DESIGN OF LANTHANIDE SUPRAMOLECULAR ARCHITECTURES

YIM KING HIM

PhD

The Hong Kong Polytechnic University

2022

The Hong Kong Polytechnic University

Department of Applied Biology and Chemical Technology

Design of Lanthanide Supramolecular Architectures

Yim King Him

A thesis submitted in partial fulfilment of the requirements for

the degree of Doctor of Philosophy

August 2021

CERTIFICATE OF ORIGINALITY

I hereby declare that this thesis is my own work and that, to the best of my knowledge and belief, it reproduces no material previously published or written, nor material that has been accepted for the award of any other degree of diploma, except where due acknowledgement has been made in the text.

_____ (Signed)

____Yim King Him_____ (Name of student)

Abstract

Self-assembly of supramolecular architectures have been widely used in catalysis and luminescent sensing. By contrast to transition metals, lanthanide self-assembled supramolecular complexes exhibit unique chemical and physical properties which have shown promising application in luminescent sensing and diagnostic applications. In Chapter 1, the background of supramolecular chemistry and lanthanides are briefly introduced. Since the applications of these lanthanide self assembled systems are all structure-dependent, this thesis aims to develop different lanthanide supramolecular compounds from small assembled units by targeting changes in ligand design and reaction conditions. The other goal is to create chiral functional materials to explore and develop the area of chiroptic by looking at the effect of chirality in structure and correlating to its optical properties and function. In this aspect, such assemblies require the control of stereoselectivity of the lanthanide supramolecular architectures. However, controlling the stereoselectivity of lanthanide complexes is rather challenging due to the kinetically labile properties and poor stereochemical preferences. In Chapter 2- point chirality as well as the linker/spacer effect will be explored.

In Chapter 2a, two pairs of linear biphenyl-linked chiral bis-tridentate ligands were prepared and the point chirality effect of four resulting lanthanide supramolecular bimetallic helicates were studied. By extending the point chirality from the two metal centers, the ability of chirality transfer was shown to be greatly

affected and diastereoselective and nondiastereoselective formation of bimetallic triple helicates were observed.

In Chapter 2b, two C_2-symmetric bis-tridentate ligands were designed based on symmetry principles where the effect of the length of the spacer towards self-assembly process was studied. Results showed that the length of the spacer greatly affected the supramolecular formation even if the offset distance of two metal chelating units remained unchanged. Higher-ordered supramolecular tetrahedron was then prepared based on the small helicate units, which resulted in an helicate-to-cage transformation. In this system, it was found that the stability of the tetrahedron was dependent on the size of the ionic radii. Hence, this study showed the importance of ionic radii and ligand design towards supramolecular transformation. Lanthanide heterometallic complexes are important for engineering optical material and is promising for creating more versatile multifunctional properties as well as improving up-conversion efficiency and enhancing optical properties. However, preparation of lanthanide heterometallic complexes is extremely difficult owing to the similar ionic radii causing issues in controlled selectively.

In Chapter 3, attempt to prepare lanthanide heterometallic tetrahedron by a simple crystallization method was reported. In this work, it was found that upon crystallization with a mixture of two different lanthanide metal helicates with very similar ionic radii, e.g. one helicate strand of Eu and Ln (Ln = Sm /Gd), a mixture of five different lanthanide tetrahedron was formed as evidenced by ESI-HRMS. The percentage amount of each tetrahedron was estimated by MS deconvolution. It was

evidenced, that the self-assembly process of the tetrahedron deviated from the statistical result. The helicate-to-tetrahedron mechanism was also investigated in this chapter.

In Chapter 4, focus here is channeled to looking at point chirality and the chiral domino effect in a lanthanide system. Hence different types of small building blocks based on amino acids were used to investigate and explore the area. The construction of enantiomeric pure lanthanide supramolecular complexes strongly relies on point chirality induced by a chiral group with the strongest point chirality effect. As a result, the ligand design is restricted by the use of a specific chiral group and the distance between the point chirality and metal centers. A series of ligands which was coupled to different types of amino acid were designed and synthesized. The design principal here is based on a chiral group being attached to the C-terminal of a short peptide which is expected to transfer chiral information to the metal center via the chiral domino effect.

Publications

1. Yim, K.-H.; Yeung, C.-T.; Probert, M. R.; Chan, W. T. K.; Macknezie, L. E.; Pal, R.; Wong, W.-T.; Law, G.-L. Helicate-to-Tetrahedron Transformation of Chiral Lanthanide Supramolecular Complexes Induced by Ionic Radii Effect and Linker Length. *Commun. Chem.* **2021**, *4*, 116.
2. Yim, K.-H.; Yeung, C.-T.; Wong, H.-Y.; Law, G.-L., Structural Variation of Self-assembled Lanthanide Supramolecular Complexes Induced by Reaction Conditions. *Inorg. Chem. Front.* **2021**, *8*, 2952-2964.
3. Wong, H.-Y.; Lo, W.-S.; Yim, K.-H.; Law, G.-L., Chirality and Chiroptics of Lanthanide Molecular and Supramolecular Assemblies. *Chem* **2019**, *5*, 3058-3095.
4. Yeung, C.-T.; Yim, K.-H.; Wong, H.-Y.; Pal, R.; Lo, W.-S.; Yan, S.-C.; Wong, M. Y.-M; Yufit, D.; Smiles, D. E.; McCormick, L. J.; Teat, S. J.; Shuh, D. K.; Wong, W.-T.; Law, G.-L., Chiral Transcription in Self-Assembled Tetrahedral Eu_4L_6 Chiral Cages Displaying Sizable Circularly Polarized Luminescence. *Nat. Commun*. **2017**, *8*, 1128-1136.
5. Yeung, C.-T.; Chan, W. T. K.; Yan, S.-C.; Yu, K.-L.; Yim, K.-H.; Wong, W.-T.; Law, G.-L. Lanthanide Supramolecular Helical Diastereoselective Breaking Induced by Point Chirality: Mixture or *P*-Helix, *M*-Helix. *Chem. Commun.* **2015**, *51*, 592-595.

Acknowledgements

I would like to express my sincere gratitude to my chief supervisor Dr. Ga-Lai Law for her motivation and encouragement. Throughout my four years PhD study, I was depressed by numerous failed experiments and my performance was far from satisfactory in the first two years. However, Dr. Law is patient and she still gave me a chance to work in her research group. Her guidance motivated me to work hard and drive for excellence during my PhD study. Also, I would like to thank my co-supervisor Prof. Wing-Tak Wong for providing me resources and support for my research.

I would like to express my appreciation to my mentor Dr. Chi-Tung Yeung. During my PhD study, he had provided me numerous guidance and support. He always shared his interesting idea and comment for improving my research project.

Also, I would like to thank Dr. Law's research group members: Dr. Ho-Yin Wong, Dr. Lixiong Dai, Dr. Benny Zhou, Dr. Weiyuan Xu, Mr. Ting-Hin Hui, Mr. James Zhang and Prof. Wong's research group: Dr. Wai-Sum Lo, Mr. Davis Liu, Dr. Karen Gu, Miss. Liz Li for their sharing of experience.

Finally, I would like to thank all the staff in Department of Applied Biology and Chemical Technology for their sincere help.

Table of contents

CERTIFICATE OF ORIGINALITY II
Abstract III
Publications VI
Acknowledgements VII
Table of contents VIII
List of Abbreviations XII
Chapter 1: Introduction to lanthanide and supramolecular coordination chemistry ... 1
1.1 Lanthanide 1
1.1.1 Background 1
1.1.2 Electronic properties 1
1.1.3 Lanthanide coordination chemistry 3
1.2 Lanthanide photophysical properties 5
1.2.1 Luminescence of lanthanide ions 5
1.2.2 Antenna effect 7
1.2.3 Dexter and Förster mechanism 8
1.3 Spectroscopic techniques for characterization of lanthanide complexes 9
1.3.1 UV-visible spectroscopy 9
1.3.2 Emission and quantum yield 10
1.3.4 Circular dichroism spectroscopy 11
1.3.5 Circular polarized luminescence spectroscopy 12
1.4 Supramolecular coordination compounds and their applications 14
1.4.1 General background 14
1.4.2 Assembling strategies: pre-organization 15
1.4.3 Assembling strategies: self-assembly 15
1.4.4 Ligand design for self-assembled helicate 17
1.4.5 Ligand design for self-assembled metal-organic tetrahedra 20
1.4.6 Examples of chiral lanthanide supramolecular complexes 21
1.5 Scope of thesis 24
1.6 References 24

Chapter 2a: Lanthanide supramolecular helical diastereoselective breaking induced by point chirality 34
2a.1 Introduction 34
2a.1.1 Introduction to chiroptical lanthanide complexes 34
2a.1.2 Chirality and preparation of chiral lanthanide complexes 35
2a.1.3 Scope of study 35
2a.2 Result and discussion 36
2a.2.1 Design and synthesis of **L1** and **L2** 36
2a.2.2 ^{1}HNMR and UV-CD titration 37
2a.2.3 Synthesis and X-ray crystal structure of [Eu_2**L1**$_3$], [Tb_2**L1**$_3$], and [Eu_2**L2**$_3$] 41
2a.2.4 NMR analysis of [Eu_2**L1**$_3$] and [Eu_2**L2**$_3$] 42
2a.2.5 Photophysical measurement 46
2a.3 Conclusion 48
2a.4 Experimental section 49
2a.4.1 Synthesis 49
2a.4.2 X-ray crystallography 62
2a.4.3 Photophysical measurement 66
2a.5 References 67
Chapter 2b: Helicate-to-tetrahedron transformation of chiral lanthanide supramolecular complexes 72
2b.1 Introduction 72
2b.1.1 Induced structural change of supramolecules 72
2b.1.2 Concentration-dependent supramolecular formation 72
2b.1.3 Cationic radii-dependent supramolecular formation 73
2b.1.4 Scope of study 74
2b.2 Result and discussion 75
2b.2.1 Design and synthesis of **L3** and **L4** 75
2b.2.2 Conformation of metal-to-ligand ratio 76
2b.2.3 Synthesis and characterization of [Eu_2**L3**$_3$] helicates 80
2b.2.4 Synthesis and characterization of [Sm_2**L3**$_3$], [Gd_2**L3**$_3$] and [Tb_2**L3**$_3$] 86
2b.2.5 Synthesis and characterization of [La_2**L3**$_3$] and [Lu_2**L3**$_3$] 87
2b.2.5 Synthesis and characterization of [Ln_2**L4**$_3$] 89

2b.2.6 Helicate-to-tetrahedron transformation 90
2b.2.7 Analysis of the effect of ligand design and ionic radii 96
2b.2.8 Photophysical studies 99
2b.3 Conclusion 101
2b.4 Experimental section 101
2b.4.1 Synthesis 101
2b.4.2 Kinetic studies 115
2b.4.3 Crystal structure of $Eu_4(\mathbf{L3^{SS}})_6$: 117
2b.4.4 Photophysical data 119
2b.5 References 121
Chapter 3: Formation of chiroptical lanthanide heterometallic Ln_4L_6 tetrahedral cage 125
3.1 Introduction 125
3.1.1 Introduction to lanthanide heterometallic systems 125
3.1.2 Preparation of lanthanide heterometallic complexes 126
3.1.3 Scope of study 128
3.2 Result and discussion 129
3.2.1 Preparation of $[Eu_nGd_{4-n}\mathbf{L3}_6]$(n = 0-4) 129
3.2.3 Variation of metal content of the heterometallic tetrahedra 135
3.2.4 Proposed mechanism of helicate-to-tetrahedron transformation process 137
3.2.4 Photophysical properties of heterometallic tetrahedra 140
3.3 Conclusion 141
3.4 Experimental 142
3.4.1 Synthesis 142
3.4.2 ESI-HRMS deconvolution analysis 148
3.4.3 Photophysical measurement 150
3.4.4 Crystal structure of $[Eu_nGd_{4-n}\mathbf{L3}_6]$ (n = 0-4) 152
3.5 References 153
Chapter 4: Remote stereo-control of chiral lanthanide supramolecular complexes 159
4.1 Introduction 159
4.1.1 Chiral domino effect induced by α, α-disubstituted amino acids 159

4.1.2 Remote control of chirality in transition metal complexes 160
4.1.3 Scope of study 162
4.2 Result and Discussion 163
4.2.1 Scheme of this study 163
4.2.2 Ligand design of **L5** 164
4.2.3 Synthesis of Aib intermediates 165
4.2.4 Synthesis of central bridging linker 167
4.2.5 Synthesis and complexation of **L5** 168
4.2.6 Synthesis and complexation of **L6** 171
4.2.7 Synthesis of Ac_6c intermediates 173
4.2.8 Synthesis and complexation of **L7** 178
4.2.9 Synthesis and complexation of **L8** 180
4.2.10 Synthesis of intermediates for **L9** 182
4.2.11 Synthesis and complexation of **L9** 185
4.2.12 Synthesis of intermediates for **L10** 187
4.2.13 Synthesis and complexation of **L10** 188
4.2.14 Review of ligand **L5-10** 190
4.3 Conclusion and future perspectives 191
4.4 Experimental 192
4.5 References 218
General experimental procedures 221
Synthesis 221
Photophysical measurement 222
Single crystal X-ray diffraction 222
Appendix 225
Chapter 2a 225
Chapter 2b 246
Chapter 3 300
Chapter 4 321

List of Abbreviations

a.u.	Arbitrary unit
Boc	Tert-butoxycarbonyl protecting group
$CHCl_3$	Chloroform
CPL	Circularly polarized luminescence
DCM	Dichloromethane
DMAP	4-Dimethylaminopyridine
DMF	Dimethylformamide
DMSO	Dimethyl sulfoxide
DNA	Deoxyribonucleic Acid
EA	Ethyl Acetate
EDCI	1-Ethyl-3-(3-dimethylaminopropyl)-carbodiimide
em	Emission
Equiv.	Equivalent
ESI	Electrospray ionization
ex	Excitation
HPLC	High Performance Liquid Chromatography
HRMS	High-resolution mass spectroscopy
Ln	Lanthanide
m/z	Mass-to-charge ratio
MeCN	Acetonitrile

MeOH	Methanol
mM	Millimolar (10^{-3}M)
ms	Millisecond (10^{-3}s)
NMR	Nuclear magnetic resonance
THF	Tetrahydrofuran
TMS	Trimethylsilyl
UV/Vis	Ultraviolet/Visible
µM	Micromolar (10^{-6}M)

Chapter 1: Introduction to lanthanide and supramolecular coordination chemistry

1.1 Lanthanide

1.1.1 Background

Lanthanide, also known as “rare earth metal”, are a group of elements located between the third-row elements barium and hafnium. The series of lanthanide consist of 15 elements from lanthanum to lutetium with atomic numbers from 57 to 71. The history of lanthanide chemistry started in 1794. A Finnish scientist called Johann Gadolin successfully isolated an ‘earth’ oxide from a black mineral known as gadolinite. Lanthanide ions exhibit a number of interesting characteristics that are different from those of d-block transition metals. For example, lanthanide ions show a very wide range of coordination numbers, small crystal field splitting as well as unique photophysical and magnetic properties.[1] Therefore, lanthanide ions are considered to be a promising candidate for developing more efficient magnetic and luminescent materials.

1.1.2 Electronic properties

The unique photophysical and magnetic properties of lanthanide ions can be attributed to their electronic configurations, in which the 4f orbitals are gradually filled across the series. Their electronic configurations can be described as $[Xe]4f^n$, where n =0-14 (table 1-1).[2,3] Compared with outer filled $5s^25p^6$ orbitals, 4f sub-shell penetrates

the xenon core appreciably.[4] Therefore, the 4f orbital cannot overlap with ligand orbitals effectively and they do not involve significantly in bonding. When lanthanide ions coordinate with a ligand, perturbation by the ligand to the lanthanide ions will be insignificant.[3] As a result, the optical spectra as well as the magnetic properties of the lanthanide complexes are generally not affected by the coordination environment.

	Atom	Ln^{2+}	Ln^{3+}	Ln^{4+}
La	$[Xe]5d^16s^2$		[Xe]	
Ce	$[Xe]4f^15d^16s^2$		$[Xe]4f^1$	[Xe]
Pr	$[Xe]4f^36s^2$		$[Xe]4f^2$	$[Xe]4f^1$
Nd	$[Xe]4f^46s^2$	$[Xe]4f^4$	$[Xe]4f^3$	$[Xe]4f^2$
Pm	$[Xe]4f^56s^2$		$[Xe]4f^4$	
Sm	$[Xe]4f^66s^2$	$[Xe]4f^6$	$[Xe]4f^5$	
Eu	$[Xe]4f^76s^2$	$[Xe]4f^7$	$[Xe]4f^6$	
Gd	$[Xe]4f^75d^16s^2$		$[Xe]4f^7$	
Tb	$[Xe]4f^96s^2$		$[Xe]4f^8$	$[Xe]4f^7$
Dy	$[Xe]4f^{10}6s^2$	$[Xe]4f^{10}$	$[Xe]4f^9$	$[Xe]4f^8$
Ho	$[Xe]4f^{11}6s^2$		$[Xe]4f^{10}$	
Er	$[Xe]4f^{12}6s^2$		$[Xe]4f^{11}$	
Tm	$[Xe]4f^{13}6s^2$	$[Xe]4f^{13}$	$[Xe]4f^{12}$	
Yb	$[Xe]4f^{14}6s^2$	$[Xe]4f^{14}$	$[Xe]4f^{13}$	
Lu	$[Xe]4f^{14}5d^16s^2$		$[Xe]4f^{14}$	

Table 1-1. *Electronic configurations of lanthanides and their common ions*.[3]

4f sub-shell is located closely to the nuclear core which leads to lanthanide contraction. The term “contraction” describes a greater-then-expect decrease in ionic radius of the elements.[5] The effect of lanthanide contraction increases with the increasing atomic number due to the positively charged nucleus would have a stronger attraction to the 4f electrons across the period (figure 1-1).

	La	Ce	Pr	Nd	Pm	Sm	Eu	Gd	Tb	Dy	Ho	Er	Tm	Yb	Lu
Atomic radii (Å)	1.877	1.825	1.828	1.821	1.810	1.802	2.042	1.802	1.782	1.773	1.766	1.757	1.746	1.940	1.734
	La^{3+}	Ce^{3+}	Pr^{3+}	Nd^{3+}	Pm^{3+}	Sm^{3+}	Eu^{3+}	Gd^{3+}	Tb^{3+}	Dy^{3+}	Ho^{3+}	Er^{3+}	Tm^{3+}	Yb^{3+}	Lu^{3+}
Ionic radii (Å, CN = 9)	1.216	1.196	1.179	1.163	1.144	1.132	1.120	1.107	1.095	1.083	1.072	1.062	1.052	1.042	1.032

Figure 1-1. Atomic radii and ionic radii of lanthanide at +3 oxidation state (coordination number = 9).[6]

1.1.3 Lanthanide coordination chemistry

Traditionally, the coordination chemistry of lanthanide ions is considered to be purely electrostatic interaction. However, recent research has demonstrated that lanthanide ions also participate in covalent bonding with ligand.[7] With the use of a combination of ligand (Cl) K-edge X-ray absorption spectroscopy (XAS) and time-dependent density functional theory (TDDFT), the covalency in $LnCl_6^{3-}$ (Ln = Ce, Nd, Sm, Eu and Gd) was investigated. Result showed that there was an insignificant amount of mixing of 3p orbital with 4f orbital.

Even if lanthanide ions do participate in covalent bonding, lanthanide ions are still considered to be hard Lewis acids because of their large ionic radii as well as high charge density, with the most stable +3 oxidation state.[8, 9] Lanthanide ions can accommodate a large coordination number in the range of 6 to 12, with a predominance for coordination number 9 for earlier lanthanide ions (La^{3+} to Eu^{3+}), and 8 for later lanthanide ions (Dy^{3+} to Lu^{3+}).[4, 10] The coordination number of a lanthanide ion is determined by either first order- or second order effect.[3] For first order effect, the saturation of lanthanide ion is determined by the number of ligand that pack around the metal centre. For second order effect, the use of bulky ligands may cause crowding around metal centre and the coordination number is governed by the steric effects generated by the ligands. Due to the second order effect, the coordination number of some exceptional lanthanide system can be as small as 3 to 4 when bulky

ligands, such as bis(isopropyl)amide, are used.[11] The coordination number also affect the coordination geometry (table 1-2). Lanthanide ions preferably interact with hard Lewis bases in the order of O>N>S.[12, 13] Typical ligands for lanthanide complexation include aminocaboxylates and β-diketonates, which are anionic ligands that can maximize the strength of interaction with lanthanide ions.

Coordination number	Geometry	Examples
2	Bent	$[Yb\{C(SiMe_3)\}]$
3	Pyramidal (solid) Planar (gas and solution)	$La[N(SiMe_3)_2]_3$,
4	Tetrahedral	$Yb[(N(SiMe_3)_2]_3(Ph_3PO)$
5	Trigonal bipyramidal	$[Nd\{P(SiMe_3)_2\}_3(THF)_2]$
6	Trigonal prismatic	$[Ln\{S_2P(cyclohexyl)_2\}_3]$.
7	Capped trigonal prismatic	Ba_2EuCl_7
	Pentagonal bipyramidal	$[Yb(C_6F_5)_2(THF)_5]$.
8	Dodecahedral	Et_4N $[Eu(S_2CNEt_2)_4]$,
	Square antiprismatic	Ph_4P $[Pr(S_2PMe_2)_4]$.
9	Tricapped trigonal prismatic	$[Ln(H_2O)_9]^{3+}$

Table 1-2. *Examples of coordination numbers and geometries of lanthanide complexes*.[3]

In view of complexation, lanthanide ions are labile in solution state and the ligands can be exchanged easily in the presence of water and methanol. Lanthanide ions highly prefer a saturation of the inner coordination sphere. Therefore, careful designing of ligand should be taken into consideration. Generally, a ligand should consist of an adequate number of donor atoms as well as an appropriate size of binding site because lanthanide tends to be saturated with large coordination number.

Otherwise, competition for lanthanide ions by solvent molecules and ligands will affect the photophysical properties of the complexes.[14, 15]

1.2 Lanthanide photophysical properties

1.2.1 Luminescence of lanthanide ions

One of the most attractive properties of lanthanide is their unique luminescence properties.[14, 16] Molecular luminescence can be classified into either fluorescence or phosphorescence according to the IUPAC rule.[17] However, for lanthanide systems, some transitions involve fluorescence, which is a process that occurs without changing the spin state of the excited electron (e.g. Yb^{3+}, $^2F_{5/2} \rightarrow {}^2F_{7/2}$), while some transitions involve phosphorescence (e.g. Eu, $^5D_0 \rightarrow {}^7F_J$).[18] Therefore, emission of lanthanide ions is commonly referred to luminescence to avoid any confusion.

The photophysical properties of lanthanide ions can be attributed to their electronic configuration. As the 4*f* electrons are well shielded by 5*s* and 5*p* orbitals, ligand perturbations are minimized and the 4*f* orbitals are thus well hidden from the external environment. Upon excitation by electromagnetic radiation, lanthanide ions give rise to characteristic needle-like emission spectra (figure 1-2 and 1-3).[19, 20] Theoretically, most lanthanide (III) ions are luminescent but some of them are more emissive than others.

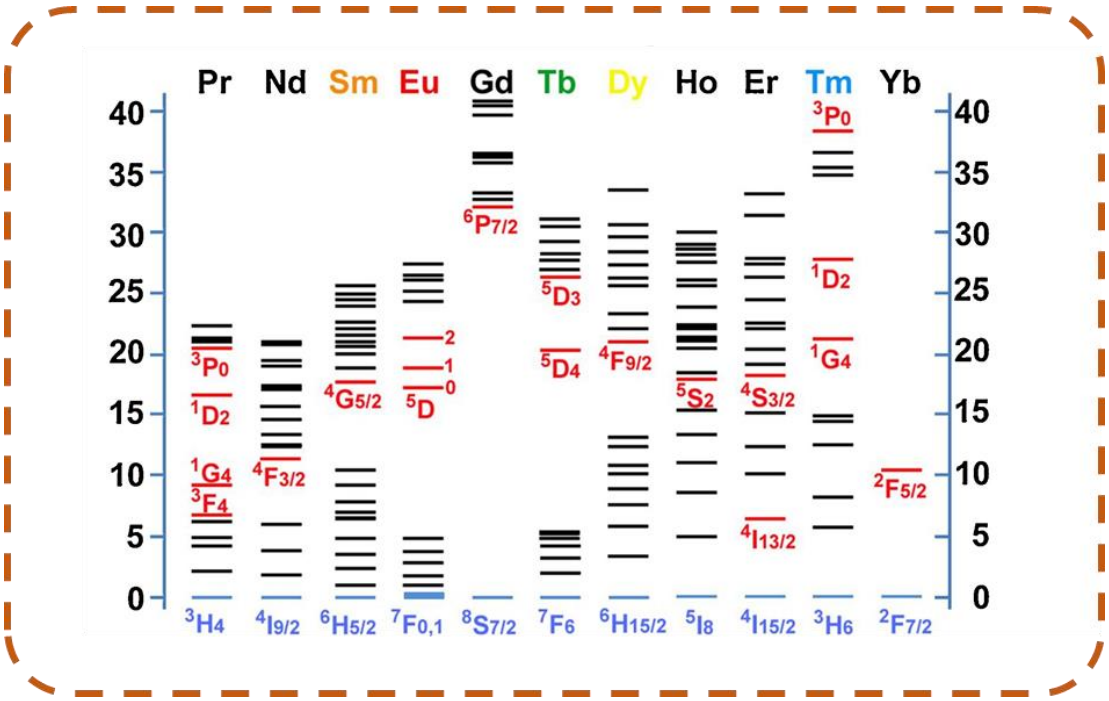

Figure 1-2. *Energy diagram of the lanthanide ions. Main luminescent levels are shown in red.*[19]

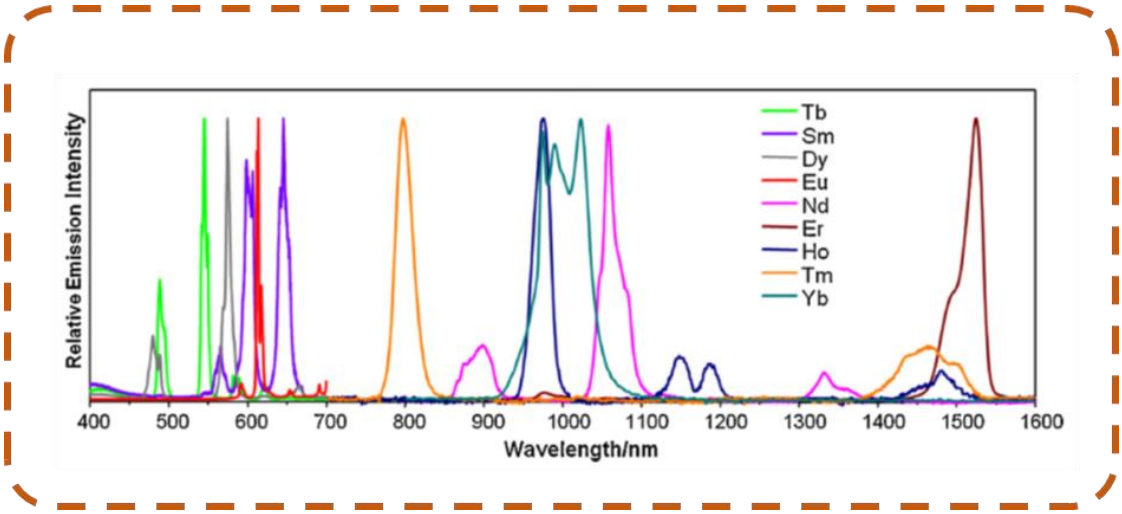

Figure 1-3. *Luminescence spectra of lanthanide complexes with narrow-like emission bands.*[20]

Lanthanide ions exhibit three different types of electronic transitions, which are 4*f*-4*f* transitions, 4*f*-5*d* transitions and charge transfer transitions. The 4*f*-4*f* transitions are the easiest to recognize as they are quite narrow and do not depend much on the chemical environment of the lanthanide ions. However, 4*f*-4*f* transitions are forbidden by the Laporte rule, which states that Δ*l* must be ± 1. 4*f*-4*f* transitions

can only be observed when there is a change in 4*f* wavefunction by vibronic coupling or mixing of parity wavefunction with 5*d* orbitals.[21] The Laporte forbidden 4*f*-4*f* transitions lead to small extinction coefficients (smaller than 10 M^{-1} cm^{-1}).[10, 11, 22]

For 4*d*-5*f* transitions, they are allowed and has a relatively larger emission intensity compared with those of 4*f*-4*f* transitions. However, 4*f*-5*d* transitions are highly dependent on ligand field effect on the d-orbitals as the 5*d* orbitals interact directly with the ligands. The 4*f*-5*d* transitions generally require high energy and only Ce^{3+}, Pr^{3+} and Tb^{3+} can be observed.[23] Similar to 4*f*-5*d* transitions, charge transfer transitions are also Laporte allowed.[24] However, they requires high energy which can be only observed for Sm^{3+}, Eu^{3+}, Tm^{3+} and Yb^{3+}.

1.2.2 Antenna effect

Since 4*f*-4*f* transitions are Laporte forbidden and 4*f*-5*d* transitions are uncommon, excitation of lanthanide ions to 4*f*-4*f* excited state remains a challenge. This problem can be solved by both direct and indirect method. In the direct method, lanthanide ions are excited using laser, but this method is not practical for biological application. The indirect method, which is called sensitization or antenna effect,[25] is a more common practice for sensitizing lanthanide ions. This method involves the coordination of a chromophore to the lanthanide ions. The chromophore will first absorb the electromagnetic radiation and then transfer the energy to the excited state of the lanthanide ions and decay through radiative 4*f*-4*f* transitions. The energy can be transferred from the ligand triplet excited state to the metal excited state, or from the ligand singlet excited state to the metal excited state (figure 1-4).[21, 26, 27]

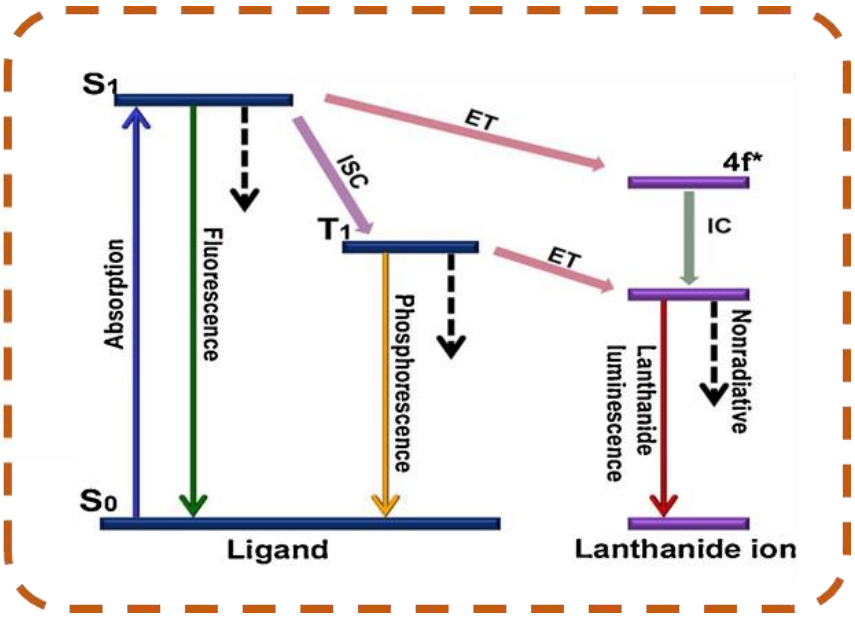

Figure 1-4. *A modified Jablonski diagram showing the energy transfer from ligand to lanthanide ion (ISC = intersystem crossing; ET = energy transfer, IC = internal conversion).*[19]

1.2.3 Dexter and Förster mechanism

Dexter and Förster mechanisms are two mechanisms that are commonly accepted to explain the antenna effect from the ligand triplet state to the excited state of lanthanide ions. Dexter mechanism describes the antenna effect as a double electron exchange between donor and acceptor through physical contact (figure 1-5a).[28] An electron is transferred from the ligand triple state to the excited state of lanthanide ions, while another electron is transferred from the highest occupied energy orbital of the lanthanide ions to the ligand. This process requires a short distance to facilitate effective overlapping of wavefunction between the ligand donor and the metal acceptor.

Förster mechanism states that energy is transferred from a ligand donor to a metal acceptor through diploe-diploe coupling (figure 1-5b).[28, 29] The donor is first

excited and then relaxes to release energy. The energy is then absorbed by the lanthanide ions.

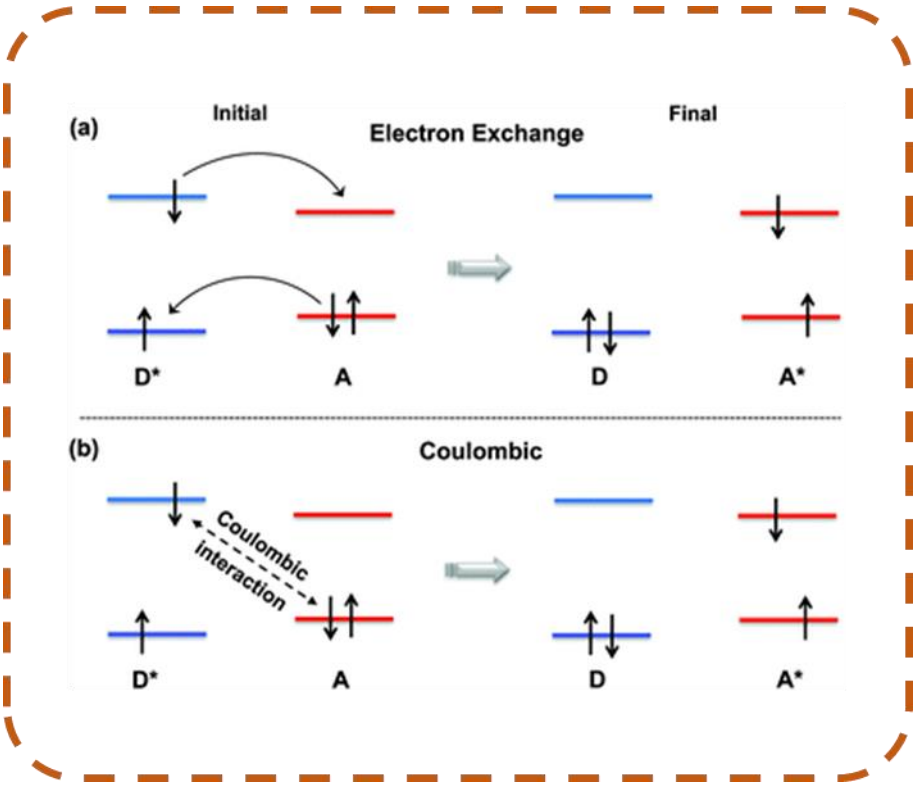

Figure 1-5. *Scheme of (a) Dexter mechanism and (b) Förster mechanism (D = energy donor; A = energy acceptor).*[28]

1.3 Spectroscopic techniques for characterization of lanthanide complexes

1.3.1 UV-visible spectroscopy

The interaction between photons and a chemical compound can be investigated by UV-visible spectroscopy. When light passes through a cuvette containing a sample, the compound will absorb the photon at a specific wavelength of light. Energy will be transferred from the photon to an electron and the electron

may be promoted to a higher energy level. The wavelength of light that is required for such a promotion depends on the energy difference between two states. The relationship between the energy difference and the wavelength of light follows Planck's equation:

$$E = hv = hc/\lambda \text{ (Eq. 1)}$$

The extinction coefficient provides an indication of the intensity of an absorption transition, which can be determined by Beer's law:

$$log(I_0/I) = A = \varepsilon cl \text{ (Eq. 2)}$$

Where A is absorbance, I_0 is the incident light intensity, I is the transmitted light intensity, ε is the extinction coefficient, c is the concentration of the sample and l is the path length of the cuvette.

1.3.2 Emission and quantum yield

Emission happens when a molecule absorbs a photon and then emits the light at a longer wavelength. The important parameters for characterizing the efficiency of emission are the quantum yield Q. The quantum yield can be expressed as

$$Q = \frac{number\ of\ emitted\ photons}{number\ of\ absorbed\ photons} \text{ (Eq. 3)}$$

There are two common methods for determining the quantum yield experimentally which are the comparative method and the absolute method. The comparative method involves the comparison between a sample and a standard with a known quantum yield.[30] For the comparative method, the quantum yield of a sample can be calculated by the following equation,

$$Q_L^{Ln} = Q_S \times \frac{E_X}{E_S} \times \frac{A_S(\lambda_S)}{A_X(\lambda_X)} \times \frac{I_S(\lambda_S)}{I_X(\lambda_X)} \times \frac{n_S^2}{n_X^2} \text{ (Eq. 4)}$$

where *E* is the corrected emission spectrum, *I* is the intensity of the excitation source and *n* is the refractive index. In order to achieve a linearity between the intensity of the emission and the concentration of the sample, the absorbance of the sample should be less than 0.1 AU to minimize re-absorption effect. For the choice of standard, the best option will be the standard compound that has the same excitation wavelength with the sample. Then measurement can be safely performed up to 0.5 AU without the problem of dissociation of the sample.

The quantum yield can also be determined by the absolute method.[31, 32] The absolute method involves the use of an integrating sphere. The integrating sphere is made up of a material with >99% reflectance and a lens that can focus the excitation light beam into the sample. The emission and the scatter can be monitored by a detector. Using integrating sphere to determine the quantum yield is more accurate since no standard is required.

1.3.4 Circular dichroism spectroscopy

Different from UV-visible spectroscopy which measures the absorption of unpolarized light, circular dichroism measures the differential absorption of left- and right-handed circularly polarized light.[33] A chiral molecule has different left- and right-handed light absorption coefficients. In circular dichroism spectroscopy, polarized light will pass through a sample and be absorbed by the sample in different proportion. The unit for circular dichroism is ellipticity ([θ]), which can be determined by the equation

$$\theta = 32.98\Delta A \text{ (Eq. 5)}$$

where ΔA is the differential absorption of left- and right-handed circularly polarized light. A chiral compound will exhibit a positive circular dichroism signal when the left-handed circularly polarized light is absorbed in a greater extent than the righted handed circularly polarized light. Circular dichroism spectroscopy is useful for studying the chiroptical information of the ground state of the sample as well as the optical activity of biological secondary structure such as protein.[34] Inherently optically active system exhibits active CD signals. Moreover, for achiral system, CD may be induced by an external magnetic field.[35]

1.3.5 Circular polarized luminescence spectroscopy

Circularly polarized luminescence spectroscopy is another technique that can characterize and give chiroptical information of chiral compounds. CPL is a more sensitive technique as it shows the emission of chiral compounds. CPL spectroscopy measures the difference in emission intensities of the left- and right-handed CPL and the result is reported in a parameter called dissymmetry factor (g_{lum}),[33] which is defined as

$$g_{lum} = 2(I_L - I_R)/(I_L + I_R) \text{ (Eq. 6)}$$

where I_L and I_R are the emission intensity of left- and right-handed CPL. The maximum of g_{lum} value is ±2.

The nature of g_{lum} can be considered as among electric dipole forbidden and magnetic dipole-allowed transitions. The luminescence dissymmetry factor can be expressed as,

$$g_{lum} = \frac{4m(cos\theta)}{\mu}$$ (Eq. 7)

Where μ and m are the electric and magnetic transition dipole vectors respectively, and θ is the angle between them.

It is expected that large g_{lum} value can be obtained when the transition involved is weak. From Eq. 7, it is expected that large g_{lum} value can be observed when electric dipole transition is forbidden but magnetic dipole transition is allowed.[36] Due to the unique electronic properties of lanthanide, circularly polarized luminescence spectroscopy is commonly used for characterizing lanthanide systems because of the magnetically allowed intra-configuration f-f transition, which can give high g_{lum} value.[37] The highest g_{lum} value that has been reported is 1.38.[33] Although the magnetically allowed f-f transition can give high g_{lum} value, the transition generally has very low intensity and thus CPL of lanthanide systems are difficult to measure.

Richardson has developed selection rules for lanthanide CPL.[38] The selection rules state that the dissymmetry factor of lanthanide transitions can be classified into three classes (*DI*, *DII* and *DIII*) based on angular momentum quantum number. The magnitude of the dissymmetry factor decreases from *DI* to *DIII*. For example, table 1-3 shows some examples of Eu^{3+} and Tb^{3+} transition. For $^5D_0$ to $^7F_1$ emission, it is predicted that this transition will exhibit the largest g_{lum} value since it is classified as DI, which is also evidenced by experimental observation.

Ion	Transition	Classification
Eu^{3+}	$^5D_0 \rightarrow {}^7F_0$	DII
	$^5D_0 \rightarrow {}^7F_1$	DI
	$^5D_0 \rightarrow {}^7F_2$	DIII
	$^5D_0 \rightarrow {}^7F_3$	DII
	$^5D_0 \rightarrow {}^7F_4$	DIII
Tb^{3+}	$^5D_4 \rightarrow {}^7F_6$	DIII
	$^5D_4 \rightarrow {}^7F_5$	DII
	$^5D_4 \rightarrow {}^7F_4$	DII
	$^5D_4 \rightarrow {}^7F_3$	DII
	$^5D_4 \rightarrow {}^7F_2$	DIII
	$^5D_4 \rightarrow {}^7F_1$	DIII
	$^5D_4 \rightarrow {}^7F_0$	DIII

Table 1-3. *Selection rule for CPL of lanthanide complexes proposed by Richardson's group.*[38]

1.4 Supramolecular coordination compounds and their applications

1.4.1 General background

The origin of supramolecular chemistry can be traced back to biology. In biological systems, there are different types of biomacromolecules that can be found in the human body such as proteins and DNAs. With a few building blocks with simple organic structure, protein can achieve specific biological functions which allow information to be stored, retrieved and processed. Supramolecular chemistry applies this concept to the molecular level by constructing well-defined structure through intermolecular noncovalent interaction. The information can then be stored in the artificial molecular level and processed at the supramolecular level. To data, numerous artificial supramolecular systems have been reported. These systems

included not only monometallic complexes, but also the higher ordered supramolecular complexes such as helicates, tetrahedra, cubes, metal-organic frameworks as well as interlocked structures.[12]

1.4.2 Assembling strategies: pre-organization

The classical method for preparing supramolecular coordination compounds involves the use of a ligand that can pre-organize a binding cavity for metal ion.[39-41] Generally, the stability of complexes that are made by pre-organization is high due to the de-solvation of water molecules. Taking lanthanides as an example, numerous lanthanide supramolecules have been built based on macrocyclic ligands such as cyclen[42-44] and calixarences.[45] These macrocycle ligands are well designed before complexation in order to contain an inner cavity with appropriate size that can encapsulate the target lanthanide ion of choice to maximize the binding between the lanthanide ions and ligand. Upon complexation, the reorganization energy of the ligand is therefore minimized.[18] A large number of macrocycle-based ligands with functional side arms have been prepared to investigate the potential application of these complexes.

1.4.3 Assembling strategies: self-assembly

Many supramolecules that are made based on pre-organization process have been reported and scientists would like to simplify the synthetic procedures. Taking advantage of the high electric field of metal ion, the small coordination building blocks can be self-assembled around the metal ions through weak intermolecular interactions.[46, 47] Different from pre-organization which has a well-defined structure and binding site for metal ion, the formation of supramolecular architectures through

self-assembly have received intense attention since it gives access to a wide range of supramolecular complexes based on multiple hydrogen bonding and donor-acceptor interactions.

Self-assembly process is governed by both internal factors and external factors.[46] Internal factors are concerned about the interaction between metal ions and ligands, such as ligand design, secondary metal coordination, hydrogen bond and van der Waals forces. Proper designing of ligand can enhance the interaction between metal ions and ligands and successful controlled formation of desired supramolecular structure with high stability will result (figure 1-6). External factors involve the concentration and stoichiometries of the reactant. The presence of foreign species is also considered an external factor since they may affect the self-assembly process through interaction with either metal ions or ligands. Moreover, since the formation of higher order of supramolecular architecture may require a progressive buildup of small units, reaction time should be taken into consideration.[46] The above factors increase the diversity of artificial supramolecules in terms of structure and function.[48]

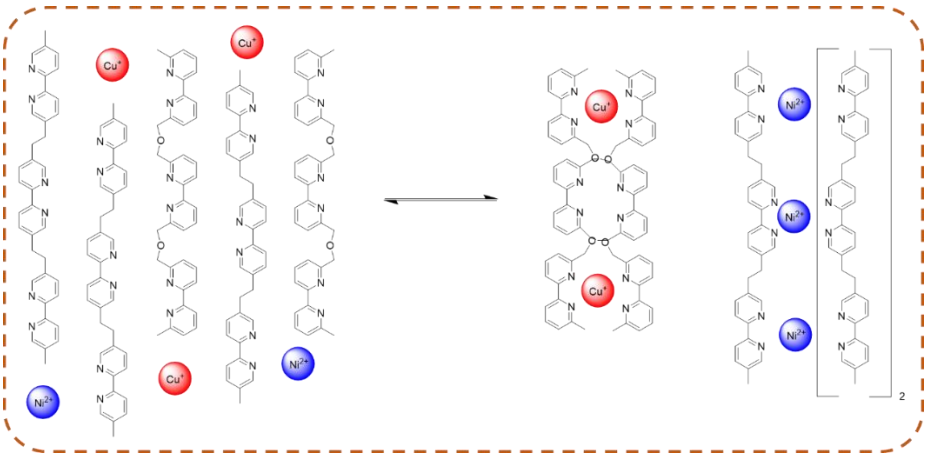

Figure 1-6. *Parallel formation of Cu^{+} double helicate and Ni^{2+} triple helicate via as self-assembly process of a mixture of two different ligands and metal ions.*[46]

To overcome the challenges mentioned above, Raymond et al. suggested three important criteria for ligand design.[49] First, the self-assembled supramolecular complexes can be constructed through multibranched chelating ligands to maximize the metal-ligand interaction. Second, any unwanted cluster and geometries can be removed by fixing the multiple chelating group within the ligand rigidly. Finally, labile metal ions are highly preferred so that mistakes can be corrected by the breaking and re-forming of metal-ligand bond.

1.4.4 Ligand design for self-assembled helicate

Helicate is one of the secondary structures that can be found in nature. Helicate can exist in either right- or left-handed structure.[50] Natural examples include amylose and DNA. In supramolecular chemistry, numerous artificial metal-based helicates have been reported and helicity can be introduced by conformation restriction of bulky side arms,[51] inter- or intramolecular hydrogen bond[52] as well as coordination geometry of metal ions.[53, 54]

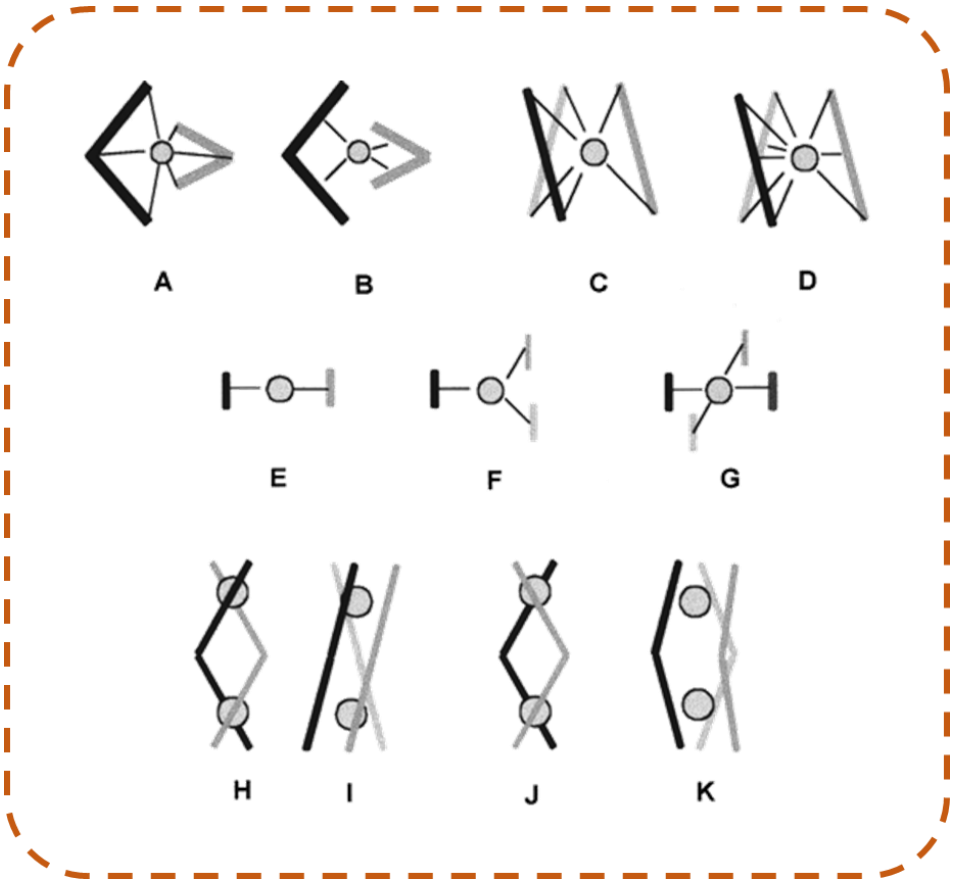

Figure 1-7. *Different types of supramolecular helicate*.[55]

Many types of helicate have been reported and all these structures can be classified in terms of the number of metal ion, the number of coordination and the presence of helical twist (figure 1-7).[55, 56] For example, (B) and (C) are coordinated tetrahedrally and octahedrally, respectively. For (E), (F) and (G), these three types do not contain any helical twist, while (H), (I), (J) and (K) are typical double- or triple-stranded that possess a helical twist and are commonly observed for self-assembled supramolecules.

The construction of helicate can be done by utilizing C_2-symmetrical ligand. For example, the D_3-symmetrical triple helicate can be formed by coordinating two metal ions with C_2-symmetrical bis(bidentate) ligand (figure 1-8).[49] To ensure the formation

of desired helical structure, the two metal-chelating planes must be parallel to each other, given that they share the same C_3 axis. The central bridging linker between two metal chelating group can be flexible or rigid but a rigid linker is highly recommended since the increased flexibility of ligand may increase the amount of unwanted cluster.

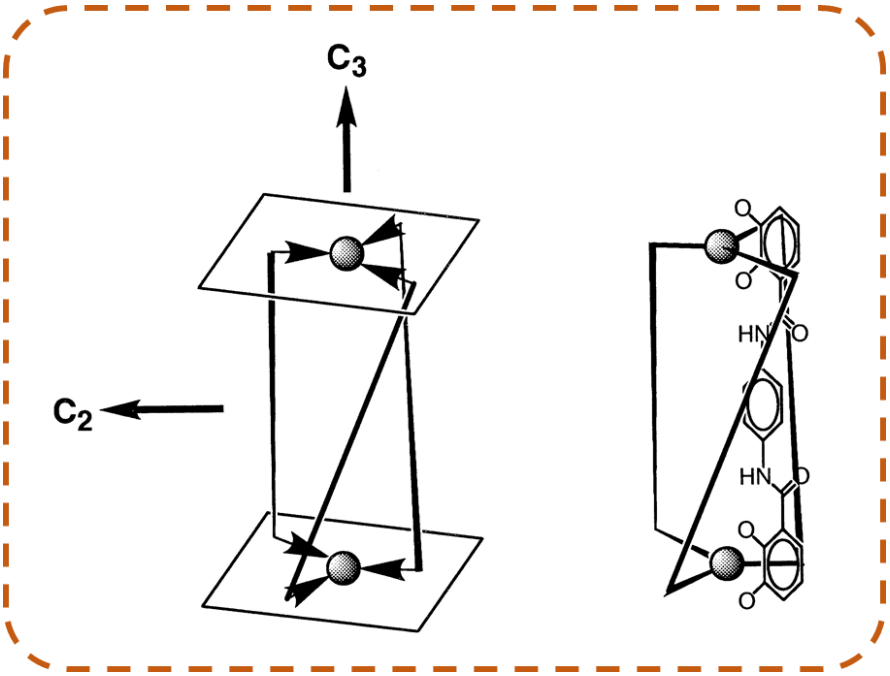

Figure 1-8. *Graphical representation of formation of D_3-symmetrical triple helicate by C_2-symmertical ligands. Two metal-chelating planes are parallel along C_3 axis.*[49]

Different from metal-organic cage, which will be discussed in the following part, helicate does not contain any inner cavity which hinders its the potential application. However, such a simple system is extremely useful in studying the mechanism of supramolecular chemistry.[57] For example, during the formation of artificial supramolecular helicates, reactants may undergo a cooperative self-assembly process to form oligonuclear complexes.[58] This problem can be solved by adding a template molecule to direct to formation of M_2L_3 helicate.[59, 60] Such a transformation depends on the number of coordinating sites of the ligand, the distance between two binding

sites as well as the geometric constraints of the resulting complex, which is also crucial when preparing other supramolecular structures.[55]

1.4.5 Ligand design for self-assembled metal-organic tetrahedra

Metal-organic tetrahedra, also known as metal-organic container, are a class of coordination driven metal complexes.[61] Compared with helicates, metal-organic cages generally exhibit well-defined shape with a specific size of an inner cavity.[62-64] The geometry of metal-organic tetrahedra can be described as polyhedron. There are two different types of polyhedron, Platonic solids and Archimedean solids (figure 1-9).[65] Platonic solids consist of multiple symmetry axes and mirror planes, while Archimedean solids are made up of unidentical polygonal planes. Most of the metal-organic cages are achiral because of the presence of inversion center and mirror plane symmetries.

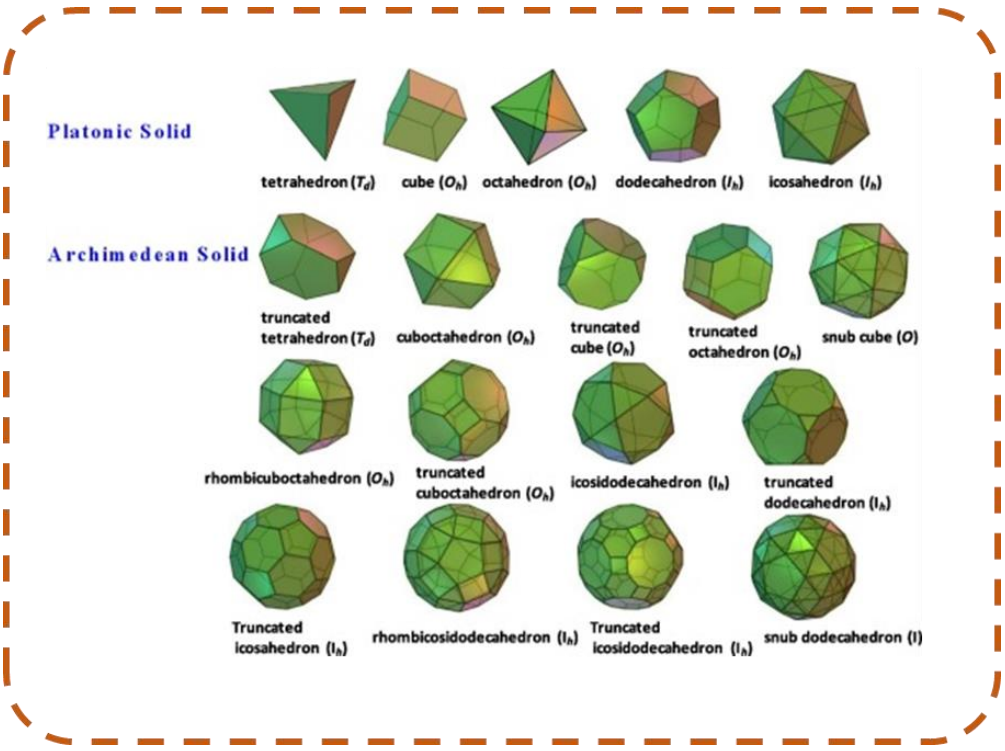

Figure 1-9. *Graphical representation of Platonic solids and Archimedean solids.*[66]

Generally, most of the metal-organic tetrahedra are constructed by two different metal-to-ligand ratios, M_4L_6 and M_4L_4.[12, 65, 66] For M_4L_6 tetrahedron, four metal ions serve as vertices and six ligands serve as edges.[67-69] In this case, C_2-symmetrical bis(bidentate) ligands with rigid backbone is used to coordinated with metal ions. Raymond et al. suggested that the angle between two chelating planes should be 70.6° so that a tetrahedral cage would be formed instead of helicate (figure 1-10a).[70] For M_4L_3 tetrahedron, a C_3-symmetrical ligand with a rigid central bridging linker should be used to avoid the coordination of two chelating groups with the same metal ion.[49] If the ligand is planar (for example, the use of a benzene as the central bridging linker), the ideal approach angle should be 19.4° (figure 1-10b).

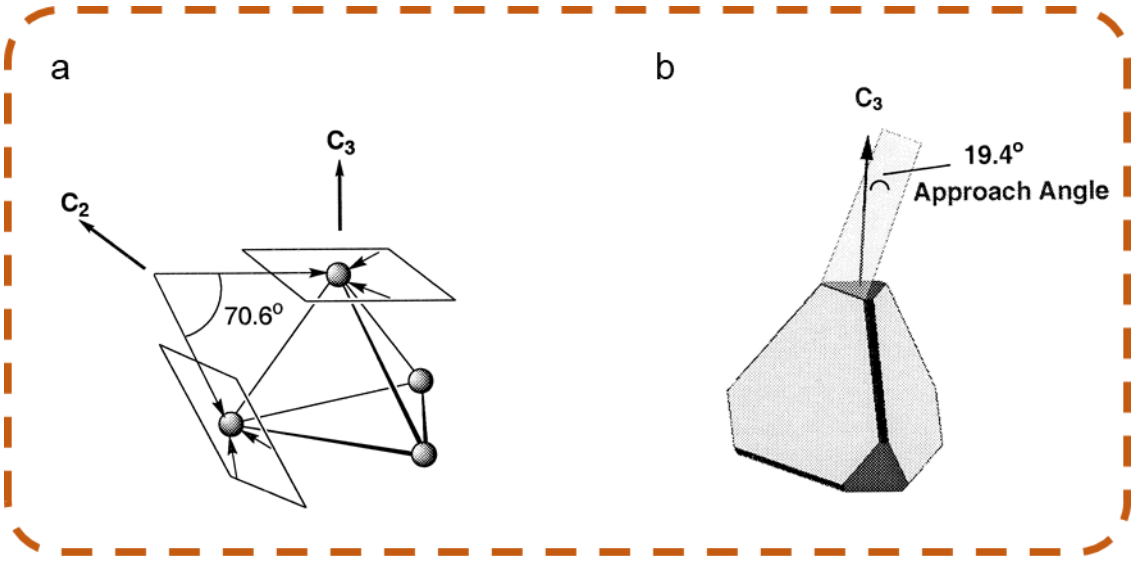

Figure 1-10. *Design principle of metal-organic tetrahedron proposed by Raymond's group. (a) Graphical representation showing the angle between two chelating planes is 70.6°. (b) Graphical representation showing the ideal approaching angle of 19.4°.*[49]

1.4.6 Examples of chiral lanthanide supramolecular complexes

Based on the ligand design principle, a number of chiral lanthanide supramolecular complexes have been reported. For example, Prof. Gunnlaugsson and

co-workers have reported the preparation of chiral lanthanide supramolecular helicates with use of bis-tridentate ligands (figure 1-11a).[71] The ligand was designed and synthesized by incorporating the pcam chelating units with a 4,4'-methylenediphenyl central bridging linker. Upon coordination with $Eu(OTf)_3$, enantiomerically pure triple-stranded helicates were prepared and exhibited CPL signal with a large g_{lum} value = -0.23 at 593 nm. Prof. Gunnlaugsson further studied the supramolecular formation of lanthanide bimetallic helicates by varying the size of linker (figure 1-11b).[72, 73] The supramolecular helicates displayed CPL signals and result showed that smaller linker could increase the stability of the helicates.

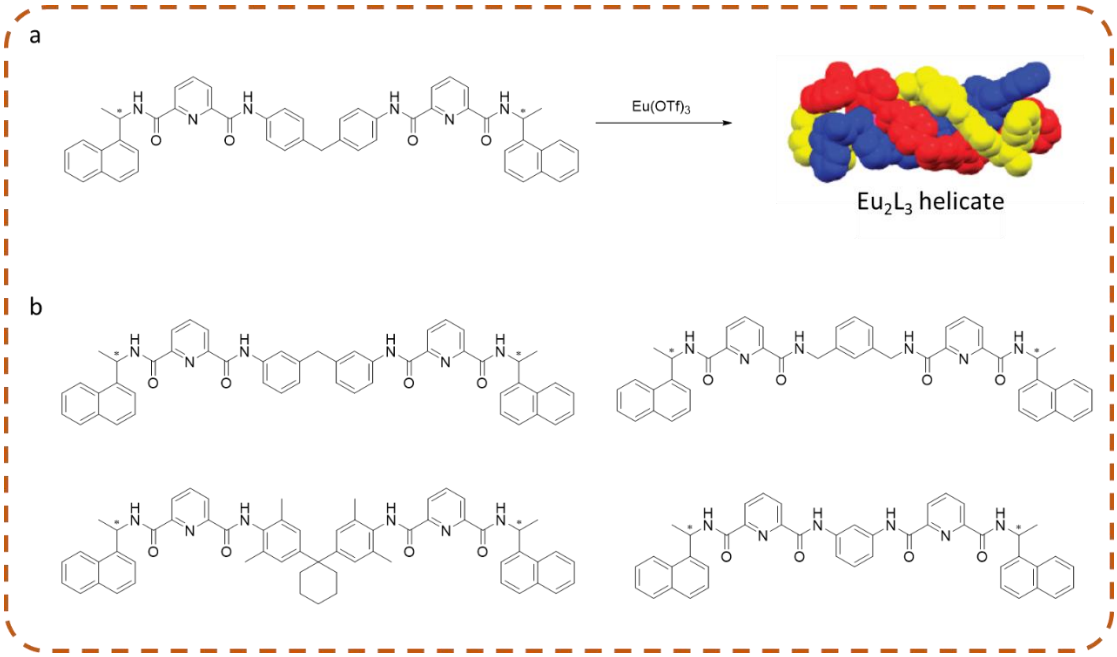

Figure 1-11. *Structure of ligand designed by Prof. Gunnlaugsson and co-workers. (a) Reaction scheme of preparation of chiral lanthanide bimetallic helicates.[71] (b) Ligands designed for studying the effect of linker effect.[72, 73]*

Apart from lanthanide bimetallic helicates, Ln_4L_6 tetrahedra are another structure that can be prepared by C_2-bistridentate ligands. The first example of

stereoselective chiral luminescent Eu^{3+} tetrahedron was reported by Prof. Sun and co-workers in 2015. Based on the ligand design principle that proposed by Prof. Raymond, the ligand was carefully designed to avoid the formation of helicate by using a naphthalene moiety as the central bridging linker. Upon coordination with Eu^{3+}, the ligand and europium ions self-assembled to form a tetrahedron topology and the structure was confirmed by X-ray crystallography.[74] The chirality from the chiral moiety was found to transferred during the self-assembly process to give enantiomeric pure product as evidenced by mirror image in CD spectra. Based on this result, numerous tetrahedra structures were reported and their ligands structures were shown in figure 1-12.[75, 76]

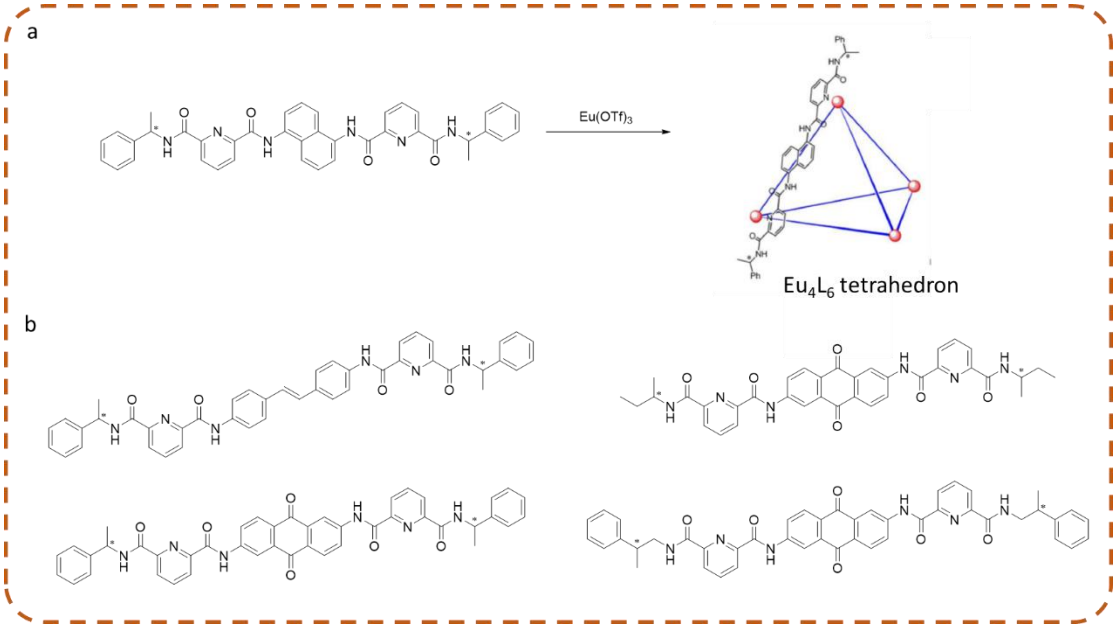

Figure 1-12. *Structure of ligand prepared for forming tetrahedron. (a) Reaction scheme of preparation of chiral lanthanide supramolecular tetrahedron reported by Prof. Sun and co-workers.[74] (b) Ligands designed for preparation of tetrahedron.[75, 76]*

1.5 Scope of thesis

This thesis demonstrates lanthanide supramolecular complexes with various topologies. This thesis aims at investigating the design principle as well as the factors that governing the structural formation of lanthanide self-assembled supramolecules. Chapter 2a is a study of preparing chiral lanthanide supramolecular helicate by point chirality effect. Chapter 2b investigates the helicate-to-tetrahedron transformation as well as the effect of ionic radii towards supramolecular formation. Chapter 3 focuses on the preparation of challenging lanthanide heterometallic tetrahedron with the use of C_2-symmetrical bis(tridentate) ligands. Chapter 4 examines the remote control of chirality in supramolecular complexes induced by chiral peptide.

1.6 References

1. Pekka, H.; Harri, H.; *Lanthanide Luminescence: Photophysical, Analytical and Biological Aspects*; Berlin, Heidelberg, 2011
2. Muller, G. Luminescent chiral lanthanide(III) complexes as potential molecular probes. *Dalton Trans.* (Cambridge, England : 2003) **2009**, *44*, 9692-9707.
3. Cotton, S.; *Lanthanide and Actinide Chemistry*; John Wiley & Sons, Ltd, 2007
4. Huang, C.-H.; *Rare Earth Coordination Chemistry: Fundamentals and Applications*; John Wiley & Sons, Ltd, 2010
5. Hughes, I. D.; Däne, M.; Ernst, A.; Hergert, W.; Lüders, M.; Poulter, J.; Staunton, J. B.; Svane, A.; Szotek, Z.; Temmerman, W. M., Lanthanide contraction and magnetism in the heavy rare earth elements. *Nature* **2007**, *446* (7136), 650-

653.

6. Shannon, R. D. Revised effective ionic radii and systematic studies of interatomic distances in halides and chalcogenides. *Acta Cryst. A.* **1976**, *32*, 751-761.

7. Löble, M. W.; Keith, J. M.; Altman, A. B.; Stieber, S. C. E.; Batista, E. R.; Boland, K. S.; Conradson, S. D.; Clark, D. L.; Lezama Pacheco, J.; Kozimor, S. A.; Martin, R. L.; Minasian, S. G.; Olson, A. C.; Scott, B. L.; Shuh, D. K.; Tyliszczak, T.; Wilkerson, M. P.; Zehnder, R. A., Covalency in lanthanides. An X-ray absorption spectroscopy and density functional theory study of $LnCl_6(x-)$ (x = 3, 2). *J. Am. Chem. Soc.* **2015**, *137* (7), 2506-2523.

8. Evans, W. J., Perspectives in reductive lanthanide chemistry. *Coord. Chem. Rev.* **2000**, *206*, 263-283.

9. Kaltsoyannis, N.; *The f elements*; Oxford University Press: Oxford Hong Kong, 1999.

10. Gunnlaugsson, T.; Leonard, J. P., Responsive lanthanide luminescent cyclen complexes: from switching/sensing to supramolecular architectures. *Chem. Commun.* **2005**, *25*, 3114.

11. Bünzli, J.-C., Benefiting from the unique properties of lanthanide ions. *Acc. Chem. Res.* **2006**, *39* (1), 53-61.

12. Barry, D. E.; Caffrey, D. F.; Gunnlaugsson, T., Lanthanide-directed synthesis of luminescent self-assembly supramolecular structures and mechanically bonded systems from acyclic coordinating organic ligands. *Chem. Soc. Rev.* **2016**, *45* (11), 3244-3274.

13. Richardson, F. S., Terbium(III) and europium(III) ions as luminescent probes and

stains for biomolecular systems. *Chem. Rev.* **1982**, *82* (5), 541-552.

14. Liu, G.; Jacquier, B.; Jacquier, B.; *Spectroscopic Properties of Rare Earths in Optical Materials*. Berlin, Heidelberg, 2005.

15. Thibon, A.; Pierre, V., Principles of responsive lanthanide-based luminescent probes for cellular imaging. *Anal. Bioanal. Chem.* **2009**, *394* (1), 107-120.

16. Cohen, I. B.; *A History of Luminescence from the Earliest Times Until 1900. Dover Publications*, 1958.

17. Melhuish, W., Nomenclature, symbols, units and their usage in spectrochemical analysis-Part VI: molecular luminescence spectroscopy. *Pure Appl. Chem.* **1984**, *56* (2), 231-245.

18. Bünzli, J.-C.; Piguet, C., Taking advantage of luminescent lanthanide ions. *Chem. Soc. Rev.* **2005**, *34* (12), 1048-1077.

19. SeethaLekshmi, S.; Ramya, A. R.; Reddy, M. L. P.; Varughese, S., Lanthanide complex-derived white-light emitting solids: a survey on design strategies. *J. Photochem. Photobiol. C: Photochem. Rev.* **2017**, *33*, 109-131.

20. Uh, H.; Petoud, S., Novel antennae for the sensitization of near infrared luminescent lanthanide cations. *C. R. Chimie* **2010**, *13*, 668-680.

21. de Sá, G. F.; Malta, O. L.; de Mello Donegá, C.; Simas, A. M.; Longo, R. L.; Santa-Cruz, P. A.; Da Silva, E. F., Spectroscopic properties and design of highly luminescent lanthanide coordination complexes. *Coord. Chem. Rev.* **2000**, *196* (1), 165-195.

22. Eliseeva, S. V.; Bünzli, J.-C, Lanthanide luminescence for functional materials and bio-sciences. *Chem. Soc. Rev.* **2009**, *39* (1), 189-227.

23. Dorenbos, P., fd transition energies of divalent lanthanides in inorganic

compounds. *J. Phys.: Condens. Matter* **2003**, *15* (3), 575-594.

24. Shionoya, S.; Yen, W. M.; Yamamoto, H.; *Phosphor Handbook*. CRC Press, 2006.

25. Buenzli, J. C.; Eliseeva, S. V., ChemInform abstract: intriguing aspects of lanthanide luminescence. *ChemInform* **2013**, *44* (35).

26. E Silva, F. R. G.; Reinhard, C.; Gudel, H.-U.; Piguet, C.; Moser, J. E.; Bunzli, J.-C. G.; Malta, O. L., Visible and near-infrared luminescence of lanthanide-containing dimetallic triple-stranded helicates: energy transfer mechanisms in the Sm (super)III and Yb (super)III molecular edifices. *J. Phys. Chem. A* **2002**, *106* (9), 1670.

27. Gonçalves E Silva, F. R.; Longo, R.; Malta, O. L.; Piguet, C.; Bünzli, J.-C., Theoretical modelling of the low quantum yield observed in an Eu(III) triple helical complex with a tridentate aromatic ligand. *PCCP* **2000**, *2* (23), 5400-5403.

28. Praveen, V. K.; Ranjith, C.; Bandini, E.; Ajayaghosh, A.; Armaroli, N., Oligo(phenylenevinylene) hybrids and self-assemblies: versatile materials for excitation energy transfer. *Chem. Soc. Rev.* **2014**, *43*, 4222-4242.

29. Hagan, A.; Zuchner, T., Lanthanide-based time-resolved luminescence immunoassays. *Anal. Bioanal. Chem.* **2011**, *400* (9), 2847-2864.

30. Williams, A. T. R.; Winfield, S. A.; Miller, J. N., Relative fluorescence quantum yields using a computer-controlled luminescence spectrometer. *The Analyst* **1983**, *108* (1290), 1067-1071.

31. De Mello, J. C.; Wittmann, H. F.; Friend, R. H., An improved experimental determination of external photoluminescence quantum efficiency. *Adv. Mater.* **1997**, *9* (3), 230-232.

32. Porrès, L.; Holland, A.; Pålsson, L.-O.; Monkman, A.; Kemp, C.; Beeby, A.,

Absolute Measurements of Photoluminescence Quantum Yields of Solutions Using an Integrating Sphere. *J. Fluoresc.* **2006**, *16* (2), 267-273.

33. Wong, H.-Y.; Lo, W.-S.; Yim, K.-H.; Law, G.-L.; Chirality and chiroptics of lanthanide molecular and supramolecular assemblies. *Chem* **2019**, *5*, 3058-3095.

34. Berova, N.; Bari, L. D.; Pescitelli, G., Application of electronic circular dichroism in configurational and conformational analysis of organic compounds. *Chem. Soc. Rev.* **2007**, *36* (6), 914-931.

35. Riehl, J. P.; Richardson, F. S., Circularly polarized luminescence spectroscopy. *Chem. Rev.* **1986**, *86* (1), 1-16.

36. Sánchez-Carnerero, E. M.; Agarrabeitia, A. R.; Moreno, F.; Maroto, B. L.; Muller, G.; Ortiz, M. J.; De La Moya, S., Circularly Polarized Luminescence from Simple Organic Molecules. *Chem. Eur. J.* **2015**, *21* (39), 13488-13500.

37. Kumar, J.; Nakashima, T.; Kawai, T., Circularly Polarized Luminescence in Chiral Molecules and Supramolecular Assemblies. *J. Phys. Chem. Lett.* **2015**, *6* (17), 3445-3452.

38. Richardson, F. S., Selection rules for lanthanide optical activity. *Inorg. Chem.* **1980**, *19* (9), 2806-2812.

39. Comby, S.; Imbert, D.; Chauvin, A.-S.; Bunzli, J.-C. G., Stable 8-hydroxyquinolinate-based podates as efficient sensitizers of lanthanide near-infrared luminescence. *Inorg. Chem.* **2006**, *45* (2), 732-743.

40. Charbonnière, L. J.; Ziessel, R., Anionically Substituted 1,1´,1"-Methylidynetris[1 H -pyrazole] Ligands for the Formation of Neutral Lanthanide Complexes in Water: Synthesis, Characterization, and Photophysical Properties.

Helv Chim Acta **2003**, *86* (10), 3402-3410.

41. Tallec, G.; Imbert, D.; Fries, P. H.; Mazzanti, M., Highly stable and soluble bis-aqua Gd, Nd, Yb complexes as potential bimodal MRI/NIR imaging agents. *Dalton Trans.* **2010**, *39* (40), 9490-9492.

42. Faulkner, S.; Burton-pye, B. P., pH Dependent self-assembly of dimetallic lanthanide complexes. *Chem. Commun.* **2005**, 2, 259-261.

43. Lukeš, I.; Kotek, J.; Vojtíšek, P.; Hermann, P., Complexes of tetraazacycles bearing methylphosphinic/phosphonic acid pendant arms with copper(II), zinc(II) and lanthanides(III). A comparison with their acetic acid analogues. *Coord. Chem. Rev.* **2001**, *216*, 287-312.

44. Plush, S. E.; Clear, N. A.; Leonard, J. P.; Fanning, A.-M.; Gunnlaugsson, T., The effect on the lanthanide luminescence of structurally simple Eu(III) cyclen complexes upon deprotonation of metal bound water molecules and amide based pendant arms. *Dalton Trans.* **2010**, *39* (15), 3644-3652.

45. Lincheneau, C.; Quinlan, E.; Kitchen, J. A.; McCabe, T.; Matthews, S. E.; Gunnlaugsson, T., Delayed lanthanide luminescent Tb(III) complexes formed from lower rim amide functionalised calix[4]arenes. *Supramol. Chem.* **2013**, *25* (12), 869-880.

46. Lehn, J.-M., Toward self-organization and complex matter. *Science* **2002**, *295* (5564), 2400-2403.

47. Alessandro, A.; Matteo, M.; Luisa De, C., Controlling and imaging biomimetic self-assembly. *Nat. Chem.* **2015**, *8* (1), 10-15

48. Reinhoudt, D. N.; Stoddart, J. F.; Ungaro, R., Supramolecular Science Where it is and where it is going. *Chem. Eur. J.* **1998**, *4* (8), 1349-1351.

49. Caulder, D. L.; Raymond, K. N., Supermolecules by Design. *Acc Chem Res* **1999,** *32* (11), 975-982.

50. Jung, J. H.; Ono, Y.; Shinkai, S., Sol-Gel Polycondensation in a Cyclohexane-Based Organogel System in Helical Silica: Creation of both Right- and Left-Handed Silica Structures by Helical Organogel Fibers. *Chem. Eur. J.* **2000,** *6* (24), 4552-4557.

51. Volker, B.; Ivan, H.; Richard, G. K.; Michael, J. K.; Jean-Marie, L., Interconversion of single and double helices formed from synthetic molecular strands. *Nature* **2000**, *407* (6805), 720.

52. Hanessian, S.; Simard, M.; Roelens, S., Molecular Recognition and Self-Assembly by Non-amidic Hydrogen Bonding. An Exceptional Assembler of Neutral and Charged Supramolecular Structures. *J. Am. Chem. Soc.* **1995**, *117* (29), 7630-7645.

53. Lehn, J. M., Programmed Chemical Systems: Multiple Subprograms and Multiple Processing/Expression of Molecular Information. *Chem. Eur. J.* **2000**, *6* (12), 2097-2102.

54. Rowan, A. E.; Nolte, R. J. M., Molekulare Programmierung von Helicität. *Angew. Chem.* **1998**, *110* (1-2), 65-71.

55. Albrecht, M., "Let's Twist Again"--Double-stranded, triple stranded, and circular helicates. *Chem. Rev.* **2001**, 3457-3497.

56. Piguet, C.; Bernardinelli, G.; Hopfgartner, G., Helicates as Versatile Supramolecular Complexes. *Chem. Rev.* **1997**, *97* (6), 2005.

57. Balzani, V.; Credi, A.; Raymo, F. M.; Stoddart, J. F., Artificial Molecular Machines. *Angew. Chem. Int. Ed.* **2000**, *39* (19), 3348-3391.

58. Funeriu, D. P.; Lehn, J. M.; Baum, G.; Fenske, D., Double subroutine self-assembly spontaneous generation of a nanocyclic dodecanuclear Cu1 inorganic architecture. *Chem. Eur. J.* **1997**, *3* (1), 99-104. 56.

59. Albrecht, M., From molecular diversity to template-directed self-assembly – new trends in metallo-supramolecular chemistry. *J. Incl. Phenom.* **2000**, *36* (2), 127-151.

60. Albrecht, M.; Kotila, S., Counter-ion induced self-assembly of a meso -helicate type molecular box. *Chem. Commun.* **1996**, (20), 2309-2310.

61. Amouri, H.; Desmarets, C.; Moussa, J., Confined nanospaces in metallocages: guest molecules, weakly encapsulated anions, and catalyst sequestration. *Chem. Rev.* **2012**, *112* (4), 2015-2041.

62. Cook, T. R.; Zheng, Y.-R.; Stang, P. J., Metal-organic frameworks and self-assembled supramolecular coordination complexes: comparing and contrasting the design, synthesis, and functionality of metal-organic materials. *Chem. Rev.* **2013**, *113* (1), 734-777.

63. Zarra, S.; Wood, D. M.; Roberts, D. A.; Nitschke, J. R., Molecular containers in complex chemical systems. *Chem. Soc. Rev.* **2014**, *44* (2), 419-432.

64. Ballester, P.; Fujita, M.; Rebek, J., Molecular containers. *Chem. Soc. Rev.* **2014**, *44* (2), 392-393.

65. Pan, M.; Wu, K.; Zhang, J.-H.; Su, C.-Y., Chiral metal–organic cages/containers (MOCs): From structural and stereochemical design to applications. *Coord. Chem. Rev.* **2019**, *378*, 333-349.

66. Wang, W.; Wang, Y.-X.; Yang, H.-B., Supramolecular transformations within discrete coordination-driven supramolecular architectures. *Chem. Soc. Rev.*

2016, *45* (9), 2656-2693.

67. Ren, D.-H.; Qiu, D.; Pang, C.-Y.; Li, Z.; Gu, Z.-G., Chiral tetrahedral iron(ii) cages: diastereoselective subcomponent self-assembly, structure interconversion and spin-crossover properties. *Chem. Commun.* **2014**, *51* (4), 788-791.

68. Liu, T.; Liu, Y.; Xuan, W.; Cui, Y., Chiral Nanoscale Metal–Organic Tetrahedral Cages: Diastereoselective Self-Assembly and Enantioselective Separation. *Angew. Chem. Int. Ed.* **2010,** *49* (24), 4121-4124.

69. Klein, C.; Gütz, C.; Bogner, M.; Topić, F.; Rissanen, K.; Lützen, A., A new structural motif for an enantiomerically pure metallosupramolecular Pd_4L_8 aggregate by anion templating. *Angew. Chem. Int. Ed.* **2014**, *53* (14), 3739-3742.

70. Caulder, D. L.; Powers, R. E.; Parac, T. N.; Raymond, K. N., The Self-Assembly of a Predesigned Tetrahedral M_4L_6 Supramolecular Cluster. *Angew. Chem. Int. Ed.* **1998**, *37* (13-14), 1840-1843.

71. Stomeo, F., Lincheneau, C., Leonard, J.P., O'Brien, J.E., Peacock, R.D., McCoy, C.P., and Gunnlaugsson, T. Metal-directed synthesis of enantiomerially pure dimetallic lanthanide luminescent triple-stranded helicates. *J. Am. Chem. Soc.* **2009**, *131*, 9636–9637.

72. Lincheneau, C., Peacock, R.D., and Gunnlaugsson, T. Europium directed synthesis of enantiomerically pure dimetallic luminescent "squeezed" triple-stranded helicates; solution studies. *Chem. Asian J.* **2010**, *5*, 500–504.

73. Kotova, O., Comby, S., Pandurangan, K., Stomeo, F., O'Brien, J.E., Feeney, M., Peacock, R.D., McCoy, C.P., and Gunnlaugsson, T. The effect of the linker size in C_2-symmetrical chiral ligands on the self-assembly formation of luminescent triple-stranded di-metallic Eu(iii) helicates in solution. *Dalton Trans.* **2018**, *47*,

12308–12317.

74. Yan, L.-L.; Tan, C.-H.; Zhang, G.-L.; Zhou, L.-P.; Bünzli, J.-C.; Sun, Q.-F. Stereocontrolled self-assembly and self-sorting of luminescent europium tetrahedral cages. *J. Am. Chem. Soc.* **2015**, 137, 8550–8555.

75. Li, X.-Z.; Zhou, L.-P.; Yan, L.-L.; Yuan, D.-Q.; Lin, C.-S.; and Sun, Q.-F. Evolution of luminescent supramolecular lanthanide $M_{2n}L_{3n}$ complexes from helicates and tetrahedra to cubes. *J. Am. Chem. Soc.* **2017**, *139*, 8237–8244.

76. Yeung, C.-T.; Yim, K.-H.; Wong, H.-Y.; Pal, R.; Lo, W.-S.; Yan, S.-C.; Wong, Y.-M. M.; Yufit, D.; Smiles, D.E.; McCormick, L. J.; Teat, S. J.; Shuh, D. K.; Wong, W.-T.; Law, G.-L. Chiral transcription in self-assembled tetrahedral Eu_4L_6 chiral cages displaying sizable circularly polarized luminescence. *Nat. Commun.* **2017**, *8*, 1128.

Chapter 2a: Lanthanide supramolecular helical diastereoselective breaking induced by point chirality

2a.1 Introduction

2a.1.1 Introduction to chiroptical lanthanide complexes

Lanthanide self-assembly supramolecular complexes have been proven to be an excellent candidate for molecular recognition due to their unique physical properties.[1] In order to apply these fascinating systems into biological research, numerous chiroptical lanthanide systems have been developed.[2-7] Chirality is essential for biological research, especially for medicinal chemistry. For example, the change in chiral centre may change the effect of drugs.[8] Therefore, development of chiroptical recognition is important for detecting chiral biomolecule such as amino acid.[9-11] To date, most of the chiral recognition by lanthanide supramolecules strongly rely on induced CPL.[1] The chiral induction was achieved by the interaction between chiral molecular and achiral lanthanide complexes. However, careful ligand design has to be taken into consideration since vacant metal site is required for induced iCPL and most of the reported iCPL lanthanide sensors are mononuclear complex with well-defined ligands.[12-15]

2a.1.2 Chirality and preparation of chiral lanthanide complexes

In order to develop chiroptical lanthanide system, control of stereoselectivity of lanthanide system is important.[16-18] Due to the labile nature and poor stereochemical preferences of lanthanide ions, precise control of stereoselective formation of desired lanthanide supramolecular complexes is challenging.[19] One of the most straightforward approach is point chirality.[20] By introduction of a predisposed point chiral group, the chiral information can be transferred from the chiral moiety to the metal centre, forcing the coordination orientation of the metal centre to be either Δ (right-handed twist) or Λ (left-handed twist). However, the control of point chirality is difficult and only few examples were reported.[2, 3, 21]

2a.1.3 Scope of study

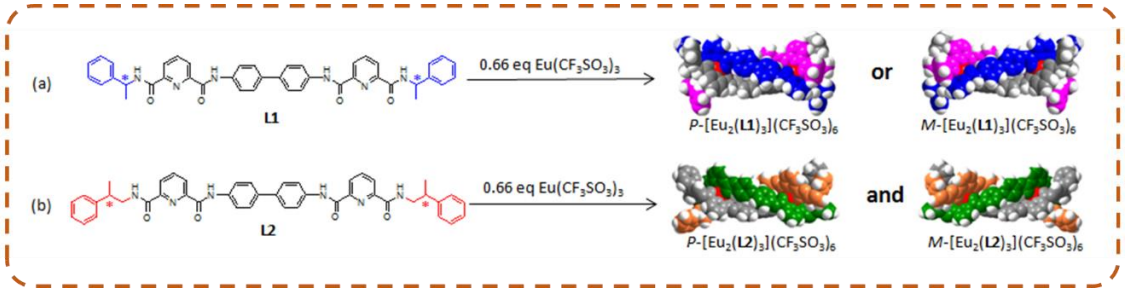

Figure 2a-1. *Stereoselective formation of **L1** and **L2** upon coordination with Eu(OTf)₃.*

This study focuses on the development of new chiral lanthanide supramolecular complexes for potential application including chiroptical sensing of biomolecules. Two pairs of chiral ligands, **L1** and **L2**, were synthesized by introducing chiral moiety next to the metal chelating group. It is expected that the chiral complexes can be form via point chirality. Compared with that of **L1**, the point chirality of **L2** is one carbon unit farther apart from the chelating unit. This slight difference in

distance between the point chirality and the metal chelating group towards the stereoselective formation is investigated.

2a.2 Result and discussion

2a.2.1 Design and synthesis of L1 and L2

L1 and **L2** were designed with the use of pyridine-2,6-dicarboxamide (pcam) moieties. Each pcam moiety contains a pyridine ring and two carbonyl groups which is able form stable nine-coordinated metal complexes with lanthanide ion.[22] Each metal chelating group was allowed to connect with a chiral moiety. A rod-like biphenyl linker was used as the linker to connect two metal chelating moieties. Although the rod-like linker is linear, recent research have demonstrated that bimetallic transition metal triple helicate can be prepared with the use of biphenyl linker.

L1 and **L2** were synthesized by using generic HATU amide coupling reactions in 2 steps. All the intermediates and final ligand products were well characterized by NMR and ESI-HRMS. The structure of **L2** was further characterized by X-ray crystallography. In the X-ray structure of **L2**, the pyridine ring and the carbonyl oxygens adopted a transoid conformations about the interannular C-C bonds (figure 2a-2).

Figure 2a-2. *X-ray crystallography of* ***L2^{RR}****.*

2a.2.2 ^{1}HNMR and UV-CD titration

Previous research has shown that the use of transition metal with similar ligand design can lead to the formation bimetallic M_2L_3 triple helicate. Therefore, it was hypothesized that the metal-to-ligand ratio is 2 to 3. This hypothesis was first tested by ^{1}HNMR titration. The ^{1}HNMR titration of **L1^{RR}** was done in a mixture of $CDCl_3$/CD_3OD/CD_3CN in a ratio of 75:5:20 due to poor ligand solubility (figure 2a-3). Upon addition of $Eu(OTf)_3$ to the ligand solution, the ^{1}HNMR signal at 1.72 ppm, which corresponds to the CH_3 group of **L1^{RR}**, decreased gradually. A new ^{1}HNMR signal gradually increased at 1.79 ppm. The new signal at 1.79 ppm was broad which corresponds to the europium complex due to the paramagnetic nature of europium ions. When 0.66 eq. of $Eu(OTf)_3$ was added, all the ligand signal disappeared. The consumption of ligand at 0.66 eq. of $Eu(OTf)_3$ indicated the metal-to-ligand ratio is 2 to 3.

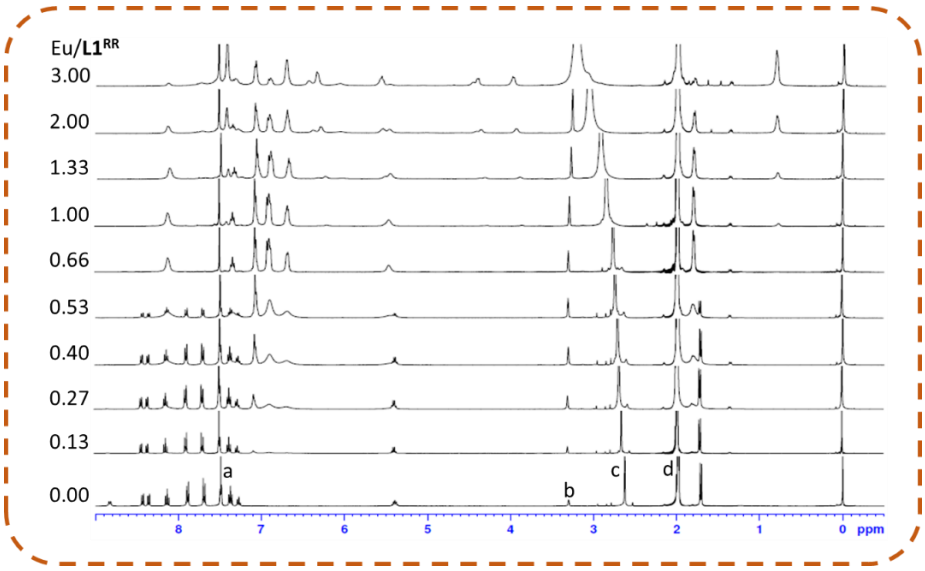

Figure 2a-3. *Variation in ^{1}H NMR spectra upon titrating **L1^{RR}** (5.11×10^{-3} M in 75:5:20, v/v/v, of $CDCl_3$/CD_3OD/CD_3CN) with Eu(OTf)$_3$ (0.271 M in CD_3OD) at 296 K. (Peaks that are marked as a, b, c and d are from the residual solvents of $CHCl_3$, MeOH, H_2O and MeCN, respectively.)*

The metal-to-ligand ratio was further examined by UV-Vis titration. UV-Vis titration was performed by slow addition of Eu(OTf)$_3$ to the ligand solution and the UV absorption of the solution was monitored (figure 2a-4). Upon addition of Eu(OTf)$_3$, the signal of ligand absorption decreased progressively at 326 nm. Simultaneously, an evolution of the absorption peak corresponding to the europium complex at 346 nm was observed. A single sharp end point was observed when 0.65 eq. Eu(OTf)$_3$ was added which conformed the hypothesis of metal-to-ligand 2 to 3.

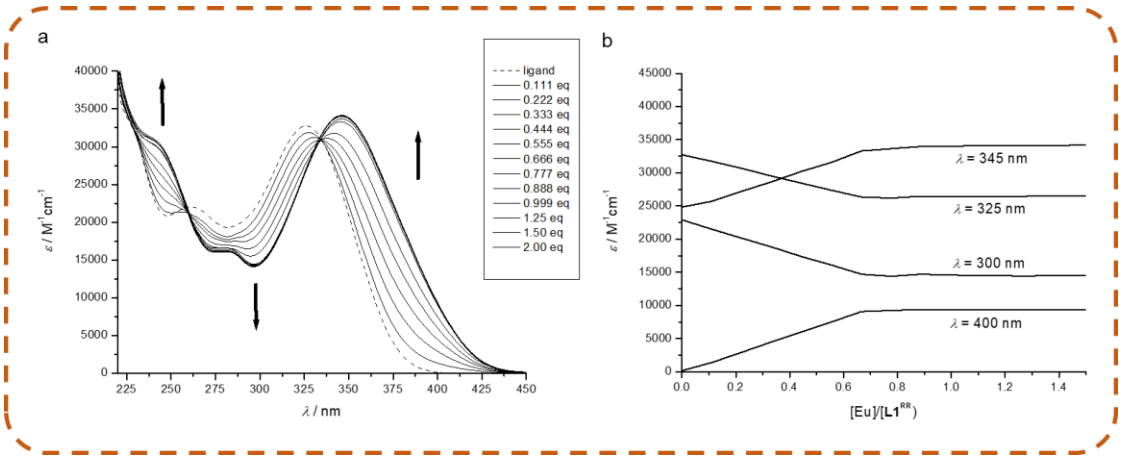

Figure 2a-4. *(a) Variation in UV-Vis absorption spectra of titrating* ***L1^{RR}*** *(1.72 × 10^{-4} M, in 73:3:24, v/v/v, of CHCl$_3$/MeOH/MeCN) with Eu(OTf)$_3$ (0.038M in MeCN) at 298 K (Eu:****L1^{RR}*** *= 0.0–2.0). (b) Variation of molar extinction coefficients at four different wavelengths upon titrating* ***L1^{RR}*** *with Eu(OTf)$_3$.*

^{1}HNMR and UV-Vis titration were also performed for **L2** to investigate the metal-to-ligand ratio. Since the ligand design of **L2** is similar with that of **L1** except for the terminal chiral group, it was expected that **L2** will also form Ln_2**L2**$_3$ species upon coordination with lanthanide ions. Indeed, similar result was observed for both UV-Vis titration. An end point of 0.66 eq. of Eu(OTf)$_3$ was observed for **L2** (figure 2a-5).

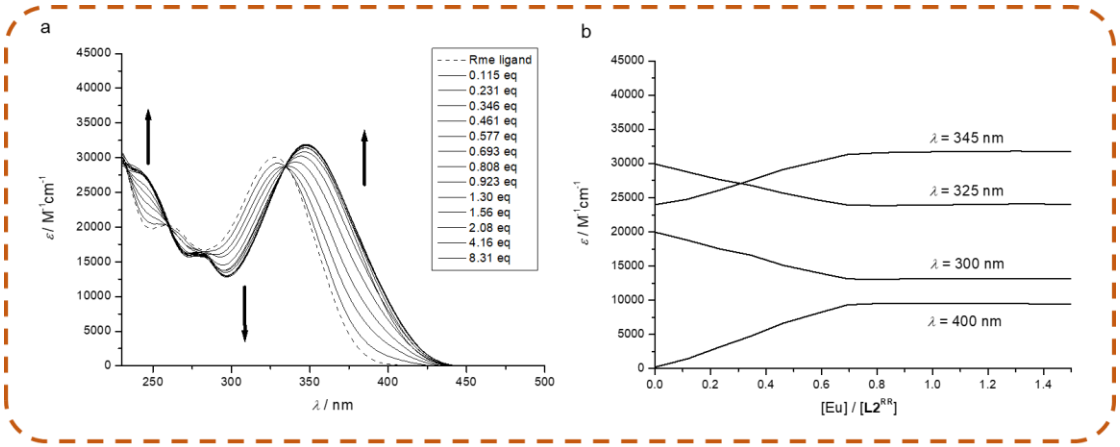

Figure 2a-5. *(a) Variation in UV-Vis absorption spectra of titrating* ***L2^{RR}*** *(1.65 × 10^{-4} M, in 73:3:24, v/v/v, of CHCl$_3$/MeOH/MeCN) with Eu(OTf)$_3$ (0.038M in MeCN) at 298 K (Eu:****L2^{RR}*** *= 0.0–2.0). (b)*

Variation of molar extinction coefficients at four different wavelengths upon titrating ***L2^{RR}*** *with* $Eu(OTf)_3$.

However, the ^{1}HNMR titration of **L2** showed a different result compared with that of **L1**. Although the disappearance of ligand signal was also observed when 0.68 eq. of $Eu(OTf)_3$ was added, two sets of signal appeared simultaneously at 0.97 and 1.40 ppm in a ratio of 1:1.1. This ^{1}HNMR titration confirmed that the metal-to-ligand ratio of **L2** was 2:3 and two species were formed upon coordination of $Eu(OTf)_3$ (figure 2a-6).

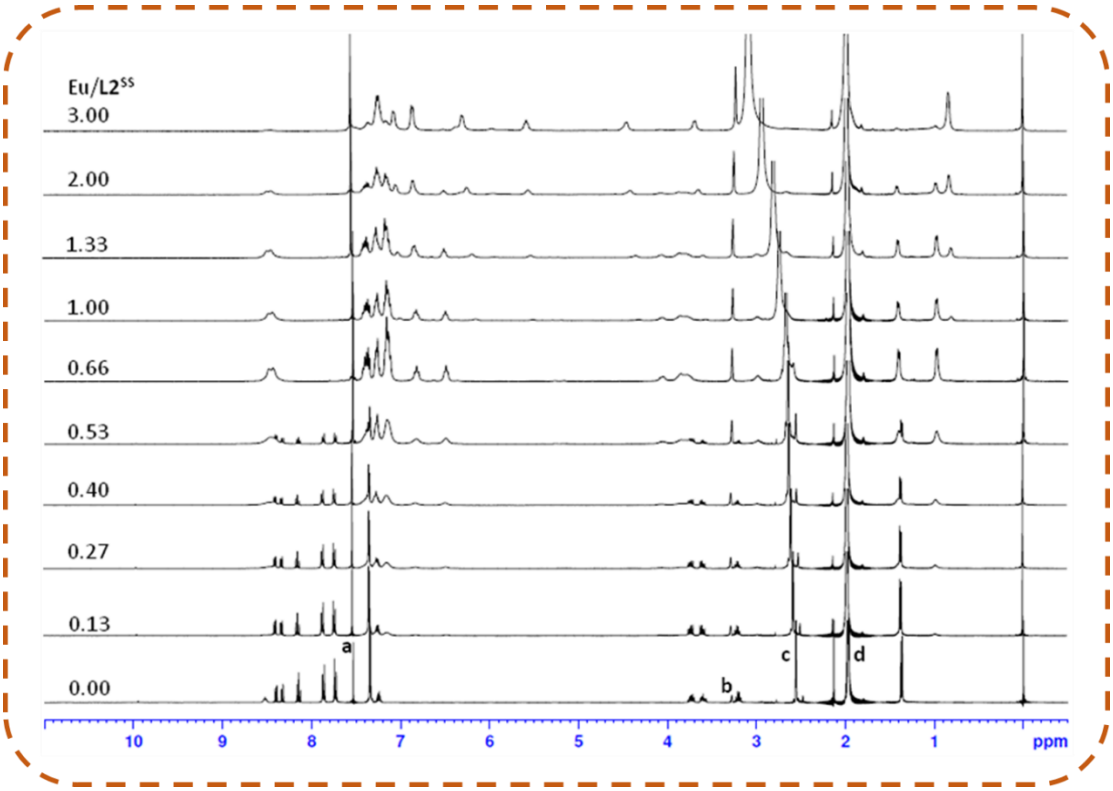

Figure 2a-6. *Variation in ^{1}H NMR (400 MHz, 295 K) spectra of titrating* ***L2^{SS}*** *(4.64×10^{-3} M in 47:6:47, v/v/v, of $CDCl_3$/CD_3OD/CD_3CN) with $Eu(OTf)_3$ (0.271 M in CD_3OD) at 296K. (Peaks that are marked as a, b, c, d are from the residual solvents.)*

2a.2.3 Synthesis and X-ray crystal structure of [Eu_2**L1**$_3$], [Tb_2**L1**$_3$], and [Eu_2**L2**$_3$]

The corresponding europium complexes with **L1** and **L2** was synthesized following the experimental condition of ^{1}HNMR titration. [Eu_2**L1**$_3$] and [Eu_2**L2**$_3$] were synthesized by reacting two equivalents of $Eu(OTf)_3$ with three equivalents of ligand. Mixture of solvent was used due to the poor solubility of **L1** and **L2**. Single crystal of both [Eu_2**L1**$_3$] and [Eu_2**L2**$_3$] can be obtained by slow evaporation of the complex in MeCN. In the crystal structure of [Eu_2**L1**$_3$], the overall *P* helicate was formed by the successive interacnnular C-N and C-C bond rotation between two metal centres and the overall helicate structure was stabilized by a total of five strong and one weak CH-π interaction (figure 2a-7a).[23] Each Eu was coordinated with three pcam moieties and exhibited the same Δ-configuration. The Eu metal centre can be best described as distorted tricapped trigonal prismatic geometry. Eu-N distances was found to be 2.532(5) to 2.566(5) Å and Eu-O distances range from 2.380(5) to 2.441(5) Å. [Tb_2**L1**$_3$] was also prepared by slow evaporation of complex solution in MeCN. Similar with [Eu_2**L1**$_3$], each terbium centre can be described as tricapped trigonal prismatic geometry. Tb-N distances range from 2.500(5) to 2.566(5) Å and Tb-O distances range from 2.377(4) to 2.432(4) Å (figure 2a-7b). A single crystal of [Eu_2**L2**$_3$] was also obtained for X-ray crystallography. Although the quality of the crystal was not suitable for analysis, it showed the overall helical structure of [Eu_2**L2**$_3$] (figure 2a-7c).

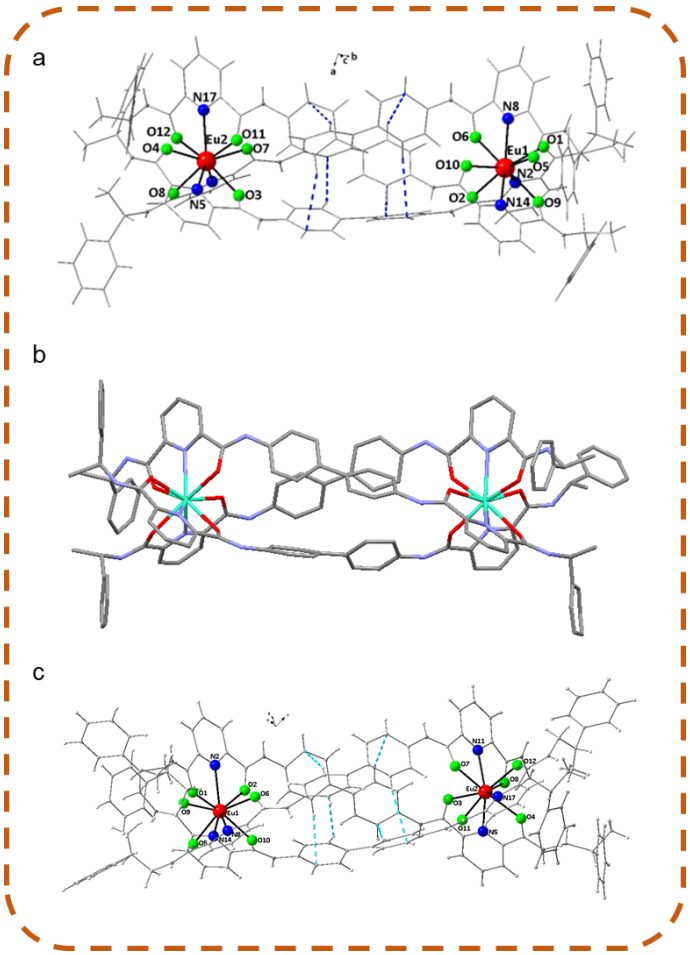

Figure 2a-7. *X-ray crystal structure of (a) [Eu_2**L1**$_3$], (b) [Tb_2**L1**$_3$].and (c) [Eu_2**L2**$_3$].*

2a.2.4 NMR analysis of [Eu_2**L1**$_3$] and [Eu_2**L2**$_3$]

After confirming the topologies of [Eu_2**L1**$_3$] and [Eu_2**L2**$_3$], [Eu_2**L1**$_3$] and [Eu_2**L2**$_3$] were then characterized by NMR. ^{1}HNMR was first done for [Eu_2**L1**$_3$]. In the ^{1}HNMR spectrum of [Eu_2**L1**$_3$], all signals are broad due to the paramagnetic nature of europium ions. The number of integrations also matched the C_2-symmetric nature of **L1** (figure 2a-8). For ^{13}CNMR, only single set of signals was observed which matched the C_2-symmetric nature of **L1** (figure 2a-9). The corresponding [La_2**L1**$_3$] complex was also synthesized for comparing with [Eu_2**L1**$_3$] (figure 2a-10). The ^{1}HNMR of [La_2**L1**$_3$] also showed single set of signals which indicated the presence of single and highly symmetric species.

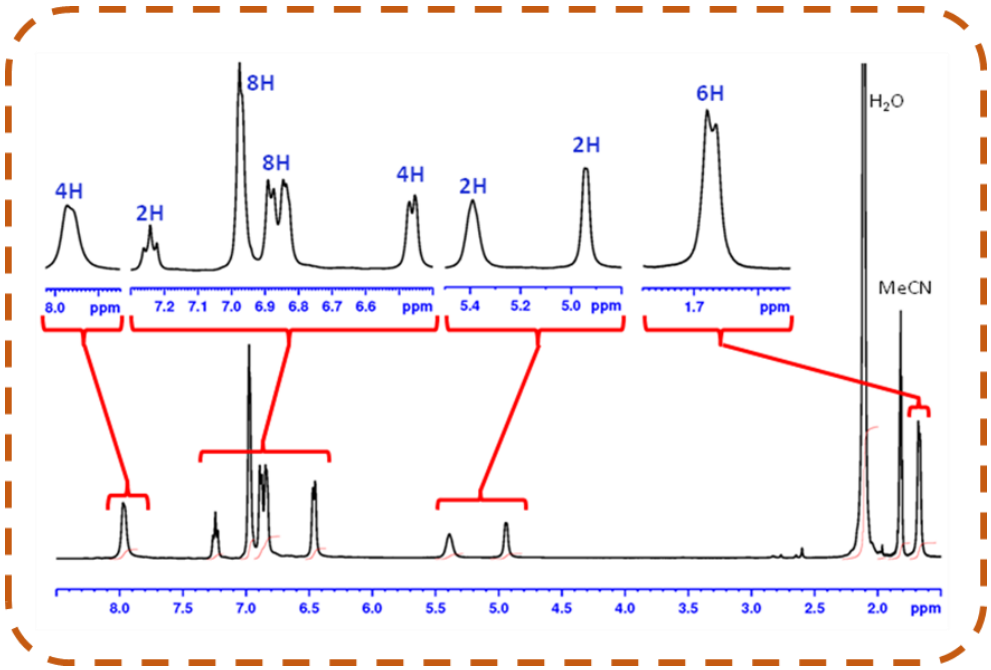

Figure 2a-8. *^{1}HNMR spectrum of* ***[Eu$_2$(L1^{RR})$_3$](CF$_3$SO$_3$)$_6$*** *(CD$_3$CN). The insets show the expansion of the corresponding region as indicated.*

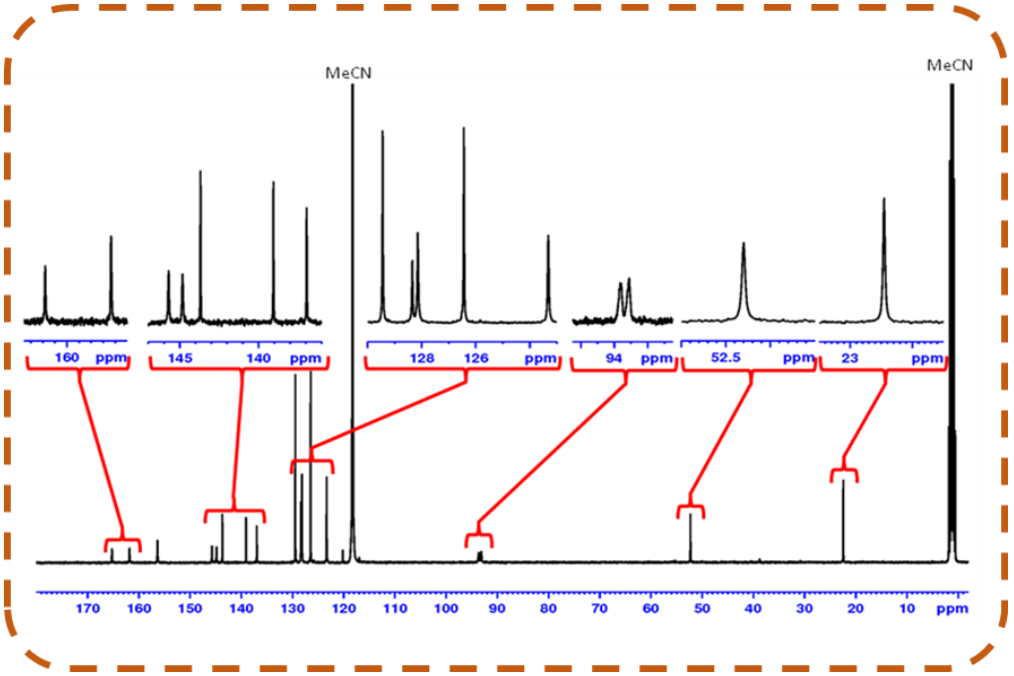

Figure 2a-9. *^{13}CNMR spectrum of* ***[Eu$_2$(L1^{RR})$_3$](CF$_3$SO$_3$)$_6$*** *(CD$_3$CN). The insets show the expansion of the corresponding region as indicated.*

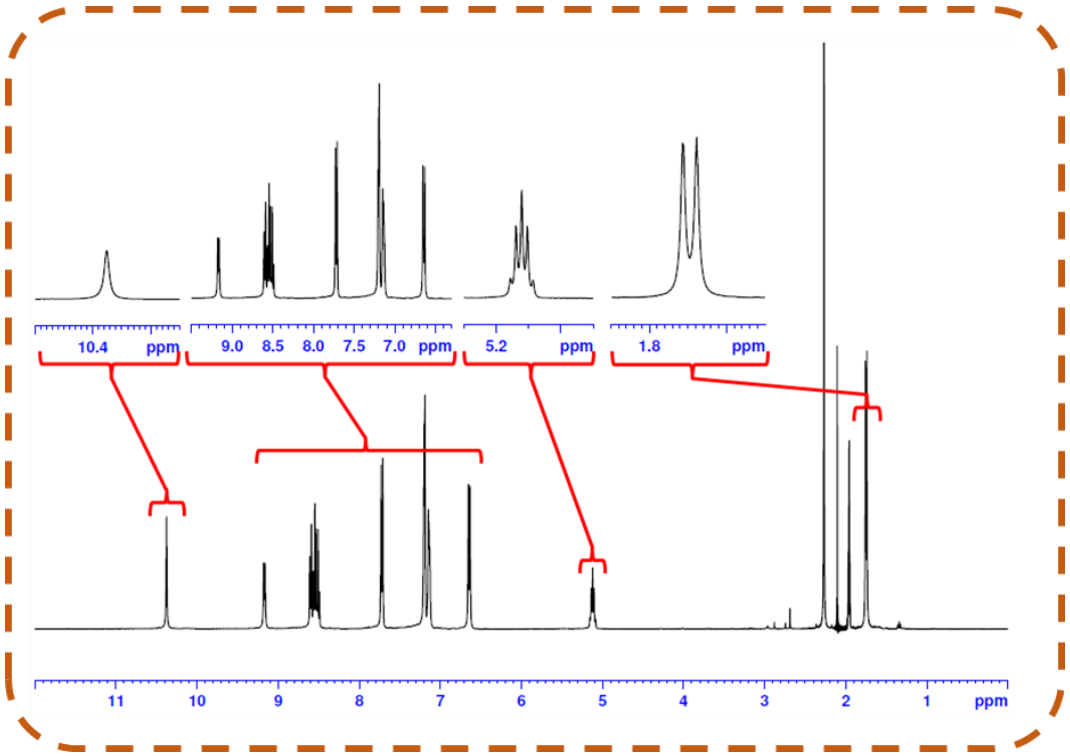

Figure 2a-10. *^{1}H NMR spectrum of* ***[La$_2$(L1^{SS})$_3$](CF$_3$SO$_3$)$_6$*** *(CD$_3$CN). The insets show the expansion of the corresponding region as indicated.*

Similar NMR studies were also performed for **L2**. However, both ^{1}HNMR (figure 2a-11) and ^{13}CNMR (figure 2a-12) of [Eu$_2$**L2**$_3$] showed a very different result compared with that of [Eu$_2$**L1**$_3$]. In the ^{1}HNMR and ^{13}CNMR spectrum of [Eu$_2$**L2**$_3$], two sets of signals were observed. Two CH_3 signals at aliphatic region (0.84 and 1.26 ppm) were observed which indicated the presence of two species. The integration of CH_3 signal showed the ratio of two species was around 1:1.1. Increasing temperature tends to alter the dynamic exchange process by shifting one to another (figure 2a-13). However, preparation of pure single species is not possible. Diamagnetic [La$_2$**L2**$_3$] was also prepared for further NMR studies (figure 2a-14). The NMR spectrum of [La$_2$**L2**$_3$] also revealed two NMR signal in a ratio of 1:1.1.

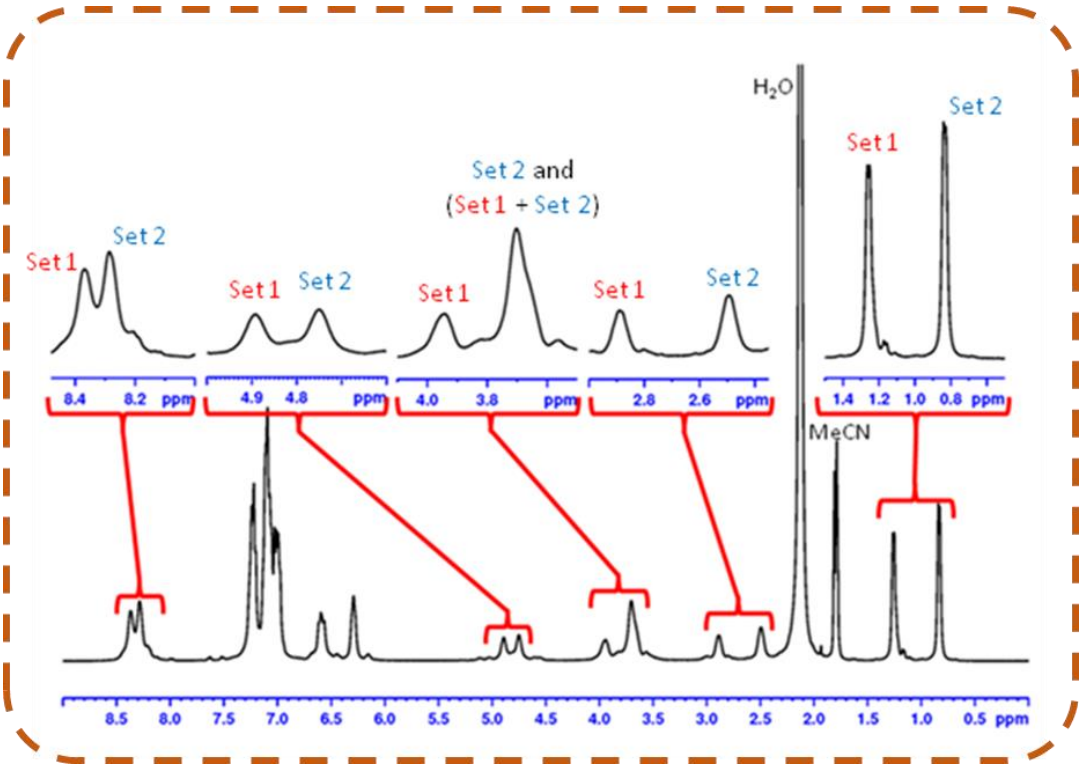

Figure 2a-11. *^{1}HNMR spectrum of* ***$[Eu_2(L2^{RR})_3](CF_3SO_3)_6$*** *($CD_3CN$). The insets show the expansion of the corresponding region as indicated. Set 1 and set 2 are preliminary assigned that based on their integration.*

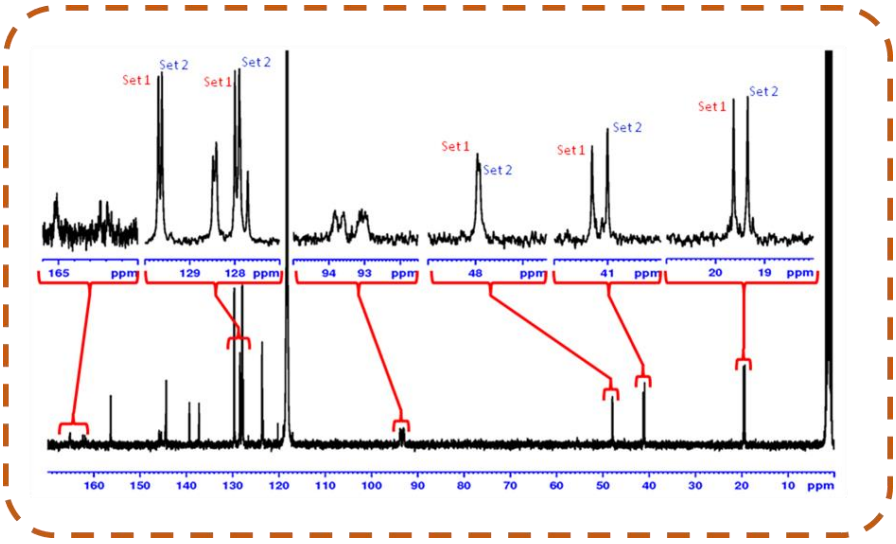

Figure 2a-12. *^{13}CNMR spectrum of* ***$[Eu_2(L2^{RR})_3](CF_3SO_3)_6$*** *($CD_3CN$). The insets show the expansion of the corresponding region as indicated. Set 1 and set 2 are preliminary assigned that based on their integration.*

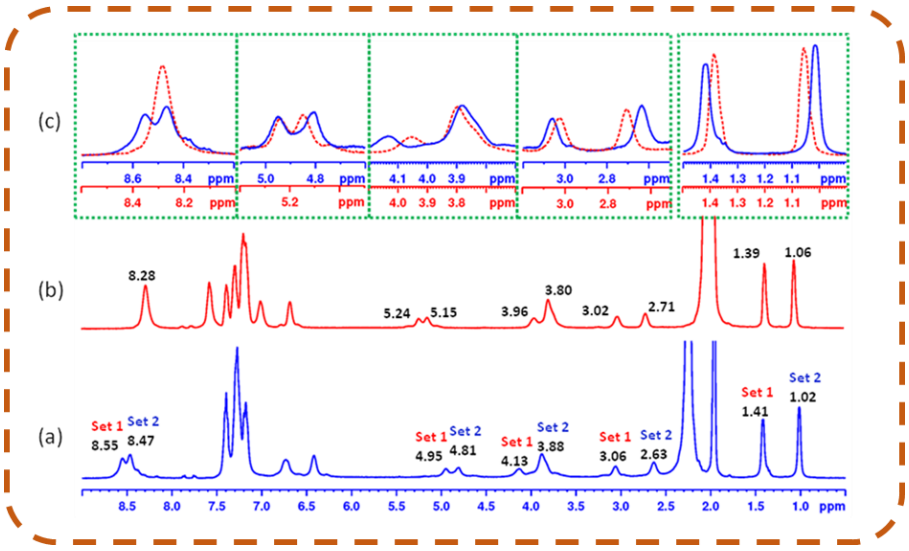

Figure 2a-13. *^{1}HNMR spectrum of* ***[Eu$_2$(L2^{RR})$_3$](CF$_3$SO$_3$)$_6$*** *(CD_3CN). a) At 295 K. b) At 345 K, c) Overlaying of the two spectra from 295 K and 345 K.*

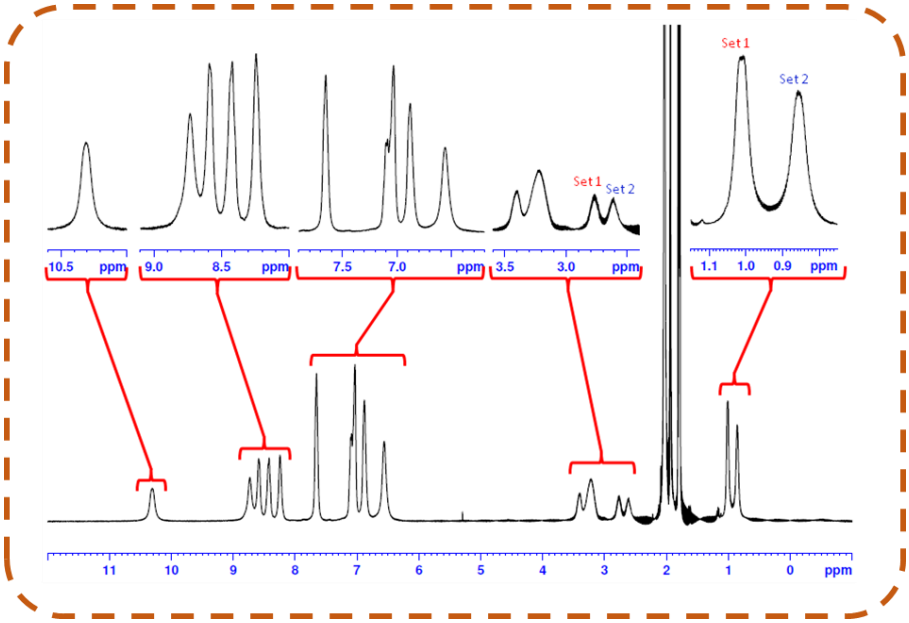

Figure 2a-14. ^{1}HNMR spectrum of **[La$_2$(L2^{SS})$_3$](CF$_3$SO$_3$)$_6$** (CD_3CN). The insets show the expansion of the corresponding region as indicated. Set 1 and set 2 are preliminary assigned that based on their integration.

2a.2.5 Photophysical measurement

Solution circular dichroism (CD) measurement was performed for both [Eu$_2$**L1**$_3$] and [Eu$_2$**L2**$_3$]. In the CD spectrum of [Eu$_2$**L1**$_3$], five strong cotton effects from π to π*

was observed at 379, 333, 283, 252 and 216 nm. Mirror image of CD spectrum was observed for *R*- and *S*-isomer which indicated the successful transfer of chiral information from the chiral moiety to metal centre (figure 2a-15a). Similar mirror image was also observed for the CD spectrum of [La_2**L1**$_3$].

For [Eu_2**L2**$_3$], different result was observed in CD spectrum. Although mirror image of CD spectrum was still observed for both *R*- and *S*- isomer, a significant decrease in CD intensity was observed (figure 2a-15b). Compared with that of [Eu_2**L1**$_3$], the percentage of decrease in CD intensity of [Eu_2**L2**$_3$] was found to be 96.8% (379 nm), 99% (333 nm), 77% (283 nm), 69% (252 nm) and 84% (216 nm) respectively. Decrease in CD intensity was also observed for [La_2**L2**$_3$]. Both NMR and CD result revealed that the diastereomeric *P* and *M* helicate were formed with the use of **L2**. The decrease in CD signal can be attributed by the presence of two isomers (*P* and *M* helicate). *P* and *M* helicate twisted into two different directions, which exhibited opposite CD signal at the same wavelength and thus the overall CD signal was decreased. ESI-HRMS showed no higher-ordered supramolecules (e.g. [Eu_4**L2**$_6$]) which confirmed the CD signals are arised from helicates only.

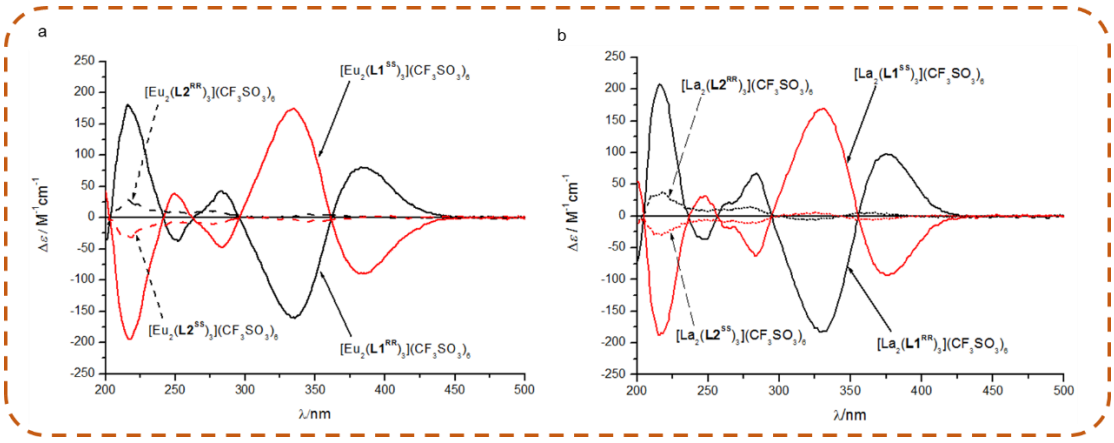

Figure 2a-15. *CD spectra of (a) $[Eu_2(\mathbf{L1})_3](CF_3SO_3)_6$ (3.23×10^{-5} M) and $[Eu_2(\mathbf{L2})_3](CF_3SO_3)_6$ (3.52×10^{-5} M) in MeCN and (b) $[La_2(\mathbf{L1})_3](CF_3SO_3)_6$ (3.58×10^{-5} M) and $[La_2(\mathbf{L2})_3](CF_3SO_3)_6$ (4.23×10^{-5} M) in MeCN.*

The luminescent properties of $[Eu_2\mathbf{L1}_3]$, and $[Eu_2\mathbf{L2}_3]$ were examined in both solid state and solution state. Generally, both $[Eu_2\mathbf{L1}_3]$, and $[Eu_2\mathbf{L2}_3]$ showed characteristic narrow Eu emission at 594, 615 and 619, 687, 697 and 704 nm, corresponding to the transition from the first excited state $^5D_0$ to the multiple ground states (^7F_J, J = 1, 2 and 4 respectively). Lifetime measurement was also performed for $[Gd_2\mathbf{L1}_3]$ at 77K and the lifetime as determined as around 0.2 to 0.4 ms, which are shorter than typical europium complex.

2a.3 Conclusion

In conclusion, this study demonstrated the strategies of preparing chiral lanthanide supramolecular complexes. With the use of linear central bridging linker, lanthanide triple stranded helicate can be prepared. Moreover, it was found that the diastereoselective and non-diastereoselective supramolecular formation was highly sensitive to the position of chiral moiety. Point-to-helical chirality transfer was efficient when the metal centre was close to the chiral group, while the non-

diastereoselective formation of lanthanide helicate was observed by just simply extending the point chirality from the metal centre. This study was important for design and preparation of chiral lanthanide supramolecular complexes.

2a.4 Experimental section

2a.4.1 Synthesis

(S)-6-((1-phenylethyl)carbamoyl)picolinic acid and (R)-6-((1-phenylethyl)carbamoyl)picolinic acid

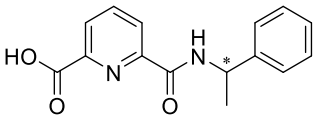

This synthesis is reported by our group previously. To a stirred solution of 2,6-pyridinedicarboxylic acid (5 g, 29.90 mmol, 2.50 equiv.) in anhydrous DMF (70 ml) at room temperature, HATU (4.55 g, 11.90 mmol, 1 equiv.) was added in portions over 10 min under nitrogen. After allowing it to stir for 20 min, (S)-(-)-1-phenylethylamine (1.53 ml, 11.97 mmol, 1 equiv.) was added dropwise and the reaction mixture was allowed to stir for 20 min. DIPEA (5.50 ml, 31.60 mmol, 2.60 equiv.) was then added to the reaction mixture over 5 min and the resulting solution was stirred at room temperature for 14 h. The reaction mixture was then diluted with H_2O (100 ml), and extracted with DCM (30 ml x 3), dried with $MgSO_4$, filtered, and concentrated in vacuo. Then dissolved it in water and extracted with EA to remove excess DMF. The resulting residue was purified by recrystallization in EtOAc solvent to give a white solid. **(S)-6-((1-phenylethyl)carbamoyl)picolinic acid**: (1.46g, 5.42 mmol, 45.39% yield), mp 110.2

– 117.3 °C. ^{1}H NMR (400 MHz, $CDCl_3$, 298K, δ): 1.65 (d, 7.0Hz, 3H), 5.37 (p, J=7.1Hz, 1H), 7.20-7.44 (m, 5H), 8.01 (d, J=8.2Hz, 1H), 8.11 (t, J=7.8Hz, 1H), 8.36 (dd, J=7.7, 1.2Hz, 1H), 8.48 (dd, J=7.8, 1.2Hz, 1H).^{13}C NMR (400MHz, $CDCl_3$, 300K, δ): 21.50, 49.14, 126.25, 126.72, 126.95, 127.48, 128.67, 139.50, 142.63, 145.37, 149.56, 162.48, 164.67. HRMS (ESI) calcd. for $C_{15}H_{14}N_2O_3Na$ [**(S)-6-((1-phenylethyl)carbamoyl)picolinic acid**+Na]$^{+}$: 293.0897, found 293.0895. The enantiomeric purity was determined with HPLC using AS-H column (Hexane/i-propanol: 80/20; flow rate 1.0 ml/min) and compared with a racemic mixture according to the elution orders with the retention times, t_S = 7.15 mins and t_R= 9.62 mins) to be > 99.9%ee. **(R)-6-((1-phenylethyl)carbamoyl)picolinic acid** was isolated, following the procedure for **(S)-6-((1-phenylethyl)carbamoyl)picolinic acid** with the use of (R)-(+)-1-phenylethylamine instead, in 55.10% yield (1.78g, 6.59 mmol): mp 110.3 – 113.9 °C. ^{1}H NMR (400 MHz, $CDCl_3$, 298K): δ 1.60 (d, J=6.9Hz, 3H), 5.34 (p, J=7.1Hz, 1H), 7.18-7.41 (m, 5H), 8.06 (t, J=7.8Hz, 1H), 8.29-8.38 (m, 2H), 8.44 (dd, J=7.8, 1.2Hz, 1H). ^{13}C NMR (100 MHz, $CDCl_3$, 300K, δ): 21.50, 30.94, 49.12, 126.23, 126.69, 126.95, 127.44, 128.63, 139.48, 142.63, 145.41, 149.52, 162.58, 164.80. HRMS (ESI) calcd. for $C_{15}H_{14}N_2O_3Na$ [**(R)- 6-((1-phenylethyl)carbamoyl)picolinic acid** +Na]$^{+}$: 293.0897, found 293.0896. The enantiomeric purity was determined to be 97.0%ee.

***N,N'*-(biphenyl-4,4'-diyl)bis[6-(*R*)-(1-phenylethylcarbamoyl)-pyridine-2-dicarboxamide] (L1^{RR}) and *N,N'*-(biphenyl-4,4'-diyl)bis[6-(*S*)-(1-phenylethylcarbamoyl)- pyridine-2-dicarboxamide] (L1^{SS})**

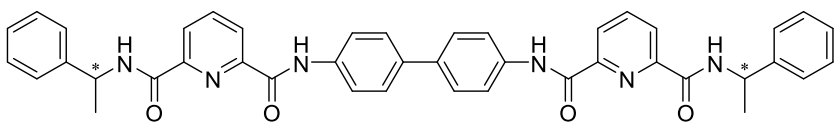

To a stirred solution of **(R)-6-((1-phenylethyl)carbamoyl)picolinic acid** (2.50 g, 9.26 mmol, 2.2 equiv.) in anhydrous DMF (40 mL) at room temperature, HATU (7.70 g, 20.3 mmol, 4.8 equiv.) was added under nitrogen. After allowing it to stir for 20 min, a benzidine (0.79 g, 4.27 mmol, 1.0 equiv.) was added and the reaction mixture was allowed to stir for 20 min in dark. DIPEA (9.24 mL, 53.03 mmol, 12.5 equiv.) was then added to the reaction mixture and the resulting solution was stirred at room temperature for 14 h. The reaction mixture was then diluted with H_2O (100 mL) and extracted with DCM (5 × 30 mL). After removing all of the organic volatile under reduced pressure, the residue was diluted with ethyl acetate (50 mL) and then washed with H_2O (5 × 30 mL) to remove the remained DMF. The organic layer was separated and then concentrated directly under reduced pressure. The residue was then diluted with MeCN (20 mL), and fine powder was progressively precipitated out. Then the solid was collected by filtration and the desired compound was isolated. **($L1^{RR}$)**: (2.53 g, 3.67 mmol, 86% yield), ^{1}H NMR (400 MHz, $(CD_3)_2SO$, 299 K, δ): 1.62 (d, *J* = 8 Hz, 6H), 5.25–5.31 (m, 2H), 7.23 (t, *J* = 8 Hz, 2H), 7.34 (t, *J* = 8 Hz, 4H), 7.45 (d, *J* = 8 Hz, 4H), 7.79 (d, *J* = 8 Hz, 4H), 7.93 (d, *J* = 8 Hz, 4H), 8.20–8.26 (m, 4H), 8.34 (d, *J* = 8 Hz, 2H), 9.60 (d, *J* = 8 Hz, 2H), 10.93 (s, 2H). ^{13}C NMR (100.6 MHz, $CD_3)_2SO$, 300 K, δ): 22.67, 49.08, 122.54, 125.79, 126.05, 127.02, 127.51, 127.69, 129.23, 136.38, 138.02, 140.62, 145.00, 149.58, 150.02, 162.62, 163.53. HRMS (ESI) calcd. for $C_{42}H_{36}N_6O_4Na$ $[M+Na]^+$: 711.2690, found 711.2681. **($L1^{SS}$)** was synthesized, following the procedure for **($L1^{RR}$)** with the use of **(S)-6-((1-phenylethyl)carbamoyl)picolinic acid** instead, in 80% yield (2.35 g, 3.42 mmol): ^{1}H NMR (400 MHz, $(CD_3)_2SO$, 299 K, δ): 1.61 (d, *J* = 8 Hz, 6H), 5.24–5.28 (m, 2H), 7.19 (t, *J* = 8 Hz, 2H), 7.30 (t, *J* = 8 Hz, 4H), 7.42 (d, *J* = 8 Hz, 4H), 7.75 (d, *J* = 8 Hz, 4H), 7.90 (d, *J* = 8 Hz, 4H), 8.18–8.21 (m, 4H), 8.31 (d, *J* = 8 Hz, 2H), 9.58 (d, *J*

= 8 Hz, 2H), 10.91 (s, 2H). ^{13}C NMR (100.6 MHz, $CD_3)_2SO$, 300 K, δ): 22.74, 49.17, 122.62, 125.86, 126.12, 127.10, 127.58, 127.76, 129.30, 136.46, 138.10, 140.68, 145.08, 149.66, 150.10, 162.70, 163.62. HRMS (ESI) calcd. for $C_{42}H_{36}N_6O_4Na$ $[M+Na]^+$: 711.2690, found 711.2682.

(*R*)-6-(2-phenylpropylcarbamoyl)picolinic acid or (*S*)-6-(2-phenylpropyl carbamoyl)picolinic acid

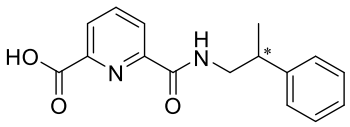

To a stirred solution of 2,6-pyridinedicarboxylic acid (9.89 g, 59.1 mmol, 4.0 equiv.) in anhydrous DMF (130 mL) at room temperature, HATU (5.64 g, 14.8 mmol, 1.0 equiv.) was added by portions over 10 min under nitrogen. After allowing it to stir for 20 min, a (*R*)-β-methylphenethylamine (2.11 mL, 14.83 mmol, 1.0 equiv.) was added dropwisely and the reaction mixture was allowed to stir for 20 min. DIPEA (5.68 mL, 32.6 mmol, 2.2 equiv.) was then added to the reaction mixture over 5 min and the resulting solution was stirred at room temperature for 18 h. The reaction mixture was then diluted with H_2O (200 mL), and extracted with DCM (5 × 50 mL), dried with $MgSO_4$, filtered, and concentrated *in vacuo*. The resulting residue was purified with flash column chromatography (DCM/EtOH 12:1, v/v) to give a white solid. **(*R*)-6-(2-phenylpropylcarbamoyl)picolinic acid**: (1.93 g, 6.8 mmol, 46% yield) ^{1}H NMR (400 MHz, CD_3OD, 299 K, δ): 1.35 (d, *J* = 8.0 Hz, 3H), 3.17 (qin, *J* = 8 Hz, 1H), 3.61 (d, *J* = 8 Hz, 2H), 7.18–7.22 (m, 1H), 7.28–7.32 (m, 4H), 8.15 (t, *J* = 8 Hz, 1H), 8.30 (d, *J* = 8 Hz, 2H), 9.42 (m, 1H). ^{13}C NMR (100.6 MHz, CD_3OD, 300 K, δ): 20.46, 41.80, 48.58, 127.34, 128.37, 129.05, 129.15, 130.36, 141.30, 146.59, 148.81, 151.99, 166.50, 168.28. HRMS

(ESI) calcd. for $C_{16}H_{16}N_2O_3Na$ $[M+Na]^+$: 307.1053, found 307.1053. The enantiomeric purity was determined with HPLC with AS-H column (Hexane/*i*-propanol: 80/20; flow rate: 0.25 ml/min) and compared with a racemic mixture according to the elution orders with retention times, t_S = 46.33 min and t_R = 49.46 min) to be 88% ee. **(*S*)-6-(2-phenylpropyl carbamoyl)picolinic acid** was isolated, following the procedure for **(*R*)-6-(2-phenylpropylcarbamoyl)picolinic acid** with the use of (*S*)-β-methylphenethylamine instead, in 43% yield (1.81 g, 6.36 mmol): ^{1}H NMR (400 MHz, CD_3OD, 299 K, δ): 1.36 (d, *J* = 8.0 Hz, 3H), 3.17 (qin, *J* = 8 Hz, 1H), 3.62 (d, *J* = 8 Hz, 2H), 7.19–7.22 (m, 1H), 7.28–7.31 (m, 4H), 8.15 (t, *J* = 8 Hz, 1H), 8.31 (d, *J* = 4 Hz, 2H). ^{13}C NMR (100.6 MHz, CD_3OD, 300 K, δ): 20.46, 41.81, 48.60, 127.34, 128.38, 129.06, 129.16, 130.37, 141.32, 146.60, 148.83, 152.00, 166.51, 168.29. HRMS (ESI) calcd. for $C_{16}H_{16}N_2O_3Na$ $[M+Na]^+$: 307.1053, found 307.1052. The enantiomeric purity was determined to be 96% ee.

***N*,*N*'-(biphenyl-4,4'-diyl)bis[6-(*R*)-(2-phenylpropylcarbamoyl)-pyridine-2,6-dicarboxamide] (L2^{RR}) and *N*,*N*'-(biphenyl-4,4'-diyl)bis[6-(*S*)-(2-phenylpropyl carbamoyl)-pyridine-2,6-dicarboxamide] (L2^{SS})**

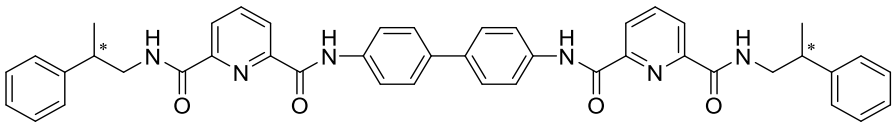

To a stirred solution of **(*R*)-6-(2-phenylpropylcarbamoyl)picolinic acid** (1.00 g, 3.52 mmol, 2.2 equiv.) in anhydrous DMF (16 mL) at room temperature, HATU (2.93 g, 7.69 mmol, 4.8 equiv.) was added under nitrogen. After allowing it to stir for 20 min, a benzidine (0.30 g, 1.61 mmol, 1.0 equiv.) was added and the reaction mixture was allowed to stir for 20 min in dark. DIPEA (3.51 mL, 20.16 mmol, 12.5 equiv.) was then

added to the reaction mixture and the resulting solution was stirred at room temperature for 14 h. The reaction mixture was then diluted with H_2O (20 mL) and extracted with DCM (5 × 30 mL). After removing all of the organic volatile under reduced pressure, the residue was diluted with ethyl acetate (20 mL) and then washed with H_2O (5 × 30 mL) to remove the remained DMF. The organic layer was separated and concentrated directly under reduced pressure. The residue was then diluted with MeCN (20 mL), and fine powder was progressively precipitated out. Then the solid was collected by filtration and the desired compound was isolated. **($L2^{RR}$)**: (0.42 g, 0.588 mmol, 73% yield), ^{1}H NMR (400 MHz, $CDCl_3$, 299K, δ): 1.42 (d, *J* = 8 Hz, 6H), 3.11–3.17 (m, 2H), 3.48–3.54 (m, 2H), 4.00–4.06 (m, 2H), 7.26–7.31 (m, 2H), 7.34–7.42 (m, 8H), 7.60–7.69 (m, 10H), 8.09 (t, *J* = 8 Hz, 2H), 8.41 (d, *J* = 8 Hz, 2H), 8.44 (d, *J* = 8 Hz, 2H), 9.20 (s, 2H). ^{13}C NMR (100.6 MHz, $CDCl_3$, 300 K, δ): 19.31, 39.97, 45.96, 120.70, 125.21, 125.45, 127.14, 127.31, 127.35, 128.95, 136.29, 136.89, 139.33, 143.91, 148.63, 148.88, 161.10, 163.09. HRMS (ESI) calcd. for $C_{44}H_{40}N_6O_4Na$ $[M+Na]^+$: 739.3003, found 739.2994. **($L2^{SS}$)** was isolated, following the procedure for **($L2^{RR}$)** with the use of **(*S*)-6-(2-phenylpropyl carbamoyl)picolinic acid** instead, in 69% yield (0.40 g, 0.555 mmol): ^{1}H NMR (400 MHz, $CDCl_3$, 298K, δ): 1.42 (d, *J* = 8 Hz, 6H), 3.13–3.15 (m, 2H), 3.48–3.53 (m, 2H), 4.01–4.06 (m, 2H), 7.27–7.31 (m, 2H), 7.35–7.42 (m, 8H), 7.58–7.60 (m, 2H), 7.65–7.70 (m, 8H), 8.10 (t, *J* = 8 Hz, 2H), 8.41 (d, *J* = 8 Hz, 2H), 8.45 (d, *J* = 8 Hz, 2H), 9.19 (s, 2H). ^{13}C NMR (100.6 MHz, $CDCl_3$, 298K, δ): 19.32, 39.99, 45.96, 120.71, 125.24, 125.48, 127.17, 127.35, 127.37, 128.97, 136.30, 136.94, 139.36, 143.92, 148.63, 148.88, 161.11, 163.02. HRMS (ESI) calcd. for $C_{44}H_{40}N_6O_4Na$ $[M+Na]^+$: 739.3003, found 739.2996.

{*N*,*N*'-(biphenyl-4,4'-diyl)bis[6-(*R*)-(1-phenylethyl-carbamoyl)-pyridine-2-dicarboxamide]}·2Eu·6(CF_3SO_3) [$Eu_2(L1^{RR})_3$] and 3{*N*,*N*'-(biphenyl-4,4'- diyl)bis[6-(*S*)-(1-phenylethylcarbamoyl)-pyridine-2-dicarboxamide]}·2Eu·6(CF_3SO_3) [$Eu_2(L1^{SS})_3$]

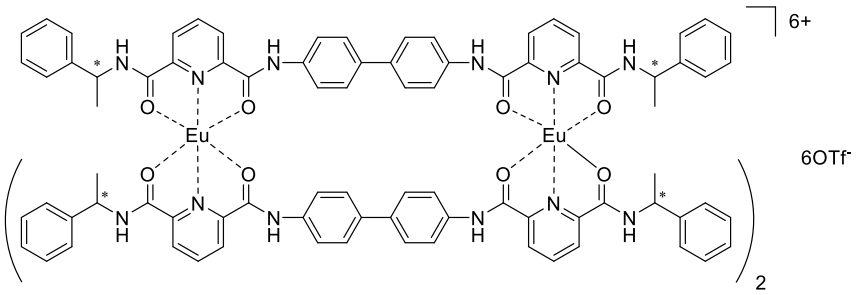

To a white suspension of **$L1^{RR}$** (0.103 g, 0.150 mmol, 1.5 equiv.) in a mixture of 13 mL of DCM/MeOH (12:1, v/v), a solution of $Eu(CF_3SO_3)_3$ (0.060 g, 0.100 mmol, 1 equiv.) in 5 mL of MeCN was added. The suspension was changed to yellow turbidity immediately. The reaction mixture was then refluxed for 16 h and the solid progressively dissolved to give a resulting homogeneous yellow solution. The solvent was removed under reduced pressure. The solid was then washed with THF to give the desired product. **[$Eu_2(L1^{RR})_3$]**: (0.140 g, 0.043 mmol, 85% yield) ^{1}H NMR (400 MHz, CD_3CN, 298 K, δ): 1.54 (s, br., 3 × 6H, C*H*$_3$), 4.95 (s, br., 3 × 2H, N-*H*), 5.27 (s, br., 3 × 2H, (CH_3)C*H*), 6.36 (s, br., 3 × 4H), 6.71 (s, br., 3 × 4H, phenyl-*H*), 6.77 (s, br., 3 × 4H, phenyl-*H*), 6.83 (s, br., 3 × 6H), 6.95 (s, br., 3 × 2H, N-*H*), 7.09 (s, br. 3 × 2H), 7.87 (s, br. 3 × 4H, phenyl-*H*). ^{13}C NMR (100.6 MHz, CD_3CN, 298 K, δ): 22.45 (*C*H_3), 52.30 (*C*H), 93.11, 93.62, 123.32, 126.44, 128.14, 128.35, 129.44, 136.95, 139.06, 143.68, 144.82, 145.70, 156.35, 161.81 (*C*O), 165.23 (*C*O). HRMS (ESI) calcd. for $C_{130}H_{108}N_{18}Eu_2O_{24}S_4F_{12}$ [M-2OTf]$^{2+}$: 1481.2431 (^{151}Eu based), found 1481.2432. Calculated for $C_{132}H_{108}N_{18}O_{30}Eu_2F_{18}S_6$·2$H_2O$: C, 48.03; H, 3.42; N, 7.64%; Found: C, 47.24; H, 3.37; N, 7.47 %; **[$Eu_2(L1^{SS})_3$]** was synthesized, following the procedure for **[$Eu_2(L1^{RR})_3$]** with the

use of **L1^{SS}** instead, in 92% yield (0.150 g, 0.046 mmol): ^{1}H NMR (400 MHz, CD_3CN, 299 K, δ): 1.53 (s, br., 3 × 6H, C*H*$_3$), 4.92 (s, br., 3 × 2H, N-*H*), 5.25 (s, br., 3 × 2H, (CH_3)C*H*), 6.36 (s, br., 3 × 4H), 6.70 (s, br., 3 × 4H, phenyl-*H*), 6.74 (s, br., 3 × 4H, phenyl-*H*), 6.82 (s, br., 3 × 6H), 6.92 (s, br., 3 × 2H, N-*H*), 7.07 (s, br. 3 × 2H), 7.85 (s, br. 3 × 4H, phenyl-*H*). ^{13}C NMR (100.6 MHz, CD_3CN, 300 K, δ): 22.46 (*C*H_3), 52.37 (*C*H), 93.34, 93.80, 123.35, 126.52, 128.19, 128.44, 129.51, 136.93, 139.12, 143.63, 144.90, 145.77, 156.35, 161.83 (*C*O), 165.23 (*C*O). HRMS (ESI) calcd. for $C_{130}H_{108}N_{18}Eu_2O_{24}S_4F_{12}$ [M-2OTf]$^{2+}$: 1481.2431 (^{151}Eu based), found 1481.2433. Calculated for $C_{132}H_{108}N_{18}O_{30}Eu_2F_{18}S_6{\cdot}2H_2O$: C, 48.03; H, 3.42; N, 7.64%; Found: C, 47.49; H, 3.42; N, 7.54 %.

3{*N*,*N*'-(biphenyl-4,4'-diyl)bis[6-(*R*)-(1-phenylethyl-carbamoyl)-pyridine-2-dicarboxamide]}·2La·6(CF_3SO_3) [La$_2$(L1^{RR})$_3$] and 3{*N*,*N*'-(biphenyl-4,4'-diyl)bis[6-(*S*)-(1-phenylethylcarbamoyl)-pyridine-2-dicarboxamide]}·2La·6(CF_3SO_3) [La$_2$(L1^{SS})$_3$]

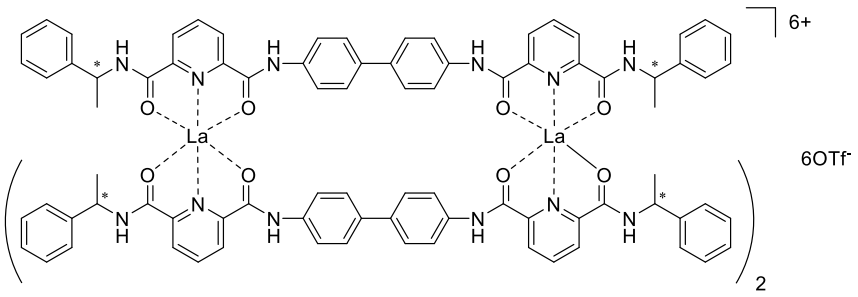

To a white suspension of **L1^{RR}** (0.050 g, 0.073 mmol, 1.5 equiv.) in a mixture of 6 mL of DCM/MeOH (12:1, v/v), a solution of La(CF_3SO_3)$_3$ (0.028 g, 0.048 mmol, 1 equiv.) in 3 mL of MeCN was added. The suspension was changed to yellow turbidity immediately. The reaction mixture was then refluxed for 16 h and the solid progressively dissolved to give a resulting homogeneous yellow solution. The solvent was removed under

reduced pressure. The solid was then washed with THF to give the desired product. **[$La_2(L1^{RR})_3$]**: (0.071 g, 0.022 mmol, 93% yield) ^{1}H NMR (400 MHz, CD_3CN, 298 K, δ): 1.75 (d, *J* = 8 Hz, 3 × 6H, C*H*$_3$), 5.08–5.16 (m, 3 × 2H, (CH_3)C*H*), 6.64 (d, *J* = 8 Hz, 3 × 4H, phenyl-*H*), 7.11–7.17 (m, 3 × 4H, phenyl-*H*), 7.18–7.23 (overlapping of two type of peaks, m, 3 × 4H, phenyl-*H* and m, 3 × 2H), 7.71 (d, *J* = 8 Hz, 3 × 4H, phenyl-*H*), 8.50–8.55 (m, 3 × 4H), 8.56–8.60 (m, 3 × 2H), 9.09 (d, *J* = 8 Hz, 3 × 2H, N-*H*), 10.32 (s, 3 × 2H, N-*H*). ^{13}C NMR (100.6 MHz, CD_3CN, 298 K, δ): 22.15 (*C*H_3), 53.71 (*C*(CH_3)H), 122.86 (*C*H), 127.38 (*C*H), 127.93 (*C*H), 128.63 (*C*H), 129.08 (*C*H), 130.05 (*C*H), 136.86, 139.19, 143.17, 144.54 (*C*H), 150.14, 150.79, 168.12 (*C*O), 168.95 (*C*O). HRMS (ESI) calcd. for $C_{129}H_{108}N_{18}La_2O_{21}S_3F_9$ [M-3OTf]$^{3+}$: 929.8355, found 929.8354. Calculated for $C_{132}H_{108}N_{18}O_{30}La_2F_{18}S_6{\cdot}5H_2O{\cdot}2CH_3OH$: C, 47.44; H, 3.74; N, 7.43%; Found: C, 46.14; H, 3.72; N, 7.32 %; **[$La_2(L1^{SS})_3$]** was synthesized, following the procedure for **[$La_2(L1^{RR})_3$]** with the use of **$L1^{SS}$** instead: (0.070 g, 0.022 mmol, 90% yield) ^{1}H NMR (400 MHz, CD_3CN, 298 K, δ): 1.75 (d, *J* = 8 Hz, 3 × 6H, C*H*$_3$), 5.09–5.16 (m, 3 × 2H, (CH_3)C*H*), 6.64 (d, *J* = 8 Hz, 3 × 4H, phenyl-*H*), 7.12–7.16 (m, 3 × 4H, phenyl-*H*), 7.18–7.23 (m, 3 × 4H, phenyl-*H;* m, 3 × 2H), 7.71 (d, *J* = 8 Hz, 3 × 4H, phenyl-*H*), 8.51 (t, *J* = 8 Hz, 3 × 2H), 8.56 (d, *J* = 8 Hz, 3 × 2H), 8.60 (d, *J* = 8 Hz, 3 × 2H), 9.09 (d, *J* = 8 Hz, 3 × 2H, N-*H*), 10.32 (s, 3 × 2H, N-*H*). ^{13}C NMR (100.6 MHz, CD_3CN, 299 K, δ): 22.16 (*C*H_3), 53.73 (*C*(CH_3)H), 122.88 (*C*H), 127.41 (*C*H), 127.96 (*C*H), 128.65 (*C*H), 129.11 (*C*H), 130.08 (*C*H), 136.87, 139.22, 143.18, 144.57 (*C*H), 150.16, 150.81, 168.15 (*C*O), 168.98 (*C*O). HRMS (ESI) calcd. for $C_{129}H_{108}N_{18}La_2O_{21}S_3F_9$ [M-3OTf]$^{3+}$: 929.8355, found 929.8352. Calculated for $C_{132}H_{108}N_{18}O_{30}La_2F_{18}S_6{\cdot}4H_2O$: C, 47.89; H, 3.53; N, 7.62%; Found: C, 47.45; H, 3.46; N, 7.53 %.

3{*N*,*N*'-(biphenyl-4,4'-diyl)bis[6-(*R*)-(2-phenylpropylcarbamoyl)-pyridine-2,6-dicarboxamide]}·2Eu·6(CF_3SO_3) [$Eu_2(L2^{RR})_3$] and 3{ *N*,*N*'-(biphenyl-4,4'-diyl)bis[6- (*S*)-(2-phenylpropylcarbamoyl)-pyridine-2,6-dicarboxamide]}·2Eu·6(CF_3SO_3) [$Eu_2(L2^{SS})_3$]

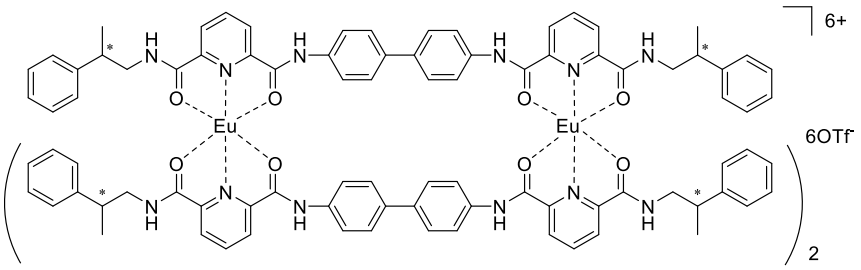

To a white suspension of **L2^{RR}** (0.107 g, 0.150 mmol, 1.5 equiv.) in a mixture of 13 mL of DCM/MeOH (12:1, v/v), a solution of $Eu(CF_3SO_3)_3$ (0.060 g, 0.100 mmol, 1 equiv.) in 5 mL of MeCN was added. The solution was changed to yellow turbidity immediately. The solution was then refluxed and the solid progressively dissolved to give a resulting homogeneous yellow solution. After for 16 h, the solvent was removed under reduced pressure. The solid was then washed with DCM to give the desired product. **[$Eu_2(L2^{RR})_3$]**: (0.154 g, 0.046 mmol, 91% yield), ^{1}H NMR (400 MHz, CD_3CN, 298 K, some of the peaks are shown two sets of peaks, **A** and **B**, respectively in ~1.1:1 ratio, δ): 1.02 (s, br., 3 × 6H, **C*H*$_3$**, **A**), 1.33 (s, br., 3 × 6H, **C*H*$_3$**, **B**), 2.56 (s, br., 3 × 2H, (CH_3)**C*H*,** **A**), 2.96 (s, br., 3 × 2H, (CH_3)**C*H*,** **B**), 3.77 (overlapping of three type of peaks, br. 3 × 2H, **C*H*H**, **A**, 3 × 2H, **CH*H***, **A** and 3 × 2H, **CH*H***, **B**), 4.01 (s, br. 3 × 2H, **C*H*H**, **B**), 4.82 (s, br. 3 × 2H, **N*H***, **A**), 4.96 (s, br. 3 × 2H, **N*H***, **B**), 6.36 (s, br. 3 × 4H, **A**), 6.64 (m, br. 3 × 4H, **B**), 7.06–7.31 (m, br. 3 × 18H, **A** and 3 × 18H **B**), 8.36 (s, br. 3 × 4H, **A**), 8.44 (s, br. 3 × 4H, **B**). ^{13}C NMR (100.6 MHz, CD_3CN, 298 K, some of the peaks are shown two sets of peaks, δ): 19.35 (***C*H*$_3$**), 19.63 (***C*H*$_3$**), 41.00 (***C*H***), 41.29 (***C*H***), 47.94 (***C*H*$_2$**), 47.96 (***C*H*$_2$**), 93.07, 93.09, 93.59, 93.89, 123.63, 127.71, 127.90, 128.00, 128.41, 128.48, 129.62, 129.70, 137.26,

137.30, 139.33, 139.38, 144.36, 144.41, 144.55, 145.42, 145.88, 156.35, 161.94 (***C*O**), 162.38 (***C*O**), 165.13 (***C*O**), 165.26 (***C*O**). HRMS (ESI) calcd. for $C_{136}H_{120}N_{18}Eu_2O_{24}S_4F_{12}$ $[M\text{-}2OTf]^{2+}$: 1523.2900 (^{151}Eu based), found 1523.2905. Calculated for $C_{138}H_{120}N_{18}O_{30}Eu_2F_{18}S_6 \cdot 2H_2O$: C, 48.97; H, 3.69; N, 7.45%; Found: C, 48.47; H, 3.63; N, 7.36 %; **$[Eu_2(L2^{SS})_3]$** was synthesized, following the procedure for **$[Eu_2(L2^{RR})_3]$** with the use of **$L2^{SS}$** instead, in 92% yield (0.154 g, 0.046 mmol): ^{1}H NMR (400 MHz, CD_3CN, 297 K, some of the signals are shown in two sets of peaks, **A** and **B**, respectively in ~ 1.1:1 ratio, δ): 0.90 (s, br., 3 × 6H, **C*H*₃**, **A**), 1.32 (s, br., 3 × 6H, **C*H*₃**, **B**), 2.54 (s, br., 3 × 2H, **C*H*, A**), 2.96 (s, br., 3 × 2H, **C*H*, B**), 3.74 (s, br. 3 × 2H, **C*H*H**, **A**), 3.78 (s, br., 3 × 2H, **CH*H***, **A** and 3 × 2H, **CH*H***, **B**), 4.02 (s, br. 3 × 2H, **C*H*H**, **B**), 4.73 (s, br. 3 × 2H, **N*H***, **A**), 4.87 (s, br. 3 × 2H, **N*H***, **B**), 6.33 (s, br. 3 × 4H, **A**), 6.64 (m, br. 3 × 4H, **B**), 7.07–7.31 (m, br. 3 × 18H, **A** and m, br. 3 × 18H **B**), 8.37 (s, br. 3 × 4H, **A**), 8.45 (s, br. 3 × 4H, **B**). ^{13}C NMR (100.6 MHz, CD_3CN, 298 K, some of the peaks are shown into two sets of peaks, δ): 19.35 (***C*H₃**), 19.63 (***C*H₃**), 41.00 (***C*H**), 41.29 (***C*H**), 47.93 (***C*H₂**), 47.98 (***C*H₂**), 93.13, 93.18, 93.71, 93.91, 123.63, 127.88, 127.91, 128.00, 128.41, 128.49, 129.62, 129.70, 137.23, 137.27, 139.34, 139.39, 144.36, 144.40, 144.60, 145.43, 145.90, 156.32, 161.91 (***C*O**), 162.36 (***C*O**), 165.13 (***C*O**), 165.26 (***C*O**). HRMS (ESI) calcd. for $C_{136}H_{120}N_{18}Eu_2O_{24}S_4F_{12}$ $[M\text{-}2OTf]^{2+}$: 1523.2900 (^{151}Eu based), found 1523.2889. Calculated for $C_{138}H_{120}N_{18}O_{30}Eu_2F_{18}S_6 \cdot 2H_2O$: C, 48.97; H, 3.69; N, 7.45%; Found: C, 48.24; H, 3.60; N, 7.31 %.

3{*N*,*N*'-(biphenyl-4,4'-diyl)bis[6-(*R*)-(2-phenylpropylcarbamoyl)-pyridine-2,6-dicarboxamide]}·2La·6(CF_3SO_3) $[La_2(L2^{RR})_3]$ and 3{ *N*,*N*'-(biphenyl-4,4'-diyl)bis[6-(*S*)-(2-phenylpropylcarbamoyl)-pyridine-2,6-dicarboxamide]}·2La·6(CF_3SO_3) $[La_2(L2^{SS})_3]$

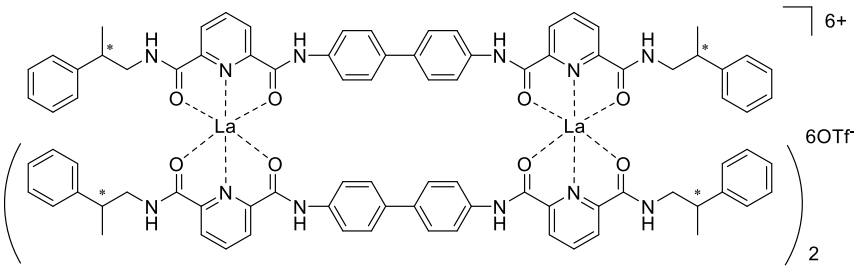

To a white suspension of **L2^{RR}** (0.040 g, 0.056 mmol, 1.5 equiv.) in a mixture of 6 mL of DCM/MeOH (8:1, v/v), a solution of $La(CF_3SO_3)_3$ (0.022 g, 0.037 mmol, 1 equiv.) in 8 mL of MeCN was added. The suspension was changed to yellow turbidity immediately. The reaction mixture was then refluxed for 16 h and the solid progressively dissolved to give a resulting homogeneous yellow solution. The solvent was removed under reduced pressure. The solid was then washed with DCM to give the desired product. **[La_2(L2^{RR})$_3$]**: (0.055 g, 0.016 mmol, 89% yield) ^{1}H NMR (400 MHz, CD_3CN, 298 K, some of the signals are shown in two sets of peaks, **A** and **B**, respectively in ~1:1.1 ratio, δ): 1.02 (s, br., 3 × 6H, A), 1.18 (s, br., 3 × 6H, B), 2.77 (s, br., 3 × 2H, B), 2.93 (s, br., 3 × 2H, A), 3.40 (s, br., 3 × 6H), 3.57 (s, br., 3 × 2H), 6.72 (s, br. 3 × 8H, A), 7.05 (s, br., 3 × 8H, B), 7.18–7.30 (m, 3 × 12H), 7.82 (s, br. 3 × 8H), 8.40 (s, br., 3 × 4H, B), 8.59 (s, br., 3 × 4H, A), 8.75 (s, br., 3 × 4H, B), 8.87 (s, br., 3 × 4H, A), 10.47 (s, br., 3 × 4H). ^{13}C NMR (100.6 MHz, CD_3CN, 298 K, some of the peaks cannot be shown clearly due to limited solubility, δ): 19.85, 19.90, 40.29, 40.51, 49.19, 49.31, 122.97, 123.00, 127.29, 127.35, 128.26, 128.33, 128.46, 128.78, 130.11, 137.01, 139.29, 144.82, 144.89, 150.43, 151.16, 151.30. HRMS (ESI) calcd. for $C_{135}H_{120}N_{18}La_2O_{21}S_3F_9$ $[M\text{-}3OTf]^{3+}$: 957.8668, found 957.8670. Calculated for $C_{138}H_{120}N_{18}O_{30}La_2F_{18}S_6{\cdot}4H_2O$: C, 48.83; H, 3.80; N, 7.43%; Found: C, 48.02; H, 3.73; N, 7.30 %; **[La_2(L2^{SS})$_3$]** was synthesized, following the procedure for **[La_2(L2^{RR})$_3$]** with the use of **L2^{SS}** instead, in 85% yield (0.052 g, 0.016

mmol): ^{1}H NMR (400 MHz, CD_3CN, 298 K, some of the signals are shown in two sets of peaks, **A** and **B**, respectively in ~1:1.1 ratio, δ): 1.02 (s, br., 3 × 6H, A), 1.16 (s, br., 3 × 6H, B), 2.77 (s, br., 3 × 2H, B), 2.93 (s, br., 3 × 2H, A), 3.39 (s, br., 3 × 6H), 3.57 (s, br., 3 × 2H), 6.72 (s, br. 3 × 8H, A), 7.04 (s, br., 3 × 8H, B), 7.17–7.39 (m, 3 × 12H), 7.82 (s, br. 3 × 8H), 8.40 (s, br., 3 × 4H, B), 8.58 (s, br., 3 × 4H, A), 8.75 (s, br., 3 × 4H, B), 8.89 (s, br., 3 × 4H, A), 10.47 (s, br., 3 × 4H). ^{13}C NMR (100.6 MHz, CD_3CN, 298 K, some of the peaks cannot be shown clearly due to limited solubility, δ): 19.87, 40.24, 40.49, 49.14, 49.37, 122.91, 123.05, 127.32, 128.28, 128.49, 128.76, 130.14, 134.20, 137.02, 139.36, 144.86, 150.44, 151.33, 168.23, 168.41. HRMS (ESI) calcd. for $C_{135}H_{120}N_{18}La_2O_{21}S_3F_9$ $[M\text{-}3OTf]^{3+}$: 957.8668, found 957.8662. Calculated for $C_{138}H_{120}N_{18}O_{30}La_2F_{18}S_6{\cdot}4H_2O$: C, 48.83; H, 3.80; N, 7.43%; Found: C, 48.00; H, 3.78; N, 7.31 %.

3{*N*,*N*'-(biphenyl-4,4'-diyl)bis[6-(*S*)-(2-phenylpropylcarbamoyl)-pyridine-2,6-dicarboxamide]}·2Gd·6(CF_3SO_3) [$Gd_2(L2^{SS})_3$]

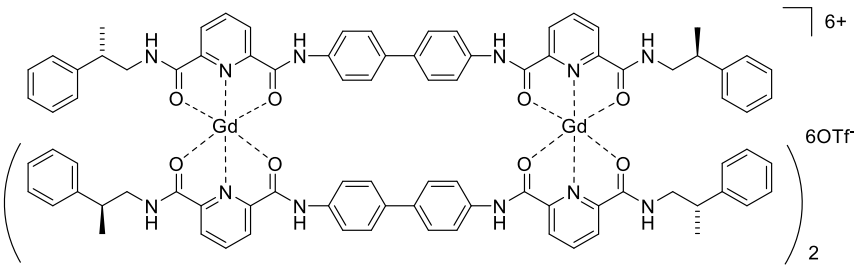

To a white suspension of **L2^{SS}** (0.050 g, 0.056 mmol, 1.5 equiv.) in a mixture of 6 mL of DCM/MeOH (12:1, v/v), a solution of $Gd(CF_3SO_3)_3$ (0.028 g, 0.047 mmol, 1 equiv.) in 8 mL of MeCN was added. The suspension was changed to yellow turbidity immediately. The reaction mixture was then refluxed for 16 h and the solid progressively dissolved to give a resulting homogeneous yellow solution. The solvent was removed under reduced pressure. The solid was then washed with DCM to give the desired product.

[$Gd_2(L2^{SS})_3$]: (0.071 g, 0.021 mmol, 90% yield) HRMS (ESI) calcd. for $C_{135}H_{120}N_{18}Gd_2O_{21}S_3F_9$ $[M\text{-}3OTf]^{3+}$: 970.5464, found 970.5457.

2a.4.2 X-ray crystallography

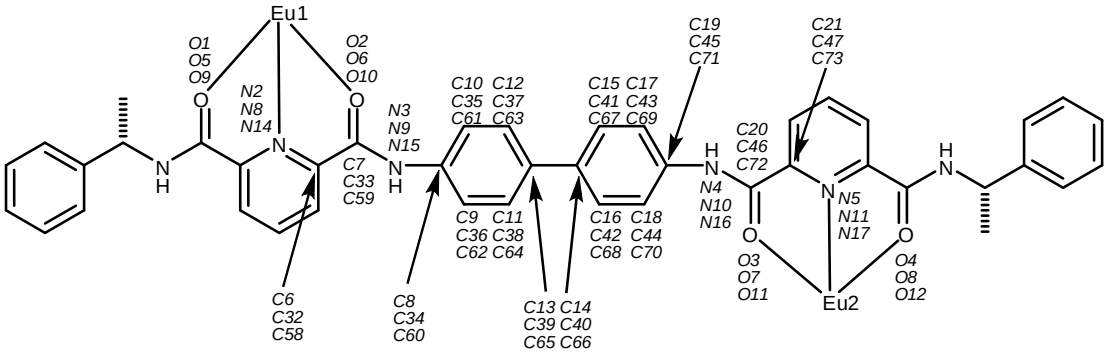

Chart S2a-1. Selected atomic numbering scheme of **[$Eu_2(L1^{SS})_3$]$(CF_3SO_3)_6$** in strand 1(top), 2 (middle), and 3 (bottom) for X-ray crystallography. The corresponding hydrogen atoms, H(number)A, with the same number of the attached carbons are not shown.

Table S2a-1. Selected structural parameters for **[$Eu_2(L1^{SS})_3$]$(CF_3SO_3)_6$**

		Distances(Å)		
	Distance(Å)	Strand 1	Strand 2	Strand 3
Eu(1)–N		N(2), 2.566(5)	N(8), 2.537(5)	N(14), 2.595(5)
Eu(1)–O		O(2), 2.438(5)	O(5), 2.404(5)	O(9), 2.380(5)
Eu(1)–O		O(1), 2.438(5)	O(6), 2.407(5)	O(10), 2.424(4)
Eu(2)–N		N(5), 2.557(6)	N(11), 2.532(5)	N(17), 2.553(5)
Eu(2)–O		O(3), 2.435(4)	O(7), 2.434(4)	O(11), 2.441(5)
Eu(2)–O		O(4), 2.427(5)	O(8), 2.409(5)	O(12), 2.429(5)
Eu(1)–Eu(2)	15.055(1)			
Bite angles				
	angles(°)			angles(°)
O(1)–Eu(1)–N(2)	62.96(17)	O(4)–Eu(2)–N(5)		63.87(17)
O(5)–Eu(1)–N(8)	63.87(18)	O(8)–Eu(2)–N(11)		62.82(16)
O(9)–Eu(1)–N(14)	63.70(16)	O(12)–Eu(2)–N(17)		62.82(18)

N(2)–Eu(1)–O(2)	62.92(16)	N(5)–Eu(2)–O(3)	67.17(18)
N(8)–Eu(1)–O(6)	62.77(17)	N(11)–Eu(2)–O(7)	63.47(16)
N(14)–Eu(1)–O(10)	62.81(16)	N(17)–Eu(2)–O(11)	64.06(17)
O(1)–Eu(1)–O(5)	77.70(16)	O(4)–Eu(2)–O(8)	76.17(17)
O(5)–Eu(1)–O(9)	75.94(16)	O(8)–Eu(2)–O(12)	73.51(16)
O(9)–Eu(1)–O(1)	75.64(16)	O(12)–Eu(2)–O(4)	74.20(16)
N(2)–Eu(1)–N(8)	119.46(17)	N(5)–Eu(2)–N(11)	122.53(18)
N(8)–Eu(1)–N(14)	121.88(17)	N(11)–Eu(2)–N(17)	117.94(17)
N(14)–Eu(1)–N(2)	117.61(15)	N(17)–Eu(2)–N(5)	119.00(18)
O(2)–Eu(1)–O(6)	76.01(16)	O(3)–Eu(2)–O(7)	76.01(14)
O(6)–Eu(1)–O(10)	77.39(15)	O(7)–Eu(2)–O(11)	73.34(15)
O(10)–Eu(1)–O(2)	76.41(16)	O(11)–Eu(2)–O(3)	73.63(15)

Torsional angles

Strand 1	angles(°)	Strand 2	angles(°)	Strand 3	angles(°)
N(2)–C(6)–C(7)–O(12)	-22.97(103)	N(8)–C(32)–C(33)–O(6)	-19.52(107)	N(14)–C(58)–C(59)–O(10)	-18.38(100)
C(6)–C(7)–N(3)–C(8)	-175.63(70)	C(32)–C(33)–N(9)–C(34)	-171.78(72)	C(58)–C(59)–N(15)–C(60)	-164.52(72)
C(7)–N(3)–C(8)–C(9)	-13.31(135)	C(33)–N(9)–C(34)–C(35)	160.48(77)	C(59)–N(15)–C(60)–C(61)	166.37(76)
C(11)–C(13)–C(14)–C(15)	150.24(75)	C(37)–C(39)–C(40)–C(41)	-44.15(102)	C(63)–C(65)–C(66)–C(67)	-35.42(103)
C(17)–C(19)–N(4)–C(20)	-5.56(126)	C(43)–C(45)–N(10)–C(46)	7.90(115)	C(69)–C(71)–N(16)–C(72)	-8.10(104)
C(19)–N(4)–C(20)–C(21)	-167.72(71)	C(45)–N(10)–C(46)–C(47)	-176.32(69)	C(71)–N(16)–C(72)–C(73)	-167.21(59)
O(3)–C(20)–C(21)–N(5)	-8.27(99)	O(7)–C(46)–C(47)–N(11)	-21.38(103)	O(11)–C(72)–C(73)–N(17)	-17.69(92)

C–H···C	Distance(Å) of (H···C)	Distance(Å) of (C···C)	Angles(°) of (C–H–C)
C38–H38A···C10	2.987(8)	3.800(11)	146.81(51)
C64–H64A···C35	2.874(8)	3.728(11)	153.19(48)
C11–H11A···C61	2.908(8)	3.702(12)	144.23(56)
C67–H67A···C18	2.897(5)	3.788(9)	160.92(48)
C15–H15A···C44	3.154(6)	3.997(10)	151.76(44)
C41–H41A···C70	2.989(9)	3.851(12)	154.92(50)

Table S2a-2. Crystal data and structure refinement of **$[Eu_2(L1^{SS})_3](CF_3SO_3)_6$**, **$[Eu_2(L2^{RR})_3](CF_3SO_3)_6$**, and **$L2^{RR}$**

	$[Eu_2(L1^{SS})_3](CF_3SO_3)_6$,	**$[Eu_2(L2^{RR})_3](CF_3SO_3)_6$**	**$L2^{RR}$**
Empirical formula	$C_{126}H_{108}Eu_2N_{18}O_{12}$	$C_{132}H_{120}Eu_2N_{18}O_{12}$	C_{44} $H_{40}N_6O_4$
Formula weight	2370.22	2454.38	716.82
Temperature	296(2) K	296(2) K	296(2) K
Wavelength	0.71073 Å	0.71073 Å	0.71073 Å
Crystal system, space group	Orthorhombic, *P* 2_1 2_1 2	Triclinic, *P*-1	Monoclinic, *P* 2_1
Unit cell dimensions	a = 26.0606(10), b = 28.4219(9), c = 23.3299(9), α = β = γ = 90	a = 16.6790(5), b = 20.3099(6), c = 24.4218(8), α = 87.025(2), β = 70.961(2), γ = 89.269(2)	a = 10.3285(6), b = 17.8133(12), c = 10.5822(7), α = 90, β = 100.506(4) α = 90
Volume	17280.3(11) $Å^3$	7809.7(4) $Å^3$	1914.3(2) $Å^3$
Z, Calculated density	4, 0.911 mg/m^3	2, 1.044 mg/m^3	2, 1.244 mg/m^3
Absorption coefficient	0.765 mm^{-1}	0.849 mm^{-1}	0.081 mm^{-1}
F(000)	4848	2520	756
Crystal size	0.20 x 0.46 x 0.48 mm	0.04 x 0.16 x 0.24 mm	0.04 x 0.36 x 0.56 mm
θ range for data collection	2.60 to 25.35 deg	2.58 to 26.37 deg	2.78 to 24.71 deg
Limiting indices	$-31 \le h \le 24$, $-34 \le k \le 34$, $-28 \le l \le 28$	$-20 \le h \le 20$, $-25 \le k \le 25$, $-30 \le l \le 30$	$-12 \le h \le 12$, $-20 \le k \le 20$, $-12 \le l \le 12$
Reflections collected / unique	144075/31600	196288/31901	23536 / 6477
Absorption correction	Semi-empirical from equivalents	Semi-empirical from equivalents	Semi-empirical from equivalents
Refinement method	Full-matrix least-squares on F^2	Full-matrix least-squares on F^2	Full-matrix least-squares on F^2
Data/restraints/ parameters	31600 / 0 / 1261	31901 / 6 / 1161	6477 / 2 / 487
Goodness-of-fit on F^2	1.010	0.952	1.021

Final R indices [I>2σ(I)]	R_1 = 0.0607, wR_2 = 0.0986	R_1 = 0.0743, wR_2 = 0.1956	R_1 = 0.0583, wR_2 = 0.1407
R indices (all data)	R_1 = 0.1062, wR_2 = 0.1073	R_1 = 0.1465, wR_2 = 0.2181	R_1 = 0.1163, wR_2 = 0.1712
Flack parameter	0.018(8)	N/A	0(2)
Extinction coefficient	N/A	N/A	0.0054(14)
Largest diff. peak and hole	0.749 and -0.355 Å^{-3}	1.034 and -0.622 Å^{-3}	0.253 and -0.193 Å^{-3}

Note: All data were collected at ambient temperature. **$[Eu_2(L1^{SS})_3](CF_3SO_3)_6$**, and **$[Eu_2(L2^{RR})_3](CF_3SO_3)_6$** were refined using PLATON/SQUEEZE, as such parameters such as empirical formula, formula weight, calculated density, etc. only reflect the refined structure as is.

Crystal data for Tb_2(**$L1^{SS}$**)$_3$: *formula*, M_r = 2372.04, *crystal system*, space group P 2_1 2_1 2, Z = 4, a = 26.075(3) Å, b = 28.363(4)Å, c = 23.396(3)Å, α =90°, β = 90°, γ = 90°, V = 17304(4) Å^3, μ(Mo$_{K\alpha}$) = 0.857 mm^{-1}, ρ_{calc} = 0.911 mgm^{-3}, T = 296(2) K. The crystallographic data for the structural analyses have been deposited with the Cambridge Crystallographic Data Centre, CCDC No. 1009616, and the data can be obtained free of charge via www.ccdc.cam.ac.uk/data_request/cif.

Information	Identifier from cif file
Empirical formula	$C_{126}H_{96}N_{18}O_{12}Tb_2$
Formula weight	2372.04
Temperature/K	296(2)
Crystal system	orthorhombic
Space group	$P2_12_12$
a/Å	26.075(3)
b/Å	28.363(4)
c/Å	23.396(3)
α/°	90
β/°	90

γ/°	90
Volume/Å^3	17304(4)
Z	4
ρ_{calc}g/cm^3	0.911
μ/mm^{-1}	0.857
F(000)	4816.0
Crystal size/mm^3	0.480 × 0.320 × 0.200
Radiation	MoKα (λ = 0.71073)
2Θ range for data collection/°	5.202 to 50.7
Index ranges	-29 ≤ h ≤ 31, -34 ≤ k ≤ 29, -28 ≤ l ≤ 28
Reflections collected	210003
Independent reflections	31661 [R_{int} = 0.0893, R_{sigma} = 0.0808]
Data/restraints/parameters	31661/17/1363
Goodness-of-fit on F^2	0.941
Final R indexes [I>=2σ (I)]	R_1 = 0.0524, wR_2 = 0.1159
Final R indexes [all data]	R_1 = 0.0774, wR_2 = 0.1240
Largest diff. peak/hole / e Å^{-3}	0.59/-0.33
Flack parameter	0.002(5)

Tb_2(**L2^{SS}**)$_3$	Shape measure (°)	
	Tricapped trigonal prism (D_{3h})	Capped square antiprism (C_{4v})
Tb1	7.04	10.89
Tb2	6.77	10.43

Table S2a-3. Results of the Shape Analysis for Tb_2(**L1^{SS}**)$_3$ helix.

Shape analysis was performed by the software developed by Raymond's group.[24, 25]. The coordination geometry of the Tb_2(**L1^{SS}**)$_3$: helix can be best described as tricapped trigonal prism.

2a.4.3 Photophysical measurement

Table S2a-1. A summary of selected photophysical properties, UV-Vis absorption and luminescence data, of **[Eu$_2$(L)$_3$](CF$_3$SO$_3$)$_6$** in acetonitrile solution[a]

	λ_{abs}^{max}	ε^{max}	λ_{em}^{max}	τ

	(nm)	($L \cdot mol^{-1} \cdot cm^{-1}$)	(nm)	(ms)
$[Eu_2(L1^{RR})_3](CF_3SO_3)_6$	340	102300	616	0.22
$[Eu_2(L1^{SS})_3](CF_3SO_3)_6$	340	107000	616	0.22
$[Eu_2(L2^{RR})_3](CF_3SO_3)_6$	340	99000	616	0.22
$[Eu_2(L2^{SS})_3](CF_3SO_3)_6$	340	98000	616	0.22
$[La_2(L1^{SS})_3](CF_3SO_3)_6$	338	103000	449[b]	0.014[b]

[a]Using a 1mm cuvette and filter 455 nm. [b]Measurement performed at 77 K in 1:4 of MeOH/EtOH and using a 10 mm cuvette.

2a.5 References

1. Wong, H.-Y.; Lo, W.-S.; Yim, K.-H.; Law, G.-L.; Chirality and chiroptics of lanthanide molecular and supramolecular assemblies. *Chem* **2019**, *5*, 3058-3095.
2. Albrecht, M.; Schmid, S.; Dehn, S.; Wickleder, C.; Zhang, S.; Bassett, A. P.; Pikramenou, Z.; Frohlich, R. Diastereoselective formation of luminescent dinuclear lanthanide(iii) helicates with enantiomerically pure tartaric acid derived bis(b-diketonate) ligands. *New J. Chem.* **2007**, *31*, 1755–1762.
3. Stomeo, F.; Lincheneau, C.; Leonard, J. P.; O'Brien, J. E.; Peacock, R. D.; McCoy, C. P.; Gunnlaugsson, T. (2009). Metal-directed synthesis of enantiomerially pure dimetallic lanthanide luminescent triple-stranded helicates. *J. Am. Chem. Soc*. **2009**, *131*, 9636–9637.
4. Lincheneau, C.; Peacock, R. D.; Gunnlaugsson, T. Europium directed synthesis of enantiomerically pure dimetallic luminescent "squeezed" triple-stranded helicates; solution studies. *Chem. Asian J.* **2010**, *5*, 500–504.

5. Yan, L.-L.; Tan, C.-H.; Zhang, G.-L.; Zhou, L.-P.; Bünzli, J.-C.; Sun, Q.-F. Stereocontrolled self-assembly and self-sorting of luminescent europium tetrahedral cages. *J. Am. Chem. Soc.* **2015**, 137, 8550–8555.

6. Yeung, C.-T.; Yim, K.-H.; Wong, H.-Y.; Pal, R.; Lo, W.-S.; Yan, S.-C.; Wong, Y.-M. M.; Yufit, D.; Smiles, D.E.; McCormick, L. J.; Teat, S. J.; Shuh, D. K.; Wong, W.-T.; Law, G.-L. Chiral transcription in self-assembled tetrahedral Eu_4L_6 chiral cages displaying sizable circularly polarized luminescence. *Nat. Commun.* **2017**, *8*, 1128.

7. Li, X.-Z.; Zhou, L.-P.; Yan, L.-L.; Yuan, D.-Q.; Lin, C.-S.; and Sun, Q.-F. Evolution of luminescent supramolecular lanthanide $M_{2n}L_{3n}$ complexes from helicates and tetrahedra to cubes. *J. Am. Chem. Soc.* **2017**, *139*, 8237–8244.

8. Kitchen, J. A. Lanthanide-based self-assemblies of 2,6-pyridyldicarboxamide ligands: recent advances and applications as next-generation luminescent and magnetic materials. *Coord. Chem. Rev.* **2017**, *340*, 232–246.

9. Iwamura, M.; Kimura, Y.; Miyamoto, R.; Nozaki, K. Chiral sensing using an achiral europium(III) complex by induced circularly polarized luminescence. *Inorg. Chem.* **2012**, *51*, 4094–4098.

10. Okutani, K.; Nozaki, K.; Iwamura, M. Specific chiral sensing of amino acids using induced circularly polarized luminescence of bis(diimine)dicarboxylic acid europium(III) complexes. *Inorg. Chem.* **2014**, *53*, 5527–5537.

11. Uchida, T. A.; Nozaki, K.; Iwamura, M. Chiral sensing of various amino acids using induced circularly polarized luminescence from europium(III) complexes of phenanthroline dicarboxylic acid derivatives. *Chem. Asian J.* **2016**, *11*, 2415–2422.

12. Smith, D. G.; Pal, R.; and Parker, D. Measuring equilibrium bicarbonate concentrations directly in cellular mitochondria and in human serum using europium/terbium emission intensity ratios. *Chemistry* **2012**, *18*, 11604–11613.

13. Neil, E. R.; Fox, M. A.; Pal, R.; Palsson, L. O.; O'Sullivan, B. A.; and Parker, D. Chiral probe development for circularly polarised luminescence: comparative study of structural factors determining the degree of induced CPL with four heptacoordinate europium(III) complexes. *Dalton Trans.* **2015**, *44*, 14937–14951.

14. Carr, R.; Di Bari, L.; Lo Piano, S.; Parker, D.; Peacock, R. D.; and Sanderson, J. M. A chiral probe for the acute phase proteins alpha-1-acid glycoprotein and alpha-1-antitrypsin based on europium luminescence. *Dalton Trans.* **2012**, *41*, 13154–13158.

15. Shuvaev, S.; Suturina, E. A.; Mason, K.; and Parker, D. Chiral probes for alpha1-AGP reporting by species-specific induced circularly polarised luminescence. *Chem. Sci.* **2018**, *9*, 2996–3003.

16. Howson, S. E.; Scott, P. Approaches to the synthesis of optically pure helicates. *Dalton Trans.* **2011**, *40*, 10268–10277.

17. Perret-Aebi, L.-E.; Zelewsky, A. V.; Neels, A. Diastereoselective preparation of Cu(I) and Ag(I) double helices by the use of chiral bis-bipyridine ligands. *New J. Chem.* **2009**, *33*, 462-465.

18. Albrecht, M. How Do They Know? Influencing the relative stereochemistry of the complex units of dinuclear triple-stranded helicate-type complexes. *Chem. Eur. J.* **2000**, *6*, 3485 – 3489.

19. Barry, D. E.; Caffrey, D. F.; Gunnlaugsson, T. Lanthanide-directed synthesis of

luminescent self-assembly supramolecular structures and mechanically bonded systems from acyclic coordinating organic ligands. *Chem. Soc. Rev.* **2016**, *45*, 3244.

20. Yeung, C.-T.; Chan, W. T. K.; Yan, S.-C.; Yu, K.-L.; Yim, K.-H.; Wong, W.-T.; Law, G.-L. Lanthanide supramolecular helical diastereoselective breaking induced by point chirality: mixture or *P*-helix, *M*-helix. *Chem. Commun.* **2015**, *51*, 592-595.

21. Lessmann, J. L.; Horrocks, W. D. Supramoelcular coordination chemistry in aqueous solution: lanthanide ion-induced triple helix formation. *Inorg. Chem.* **2000**, *39*, 3114-3124.

22. Tanase, S.; Gallego, P. M.; Gelder, R.; Fu, W. T. Synthesis, crystal structure and photophysical properties of europium(III) and terbium(III) complexes with pyridine-2,6-dicarboxamide. *Inorg. Chim. Acta* **2007**, *360*, 102-108.

23. Suezawa, H.; Ishihara, S.; Umezawa, Y.; Tsuboyama, S.; Nishio, M. The aromatic CH/π hydrogen bond as an important factor in determining the relative stability of diastereomeric salts relevant to enantiomeric resolution - a crystallographic database study. *Eur. J. Org. Chem.* **2004**, 4816-4822

24. Xu, J.; Radkov, E.; Zieglar, M.; Raymond, K. N. Plutonium(IV) sequestration: structural and thermodynamic evaluation of the extraordinarily stable cerium(IV) hydroxypyridinonate complexes[1]. *Inorg. Chem.* **2000**, *39* (18), 4156-4164.

25. Daumann, L. J.; Tatum, D. S.; Andolina, C. M.; Pacold, J. I.; D'Aléo, A.; Law, G.-L.; Xu, J.; Raymond, K. N. Effects of ligand geometry on the photophysical properties of photoluminescent Eu(III) and Sm(III) 1-hydroxypyridin-2-one

complexes in aqueous solution. *Inorg. Chem.* **2016**, *55* (1) 114-124.

Chapter 2b: Helicate-to-tetrahedron transformation of chiral lanthanide supramolecular complexes

2b.1 Introduction

2b.1.1 Induced structural change of supramolecules

Self-assembly supramolecular complexes have been proven to be an excellent candidate for various application such as catalysts[1,2] and luminescent sensors.[3,4] The applications of these self-assembled complex are all structural dependent and in-depth investigation of ligand design principle was performed.[5] Beyond the ligand design principles, understanding the factors that affect the structural formation of self-assembled complexes is important for engineering functional supramolecular complexes. In terms of lanthanide systems, recent research has been demonstrated that the formation of supramolecular structures is governed by five factors including concentration,[6,7] anion and solvent,[8,9] ionic radii of cation,[10,11] stoichiometric [ratio12-14] and UV.[15] This chapter will focus on concentration- and cationic radii dependent supramolecular formation.

2b.1.2 Concentration-dependent supramolecular formation

Generally, lanthanide ions coordinate with organic ligands by weak non-covalent interaction. Upon self-assembly of lanthanide ions with ligands, different

supramolecular products can co-exist in solution state if there is no clear thermodynamic preference. Due to the labile feature of lanthanides, the supramolecular products can be changed from one to another depending on the external environment. In the case of concentration effect, increasing either complex or ligand concentration can promote the formation of higher order supramolecular products due to the aggregation of building blocks.[16] An example is shown in figure 2b-1. Ln_2L_3 helicate was formed at low ligand concentration (6mM). When ligand concentration was increased to 48 mM, higher ordered Ln_4L_6 tetrahedron was formed.[17]

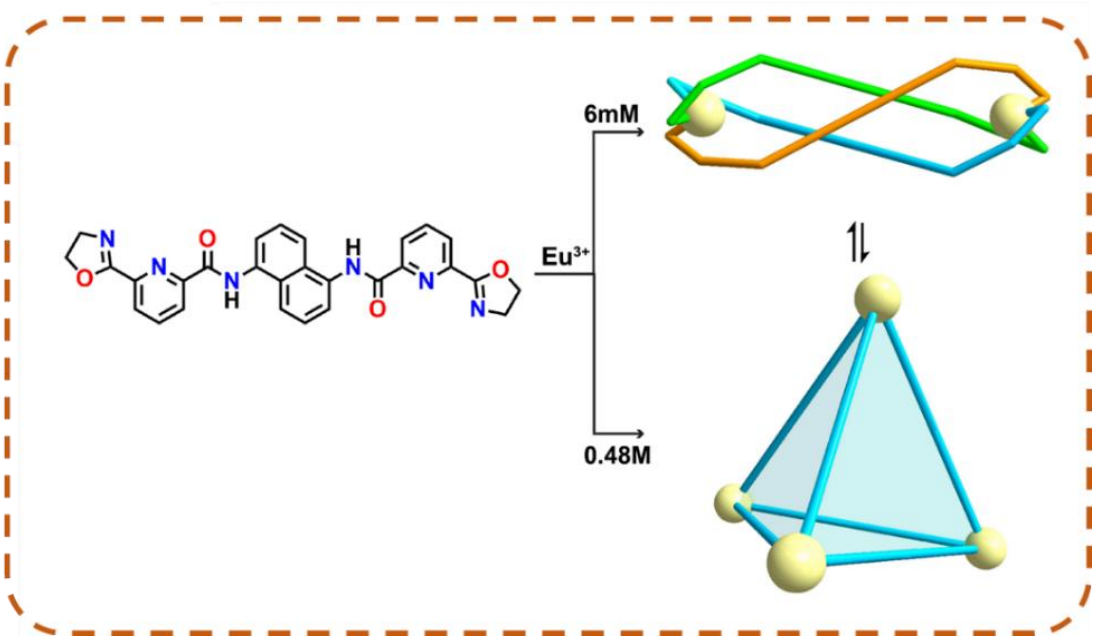

Figure 2b-1. *Concentration supramolecular formation reported by Sun's and co-workers.*[17]

2b.1.3 Cationic radii-dependent supramolecular formation

Unlike preorganized ligand such as cyclen, the coordinating sites of dipodal ligands and tripodal ligands are not well defined.[18-20] Slight change in reaction condition may lead to a different supramolecular product. As mentioned in chapter 1,

lanthanide ions are considered as having similar ionic radii and thus should exhibited similar reactivity profile. However, recent research has demonstrated that the cationic radii of lanthanide ions would affect the self-assembly process. Differences in ionic radii may affect the binding between ligands and metal ions, leading to different supramolecular products. One of the examples was shown in figure 2b-2. Coordination of ligand with light lanthanide led to the formation of cubane core, while the use of heavy lanthanide will lead to the formation of dimer core.[21]

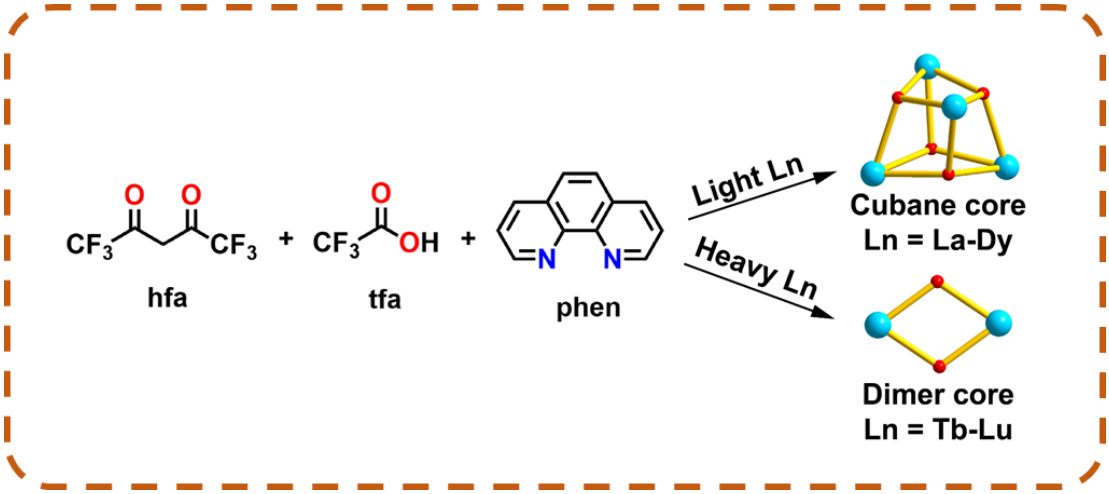

Figure 2b-2. *Cationic radii-dependent supramolecular formation reported by our group.*[21]

2b.1.4 Scope of study

Recent research has reported that the offset distance of coordination units leads to an influence on the supramolecular formation. In this chapter, two pairs of new C_2-symmetric bis-tridentate ligands **L3** and **L4** were designed and synthesized. The offset distance of the coordination units in **L1**, **L3** and **L4** remained unchanged, and the effect of linker length was investigated. By varying the length of the linker, supramolecular transformation was observed for **L3**. Effect of concentration and cationic radii towards supramolecular formation will be also examined.

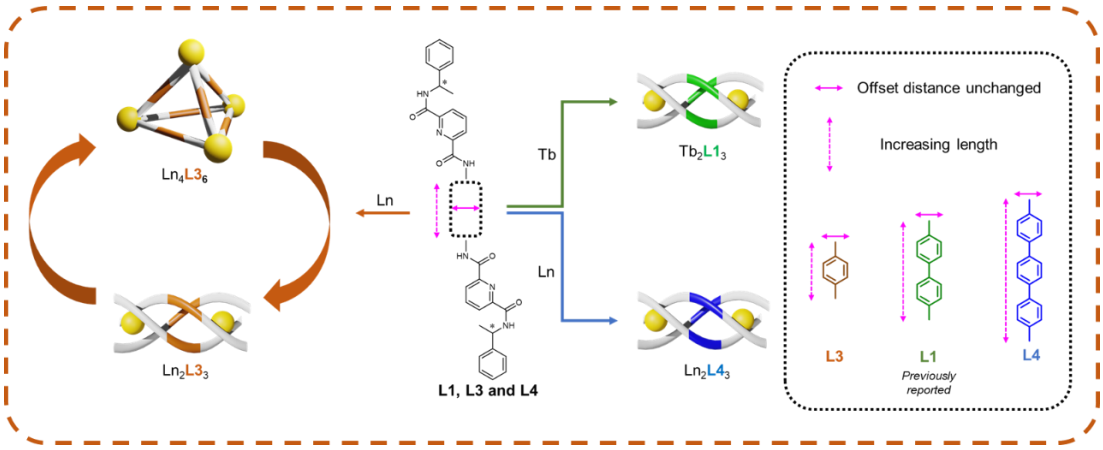

Figure 2b-3. *Supramolecular formation of **L1**, **L2** and **L3**.*

2b.2 Result and discussion

2b.2.1 Design and synthesis of L3 and L4

In the previous chapter, **L1** was found to form enantiomeric pure lanthanide bimetallic triple helicate induced by point chirality effect. Based on this result, the length of the central bridging linker was varied and the coordinating sites was kept to the same. The structures of ligands were shown in figure 2b-4.

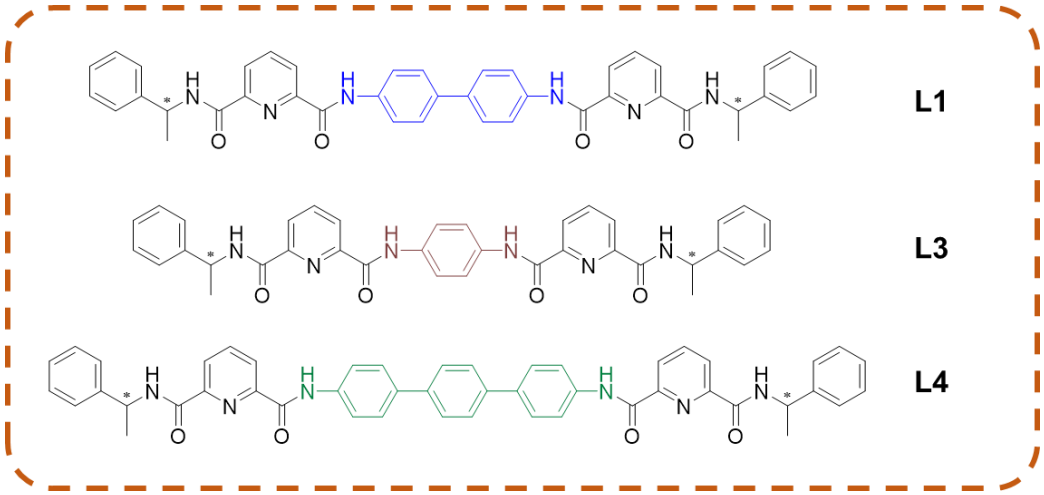

Figure 2b-4. *Ligand structures of **L1**, **L3** and **L4**.*

Similar to the design of **L1**, pyridine-2,6-dicarboxamide (pcam) moieties were employed as coordinating units in **L3** and **L4**, which tends to form stable nine-coordinated lanthanide complexes.[22] The shorter ligand **L3** was prepared by connecting two chiral metal chelating pcam moieties with a monophenyl linker. For **L4**, a longer triphenyl linker was employed. Compare the ligand design of **L1** with **L3** and **L4**, the offset distance of two chelating moieties did not change and we expected that both **L3** and **L4** could also form stable Ln_2L_3 (L = **L3** and **L4**) helicates. Following the previous procedures, two pairs of ligands $\mathbf{L3^{R/S}}$ and $\mathbf{L4^{R/S}}$ were prepared in two steps using generic HATU peptide coupling reactions and were fully characterized.

2b.2.2 Conformation of metal-to-ligand ratio

The metal-to-ligand ratio is essential for complexation and it can be determined by ^{1}H NMR and UV-CD titration. Poor ligand solubility was the major challenge when performing titration as it is only soluble in a mixture of chloroform and methanol. Addition methanol may cause dissocation of lanthanide complex. Therefore, ^{1}H NMR and UV-CD titration were done by using a mixture of $CHCl_3$/MeOH/MeCN in a ratio of 50:5:45 and 12:1:12 respectively to minimize the effect brought by methanol.

^{1}H NMR and UV-CD titration were performed by adding metal into a solution of ligand and then observed the changes. For ^{1}H NMR titration (figure 2b-5), the ^{1}H NMR signal at 1.7 ppm, which corresponds to the CH_3 group of the ligand, decreased gradually upon addition of $Eu(OTf)_3$ to a solvent mixture containing **L3** and a new siganl at 2.1 ppm in the aliphatic region increased progressively. When 0.67 eq. of $Eu(OTf)_3$

was added, all the ligand peaks disappeared when confirmed the metal-to-ligand ratio was 2 to 3.

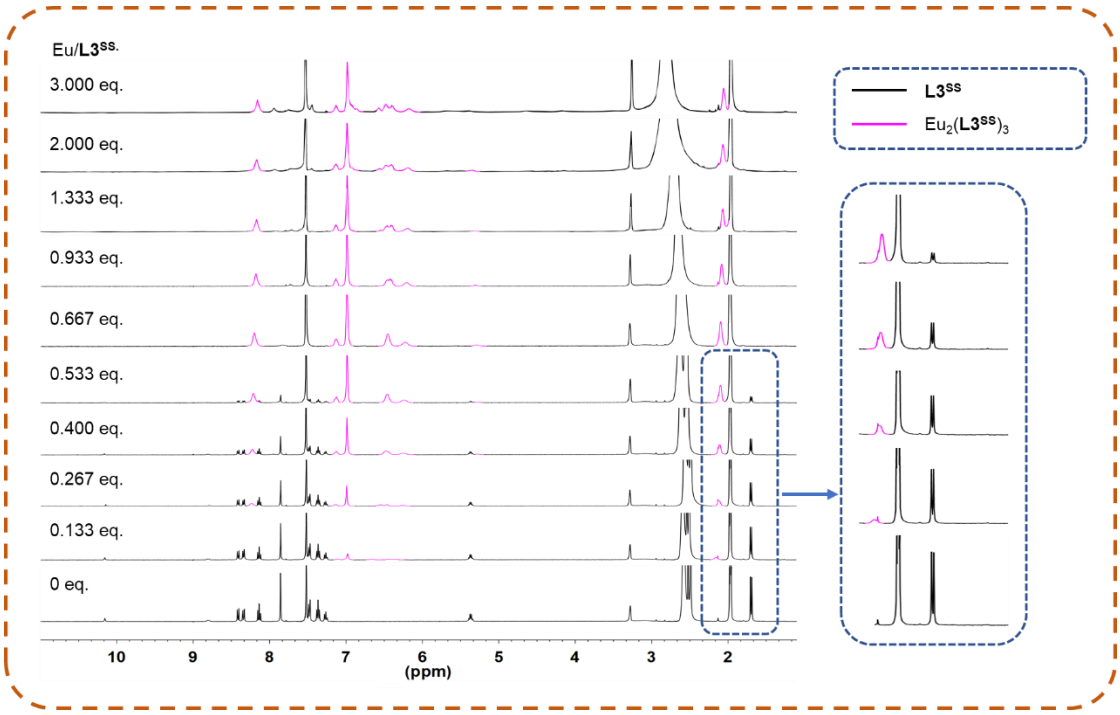

Figure 2b-5. *^{1}H NMR titration of **L1^{SS}** (1.09 x 10^{-3}M in 50:5:45, v/v/v of $CDCl_3$/CD_3OD/CD_3CN) with $Eu(OTf)_3$ (0.108M in CD_3OD) at 298 K.*

Similar result was also observed for UV-Vis titration. UV-Vis titration for **L3** was performed in a solvent mixture of $CHCl_3$/MeOH/MeCN (12:1:12, v/v/v). Upon addition of $Eu(OTf)_3$ to the ligand solution **L3**, a progressive decrease of 281, 315 and 353 nm was observed which corresponded to the ligand absorption (figure 2b-6). As evolution of complex absorption at 320 nm was observed simultaneously. A plot of changes in molar absorptivity at four wavelengths reveal an end point of 0.67.

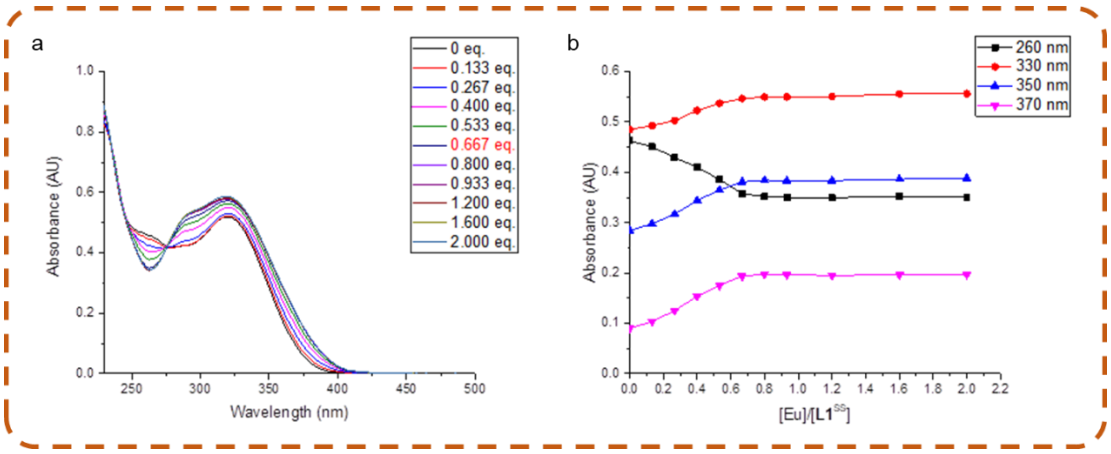

Figure 2b-6. *UV-Vis titration of* ***L3*** *with* $Eu(OTf)_3$*.(a) Variation in UV-Vis absorption spectra of titrating* $\boldsymbol{L3^{SS}}$ *(2.79 x* 10^{-4}*M, in 12:1:12, v/v/v, of* $CHCl_3/MeOH/CH_3CN$*) with* $Eu(OTf)_3$ *(0.036M in MeOH) at 298K (Eu:*$\boldsymbol{L3^{SS}}$ *= 0.0–2.0). (b) Variation of absorbance at four different wavelengths upon titrating* $\boldsymbol{L3^{SS}}$ *with* $Eu(OTf)_3$*.*

Given that **L4** exhibit similar ligand design and coordinating site, a hypothesis of metal-to-ligand ratio 2 to 3 was also investigated by ^{1}H NMR and UV-CD titration. For ^{1}H NMR titration, the signal at 5.3 ppm corresponding to the chiral proton of the ligand was monitored (figure 2b-7). Upon addition of $Eu(OTf)_3$ to a solution of **L4**, the proton signal at 5.3 ppm decreased gradually and a A new chiral proton signal at 5.5 ppm increased progressively. When 0.67 eq. of $Eu(OTf)_3$ was added, all the ligand signal disappeared which confirmed the metal-to-ligand ratio is 2 to 3. Similar result was also observed for UV-Vis titration and an end point of 0.67 was observed (figure 2b-8).

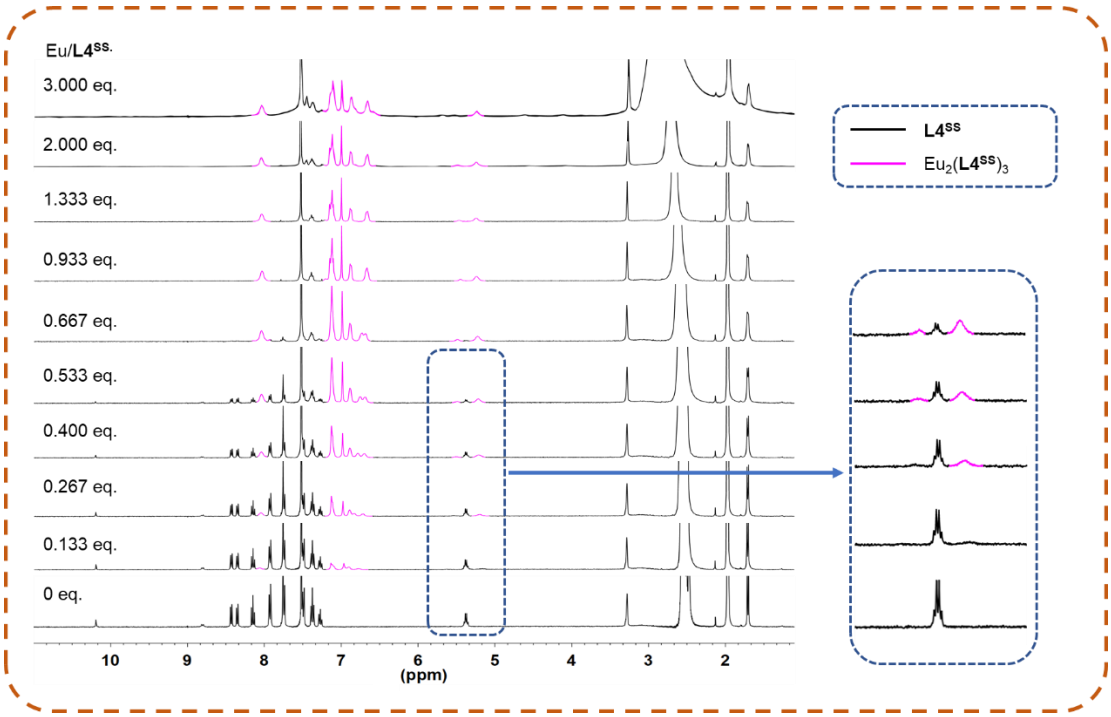

Figure 2b-7. *^{1}HNMR titration of **L4^{SS}** (1.09 x 10^{-3}M in 50:5:45, v/v/v of $CDCl_3$/CD_3OD/CD_3CN) with $Eu(OTf)_3$ (0.108M in CD_3OD) at 298 K.*

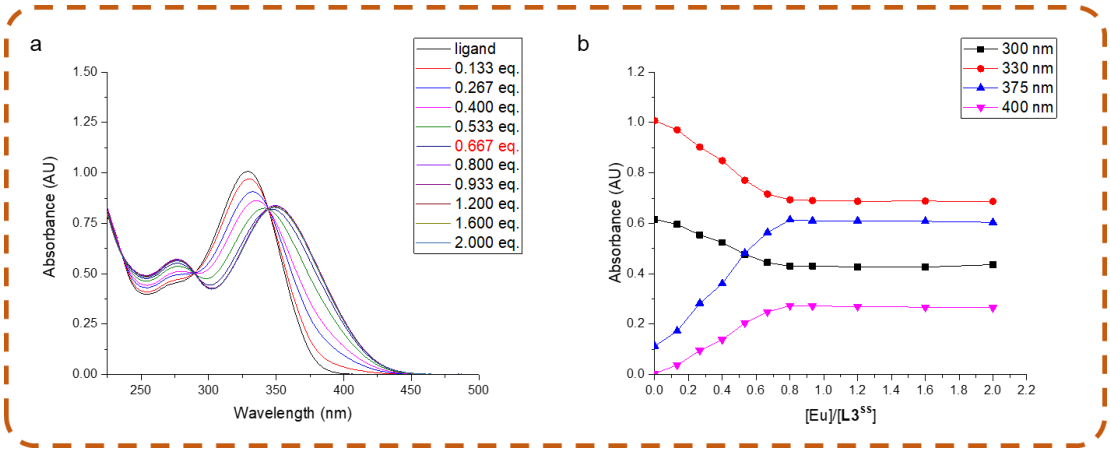

Figure 2b-8. *UV-Vis titration of **L4** with $Eu(OTf)_3$.(a) Variation in UV-Vis absorption spectra of titrating **L4^{SS}** (1.96 x 10^{-4}M, in 12:1:12, v/v/v, of $CHCl_3$/MeOH/CH_3CN) with $Eu(OTf)_3$ (0.014M in MeOH) at 298K (Eu:**L4^{SS}** = 0.0–2.0). (b) Variation of absorbance at four different wavelengths upon titrating **L4^{SS}** with $Eu(OTf)_3$.*

2b.2.3 Synthesis and characterization of [Eu_2**L3**$_3$] helicates

The Eu metal complex was synthesized by treating 8 x 10^{-3} M ligand with 0.67 equivalents of $Eu(OTf)_3$ in a mixed solution of $CHCl_3$/MeOH/CH_3CN (12/1/12, v/v/v).By comparing the ^1H NMR of free ligand, most signals arising from the europium complexes are shifted due to the formation of paramagnetic europium complex. Interestingly, two sets of signals in a ratio of ~96:4 was observed and the signal of minor species disappeared after dissolution in CD_3CN for three days (figure 2b-9).

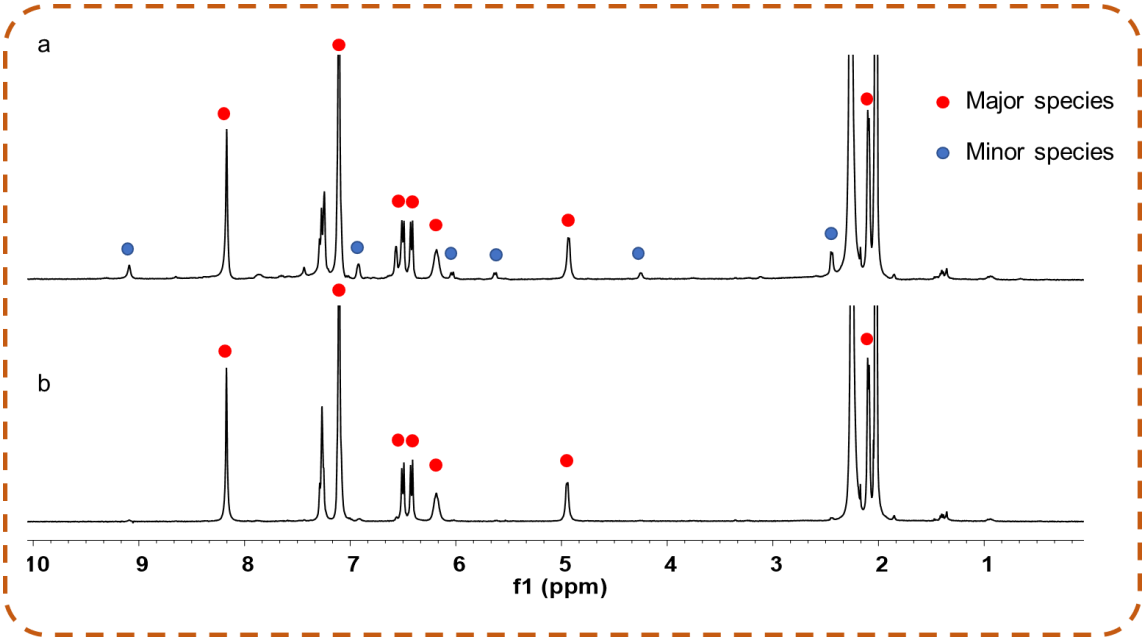

Figure 2b-9. *(a) ^1H NMR of crude Eu complex mixture containing both of major species and minor species in a ratio of 96:4. (b) ^{1}HNMR showing pure major species by dissolving crude mixture after 3 days.*

Several investigations were done to promote the formation of either minor species or major species including solvent effect, counterion effect and concentration effect.

For solvent effect, the role of methanol in complexation was investigated. Since methanol is well known to compete with ligands for lanthanide ions during complexation, the self-assembly process may be affected. Therefore, complexation was done without the use of methanol. ^{1}H NMR result showed that the addition of methanol was not necessary as the it did not affect the result of complexation (figure 2b-10). Lanthanide complexes was found to be stable in 4% methanol without dissociation. To keep consistent to the complexation condition of ^{1}H NMR titration, methanol was added in further preparation of different lanthanide complexes.

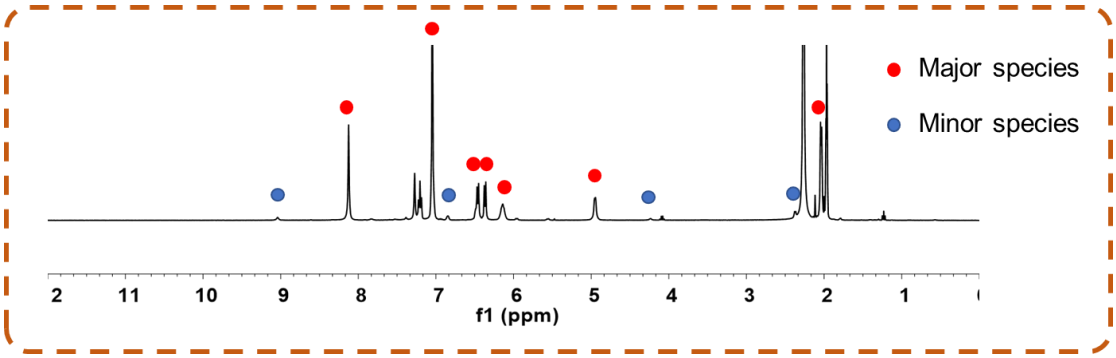

Figure 2b-10. *^{1}HNMR of crude Eu complex mixture prepared using CD_3Cl and CD_3CN as solvent.*

Triflate ion was replaced by chloride and perchlorate to investigate the counterions effect. Similar result was also observed when counterion was changed to chloride and perchlorate and Eu_2**L3**$_3$ was formed as major species. However, both chloride and perchlorate ion were not suitable for further experiment due to poor stability of resulting complexes. For perchlorate ion, the water content of the stock Europium perchlorate solution is too high (50%) and high-water content interfered the complexation. Free ligand signals were observed in ^{1}H NMR spectrum (figure 2b-11). For chloride ion, the complex was only soluble in methanol and dissociation of complex was found in ESI-HRMS (figure 2b-12).

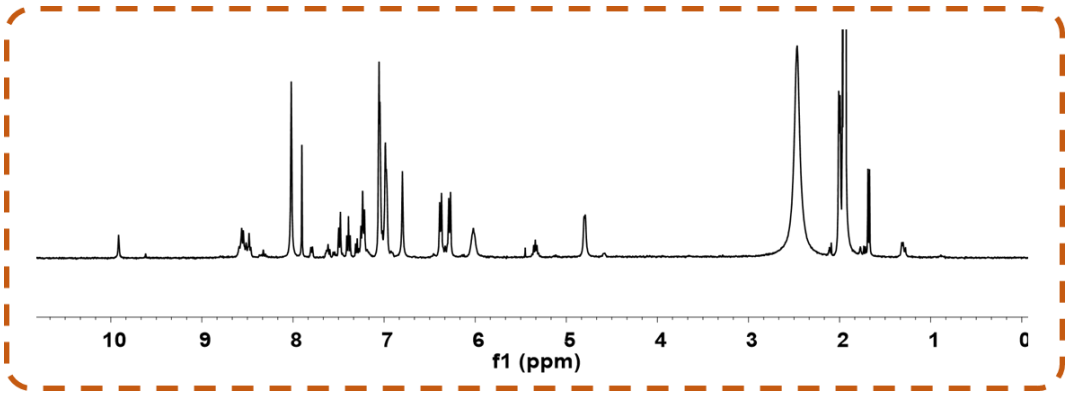

Figure 2b-11. *^{1}HNMR of $[Eu_2\mathbf{L3}_3](ClO_4)_6$.*

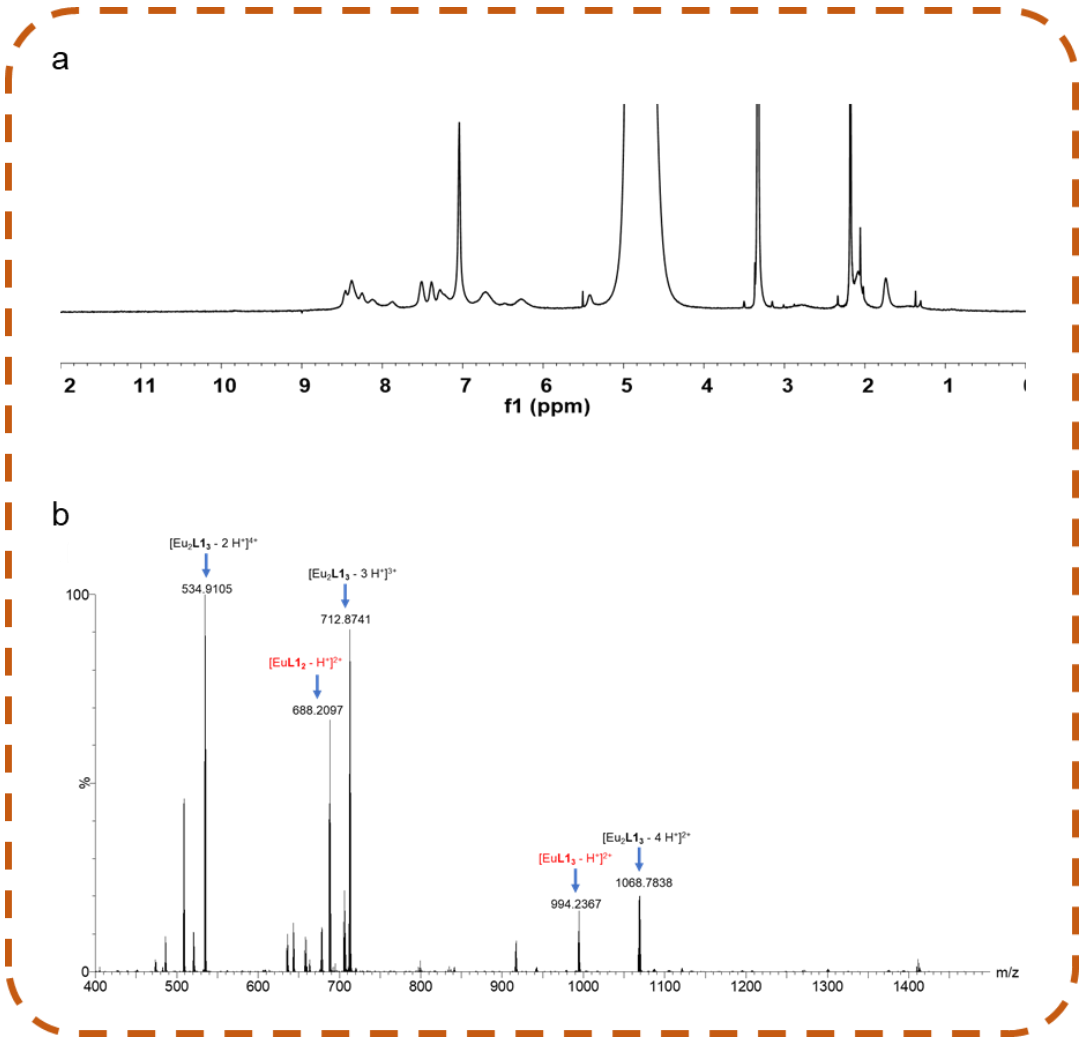

Figure 2b-12. *(a) ^{1}HNMR and (b) ESI-HRMS of $[Eu_2\mathbf{L3}_3]Cl_6$.*

Ligand concentration was found to have a great influence towards the supramolecular formation of **L3**. In a lower ligand concentration (1 x 10^{-3} M), only single species was observed in ^{1}H NMR (figure 2b-13). When the ligand concentration increased, another minor species was observed as evidenced by another ^{1}H NMR titration, in which the minor species can be observed when 2.15 x 10^{-3} M of ligand was titrated with $Eu(OTf)_3$ (figure 2b-14).

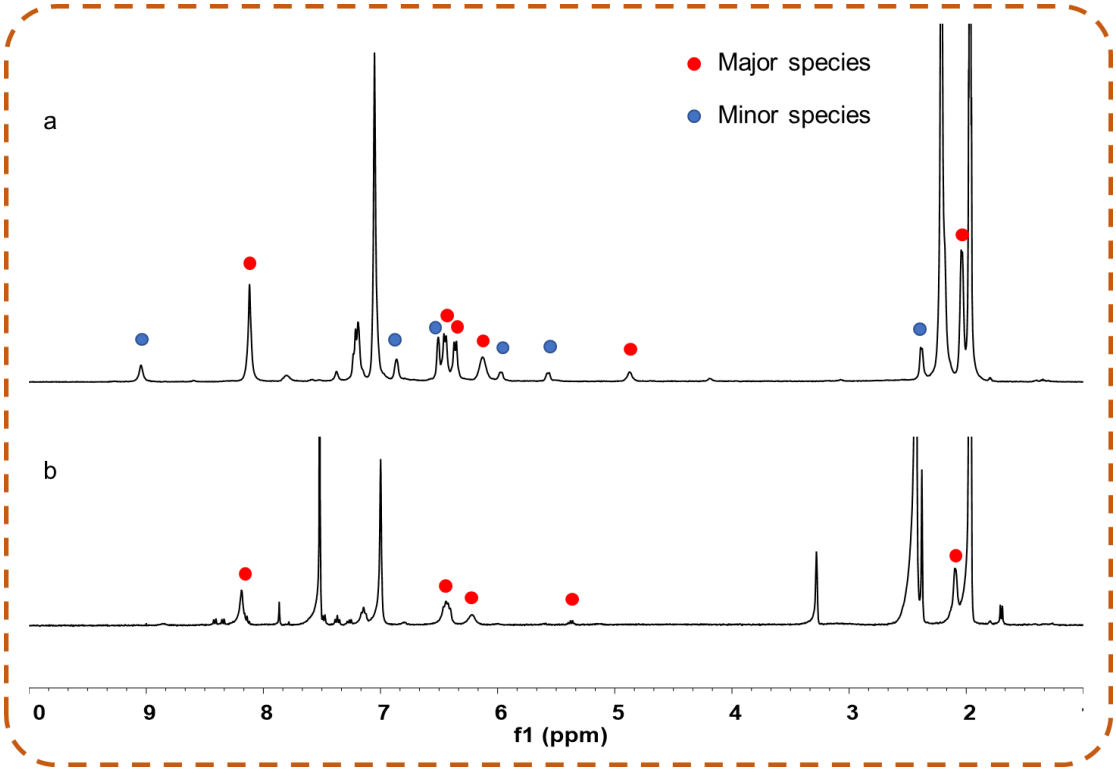

Figure 2b-13. *^{1}HNMR of (a) crude Eu complexes prepared by 0.008M **L3** and (b) 0.0001M **L3** in $CDCl_3$/MeOD/CD_3CN (12/1/12, v/v/v).*

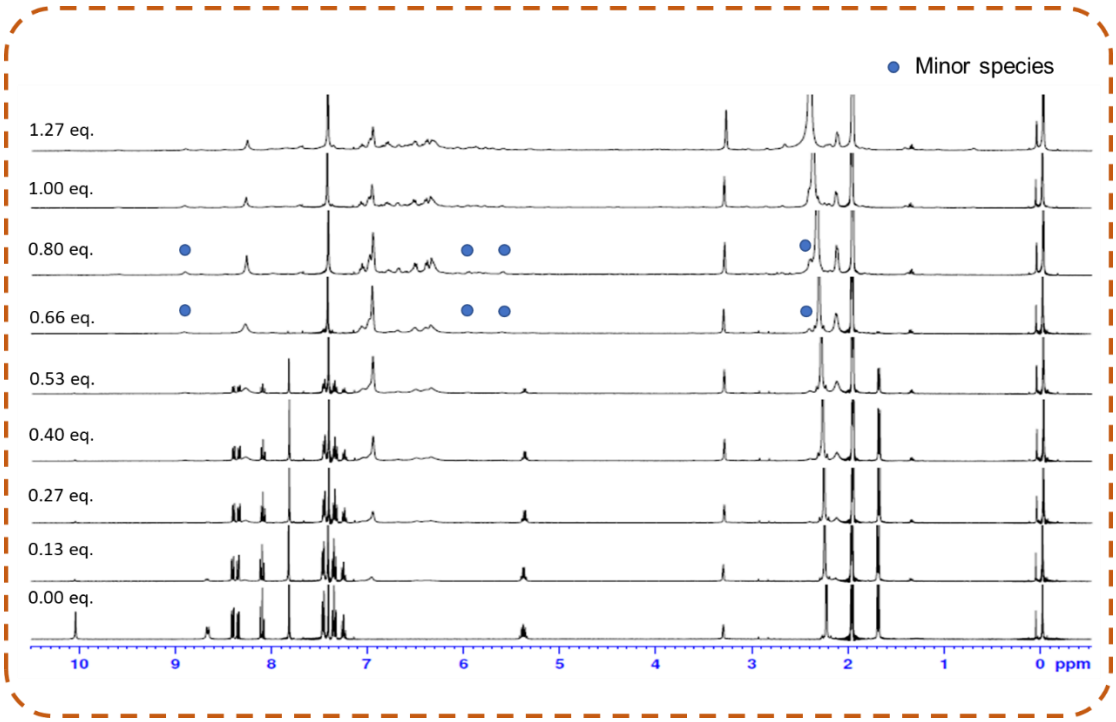

Figure 2b-14. *^{1}HNMR titration of **L3** (2.15 x 10^{-3}M in 70:5:25, v/v/v of $CDCl_3$/CD_3OD/CD_3CN) with Eu(OTf)3 (0.09M in CD_3OD) at 298 K.*

Due to the poor ligand solubility, attempt to prepare pure minor species was not successful. The high ligand concentration was then mimicked by dissolving Eu complexes and observed the ^{1}H NMR. Generally, increasing the Eu complex concentration will lead to an increase in formation of minor species. The maximum ratio of major species to minor species was determined to be 2.9:1 when ligand concentration is 88.9 mM. Further increase in ligand concentration will not affect the ratio significantly (figure 2b-15).

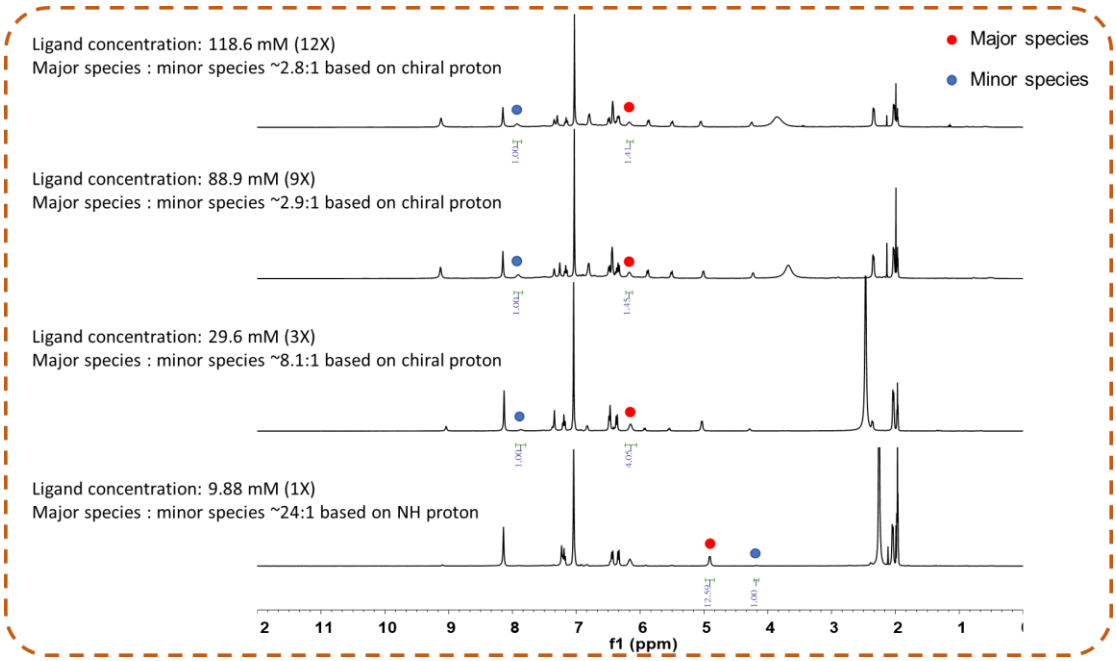

Figure 2b-15. *^{1}HNMR spectra of [Eu major species]/[Eu minor species] at different ligand concentration in CD_3CN at 298 K.*

The metal-to-ligand ratio of major species was also confirmed by ESI-HRMS. From the ESI-HRMS spectrum, only single set of independent signal series was observed corresponding to the dinuclear species $[Eu_2\mathbf{L3}_3]$. Three different clusters of signals can be observed which correspond to three different charged $[Eu_2\mathbf{L3}_3]$ species (+2, +3 and +4). Each signal can be assigned to the charged species with the loss of either triflate ion or proton. For example, signal with peaks with *m/z* equal to 1369.1962, 1294.2137 and 1219.2385 can be assigned to the species of $[\{[Eu_2\mathbf{L1}^{\mathbf{SS}}_3](OTf)_m\}\text{-}H_n]^{2+}$ with m = 4, n = 0; m = 3, n = 1; m = 2, n = 2. The assignments for each signal were also further confirmed by comparing the corresponding experimental isotopic pattern to the stimulated isotopic pattern.

2b.2.4 Synthesis and characterization of [Sm_2**L3**$_3$], [Gd_2**L3**$_3$] and [Tb_2**L3**$_3$]

Sm was used to replace Eu for preparing [Sm_2**L3**$_3$] complexes. By using the same protocol, similar result was observed. The ^{1}H NMR showed the existence of a major species and a minor species in a ratio of 94:6 and the minor species was found to undergo transformation to the major species after 3 days (figure 2b-16). The ESI-HMRS of the Sm major species showed only single set of independent peak series, corresponding to the [Sm_2**L3**$_3$] complex with different charges. The preparation of [Gd_2**L3**$_3$] and [Tb_2**L3**$_3$] complexes were done by treating 1 x 10^{-3} M ligand with the correspond $Gd(OTf)_3$ and $Tb(OTf)_3$. Characterization by NMR is not possible due to the strong paramagnetic nature. The ESI-HRMS revealed single species corresponding to [Gd_2**L1**$_3$] and [Tb_2**L1**$_3$] with different clusters corresponding to the progressive loss of triflate anion and proton.

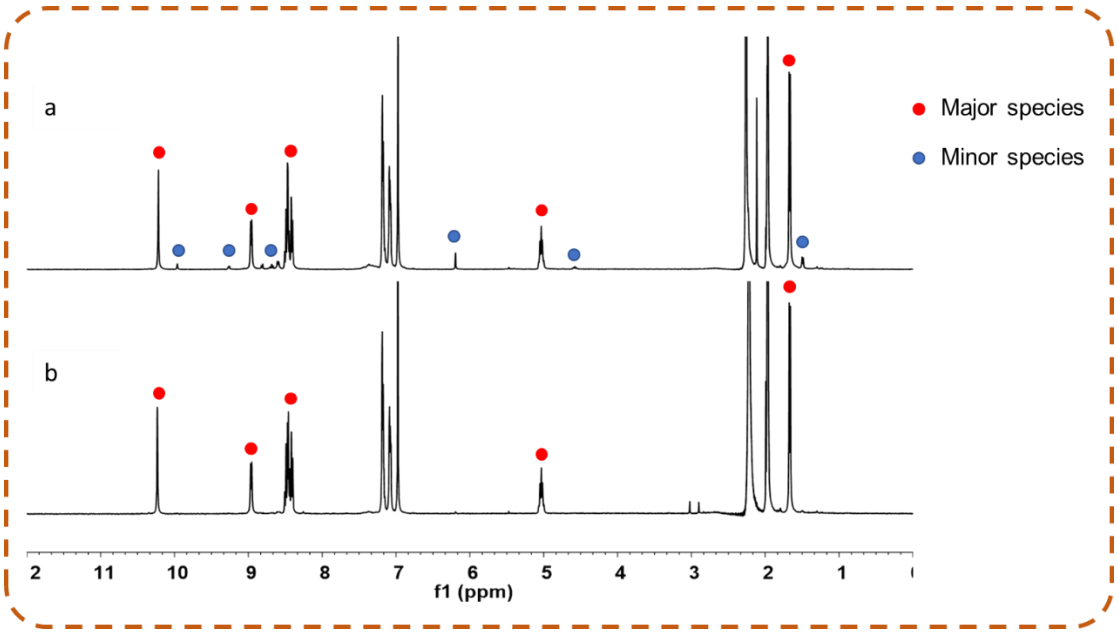

Figure 2b-16. *(a) ^{1}H NMR of crude Sm complex mixture containing both of major species and minor species in a ratio of 94:6. (b) ^{1}HNMR showing pure major species by dissolving crude mixture after 3 days.*

2b.2.5 Synthesis and characterization of [La_2**L3**$_3$] and [Lu_2**L3**$_3$]

The corresponding La and Lu complexes were synthesized by treating 2 eq. of lanthanide ions to 3 eq. of **L3**. For La complexes, the crude NMR showed two different sets of signals corresponding to a major and minor species. However, unlike the minor species of Eu complex, which transformed to major species slowly upon dilution (figure 2b-17), the La minor species exhibited a fast transformation upon dilution (figure 2b-18).

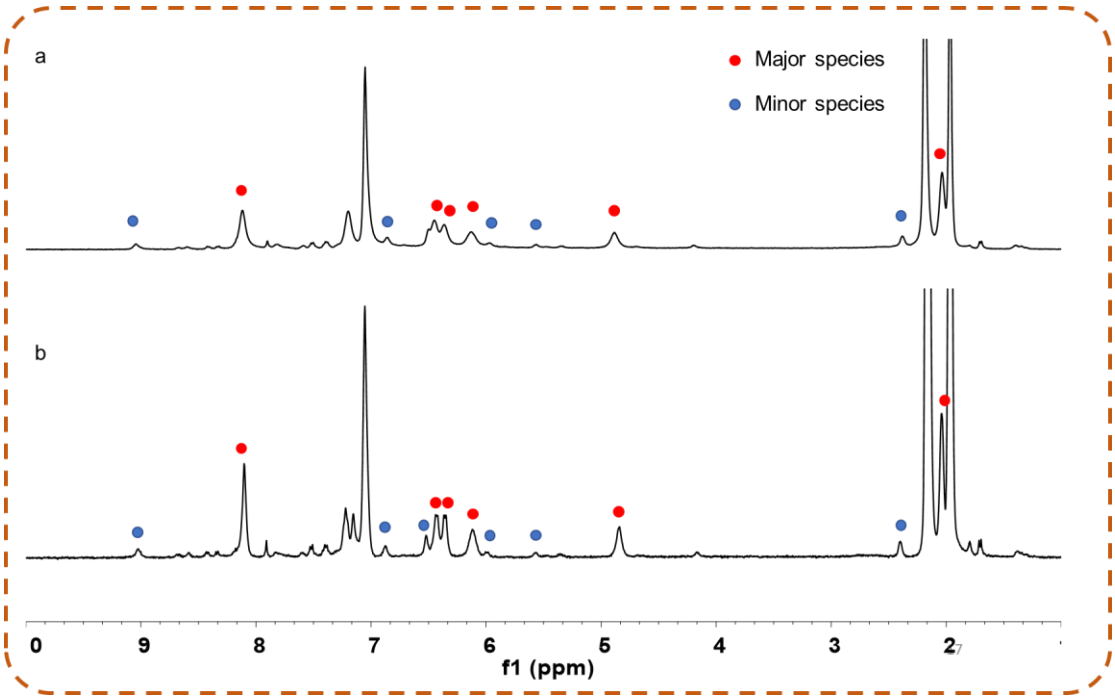

Figure 2b-17. *^{1}HNMR of (a) crude Eu complexes prepared by 0.006M **L3** in CD_3CN and (b) subjected to 5-fold dilution and performed ^{1}HNMR instantaneously.*

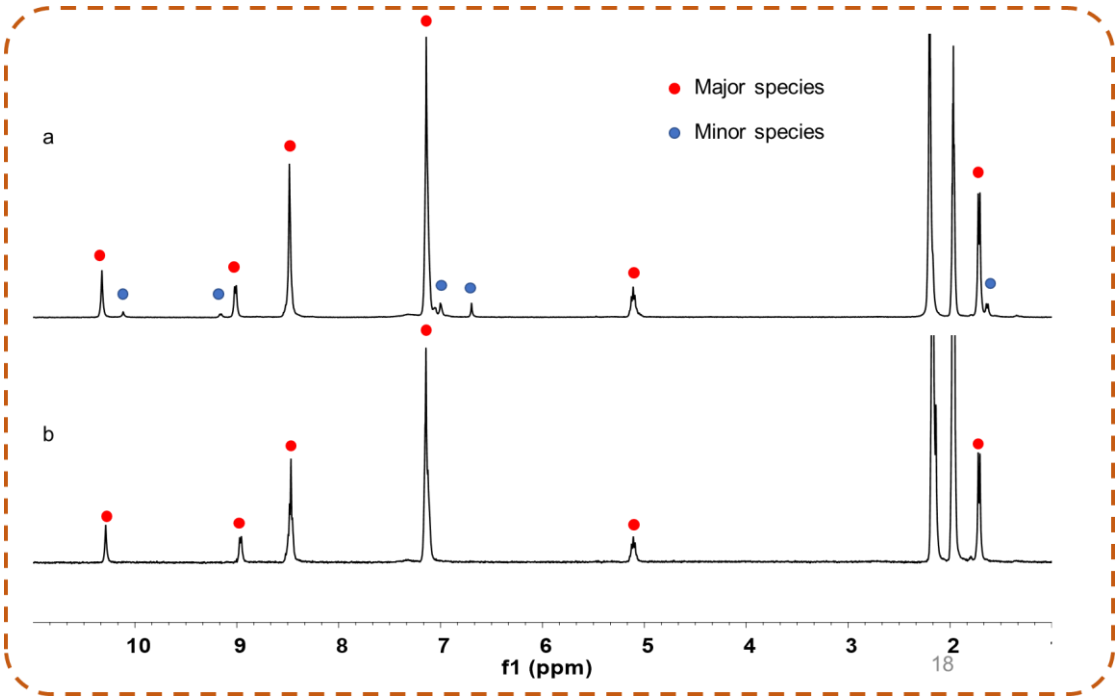

Figure 2b-18. *^{1}HNMR of (a) crude La complexes prepared by 0.006M **L3** in CD_3CN and (b) subjected to 5-fold dilution and performed ^{1}HNMR instantaneously.*

For Lu complexes, insignificant amount of minor species was observed when 0.008M L3 was treated with $Lu(OTf)_3$. Similar with the result of Eu and Sm, pure major species can be obtained by decreasing the ligand concentration to 0.001M (figure 2b-19). The metal-to-ligand ratio of both La and Lu complexes were even evidenced by ESI-HRMS in which only [Ln_2**L3**$_3$] were shown in the spectrum and no other supramolecular species can be observed.

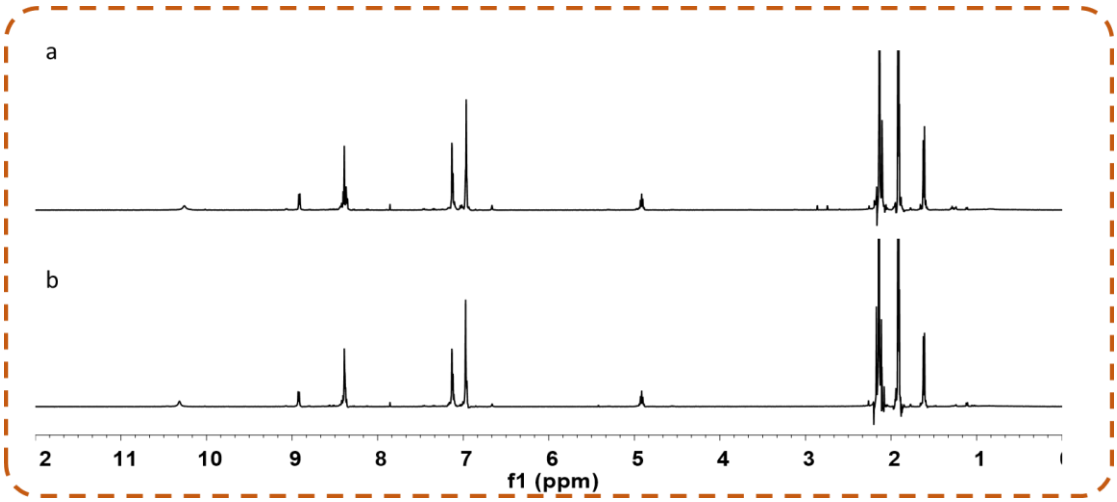

Figure 2b-19. *^{1}HNMR of (a) crude Lu complexes prepared by 0.008M **L3**, (B) crude Lu complexes prepared by 0.001M **L3**.*

2b.2.5 Synthesis and characterization of [Ln_2**L4**$_3$]

Following the previous synthetic procedures of [Ln_2**L1**$_3$], the corresponding [Eu_2**L4**$_3$] was prepared by addition of two equivalents $Eu(OTf)_3$ into the solution containing three equivalent of **L4**. Due to the paramagnetic europium ions, most NMR signal of the [Eu_2**L4**$_3$] was shifted which indicated the successful coordination of europium ion to the ligand. The ^{1}H NMR displayed only single set of signals and the ESI-HRMS revealed one set of independent peak series, corresponding to the dinuclear species [Eu_2**L4**$_3$]. In the ESI-HRMS spectrum, [Eu_2**L4**$_3$] exhibits three different clusters of peaks which correspond to three different species with +3 and +4 charged states. For example, peaks with *m/z* equal to 1015.2181, 965.2259, 915.2409 and 865.2620 can be assigned to the species of $[\{[Eu_2\mathbf{L4}^{\mathbf{SS}}{}_3](OTf)_m\}\text{-}H_n]^{3+}$ with m = 3, n = 0; m = 2, n = 1; m = 1, n = 2; m = 0, n = 3. Other lanthanide ions were used to replace Eu for preparation of a series of [Ln_2**L4**$_3$] including La, Sm, Gd, Tb and Lu. All the [Ln_2**L4**$_3$] were successfully synthesized and well characterized by NMR and ESI-HRMS.

2b.2.6 Helicate-to-tetrahedron transformation

Single X-ray diffraction is a powerful tool to determine the exact structure of a supramolecular complex. Several attempts were done to prepare crystal of [Eu_2**L3**$^{SS}{}_3$] including evaporation and solvent diffusion. A single crystal of Eu complex was obtained by slow diffusion of diisopropyl ether into an acetonitrile solution of the complex. Similar result was observed when ether was used including methyl t- butyl ether, diethyl ether, diisopropyl ether. No crystal can be formed when ether was replaced by ethyl acetate, dichloromethane and acetone.

Single X-ray diffraction showed a [Eu_4**L3**$^{SS}{}_6$] tetrahedral structure which confirmed a helicate-to-tetrahedron transformation through crystallization (figure 2b-20). In the crystal structure of [Eu_4**L3**$^{SS}{}_6$] tetrahedron, each europium metal centre can be best described as tricapped trigonal prism. Four metal ions adopted the same Δ-configurations, which shows the successful transfer of chiral information from the chiral moiety to the metal centre. In the tetrahedron structure, four europium ions occupied the vertices, and six ligands act as the edges. Eu-N distances range from 2.52(2) to 2.59(2) Å and Eu-O distances range from 2.38(2) to 2.44(2) Å.

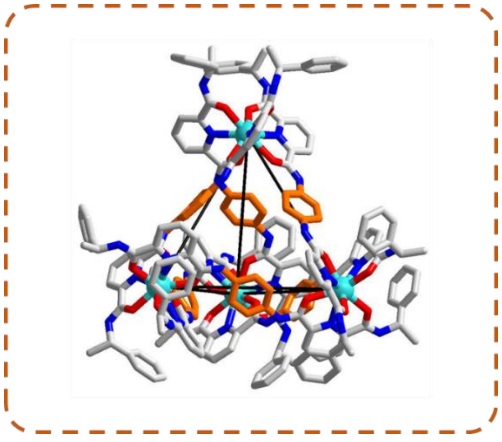

Figure 2b-20. *X ray crystal structure of [Eu_4**L3**$^{SS}{}_6$] showing a tetrahedron structure.*

Further characterization of $[Eu_4(\mathbf{L3}^{SS})_6]$ was done by washing the crystal with diisopropyl ether and then dried under vacuum. Compared with $[Eu_2(\mathbf{L3})_3]$ helicate, $[Eu_4(\mathbf{L3})_6]$ showed a very different ^{1}H NMR signal, which suggested that only pure $[Eu_4(\mathbf{L3})_6]$ in the solution (figure 2b-21). The integration of $[Eu_4(\mathbf{L3})_6]$ integrations are equivalent to the ligand in C_2-symmetric nature which revealed the similar lanthanide geometry with $[Eu_2(\mathbf{L3})_3]$.

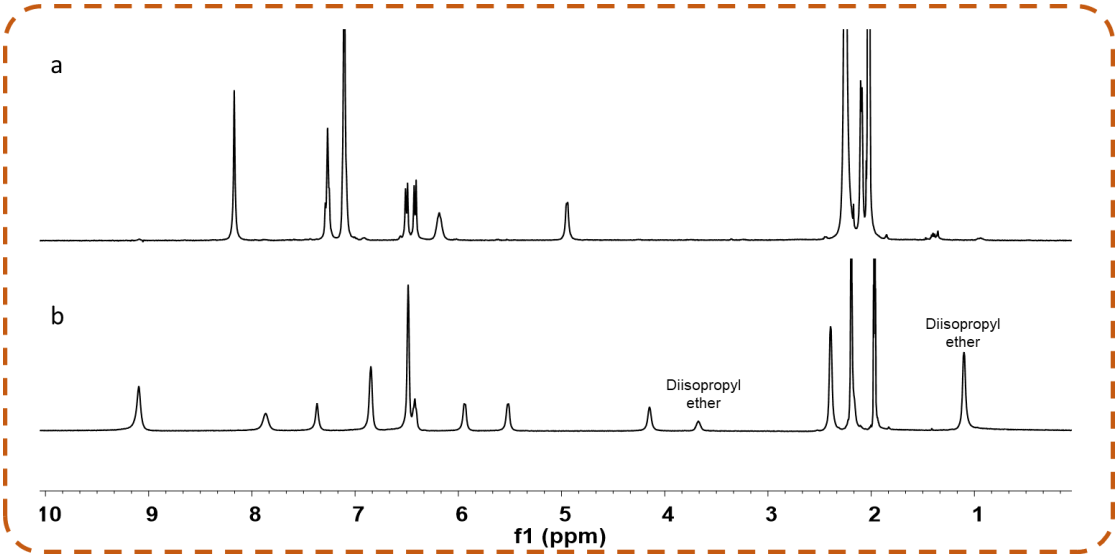

Figure 2b-21. *^{1}H NMR of (a) pure $[Eu_2\mathbf{L1}_3]$ and (b) pure $[Eu_4\mathbf{L1}_6]$ that was done simultaneously after dissolution of $[Eu_4\mathbf{L1}_6]$.*

Comparing the ^{1}H NMR of $[Eu_2(\mathbf{L3})_3]$ with $[Eu_4(\mathbf{L3})_6]$, the peaks of $[Eu_4(\mathbf{L3})_6]$ are relatively broad (figure 2b-22) The broadening of peaks can be attributed to the pseudocontact shifts of paramagnetic europium ion. Since the pseudocontact shifts is governed by the distance between the paramagnetic metal ion and proton, it can be deduced that the proton in $[Eu_4(\mathbf{L3})_6]$ experienced a stronger paramagnetic shift. The chemical formulas of $[Eu_4(\mathbf{L3})_6]$ was further characterized by ESI-HRMS. In the ESI-HRMS spectrum, only single set of independent peaks was observed. Each cluster of peaks can be assigned to the tetranuclear species with the progressive loss of anions

and protons. For example, peaks with *m/z* equal to 1065.3668, 1035.3778, 1005.3876 and 975.3884 can be assigned to the species of $[\{[Eu_4\mathbf{L3^{SS}}_6](OTf)_m\}\text{-}H_n]^{5+}$ with m =7, n = 0; m = 6, n = 1; m = 5, n = 2; m = 4, n = 3. Upon dilution of $[Eu_4(\mathbf{L3^{SS}})_6]$ in MeCN, the tetrahedral $[Eu_4(\mathbf{L3^{SS}})_6]$ is unstable and will slowly rearranged back to $[Eu_2(\mathbf{L3^{SS}})_3]$ in 11 days (figure 2b-23).

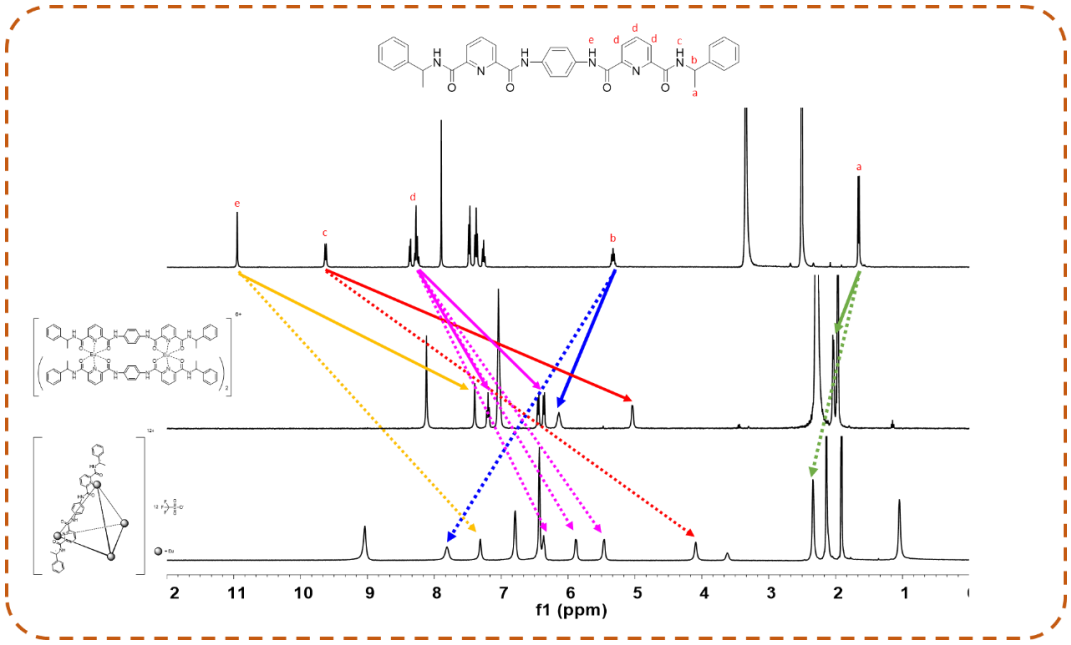

Figure 2b-22. *Paramagnetic shift of $[Eu_2(\mathbf{L3})_3]$ and $[Eu_4(\mathbf{L3})_6]$ in CD_3CN.*

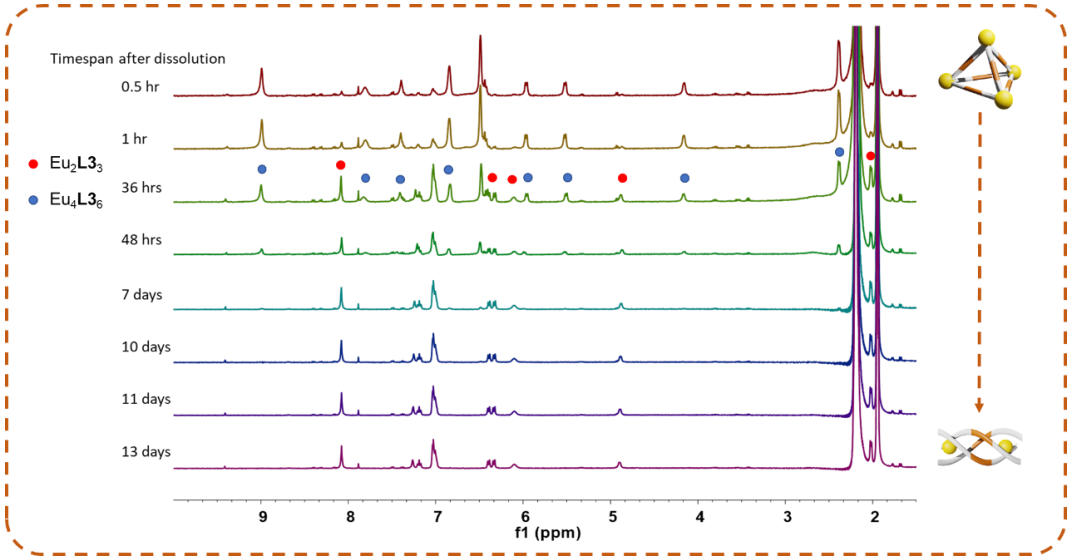

Figure 2b-23. *Tetrahedron-to-helicate transformation from $[Eu_4\mathbf{L3}_6]$ to $[Eu_2\mathbf{L3}_3]$ (4.53 x 10^{-4}M in CD_3CN).*

With this interesting helicate-to-tetrahedron transformation via ether crystallization, the effect of lanthanide ionic radii towards this transformation was further investigated. By replacing Eu to Sm for coordination, helicate-to-tetrahedron transformation was also observed. Single crystal of [Sm_4**L3**$_6$] was obtained upon slow diffusion of diisopropyl ether into a solution containing pure [Sm_2**L3**$_3$]. The crystal was then dried and characterized by NMR and ESI-HRMS. In the ^{1}H NMR spectrum, the [Sm_4**L3**$_6$] showed a different signal compared with that of [Sm_2**L1**$_3$] (figure 2b-24). Similar with [Eu_4**L3**$_6$], [Sm_4**L3**$_6$] is unstable upon dissolution in MeCN and will slowly transform back to [Sm_2**L3**$_3$] in 14 days.

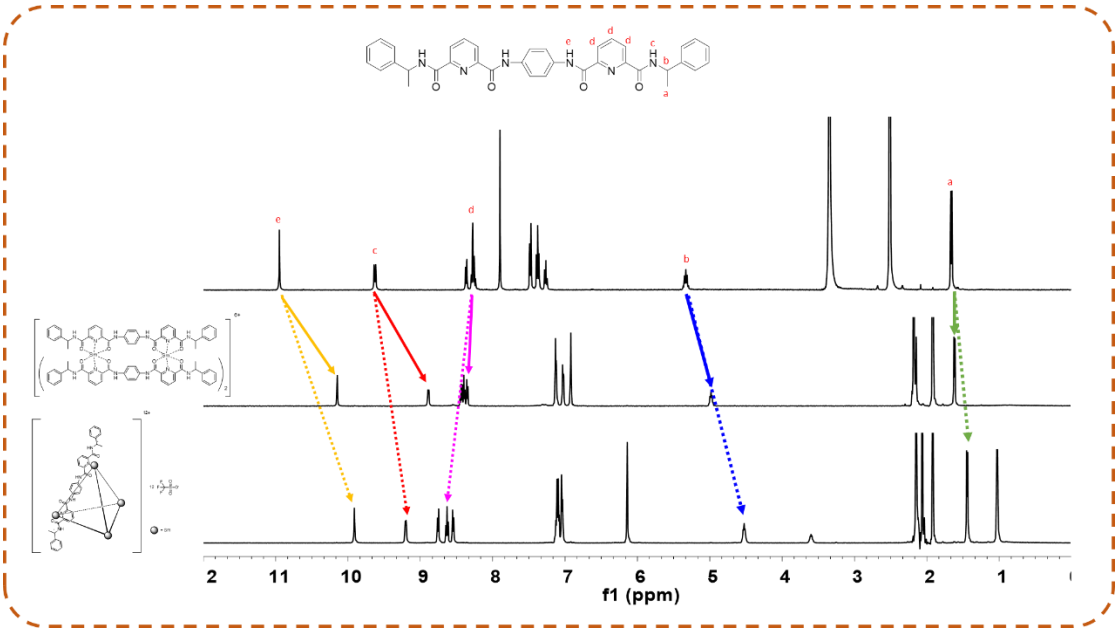

Figure 2b-24. *Chemical shift of [Sm_2(**L3**)$_3$] and [Sm_4(**L3**)$_6$] in CD_3CN.*

By replacing Eu with Gd and Tb, similar helicate-to-tetrahedron was also observed as evidenced by ESI-HRMS. However, characterization by NMR is not possible due to the strong paramagnetic nature of Gd and Tb. Tetrahedron-to-helicate transformation process was monitored by dissolving the tetrahedron in MeCN and

wait for 14 days before performing ESI-HRMS. Result showed that that [Gd_4**L3**$_6$] and [Tb_4**L3**$_6$] are unstable upon dissolution in MeCN and will rearrange back to [Gd_2**L3**$_3$] and [Tb_2**L3**$_3$] respectively (figure 2b-25).

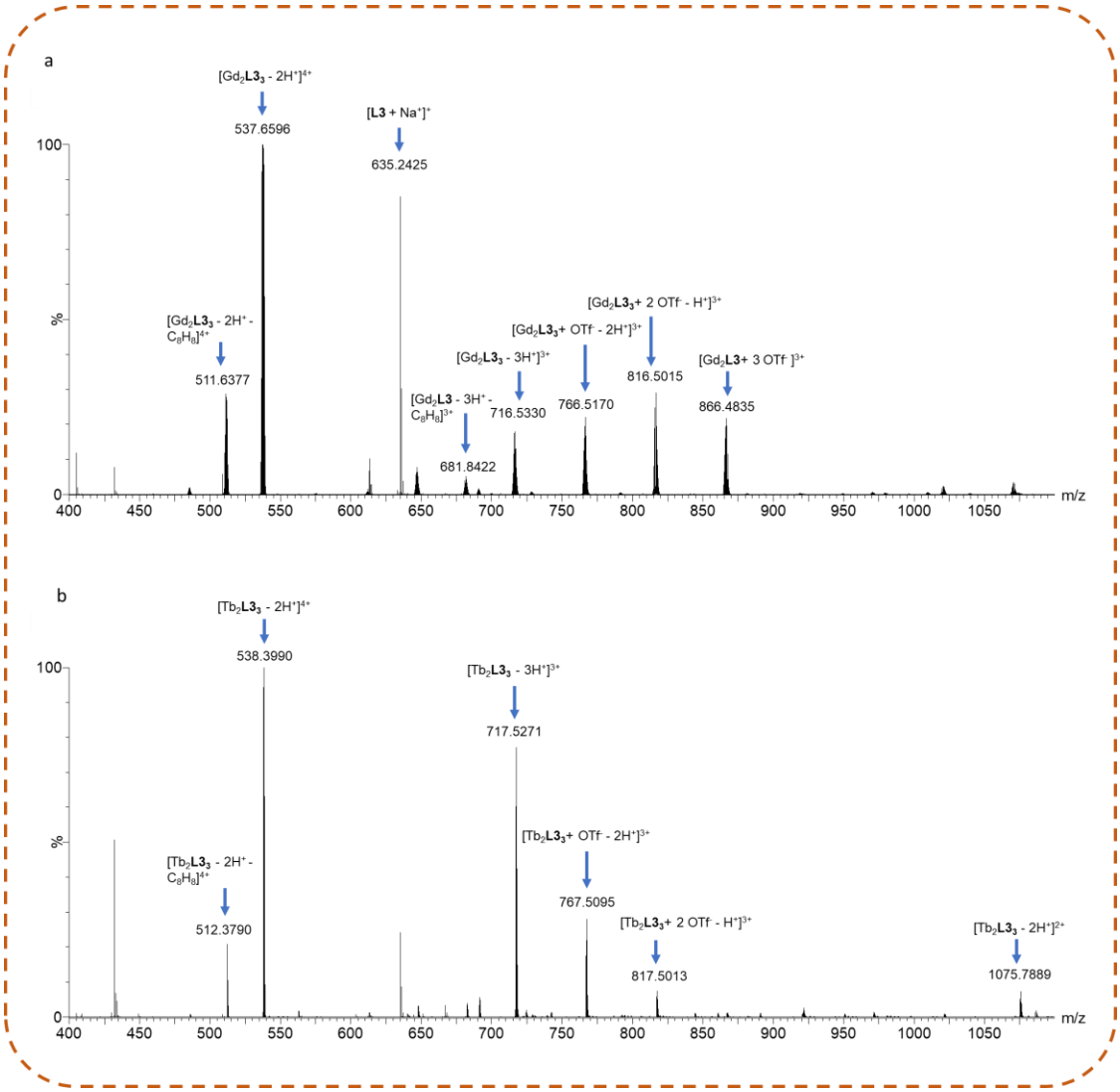

Figure 2b-25. *ESI-HRMS of tetrahedron-to-helicate transformation after dissolution in CH_3CN for 14 days (a) [Gd_4**L3**$_6$] and (b) [Tb_4**L3**$_6$].*

When Eu was replaced by Lu, [Lu_4**L3**$_6$] can be also prepared by helicate-to-tetrahedron transformation through ether crystallization. The chemical formula and structure were well characterized by NMR and ESI-HRMS. Similar with [Eu_4**L3**$_6$] and [Sm_4**L3**$_6$], the ^{1}H NMR of [Lu_4**L3**$_6$] also showed a very different signal compared with

that of [Lu_2**L3**$_3$] (figure 2b-26). Interestingly, different from that of [Eu_4**L3**$_6$] and [Sm_4**L3**$_6$], [Lu_4**L3**$_6$] was found to be relatively stable and only insignificant amount of [Lu_2**L3**$_3$] was found upon dissolution in MeCN after 10 days (figure 2b-27).

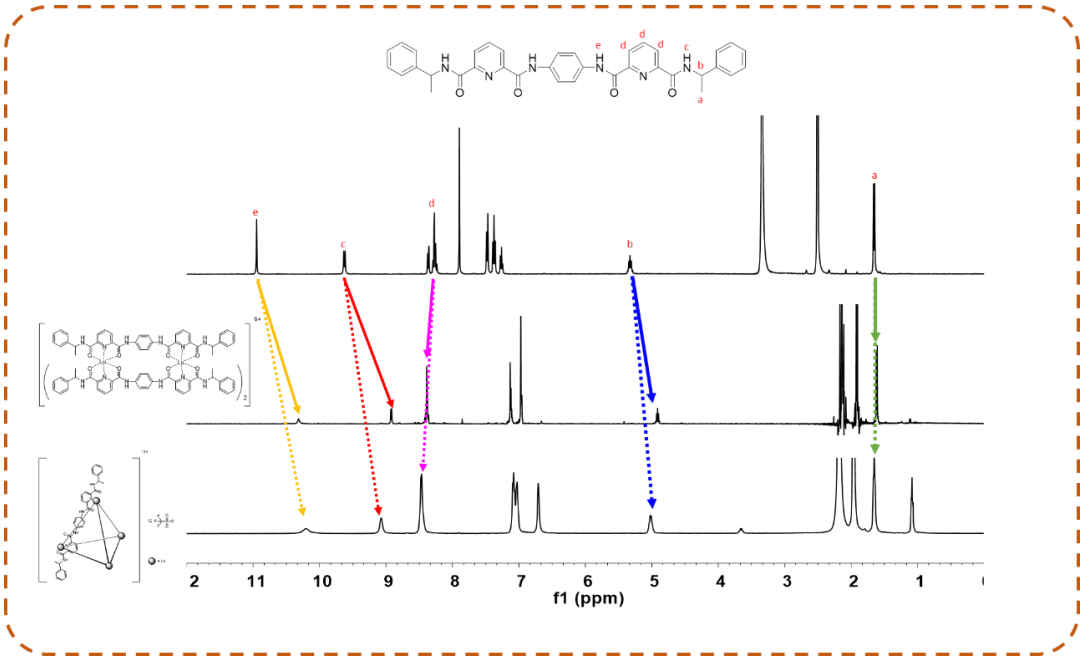

Figure 2b-26. *Chemical shift of [Lu_2(**L3**)$_3$] and [Lu_4(**L3**)$_6$] in CD_3CN.*

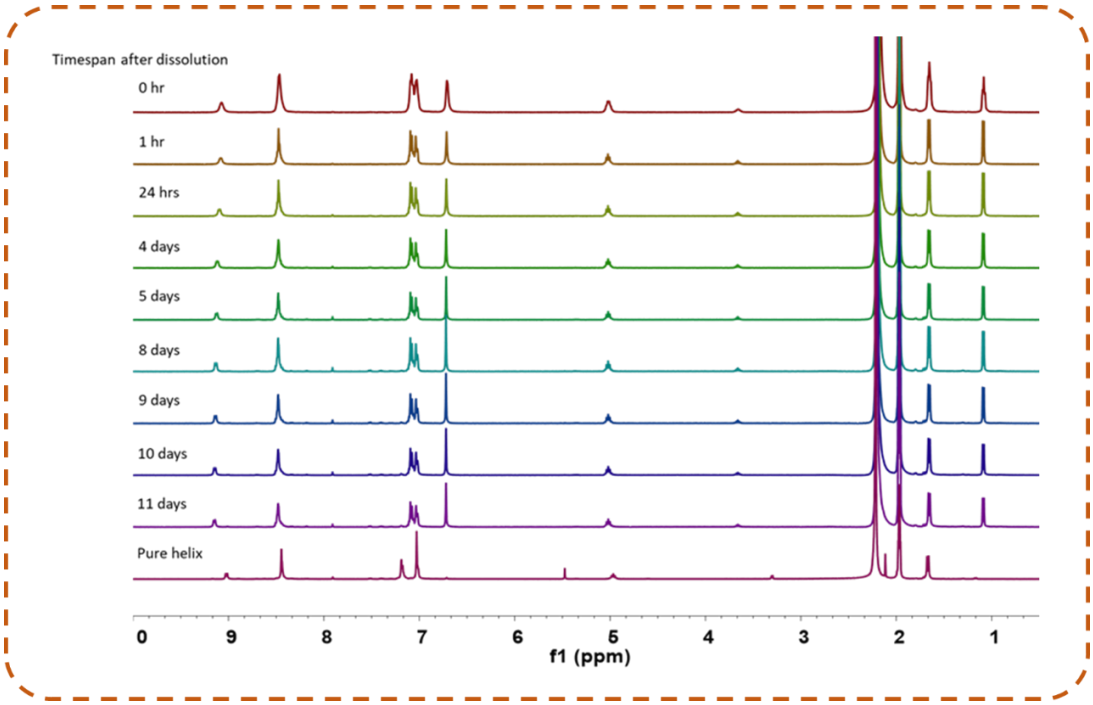

Figure 2b-27. *^{1}H NMR of [Lu_4(**L3**)$_6$] upon dissolution in CD_3CN at different timespan.*

When the metal source is changed from Eu to La, no crystal can be obtained by slow diffusion of ether into a solution containing [La_2**L3**$_3$]. The powder that obtained from diffusion of ether was then characterized by NMR. The ^{1}HNMR of the powder revealed that the La complex remained in the most stable form [La_2**L3**$_3$] helicate form and no other supramolecular complexes can be observed (figure 2b-28).

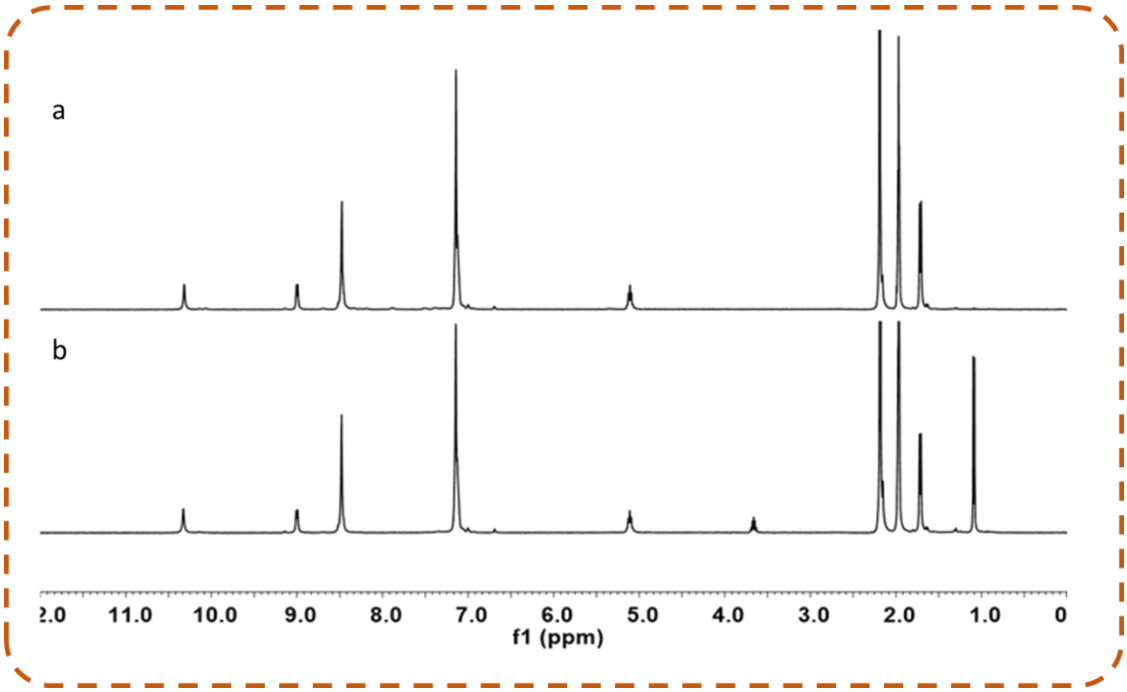

Figure 2b-28. *^{1}HNMR of (a) [La_2(**L3**)$_3$] in CD_3CN and (b) the powder left after diffusing ether into a solution containing [La_2(**L3**)$_3$].*

2b.2.7 Analysis of the effect of ligand design and ionic radii

Result showed that the ligand design has a great influence towards the supramolecular formation as well as the helicate-to-tetrahedron transformation. In this study, both **L3** and **L4** were expected to form stable Ln_2L_3 helicate as the two metal ions shared the same C_3 axis upon coordination. According to the symmetry design principle that proposed by Raymond and co-workers, the use of longer and flexible central bridging linker should be avoided since it may increase the chance of forming

unwanted clusters.[23] In the previous chapter, diphenyl unit was used as central bridging linker in **L1** and **L2** and both can form stable Ln_2L_3 helicate. In this study, monophenyl unit was used as central bridging linker in **L3** and it is expected form Ln_2**L3**$_3$ helicate since shorter linker may promote the formation of helicate without other unwanted supramolecular clusters. Interestingly, helicate-to-tetrahedron transformation was observed for **L3** and pure tetrahedron can be isolated through either crystallization. Apart from the offset distance of two chelating groups, this study showed that the distance of two metal ions also plays an important role in supramolecular formation.

The stability of the supramolecular complex also varies across the lanthanide series (figure 2b-29). Generally, lanthanide ions are considered as having similar physical and chemical properties due to their similar ionic radii. In this study, the stability and the supramolecular formation were governed by the ionic radii which is consistent with the work that reported by Hamacek and co-workers.[24] When the largest La ion was used, formation of stable [La_2(**L3**)$_3$] helicate was highly preferred and labile [La_4(**L3**)$_6$] tetrahedron can be only observed under high ligand concentration. Stable helicate and tetrahedron can be formed when the smallest Lu ion was used. The lanthanide ions that lies between La and Lu (Sm, Eu, Gd and Tb) were found to form stable helicate at low concentration and stable tetrahedron at high ligand concentration.

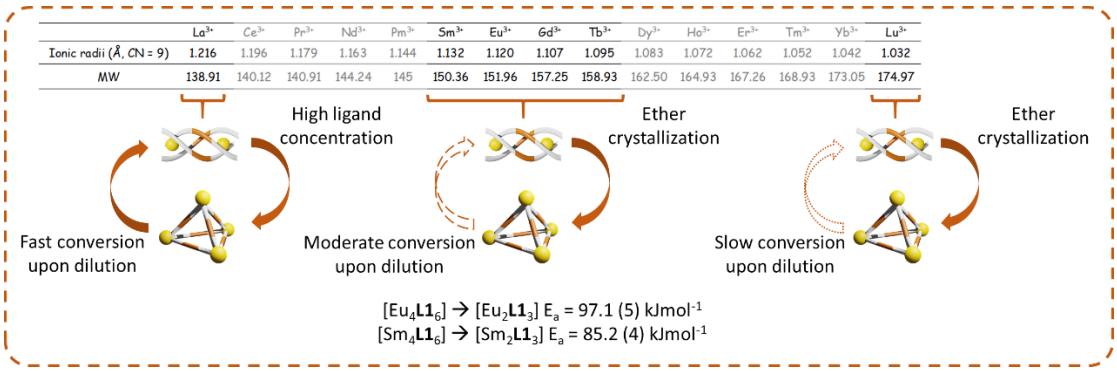

Figure 2b-29. *Summary of helicate-to-tetrahedron transformation governed by different lanthanide ions.*

Kinetic studies were done to estimate the activation parameter of tetrahedron-to-helicate transformation process. Arrhenius plot was used since the tetrahedron-to-helicate transformation is not an equilibrium process. The transformation process was monitored by NMR and two experimental error were observed. Firstly, tetrahedron did not undergo transformation to helicate even heating at 338K. Moreover, the rate of conversion at 338K is slower than that of 328K in some of the trials. 8 trials were performed for Eu complex and 5 trials were performed for Sm complex. After omitting the outliner, the kinetic studies showed that both [Eu_4**L3**$_6$] and [Sm_4**L3**$_6$] exhibited similar activation energy which was 97.1 (5) and 85.2 (4) $kJmol^{-1}$ respectively due to the similar ionic radii of Eu and Sm. The positive value of ΔH_{298} also showed that the tetrahedron-to-helicate transformation is endothermic.

This study also revealed that the Ln_2**L3**$_3$ helicate is an essential intermediate for the formation of Ln_4L_6 tetrahedron. It was proposed that the ligand and lanthanide ion will first self-assembled to form the entropically favored helicate. Then the helicate will rearrange to form the Ln_4**L3**$_6$ tetrahedron under high ligand concentration.

Crystallization process was proven to be an alternative way to mimic high ligand concentration environment. This hypothesis was supported by attempting to prepare Lu tetrahedron in a one pot self-assembly reaction. Despite varying the reaction condition such as temperature and solvent, direction formation of Lu tetrahedron was unsuccessful. All the tetrahedron seems to form by crystallization of a solution of helicate only.

2b.2.8 Photophysical studies

Photophysical measurement was done for the complex of **L3** and **L4**. To avoid tetrahedron-to-helicate transformation, all the [Ln_4**L3**$_6$] tetrahedron were performed within 1 hr after dissolution of sample. For UV-Vis absorption measurement, the λ_{max} of [Eu_2**L3**$_3$] was blueshifted for 19 nm compared with that of [Eu_4**L3**$_6$] (figure 2b-30).

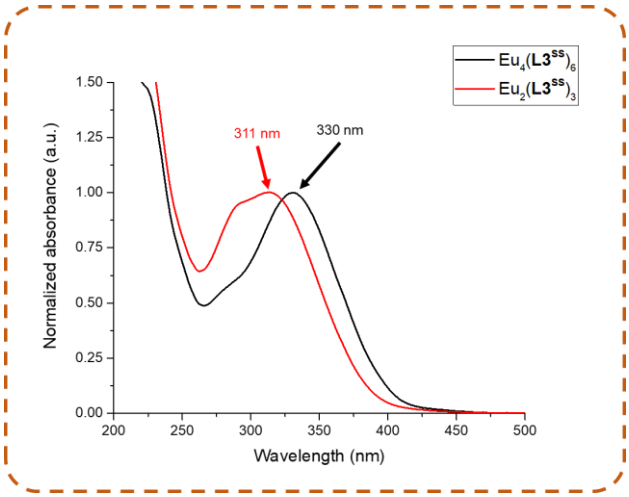

Figure 2b-30. *Normalized UV-Vis spectrum of [Eu_2(**L3**^{SS})$_3$] and [Eu_4(**L3**^{SS})$_6$] in CH_3CN.*

The chiroptic properties of Eu complexes were examined by solution CD and CPL measurement. Similar with that of UV-Vis absorption, [Ln_2**L3**$_3$] and [Ln_4**L3**$_6$] (Ln = La, Eu and Sm) also showed slight differences in the CD absorption. For [Ln_2**L3**$_3$], strong cotton effects were observed at 212, 240, 259, 273, 312 and 381 nm while for [Ln_4**L3**$_6$],

strong cotton effects were observed at 212, 240, 259, 273, 312 and 362 nm. Mirror image of CD spectrum were observed for *R*- and *S*-isomers. For [Ln_2**L3**$_3$] (Ln = La and Eu), strong Cotton effects were observed at 209, 240, 263, 290, 334 and 381 nm.

For CPL measurement, both [Eu_2**L3**$^{SS}_3$] and [Eu_4**L3**$^{SS}_6$] exhibited fairly strong CPL signal for the for the $^5D_0$ -> $^7F_1$ transition, with g_{lum} = +0.10 for both complexes. Weaker g_{lum} value of -0.02 was observed for the the $^5D_0$ -> $^7F_2$ transition. Mirror CPL spectrum was also observed for these Eu complexes (figure 2b-31a). The CD and CPL result were consistent with the diastereoselective and diastereoselective breaking supramolecular formation behaviour that reported in Chapter 2a.

The luminescent properties of [Eu_2**L3**$_3$] and [Eu_4**L3**$_6$] were examined. Upon excitation of [Eu_2**L3**$_3$] at 311 nm, characteristics narrow Eu red emission lines at 595, 616, 688 and 697 nm were observed which indicated the successful sensitization of Eu^{III} $^5D_0$ excited state via antenna effect (figure 2b-31b). Similar result was observed upon excitation of [Eu_4**L3**$_6$] at 330 nm. The relative quantum yield of [Eu_2**L3**$^{RR}_3$] was determined to be 4.41% which is higher than that of [Eu_4**L3**$^{RR}_6$] (0.83%).

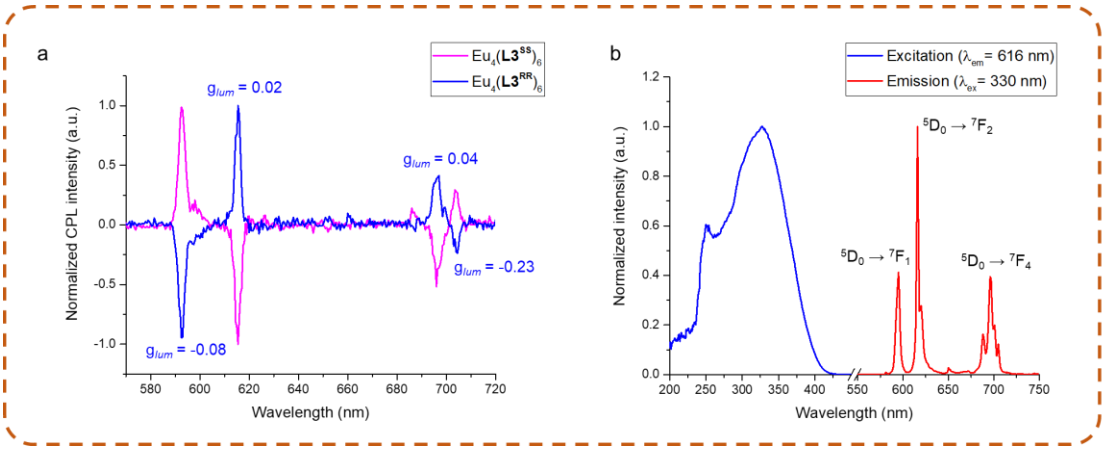

Figure 2b-31. (a) Normalized CPL spectra of [Eu_4**L1**$^{RR/SS}_6$] in MeCN. (b) Normalized excitation and emission spectra of [Eu_4**L1**$^{RR/SS}_6$] in MeCN.

2b.3 Conclusion

In conclusion, this work demonstrated that the lanthanide self-assembly supramolecular formation is highly sensitive to the lanthanide ionic radii as well as the length of central bridging linker. The formation of higher ordered tetrahedron can be favored by varying the distance of two metal chelating groups. Result showed that the formation of helicates is favored when larger lanthanide ion was used, while smaller lanthanide ions tend to form tetrahedron. This work is important as it demonstrated two important parameters for designing supramolecular lanthanide edifices.

2b.4 Experimental section

2b.4.1 Synthesis

N^2,$N^{2'}$-(1,4-phenylene)bis(N^6-((*S*)-1-phenylethyl)pyridine-2,6-dicarboxamide) ($L3^{SS}$) and N^2,$N^{2'}$-(1,4-phenylene)bis(N^6-((*R*)-1-phenylethyl)pyridine-2,6-dicarboxamide) ($L3^{RR}$)

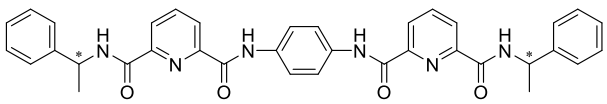

To a stirred solution of **(R)-6-((1-phenylethyl)carbamoyl)picolinic acid** (0.25 g, 0.92 mmol, 2.2 equiv.) in anhydrous DMF (4 mL) at room temperature, HATU (0.765 g, 2.01 mmol, 4.8 equiv.) was added under nitrogen. After allowing it to stir for 20 min, a 4,4'-diamino-p-terphenyl (0.045 g, 0.417 mmol, 1.0 equiv.) was added and the reaction mixture was allowed to stir for 20 min in dark. DIPEA (0.89 mL, 5.1 mmol, 12.5 equiv.) was then added to the reaction mixture and the resulting solution was stirred at room

temperature for 14 h. The reaction mixture was then diluted with H_2O (10 mL) and extracted with DCM (5 × 3 mL). After removing the organic volatile under reduced pressure, the residue was then washed with CH_3CN (10 mL), and fine powder was progressively precipitated out. Then the solid was collected by centrifugation and the desired compound was isolated. **(L3^{RR})**: (0.20 g, 0.33 mmol, 70% yield), ^{1}H NMR (400 MHz, $(CD_3)_2SO$, 299 K, δ): 1.67 (d, *J* = 8 Hz, 6H), 5.35–5.45 (m, 2H), 7.24 (t, *J* = 8 Hz, 2H), 7.34 (t, *J* = 8 Hz, 4H), 7.45 (d, *J* = 8 Hz, 4H), 7.70 (s, 4H), 8.07 (t, *J* = 8 Hz, 2H), 8.35 (d, *J* = 8 Hz, 2H), 8.39 (d, *J* = 8 Hz, 2H), 9.27 (d, *J* = 8 Hz, 2H). ^{13}C NMR (100 MHz, $(CD_3)_2SO$, 300 K, δ): 22.17(CH_3), 48.81(CH), 122.36, 125.41, 126.52, 127.28, 128.80, 134.71, 140.20, 144.52, 149.14, 149.42, 162.28, 163.39. HRMS (ESI) calcd. for $C_{72}H_{64}N_{12}O_8Na$ [2**L3^{RR}**+Na]$^+$: 1247.4862, found 1247.4850. **(L3^{SS})** was synthesized, following the procedure for **(L3^{RR})** with the use of **(S)-6-((1-phenylethyl)carbamoyl)picolinic acid** instead, in 60% yield (0.17 g, 0.28 mmol): ^{1}H NMR (400 MHz, $(CD_3)_2SO$, 299 K, δ): 1.67 (d, *J* = 8 Hz, 6H), 5.35–5.45 (m, 2H), 7.24 (t, *J* = 8 Hz, 2H), 7.34 (t, *J* = 8 Hz, 4H), 7.45 (d, *J* = 8 Hz, 4H), 7.70 (s, 4H), 8.07 (t, *J* = 8 Hz, 2H), 8.35 (d, *J* = 8 Hz, 2H), 8.39 (d, *J* = 8 Hz, 2H), 9.27 (d, *J* = 8 Hz, 2H). ^{13}C NMR (100 MHz, $(CD_3)_2SO$, 300 K, δ): 22.15, 48.78, 122.35, 125.39, 125.58, 126.51, 127.26, 128.78, 134.71, 140.19, 144.51, 149.13, 149.41, 162.28, 163.20. HRMS (ESI) calcd. for $C_{72}H_{64}N_{12}O_8Na$ [2**L3^{SS}**+Na]$^+$: 1247.4862, found 1247.4850.

N^2,$N^{2'}$-([1,1':4',1''-terphenyl]-4,4''-diyl)bis(N^6-((R)-1-phenylethyl)pyridine-2,6-dicarboxamide) (L4^{RR}) and N^2,$N^{2'}$-([1,1':4',1''-terphenyl]-4,4''-diyl)bis(N^6-((R)-1-phenylethyl)pyridine-2,6-dicarboxamide) (L4^{RR})

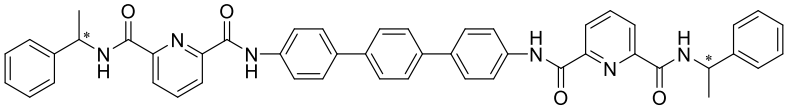

To a stirred solution of **(R)-6-((1-phenylethyl)carbamoyl)picolinic acid** (0.5 g, 1.85 mmol, 2.2 equiv.) in anhydrous DMF (8 mL) at room temperature, HATU (1.65 g, 4.06 mmol, 4.8 equiv.) was added under nitrogen. After allowing it to stir for 20 min, a 4,4'-diamino-p-terphenyl (1.10 g, 4.21 mmol, 1.0 equiv.) was added and the reaction mixture was allowed to stir for 20 min in dark. DIPEA (1.78 mL, 10.2 mmol, 12.5 equiv.) was then added to the reaction mixture and the resulting solution was stirred at room temperature for 14 h. The reaction mixture was then diluted with H_2O (20 mL) and extracted with DCM (5 × 6 mL). After removing all of the organic volatile under reduced pressure, the residue was then washed with CH_3CN three times (20 mL x 3), and fine powder was progressively precipitated out. Then the solid was collected by filtration and the desired compound was isolated. **(L4^{RR})**: (0.62 g, 0.81 mmol, 95.28% yield), ^{1}H NMR (400 MHz, $(CD_3)_2SO$, 299 K, δ): 1.69 (d, *J* = 6.96 Hz, 6H), 5.35–5.45 (m, 2H), 7.29 (t, *J* = 2.65 Hz, 2H), 7.39 (t, *J* = 8 Hz, 4H), 7.46 (d, *J* = 8 Hz, 4H), 7.66 (d, *J* = 8 Hz, 8H), 7.78 (d, *J* = 8 Hz, 4H), 8.09 (t, *J* = 8 Hz, 2H), 8.38 (d, *J* = 8 Hz, 2H), 8.44 (d, *J* = 8 Hz, 2H), 8.54 (d, *J* = 8 Hz, 2H), 10.01 (s, 2H). ^{13}C NMR (101 MHz, 300 K, δ): ^{13}C NMR (101 MHz, $(CD_3)_2SO$, 300K, δ): 163.11, 162.22, 149.59, 149.14, 144.60, 140.23, 138.74, 137.85, 135.95, 128.83, 127.29, 126.62, 125.66, 125.40, 122.16, 48.68, 22.28. HRMS (ESI) calcd. for $C_{48}H_{40}N_6O_4Na$ [**L4^{RR}**+Na]$^+$: 787.3003, found 787.3038. **(L4^{SS})** was synthesized, following the procedure for **(L4^{RR})** with the use of **(S)-6-((1-phenylethyl)carbamoyl)picolinic acid** instead, in 80% yield (0.4 g, 0.52 mmol): ^{1}H NMR (400 MHz, $(CD_3)_2SO$, 299 K, δ): 1.72 (d, *J* = 8 Hz, 6H), 5.40–5.48 (m, 2H), 7.30 (t, *J* = 8

Hz, 2H), 7.41 (t, *J* = 8 Hz, 4H), 7.49 (d, *J* = 8 Hz, 4H), 7.70 (d, *J* = 8 Hz, 8H), 7.83 (d, *J* = 8 Hz, 4H), 8.13 (t, 2H), 8.40 (d, *J* = 8 Hz, 2H), 8.47 (d, *J* = 8 Hz, 2H), 8.77 (d, *J* = 8 Hz, 2H). ^{13}C NMR (100 MHz, $(CD_3)_2SO$, 300 K, δ): 163.11, 162.22, 149.61, 149.15, 144.60, 140.23, 138.75, 137.86, 135.95, 128.83, 127.29, 126.62, 125.65, 125.40, 122.15, 48.67, 22.28. HRMS (ESI) calcd. for $C_{48}H_{40}N_6O_4Na$ [**L4^{RR}**+Na]$^+$: 787.3003, found 787.3038.

General synthetic procedures of [Ln_2**L3**$_3$]

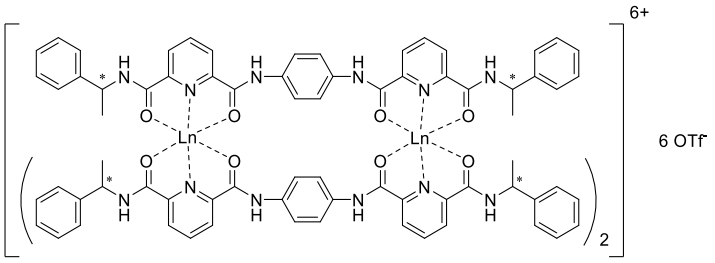

To a white suspension of **L3** (10 mg, 0.016 mmol, 1.5 equiv.) in a mixture of 8.49 ml of DCM/MeOH (12:1, v/v), a solution of $Ln(OTf)_3$ (0.011 mmol, 1 equiv.) (Ln = La, Sm, Eu, Gd, Tb and Lu) in 7.83 ml of CH_3CN was added. The solution was changed to homogeneous colorless solution immediately. The solution was then reacted for 16 hrs at room temperature and pressure. After 16 hrs, the solvent was removed under reduced pressure to give desired product.

[La_2**L3^{SS}**$_3$]: (12.0 mg, 3.99 x 10^{-3} mmol, 73.3% yield), ^{1}H NMR (400 MHz, CD_3CN, 299 K, δ): δ 10.32 (s, 3 x 2H), 9.00 (d, *J* = 6.9 Hz, 3 x 2H), 8.56 – 8.35 (m, 3 x 6H), 7.24 – 7.01 (m, 3 x 14H), 5.11 (p, *J* = 7.0 Hz, 3 x 2H), 1.71 (d, *J* = 7.1 Hz, 3 x 6H). ^{13}C NMR (100 MHz, CD_3CN, 300 K, δ): 167.57, 166.99, 148.75, 148.51, 143.14, 141.70, 133.52, 128.51, 127.66, 126.60, 126.31, 125.93, 123.56, 52.25, 20.61. HRMS (ESI) calcd. for $C_{112}H_{96}F_{12}La_2N_{18}O_{24}S_4$ [La_2(**L3^{SS}**)$_3$ + 4OTf^-]$^{2+}$: 1355.6841, found 1355.6792. Elemental

analysis calcd. for $C_{114}H_{96}F_{18}La_2N_{18}O_{30}S_6 \cdot 8H_2O$: C 43.41, H 3.58, N 7.99, found: C 43.35, H 3.60, N 7.92.

[La_2**L3**$^{RR}{}_3$]: (13.5 mg, 4.48 x 10^{-3} mmol, 82.4% yield), ^{1}H NMR (400 MHz, CD_3CN, 299 K, δ): 10.34 (s, 3 x 2H), 9.01 (d, *J* = 7.0 Hz, 3 x 2H), 8.61 – 8.39 (m, 3 x 6H), 7.25 – 6.97 (m, 3 x 14H), 5.11 (p, *J* = 7.0 Hz, 3 x 2H), 1.71 (d, *J* = 7.1 Hz, 3 x 6H). ^{13}C NMR (101 MHz, CD_3CN, 300 K, δ): 167.52, 166.92, 148.69, 148.45, 143.05, 141.64, 133.46, 128.44, 127.59, 126.53, 126.25, 125.86, 123.48, 52.21, 20.55. HRMS (ESI) calcd. for $C_{111}H_{95}F_9La_2N_{18}O_{21}S_3$ [La_2(**L3**^{RR}**)**$_3$ + 3OTf^- - H^+]$^{2+}$: 1280.7042, found 1280.7103. Elemental analysis calcd. for $C_{114}H_{96}F_{18}La_2N_{18}O_{30}S_6 \cdot 19H_2O$: C 40.80, H 4.03, N 7.52, found: C 40.90, H 3.57, N 7.30.

[Sm_2**L3**$^{SS}{}_3$]: (14.5 mg, 4.78 x 10^{-3} mmol, 87.9% yield), ^{1}H NMR (400 MHz, CD_3CN, 299 K, δ): 10.40 (s, 3 x 2H), 9.11 (d, *J* = 6.8 Hz, 3 x 2H), 8.59 – 8.31 (m, 3 x 6H), 7.18 (dd, *J* = 5.2, 1.9 Hz, 3 x 6H), 7.07 (dd, *J* = 6.8, 2.8 Hz, 3 x 4H), 6.98 (s, 3 x 4H), 5.08 – 4.92 (m, 3 x 2H), 1.66 (d, *J* = 7.0 Hz, 3 x 6H). ^{13}C NMR (125 MHz, CD_3CN, 300 K, δ): 169.49, 168.71, 149.49, 149.22, 143.59, 141.77, 133.34, 128.61, 127.66, 125.87, 125.66, 125.32, 123.32, 52.29, 20.63. HRMS (ESI) calcd. for $C_{111}H_{96}F_9N_{18}O_{21}S_3Sm_2$ [Sm_2(**L3**^{SS}**)**$_3$ + 3OTf^-]$^{3+}$: 861.8131, found 861.8192. Elemental analysis calcd. for $C_{114}H_{96}F_{18}Sm_2N_{18}O_{30}S_6 \cdot 18H_2O$: C 40.78, H 3.96, N 7.51, found: C 40.80, H 3.53, N 7.42.

[Sm_2**L3**$^{RR}{}_3$]: (12.1 mg, 3.99 x 10^{-3} mmol, 73.3% yield), ^{1}H NMR (495 MHz, CD_3CN, 299 K, δ): 10.15 (s, 3 x 2H), 8.89 (s, 3 x 2H), 8.45 – 8.32 (m, 3 x 6H), 7.13 (s, 3 x 6H), 7.03 (s, 3 x 4H), 6.92 (s, 3 x 4H), 5.01 – 4.95 (m, 3 x 2H), 1.72 – 1.50 (m, 3 x 6H). ^{13}C NMR (125 MHz, CD_3CN, 300 K, δ): 169.48, 168.71, 149.49, 149.23, 143.59, 141.76, 133.34, 128.61, 127.67, 125.87, 125.66, 125.31, 123.32, 52.28, 20.63. HRMS (ESI) calcd. for

$C_{111}H_{96}F_9N_{18}O_{21}S_3Sm_2$ [Sm_2(**L3^{RR}**)$_3$ + 3OTf$^-$]$^{3+}$: 861.8131, found 861.8160. Elemental analysis calcd. for $C_{114}H_{96}F_{18}Sm_2N_{18}O_{30}S_6 \cdot 18H_2O$: C 40.78, H 3.96, N 7.51, found: C 40.80, H 3.36, N 7.35.

[Eu_2**L3$^{SS}_3$**]: (14.1 mg, 4.64 x 10^{-3} mmol, 85.4% yield), ^{1}H NMR (400 MHz, CD_3CN, 299 K, δ): 8.12 (s, 3 x 4H), 7.40 (s, 3 x 2H), 7.20 (t, *J* = 7.9 Hz, 3 x 2H), 7.05 (d, *J* = 3.9 Hz, 3 x 10H), 6.45 (d, *J* = 8.0 Hz, 3 x 2H), 6.36 (d, *J* = 7.9 Hz, 3 x 2H), 6.14 (s, 3 x 2H), 5.04 (s, 3 x 2H), 2.04 (d, *J* = 6.0 Hz, 3 x 6H). ^{13}C NMR (125 MHz, CD_3CN, 300 K, δ): 160.24, 155.37, 142.84, 142.47, 141.94, 134.83, 128.50, 127.50, 125.65, 125.29, 91.92, 91.80, 51.70, 21.73. HRMS (ESI) calcd. for $C_{112}H_{96}Eu_2F_{12}N_{18}O_{24}S_4$ [Eu_2(**L3^{SS}**)$_3$ + 4OTf$^-$]$^{2+}$: 1369.1985, found 1369.1962. Elemental analysis calcd. for $C_{114}H_{96}F_{18}Eu_2N_{18}O_{30}S_6 \cdot 18H_2O$: C 40.74, H 3.96, N 7.50, found: C 40.83, H 3.56, N 7.44.

[Eu_2**L3$^{RR}_3$**]: (13.6 mg, 4.48 x 10^{-3} mmol, 82.3% yield), ^{1}H NMR (400 MHz, CD_3CN, 299 K, δ): 8.07 (s, 3 x 4H), 7.13 (d, *J* = 15.9 Hz, 3 x 4H), 6.99 (s, 3 x 10H), 6.37 (s, 3 x 2H), 6.28 (d, *J* = 8.2 Hz, 3 x 2H), 6.09 (s, 3 x 2H), 4.80 (s, 3 x 2H), 1.99 (s, 3 x 6H). ^{13}C NMR (125 MHz, CD_3CN, 300 K, δ): 163.43, 160.28, 155.37, 142.83, 142.46, 142.02, 134.81, 128.50, 127.50, 125.66, 125.29, 91.94, 91.80, 51.70, 21.73. HRMS (ESI) calcd. for $C_{112}H_{96}Eu_2F_{12}N_{18}O_{24}S_4$ [Eu_2(**L3^{RR}**)$_3$ + 4OTf$^-$]$^{2+}$: 1369.1985, found 1369.1949. Elemental analysis calcd. for $C_{114}H_{96}F_{18}Eu_2N_{18}O_{30}S_6 \cdot 4H_2O$: C 44.05, H 3.37, N 8.11, found: C 44.10, H 3.38, N 7.99.

[Gd_2**L3$^{SS}_3$**]: (12.5 mg, 4.10 x 10^{-3} mmol, 75.4% yield), HRMS (ESI) calcd. for $C_{111}H_{96}F_9N_{18}O_{21}S_3Gd_2$ [Gd_2(**L3^{SS}**)$_3$ + 3OTf$^-$]$^{3+}$: 866.4836, found 861.4828. Elemental analysis calcd. for $C_{114}H_{96}F_{18}Gd_2N_{18}O_{30}S_6 \cdot 21H_2O$: C 39.98, H 4.06, N 7.36, found: C 40.01, H 3.54, N 7.30.

[Gd_2**L3**$^{RR}{}_3$]: (14.3 mg, 4.69 x 10^{-3} mmol, 86.2% yield), HRMS (ESI) calcd. for $C_{111}H_{96}F_9N_{18}O_{21}S_3Gd_2$ [Gd_2(**L3**^{RR})$_3$ + $3OTf^-$]$^{3+}$: 866.4836, found 861.4865. Elemental analysis calcd. for $C_{114}H_{96}F_{18}Gd_2N_{18}O_{30}S_6 \cdot 22H_2O$: C 39.77, H 4.10, N 7.32, found: C 39.88, H 3.30, N 7.20.

[Tb_2**L3**$^{SS}{}_3$]: (14.7 g, 4.82 x 10^{-3} mmol, 88.6% yield), HRMS (ESI) calcd. for $C_{109}H_{94}F_3N_{18}O_{15}STb_2$ [Tb_2(**L3**^{SS})$_3$ + OTf^- - $2H^+$]$^{3+}$: 767.5113, found 767.5154. Elemental analysis calcd. for $C_{114}H_{96}F_{18}Tb_2N_{18}O_{30}S_6 \cdot 16H_2O$: C 41.01, H 3.86, N 7.55, found: C 41.07, H 3.49, N 7.48.

[Tb_2**L3**$^{RR}{}_3$]: (13.6 g, 4.46 x 10^{-3} mmol, 81.9% yield), HRMS (ESI) calcd. for $C_{112}H_{96}Eu_2F_{12}N_{18}O_{24}S_4$ [Tb_2(**L3**^{RR})$_3$ + $4OTf^-$]$^{2+}$: 1300.7232, found 1300.7169. Elemental analysis calcd. for $C_{114}H_{96}F_{18}Tb_2N_{18}O_{30}S_6 \cdot 15H_2O$: C 41.24, H 3.82, N 7.59, found: C 41.36, H 3.33, N 7.48.

[Lu_2**L3**$^{SS}{}_3$]: (14.2 g, 4.61 x 10^{-3} mmol, 84.7% yield), ^{1}H NMR (400 MHz, CD_3CN, 299 K, δ): 10.42 (s, 3 x 2H), 9.02 (d, *J* = 6.8 Hz, 3 x 2H), 8.56 – 8.33 (m, 3 x 6H), 7.17 (ddd, *J* = 8.9, 5.5, 3.3 Hz, 3 x 6H), 7.02 (d, *J* = 5.0 Hz, 3 x 8H), 4.97 (p, *J* = 6.9 Hz, 3 x 2H), 1.75 – 1.58 (m, 3 x 6H). ^{13}C NMR (125 MHz, CD_3CN, 300 K, δ): 166.82, 166.38, 147.04, 146.66, 143.08, 141.74, 133.26, 128.66, 127.61, 126.31, 125.79, 125.69, 123.07, 52.29, 20.77. HRMS (ESI) calcd. for $C_{111}H_{96}F_9Lu_2N_{18}O_{21}S_3$ [Lu_2(**L3**^{SS})$_3$ + $3OTf^-$]$^{3+}$: 878.1615, found 878.1616. Elemental analysis calcd. for $C_{114}H_{96}F_{18}Lu_2N_{18}O_{30}S_6 \cdot 7H_2O$: C 42.68, H 3.46, N 7.86, found: C 42.66, H 3.39, N 7.77.

[Lu_2**L3**$^{RR}{}_3$]: (14.4 g, 4.67 x 10^{-3} mmol, 85.9% yield), ^{1}H NMR (400 MHz, CD_3CN, 299 K, δ): 10.31 (s, 3 x 2H), 8.93 (s, 3 x 2H), 8.38 (s, 3 x 6H), 7.13 (s, 3 x 6H), 6.97 (s, 3 x 8H),

4.92 (d, *J* = 7.5 Hz, 3 x 2H), 1.61 (d, *J* = 7.1 Hz, 3 x 6H). ^{13}C NMR (125 MHz, CD_3CN, 300 K, δ): 166.41, 165.98, 146.63, 146.33, 142.69, 141.32, 128.26, 127.21, 125.87, 125.43, 125.29, 122.64, 51.86, 20.36. HRMS (ESI) calcd. for $C_{112}H_{96}F_{12}Lu_2N_{18}O_{24}S_4$ [Lu_2(**L3^{RR}**)$_3$ + 4OTf$^-$]$^{2+}$: 1391.7185, found 1391.7209. Elemental analysis calcd. for $C_{114}H_{96}F_{18}Lu_2N_{18}O_{30}S_6 \cdot 7H_2O$: C 42.68, H 3.46, N 7.86, found: C 42.74, H 3.54, N 7.84.

General synthetic procedures of [Ln_4**L3**$_6$]

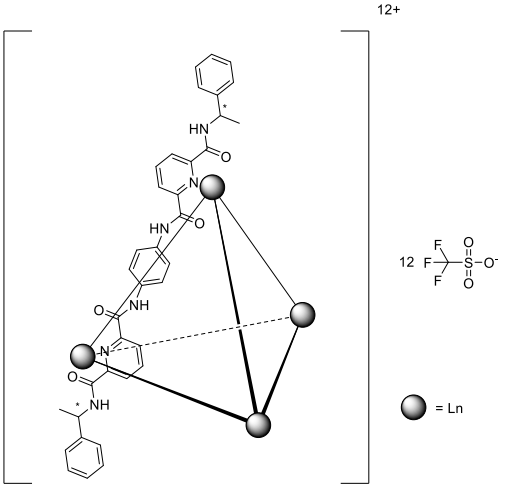

Ln_2**L3**$_3$ (0.66 mmol) were dissolved in CH_3CN (0.6 ml) and ether was allowed to slowly diffuse into the solution. The solution was decanted, and the crystal was washed with ether and dried under vacuum to obtain the homometallic tetrahedron crystal.

[Eu_4**L3^{SS}**$_6$]: (1.80 mg, 2.96 x 10^{-4} mmol, 90.0% yield), ^{1}H NMR (495 MHz, CD_3CN, 299 K, δ): 9.04 (s, 6 x 4H), 7.81 (s, 6 x 2H), 7.31 (s, 6 x 2H), 6.79 (s, 6 x 4H), 6.40 (d, *J* = 31.8 Hz, 6 x 8H), 5.88 (s, 6 x 2H), 5.47 (s, 6 x 2H), 4.09 (s, 6 x 2H), 2.34 (s, 6 x 6H). ^{13}C NMR (125 MHz, CD_3CN, 300 K, δ): 161.73, 156.50, 153.58, 142.91, 136.72, 135.57, 133.80, 127.79, 126.76, 125.52, 124.96, 121.93, 119.36, 92.00, 91.32, 52.29, 22.27. HRMS (ESI) calcd. for $C_{225}H_{192}Eu_4F_{27}N_{36}O_{51}S_9$ [Eu_4(**L3^{SS}**)$_6$ + 9 OTf$^-$]$^{3+}$: 1875.2490, found 1875.2516.

Elemental analysis calcd. for $C_{228}H_{192}Eu_4F_{36}N_{36}O_{60}S_{12}\cdot 11H_2O\cdot C_6H_{14}O$: C 44.10, H 3.61, N 7.91, found: C 44.12, H 3.68, N 7.83.

[Eu_4**L3^{RR}**$_6$]: (1.68 mg, 2.77 x 10^{-4} mmol, 83.8% yield), ^{1}H NMR (495 MHz, CD_3CN, 299 K, δ) 9.03 (s, 6 x 4H), 7.80 (s, 6 x 2H), 7.33 (s, 6 x 2H), 6.79 (s, 6 x 4H), 6.40 (d, *J* = 30.9 Hz, 6 x 8H), 5.89 (s, 6 x 2H), 5.47 (s, 6 x 2H), 4.11 (s, 6 x 2H), 2.33 (s, 6 x 6H). ^{13}C NMR (125 MHz, CD_3CN, 300 K, δ): 161.81, 156.51, 153.57, 142.91, 136.77, 135.56, 133.85, 128.50, 127.79, 126.76, 125.52, 124.96, 121.96, 119.39, 92.10, 91.38, 52.29, 22.26. HRMS (ESI) calcd. for $C_{225}H_{192}Eu_4F_{27}N_{36}O_{51}S_9$ [Eu_4(**L3^{RR}**)$_6$ + 9 OTf^-]$^{3+}$: 1875.2490, found 1875.2516. Elemental analysis calcd. for $C_{228}H_{192}Eu_4F_{36}N_{36}O_{60}S_{12}\cdot 14H_2O\cdot 2(C_6H_{14}O)$: C 44.15, H 3.83, N 7.72, found: C 44.13, H 3.78, N 7.72.

[Sm_4**L3^{SS}**$_6$]: (1.74 mg, 2.87 x 10^{-4} mmol, 86.9% yield), ^{1}H NMR (495 MHz, CD_3CN, 299 K, δ) 9.91 (s, 6 x 2H), 9.20 (s, 6 x 2H), 8.76 (d, *J* = 9.6 Hz, 6 x 2H), 8.63 (s, 6 x 2H), 8.54 (d, *J* = 8.6 Hz, 6 x 2H), 7.19 – 6.98 (m, 6 x 10H), 6.14 (s, 6 x 4H), 4.52 (d, *J* = 8.7 Hz, 6 x 2H), 1.43 (s, 6 x 6H). ^{13}C NMR (125 MHz, CD_3CN, 300 K, δ): 170.25, 167.32, 150.56, 148.82, 143.61, 142.40, 132.68, 128.54, 127.64, 126.67, 125.68, 125.39, 122.20, 121.60, 119.64, 52.47, 20.73. HRMS (ESI) calcd. for $C_{222}H_{191}F_{18}N_{36}O_{42}S_6Sm_4$ [Sm_4(**L3^{SS}**)$_6$ + 6 OTf^- - H^+]$^{5+}$: 1034.1745, found 1034.1748. Elemental analysis calcd. for $C_{228}H_{192}Sm_4F_{36}N_{36}O_{60}S_{12}\cdot 15H_2O\cdot 2(C_6H_{14}O)$: C 44.07, H 3.85, N 7.71, found: C 43.91, H 3.51, N 7.76.

[Sm_4**L3^{RR}**$_6$]: (1.89 g, 3.12 x 10^{-4} mmol, 94.4% yield), ^{1}H NMR (495 MHz, CD_3CN, 299 K, δ) ^{1}H NMR (495 MHz, Acetonitrile-d_3) δ 9.93 (s, 6 x 2H), 9.22 (s, 6 x 2H), 8.76 (d, *J* = 8.9 Hz, 6 x 2H), 8.74 – 8.59 (m, 6 x 2H), 8.54 (d, *J* = 9.3 Hz, 6 x 2H), 7.07 (dd, *J* = 29.5, 9.9 Hz, 6 x 10H), 6.13 (s, 6 x 4H), 4.52 (s, 6 x 2H), 1.44 (s, 6 x 6H). ^{13}C NMR (125 MHz, CD_3CN,

300 K, δ): 170.26, 167.34, 150.55, 148.83, 143.61, 142.42, 132.68, 128.54, 127.64, 126.67, 125.86, 125.67, 125.41, 122.21, 121.62, 119.64, 52.47, 20.73. HRMS (ESI) calcd. for $C_{225}H_{192}Sm_4F_{27}N_{36}O_{51}S_9$ [Sm_4(**L3^{RR}**)$_6$ + 9 OTf^-]$^{3+}$: 1873.2460, found 1873.2405. Elemental analysis calcd. for $C_{228}H_{192}Sm_4F_{36}N_{36}O_{60}S_{12}\cdot 12H_2O\cdot C_6H_{14}O$: C 44.02, H 3.63, N 7.90, found: C 44.03, H 3.72, N 7.92.

[Gd_4**L3^{SS}**$_6$]: (1.45 mg, 2.38 x 10^{-4} mmol, 72.1% yield), HRMS (ESI) calcd for $C_{224}H_{192}F_{24}Gd_4N_{36}O_{48}S_8$ [Gd_4(**L3^{SS}**)$_6$ + 8 OTf^-]$^{4+}$ is 1374.4520, found 1374.4512. Elemental analysis calcd. for $C_{228}H_{192}Gd_4F_{36}N_{36}O_{60}S_{12}\cdot 12H_2O$: C 43.40, H 3.45, N 7.99, found: C 43.31, H 3.38, N 7.78.

[Gd_4**L3^{RR}**$_6$]: (1.23 mg, 2.02 x 10^{-4} mmol, 61.2% yield), HRMS (ESI) calcd for $C_{225}H_{192}F_{27}Gd_4N_{36}O_{51}S_9$ [Gd_4(**L1^{RR}**)$_6$ + 9 OTf^-]$^{4+}$ is 1882.2535 (100%), found 1882.2499. Elemental analysis calcd. for $C_{228}H_{192}Gd_4F_{36}N_{36}O_{60}S_{12}\cdot 13H_2O$: C 43.28, H 3.47, N 7.97, found: C 43.22, H 3.58, N 7.85.

[Tb_4**L3^{SS}**$_6$]: (1.37 mg, 2.25 x 10^{-4} mmol, 68.1% yield), HRMS (ESI) calcd for $C_{222}H_{191}F_{18}N_{36}O_{42}S_6Tb_4$ [Tb_4(**L3^{SS}**)$_6$ + 6 OTf^- - H^+]$^{5+}$ is 1040.9802, found 1040.9800. Elemental analysis calcd. for $C_{228}H_{192}Tb_4F_{36}N_{36}O_{60}S_{12}\cdot 12H_2O\cdot C_6H_{14}O$: C 43.79, H 3.61, N 7.86, found: C 43.74, H 3.68, N 7.81.

[Tb_4**L3^{RR}**$_6$]: (1.66 mg, 2.72 x 10^{-4} mmol, 82.5% yield), HRMS (ESI) calcd for $C_{222}H_{191}F_{18}N_{36}O_{42}S_6Tb_4$ [Tb_4(**L3^{SS}**)$_6$ + 6 OTf^- - H^+]$^{5+}$ is 1040.9802, found 1040.9839. Elemental analysis calcd. for $C_{228}H_{192}Tb_4F_{36}N_{36}O_{60}S_{12}\cdot 17H_2O\cdot C_6H_{14}O$: C 43.18, H 3.72, N 7.75, found: C 43.13, H 3.46, N 7.67.

[Lu_4**L3**$^{SS}{}_6$]: (1.89 mg, 3.07 x 10^{-4} mmol, 92.9% yield), ^{1}H NMR (400 MHz, CD_3CN, 299 K, δ) 10.20 (s, 6 x 2H), 9.07 (s, 6 x 2H), 8.46 (dd, *J* = 10.6, 5.7 Hz, 6 x 6H), 7.05 (dt, *J* = 21.9, 6.3 Hz, 6 x 10H), 6.71 (d, *J* = 4.9 Hz, 6 x 4H), 5.02 (q, *J* = 6.5 Hz, 6 x 2H), 1.65 (t, *J* = 5.9 Hz, 6 x 6H). HRMS (ESI) calcd. for $C_{225}H_{192}Lu_4F_{27}N_{36}O_{51}S_9$ [Lu_4(**L3**^{SS})$_6$ + 9 OTf^-]$^{3+}$: 1905.6090, found 1905.6060.

[Lu_4**L3**$^{RR}{}_6$]: (1.34 mg, 2.17 x 10^{-4} mmol, 65.9% yield), ^{1}H NMR (405 MHz, CD_3CN, 299 K, δ) 10.22 (s, 6 x 2H), 9.07 (s, 6 x 2H), 8.47 (d, *J* = 5.5 Hz, 6 x 6H), 7.21 – 6.91 (m, 6 x 10H), 6.72 (s, 6 x 4H), 5.02 (p, *J* = 7.0 Hz, 6 x 2H), 1.66 (d, *J* = 7.1 Hz, 6 x 6H). HRMS (ESI) calcd. for $C_{225}H_{192}Lu_4F_{27}N_{36}O_{51}S_9$ [Lu_4(**L3**^{RR})$_6$ + 9 OTf^-]$^{3+}$: 1905.6090, found 1905.6080.

General synthetic procedures of [Ln_2**L4**$_3$]

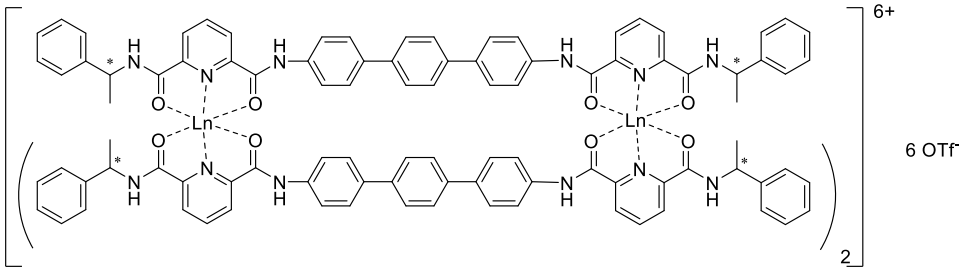

To a white suspension of **L4** (30 mg, 0.039 mmol, 1.5 equiv.) in a mixture of 2.55 ml of DCM/MeOH (12:1, v/v), a solution of $Ln(OTf)_3$ (0.026 mmol, 1 equiv.) (Ln = La, Sm, Eu, Gd, Tb and Lu) in 2.35 ml of CH_3CN was added. The solution was changed to yellow immediately. The solution was then reacted for 16 hrs at room temperature and pressure. After 16 hrs, the solvent was removed under reduced pressure to give desired product.

[La_2**L4**$^{SS}{}_3$]: (39.4 mg, 0.114 mmol, 86.9% yield), ^{1}H NMR (400 MHz, CD_3CN, 299 K, δ): 10.21 (s, 3 x 2H), 9.07 (d, *J* = 7.1 Hz, 3 x 2H), 8.67 – 8.40 (m, 3 x 6H), 7.88 (d, *J* = 8.3 Hz,

3 x 4H), 7.31 – 7.20 (m, 3 x 6H), 7.14 (s, 3 x 4H), 7.02 (d, *J* = 8.3 Hz, 3 x 4H), 6.95 (s, 3 x 4H), 5.14 – 5.05 (m, 3 x 2H), 1.76 (d, *J* = 7.1 Hz, 3 x 6H). ^{13}C NMR (101 MHz, CD_3CN, 300 K, δ): 168.78, 168.17, 150.80, 150.04, 144.52, 142.98, 139.58, 130.07, 129.10, 128.65, 128.40, 127.82, 127.37, 123.02, 119.33, 118.78, 55.51, 22.11. HRMS (ESI) calcd. for $C_{147}H_{120}F_9La_2N_{18}O_{21}S_3$ [La_2(**L4^{SS}**)$_3$ + 3 OTf^-]$^{3+}$: 1006.2012, found 1006.2037. Elemental analysis calcd. for $C_{150}H_{120}F_{18}N_{18}O_{30}S_6La_2 \cdot 7H_2O$: C 50.14, H 3.76, N 7.02, found: C 50.24, H 4.21, N 6.71.

[La_2**L4^{RR}**$_3$]: (37.9 mg, 0.109 mmol, 83.7% yield), ^{1}H NMR (400 MHz, CD_3CN, 299 K, δ): 10.21 (s, 3 x 2H), 9.07 (d, *J* = 6.6 Hz, 3 x 2H), 8.54 (d, *J* = 21.5 Hz, 3 x 6H), 7.88 (d, *J* = 8.3 Hz, 3 x 4H), 7.25 (s, 3 x 6H), 7.13 (s, 3 x 4H), 7.02 (d, *J* = 8.2 Hz, 3 x 4H), 6.96 (s, 3 x 4H), 5.08 (s, 3 x 2H), 1.76 (d, *J* = 7.1 Hz, 3 x 6H). ^{13}C NMR (125 MHz, CD_3CN, 300 K, δ): 167.40, 166.79, 149.42, 148.66, 143.13, 141.62, 138.50, 138.19, 135.54, 128.70, 127.72, 127.27, 127.02, 126.39, 125.98, 121.64, 52.14, 22.24. HRMS (ESI) calcd. for $C_{147}H_{120}F_9La_2N_{18}O_{21}S_3$ [La_2(**L4^{RR}**)$_3$ + 3 OTf^-]$^{3+}$: 1006.2012, found 1006.2037. Elemental analysis calcd. for $C_{150}H_{120}F_{18}N_{18}O_{30}S_6La_2 \cdot 6H_2O$: C 50.40, H 3.72, N 7.05, found: C 50.42, H 3.95, N 6.90.

[Sm_2**L4^{SS}**$_3$]: (38.1 mg, 0.0109 mmol, 83.5% yield), ^{1}H NMR (400 MHz, CD_3CN, 299 K, δ): 10.15 (s, 3 x 2H), 9.03 (d, *J* = 7.0 Hz, 3 x 2H), 8.44 (dq, *J* = 7.3, 4.3, 3.5 Hz, 3 x 6H), 7.89 (d, *J* = 8.3 Hz, 3 x 4H), 7.35 – 7.16 (m, 3 x 6H), 7.10 (dd, *J* = 7.0, 2.5 Hz, 3 x 4H), 6.98 (d, *J* = 8.2 Hz, 3 x 4H), 6.91 (s, 3 x 4H), 5.19 (q, *J* = 7.0 Hz, 3 x 2H), 1.77 (d, *J* = 6.9 Hz, 3 x 6H). ^{13}C NMR (101 MHz, CD_3CN, 300K, δ): 169.41, 168.43, 149.63, 148.99, 143.29, 141.71, 138.44, 137.96, 135.57, 128.69, 127.62, 127.20, 126.80, 125.81, 125.20, 121.36, 52.31, 20.90. HRMS (ESI) calcd. for $C_{147}H_{120}F_9Sm_2N_{18}O_{21}S_3$ [Sm_2(**L4^{SS}**)$_3$ + 3

$OTf^-]^{3+}$: 1013.8759, found 1013.8749. Elemental analysis calcd. for $C_{150}H_{120}F_{18}N_{18}O_{30}S_6Sm_2 \cdot 8H_2O$: C 49.58, H 3.77, N 6.94, found: C 49.59, H 4.07, N 6.81.

[Sm_2**L4**$^{RR}{}_3$]: (36.5 mg, 0.0104 mmol, 79.9% yield), ^{1}H NMR (400 MHz, CD_3CN, 299 K, δ): 10.11 (s, 3 x 2H), 9.00 (d, *J* = 7.0 Hz, 3 x 2H), 8.43 (dq, *J* = 7.3, 4.3, 3.5 Hz, 3 x 6H), 7.89 (d, *J* = 8.3 Hz, 3 x 4H), 7.42 – 7.17 (m, 3 x 6H), 7.10 (dd, *J* = 7.0, 2.5 Hz, 3 x 4H), 6.98 (d, *J* = 8.2 Hz, 3 x 4H), 6.91 (s, 3 x 4H), 5.19 (q, *J* = 7.0 Hz, 3 x 2H), 1.78 (d, *J* = 6.9 Hz, 3 x 6H). ^{13}C NMR (101 MHz, CD_3CN, 300K, δ): 169.42, 168.46, 149.74, 149.03, 143.40, 141.67, 138.49, 138.02, 135.53, 128.68, 127.62, 127.22, 126.87, 125.80, 125.25, 121.32, 52.25, 20.81. HRMS (ESI) calcd. for $C_{144}H_{118}N_{18}O_{12}Sm_2$ [Sm_2(**L4**^{RR}**)**$_3$ – $3H^+]^{3+}$: 863.9162, found 863.9186. Elemental analysis calcd. for $C_{150}H_{120}F_{18}N_{18}O_{30}S_6Sm_2 \cdot 17H_2O$: C 47.46, H 4.09, N 6.64, found: C 47.34, H 3.96, N 6.48.

[Eu_2**L4**$^{SS}{}_3$]: (36.4 mg, 0.0104 mmol, 79.8 % yield), ^{1}H NMR (400 MHz, CD_3CN, 299 K, δ): 8.21 – 7.96 (m, 3 x 4H), 7.42 (s, 3 x 2H), 7.24 (s, 3 x 4H), 7.15 (d, *J* = 5.8 Hz, 3 x 6H), 7.08 (s, 3 x 4H), 6.96 (s, 3 x 4H), 6.76 (s, 3 x 2H), 6.58 (s, 3 x 4H), 5.36 (s, 3 x 2H), 4.99 (s, 3 x 2H), 1.76 (s, 3 x 6H). ^{13}C NMR (125 MHz, CD_3CN, 300 K, δ): 155.25, 142.22, 138.62, 137.71, 135.36, 128.25, 127.19, 126.81, 126.69, 125.21, 122.15, 92.13, 91.52, 50.88, 21.13. HRMS (ESI) calcd. for $C_{147}H_{120}Eu_2F_9N_{18}O_{21}S_3$ [Eu_2(**L4**^{SS}**)**$_3$ + $3OTf^-]^{3+}$: 1015.2111, found 1015.2097. Elemental analysis calcd. for $C_{150}H_{120}F_{18}N_{18}O_{30}S_6Eu_2 \cdot 4H_2O$: C 50.54, H 3.62, N 7.07, found: C 50.55, H 3.90, N 6.50.

[Eu_2**L4**$^{RR}{}_3$]: (37.6 mg, 0.0108 mmol, 82.3% yield), ^{1}H NMR (400 MHz, CD_3CN, 299 K, δ): 8.02 (d, *J* = 49.6 Hz, 3 x 4H), 7.47 (d, *J* = 38.6 Hz, 3 x 2H), 7.23 (s, 3 x 4H), 7.16 (d, *J* = 5.2 Hz, 3 x 6H), 7.07 (s, 3 x 4H), 6.97 (s, 3 x 4H), 6.79 (s, 3 x 2H), 6.59 (s, 3 x 4H), 5.36 (s, 3 x 2H), 5.03 (s, 3 x 2H), 1.73 (d, *J* = 22.2 Hz, 3 x 6H). ^{13}C NMR (125 MHz, CD_3CN, 300 K,

δ): 155.62, 142.66, 138.99, 138.10, 135.80, 128.64, 127.58, 127.20, 127.07, 125.61, 122.56, 92.56, 91.97, 51.29, 21.55. HRMS (ESI) calcd. for $C_{147}H_{120}Eu_2F_9N_{18}O_{21}S_3$ [Eu_2(**L4^{RR}**)$_3$ + 3OTf$^-$]$^{3+}$: 1015.2111, found 1015.2097. Elemental analysis calcd. for $C_{150}H_{120}F_{18}N_{18}O_{30}S_6Eu_2 \cdot 5H_2O$: C 50.28, H 3.66, N 7.04, found: C 50.26, H 4.03, N 6.99.

[Gd_2**L4$^{SS}_3$**]: (39.5 mg, 0.0113 mmol, 86.2% yield), HRMS (ESI) calcd. for $C_{144}H_{117}Gd_2N_{18}O_{12}$ [Gd_2(**L4^{SS}**)$_3$ – 3H$^+$]$^{3+}$: 868.5869, found 868.5845. Elemental analysis calcd. for $C_{150}H_{120}F_{18}N_{18}O_{30}S_6Gd_2 \cdot 18H_2O$: C 47.07, H 4.11, N 6.59, found: C 46.97, H 3.72, N 6.40.

[Gd_2**L4$^{RR}_3$**]: (37.6 mg, 0.0107 mmol, 82.0% yield), HRMS (ESI) calcd. for $C_{147}H_{120}F_9Gd_2N_{18}O_{21}S_3$ [Gd_2(**L4^{RR}**)$_3$ + 3OTf$^-$]$^{3+}$: 1018.5452, found 1018.5465. Elemental analysis calcd. for $C_{150}H_{120}F_{18}N_{18}O_{30}S_6Gd_2 \cdot 23H_2O$: C 45.99, H 4.27, N 6.44, found: C 45.88, H 3.76, N 6.21.

[Tb_2**L4$^{SS}_3$**]: (37.2 mg, 0.0106 mmol, 81.1% yield), HRMS (ESI) calcd. for $C_{147}H_{120}F_9Tb_2N_{18}O_{21}S_3$ [Tb_2(**L4^{SS}**)$_3$ + 3OTf$^-$]$^{3+}$: 1019.5472, found 1019.5485. Elemental analysis calcd. for $C_{150}H_{120}F_{18}N_{18}O_{30}S_6Tb_2 \cdot 16H_2O$: C 47.47, H 4.04, N 6.64, found: C 47.58, H 3.87, N 6.56.

[Tb_2**L4$^{RR}_3$**]: (38.6 g, 0.0110 mmol, 84.1% yield), HRMS (ESI) calcd. for $C_{147}H_{120}F_9Tb_2N_{18}O_{21}S_3$ [Tb_2(**L4^{RR}**)$_3$ + 3OTf$^-$]$^{3+}$: 1019.5472, found 1019.5485. Elemental analysis calcd. for $C_{150}H_{120}F_{18}N_{18}O_{30}S_6Tb_2 \cdot 18H_2O$: C 47.03, H 4.10, N 6.58, found: C 47.02, H 4.06, N 6.19.

[Lu_2**L4$^{SS}_3$**]: (38.6 mg, 0.0109 mmol, 83.4% yield), ^{1}H NMR (400 MHz, CD_3CN, 299 K, δ): 10.13 (s, 3 x 2H), 8.99 (d, *J* = 7.0 Hz, 3 x 2H), 8.54 (dd, *J* = 6.0, 2.8 Hz, 3 x 2H), 8.46 (d, *J*

= 6.0 Hz, 3 x 4H), 7.83 – 7.66 (m, 3 x 4H), 7.27 (dt, *J* = 5.6, 2.8 Hz, 3 x 6H), 7.12 – 7.00 (m, 3 x 4H), 6.89 (d, *J* = 8.5 Hz, 3 x 4H), 6.83 (s, 3 x 4H), 4.95 (t, *J* = 7.0 Hz, 3 x 2H), 1.69 (d, *J* = 7.0 Hz, 3 x 6H). ^{13}C NMR (101 MHz, CD_3CN, 300K, δ): 166.79, 166.00, 147.36, 146.91, 142.84, 141.66, 138.40, 137.88, 135.37, 128.72, 127.58, 127.16, 126.75, 126.06, 125.62, 120.98, 52.16, 20.90. HRMS (ESI) calcd. for $C_{145}H_{118}F_3Lu_2N_{18}O_{15}S$ $[Lu_2(\mathbf{L4^{SS}})_3 + OTf^- - 2H^+]^{3+}$: 930.2509, found 930.2584. Elemental analysis calcd. for $C_{150}H_{120}F_{18}N_{18}O_{30}S_6Lu_2 \cdot 3H_2O$: C 50.14, H 3.53, N 7.02, found: C 50.10, H 3.74, N 6.90.

$[Lu_2\mathbf{L4^{RR}}_3]$: (39.3 mg, 0.0111 mmol, 85.0% yield), ^{1}H NMR (400 MHz, CD_3CN, 299 K, δ): 10.18 (s, 3 x 2H), 9.03 (d, *J* = 7.1 Hz, 3 x 2H), 8.54 (d, *J* = 6.2 Hz, 3 x 2H), 8.52 – 8.38 (m, 3 x 4H), 7.76 (d, *J* = 8.4 Hz, 2H), 7.36 – 7.21 (m, 3 x 4H), 7.11 – 6.99 (m, 3 x 4H), 6.89 (d, *J* = 8.5 Hz, 3 x 4H), 6.83 (s, 3 x 4H), 4.94 (t, *J* = 7.0 Hz, 3 x 2H), 1.69 (d, *J* = 7.0 Hz, 3 x 6H). ^{13}C NMR (101 MHz, CD_3CN, 300 K, δ): 166.79, 165.98, 147.36, 146.92, 142.82, 141.67, 138.38, 137.83, 135.37, 128.72, 127.58, 127.14, 126.74, 126.07, 125.63, 120.99, 52.18, 20.92. HRMS (ESI) calcd. for $C_{147}H_{120}F_9Lu_2N_{18}O_{21}S_3$ $[Lu_2(\mathbf{L4^{SS}})_3 + 3OTf^-]^{3+}$: 1030.2241, found 1030.2292. Elemental analysis calcd. for $C_{150}H_{120}F_{18}N_{18}O_{30}S_6Lu_2 \cdot 3H_2O$: C 50.14, H 3.53, N 7.02, found: C 50.09, H 3.95, N 7.00.

2b.4.2 Kinetic studies

The activation energy of tetrahedron-to-helicate transformation was determined by Arrhenius Equation that shown below,

$$lnk = lnA - \frac{E_a}{RT}$$

where *k* is the rate constant, A is the frequency factor, E_a is the activation energy ($Jmol^{-1}$), R is the gas constant (8.314 $JK^{-1}mol^{-1}$), T is the temperature (K).

Enthalpy ΔH was determined by the following equation

$$E_a = \Delta H + RT$$

where E_a is the activation energy ($Jmol^{-1}$), R is the gas constant (8.314 $JK^{-1}mol^{-1}$), T is the temperature (K).

Activation energy was determined by dissolving Eu or Sm tetrahedron in CD_3CN. The stock solution was transferred to five NMR tubes after performing the first NMR data point. The temperature (308K, 318K, 328K, 338K) of NMR tubes were maintained by water bath. The concentration of the mixture of tetrahedron and helicate was calculated by the following equations depending on the resolution of NMR spectrum:

2 [Ln_2**L3**$_3$] / 4[Ln_4**L3**$_6$] = integration of linker proton in helicate / integration of linker proton in tetrahedron OR 6 [Ln_2**L3**$_3$] / 4[Ln_4**L3**$_6$] = integration of [NH+phenyl proton] in helicate / integration of linker proton in tetrahedron WITH 3 [Ln_2**L3**$_3$] + 6 [Ln_4**L3**$_6$] = [**L3**].

	E_a ($kJmol^{-1}$)	A	ΔH_{298} ($kJmol^{-1}$)
Eu_A	90.1	2.93×10^{13}	+87.6
Eu_B	98.8	2.63×10^{13}	+96.3
Eu_C	102.3	1.16×10^{15}	+99.8
Average	97.1 (5)	4.05×10^{14}	+94.6 (5)

Table S2b-4. Kinetic data of Eu tetrahedron-to-helicate transformation.

	E_a (kJmol^{-1})	A	ΔH_{298} (kJmol^{-1})
Sm_A	78.8	2.25 x 10^{11}	+76.3
Sm_B	89.5	2.06 x 10^{13}	+87.0
Sm_C	84.5	4.51 x 10^{12}	+82.0
Sm_D	88.1	2.17 x 10^{13}	+85.6
Average	85.2 (4)	1.18 x 10^{13}	+82.7 (4)

Table S2b-5. Kinetic data of Sm tetrahedron-to-helicate transformation.

2b.4.3 Crystal structure of $Eu_4(L3^{SS})_6$:

Information	Identifier from cif file
Empirical formula	$C_{225}H_{192}Eu_4F_{27}N_{36}O_{51}S_9$
Formula weight	5625.51
Temperature/K	220.0
Crystal system	trigonal
Space group	R3
a/Å	29.9510(4)
b/Å	29.9510(4)
c/Å	71.8428(16)
α/°	90
β/°	90
γ/°	120
Volume/Å^3	55813.1(19)
Z	6
ρ_{calc}g/cm^3	1.004
μ/mm^{-1}	5.808
F(000)	17046.0
Crystal size/mm^3	0.24 × 0.17 × 0.14
Radiation	CuKα (λ = 1.54178)
2Θ range for data collection/°	5.902 to 100.82

Index ranges	-28 ≤ h ≤ 27, -27 ≤ k ≤ 29, -69 ≤ l ≤ 71
Reflections collected	41125
Independent reflections	20620 [R_{int} = 0.0639, R_{sigma} = 0.0648]
Data/restraints/parameters	20620/1946/2017
Goodness-of-fit on F^2	1.055
Final R indexes [I>=2σ (I)]	R_1 = 0.0553, wR_2 = 0.1497
Final R indexes [all data]	R_1 = 0.0685, wR_2 = 0.1594
Largest diff. peak/hole / e $Å^{-3}$	0.66/-0.18
Flack parameter	0.030(4)

Eu_4(**L3^{SS}**)$_6$	Shape measure (°)	
	Tricapped trigonal prism (D_{3h})	Capped square antiprism (C_{4v})
Eu1	6.45	11.13
Eu2	5.82	10.33
Eu3	5.94	10.23
Eu4	6.11	10.93

Supplementary Table 7. Results of the Shape Analysis for Eu_4(**L3^{SS}**)$_6$ tetrahedron.

Shape analysis was performed by the software developed by Raymond's group.[25-26] The coordination geometry of the Eu_4(**L3^{SS}**)$_6$ tetrahedron can be best described as tricapped trigonal prism.

2b.4.4 Photophysical data

	λ_{abs}^{max} (nm)	ε^{max} ($L \cdot mol^{-1} \cdot cm^{-1}$)
$[La_2(\mathbf{L4^{SS}})_3](CF_3SO_3)_6$	345	125117.0
$[La_2(\mathbf{L4^{RR}})_3](CF_3SO_3)_6$	345	128419.6
$[Sm_2(\mathbf{L4^{SS}})_3](CF_3SO_3)_6$	345	104030.4
$[Sm_2(\mathbf{L4^{RR}})_3](CF_3SO_3)_6$	345	104038.3
$[Eu_2(\mathbf{L4^{SS}})_3](CF_3SO_3)_6$	345	124128.9
$[Eu_2(\mathbf{L4^{RR}})_3](CF_3SO_3)_6$	345	125331.4
$[Gd_2(\mathbf{L4^{SS}})_3](CF_3SO_3)_6$	345	108324.9
$[Gd_2(\mathbf{L4^{RR}})_3](CF_3SO_3)_6$	345	115018.7
$[Tb_2(\mathbf{L4^{SS}})_3](CF_3SO_3)_6$	345	114213.3
$[Tb_2(\mathbf{L4^{RR}})_3](CF_3SO_3)_6$	345	119793.5
$[Lu_2(\mathbf{L4^{SS}})_3](CF_3SO_3)_6$	345	117521.9
$[Lu_2(\mathbf{L4^{RR}})_3](CF_3SO_3)_6$	345	115357.7

Table S2b-1. A summary of selected photophysical properties, UV-Vis absorption and luminescence data of $[Ln_2\mathbf{L4}_3]$ in acetonitrile solution using a 10 mm cuvette and filter 380 nm.

	λ_{abs}^{max} (nm)	ε^{max} ($L \cdot mol^{-1} \cdot cm^{-1}$)	λ_{em}^{max} (nm)	ϕ_x[b] (%)	τ (ms)
$[La_2(\mathbf{L3^{SS}})_3](CF_3SO_3)_6$	311	59052.4	/	/	/
$[La_2(\mathbf{L3^{RR}})_3](CF_3SO_3)_6$	311	58787.3	/	/	/
$[Sm_2(\mathbf{L3^{SS}})_3](CF_3SO_3)_6$	311	60056.4	/	/	/
$[Sm_2(\mathbf{L3^{RR}})_3](CF_3SO_3)_6$	311	62036.6	/	/	/
$[Eu_2(\mathbf{L3^{SS}})_3](CF_3SO_3)_6$	311	62925.5	616	4.07 (0.015)	1.42
$[Eu_2(\mathbf{L3^{RR}})_3](CF_3SO_3)_6$	311	61958.6	616	4.41 (0.005)	1.41
$[Gd_2(\mathbf{L3^{SS}})_3](CF_3SO_3)_6$	311	58396.8	462	/	0.0073
$[Gd_2(\mathbf{L3^{RR}})_3](CF_3SO_3)_6$	311	59227.0	/	/	/
$[Tb_2(\mathbf{L3^{SS}})_3](CF_3SO_3)_6$	311	61469.6	/	/	/
$[Tb_2(\mathbf{L3^{RR}})_3](CF_3SO_3)_6$	311	60113.3	/	/	/
$[Lu_2(\mathbf{L3^{SS}})_3](CF_3SO_3)_6$	311	60668.1	/	/	/
$[Lu_2(\mathbf{L3^{RR}})_3](CF_3SO_3)_6$	311	59773.5	/	/	/
$[Sm_4(\mathbf{L3^{SS}})_6](CF_3SO_3)_{12}$	330	130019.8	/	/	/
$[Sm_4(\mathbf{L3^{RR}})_6](CF_3SO_3)_{12}$	330	139354.6	/	/	/
$[Eu_4(\mathbf{L3^{SS}})_6](CF_3SO_3)_{12}$	330	123947.0	616	0.81 (0.035)	1.28
$[Eu_4(\mathbf{L3^{RR}})_6](CF_3SO_3)_{12}$	330	121335.7	616	0.83 (0.035)	1.27
$[Gd_4(\mathbf{L3^{SS}})_6](CF_3SO_3)_{12}$	330	123657.1	/	/	/
$[Gd_4(\mathbf{L3^{RR}})_6](CF_3SO_3)_{12}$	330	121829.6	466	/	0.0087[c]
$[Tb_4(\mathbf{L3^{SS}})_6](CF_3SO_3)_{12}$	330	131075.9	/	/	/
$[Tb_4(\mathbf{L3^{RR}})_6](CF_3SO_3)_{12}$	330	127713.5	/	/	/
$[Lu_4(\mathbf{L3^{SS}})_6](CF_3SO_3)_{12}$	330	110557.9	/	/	/
$[Lu_4(\mathbf{L3^{RR}})_6](CF_3SO_3)_{12}$	330	112691.3	/	/	/

Table S2b-2. A summary of selected photophysical properties, UV-Vis absorption and luminescence data of $[Ln_2\mathbf{L3}_3]$ and $[Ln_4\mathbf{L3}_6]$ complexes in acetonitrile solution[a]. [a]using a 10 mm cuvette and filter 380 nm. [b]The relative quantum yields were referenced with quinine sulfate in 0.1 M sulfuric acid (ϕ= 0.577, λ_{ex} = 350nm) with 10 mm cuvette. [c]Measurement performed at 77K in 1:4 MeOH/EtOH.

	g_{lum}			
Complex	$^5D_0$ -> $^7F_1$ ΔJ = 1 (592.5 nm)	$^5D_0$ -> $^7F_2$ ΔJ = 2 (615 nm)	$^5D_0$ -> $^7F_4$ ΔJ = 4 (695.5 nm)	$^5D_0$ -> $^7F_4$ ΔJ = 4 (704 nm)
$[Eu_2(\mathbf{L3^{SS}})_3]$	+0.10	-0.02	—	—
$[Eu_2(\mathbf{L3^{RR}})_3]$	- 0.10	+0.02	—	—
$[Eu_4(\mathbf{L3^{SS}})_6]$	+0.10	-0.02	-0.05	+0.23
$[Eu_4(\mathbf{L3^{RR}})_6]$	- 0.08	+0.02	+0.04	-0.23

*All g_{lum} values have associated nominal assumed instrumental uncertainty of ± 0.01.

Table S2b-3. g_{lum} values for $[Eu_2(\mathbf{L3^{SS/RR}})_3]$ and $[Eu_4(\mathbf{L3^{SS/RR}})_6]$ calculated from total intensity and CPL spectra.

2b.5 References

1. Jing, X.; He, C.; Yang, Y.; Duan, C. A metal–organic tetrahedron as a redox vehicle to encapsulate organic dyes for photocatalytic proton reduction, *J. Am. Chem. Soc.*, **2015**, *137*, 3967-3974.
2. Zhao, C.; Sun, Q.-F.; Hart-Cooper, W. M.; DiPasquale, A. G.; Toste, F. D.; Bergman, R. G.; Raymond, K. N., Chiral amide directed assembly of a diastereo- and enantiopure supramolecular host and its application to enantioselective catalysis of neutral substrates, *J. Am. Chem. Soc.*, **2013**, *135*, 18802-18805.
3. Montgomery, C. P.; Murray, B. S.; New, E. J.; Pal, R.; Parker, D. Cell-penetrating metal complex optical probes: targeted and responsive systems based on lanthanide luminescence, *Acc. Chem. Res.*, **2009**, *42*, 925-937.
4. Liu, X.; Wu, X.; He, C.; Zhang, R.; Duan, C. A truncated octahedral nanocage for fluorescent detection of nucleoside, *Dalton Trans.*, **2008**, *43*, 5866-5868.

5. Yim, K.-H.; Yeung, C.-T.; Wong, H.-Y.; Law, G.-L. Structural variation of self-assembled lanthanide supramolecular complexes induced by reaction conditions. *Inorg. Chem. Front.* **2021**, *8*, 2952-2964. G.

6. Bozoklu, G.; Marchal, C.; Gateau, C.; Pécaut, J.; Imbert, D.; Mazzanti, M. Diastereoselective self-assembly of a homochiral europium triangle from a bipyoxazoline-carboxylate ligand, *Chem. Eur. J.*, **2010**, *16*, 6159-6163.

7. Li, X.-Z.; Zhou, L.-P.; Yan, L.-L.; Yuan, D.-Q.; Lin, C.-S.; Sun, Q.-F. Evolution of luminescent supramolecular lanthanide $M_{2n}L_{3n}$ complexes from helicates and tetrahedra to cubes, *J. Am. Chem. Soc.*, **2017**, *139*, 8237-8244.

8. Wang, B.; Zang, Z.; Wang, H.; Dou, W.; Tang, X.; Liu, W.; Shao, Y.; Ma, J.; Li, Y.; Zhou, J. Multiple lanthanide helicate clusters and the effects of anions on their configuration, *Angew. Chem. Int. Ed.*, **2013**, *52*, 3756-3759.

9. Zhang, Y.; Ali, B.; Wu, J.; Guo, M.; Yu, Y.; Liu, Z.; Tang, J. Construction of metallosupramolecular coordination complexes: from lanthanide helicates to octahedral cages showing single-molecule magnet behavior, *Inorg. Chem.*, **2019**, *58*, 3167-3174.

10. Li, X.; Liu, W.; Guo, Z.; Tan, M. Trinuclear to dinuclear: a radii dependence lanthanide (III) self-assembly coordination behavior of an amide-type tripodal ligand, *Inorg. Chem.*, **2003**, *42*, 8735-8738.

11. Wang, Y.-W.; Zhang, Y.-L.; Dou, W.; Zhang, A.-J.; Qin, W.-W.; Liu, W.-S. Synthesis, radii dependent self-assembly crystal structures and luminescent properties of rare earth (III) complexes with a tripodal salicylic derivative, *Dalton Trans.*, **2010**, *39*, 9013-9021.

12. Bretonnière, Y.; Mazzanti, M.; Pécaut, J.; Olmstead, M. M. Cation-controlled

self-assembly of a hexameric europium wheel, *J. Am. Chem. Soc.*, **2002**, *124*, 9012-9013.

13. Chen, X.-Y., Bretonnière, Y.; Pécaut, J.; Imbert, D.; Bünzli, J.-C.; Mazzanti, M. Selective self-assembly of hexameric homo-and heteropolymetallic lanthanide wheels: Synthesis, structure, and photophysical studies, *Inorg. Chem.*, **2007**, *46*, 625-637.
14. Bozoklu, G. I.; Gateau, C.; Imbert, D.; Pécaut, J.; Robeyns, K.; Filinchuk, Y.; Memon, F.; Muller, G.; Mazzanti, M. Metal-controlled diastereoselective self-assembly and circularly polarized luminescence of a chiral heptanuclear europium wheel, *J. Am. Chem Soc.*, **2012**, *134*, 8372-8375.
15. Cai, L.-X.; Yan, L.-L.; Li, S.-C.; Zhou, L.-P.; Sun, Q.-F. Stereocontrolled self-assembly and photochromic transformation of lanthanide supramolecular helicates, *Dalton Trans.*, **2018**, *47*, 14204-14210.
16. Wang, W.; Wang, Y.-X.; Yang, H.-B. Supramolecular transformations within discrete coordination-driven supramolecular architectures, *Chem. Soc. Rev.*, **2016**, *45*, 2656-2693.
17. Liu, C.-L.; Zhou, L.-P.; Tripathy, D.; Sun, Q.-F. Self-assembly of stable luminescent lanthanide supramolecular M_4L_6 cages with sensing properties toward nitroaromatics, *Chem. Commun.*, **2017**, *53*, 2459-2462.
18. Faulkner, S.; Burton-Pye, B. P.; pH dependent self-assembly of dimetallic lanthanide complexes, *Chem. Commun.*, **2005**, 259-261.
19. Lukeš, I.; Kotek, J.; Vojtíšek, P.; Hermann, P. Complexes of tetraazacycles bearing methylphosphinic/phosphonic acid pendant arms with copper(II), zinc(II) and lanthanides(III). A comparison with their acetic acid analogues,

Coord. Chem. Rev., **2001**, *216-217*, 287-312.

20. Plush, S. E.; Clear, N. A.; Leonard, J. P.; Fanning, A.-M.; Gunnlaugsson, T. The effect on the lanthanide luminescence of structurally simple Eu(iii) cyclen complexes upon deprotonation of metal bound water molecules and amide based pendant arms, *Dalton Trans.*, **2010**, *39*, 3644-3652.

21. Wong, H.-Y.; Chan, W. T. K.; Law, G.-L. Assembly of lanthanide (III) cubanes and dimers with single-molecule magnetism and photoluminescence, *Inorg. Chem.*, **2018**, *57*, 6893-6902.

22. Leonard, J. P.; Jensen, P.; McCabe, T.; O'Brien, J. E.; Peacock, R. D.; Kruger, P. E.; Gunnlaugsson, T. Self-assembly of chiral luminescent lanthanide coordination bundles. *J. Am. Chem. Soc.* **2007**, *129*, 10986-10987.

23. Caulder, D. L.; Raymond, K. N. Supermolecules by design. *Acc. Chem. Res.* **1999**, *32*, 975-982.

24. Li, G.; Zhao, X.; Han, Q.; Wang, L.; Liu, W. Radii-dependent self-assembly of chiral lanthanide complexes: synthesis, chirality, and single-molecule magnet behavior, *Dalton Trans.* **2020**, *49*, 10120-10126.

25. Xu, J.; Radkov, E.; Zieglar, M.; Raymond, K. N. Plutonium(IV) sequestration: structural and thermodynamic evaluation of the extraordinarily stable cerium(IV) hydroxypyridinonate complexes[1]. *Inorg. Chem.* **2000**, *39* (18), 4156-4164.

26. Daumann, L. J.; Tatum, D. S.; Andolina, C. M.; Pacold, J. I.; D'Aléo, A.; Law, G.-L.; Xu, J.; Raymond, K. N. Effects of ligand geometry on the photophysical properties of photoluminescent Eu(III) and Sm(III) 1-hydroxypyridin-2-one complexes in aqueous solution. *Inorg. Chem.* **2016**, *55* (1) 114-124.

Chapter 3: Formation of chiroptical lanthanide heterometallic Ln_4L_6 tetrahedral cage

3.1 Introduction

3.1.1 Introduction to lanthanide heterometallic systems

Transition metal based supramolecular complexes have been proven to be an excellent candidate for various applications including catalyst[1-5] and luminescent probes.[6-8] In order to fine tune the functional role of supramolecular materials, numerous hybrid metal supramolecular systems have been reported. For instance, some supramolecular catalysts involved the use of two different metal ions.[9-11] One can act as structural nodes to provide a well-defined structure for matching substrate, while another one act as a catalytic centre to interact with target substrates.

For lanthanide supramolecular complexes, numerous d-f hybrid complexes topologies[12-14] as well as heterometallic lanthanide based supramolecular complexes have been prepared.[15-20] It was found that the combination of different lanthanide ions can lead to an enhancement in photophysical properties including improvement in up-conversion efficiency[21] as well as better optimization in the optical properties.[22] The enhancement in photophysical properties can help to develop potential dual imaging agent that cover both visible and near-infrared region.[23]

3.1.2 Preparation of lanthanide heterometallic complexes

As mentioned in the previous chapters, preparation of lanthanide supramolecular complexes is difficult compared with transition metal due to their labile coordination number and poor stereochemical preferences. Preparation of lanthanide heterometallic systems is more challenging due to the similar ionic radii and chemical properties of lanthanide ions.[24] During the one-pot mixed lanthanide self-assembly process, lanthanide ions will bind to the ligand randomly and complexes with different lanthanide content will result.

Generally, there are two strategies for preparing lanthanide heterometallic complexes. The first strategy is to synthesize an organic ligand that consists of two different chelating groups.[25-27] These two coordination sites are well designed so that they can bind to the lanthanide ions selectively. However, selective coordination with different lanthanide ions is difficult using the same ligand. Undesired supramolecular products with different fractions of lanthanide content can be only partially removed from the reaction mixture and thus the complexes can be only studied as a part of a statistical mixture.[26] Rare successful examples of pure heterometallic complexes were demonstrated by Aromí's group.[26] They have synthesized a series of asymmetric ligands with excellent selectivity towards lanthanide ions by employing β-diketone and dipicolinate-like as the coordination sites. Figure 3-1 showed the ligand examples.

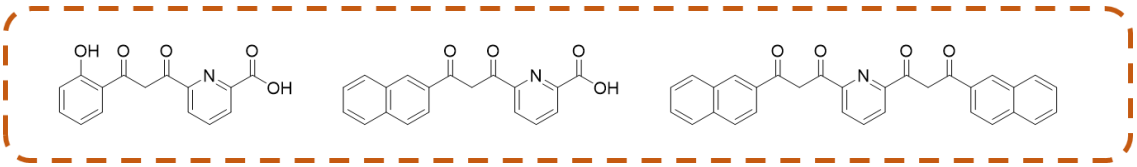

Figure 3-1. *Ligand examples reported by Aromí's group.*[26]

Lanthanide heterometallic complexes can be also prepared by stepwise reaction. Different from one-pot self-assembly process, stepwise reaction approach required the preparation of lanthanide complexes followed by the attachment of two lanthanide complexes.[28, 29] Stepwise reaction approach is a better approach since the lanthanide contents of the resulting complexes can be controlled easily. However, this strategy strongly depends on the use of ligand having strong chelating power such as macrocyclic ligands.[30-32] Otherwise, the complexes are not stable enough to survive the next steps in the reaction. Figure 3-2 showed an example of lanthanide heterometallic complexes that prepared by stepwise reaction approach.[32]

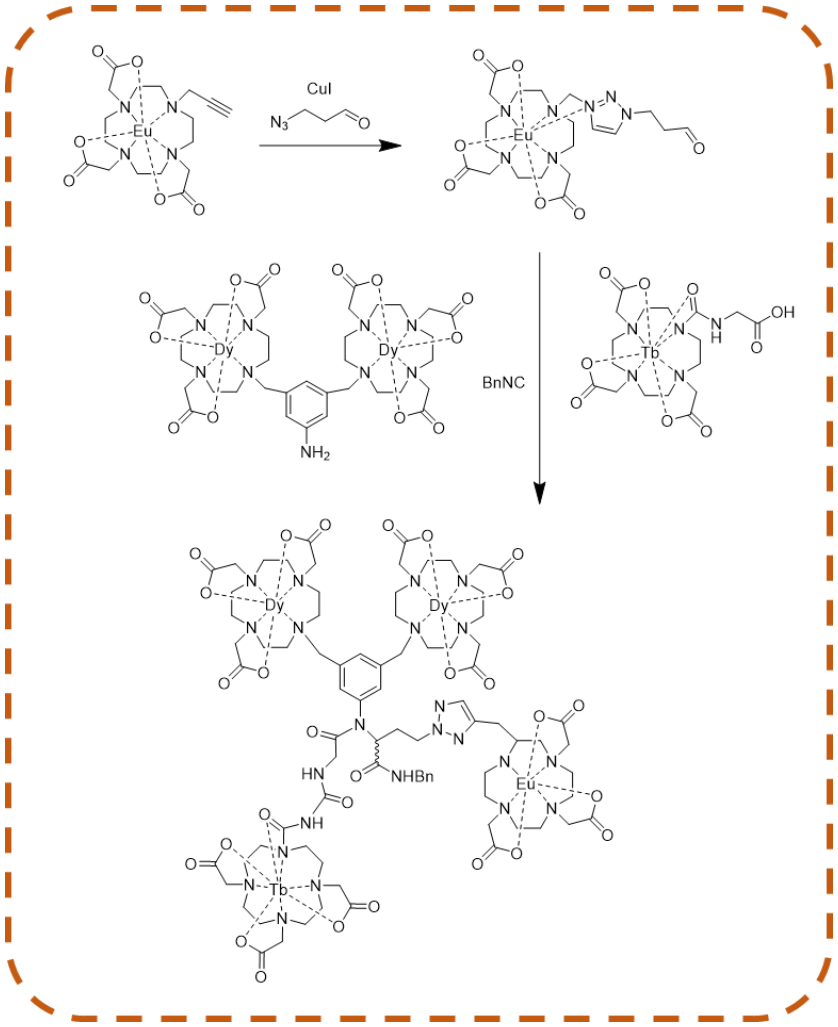

Figure 3-2. *Lanthanide heterometallic complexes prepared by stepwise reaction approach.*[32]

3.1.3 Scope of study

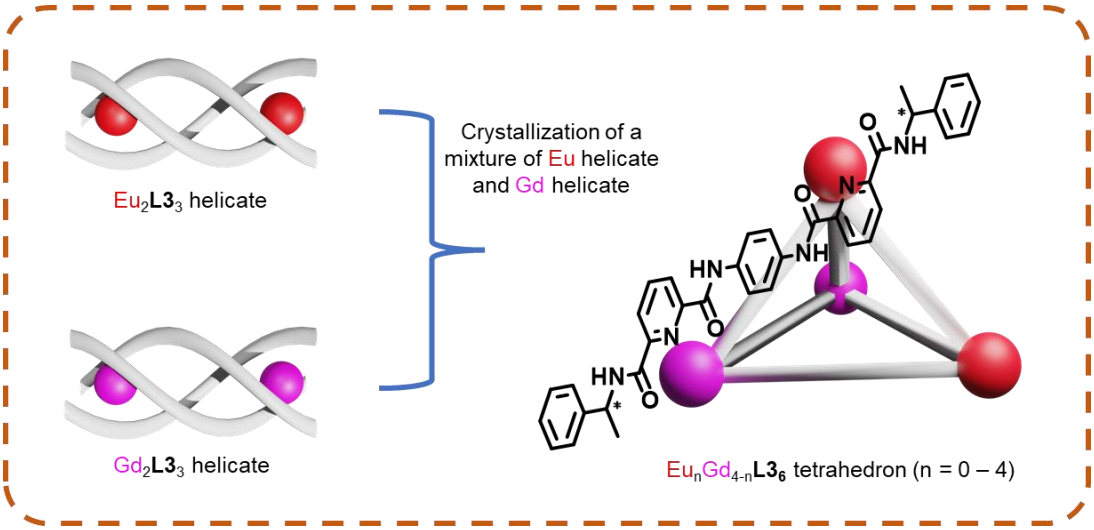

Figure 3-3. *Self-assembly of a mixed heterometallic tetrahedron from metal helicates by one-step process by ether diffusion crystallization. The heterometallic tetrahedron consists of Eu and Gd in a ratio of 1:1.*

Inspired by the potential application of heterometallic lanthanide systems, we investigate the possibility of developing heterometallic lanthanide tetrahedron via crystallization. In this chapter, a series of mixed lanthanide heterometallic tetrahedra were developed with the use of C_2-symmetical bis(tridentate) ligand. Crystallization of two lanthanide helicates by slow diffusion of diisopropyl ether leads to a formation of mixed heterometallic tetrahedron. Detailed ESI-HRMS deconvolution was done to analyze the percentage amount of tetrahedron. The effect of ionic radii towards the formation of heterometallic tetrahedron was also investigated. By varying the ratio of two different lanthanide helicates, the percentage amount of tetrahedra varies. Photophysical studies of the tetrahedra were further investigated.

3.2 Result and discussion

3.2.1 Preparation of [Eu_nGd_{4-n}**L3**$_6$](n = 0-4)

A C_2-symmetrical bis(tridentate) ligand **L3** was reported in Chapter 2b and the corresponding lanthanide helicate was found to have an helicate-to-tetrahedron transformation. Such helicate-to-tetrahedron transformation depends on the size of lanthanide cations and the linker length and pure tetrahedron can be only isolated via crystallization. With this interesting findings, further investigation of the helicate-to-tetrahedron transformation was done by crystallization of different mixture of [Ln_2**L3**$_3$] helicate. It was hypothesized that the helicate will either undergo a self-sorting behavior to form pure homometallic tetrahedron or forming a mixture of tetrahedron with different metal content due to the similar ionic radii of lanthanide ions.

Interestingly, upon crystallization of a mixture of [Eu_2(**L3**)$_3$] and [Gd_2(**L3**)$_3$] helicates in a ratio of 1 to 1, a single crystal of mixed heterometallic [Eu_nGd_{4-n}**L3**$_6$] (n = 0-4) was obtained. X-ray crystal structure of [Eu_nGd_{4-n}**L3**$_6$] (n = 0-4) revealed a tetrahedral topology constructed by four lanthanide ions and six ligands (figure 3-4).

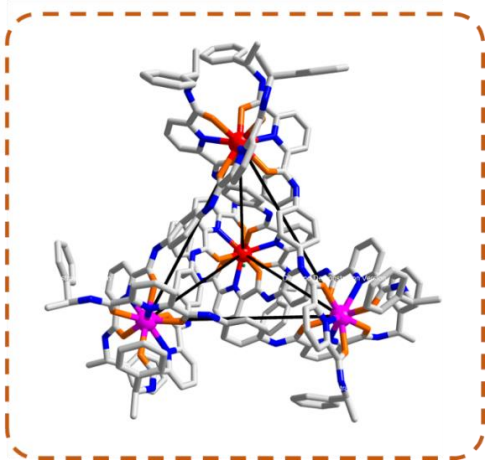

Figure 3-4. *X-ray crystal structure of [Eu_nGd_{4-n}**L3**$_6$] (n = 0-4). The Eu and Gd metal centers were refined as 50:50 by X-ray crystallography however depicted as a single element in the illustration.*

Precise differentiation by X-ray crystallography between Eu and Gd metal centre is no possible due to their similar electron density. Thus, each Eu and Gd metal centre is refined as 50:50. In the crystal structure, all the lanthanide centres are arranged in the same Δ-configurations and each metal centre can be best described as as tricapped trigonal prism. Average Ln – N (Ln = Eu or Gd) distance is 2.553 Å, comparable to an average Eu – N (2.561 Å) and Gd – N (2.581 Å) distance of pyridinedicarboxylic chelating unit. Average Ln – O distance was found to be 2.406 Å, which is also comparable to the average Gd – O and distance Eu – O (2.426 Å and 2.423 Å) that reported in literature.[33] Characterization by NMR is not possible due to the strong paramagnetic nature of Gd. Therefore, the chemical formulas were examined by ESI-HRMS. In the ESI-HRMS spectrum, peaks series were observed corresponding to the heterometallic [Eu_nGd_{4-n}**L3**$_6$] (n = 0-4) species with the progressive loss of anions and protons (figure 3-5).

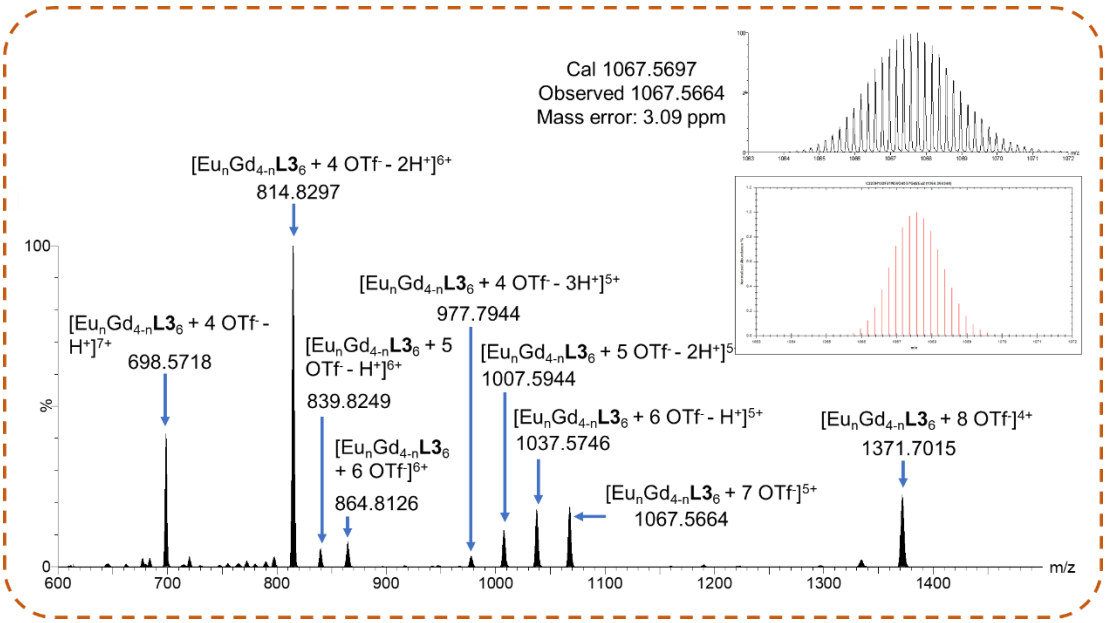

Figure 3-5. *ESI-HRMS spectra of [Eu_nGd_{4-n}**L3**$_6$] (n = 0-4) with insets showing the observed and isotropic pattern of the peaks corresponding to [Eu_2Gd_2**L3**$_6$ + 7OTf^-]$^{5+}$.*

3.2.3 Effect of difference in ionic radii

Gd was replaced by other lanthanide ions to investigate the effect of ionic radii. When Gd was replaced by Sm, which exhibited less paramagnetic nature and a slightly small ionic radii difference with Eu ($\Delta r_{Eu\text{-}Gd}$ 1.3 pm vs $\Delta r_{Eu\text{-}Sm}$ 1.2 pm),[34] similar mixed heterometallic tetrahedron was formed upon crystallization of a mixture of [Eu_2(**L3**)$_3$] and [Sm_2(**L3**)$_3$] in a ratio of 1 to 1. The chemical formulas were also confirmed by ESI-HRMS, in which single set of peaks corresponding to [Eu_nSm_{4-n}**L3**$_6$] (n = 0-4) species were observed (figure 3-6). Similar with the result in chapter 2b, ^{1}H NMR revealed that [Eu_2Sm_2**L3**$_6$] was not stable upon dissolution and it slowly transformed back to a mixture of [Eu_2(**L3**)$_3$], [EuSm(**L3**)$_3$] and [Sm_2(**L3**)$_3$] after 13 days (figure 3-7).

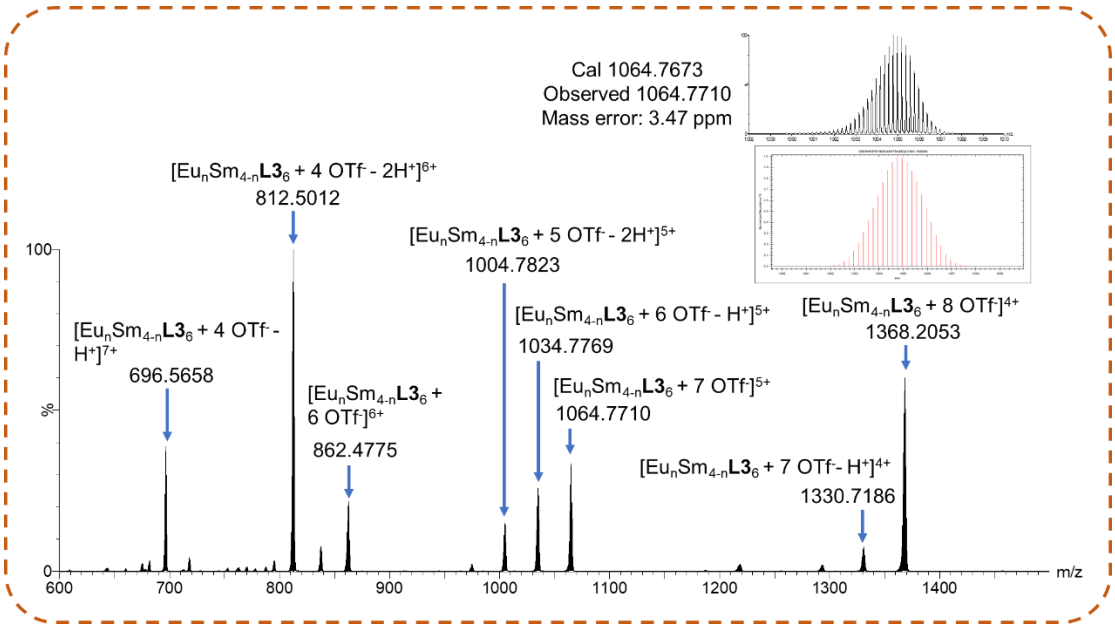

Figure 3-6. *ESI-HRMS spectra of [Eu_nSm_{4-n}**L3**$_6$] (n = 0-4) with insets showing the observed and isotropic pattern of the peaks corresponding to [Eu_2Sm_2**L3**$_6$ + 7OTf^-]$^{5+}$.*

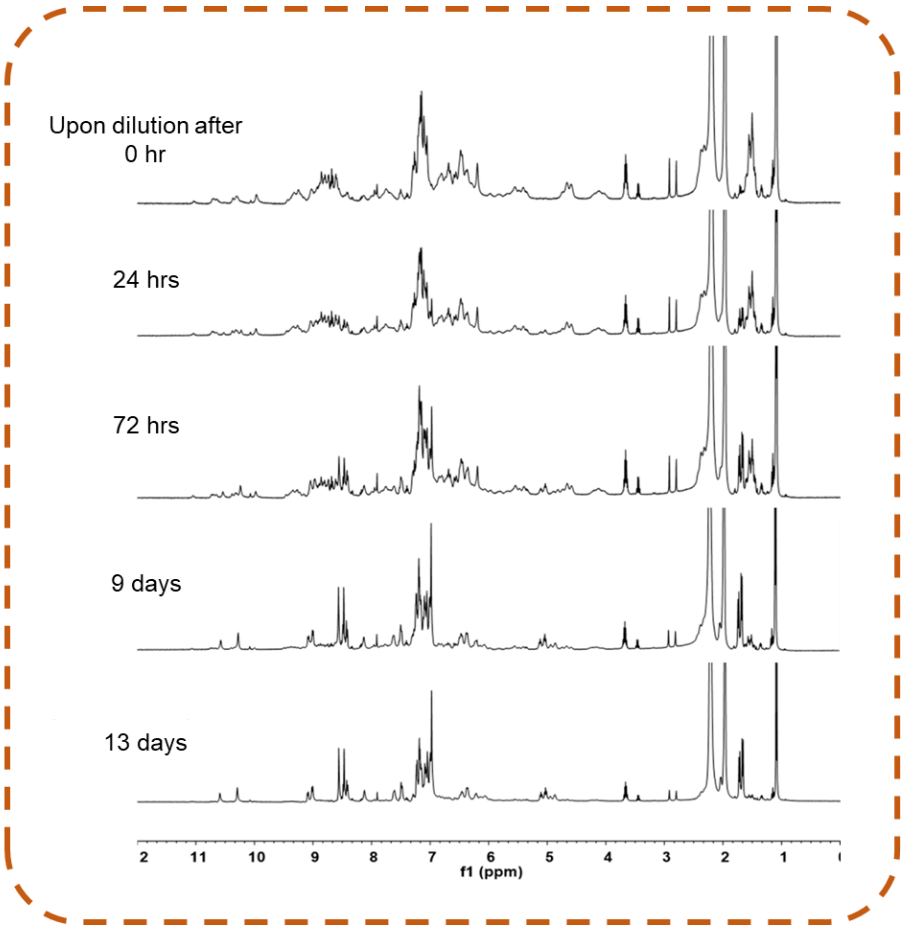

Figure 3-7. *Variation of ^{1}H NMR of [Eu_nSm_{4-n}**L3**$_6$] (n = 0-4) upon dissolution in CD_3CN.*

Different result was obtained when La, Tb and Lu were used to replace Gd. In the case of Tb, five different types of tetrahedra were observed in the ESI-HRMS upon crystallization of a mixture of [Eu_2**L3**$_3$] and [Tb_2**L3**$_3$] in a ratio of 1 to 1. These five tetrahedra can be assigned as [Eu_4**L3**$_6$], [Eu_3Tb**L3**$_6$] [Eu_2Tb_2**L3**$_6$], [$EuTb_3$**L3**$_6$] and [Tb_4**L3**$_6$] (figure 3-8). Similar result was also observed when Gd was replaced by Lu. The ESI-HRMS also showed the existence of a mixture of [Eu_4**L3**$_6$], [Eu_3Lu**L3**$_6$] [Eu_2Lu_2**L3**$_6$], [$EuLu_3$**L3**$_6$] and [Lu_4**L3**$_6$] (figure 3-9).

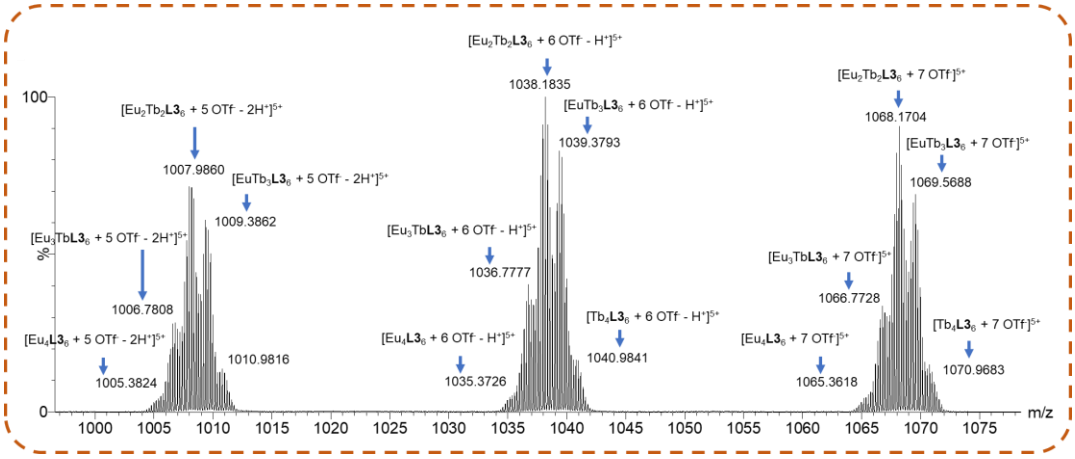

Figure 3-8. *Expanded region of the ESI-HRMS spectrum of a mixture of [Eu_4**L3**$_6$], [Eu_3Tb**L3**$_6$], [Eu_2Tb_2**L3**$_6$], [$EuTb_3$**L3**$_6$] and [Tb_4**L3**$_6$].*

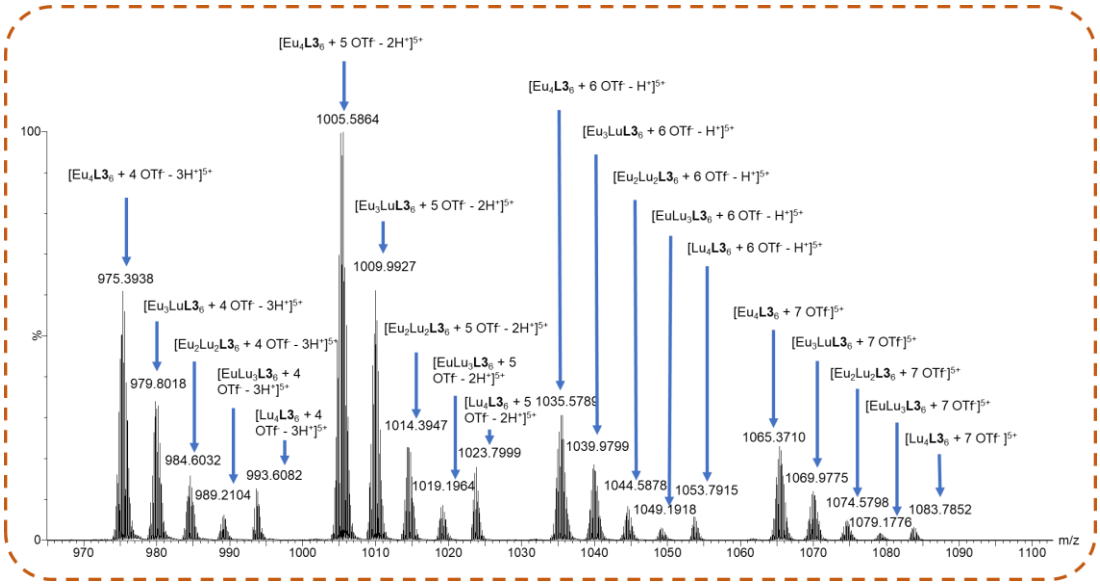

Figure 3-9. *Expanded region of the ESI-HRMS spectrum of a mixture of [Eu_4**L3**$_6$], [Eu_3Lu**L3**$_6$], [Eu_2Lu_2**L3**$_6$], [$EuLu_3$**L3**$_6$] and [Lu_4**L3**$_6$].*

When Gd was replaced by La, ESI-HRMS result revealed that the major species were [La_2**L3**$_3$], [EuLa**L3**$_3$] and [Eu_2**L3**$_3$], and minor species were found to be [Eu_2La_2**L3**$_6$] and [Eu_3La**L3**$_6$] (figure 3-10). As discussed in chapter 2b, La highly prefers to form helicates upon coordinating with lanthanide. Thus, it is expected that La also biases the helicate-to-tetrahedron transformation. [La_2**L3**$_3$] was also observed in the crystallized product.

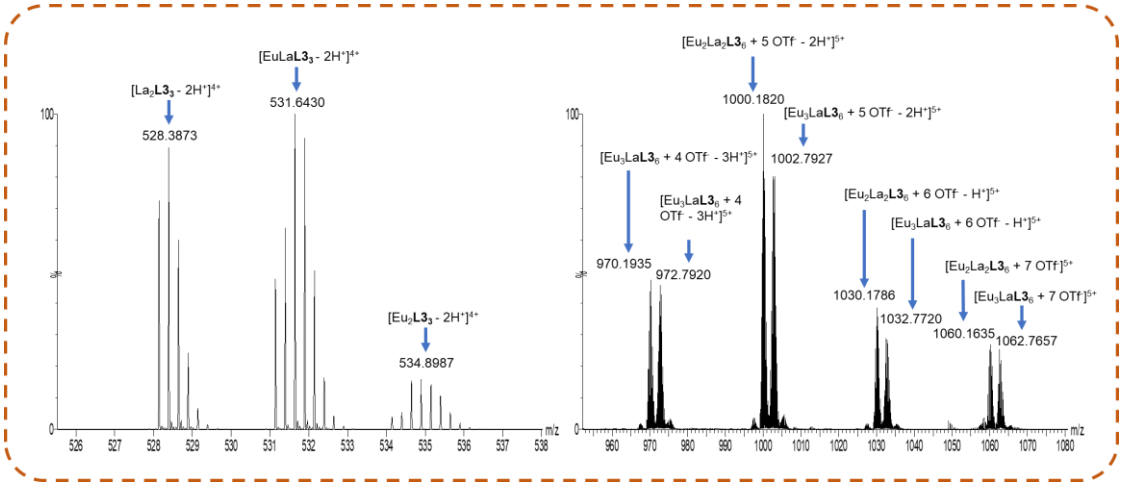

Figure 3-10. *Expanded region of the ESI-HRMS spectrum of a mixture of [Eu_2**L3**$_3$], [EuLa**L3**$_3$], [La_2**L3**$_3$], [Eu_2La_2**L3**$_6$] and [Eu_3La**L3**$_6$].*

Mass deconvolution using OrginPro was performed and figure 3-11 summarizes the effect of ionic radii towards the helicate-to-tetrahedron transformation via crystallization. Generally, the formation of lanthanide heterometallic tetrahedron is highly sensitive to the difference of ionic radii between the lanthanide ions used in crystallization. In the case of Eu and Gd, the ionic radii differ from 1.3 pm, and the largest percentage amount of complex was found to be [Eu_2Gd_2**L3**$_6$] heterometallic tetrahedron. Similar result can be observed when the difference of ionic radii slightly decreased to 2.5 pm, which is the case of Eu and Tb.

Interestingly, the intensity of [$Ln_2Ln'_2$**L3**$_6$] heterometallic tetrahedron also decreased if the difference of ionic radii increased. As evidenced in the combination of Eu and Lu, the major species was found to be [Eu_4**L3**$_6$] and the heterometallic [Eu_2Lu_2**L3**$_6$] became minor species when the difference of ionic radii became 8.8 pm.

The maximum difference of ionic radii that this system can tolerate to form heterometallic tetrahedron, i.e., the cutoff ionic radii, was further investigated by utilizing different pairs of lanthanides. Due to the similar mass difference, selection of lanthanide pairs was challenging. Based on the MS deconvolution result, the cutoff ionic radii was found to be 8.8 pm in the combination of Eu and Lu.

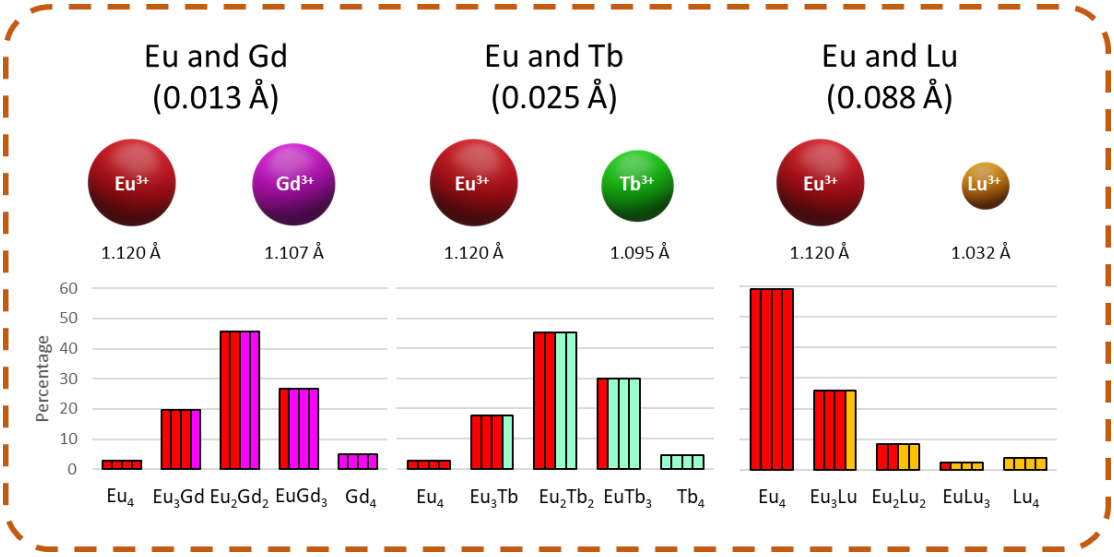

Figure 3-11. *Quantitative analysis of the lanthanide heterometallic tetrahedra. The ESI-MS data was calculated based on the intensity of [complex + 9 OTf$^-$]$^{3+}$*

3.2.3 Variation of metal content of the heterometallic tetrahedra

The preferential formation of heterometallic tetrahedra via crystallization is important for preparing of lanthanide heterometallic material. Further investigation has been done to study the formation process. However, the entire process of

helicate-to-tetrahedron transformation via crystallization cannot be monitored by NMR and ESI-HRMS. Therefore, the solution state of the mixed complexes first studied before crystallization. Interestingly, formation of intermediate was observed in ^{1}HNMR. Upon mixing [Eu_2**L3**$_3$] and [Sm_2**L3**$_3$] in MeCN, ^{1}HNMR revealed a formation of new species correspond to the heterometallic helicate [EuSm**L3**$_3$] (figure 3-12). The signal of [EuSm**L3**$_3$] increased gradually. After 5 hrs, the system reached to an equilibrium and the ratio of [Eu_2**L3**$_3$]: [Sm_2**L3**$_3$]: [EuSm**L3**$_3$] was found to be 1:1:1.

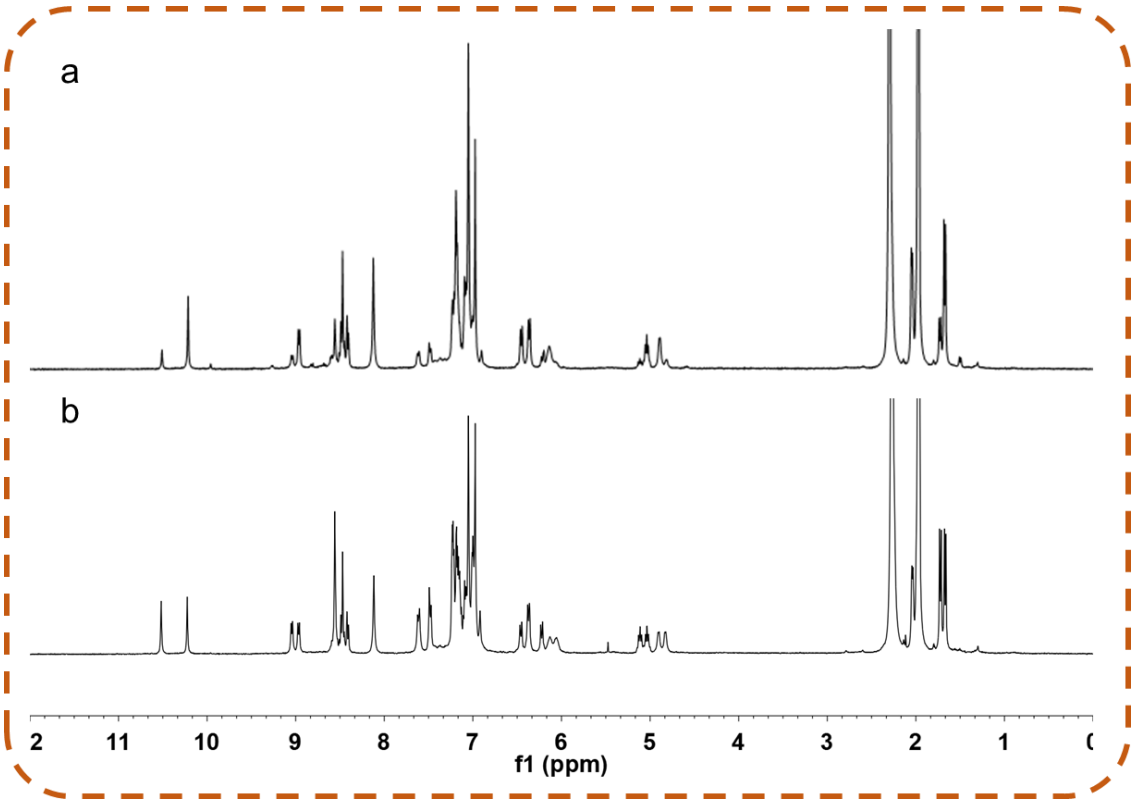

Figure 3-12. *Variation of ^{1}H NMR when [Eu_2**L3**$_3$] was mixed with [Sm_2**L3**$_3$] after (A) 0 hr and (B) 5 hrs in CD_3CN.*

The ionic radii also governed the transformation process from homometallic- to heterometallic helicate. Upon mixing [Eu_2**L3**$_3$] and [Lu_2**L3**$_3$] in MeCN, similar homometallic- to heterometallic helicate transformation was observed. However, the

rate was slower compared with that of the case in Eu and Sm. No new NMR signal can be observed after mixing [Eu_2**L3**$_3$] and [Lu_2**L3**$_3$] for 5 hrs and insignificant amount of [EuLu**L3**$_3$] was formed after 7 days (figure 3-13).

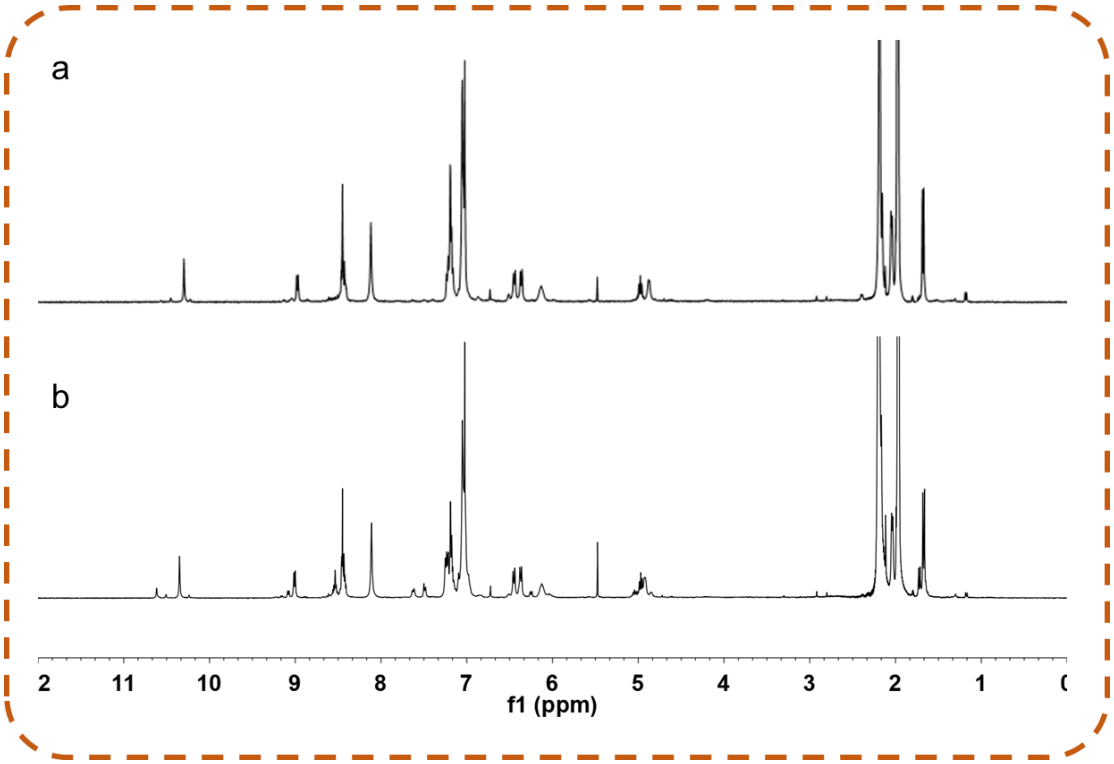

Figure 3-13. *Variation of ^{1}H NMR when [Eu_2**L3**$_3$] was mixed with [Lu_2**L3**$_3$] after (A) 5 hrs and (B) 7 days in CD_3CN.*

3.2.4 Proposed mechanism of helicate-to-tetrahedron transformation process

During the crystallization process, no precipitate was observed. As ligand was not soluble in MeCN, it was hypothesized that the helicate did not undergo complete dissociation during helicate-to-tetrahedron transformation. Based on the above homometallic helicate-to-heterometallic helicate transformation study, it was further hypothesized the rate of association and dissociation of lanthanide ions was governed by the ionic radii. The statistical and experimental result were shown in figure 3-14.

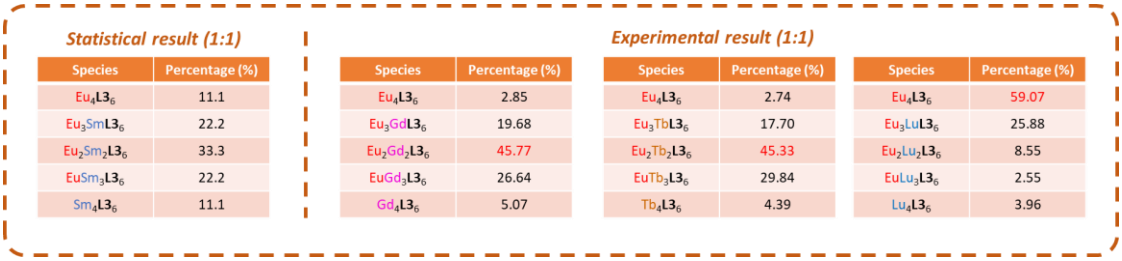

Figure 3-14. *Comparison of statistical and experimental result of MS deconvolution of mixed lanthanide heterometallic tetrahedra.*

It was hypothesized that lanthanide ions having similar ionic radii will have similar rate of association and dissociation, which lead to the formation of heterometallic tetrahedron. Therefore, the crystallization process is governed by both ionic radii as well as the ratio of lanthanide ions that present in the helicate solution. It was then suggested that the metal ratio of the resulting tetrahedron can be simply altered by varying the ratio of the two lanthanide helicates in the mixed solution before crystallization. Upon crystallization of a mixture containing $[Eu_2(\mathbf{L3})_3]$ and $[Gd_2(\mathbf{L3})_3]$ helicates in a ratio of 3:1, the MS deconvolution result showed the formation of highest amount of heterometallic $[Eu_3Gd\mathbf{L3}_6]$ (figure 3-15). The metal content of the tetrahedron was further varied by changing the ratio of the helicate and similar result was observed in the MS deconvolution spectra (figure 3-16).

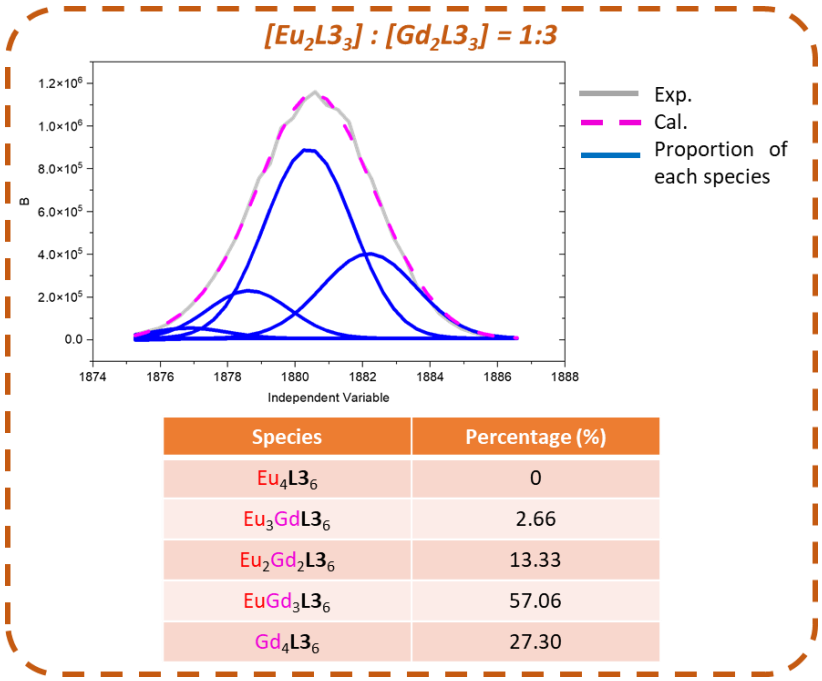

Species	Percentage (%)
Eu_4L3_6	0
Eu_3GdL3_6	2.66
$Eu_2Gd_2L3_6$	13.33
$EuGd_3L3_6$	57.06
Gd_4L3_6	27.30

Figure 3-15. *MS deconvolution result of [Eu_nGd_{4-n}**L3**$_6$] (n = 0-4) prepared by crystallization of a mixture of [Eu_2**L3**$_3$] and [Gd_2**L3**$_3$] in a ratio of 1:3.*

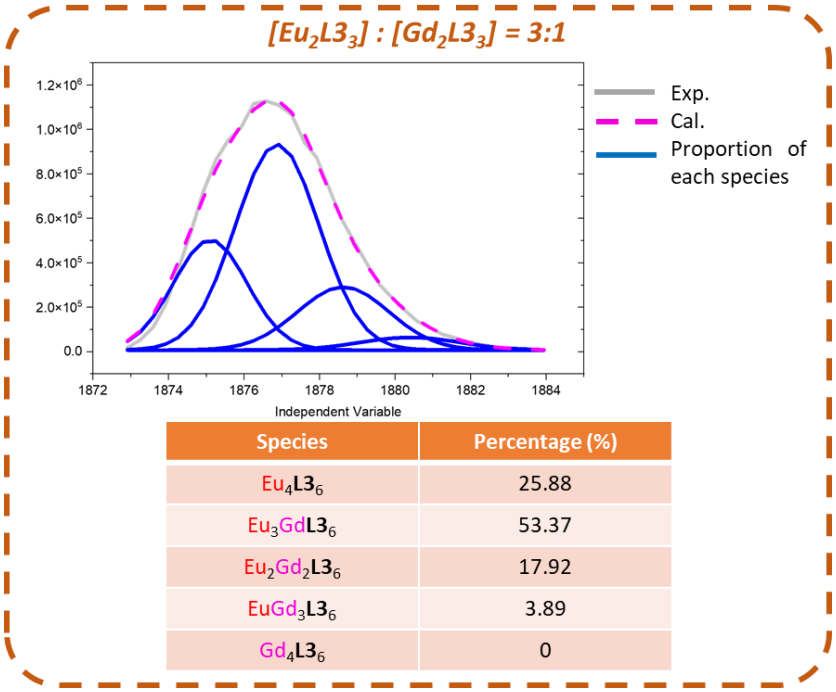

Species	Percentage (%)
Eu_4L3_6	25.88
Eu_3GdL3_6	53.37
$Eu_2Gd_2L3_6$	17.92
$EuGd_3L3_6$	3.89
Gd_4L3_6	0

Figure 3-15. *MS deconvolution result of [Eu_nGd_{4-n}**L3**$_6$] (n = 0-4) prepared by crystallization of a mixture of [Eu_2**L3**$_3$] and [Gd_2**L3**$_3$] in a ratio of 3:1.*

3.2.4 Photophysical properties of heterometallic tetrahedra

The photophysical properties of emissive heterometallic tetrahedra [Eu_nGd_{4-n}**L3**$_6$] (n = 0-4) prepared by different ratio of helicate were examined. Upon excitation at 330 nm, successful sensitization of Eu^{3+} $^5D_0$ excited state through antenna effect was observed. The luminescence spectrum revealed four narrow Eu emission lines at 595, 616, 688 and 697 nm, which corresponds to the transition $^5D_0$ to ^7F_J (J = 1, 2 and 4) transitions (figure 3-16a). Quantum yield measurement was also done and [Eu_4**L3**$^{RR}_6$] exhibited the highest quantum yield of 0.83%. Due to the decrease in luminescent Eu^{3+} content of the tetrahedron, the quantum yield decreased gradually from 0.70% [Eu_nGd_{4-n}**L3**$^{RR}_6$] (prepared by ratio Eu/Gd: 3/1) to 0.50% [Eu_nGd_{4-n}**L3**$^{RR}_6$] (prepared by ratio Eu/Gd: 1/1) to 0.34% [Eu_nGd_{4-n}**L3**$^{RR}_6$] (prepared by ratio Eu/Gd: 1/3).

Solution circular dichroism and circularly polarized luminescence were also done to investigate the chiroptical properties of lanthanide heterometallic tetrahedra [Eu_nGd_{4-n}**L3**$_6$] (n = 0-4). Generally, five tetrahedra showed similar CD spectrum. Mirror image and strong cotton effects were observed for *R*- and *S*-isomers at 212, 240, 259, 273, 312 and 362 nm. Four Eu^{3+}-containing heterometallic tetrahedra also exhibit CPL. Based on the luminescence result, tetrahedron with the highest content of emissive Eu^{3+} ions were expected to have the strongest CPL intensity. Indeed, [Eu_4**L3**$_6$] was found to exhibit the highest CPL intensity. The normalized CPL intensity decreased gradually from [Eu_nGd_{4-n}**L3**$^{RR}_6$] (prepared by ratio Eu/Gd: 3/1) to 0.50% [Eu_nGd_{4-n}**L3**$^{RR}_6$] (prepared by ratio Eu/Gd: 1/1) to 0.34% [Eu_nGd_{4-n}**L3**$^{RR}_6$] (prepared by ratio Eu/Gd: 1/3) as expected. Four Eu^{3+}-containing tetrahedra were found to have the same g_{lum} value

(587 nm) = 0.15 and mirror image of CPL spectra confirmed the successful stereoselective control via point chirality (figure 3-16b).

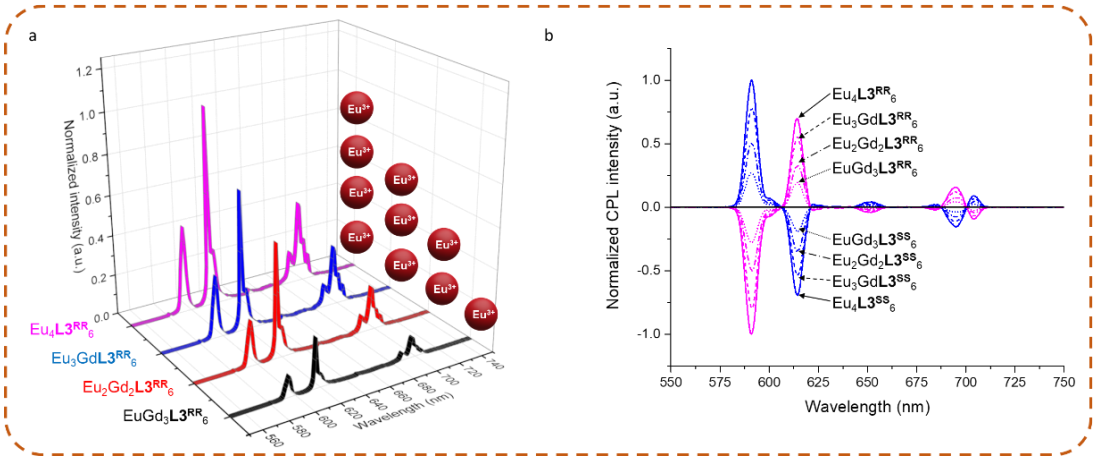

Figure 3-16. *Photophysical properties of Eu^{3+}-containing tetrahedra. (a) Normalized emission spectrum and (b) Normalized CPL spectrum of [Eu_nGd_{4-n}**L3**$_6$].*

3.3 Conclusion

To conclude, with the use of C_2-symmetrical bis(tridentate) ligand **L3**, a mixture of heterometallic tetrahedra [Eu_nGd_{4-n}**L3**$_6$] (n = 0-4) can be prepared via crystallization. The chemical formulae of the tetrahedra were confirmed by ESI-HRMS and X-ray crystallography. The formation of heterometallic tetrahedra was highly sensitive to the ionic radii of lanthanide ions. By varying the ratio of helicate solution before crystallization, the metal content of the tetrahedron can be fine-tuned. The Eu^{3+}-containing tetrahedra were luminescent and exhibited CPL signal with g_{lum} (587 nm) value = 0.15.

3.4 Experimental

3.4.1 Synthesis

General synthetic procedures of [Ln_2**L3**$_3$]

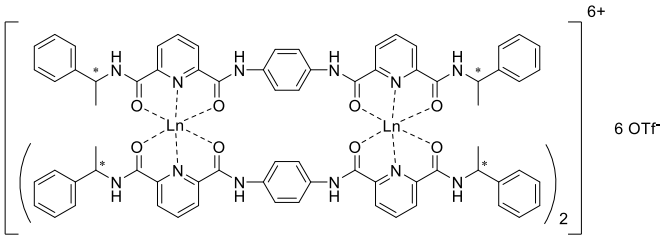

To a white suspension of **L3** (10 mg, 0.016 mmol, 1.5 equiv.) in a mixture of 8.49 ml of DCM/MeOH (12:1, v/v), a solution of $Ln(OTf)_3$ (0.011 mmol, 1 equiv.) (Ln = Dy and Ho) in 7.83 ml of MeCN was added. The solution was changed to homogeneous colorless solution immediately. The solution was then reacted for 16 hrs at room temperature and pressure. After 16 hrs, the solvent was removed under reduced pressure to give desired product.

[Dy_2**L3**$^{SS}{}_3$]: (14.2 mg, 4.64 x 10^{-3} mmol, 85.4% yield), HRMS (ESI) calcd. for $C_{112}H_{96}Dy_2F_{12}N_{18}O_{24}S_4$ [Dy_2(**L3**^{SS})$_3$ + 4OTf^-]$^{2+}$: 1379.7060, found 1379.7075. Elemental analysis calcd. for $C_{114}H_{96}F_{18}Dy_2N_{18}O_{30}S_6 \cdot 11H_2O$: C 42.06, H 3.65, N 7.74, found: C 42.10, H 3.14, N 7.78.

[Ho_2**L3**$^{SS}{}_3$]: (13.9 mg, 4.54 x 10^{-3} mmol, 83.4% yield), HRMS (ESI) calcd. for $C_{112}H_{96}Eu_2F_{12}N_{18}O_{24}S_4$ [Ho_2(**L3**^{SS})$_3$ + 4OTf^-]$^{2+}$: 1381.7072, found 1381.7081. Elemental analysis calcd. for $C_{114}H_{96}F_{18}Ho_2N_{18}O_{30}S_6 \cdot 20H_2O$: C 40.01, H 4.01, N 7.37, found: C 40.07, H 3.29, N 7.24.

General procedures for preparing homometallic tetrahedra

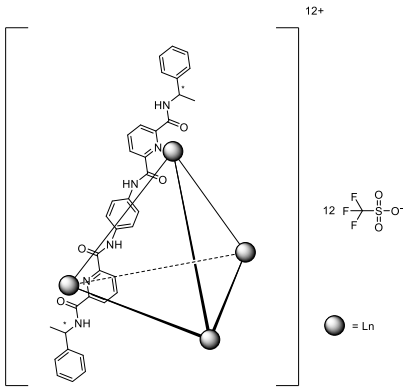

Ln_2**L3**$_3$ (0.66 mmol) was dissolved in MeCN (0.6 ml) and ether was allowed to slowly diffuse into the solution containing Ln_2**L**$_3$. The solution was decanted, and the crystal was washed with ether and dried under vacuum to obtain the homometallic tetrahedra crystal.

Dy_4**L3**$^{SS}_6$: (1.66 mg, 2.71 x 10^{-4} mmol, 82.4% yield), HRMS (ESI): *m/z* calcd. for $C_{223}H_{192}Dy_4F_{21}N_{36}O_{45}S_7$ [Dy_4**L3**$^{SS}_6$ + 7 OTf^-]$^{5+}$: 1073.9743, found 1073.9764; Calcd for $C_{222}H_{191}Dy_4F_{18}N_{36}O_{42}S_6$ [Dy_4**L3**$^{SS}_6$ + 6 OTf^- - H^+]$^{5+}$: 1043.7821, found 1043.7826; Calcd. for $C_{221}H_{190}Dy_4F_{15}N_{36}O_{39}S_5$ [Dy_4**L3**$^{SS}_6$ + 5 OTf^- - 2H^+]$^{5+}$: 1013.7902, found 1013.7969; Calcd. for $C_{220}H_{189}Dy_4F_{12}N_{36}O_{36}S_4$ [Dy_4**L3**$^{SS}_6$ + 4 OTf^- - 3H^+]$^{5+}$: 983.7983, found 983.7963; Calcd. for $C_{220}H_{190}Dy_4F_{12}N_{36}O_{36}S_4$ [Dy_4**L3**$^{SS}_6$ + 4 OTf^- - 2H^+]$^{6+}$: 819.9998, found 820.0034. Elemental analysis calcd. for $C_{228}H_{192}F_{36}$ $Dy_3TbN_{36}O_{60}S_{12}\cdot 11H_2O\cdot C_6H_{14}O$: C 43.81, H 3.58, N 7.86, found: C 43.88, H 3.63, N 7.46.

General procedures for preparing heterometallic tetrahedra

Ln_2**L3**$_3$ and Ln'_2**L3**$_3$ (depends on different mole ratio) were dissolved in MeCN (0.6 ml) and ether was allowed to slowly diffuse into the solution containing a mixture of Ln_2**L3**$_3$ and Ln'_2**L3**$_3$. The solution was decanted, and the crystal was washed with ether and dried under vacuum to obtain the homometallic tetrahedra crystal.

[Eu_nGd_{4-n}**L3**$^{SS}_6$] (prepared by ratio Eu/Gd: 3/1): (1.49 mg, 2.45 x 10^{-4} mmol, 74.3% yield), HRMS (ESI): *m/z* calcd. for $C_{225}H_{192}Eu_3F_{27}GdN_{36}O_{51}S_9$ [Eu_3Gd**L3**$^{SS}_6$ + 9 OTf^-]$^{3+}$: 1876.9166, found 1876.9222; Calcd. for $C_{223}H_{191}Eu_3F_{21}GdN_{36}O_{45}S_7$ [Eu_3Gd**L3**$^{SS}_6$ + 7 OTf^- - H^+]$^{4+}$: 1332.9595, found 1335.9584; Calcd. for $C_{223}H_{192}Eu_3F_{21}GdN_{36}O_{45}S_7$ [Eu_3Gd**L3**$^{SS}_6$ + 7 OTf^-]$^{5+}$: 1066.5690, found 1066.5699; Calcd. for $C_{222}H_{191}Eu_3F_{18}GdN_{36}O_{42}S_6$ [Eu_3Gd**L3**$^{SS}_6$ + 6 OTf^- - H^+]$^{5+}$: 1036.3769, found 1036.3811; Calcd. for $C_{220}H_{190}Eu_3F_{12}GdN_{36}O_{36}S_4$ [Eu_3Gd**L3**$^{SS}_6$ + 4 OTf^- - 2H^+]$^{6+}$: 813.8287, found 813.8317. Elemental analysis calcd. for $C_{228}H_{192}F_{36}Eu_3GdN_{36}O_{60}S_{12}\cdot 14H_2O$: C 43.26, H 3.50, N 7.97, found: C 43.20, H 3.32, N 7.92.

[Eu_nGd_{4-n}**L3**$^{RR}_6$] (prepared by ratio Eu/Gd: 3/1): (1.57 mg, 2.58 x 10^{-4} mmol, 78.3% yield), HRMS (ESI): *m/z* calcd. for $C_{225}H_{192}Eu_3F_{27}GdN_{36}O_{51}S_9$ [Eu_3Gd**L3**$^{RR}_6$ + 9 OTf^-]$^{3+}$: 1876.9166, found 1876.9133; Calcd. for $C_{223}H_{192}Eu_3F_{21}GdN_{36}O_{45}S_7$ [Eu_3Gd**L3**$^{RR}_6$ + 7 OTf^-]$^{5+}$: 1066.5690, found 1066.5623; Calcd. for $C_{222}H_{191}Eu_3F_{18}GdN_{36}O_{42}S_6$ [Eu_3Gd**L3**$^{RR}_6$ + 6 OTf^- - H^+]$^{5+}$: 1036.3769, found 1036.3728; Calcd. for $C_{221}H_{190}Eu_3F_{15}GdN_{36}O_{39}S_5$ [Eu_3Gd**L3**$^{RR}_6$ + 5 OTf^- - 2H^+]$^{5+}$: 1006.3850, found 1006.3813; Calcd. for $C_{220}H_{190}Eu_3F_{12}GdN_{36}O_{36}S_4$ [Eu_3Gd**L3**$^{RR}_6$ + 4 OTf^- - 2H^+]$^{6+}$: 813.8287, found 813.8316. Elemental analysis calcd. for $C_{228}H_{192}F_{36}Eu_3GdN_{36}O_{60}S_{12}\cdot 13H_2O$: C 43.38, H 3.48, N 7.99, found: C 43.35, H 3.35, N 7.88.

[Eu_nGd_{4-n}**L3**$^{SS}_6$] (prepared by ratio Eu/Gd: 1/1): (1.72 mg, 2.83 x 10^{-4} mmol, 85.7% yield), HRMS (ESI): *m/z* calcd. for $C_{224}H_{192}Eu_2F_{24}Gd_2N_{36}O_{48}S_8$ [Eu_2Gd_2**L3**$^{SS}_6$ + 8 OTf^-]$^{4+}$: 1371.7002, found 1371.7015; Calcd. for $C_{223}H_{192}Eu_2F_{21}Gd_2N_{36}O_{45}S_7$ [Eu_2Gd_2**L3**$^{SS}_6$ + 7 OTf^-]$^{5+}$: 1067.5697, found 1067.5664; Calcd. for $C_{222}H_{191}Eu_2F_{18}Gd_2N_{36}O_{42}S_6$ [Eu_2Gd_2**L3**$^{SS}_6$ + 6 OTf^- - H^+]$^{5+}$: 1037.5777, found 1037.5746; Calcd. for

$C_{222}H_{192}Eu_2F_{18}Gd_2N_{36}O_{42}S_6$ [Eu_2Gd_2**L3**$^{SS}_6$ + 6 OTf^-]$^{6+}$: 864.8160, found 864.8126; Calcd. for $C_{220}H_{190}Eu_2F_{12}Gd_2N_{36}O_{36}S_4$ [Eu_2Gd_2**L3**$^{SS}_6$ + 4 OTf^- - 2H^+]$^{6+}$: 814.8295, found 814.8297. Elemental analysis calcd. for $C_{228}H_{192}F_{36}Eu_2Gd_2N_{36}O_{60}S_{12}\cdot14H_2O$: C 43.22, H 3.50, N 7.96, found: C 43.26, H 3.54, N 8.00.

[Eu_nGd_{4-n}**L3**$^{RR}_6$] (prepared by ratio Eu/Gd: 1/1): (1.70 mg, 2.79 x 10^{-4} mmol, 84.7% yield), HRMS (ESI): *m/z* calcd. for $C_{225}H_{192}Eu_2F_{27}Gd_2N_{36}O_{51}S_9$ [Eu_2Gd_2**L3**$^{RR}_6$ + 9 OTf^-]$^{3+}$: 1878.5844, found 1878.5778; Calcd. for $C_{223}H_{192}Eu_2F_{21}Gd_2N_{36}O_{45}S_7$ [Eu_2Gd_2**L3**$^{RR}_6$ + 7 OTf^-]$^{5+}$: 1067.5697, found 1067.5664; Calcd. for $C_{221}H_{190}Eu_2F_{15}Gd_2N_{36}O_{39}S_5$ [Eu_2Gd_2**L3**$^{RR}_6$ + 5 OTf^- - 2H^+]$^{5+}$: 1007.5858, found 1007.5864; Calcd. for $C_{222}H_{192}Eu_2F_{18}Gd_2N_{36}O_{42}S_6$ [Eu_2Gd_2**L3**$^{RR}_6$ + 6 OTf^-]$^{6+}$: 864.8160, found 864.8129; Calcd. for $C_{220}H_{190}Eu_2F_{12}Gd_2N_{36}O_{36}S_4$ [Eu_2Gd_2**L3**$^{RR}_6$ + 4 OTf^- - 2H^+]$^{6+}$: 814.8295, found 814.8281. Elemental analysis calcd. for $C_{228}H_{192}F_{36}Eu_2Gd_2N_{36}O_{60}S_{12}\cdot13H_2O$: C 43.35, H 3.48, N 7.98, found: C 43.36, H 3.39, N 7.92.

[Eu_nGd_{4-n}**L3**$^{SS}_6$] (prepared by ratio Eu/Gd: 1/3): (1.66 mg, 2.73 x 10^{-4} mmol, 82.6% yield), HRMS (ESI): *m/z* calcd. for $C_{225}H_{192}EuF_{27}Gd_3N_{36}O_{51}S_9$ [$EuGd_3$**L3**$^{SS}_6$ + 9 OTf^-]$^{3+}$: 1880.2521, found 1880.2518; Calcd. for $C_{224}H_{192}EuF_{24}Gd_3N_{36}O_{48}S_8$ [$EuGd_3$**L3**$^{SS}_6$ + 8 OTf^-]$^{4+}$: 1372.9510, found 1372.9503; Calcd. for $C_{223}H_{192}EuF_{21}Gd_3N_{36}O_{45}S_7$ [$EuGd_3$**L3**$^{SS}_6$ + 7 OTf^-]$^{5+}$: 1068.5703, found 1068.5665; Calcd. for $C_{222}H_{191}EuF_{18}Gd_3N_{36}O_{42}S_6$ [Eu_2Gd_2**L3**$^{SS}_6$ + 6 OTf^- - H^+]$^{5+}$: 1038.5784, found 1038.5743; Calcd. for $C_{220}H_{190}EuF_{12}Gd_3N_{36}O_{36}S_4$ [Eu_2Gd_2**L3**$^{SS}_6$ + 4 OTf^- - 2H^+]$^{6+}$: 815.6633, found 815.6631. Elemental analysis calcd. for $C_{228}H_{192}F_{36}EuGd_3N_{36}O_{60}S_{12}\cdot15H_2O\cdot C_6H_{14}O$: C 43.50, H 3.68, N 7.80, found: C 43.43, H 3.68, N 7.82.

[Eu_nGd_{4-n}**L3**$^{RR}{}_6$] (prepared by ratio Eu/Gd: 1/3): (1.75 mg, 2.87 x 10^{-4} mmol, 87.1% yield), HRMS (ESI): *m/z* calcd. for $C_{225}H_{192}EuF_{27}Gd_3N_{36}O_{51}S_9$ [$EuGd_3$**L3**$^{RR}{}_6$ + 9 OTf^-]$^{3+}$: 1880.2521, found 1880.2430; Calcd. for $C_{224}H_{192}EuF_{24}Gd_3N_{36}O_{48}S_8$ [$EuGd_3$**L3**$^{RR}{}_6$ + 8 OTf^-]$^{4+}$: 1372.9510, found 1372.9489; Calcd. for $C_{221}H_{190}EuF_{15}Gd_3N_{36}O_{39}S_5$ [$EuGd_3$**L3**$^{RR}{}_6$ + 5 OTf^- - $2H^+$]$^{5+}$: 1008.5864, 1008.5843; Calcd. for $C_{220}H_{190}EuF_{12}Gd_3N_{36}O_{36}S_4$ [$EuGd_3$**L3**$^{RR}{}_6$ + 4 OTf^- - $2H^+$]$^{6+}$: 815.6633, found 815.6630; Calcd. for $C_{220}H_{192}EuF_{12}Gd_3N_{36}O_{36}S_4$ [$EuGd_3$**L3**$^{RR}{}_6$ + 4 OTf^- - $2H^+$]$^{7+}$: 699.2839, found 699.2811. Elemental analysis calcd. for $C_{228}H_{192}F_{36}EuGd_3N_{36}O_{60}S_{12}\cdot 15H_2O\cdot C_6H_{14}O$: C 43.50, H 3.68, N 7.80, found: C 43.53, H 3.42, N 7.89.

[Eu_nSm_{4-n}**L3**$^{SS}{}_6$] (prepared by ratio Eu/Sm: 1/1): (1.79 mg, 2.95 x 10^{-4} mmol, 89.4% yield), HRMS (ESI): *m/z* calcd. for $C_{223}H_{192}Eu_2F_{21}N_{36}O_{45}S_7Sm_2$ [Eu_2Sm_2**L3**$^{SS}{}_6$ + 7 OTf^-]$^{5+}$: 1064.7673, found 1064.7710; Calcd. for $C_{222}H_{191}Eu_2F_{18}N_{36}O_{42}S_6Sm_2$ [Eu_2Sm_2**L3**$^{SS}{}_6$ + 6 OTf^- - H^+]$^{5+}$: 1034.7754, found 1034.7769; Calcd. for $C_{221}H_{190}Eu_2F_{15}N_{36}O_{39}S_5Sm_2$ [Eu_2Sm_2**L3**$^{SS}{}_6$ + 5 OTf^- - $2H^+$]$^{5+}$: 1004.7834, found 1004.7823; Calcd. for $C_{222}H_{192}Eu_2F_{18}N_{36}O_{42}S_6Sm_2$ [Eu_2Sm_2**L3**$^{SS}{}_6$ + 6 OTf^-]$^{6+}$: 862.4807, found 862.4775; Calcd. for $C_{220}H_{191}Eu_2F_{12}N_{36}O_{36}S_4Sm_2$ [Eu_2Sm_2**L3**$^{SS}{}_6$ + 4 OTf^- - H^+]$^{7+}$: 696.5675, 696.5658. Elemental analysis calcd. for $C_{228}H_{192}F_{36}Eu_2Sm_2N_{36}O_{60}S_{12}\cdot 14H_2O\cdot 2(C_6H_{14}O)$: C 44.17, H 3.83, N 7.73, found: C 44.11, H 3.54, N 7.75.

[Eu_nSm_{4-n}**L3**$^{RR}{}_6$] (prepared by ratio Eu/Sm: 1/1): (1.68 mg, 2.77 x 10^{-4} mmol, 83.9% yield), HRMS (ESI): *m/z* calcd. for $C_{225}H_{192}Eu_2F_{27}N_{36}O_{51}S_9Sm_2$ [Eu_2Sm_2**L3**$^{RR}{}_6$ + 9 OTf^-]$^{3+}$: 1873.9137, found 1873.9077; Calcd. for $C_{224}H_{192}Eu_2F_{24}N_{36}O_{48}S_8Sm_2$ [Eu_2Sm_2**L3**$^{RR}{}_6$ + 8 OTf^-]$^{4+}$: 1368.1972, found 1368.1980; Calcd. for $C_{223}H_{191}Eu_2F_{21}N_{36}O_{45}S_7Sm_2$ [Eu_2Sm_2**L3**$^{RR}{}_6$ + 7 OTf^- - H^+]$^{4+}$: 1330.7073, found 1330.7100; Calcd. for

$C_{223}H_{192}Eu_2F_{21}N_{36}O_{45}S_7Sm_2$ [Eu_2Sm_2**L3**$^{RR}_6$ + 7 OTf^-]$^{5+}$: 1064.7673, found 1064.7668; Calcd. for $C_{222}H_{191}Eu_2F_{18}N_{36}O_{42}S_6Sm_2$ [Eu_2Sm_2**L3**$^{RR}_6$ + 6 OTf^- - H^+]$^{5+}$: 1034.7754, found 1034.7715; Elemental analysis calcd. for $C_{228}H_{192}F_{36}Eu_2Sm_2N_{36}O_{60}S_{12}\cdot12H_2O\cdot2(C_6H_{14}O)$: C 44.42, H 3.79, N 7.77, found: C 44.40, H 3.82, N 7.80.

Dy_4**L3**$^{SS}_6$: (1.66 mg, 2.71 x 10^{-4} mmol, 82.4% yield), HRMS (ESI): *m/z* calcd. for $C_{223}H_{192}Dy_4F_{21}N_{36}O_{45}S_7$ [Dy_4**L3**$^{SS}_6$ + 7 OTf^-]$^{5+}$: 1073.9743, found 1073.9764; Calcd for $C_{222}H_{191}Dy_4F_{18}N_{36}O_{42}S_6$ [Dy_4**L3**$^{SS}_6$ + 6 OTf^-- H^+]$^{5+}$: 1043.7821, found 1043.7826; Calcd. for $C_{221}H_{190}Dy_4F_{15}N_{36}O_{39}S_5$ [Dy_4**L3**$^{SS}_6$ + 5 OTf^-- $2H^+$]$^{5+}$: 1013.7902, found 1013.7969; Calcd. for $C_{220}H_{189}Dy_4F_{12}N_{36}O_{36}S_4$ [Dy_4**L3**$^{SS}_6$ + 4 OTf^-- $3H^+$]$^{5+}$: 983.7983, found 983.7963; Calcd. for $C_{220}H_{190}Dy_4F_{12}N_{36}O_{36}S_4$ [Dy_4**L3**$^{SS}_6$ + 4 OTf^- - $2H^+$]$^{6+}$: 819.9998, found 820.0034. Elemental analysis calcd. for $C_{228}H_{192}F_{36}$ $Dy_3TbN_{36}O_{60}S_{12}\cdot11H_2O\cdot C_6H_{14}O$: C 43.81, H 3.58, N 7.86, found: C 43.88, H 3.63, N 7.46.

3.4.2 ESI-HRMS deconvolution analysis

	Precentage (%)
$[Eu_4\mathbf{L3}_6 + 9OTf^-]^{3+}$	2.85
$[Eu_3Gd\mathbf{L3}_6 + 9OTf^-]^{3+}$	19.68
$[Eu_2Gd_2\mathbf{L3}_6 + 9OTf^-]^{3+}$	45.77
$[EuGd_3\mathbf{L3}_6 + 9OTf^-]^{3+}$	26.64
$[Gd_4\mathbf{L3}_6 + 9OTf^-]^{3+}$	5.07

Table S3-1. Percentage of the selected ESI-HRMS peak for $[Eu_nGd_{4-n}\mathbf{L3}_6]$ (n = 0-4), Eu/Gd: 1:1.

	Percentage (%)
$[Eu_4\mathbf{L3}_6 + 9OTf^-]^{3+}$	2.74
$[Eu_3Tb\mathbf{L3}_6 + 9OTf^-]^{3+}$	17.70
$[Eu_2Tb_2\mathbf{L3}_6 + 9OTf^-]^{3+}$	45.33
$[EuTb_3\mathbf{L3}_6 + 9OTf^-]^{3+}$	29.84
$[Eu_4\mathbf{L3}_6 + 9OTf^-]^{3+}$	4.39

Table S3-2. Percenatge of the selected ESI-HRMS peak for $[Eu_nTb_{4-n}\mathbf{L3}_6]$ (n = 0-4), Eu/Tb: 1:1.

	Percentage (%)
$[Eu_4\mathbf{L3}_6 + 9OTf^-]^{3+}$	59.07
$[Eu_3Lu\mathbf{L3}_6 + 9OTf^-]^{3+}$	25.88
$[Eu_2Lu_2\mathbf{L3}_6 + 9OTf^-]^{3+}$	8.55
$[EuLu_3\mathbf{L3}_6 + 9OTf^-]^{3+}$	2.55
$[Lu_4\mathbf{L3}_6 + 9OTf^-]^{3+}$	3.96

Table S3-3. Percenatge of the selected ESI-HRMS peak for $[Eu_nLu_{4-n}\mathbf{L3}_6]$ (n = 0-4), Eu/Lu: 1:1.

	Percentage
$[Eu_4\mathbf{L3}_6 + 9OTf^-]^{3+}$	25.88
$[Eu_3Gd\mathbf{L3}_6 + 9OTf^-]^{3+}$	53.37
$[Eu_2Gd_2\mathbf{L3}_6 + 9OTf^-]^{3+}$	17.92
$[EuGd_3\mathbf{L3}_6 + 9OTf^-]^{3+}$	3.89
$[Gd_4\mathbf{L3}_6 + 9OTf^-]^{3+}$	0

Table S3-4. Percentage of the selected ESI-HRMS peak for $[Eu_nGd_{4-n}\mathbf{L3}_6]$ (n = 0-4), Eu/Gd: 3:1.

	Percentage
$[Eu_4\mathbf{L3}_6 + 9OTf^-]^{3+}$	0
$[Eu_3Gd\mathbf{L3}_6 + 9OTf^-]^{3+}$	2.66
$[Eu_2Gd_2\mathbf{L3}_6 + 9OTf^-]^{3+}$	13.33
$[EuGd_3\mathbf{L3}_6 + 9OTf^-]^{3+}$	57.06
$[Gd_4\mathbf{L3}_6 + 9OTf^-]^{3+}$	27.30

Table S3-5. Percentage of the selected ESI-HRMS peak for $[Eu_nGd_{4-n}\mathbf{L3}_6]$ (n = 0-4), Eu/Gd: 1:3.

3.4.3 Photophysical measurement

Electronic transition	λ (nm)	g_{lum}							
		$[Eu_4\mathbf{L3}^{S}{}_{6}^{S}]$	$[Eu_4\mathbf{L3}^{R}{}_{6}^{R}]$	$[Eu_nGd_{4-n}\mathbf{L3}_6{}^{SS}]$ (n = 0-4), Eu/Gd: 3:1	$[Eu_nGd_{4-n}\mathbf{L3}_6{}^{RR}]$ (n = 0-4), Eu/Gd: 3:1	$[Eu_nGd_{4-n}\mathbf{L3}_6{}^{SS}]$ (n = 0-4), Eu/Gd: 1:1	$[Eu_nGd_{4-n}\mathbf{L3}_6{}^{RR}]$ (n = 0-4), Eu/Gd: 1:1	$[Eu_nGd_{4-n}\mathbf{L3}_6{}^{SS}]$ (n = 0-4), Eu/Gd: 1:3	$[Eu_nGd_{4-n}\mathbf{L3}_6{}^{RR}]$ (n = 0-4), Eu/Gd: 1:3
$^5D_0 \rightarrow {}^7F_1$	587	0.15	-0.15	0.14	-0.15	0.15	-0.15	0.14	-0.15
	601	0.06	-0.06	0.05	-0.06	0.06	-0.05	0.06	-0.06
$^5D_0 \rightarrow {}^7F_2$	613	-0.05	0.04	0.04	-0.05	-0.05	0.05	-0.04	0.04
$^5D_0 \rightarrow {}^7F_3$	652	0.12	-0.11	0.10	-0.10	0.06	-0.06	0.03	-0.04
$^5D_0 \rightarrow {}^7F_4$	685	0.01	-0.01	0.01	-0.01	0.02	-0.01	0.02	-0.01
	697	-0.04	0.04	-0.04	0.04	-0.04	0.04	-0.05	0.05
	704	0.12	-0.12	0.10	-0.11	0.11	-0.10	0.07	-0.07

Table S3-6. Summary of CPL results for the eight homometallic and heterometallic tetrahedra.

	λ_{abs}^{max} (nm)	ε^{max} ($L \cdot mol^{-1} \cdot cm^{-1}$)	λ_{em}^{max} (nm)	ϕ_x[b] (%)	τ (ms)
$[Eu_4(\mathbf{L3^{SS}})_6](CF_3SO_3)_{12}$	330	121335.7	616	0.81 (0.035)	1.28
$[Eu_4(\mathbf{L3^{RR}})_6](CF_3SO_3)_{12}$	330	123947.0	616	0.83 (0.035)	1.27
$[Eu_nGd_{4-n}\mathbf{L3}_6{}^{SS}]$ (n = 0-4), Eu/Gd: 3:1	330	122963.9	616	0.76 (0.03)	1.27
$[Eu_nGd_{4-n}\mathbf{L3}_6{}^{RR}]$ (n = 0-4), Eu/Gd: 3:1	330	124822.0	616	0.70 (0.025)	1.27
$[Eu_nGd_{4-n}\mathbf{L3}_6{}^{SS}]$ (n = 0-4), Eu/Gd: 1:1	330	124869.7	616	0.49 (0.025)	1.28
$[Eu_nGd_{4-n}\mathbf{L3}_6{}^{RR}]$ (n = 0-4), Eu/Gd: 1:1	330	125035.4	616	0.50 (0.02)	1.27
$[Eu_nGd_{4-n}\mathbf{L3}_6{}^{SS}]$ (n = 0-4), Eu/Gd: 1:3	330	123626.7	616	0.30 (0.02)	1.27
$[Eu_nGd_{4-n}\mathbf{L3}_6{}^{RR}]$ (n = 0-4), Eu/Gd: 1:3	330	131345.8	616	0.34 (0.03)	1.27
$[Gd_4(\mathbf{L3^{SS}})_6](CF_3SO_3)_{12}$	330	121829.6	/	/	/
$[Gd_4(\mathbf{L3^{RR}})_6](CF_3SO_3)_{12}$	330	123657.1	466	/	0.0087[c]
$[Eu_nSm_{4-n}\mathbf{L3}_6{}^{SS}]$ (n = 0-4), Eu/Sm: 1:1	330	130409.0	616	0.33 (0.045)	1.27
$[Eu_nSm_{4-n}\mathbf{L3}_6{}^{RR}]$ (n = 0-4), Eu/Sm: 1:1	330	119229.7	616	0.34 (0.03)	1.28

Table S3-7. A summary of selected photophysical properties, UV-Vis absorption and luminescence data of lanthanide complexes in acetonitrile solution[a]. [a]using a 10 mm cuvette and filter 380 nm. [b]The relative quantum yields were referenced with quinine sulfate in 0.1 M sulfuric acid (ϕ= 0.577, λ_{ex} = 350nm) with 10 mm cuvette. [c]Measurement performed at 77K in 1:4 MeOH/EtOH.

3.4.4 Crystal structure of [$Eu_nGd_{4-n}L3_6$] (n = 0-4)

Crystal Data for $C_{224.998875}H_{191.99904}Eu_{1.99999}F_{26.999865}Gd_{1.99999}N_{35.99982}O_{50.999745}S_{8.999955}$ (*M* =5636.07 g/mol): trigonal, space group R3 (no. 146), *a* = 30.0304(9) Å, *c* = 71.671(3) Å, *V* = 55975(4) Å^3, *Z* = 6.00003, *T* = 220.0 K, μ(CuKα) = 5.684 mm^{-1}, *Dcalc* = 1.003 g/cm^3, 70262 reflections measured (5.886° ≤ 2Θ ≤ 117.84°), 34927 unique (R_{int} = 0.0543, R_{sigma} = 0.0620) which were used in all calculations. The final R_1 was 0.0655 (I > 2σ(I)) and wR_2 was 0.1960 (all data). The crystallographic data for the structural analyses have been deposited with the Cambridge Crystallographic Data Centre, CCDC No. 2092789, and the data can be obtained free of charge via www.ccdc.cam.ac.uk/data_request/cif.

Information	Identifier from cif file
Empirical formula	$C_{225}H_{192}Eu_2F_{27}Gd_2N_{36}O_{51}S_9$
Formula weight	5636.07
Temperature/K	220.0
Crystal system	trigonal
Space group	R3
a/Å	30.0304(9)
b/Å	30.0304(9)
c/Å	71.671(3)
α/°	90
β/°	90
γ/°	120
Volume/Å^3	55975(4)
Z	6.00003
ρ_{calc}g/cm^3	1.003
μ/mm^{-1}	5.684
F(000)	17058.0
Crystal size/mm^3	0.23 × 0.18 × 0.13
Radiation	CuKα (λ = 1.54178)

2Θ range for data collection/°	5.886 to 117.84
Index ranges	-33 ≤ h ≤ 33, -33 ≤ k ≤ 33, -79 ≤ l ≤ 79
Reflections collected	70262
Independent reflections	34927 [R_{int} = 0.0543, R_{sigma} = 0.0620]
Data/restraints/parameters	34927/2794/1969
Goodness-of-fit on F^2	0.983
Final R indexes [I>=2σ (I)]	R_1 = 0.0655, wR_2 = 0.1771
Final R indexes [all data]	R_1 = 0.0805, wR_2 = 0.1960
Largest diff. peak/hole / e $Å^{-3}$	0.80/-0.82
Flack parameter	0.011(3)

	Shape measure (°)	
	Tricapped trigonal prism (D_{3h})	Capped square antiprism (C_{4v})
Eu1	5.70	10.30
Eu2	5.70	10.30
Eu3	5.78	10.79
Eu4	5.70	10.30

Table S3-8. Results of the Shape Analysis for Eu_2Gd_2(**L3^{SS}**)$_6$

Shape analysis was performed using the software that developed by Raymond's group.[35-36] The coordination geometry of the Eu_2Gd_2(**L3^{SS}**)$_6$ can be best described as tricapped trigonal prism.

3.5 References

1. Jing, X.; He, C.; Yang, T.; Duan, C. A metal–organic tetrahedron as a redox vehicle to encapsulate organic dyes for photocatalytic proton reduction. *J. Am. Chem. Soc.* **2015**, *137* (11), 9224-9229.

2. Ramsay, W. J.; Ronson, T. K.; Clegg, J. K.; Nitschke, J. R. Bidirectional regulation

of halide binding in a heterometallic supramolecular cube. *Angew. Chem. Int. Ed.* **2013**, *52*, 13439-13443.

3. Zhang, D.; Ronson, T. K.; Nitschke, J. R. Functional capsules via subcomponent self-assembly. *Acc. Chem. Res.* **2018**, *51* (10), 2423-2436.

4. Hong, C. M.; Bergman, R. G.; Raymond, K. N.; Toste, F. D. Self-assembled tetrahedral hosts as supramolecular catalysts. *Acc. Chem. Res.* **2018**, *51* (10), 2447-2455.

5. Bender, T. A.; Bergman, R. G.; Raymond, K. N.; Toste, F. D. A Supramolecular strategy for selective catalytic hydrogenation independent of remote chain length. *J. Am. Chem. Soc.* **2019**, *141* (30), 11806-11810.

6. Montgomery, C. P.; Murray, B. S.; New, E. J.; Pal, R.; Parker, D. Cell-penetrating metal complex optical probes: targeted and responsive systems based on lanthanide luminescence. *Acc. Chem. Res.* **2009**, *42* (7), 925-937.

7. Liu, Y.; Wu, X.; He, C.; Zhang, R.; Duan, C. A Truncated octahedral nanocage for fluorescent detection of nucleoside. *Dalton Trans.* **2008**, 5866-5868.

8. Aletti, A. B.; Gillen, D. M.; Gunnlaugsson, T. Luminescent/colorimetric probes and (chemo-) sensors for detecting anions based on transition and lanthanide Ion receptor/binding complexes. *Coord. Chem. Rev.* **2018**, *354*, 98-120.

9. Gao, W.-X.; Zhang, H.-N.; Jin, G.-X. Supramolecular catalysis based on discrete heterometallic coordination-driven metallacycles and metallacages. *Coord. Chem. Rev.* **2019**, *386*, 69-84.

10. Li, K.; Zhang, L.-Y.; Yan, C.; Wei, S.-C.; Pan, M.; Zhang, L.; Su, C.-Y. Stepwise assembly of $Pd_6(RuL_3)_8$ nanoscale rhombododecahedral metal-organic cages via metalloligand strategy for guest trapping and protection. *J. Am. Chem. Soc.*

2014, *136*, 4456-4459.

11. Chen, S.; Li, K.; Zhao, F.; Zhang, L.; Pan. M.; Fan, Y.-Z.; Guo, J.; Shi, J.; Su, C.-Y. A metal-organic cage incorporating multiple light harvesting and catalytic centres for photochemical hydrogen production. *Nat. Commun.* **2016**, *7*, 13169.
12. Koullourou, T.; Natrajan, L. S.; Bhavsar, H.; Pope, S. J. A.; Feng, J.; Narvainen, J.; Shaw, R.; Scales, E.; Kauppinen, R.; Kenwright, A. M.; Faulkner, S. Synthesis and spectroscopic properties of a prototype single molecule dual imaging agent comprising a heterobimetallic Rhenium-Gadolinium complex. *J. Am. Chem. Soc.* **2008**, *130*, 2178-2179.
13. Nonat, A. M.; Allain, C.; Faulkner, S.; Gunnlaugsson, T. Mixed d-f_3 coordination complexes possessing improved near-infrared (NIR) lanthanide luminescent properties in aqueous solution. *Inorg. Chem.* **2010**, *49* (18), 8449-8456.
14. Sénéchal-David, K.; Pope, S. J. A.; Faulkner, S.; Gunnlausson, T. Sensitized near-infrared lanthanide luminescence from Nd(III)- and Yb(III)-based cyclen-ruthenium coordination conjugates. *Inorg. Chem*. **2006**, *45* (25), 10040-10042.
15. Yeung, C.-T.; Chan, W. T. K.; Yan, S.-C.; Yu, K.-L.; Yim, K.-H.; Wong, W.-T.; Law, G.-L. Lanthanide supramolecular helical diastereoselective breaking induced by point chirality: mixture or *P*-helix, *M*-helix. *Chem. Commun.* **2015**, *51*, 592-595.
16. Yeung, C.-T.; Yim, K.-H.; Wong, H.-Y.; Pal, R.; Lo, W.-S.; Yan, S.-C.; Wong, M. Y.-M.; Yufit, D.; Smiles, D. E.; McCormick, L. J.; Teat, S. J.; Shuh, D. K.; Wong, W.-T.; Law, G.-L. Chiral transcription in self-assembled tetrahedral Eu_4L_6 chiral cages displaying sizable circularly polarized luminescence. *Nat. Commun.* **2017**, *8*, 1128.

17. Yan, L.-L.; Tan, C.-H.; Zhang, G.-L.; Zhou, L.-P.; Bünzli, J.-C.; Sun, Q.-F. Stereocontrolled self-assembly and self-sorting of luminescent europium tetrahedral cages. *J. Am. Chem. Soc.* **2015**, *137* (26), 8550-8555.

18. Liu, C.-L.; Zhou, L.-P.; Tripathy, D.; Sun, Q.-F. Self-assembly of stable luminescent lanthanide supramolecular M_4L_6 cages with sensing properties toward nitroaromatics. *Chem. Commun.* **2017**, *53*, 2459-2462.

19. Kotova, O.; Comby, S.; Pandurangan, K.; Stomeo, F.; O'Brien, J. E.; Feeney, M.; Peacock, R. D.; McCoy, C. P.; Gunnlaugsson, T. The effect of the linker size in C_2 -symmetrical chiral ligands on the self-assembly dormation of luminescent triple-stranded di-metallic Eu(III) helicates in solution. *Dalton. Trans.* **2018**, *47*, 12308-12317.

20. Yim, K.-H.; Yeung, C.-T.; Wong, H.-Y.; Law, G.-L. Structural variation of self-assembled lanthanide supramolecular complexes induced by reaction conditions. *Inorg. Chem. Front.* **2021**, *8*, 2952-2964.

21. Zhou, J.; Liu, Q.; Feng, W.; Sun, Y.; Li, F. Upconversion luminescent materials: advances and applications. *Chem. Rev.* **2015**, *115* (1), 395-465.

22. Guillou, O.; Daiguebonne, C.; Calvez, G.; Bernot, K. A long journey in lanthanide chemistry: from fundamental crystallogenesis studies to commercial anticounterfeiting taggants. *Acc. Chem. Res.* **2016**, *49* (5), 844-856.

23. Mamedov, I.; Parac-Vogt, T. N.; Logothetis, N. K.; Angelovski, G. Synthesis and characterization of dinuclear heterometallic lanthanide complexes exhibiting MRI and luminescence response. *Dalton. Trans*. **2010**, *39*, 5721-5727.

24. Faulkner, S.; Pope, S. J. A. Lanthanide-sensitized lanthanide luminescence: terbium-sensitized ytterbium luminescence in a trinuclear complex. *J. Am.*

Chem. Soc. **2003**, *125* (35), 10526-10527.

25. Aguilà, D.; Barrios, L. A.; Velasco, V.; Roubeau, O.; Repollés, A.; Alonso, P. J.; Sesé, J.; Teat, S. J.; Luis, F.; Aromí, G. Heterodimetallic [LnLn'] lanthanide complexes: toward a chemical design of two-qubit molecular spin quantum gates. *J. Am. Chem. Soc.* **2014**, *136* (40), 14215-14222.
26. Velasco, V.; Barrios, L. A.; Schütze, M.; Roubeau, O.; Luis, F.; Teat, S. J.; Aguilà, D.; Aromí, G. Controlled heterometallic composition in linear trinuclear [LnCeLn] lanthanide molecular assemblies. *Chem. Eur. J.* **2019**, *25*, 15228-15232.
27. Aguilà, D.; Velasco, V.; Barrios, L. A.; González-Fabra, J.; Bo, C.; Teat, S. J.; Roubeau, O.; Aromí, G. Selective lanthanide distribution within a comprehensive series of heterometallic [LnPr] complexes. *Inorg. Chem.* **2019**, *57* (14), 8429-8439.
28. Costes, J.-P.; Dahan, F.; Nicodème, F. Structure-based description of a systematic synthesis of homo-and heteronuclear (4f, 4f) lanthanide complexes. *Inorg. Chem.* **2003**, *42* (20), 6556-6563.
29. Chen, X.-Y.; Bretonnière, Y.; Pécaut, J.; Bünzli, J.-C.; Mazzanti, M. Selective self-assembly of hexameric Homo- and heteropolymetallic lanthanide wheels: synthesis, structure, and photophysical studies. *Inorg. Chem.* **2007**, *46* (3), 625-637.
30. Tilney, J. A.; Sørensen, T. J.; Burton-Pye, B. P.; Faulkner, S. Self-assembly between dicarboxylate ions and a binuclear europium complex: formation of stable adducts and heterometallic lanthanide complexes. *Dalton. Trans.* **2011**, *40*, 12063-12066.

31. Lewis, D. J.; Glover, P. B.; Solomons, M. C.; Pikramenou, Z. Purely heterometallic lanthanide(III) macrocycles through controlled assembly of disulfide bonds for dual color emission. *J. Am. Chem. Soc.* **2011**, *133* (4), 1033-1043.

32. Sørensen, T. J.; Tropiano, M.; Blackburn, O. A.; Tilney, J. A.; Kenwright, A. M.; Faulkner, S. Preparation and study of an f,f,f,f covalently linked tetranuclear hetero-trimetallic complex a Europium, Terbium, Dysprosium triad. *Chem. Commun.* **2012**, *49*, 783-785.

33. Search of the cambridge structural database using conQuest of the CSD-system software suite.

34. Shannon, R. D. Revised effective ionic radii and systematic studies of interatomic distances in halides and chalcogenides. *Acta Cryst. A.* **1976**, *32*, 751-761.

35. Xu, J.; Radkov, E.; Zieglar, M.; Raymond, K. N. Plutonium(IV) sequestration: structural and thermodynamic evaluation of the extraordinarily stable cerium(IV) hydroxypyridinonate complexes[1]. *Inorg. Chem.* **2000**, *39* (18), 4156-4164.

36. Daumann, L. J.; Tatum, D. S.; Andolina, C. M.; Pacold, J. I.; D'Aléo, A.; Law, G.-L.; Xu, J.; Raymond, K. N. Effects of ligand geometry on the photophysical properties of photoluminescent Eu(III) and Sm(III) 1-hydroxypyridin-2-one complexes in aqueous solution. *Inorg. Chem.* **2016**, *55* (1) 114-124.

Chapter 4: Remote stereo-control of chiral lanthanide supramolecular complexes

4.1 Introduction

4.1.1 Chiral domino effect induced by α, α-disubstituted amino acids

Helical peptides are inherently chiral even if they lack asymmetric centers in the peptide backbone.[1] However, isomers of the helical peptides are isoenergetic and thus they have an equal population in the achiral environment. Control chirality of peptides is essential for biological application. Therefore, scientists were interested in restricting the conformation of peptides through chiral domino effect.

'Domino effect' is a term that describes the transfer and amplification of chiral information from the chiral moiety to the rest of the achiral moiety. For covalent chiral domino effect on peptides, it strongly relies on the presence of chiral amino acid units to transfer the chiral information throughout the entire peptide.[2-4]

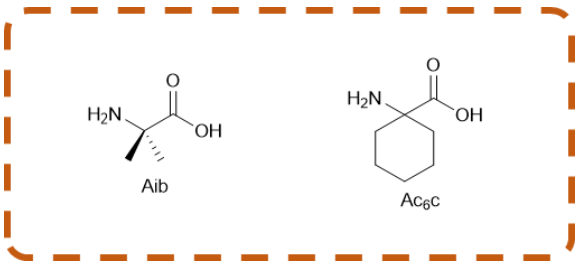

Figure 4-1. *Structures of Aib and Ac6c.*

One of the solutions is the use of α, α-disubstituted amino acids.[5] Replacement of the α-hydrogen with an alkyl substituent can increase the chemical stability and restrict the conformational freedom of the peptide. Common α, α-disubstituted amino acids include α-aminoisobutyric acid (Aib) and 1-aminocyclohexanecarboxylic acid (Ac_6c) (figure 4-1).[6]

The secondary structures of peptide containing Aib has been well investigated. Homopeptide consists of Aib is preferred to form 3_{10} helicates in both solution and crystal state. The enantiomeric ratio of right-handed helicates and left-handed helicates is 1 to 1.[7-8] There is no critical chain length for the formation of 3_{10} helicates.[9] The minimal number of amino acids for 3_{10} helicates might be 3. When the L-α-amino acid residue is incorporated with Aib units, right-handed helicates will be preferred. It is found that the peptides prefer to form 3_{10} helicates when it is short (<7 amino acid units) and containing high percentage of Aib (>50%),[10] while α-helices will be formed when the peptide is long (>9 amino acid units) and contains little Aib residue (<50%).[11]

4.1.2 Remote control of chirality in transition metal complexes

Control of the chirality of the self-assembly supramolecule is one of the major research areas. In most of the examples, chirality of the metal complexes can be successfully controlled by the chiral group in the ligand through covalent domino effect.[12] However, the position of the chiral group should be close enough to the chelating group so that the chiral information could be transmitted to the metal ion.

In 2011, Yashima's group reported an example of remote control of chirality of a metal complex.[13] The complex was coordinated by a ligand bearing a helical oligopeptide. The general idea of the remote control of chirality was based on the

covalent chiral domino effect. Although the chiral Val residue was located far from the metal center, chiral information can be still transferred through the strongly helicogenic achiral peptide. The mechanism involved the transfer of chiral information along the whole peptide, resulting in either *P*- (right-handed twisted) or *M*- (left-handed twisted) helix. The handedness can control the chirality of the metal center. It was found the most effective distance is 4 amino acid units (n=2), while no stereocontrol effect can be found when n =0 or 1.

Based on the result in 2011, Yashima's group further demonstrated the concept of remote control of chirality by helical peptides with self-assembly supramolecular complexes (figure 4-2).[14] One of the interesting results was the transformation between the 3_{10} helicates and α-helix by the addition of fluoroalcohols. The α-helix will freeze the rotation of the peptide because of the increased helix width. As a result, the complex containing higher 3_{10} helicates content will have a stronger CD intensity compared with that of α-helix.

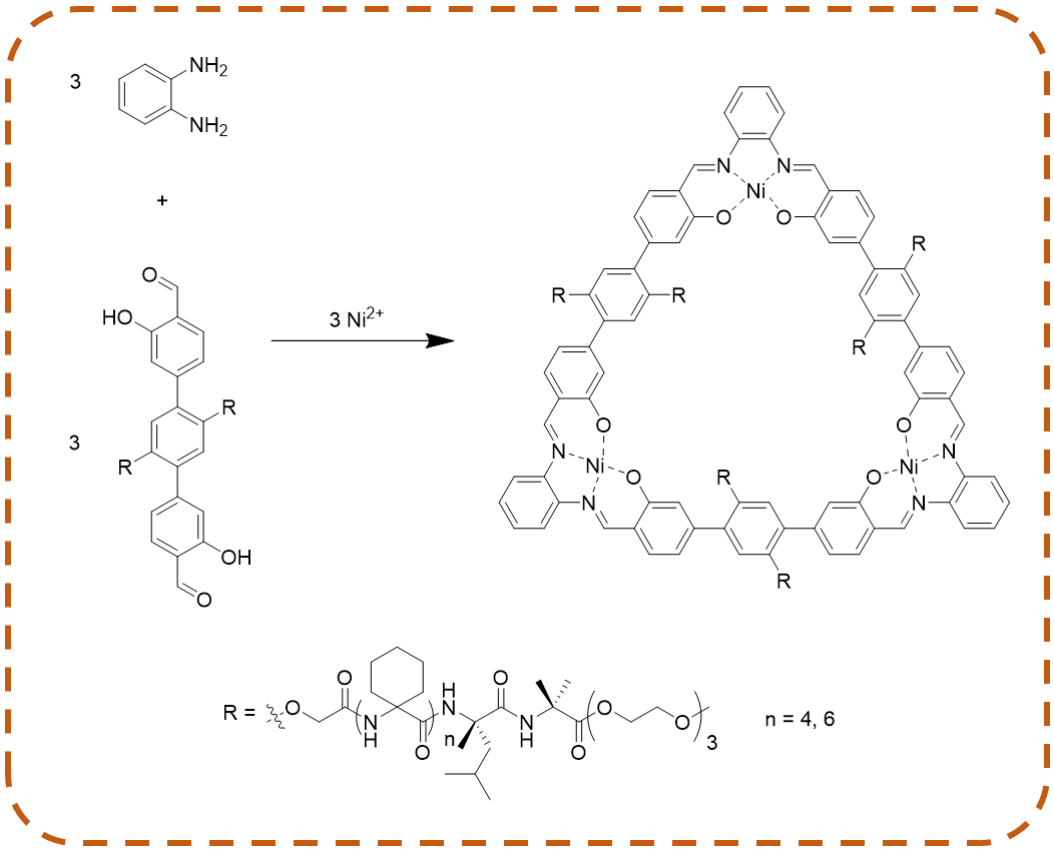

Figure 4-2. *Remote control of chirality by helical peptide supramolecular Ni complex.*[14]

4.1.3 Scope of study

In this study, the concept of remote control of chirality was applied to lanthanide complexes. Chiral ligands consist of short amino acid sequences were prepared. Position, length and types of amino acid was varied to investigate the effect of peptide towards the supramolecular formation. It was expected that the chiral information could be transmitted by chiral domino effect induced by the helical twisting of bulky disubstituted amino acid units.

4.2 Result and Discussion

4.2.1 Scheme of this study

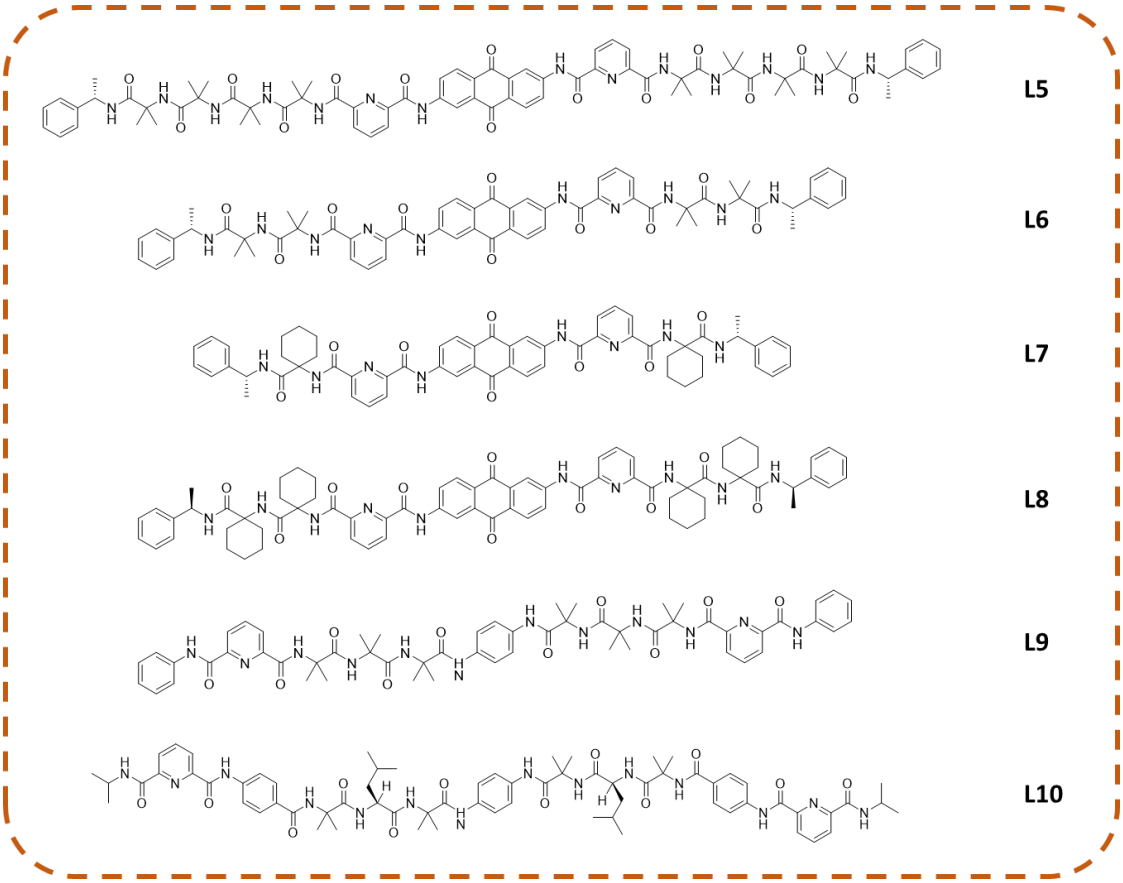

Figure 4-3. *Structures of* ***L5-10****.*

In this chapter, six ligands were synthesized and their structures are shown in figure 4-3. **L5** was designed based on literature and it was expected to form chiral lanthanide supramolecular tetrahedron through chiral domino effect. However, no desired supramolecular product was observed in both ^{1}HNMR and ESI-HRMS. Therefore, five different ligands were synthesized and the supramolecular formation using peptide-consisted ligands was investigated. The scheme of this study was shown in figure 4-4.

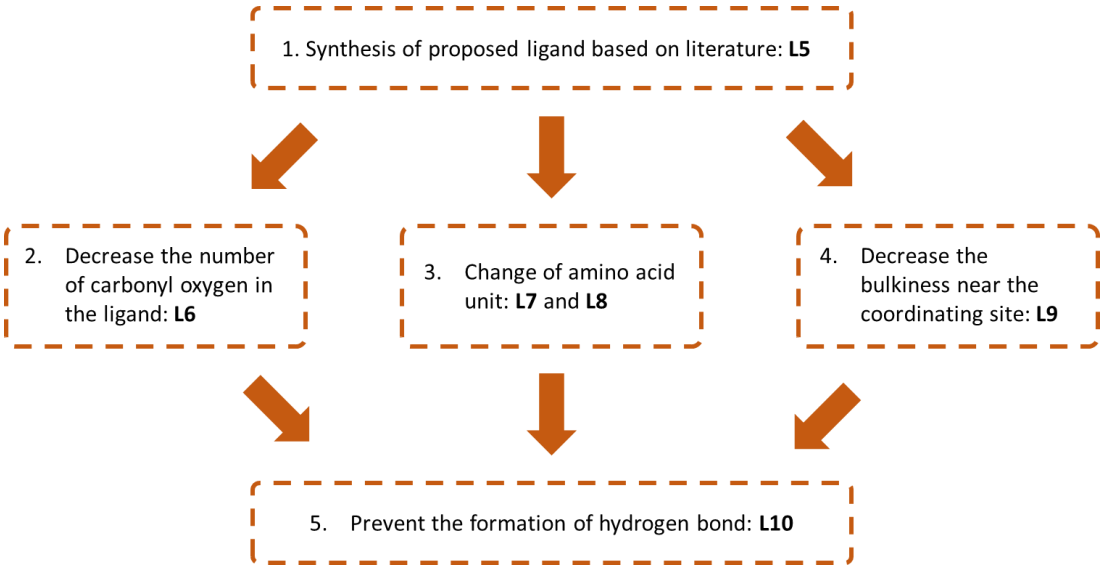

Figure 4-4. *Scheme showing the investigation of supramolecular formation using peptide ligands.*

4.2.2 Ligand design of L5

L5 was designed based on the reported literature. The ligand consists of four parts, which are the chiral group, peptide, metal chelator and bridging unit. The chiral group and metal chelator are chosen to be 1-phenylethan-1-amine and pyridinedicarboxylamide (pcam). The designed bridging unit is 2,6-diaminoanthracene-9,10-dione. The incorporation of the above three parts with europium shows bright red luminescence. The peptide part would be composed of four Aib residues, which was found to have a strong helix-forming ability due to its steric hinderance. It was expected that the chirality can be transmitted from the chiral group to the metal center through covalent chiral effect.

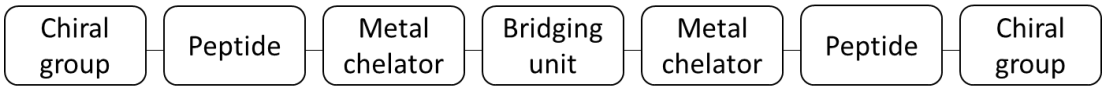

Figure 4-5. *The component of the proposed **L5**.*

4.2.3 Synthesis of Aib intermediates

Step 1:

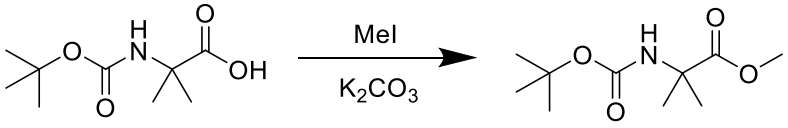

Step 1 involved the esterification of Boc-Aib-OH using iodomethane. The desired Boc-Aib-OMe was successfully synthesized and the highest yield that obtained was 89.8%.

Step 2:

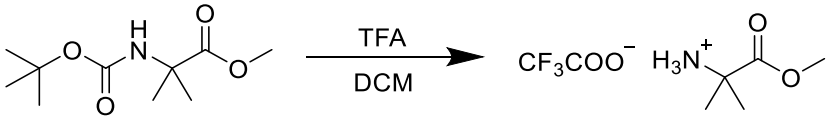

In the next step, TFA was used to deprotect the Boc group in the amino acid. The highest yield that obtained was 88.15%.

Step 3:

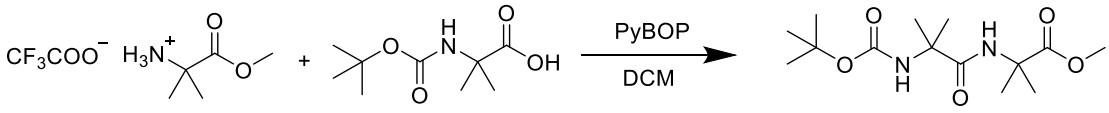

Boc-Aib-Aib-OMe was prepared by coupling H_3N^+-Aib-OMe and Boc-Aib-OH using PyBOP as the coupling reagent. The amide coupled product can be purified by simply washing with acid and base. Result showed that 2 M HCl will deprotect the Boc group. Therefore, the concentration of acid was set to 0.5 M. Different coupling reagents were tested in this step including thinoyl chloride, oxalyl chloride, HOBt and EEDQ. However, PyBOP was found to be the most efficient coupling reagent since the

yield was high (up to 75.0%) and the reaction time was relatively short (16 hrs) compared to other coupling reagent.

Step 4:

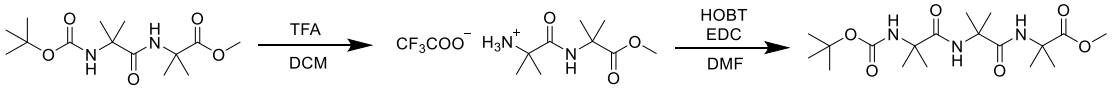

Boc-Aib-Aib-Aib-OMe was prepared by in-situ deprotection of Boc-Aib-Aib-OMe followed by amide coupling reaction with Boc-Aib-OH. Different from general procedure, which suggested that deprotection of Boc group can be completed within an hour with the use of TFA, 3 hrs were required for deprotection in this step. The crude Boc-Aib-Aib-Aib-OMe can be purified simply by washing with acid, base and diethyl ether.

Step 5:

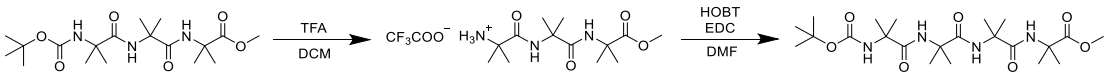

Boc-$(Aib)_4$-OMe was synthesized by in-situ deprotection of Boc-Aib-Aib-Aib-OMe followed by coupling with Boc-Aib-OH. The highest yield was found to be 54.3%.

Step 6:

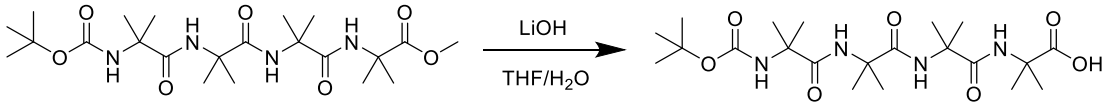

Boc-$(Aib)_4$-OH was prepared by alkaline hydrolysis to Boc-$(Aib)_4$-OMe to deprotect the methyl ester group. The highest yield was found to be 85.1%.

Step 7:

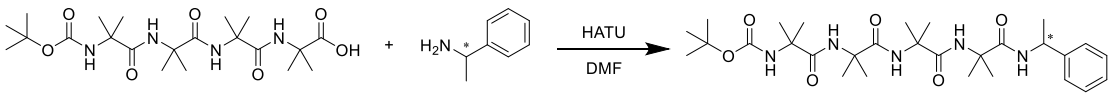

Boc-$(Aib)_4$-spy was synthesized by classical HOBt, EDC coupling and purified by washing with acid and base. The product was only slightly soluble in ethyl acetate and diethyl ether, and highly soluble in DCM.

Step 8:

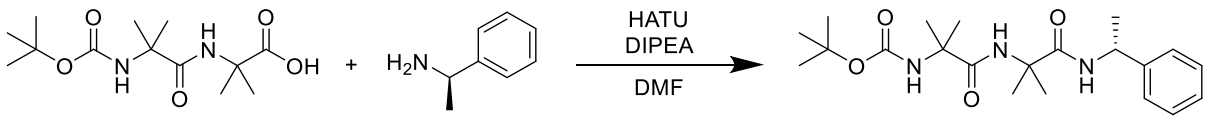

Boc-Aib-Aib-OH was successfully coupled with chiral group following the procedure of Boc-$(Aib)_4$-spy. The highest yield was 92.3%.

4.2.4 Synthesis of central bridging linker

Step 1:

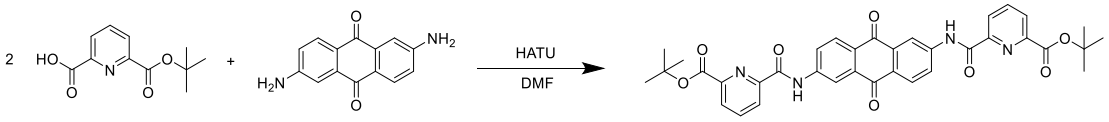

Di-tert-butyl 6,6'-(((9,10-dioxo-9,10-dihydroanthracene-2,6-diyl)bis(azanediyl))bis(carbonyl))dipicolinate was prepared by coupling two equivalents of 6-(tert-butoxycarbonyl)picolinic acid with one equivalent of 2,6-diaminoanthracene-9,10-dione for 32 hrs. The pure product could be obtained by simply washing the crude product with water and MeCN. The yield was found to be 92.4%.

Step 2:

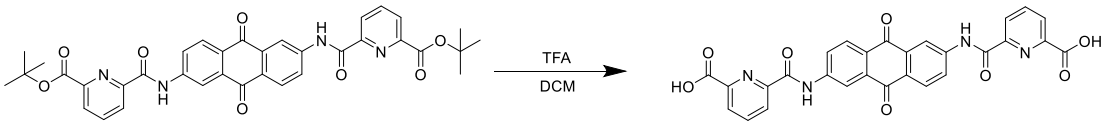

The central bridging linker of 6,6'-(((9,10-dioxo-9,10-dihydroanthracene-2,6-diyl)bis(azanediyl))bis(carbonyl))dipicolinic acid was prepared by deprotection of t-butyl group in DCM. After 16 hrs, the solvent was evaporated, and the crude product was washed with diethyl ether. The highest yield that obtained for this step is 99.3% yield.

4.2.5 Synthesis and complexation of L5

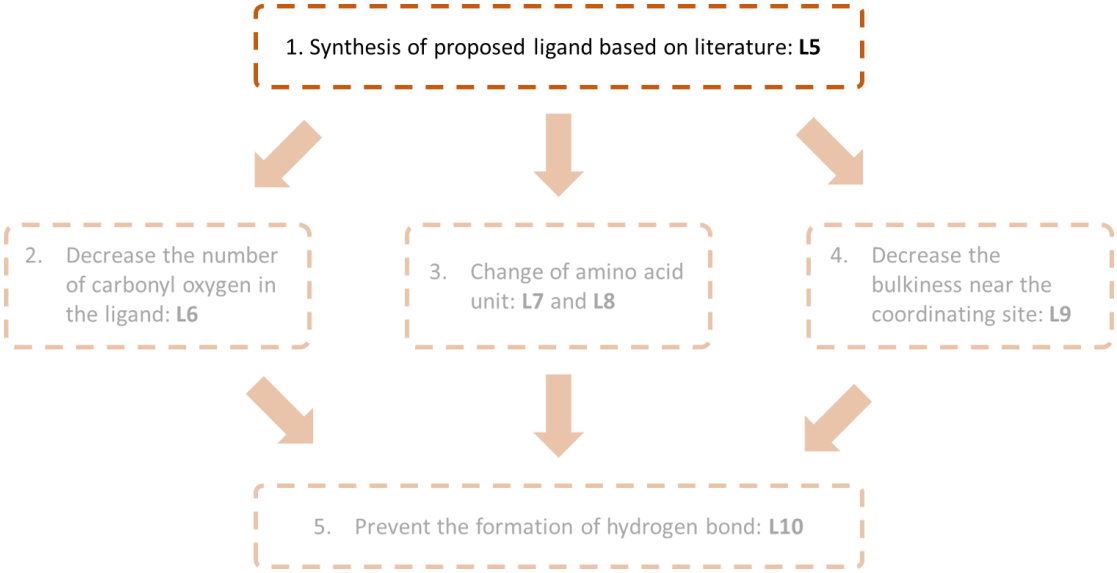

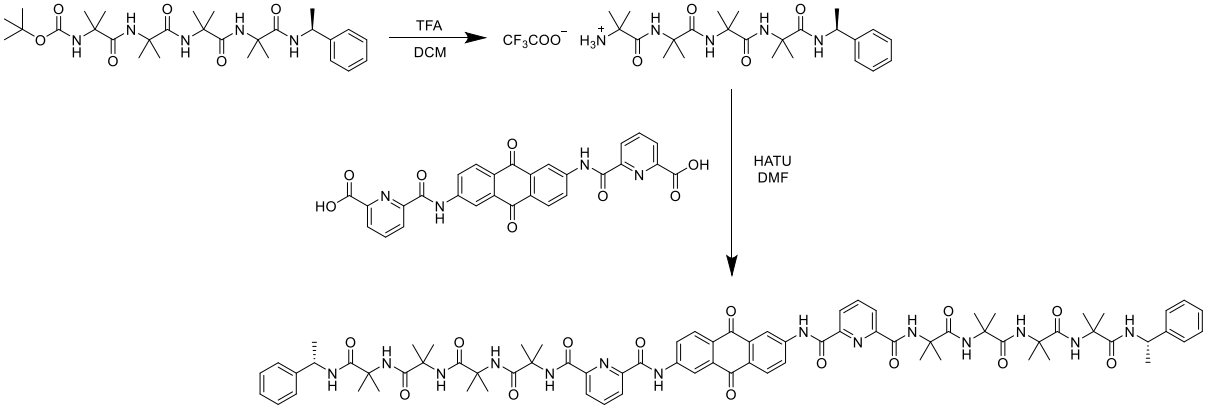

L5 was synthesized by in-situ deprotection of Boc-$(Aib)_4$-spy followed by coupling with the central bridging linker 6,6'-(((9,10-dioxo-9,10-dihydroanthracene-2,6-diyl)bis(azanediyl))bis(carbonyl))dipicolinic acid using HATU as the coupling reagent. The ligand was purified by simply washing with MeCN to obtain 49.6% yield.

Three equivalents of **L5** was allowed to coordinate with two equivalents of $Eu(OTf)_3$ in a mixture of MeCN and DCM at 60^oC for 3 hrs. ^{1}HNMR revealed the disappearance of ligand peaks, indicating the successful coordination of ligand with Eu. Compared with free ligand, the NMR signals arising from the complex are shifted due to the coordination to paramagnetic europium(III) ions. Diamagnetic La complex was also synthesized by replacing Eu with La and the ^{1}HNMR was done to confirm the complexation. However, compared the NMR spectrum with other lanthanide complexes from chapter 2 and 3, the NMR of Eu and La complexes with **L5** were weak (figure 4-6). ESI-HRMS was also performed for both Eu and La complexes. In the ESI-HRMS specta, mononuclear species Ln**L5** was found to be the only species in solution state and no other higher order supramolecular complex can be observed (figure 4-7). For the structure of Ln**L5**, it was hypothesized that one Ln ion coordinate with one **L5** and the coordination sphere of Ln was saturated by both ligand and solvent molecules. However, due to the lack of X-ray crystal structure, exact determination of structure of Ln**L5** was not possible. Result showed that the formation of desired tetrahedron was unsuccessful using **L5**.

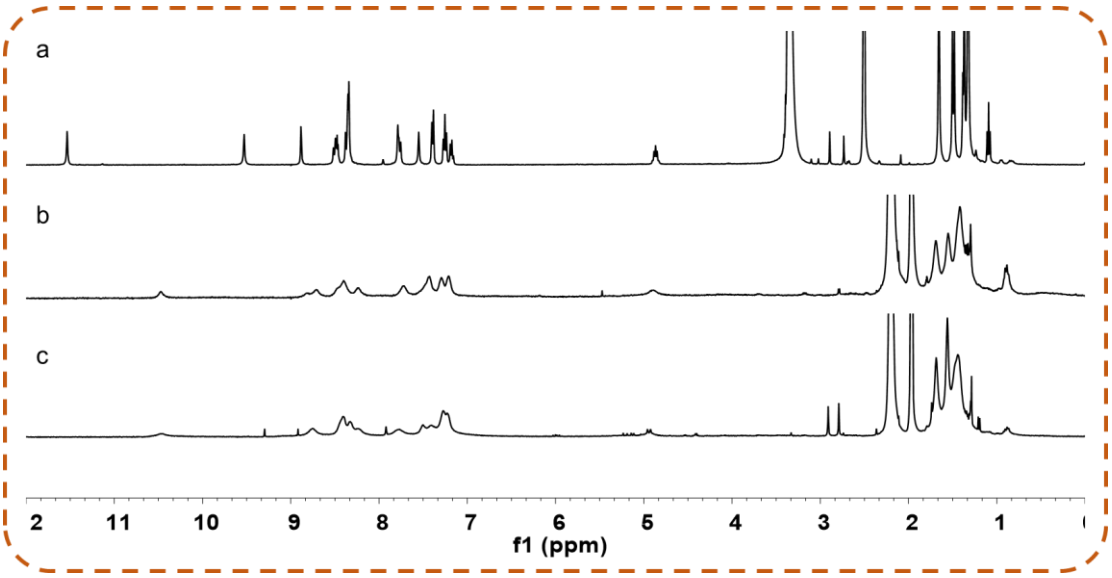

Figure 4-6. *^{1}HNMR of (a) free ligand **L5** in $(CD_3)_2SO$, (b) Eu complex of **L5** in CD_3CN and (c) La complex of **L5** in CD_3CN.*

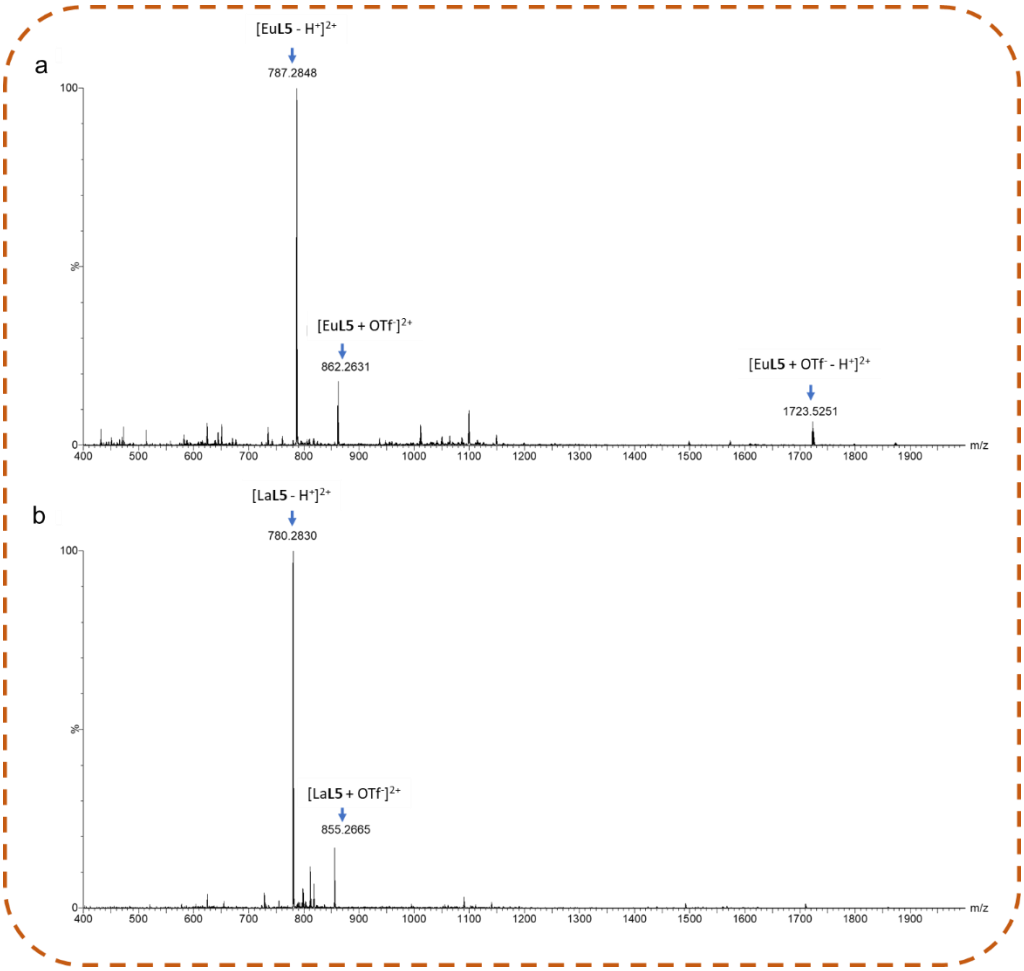

Figure 4-7. *ESI-HRMS of (a) Eu complex of **L5** (b) La complex of **L5**.*

4.2.6 Synthesis and complexation of L6

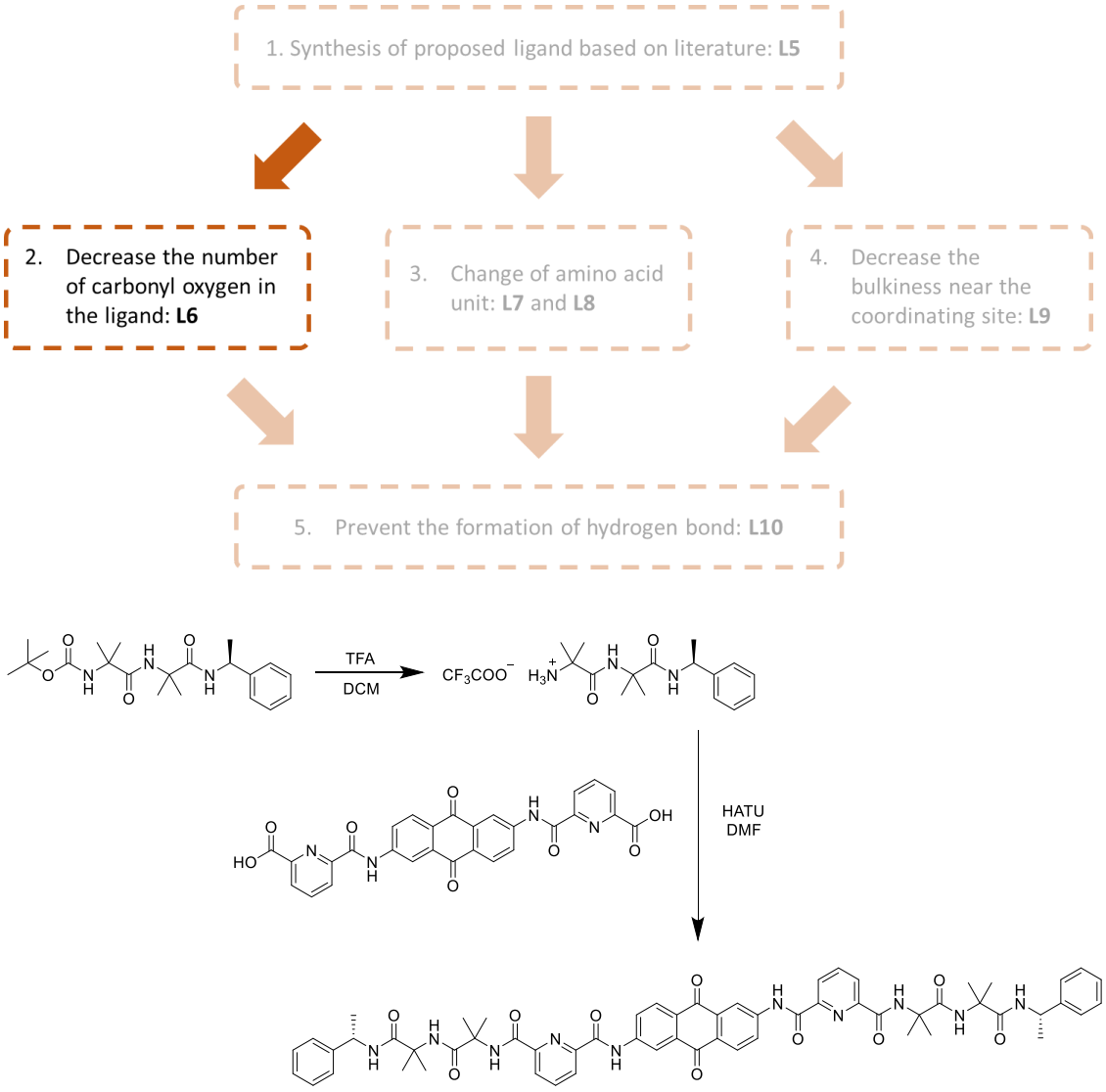

Based on the result from **L5**, it showed that **L5** can successfully coordinate with Eu and La. However, there were some factors that affect the supramolecular formation. Thus, **L6** was prepared to compare the result with **L5**. Different from **L5**, **L6** only consists of two Aib units. It was expected to form 3_{10} helix so that the chiral information can be transferred from the chiral group to the metal centre. It was hypothesized that large number of carbonyl oxygen may affect the lanthanide supramolecular formation since carbonyl oxygen may act as a donor to coordinate with lanthanide ions. Therefore, the number of carbonyl oxygen was reduced in **L6**.

Similar to **L5**, **L6** was synthesized by in-situ deprotection of Boc-Aib-Aib-spy followed by coupling with the central bridging linker 6,6'-(((9,10-dioxo-9,10-dihydroanthracene-2,6-diyl)bis(azanediyl))bis(carbonyl))dipicolinic acid using HATU as the coupling reagent. The product can be simply washed with chloroform and the yield was found to be 53.6%.

Three equivalents of **L6** was allowed to coordinate with two equivalents of $Eu(OTf)_3$ in a mixture of MeCN and DCM at 60°C for 3 hrs. In the ^{1}HNMR spectrum of the Eu complex, similar result was observed compared with that of **L5**. All signals corresponding to the ligand were disappeared and broad peaks were observed due to the paramagnetic europium(III) ions (figure 4-8).

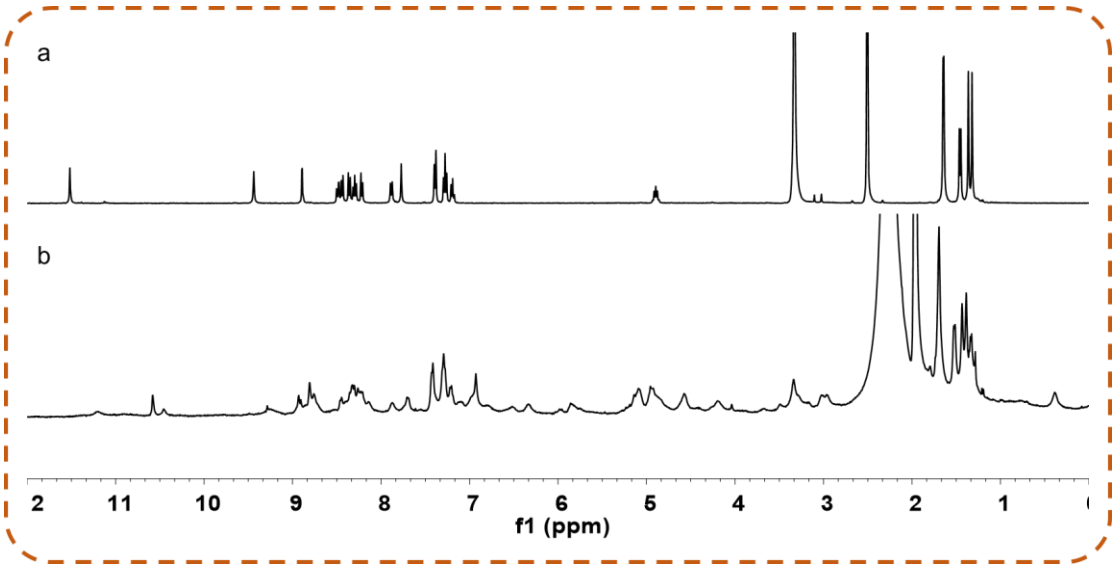

Figure 4-8. *^{1}HNMR of (a) free ligand **L6** in $(CD_3)_2SO$ and (b) Eu complex of **L5** in CD_3CN.*

The Eu complex of **L6** was further characterized by ESI-HMRS (figure 4-9). In the ESI-HRMS spectrum, the resolved peaks are either in +2 and +3 charge and the major species was found to be Eu_2**L6**$_2$. No desired tetrahedron or helicate can be observed.

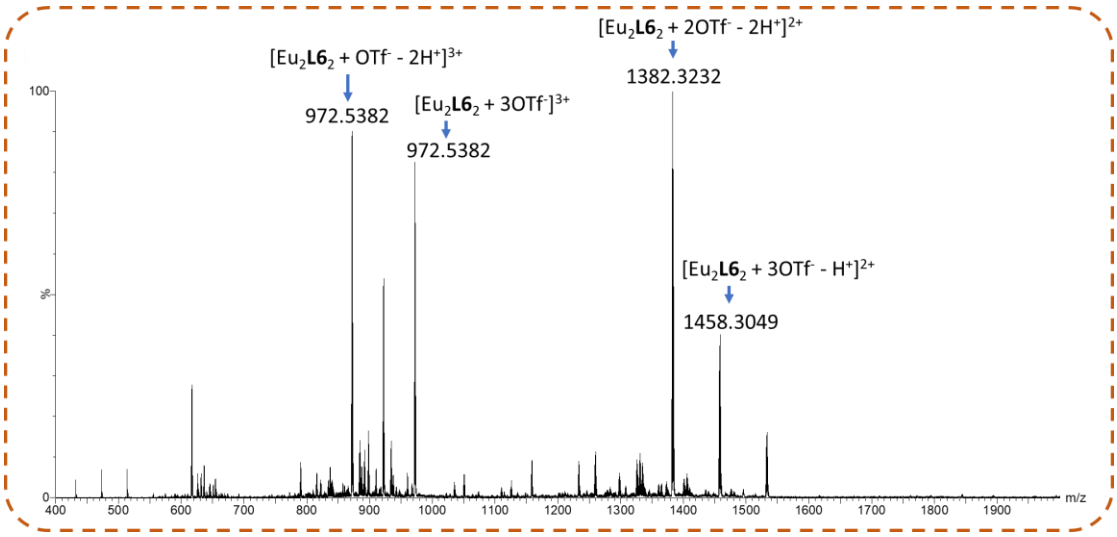

Figure 4-9. *ESI-HRMS of Eu complex of* ***L6****.*

4.2.7 Synthesis of Ac_6c intermediates

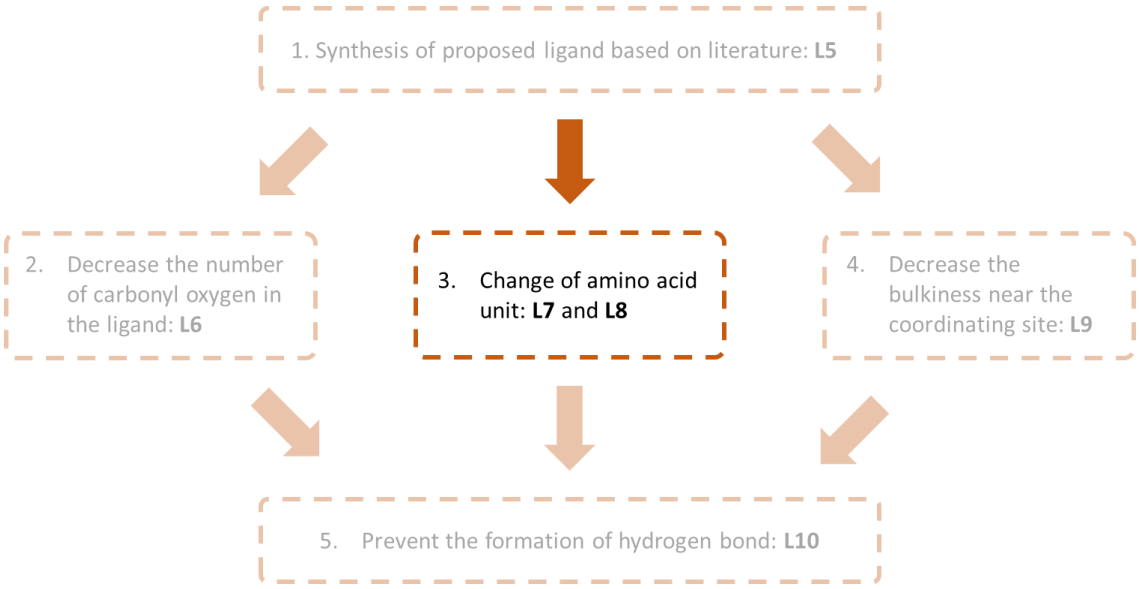

Two more ligands, **L7** and **L8**, were designed and synthesized. Different from **L5** and **L6**, both **L7** and **L7** consist of another type of bulky amino acid units. Ac_6c amino acid was used for chiral domino effect. Complexation was done for **L7** and **L8** to observe the effect of changing another type of amino acid towards supramolecular formation. In order to avoid the coordination between metal ion and carbonyl oxygen, the number of amino acids was greatly reduced (one for **L7**, and two for **L8**).

Step 1:

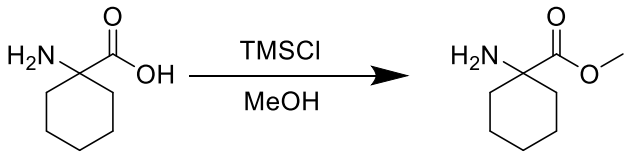

The first step is to prepare the H_2N-Ac_6c-OMe. According to the literature, this step can be achieved by using thionyl chloride and methanol and the carboxylic acid group can be protected by a methyl group. The following table shows five trials for this reaction.

Trial	Reaction time	Reagent	Yield/Result
1	16 hrs	Thionyl chloride	30.2%
2	16 hrs	Oxalyl chloride	No product can be obtained
3	96 hrs	Thionyl chloride	35.9%
4	7 days		46.1%
5	10 days		No product can be obtained

Table 4-1. *Trials for synthesizing H-Ac_6c-OMe.*

Although this method can synthesize the product successfully, the yield is relatively low. The unreacted thionyl chloride is difficult to be removed and some of the product would be precipitated out in a form of acidic salt. The acidic product may affect the next step reaction since the amide coupling reaction requires a basic environment.

An alternative synthetic procedure to prepare H_2N-Ac_6c-OMe. Although the H_3N-Ac_6c-OMe could be synthesized by the Boc group protection of the H-Ac_6c-OH followed by the methylation by iodomethane and TFA deprotection in good yield.

However, three steps are required, and the reaction time is long in order to achieve high yield. Therefore, an alternative method is needed to increase the efficiency.

The new method is based on the findings by Sha's group.[15] In 2008, Sha's group reported a convenient synthesis of amino acid methyl esters by employing trimethylchlorosilane (TMSCl) as the methylation reagent. The result shows that the use of TMSCl could obtain a high yield, which is comparable or even higher than those obtained with the use of thionyl chloride. TMSCl has a relatively lower boiling point compared with thionyl chloride which is easier for purification. Several attempts were done, and the results are summarized in the following table.

Trial	Reaction Time (hrs)	Temperature (°C)	Yield
1	16	rtp	22.8%
2	24	rtp	28.3%
3	16	50	51.5%
4	24	50	52.9%

Table 4-2. *Trials for synthesizing H_2N -Ac_6c-OMe by TMSCl.*

Based on the result, the condition in trial 3 is the most efficient since the reaction time is shorter and it provides a reasonable yield.

Step 2:

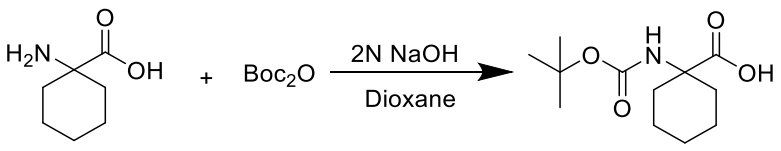

The second step is to prepare the Boc-Ac_6c-OH. Several trials were tested to prepare it since the Boc-protection reaction is simple. The following table summarized the details of different trials.

Trial	Base	Solvent	Reaction time	Temperature	Yield//Result
1	KOH	THF/Water	16 hrs	0 °C	5.21%
2	TEA	DCM	16 hrs	rtp	No product can be found in NMR
3	NaOH	MeOH/Water	16 hrs	0 °C	No product can be found in NMR
4	NaOH	Dioxane	16 hrs	0 °C	27.0%
5			32 hrs	0 °C	46.4%
6			16 hrs	rtp	64.5%

Table 4-3. *Trials for synthesizing Boc-Ac_6c-OH.*

Based on the theory of Boc group protection, the reaction should be done in anhydrous solvent since the reactant, Boc_2O, would react with water to generate carbon dioxide. Therefore, the first five trials were done in either rtp in dry solvent or 0°C in water in order to suppress the reaction between Boc_2O and water. Based on the result of trial 6, it shows that this reaction can also be done in water containing solvent and produce an acceptable yield.

Step 3:

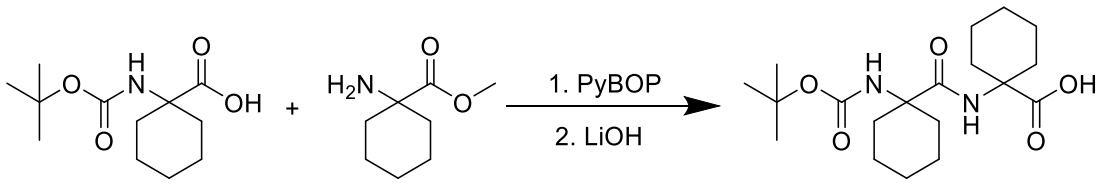

Reaction 3 is the preparation of dipeptide Boc-Ac_6c-Ac_6c-OMe. It involves the coupling between Boc-Ac_6c-OH and H_2N-Ac_6c-OMe. Based on the experience in synthesizing the Boc-Aib-Aib-OMe, the dipeptide was the most challenging reaction. In the case of Boc-Aib-Aib-OMe, it was just a very short peptide and the hydrophobic character is not "obvious". For example, the Boc-Aib-Aib-OMe is slightly soluble in both hexane and diethyl ether, while the tripeptide (Boc-Aib-Aib-Aib-OMe) and tetrapeptide (Boc-Aib-Aib-Aib-Aib-OMe) are completely insoluble in hexane and diethyl ether. The solubility issue created a challenge in obtaining the pure product in high yield.

When preparing Boc-Ac_6c-Ac_6c-OMe, similar result was observed. The crude compound contained three UV-active impurities. The difference of the R_f value of the impurities and the desired product was quite large, but they cannot be completely separated by flash column chromatography. One of the attempts was the direct deprotection of methyl ester by lithium hydroxide monohydrate without further purification. Result shows that the UV-active impurities will not react with lithium hydroxide monohydrate and can be washed away by dichloromethane. The Boc-Ac_6c-Ac_6c-OH can be protonated and extracted by dichloromethane afterwards.

This reaction was repeated to prepare more intermediate compound and the reaction was summarized in the following table.

Trial	Yield
1	66.7%
2	73.0%

Table 4-4. *Trials for synthesizing Boc-Ac_6c-Ac_6c-OH.*

Step 4:

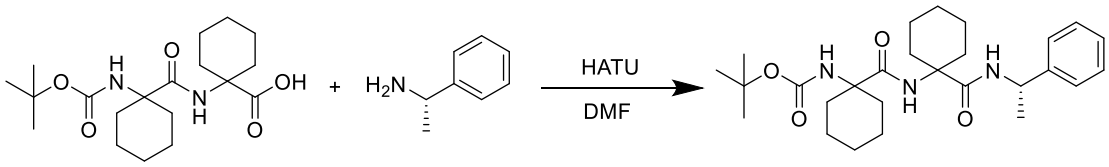

Boc-Ac$_6$c-Ac$_6$c-rpy was synthesized following the procedures of Boc-Aib-Aib-spy. The reaction and workup were relatively easier, and the product can be purified by column chromatography to yield the desired white solid in 50.9% yield.

Step 5:

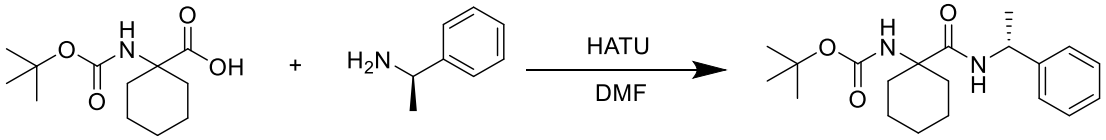

Boc-Ac$_6$c-OH were allowed to react with (R)-1-phenylethan-1-amine. The mixture was reacted for 48 hrs with the use of HATU as the coupling reagent. The workup was simple, and the pure product could be obtained by simply washing with acid and base. The yield was found to be 90.9% for Boc-Ac$_6$c-rpy.

4.2.8 Synthesis and complexation of L7

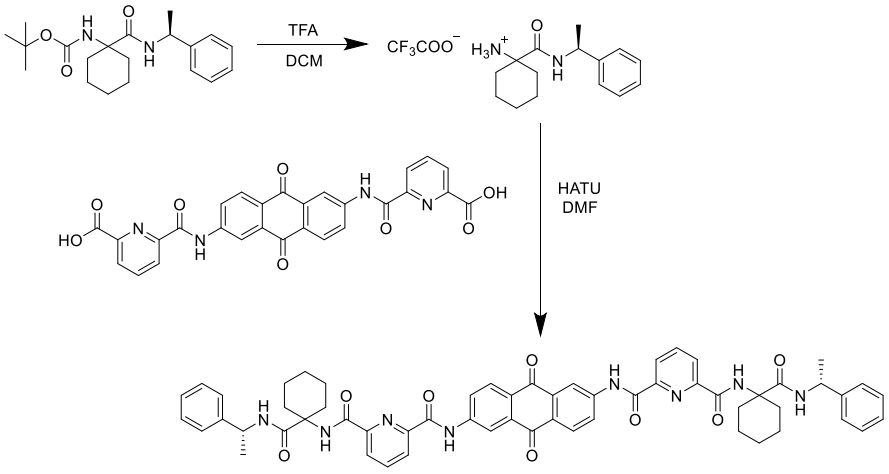

L7 was allowed to react with $Eu(OTf)_3$ in a ratio of 3 to 2. The solution turned to red luminescence which confirmed the complexation with Eu^{3+}. However, the proton NMR signal was very weak (figure 4-10). Diamagnetic La complex of **L7** was also prepared. However, unresolved broad peaks were observed in proton NMR and no conclusion can be drawn. ESI-HRMS was also performed for characterization of both Eu and La complexes. For Eu complex, undesired supramolecular Eu_2**L7**$_3$ complex was observed in the ESI-HRMS spectrum, and it was hypothesized that Eu_2**L7**$_3$ exhibited a helicate stucture. Due to the lack of X-ray crystal structure, confirmation of exact topology was not possible. Although **L7** can form Eu_2**L7**$_3$ complex with Eu, La complex showed undesired La_2**L7**$_2$ lanthanide cluster. For Eu_2**L7**$_3$ complex, the stoichiometric ratio was confirmed by ESI-HRMS (figure 4-11). However, no structural information can be obtained from the NMR spectrum and further investigation is needed.

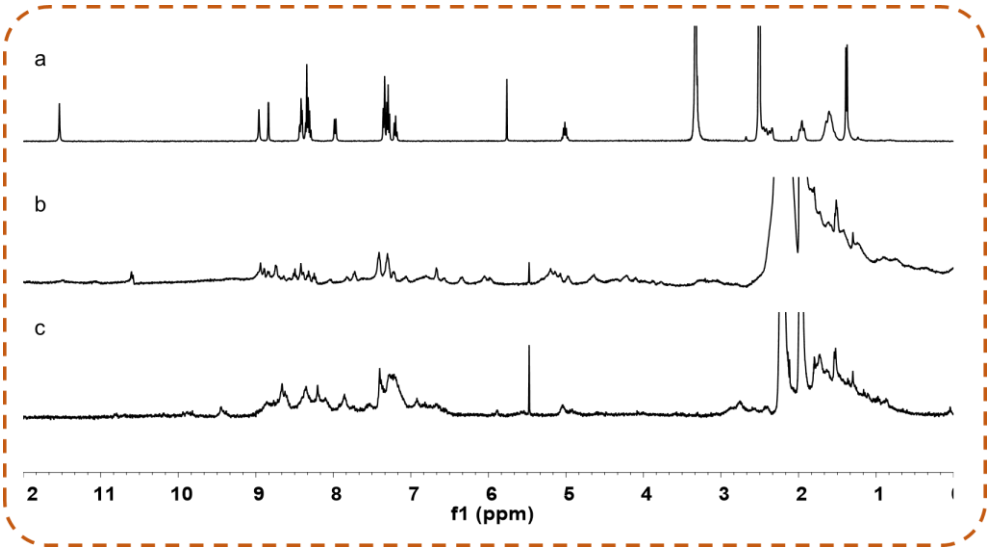

Figure 4-10. *^{1}HNMR of (a) free ligand **L7** in $(CD_3)_2SO$, (b) Eu complex of **L7** in CD_3CN and (c) La complex of **L7** in CD_3CN.*

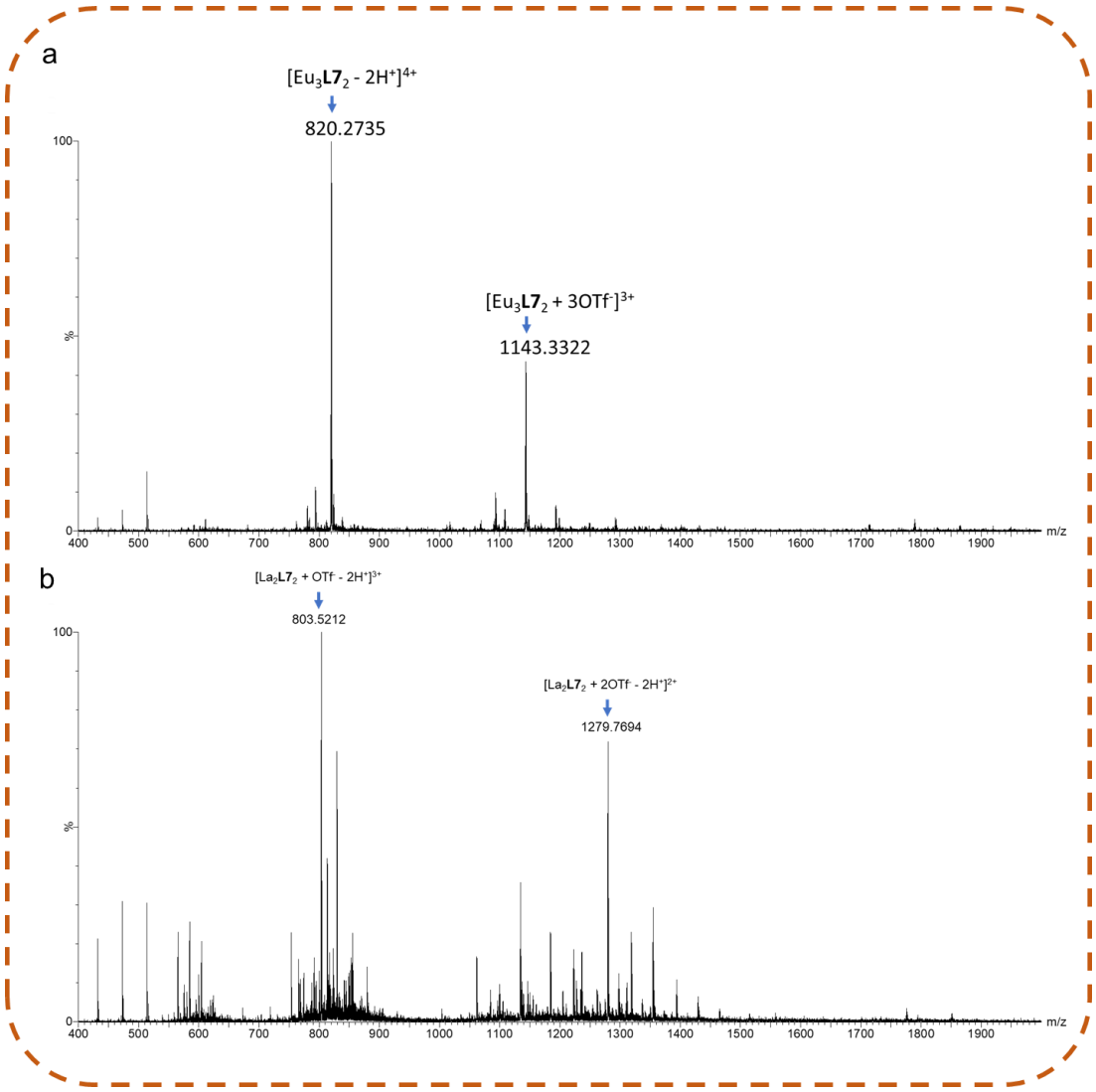

Figure 4-11. *ESI-HRMS of (a) Eu complex of **L7** (b) La complex of **L7**.*

4.2.9 Synthesis and complexation of L8

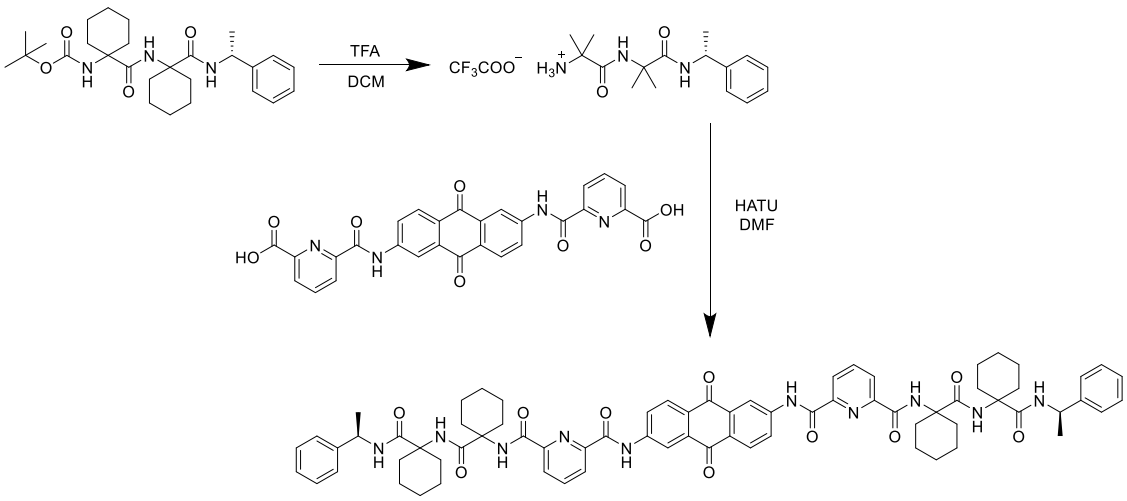

Ligand with 2 Ac_6c units (**L8**) was allowed to react with $La(OTf)_3$ and Eu $La(OTf)_3$. Similar with the result of **L7**, red luminescence was also observed for Eu^{3+}, indicating the successful coordination between **L8** and Eu^{3+}. However, the proton NMR signal was very weak (figure 4-12). Similar result was obtained for La complex. ESI-HRMS result revealed both Eu and La complexes exhibited as Ln_2**L8**$_2$ lanthanide cluster in solution state no desired higher ordered supramolecular complex can be observed (figure 4-13).

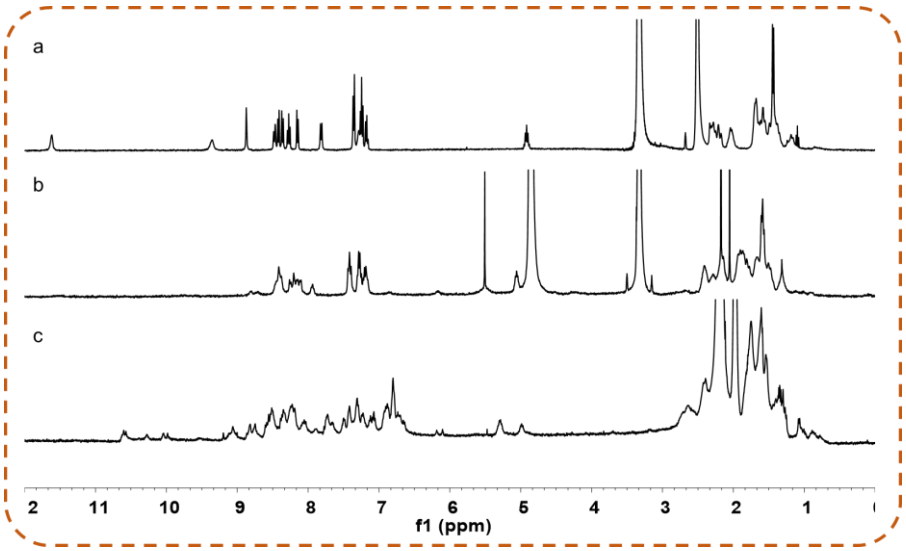

Figure 4-12. *^{1}HNMR of (a) free ligand **L8** in $(CD_3)_2SO$, (b) Eu complex of **L8** in CD_3CN and (c) La complex of **L8** in CD_3CN.*

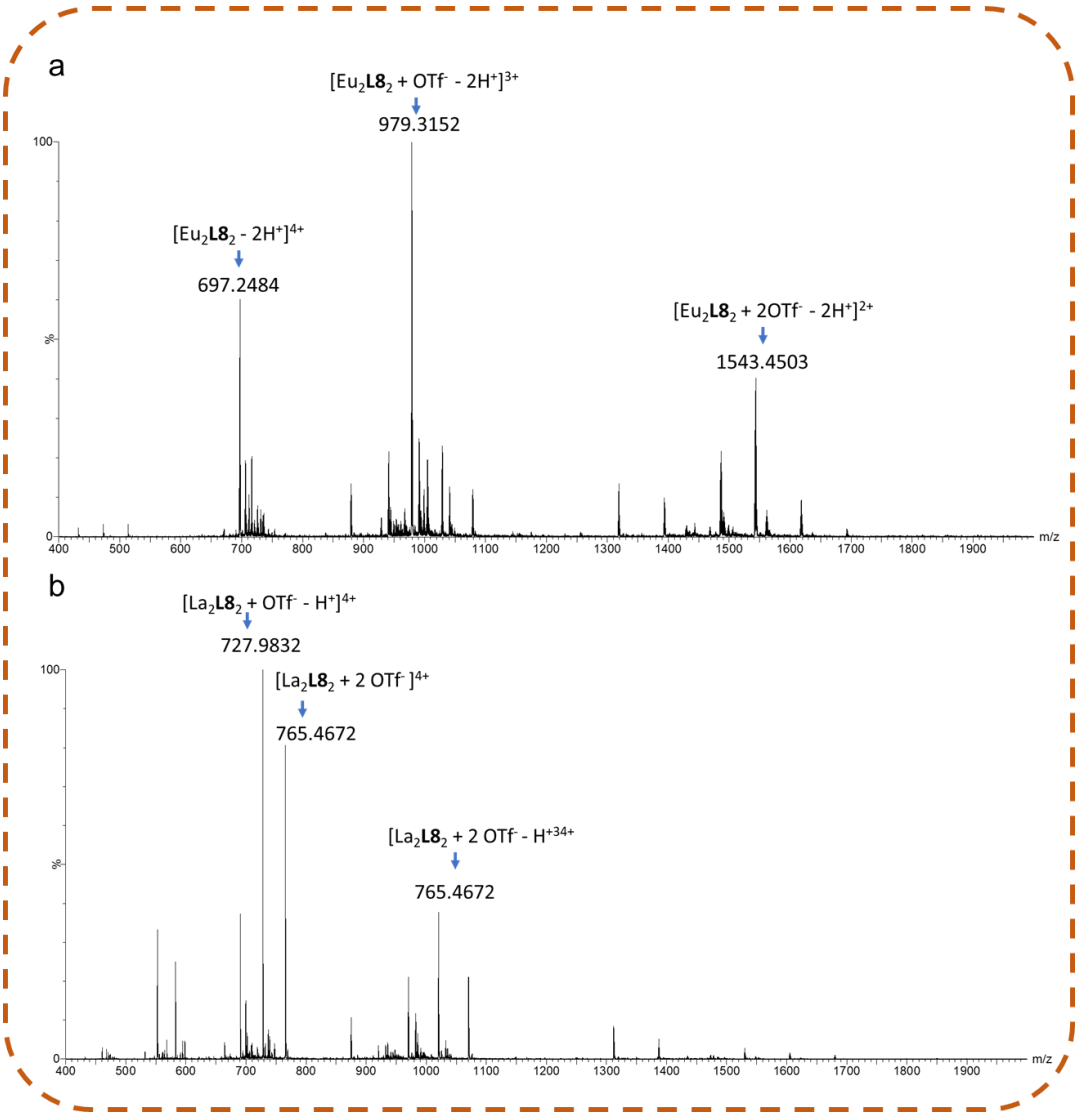

Figure 4-13. *ESI-HRMS of (a) Eu complex of **L8** (b) La complex of **L8**.*

4.2.10 Synthesis of intermediates for L9

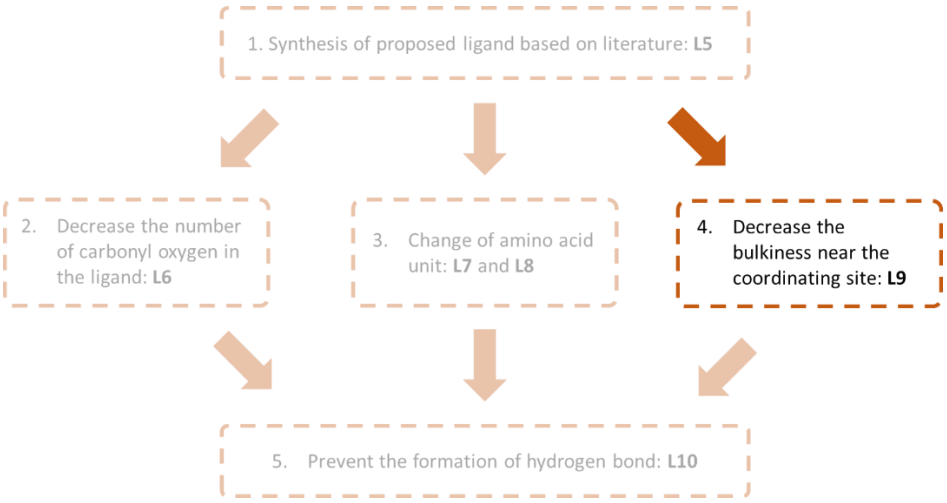

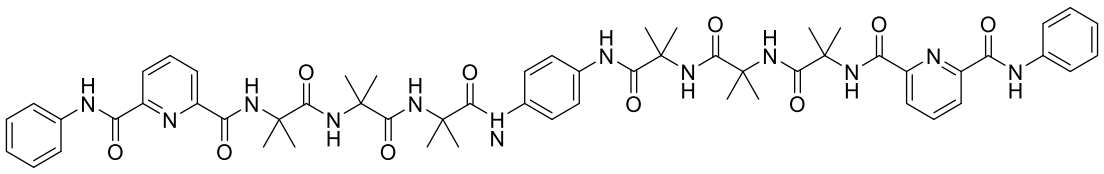

Since **L5-8** cannot form desired supramolecular tetrahedron with lanthanide ions, it was hypothesized that the short peptide may create a large steric hindrance which prevent the formation of stable nine coordinated lanthanide centre. Therefore, **L9** was designed based on two pyridine-2,6-dicarboxamide (pcam) moieties, which tends to form stable nine-coordinated lanthanide complexes. Two pcam metal chelating pcam moieties are connected with a short Aib peptide to remove the bulkiness at the terminal site of the ligand. It is expected to form a stable bimetallic helicate since a monophenyl linker was used to connect two metal chelating units.

Step 1:

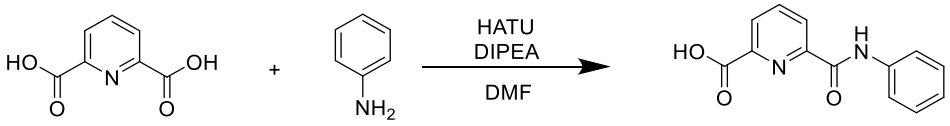

The first step involved the amide coupling of aniline with pyridine dicarboxylic acid. In the first trial, aniline was successfully coupled with pyridine dicarboxylic acid but the yield was low (30%). Possible reason may due to the fact that slightly excess amount of base (DIPEA) was added. More pyridine dicarboxylic acid was deprotected and react with the coupling reagent HATU. Therefore, more decoupling product was expected to be formed rather than the desired monocoupling product. However, in the second trial, the yield was low even limited amount of base was added. Possible reason may be due to the resonance structure of aniline, in which the nucleophilicity

of the NH_2 group is stabilized by the resonance structure (figure 4-14). Therefore, the yield is low even if the reaction was performed under reflux

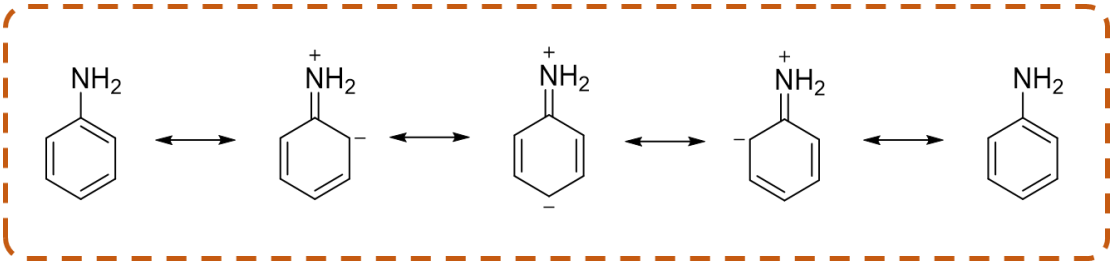

Figure 4-14. *Resonance structure of aniline.*

Step 2:

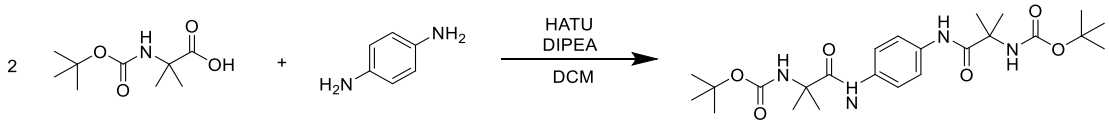

The second step involved the amide coupling of Boc-Aib-OH with the central bridging linker benzene-1,4-diamine using HATU as the coupling reagent. Pure product can be obtained easily by simply washing with MeCN. The highest yield was found to be 94%.

Step 3:

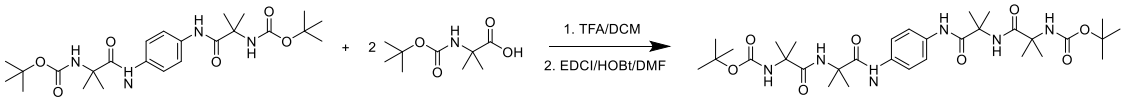

The third step involve the amide coupling Boc-Aib-OH with *Di-tert*-butyl ((1,4-phenylenebis(azanediyl))bis(2-methyl-1-oxopropane-1,2-diyl))dicarbamate. EDCI/HOBt was used as the coupling reagent. Coupling α, α-disubstituted amino acids was difficult due to the steric hinderance and the highest yield was found to be 32.5%.

Step 4:

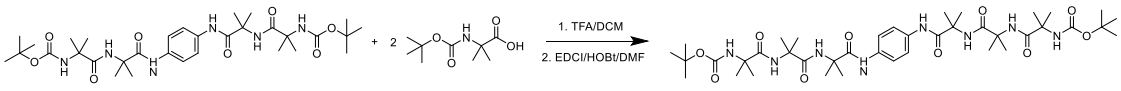

Following the previous step, desired *Di-tert*-butyl ((((((1,4-phenylenebis(azanediyl))bis(2-methyl-1-oxopropane-1,2-diyl))bis(azanediyl))bis(2-methyl-1-oxopropane-1,2-diyl))bis(azanediyl))bis(2-methyl-1-oxopropane-1,2-diyl))dicarbamate can be prepared in 19% yield using EDCI/HOBt as the coupling reagent. Characterization by ^{13}CNMR was not possible due to poor solubility.

4.2.11 Synthesis and complexation of L9

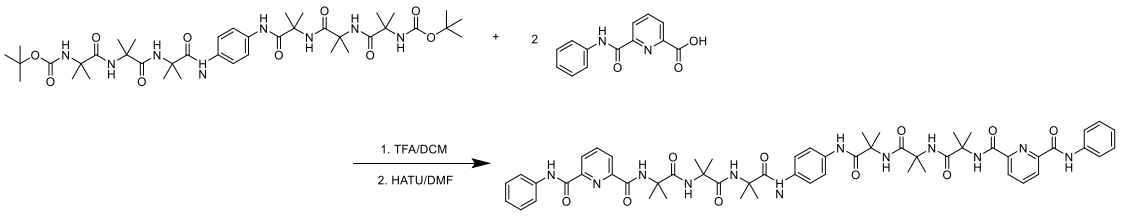

L9 was synthesized by in-situ deprotection of *di-tert*-butyl ((((((1,4-phenylenebis(azanediyl))bis(2-methyl-1-oxopropane-1,2-diyl))bis(azanediyl))bis(2-methyl-1-oxopropane-1,2-diyl))bis(azanediyl))bis(2-methyl-1-oxopropane-1,2-diyl))dicarbamate followed by coupling with two equivalents of 6-(phenylcarbamoyl)picolinic acid. The yield was 41.0%.

Then **L9** was allowed to coordinate with $Eu(OTf)_3$ and $La(OTf)_3$ in a ratio of 3:2. The turbid ligand solution turned to be clear upon addition of lanthanide and the corresponding lanthanide complexes were characterized by NMR. The ^{1}HNMR was expected to be more complicated since no chiral group is introduced in the ligand and thus different isomers can be formed. Similar with **L8**, the ^{1}HNMR signal for both Eu and La complexes were very weak (figure 4-14). The ESI-HRMS showed a lot of

fragments of Ln complexes and the major species was found to be mononuclear Ln**L9** for both Eu and La complexes (figure 4-15).

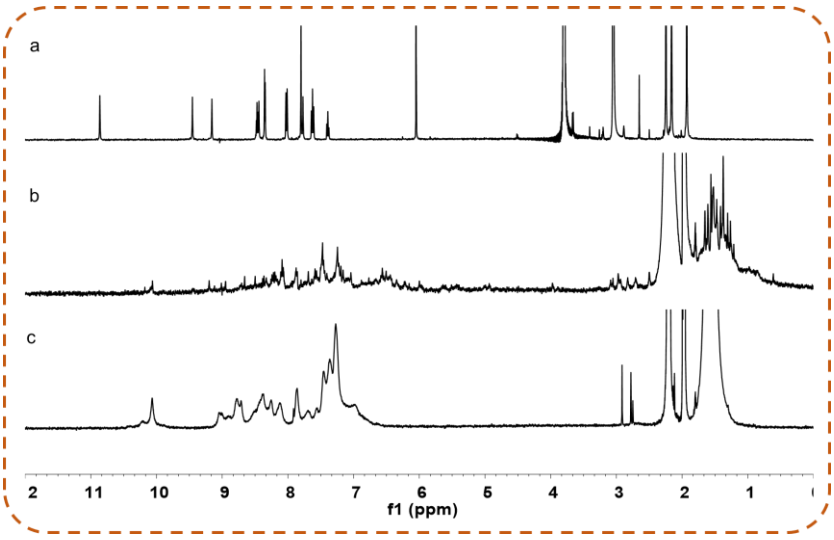

Figure 4-14. *^{1}HNMR of (a) free ligand **L9** in $(CD_3)_2SO$, (b) Eu complex of **L9** in CD_3CN and (c) La complex of **L9** in CD_3CN.*

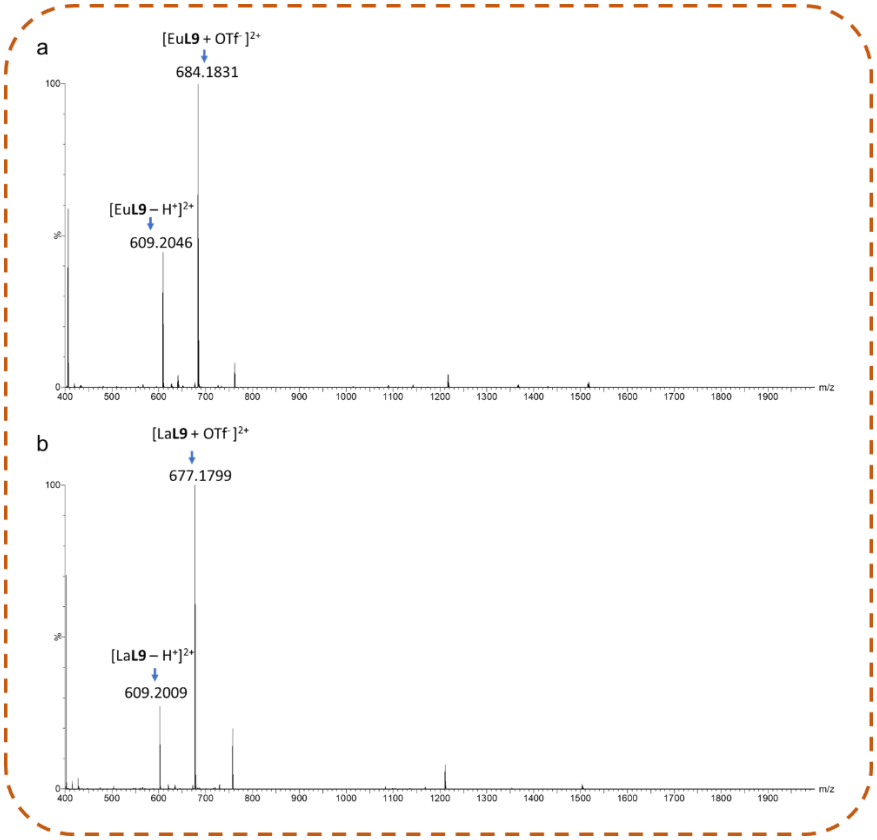

Figure 4-15. *ESI-HRMS of (a) Eu complex of **L9** (b) La complex of **L9**.*

4.2.12 Synthesis of intermediates for L10

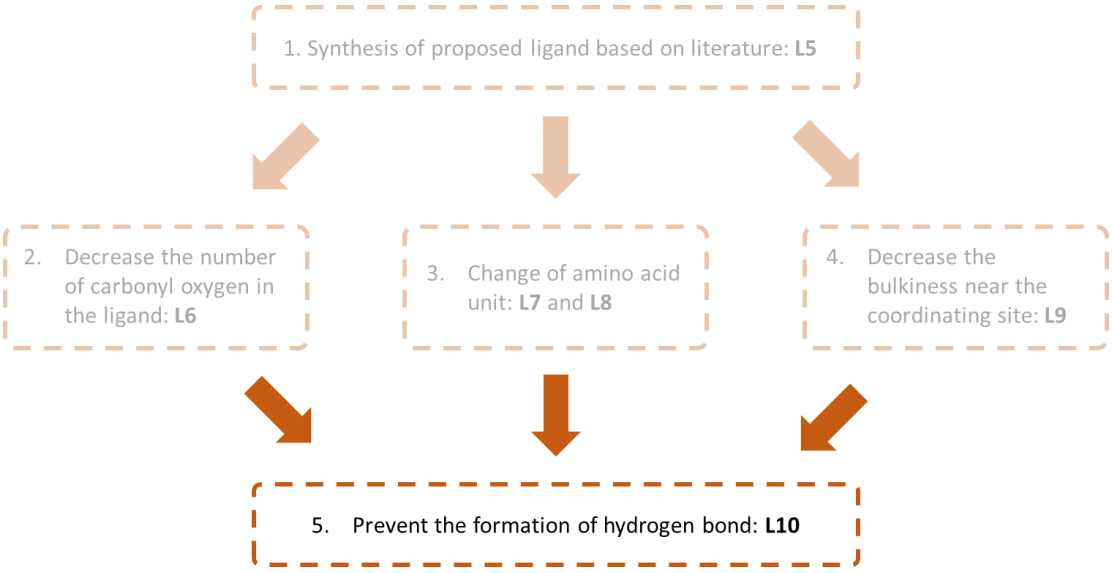

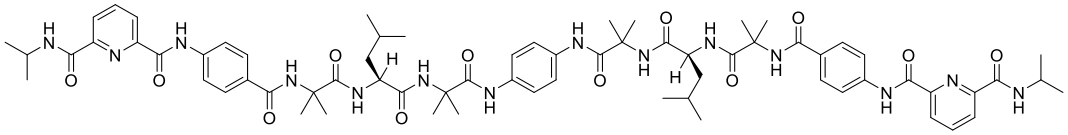

Another ligand **L10** was synthesis for preventing the formation of intramolecular hydrogen bond. Intramolecular hydrogen bond can be formed between the carbonyl oxygen and amide NH group. Aib amino acid unit was found to form stable 3_{10} helix, which means a helix is formed by 3 amino acid unit consisting of 10 atoms. The carbonyl oxygen in the pcam chelating moiety can be also participate in the helical formation by forming intramolecular hydrogen bond with the Aib peptide. Thus, the coordination power of the pcam moiety will be weakened. Moreover, the flexibility of the chelating group will be locked because of the intramolecular hydrogen bond of the peptide, which hindered the fine tuning of the whole supramolecular complex.

In **L10**, two pcam metal chelating moieties are first connected with a phenyl ring, which aims at separating the pcam chelating moiety with the peptide. It is

expected that the formation of intramolecular hydrogen bond between the pcam unit and the peptide will be avoided. Chiral amino acid unit Leu will be coupled into the peptide to introduced point chirality. Peptide chain Aib-Leu-Aib is expected to form a stable 3_{10} helix through intramolecular hydrogen bond which can transmit the chiral information from Leu to the metal chelating unit.

Following the previous protocol of synthesizing **L9**, all the intermediates for **L10** can be prepared in 4 steps and the synthetic route was shown in figure 4-16.

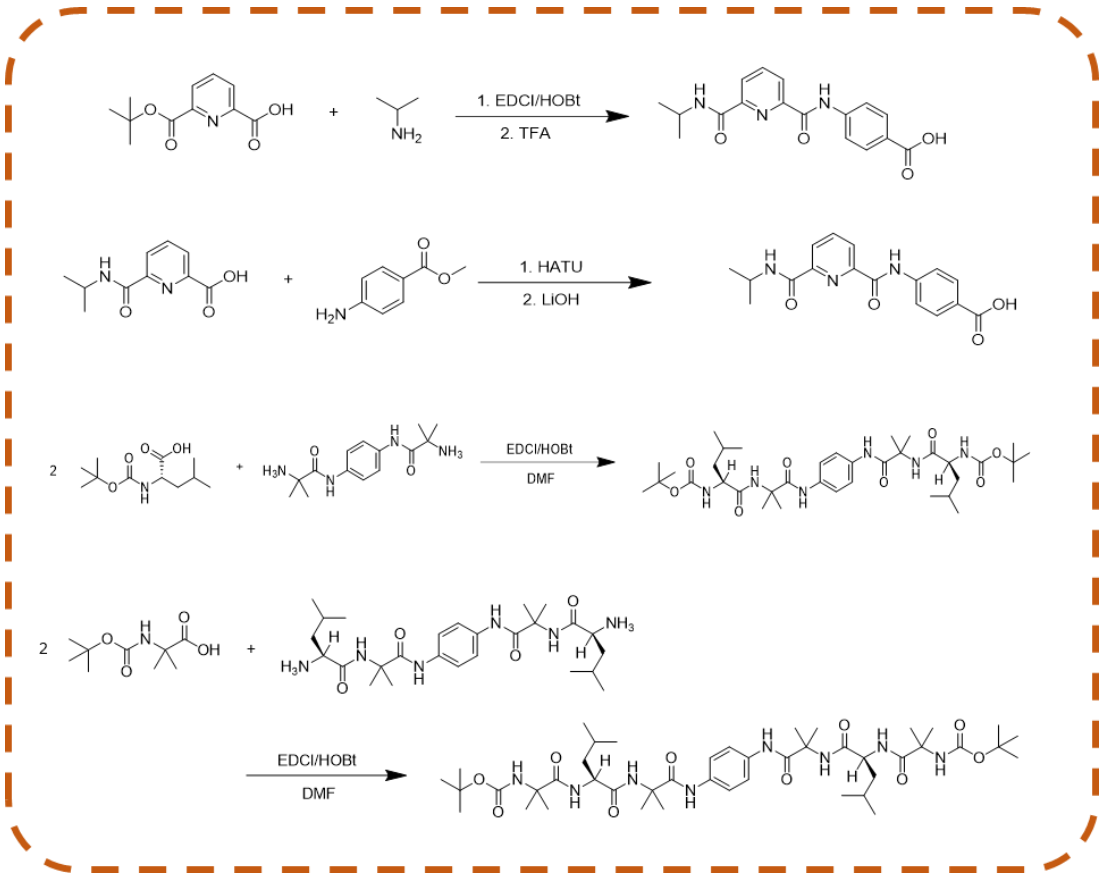

Figure 4-16. *Synthetic route for preparation of* ***L10*** *intermediates.*

4.2.13 Synthesis and complexation of L10

L10 was synthesized by in-situ deprotection of di-tert-butyl ((((2S,2'S)-(((1,4-phenylenebis(azanediyl))bis(2-methyl-1-oxopropane-1,2-diyl))bis(azanediyl))bis(4-

methyl-1-oxopentane-1,2-diyl))bis(azanediyl))bis(2-methyl-1-oxopropane-1,2-diyl))dicarbamate followed by coupling with two equivalents of 4-(6-(isopropylcarbamoyl)picolinamido)benzoic acid. The yield was found to be 26.8%.

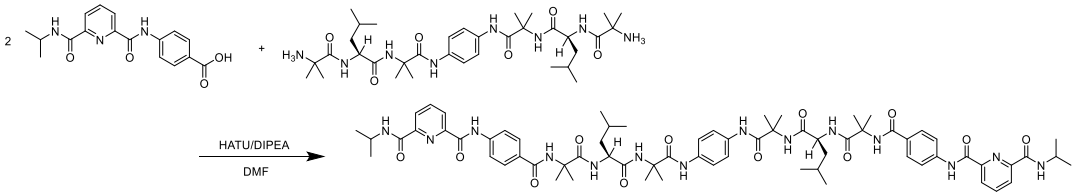

Upon coordination of **L10** with $Eu(OTf)_3$ in a ratio of 3:2. The ^{1}HNMR of the corresponding Eu complex showed no signal. For La complex, very weak signal was observed (figure 4-17). In the ESI-HRMS spectrum, the major species for Eu complex was found to be Eu_2**L10**$_2$ and Eu**L10**$_2$. For La complex, the major species was found to be La_2**L10**$_2$. No desired supramolecular tetrahedron can be observed (figure 4-18).

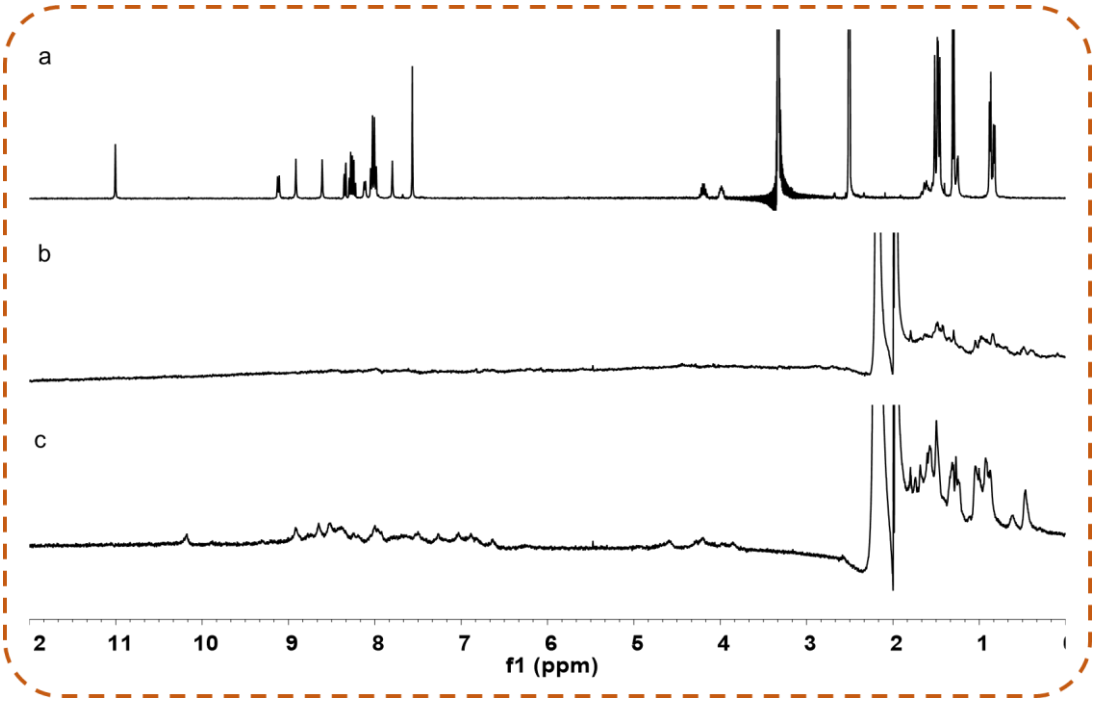

Figure 4-17. *^{1}HNMR of (a) free ligand **L10** in $(CD_3)_2SO$, (b) Eu complex of **L10** in CD_3CN and (c) La complex of **L10** in CD_3CN.*

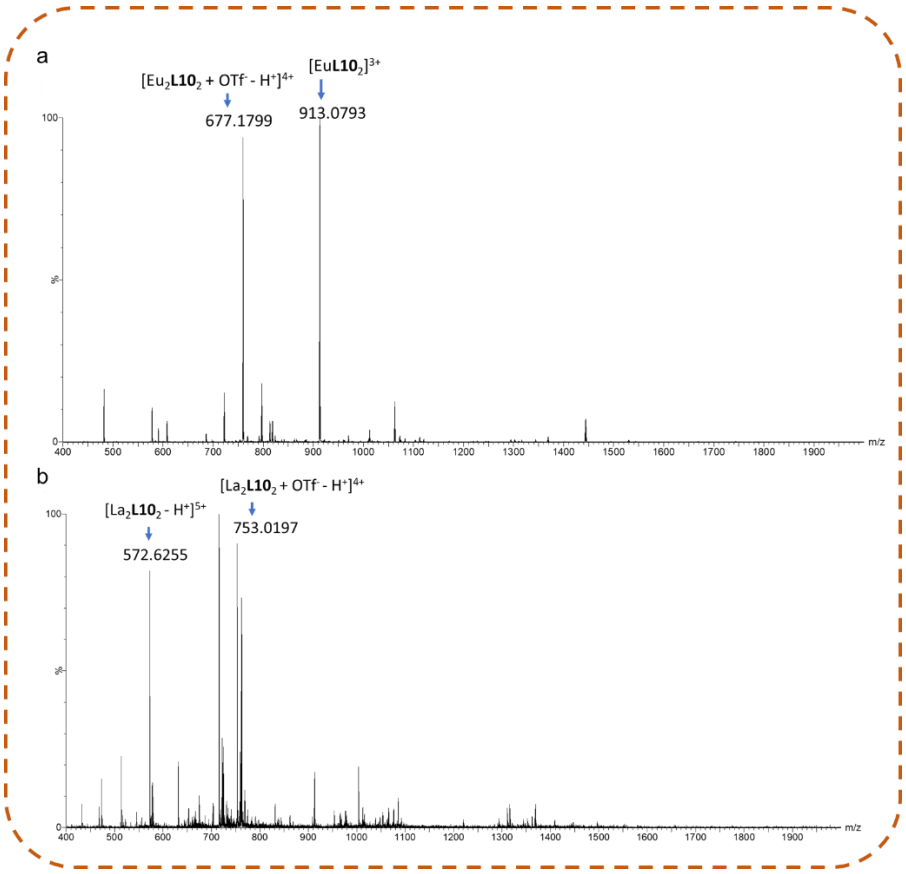

Figure 4-18. *ESI-HRMS of (a) Eu complex of* ***L10*** *(b) La complex of* ***L10****.*

4.2.14 Review of ligand L5-10

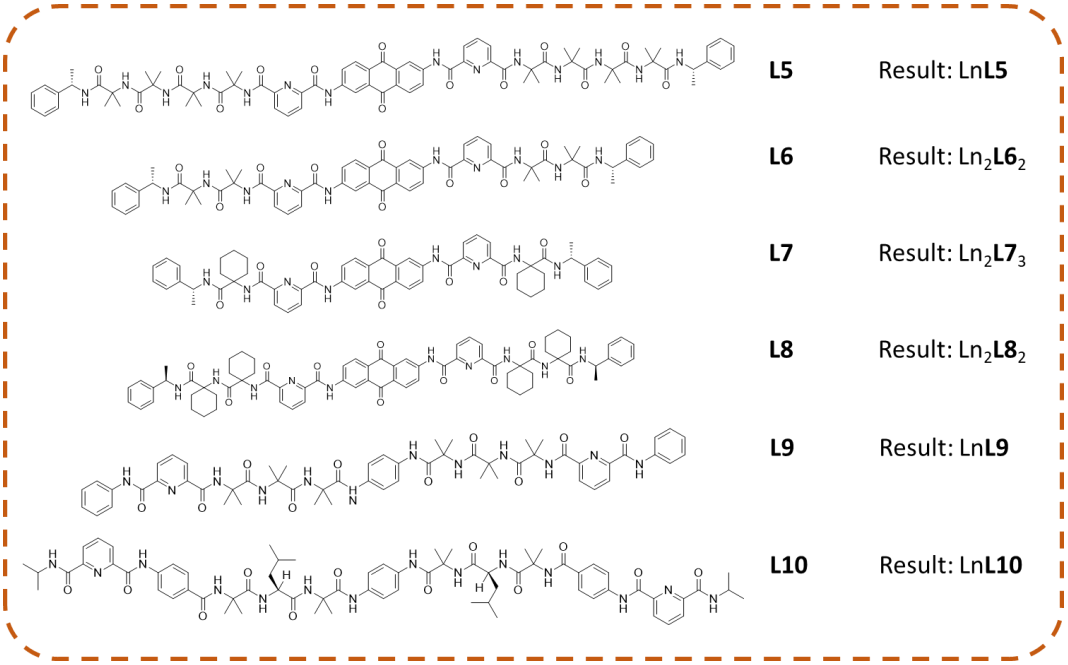

Figure 4-19. *Structure and complexation result of peptide ligands* ***L5-L10****.*

Figure 4-19 showed the peptide ligands that have synthesized. The original ligand design principle depends on two factors, which were the choice of amino acid and the length of the peptide units. It was believed that the peptide sequence will not form helicate when the length is short. As a result, no intramolecular hydrogen bond between the carbonyl oxygen and amide NH group will be formed and the coordination site will not be affected. However, based on the result, we believed that the presence of two amide group will strongly affect the coordination. Although **L7** can form Eu_2**L7**$_3$ complex, the structure cannot be confirmed by ^{1}HNMR. For **L10**, it was proposed that the coordination site will not be affect by hydrogen bonding since the short peptide was separated from the chelating group by a phenyl group. However, no supramolecular complexes can be observed upon coordination with lanthanide ions.

4.3 Conclusion and future perspectives

Various peptide ligand derivatives were synthesized in order to study the supramolecular formation. Although lanthanide ions can successfully coordinate with the metal chelating moiety, major product was found to be M_2L_2 and ML_2. Result showed that the steric bulkiness and the choice of the amino acid unit does not have an effect towards the coordination with lanthanide ion. Moreover, the presence of two amide bonds may hinder the formation of lanthanide supramolecular complexes.

One of the possible solutions is to change the metal chelating unit. Although pcam was found to be well known for coordinating with lanthanide ions to form nine-coordinated complexes, the complexes were unstable due to the neutral nature of the

chelating group. It is believed that using other charged chelating group or macrocyclic ligand can help to improve the coordinating power.

4.4 Experimental

Methyl 2-((*tert*-butoxycarbonyl)amino)-2-methylpropanoate, **Boc-Aib-OMe**

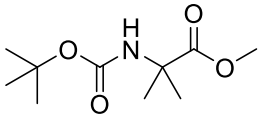

Iodomethane (1 ml, 12.3 mmol, 5 eq.) was added to a pressure vessel containing Boc-Aib-OH (0.5 g, 2.46 mmol, 1 eq.) and potassium carbonate (0.68 g, 4.92 mmol, 2 eq.). The reaction mixture was allowed to stir for 16 hrs. Dichloromethane (15 ml) was then added and the insoluble white solid was filtered. The crude product was purified by column chromatography (DCM/MeOH, 40:1, v/v) to give the desired white solid. **Boc-Aib-OMe**: (0.347g, 1.60 mmol, 64.9% yield), ^{1}H NMR (400 MHz, $CDCl_3$, 298K, δ): 1.43 (s, 9H), 1.49 (s, 6H), 3.73 (s, 3H), 4.99 (s, 1H). ^{13}C NMR (101 MHz, $CDCl_3$, 298K, δ): 175.26, 154.56, 56.10, 52.32, 28.25, 23.35. HRMS (ESI) calcd for $C_{10}H_{19}NO_4Na$ $[M+Na]^+$:240.26, found 240.12.

1-methoxy-2-methyl-1-oxopropan-2-aminium 2,2,2-trifluoroacetate, **H_3N^+-Aib-OMe**

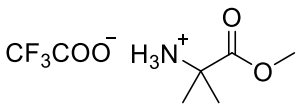

Boc-Aib-OMe (0.15 g, 0.69 mmol) was added to a mixture of DCM/TFA (4:1, v/v). The solution was allowed to stir for 2 hours. The solvent was then evaporated, and diethyl ether was added to precipitate out the desired white solid. **H_3N^+-Aib-OMe**: (0.0279g,

0.0435 mmol, 71.7% yield), ^{1}H NMR (400 MHz, $(CD_3)_2SO$, 298K, δ): 1.25 (d, J = 7.0 Hz, 3H), 7.02 - 7.41 (m, 5H), 7.84 (s, 2H), 8.09 - 8.38 (m, 3H), 9.46 (t, J = 6.1 Hz, 1H), 10.77 (s, 1H). ^{13}C NMR (101 MHz, $CDCl_3$, 298K, δ): 172.45, 56.28, 53.61, 23.87. HRMS (ESI) calcd for $C_5H_{12}NO_2$ $[M+H]^+$:118.15, found 118.10.

Methyl 2-(2-((*tert*-butoxycarbonyl)amino)-2-methylpropanamido)-2-methylpropanoate, **Boc-Aib-Aib-OMe**

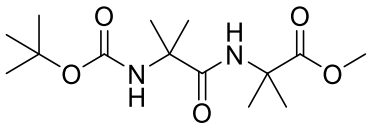

To a stirred solution of Boc-Aib-OH (2 g, 9.84 mmol, 1.0 eq) in anhydrous DCM (30 ml), DIPEA (5.14 ml, 29.52 mmol, 3.0 eq) was added. The solution was stirred for 1 hr. The PyBOP (5.12 g, 9.84 mmol, 1.0 eq) was added. Then the H_3N^+-Aib-OMe (2.5 g, 10.82 mmol, 1.1 eq) was added and the mixture was reacted for 16 hrs at rtp. The DCM was evaporated and EA (150 ml) was added. The organic layer was washed by 5% HCl (3 x 50 ml), 5% NaHCO3 (3 x 50 ml), brine (3 x 50 ml) and then dried with anhydrous MgSO4. The crude oil was then purified by column chromatography (hex/EA: 1/1) to obtain a white solid. **Boc-Aib-Aib-OMe**: (2.23 g, 7.38 mmol, 75.0% yield), ^{1}H NMR (400 MHz, $(CD_3)_2SO$, 298K, δ): 1.14-1.43 (m, 21H), 3.52 (s, 1H), 6.71 (s, 1H), 7.58 (s, 1H). ^{13}C NMR (101 MHz, $(CD_3)_2SO$, 298K, δ): 175.01, 174.44, 154.61, 55.94, 55.52, 52.23, 28.57, 25.17. HRMS (ESI) calcd for $C_{14}H_{26}N_2O_5$ $[M+Na]^+$:325.37, found 325.13.

2-(2-((tert-butoxycarbonyl)amino)-2-methylpropanamido)-2-methylpropanoic acid, **Boc-Aib-Aib-OH**

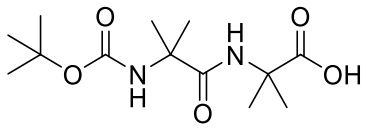

To a stirred solution of Boc-Aib-Aib-OMe (1 g, 3.31 mmol, 1.0 eq) in THF (26 ml), lithium hydroxide monohydrate (0.42 g, 9.92 mmol, 3.0 eq) in water (13.2 ml) was added. The reaction was stirred for 16 hrs at rtp. The THF was evaporated and the water phase was concentrated to 8 ml. 1% HCl was added dropwise to acidify the water phase to pH 3. Then DCM (5 x 30 ml) was added and the organic phase was collected, dried to obtain the desired white solid. **Boc-Aib-Aib-OH**: (0.86 g, 2.99 mmol, 90.5%), ^{1}H NMR (400 MHz, $(CD_3)_2SO$, 298K, δ): 1.26 (s, 6H), 1.35 (s, 15H), 6.85 (s, 1H), 7.43 (s, 1H). HRMS (ESI) calcd. for $C_{13}H_{24}N_2O_5$ $[M-H]^-$:287.34, found 287.60. ^{13}C NMR (125 MHz, $(CD_3)_2SO$, 298K, δ): 176.45, 174.23, 154.73, 56.23, 55.55, 28.64, 25.42, 24.87.

Methyl 2,2,6,6,9,9,12,12-octamethyl-4,7,10-trioxo-3-oxa-5,8,11-triazatridecan-13-oate, **Boc-Aib-Aib-Aib-OMe**

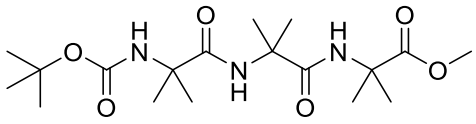

To a stirred solution of Boc-Aib-Aib-OH (0.2 g, 0.69 mmol, 1.0 eq) in anhydrous DMF (3 ml), DIPEA (0.26ml, 1.53 mmol, 2.2 eq) was added. The solution was stirred for 1 hr. HATU (0.26 g, 0.69 mmol, 1.0 eq) was then added. Then the H_3N^+-Aib-OMe (0.16 g, 0.69 mmol, 1.0 eq) was added and the mixture was reacted for 12 hrs at rtp. DCM was evaporated and EA (30 ml) was added. The organic layer was washed with 1 M LiCl solution (10 ml), 5% HCl (3 x 10 ml), brine (10 ml), 0.5M K_2CO_3 (3 x 10 ml), brine (10

ml) and then dried with anhydrous $MgSO_4$. The crude oil was then purified by column chromatography (hex/EA: 1/1) to obtain a white solid. **Boc-Aib-Aib-Aib-OMe**: (17.3 mg, 0.047 mmol, 6.4% yield), ^{1}H NMR (400 MHz, $(CD_3)_2SO$, 298K, δ): 1.11-1.51 (m, 27H), 3.51 (s, 3H), 7.20 (s, 1H), 7.57 (s, 2H); ^{13}C NMR (101 MHz, $(CD_3)_2SO$, 298K, δ): 174.88, 174.31, 173.66, 155.62, 79.14, 56.28, 55.87, 55.36, 52.10, 28.57, 25.28, 25.07. HRMS (ESI) calcd. for $C_{18}H_{33}N_3O_6$ $[M+Na]^+$: 410.48, found 410.17.

Methyl 2,2,6,6,9,9,12,12,15,15-decamethyl-4,7,10,13-tetraoxo-3-oxa-5,8,11,14-tetraazahexadecan-16-oate, **Boc-$(Aib)_4$-OMe**

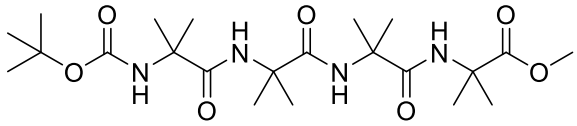

Boc-Aib-Aib-Aib-OMe (1 g, 2.68 mmol, 1.0 eq.) was dissolved in 10 ml of DCM. 10 ml of trifluoroacetic acid was added and the reaction was maintained in room temperature for 3 hrs. The solvent was then evaporated to obtain a viscous oil. The residue was dissolved in 10 ml of DMF and to this solution is added Boc-Aib-OH (0.54 g, 2.68 mmol, 1.0 eq.), HOBt (0.36 g, 2.68 mmol, 1.0 eq.), EDC (0.51 g, 2.68 mmol, 1.0 eq.) and DIPEA (1.40 ml, 8.03 mmol, 3.0 eq.). The reaction was stirred at 40^{o}C for 48 hrs. The solvent was removed and the residue was dissolved in ethyl acetate (100 ml). The organic layer was washed with 1 M LiCl solution (20 ml),5% HCl (3 x 20 ml), brine (20 ml), 0.5M K_2CO_3 (3 x 20 ml), brine (20 ml) and then dried with anhydrous $MgSO_4$. The solvent was then removed to obtain a yellowish gummy solid. The gummy solid was then washed with diethyl ether (3 x 10 ml) to obtain a white solid. **Boc-$(Aib)_4$-OMe**: (0.69 g, 1.45 mmol, 54.3%), ^{1}H NMR (400 MHz, $(CD_3)_2SO$, 298K, δ): 1.18-1.52 (m, 33H), 3.53 (s, 1H), 7.53 (d, J = 5.3 Hz, 2H), 8.15 (s, 1H). ^{13}C NMR (101 MHz, $(CD_3)_2SO$,

298K, δ): 174.88, 174.31, 173.65, 155.61, 79.14, 56.28, 55.86, 55.35, 52.10, 28.57, 25.29, 25.07. HRMS (ESI) calcd for $C_{22}H_{41}N_4O_7$ $[M+H]^+$: 473.2970, found 473.2981.

2,2,6,6,9,9,12,12,15,15-decamethyl-4,7,10,13-tetraoxo-3-oxa-5,8,11,14-tetraazahexadecan-16-oic acid, **Boc-(Aib)$_4$-OH**

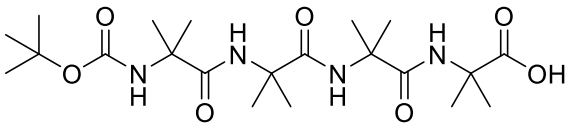

To a stirred solution of Boc-(Aib)$_4$-OMe (0.3 g, 0.64 mmol, 1.0 eq) in THF (4 ml), lithium hydroxide monohydrate (0.080 g, 1.90 mmol, 3.0 eq) in minimum amount of water was added. The reaction was stirred for 16 hrs at rtp. The THF was evaporated. Water (10 ml) was then added. 1% HCl was added dropwise to acidify the water phase to pH 2. Then DCM (5 x 10 ml) was added and the organic phase was collected, dried to obtain the desired white solid. **Boc-(Aib)$_4$-OH**: (0.25 g, 0.54 mmol, 85.1%), ^{1}H NMR (400 MHz, $(CD_3)_2SO$, 298K, δ): 1.29 (dd, J = 19.7, 8.3 Hz, 24H), 1.42 (s, 9H), 7.34 (s, 1H), 7.44 (s, 1H), 7.53 (s, 1H), 8.11 (s, 1H), 11.83 (s, 1H). ^{13}C NMR (101 MHz, $(CD_3)_2SO$, 298K, δ): 176.07, 175.50, 173.95, 173.77, 155.80, 79.41, 56.39, 56.17, 55.06, 28.57, 25.64, 25.14. HRMS (ESI) calcd for $C_{21}H_{37}N_4O_7$ $[M-H]^-$: 457.2668, found 457.2674.

tert-butyl (S)-(2-methyl-1-((2-methyl-1-oxo-1-((1-phenylethyl)amino)propan-2-yl)amino)-1-oxopropan-2-yl)carbamate, **Boc-Aib-Aib-spy**

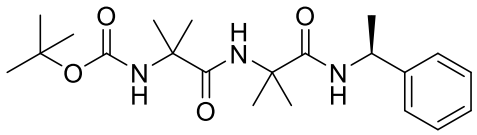

To a stirred solution of Boc-Aib-Aib-OH (5 g, 17.34 mmol, 1.0 eq) in anhydrous DMF (75 ml), DIPEA (6.63 ml, 52.02 mmol, 3.0 eq) was added. The solution was stirred for

20 mins. HATU (7.25 g, 19.07 mmol, 1.1 eq) was then added. Then the (S)-1-phenylethan-1-amine (2.21 ml, 17.34 mmol, 1.0 eq) was added and the mixture was reacted for 3 days at rtp. The reaction mixture was diluted with ethyl acetate (200 ml). The organic layer was washed by 0.5 M LiCl (3 x 50 ml),5% HCl (3 x 50 ml), 0.5 M K_2CO_3 (3 x 50 ml), brine (3 x 50 ml) and then dried with anhydrous $MgSO_4$. to obtain the desired pure white solid. **Boc-Aib-Aib-spy**: (6.27 g, 16.0 mmol, 92.3%), ^{1}H NMR (400 MHz, $(CD_3)_2SO$, 298K, δ): 7.80 (d, *J* = 7.9 Hz, 1H), 7.58 (s, 1H), 7.23 (ddd, *J* = 33.1, 17.7, 7.3 Hz, 6H), 4.83 (p, *J* = 7.2 Hz, 1H), 1.52 – 1.11 (m, 24H). ^{13}C NMR (101 MHz, $(CD_3)_2SO$, 298K, δ): 173.93, 155.69, 145.44, 128.41, 126.71, 126.37, 79.19, 56.37, 56.20, 48.61, 28.56, 25.40, 23.06. HRMS (ESI) calcd for $C_{21}H_{33}N_3O_4Na$ $[M+Na]^+$:414.2363, found 414.2375.

Tert-butyl (S)-(5,5,8,8,11,11,14-heptamethyl-4,7,10,13-tetraoxo-2-phenyl-3,6,9,12-tetraazapentadecan-14-yl)carbamate, **Boc-$(Aib)_4$-spy**

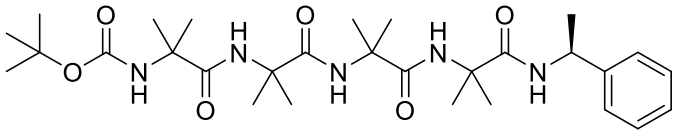

To a stirred solution of Boc-$(Aib)_4$-OH (0.1 g, 0.22 mmol, 1.0 eq) in anhydrous DMF (2 ml), DIPEA (0.11 ml, 0.085 mmol, 3.0 eq) was added. The solution was stirred for 1 hr. HATU (0.083 g, 0.22 mmol, 1.0 eq) was then added. Then the (S)-1-phenylethan-1-amine (0.028 ml 0.22 mmol, 1.0 eq) was added and the mixture was reacted for 12 hrs at rtp. DCM was evaporated and EA (30 ml) was added. The organic layer was washed with 1 M LiCl solution (10 ml),5% HCl (3 x 10 ml), brine (10 ml), 0.5M K_2CO_3 (3 x 10 ml),

brine (10 ml) and then dried with anhydrous $MgSO_4$. to obtain a white solid. **Boc-(Aib)$_4$-spy**: (24.7 mg, 0.044 mmol, 20.2% yield), ^{1}H NMR (400 MHz, $(CD_3)_2SO$, 298K, δ): 1.19-1.55 (m, 33H, 4.86 (t, J = 7.3 Hz, 1H), 7.09-7.44 (m, 6H), 7.57 (s, 1H), 7.72 (d, J = 8.2 Hz, 1H), 7.91 (s, 1H), 8.27 (s, 1H). ^{13}C NMR (101 MHz, $(CD_3)_2SO$, 298K, δ): 175.73, 173.82, 155.95, 145.77, 128.36, 126.62, 126.35, 79.52, 56.60, 56.55, 56.42, 56.18, 48.56, 28.59, 25.83, 25.52, 25.04, 23.58. HRMS (ESI) calcd. for $C_{29}H_{47}N_5O_6Na$ $[M+Na]^+$: 584.3419, found 584.3429.

Di-tert-butyl 6,6'-(((9,10-dioxo-9,10-dihydroanthracene-2,6-diyl)bis(azanediyl))bis(carbonyl))dipicolinate

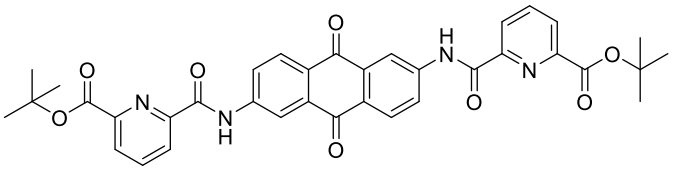

To a stirred solution of 6-(tert-butoxycarbonyl)picolinic acid (0.3 g, 1.34 mmol, 3.0 eq.) in DMF (5ml), DIPEA (0.97 ml, 5.60 mmol, 12.5 eq.) and HATU (1.02 g, 2.69 mmol, 6.0 eq.) was added. The solution was allowed to stir for 20 mins before the addition of 2,6-diaminoanthracene-9,10-dione (0.11g, 0.45 mmol, 1.0 eq.). The reaction mixture was allowed to stir at room temperature and pressure for 16 hrs. The mixture was washed with water (3 x 10 ml) and MeCN (3 x 10 ml) to obtain the desired yellow product. **Di-tert-butyl 6,6'-(((9,10-dioxo-9,10-dihydroanthracene-2,6-diyl)bis(azanediyl))bis(carbonyl))dipicolinate**: (0.27 g, 0.45 mmol, 93.5%), ^{1}H NMR (400 MHz, $CDCl_3$, 298K, δ): 1.73 (s, 9H), 8.10 (t, *J* = 7.8 Hz, 1H), 8.27 (d, *J* = 7.6 Hz, 1H), 8.41 (d, *J* = 8.5 Hz, 1H), 8.46 – 8.58 (m, 3H), 10.67 (s, 1H). ^{13}C NMR (101 MHz, $CDCl_3$, 298K, δ): 181.80, 163.11, 161.92, 149.34, 147.94, 143.17, 138.93, 134.98, 129.60,

129.23, 127.65, 125.42, 124.30, 117.42, 83.22, 29.71, 28.13, 1.02, -0.01. HRMS (ESI) calcd. for $C_{36}H_{32}N_4O_8$ $[M+Na]^+$: 671.67, found 671.00.

6,6'-(((9,10-dioxo-9,10-dihydroanthracene-2,6-diyl)bis(azanediyl))bis(carbonyl))dipicolinic acid

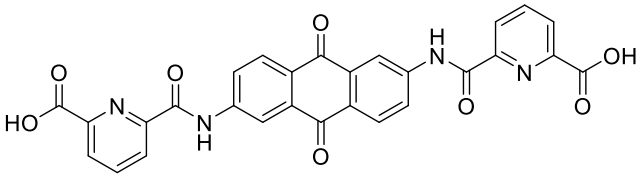

TFA (5 ml) was added to a solution containing di-tert-butyl 6,6'-(((9,10-dioxo-9,10-dihydroanthracene-2,6-diyl)bis(azanediyl))bis(carbonyl))dipicolinate (0.2 g, 0.31 mmol) in DCM (5 ml). The mixture was allowed to stir for 2 hrs. The solvent was then evaporated and washed with diethyl ether (3 x 10 ml) to obtain the desired yellow product. **6,6'-(((9,10-dioxo-9,10-dihydroanthracene-2,6-diyl)bis(azanediyl))bis(carbonyl))dipicolinic acid**: (0.15 g, 0.27 mmol, 89.0%), ^{1}H NMR (400 MHz, $(CD_3)_2SO$, 298K, δ): 8.23 – 8.57 (m, 6H), 8.71 (d, *J* = 2.2 Hz, 1H), 11.36 (s, 1H).

N^2,$N^{2'}$-(9,10-dioxo-9,10-dihydroanthracene-2,6-diyl)bis(N^6-((S)-5,5,8,8,11,11,14-heptamethyl-4,7,10,13-tetraoxo-2-phenyl-3,6,9,12-tetraazapentadecan-14-yl)pyridine-2,6-dicarboxamide), **L5**

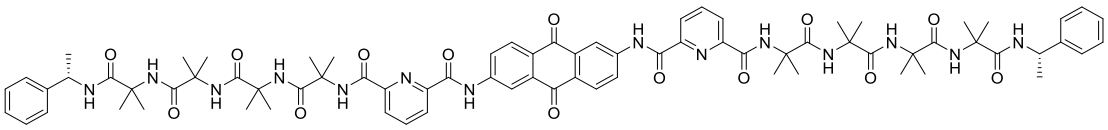

Tert-butyl (S)-(5,5,8,8,11,11,14-heptamethyl-4,7,10,13-tetraoxo-2-phenyl-3,6,9,12 tetraazapentadecan-14-yl)carbamate (0.31 g, 0.56 mmol, 3.0 eq.) was dissolved in 4 ml of DCM. 2 ml of trifluoroacetic acid was added and the reaction was maintained in

room temperature for 3 hrs. The solvent was then evaporated to obtain a viscous oil. The residue was dissolved in 6 ml of DMF and to this solution is added 6,6'-(((9,10 dioxo-9,10-dihydroanthracene-2,6-diyl)bis(azanediyl))bis(carbonyl))dipicolinic acid (0.10 g, 0.19 mmol, 1.0 eq.), HATU (0.43 g, 1.12 mmol, 6.0 eq.) and DIPEA (0.41 ml, 2.33 mmol, 12.5 eq.). The reaction was stirred for 16 hrs at room temperature and pressure. The solvent was then washed with water (2 x 20 ml) and MeCN (2 x 10 ml) to obtain the desired yellow product. **L5**: (0.13 g, 0.09 mmol, 49.6%), ^{1}H NMR (400 MHz, $(CD_3)_2SO$, 298K, δ): 1.28 – 1.42(m, 15H), 1.49 (d, *J* = 9.2 Hz, 6H), 1.66 (d, *J* = 3.1 Hz, 6H), 4.86 (q, *J* = 7.4 Hz, 1H), 7.21 (dt, *J* = 31.4, 7.2 Hz, 3H), 7.39 (d, *J* = 7.5 Hz, 2H), 7.66 – 7.91 (m, 2H), 8.27 – 8.43 (m, 4H), 8.43 – 8.61 (m, 2H), 8.88 (d, *J* = 2.1 Hz, 1H), 9.53 (s, 1H), 11.53 (s, 1H). ^{13}C NMR (125 MHz, $(CD_3)_2SO$, 298K, δ): 182.05, 175.73, 174.94, 174.20, 173.89, 163.96, 163.13, 149.15, 148.82, 145.89, 144.24, 134.90, 129.50, 128.54, 126.47, 57.07, 56.76, 56.72, 56.57, 25.19, 23.75. HRMS (ESI) calcd for $C_{76}H_{90}N_{14}O_{14}Na$ $[M+Na]^+$: 1445.6653, found 1445.6676.

N^2,$N^{2'}$-(9,10-dioxo-9,10-dihydroanthracene-2,6-diyl)bis(N^6-(2-methyl-1-((2-methyl-1-oxo-1-(((S)-1-phenylethyl)amino)propan-2-yl)amino)-1-oxopropan-2-yl)pyridine-2,6-dicarboxamide), **L6**

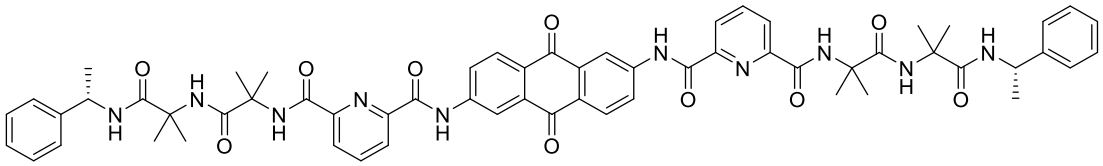

Tert-butyl (S)-(2-methyl-1-((2-methyl-1-oxo-1-((1-phenylethyl)amino)propan-2-yl)amino)-1-oxopropan-2-yl)carbamate (0.11 g, 0.28 mmol, 3.0 eq.) was dissolved in 2 ml of DCM. 1 ml of trifluoroacetic acid was added and the reaction was maintained in

room temperature for 3 hrs. The solvent was then evaporated to obtain a viscous oil. The residue was dissolved in 5 ml of DMF and to this solution is added 6,6'-(((9,10 dioxo-9,10-dihydroanthracene-2,6-diyl)bis(azanediyl))bis(carbonyl))dipicolinic acid (50.0 mg, 0.093 mmol, 1.0 eq.), HATU (0.21 g, 0.56 mmol, 6.0 eq.) and DIPEA (0.20 ml, 1.17 mmol, 12.5 eq.). The reaction was stirred for 16 hrs at room temperature and pressure. The solvent was then washed with water (2 x 10 ml) and MeCN (2 x 10 ml) to obtain the desired yellow product. **L6**: (54.10 mg, 0.05 mmol, 53.6%), ^{1}H NMR (400 MHz, $(CD_3)_2SO$, 298K, δ): 1.34 (d, *J* = 16.7 Hz, 6H), 1.46 (d, *J* = 7.0 Hz, 3H), 1.64 (d, *J* = 3.7 Hz, 6H), 4.90 (p, *J* = 7.1 Hz, 1H), 7.19 (t, *J* = 7.1 Hz, 1H), 7.28 (t, *J* = 7.5 Hz, 2H), 7.39 (d, *J* = 7.3 Hz, 2H), 7.77 (s, 1H), 7.88 (d, *J* = 8.1 Hz, 1H), 8.22 (dd, *J* = 7.5 Hz, 2H), 8.30 (t, *J* = 7.7 Hz, 1H), 8.36 (d, *J* = 8.36 Hz, 1H), 8.40 – 8.53 (m, 2H), 8.89 (d, *J* = 2.2 Hz, 1H), 9.44 (s, 1H), 11.52 (s, 1H). ^{13}C NMR (125 MHz, $(CD_3)_2SO$, 298K, δ): 182.02, 173.93, 173.28, 163.74, 163.15, 149.24, 148.81, 145.64, 144.26, 140.48, 134.87, 129.45, 129.10, 128.55, 126.81, 126.54, 126.12, 125.85, 125.67, 118.07, 57.29, 56.76, 48.72, 25.75, 25.57, 25.40, 23.34. HRMS (ESI) calcd for $C_{60}H_{62}N_{10}O_{10}Na$ $[M+Na]^+$: 1105.4543, found 1105.4554.

Methyl 1-aminocyclohexane-1-carboxylate, **H_2N- Ac_6c-OMe**

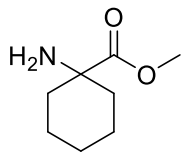

To a stirred solution of 1-aminocyclohexane-1-carboxylic acid (5 g, 34.92 mmol, 1.0 eq.) in methanol (50 ml), trimethylchlorosilane (8.86 ml, 69.84 mmol, 2.0 eq.) was added dropwise at 0^{o}C. The mixture was allowed to react at 50^{o}C for 16 hrs. The

solvent was evaporated and redissolved in water (50 ml). The crude product was washed with dichloromethane (3 x 20 ml) and $NaHCO_3$ was added to the aqueous layer with pH ~ 8. Dichloromethane (3 x 50 ml) was added and the organic layer was concentrated on a rotary evaporator to give the desired product as a yellow oil. **H_2N-Ac_6c-OMe**: (2.83 g, 18.00 mmol, 51.5%), ^1H NMR (400 MHz, $(CD_3)_2SO$, 298K, δ): 1.21 – 1.40 (m, 6H), 1.60 (ddd, *J* = 11.6, 9.1 6.1 Hz, 2H), 1.68 – 1.81 (m, 4H), 3.59 (s, 3H). ^{13}C NMR (101 MHz, MeOD, 298K, δ): 176.80, 57.04, 51.16, 34.96, 24.99, 21.71. HRMS (ESI) calcd for $C_8H_{16}NO_2$ $[M+H]^+$: 158.1176, found 158.1181.

1-((tert-butoxycarbonyl)amino)cyclohexane-1-carboxylic acid, **Boc-Ac_6c-OH**

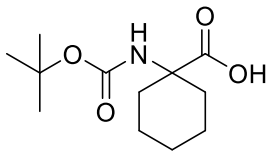

To a stirred solution of 1-aminocyclohexane-1-carboxylic acid (10.52 g, 73.47 mmol, 1.0 eq.) in 2 N NaOH (110 ml), Boc_2O (19.24 g, 88.17 mmol, 1.2 eq.) in dioxane (110 ml) was added dropwise. The reaction was stirred for 16 hrs at rtp. The dioxane was then evaporated and water (200 ml) was added. The aqueous phase was washed with diethyl ether (3 x 60 ml) and then acidified to pH ~ 4 by 5% HCl. The product was then collected by filtration and washed with brine (3 x 60 ml) to obtain the desired white product. **Boc-Ac_6c-OH**: (8.77 g, 36.06 mmol, 49.1%), ^1H NMR (400 MHz, $(CD_3)_2SO$, 298K, δ): 1.22 (d, *J* = 10.9 Hz, 2H), 1.28 – 1.53 (m, 14H), 1.61 (dt, *J* = 14.1, 7.4 Hz, 2H), 1.90 (s, 2H), 6.87 (s, 1H), 12.09 (s, 1H). ^{13}C NMR (101 MHz, MeOD, 298K, δ): 177.41, 155.95, 32.22, 27.39, 26.20, 25.14, 21.07. HRMS (ESI) calcd for $C_{12}H_{20}NO_4$ $[M-H]^-$: 242.1398, found 242.1400.

1-(1-((tert-butoxycarbonyl)amino)cyclohexane-1-carboxamido)cyclohexane-1-carboxylic acid, **Boc-Ac$_6$c-Ac$_6$c-OH**

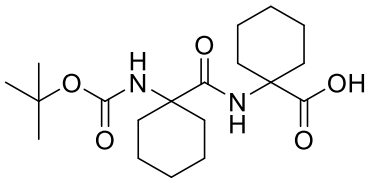

To a stirred solution of Boc-Ac$_6$c-OH (5 g, 20.55 mmol, 1.0 eq.) in anhydrous DMF (50 ml), DIPEA (10.74 ml, 61.65 mmol, 3.0 eq.) was added. The solution was stirred for 20 mins. The PyBOP (11.76 g, 22.61 mmol, 1.1 eq.) was added. Then the H-Ac$_6$c-OMe (3.23 g, 20.55 mmol, 1.0 eq.) was added and the mixture was reacted for 16 hrs at rtp. The reaction mixture was diluted with ethyl acetate (150 ml). The organic layer was washed by 0.5 M LiCl (3 x 50 ml), 5% HCl (3 x 50 ml), 0.5 M K_2CO_3 (3 x 50 ml), brine (3 x 50 ml) and then dried with anhydrous $MgSO_4$. The organic layer was concentrated. The residue was redissoved in THF (100 ml), lithium hydroxide monohydrate (2.59 g, 61.65 mmol, 3.0 eq.) in water (100 ml) was added. The reaction was stirred for 2 days at rtp. The solvent was evaporated. 5% HCl was added dropwise to acidify the aqueous phase to pH 4. Then DCM (5 x 50 ml) was added and the organic phase was collected, dried to obtain the desired white solid. **Boc-Ac$_6$c-Ac$_6$c-OH**: (5.53g, 15.00 mmol, 73.0%), ^{1}H NMR (400 MHz, $(CD_3)_2SO$, 298K, δ): 1.17 (d, *J* = 13.4 Hz, 2H), 1.41 (d, *J* = 25.2 Hz, 23H), 1.97 (d, *J* = 13.1Hz, 4H), 6.64 (s, 1H), 7.11 (s, 1H), 11.98 (s, 1H). ^{13}C NMR (101 MHz, $(CD_3)_2SO$, 298K, δ): 21.14, 21.35, 25.40, 25.49, 28.58, 31.75, 31.98, 57.79, 58.87, 78.57, 155.04, 174.62, 176.04. HRMS (ESI) calcd for $C_{19}H_{31}N_2O_5$ $[M-H]^-$: 367.2238, found 367.2285.

tert-butyl (S)-(1-((1-phenylethyl)carbamoyl)cyclohexyl)carbamate, **Boc-Ac$_6$c-rpy**

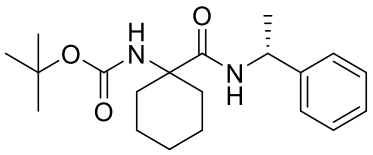

To a stirred solution of Boc-Ac_6c-OH (1 g, 4.11 mmol, 1.0 eq) in anhydrous DMF (40 ml), DIPEA (2.15 ml, 12.33 mmol, 3.0 eq) was added. The solution was stirred for 20 mins. HATU (1.72 g, 4.52 mmol, 1.1 eq) was then added. Then the (R)-1-phenylethan-1-amine (0.52 ml, 4.11 mmol, 1.0 eq) was added and the mixture was reacted for 3 days at rtp. The reaction mixture was diluted with ethyl acetate (100 ml). The organic layer was washed by 0.5 M LiCl (3 x 30 ml),5% HCl (3 x 30 ml), 0.5 M K_2CO_3 (3 x 30 ml), brine (3 x 30 ml) and then dried with anhydrous $MgSO_4$. The crude product was then purified by column chromatography (DCM/EtOH, 100/1, v/v) to obtain the desired pure white solid. **Boc-Ac_6c-rpy**: (0.13 g, 0.28 mmol, 50.9%), ^{1}H NMR (400 MHz, $(CD_3)_2SO$, 298K, δ): 7.59 (d, *J* = 8.1 Hz, 1H), 7.29 (d, *J* = 5.8 Hz, 3H), 7.27 – 7.14 (m, 1H), 6.51 (s, 1H), 4.89 (p, *J* = 7.1 Hz, 1H), 1.95 (s, 2H), 1.73 – 1.07 (m, 19H). ^{13}C NMR (101 MHz, $(CD_3)_2SO$, 298K, δ): 174.19, 154.83, 145.08, 128.52, 126.90, 126.33, 58.87, 48.05, 28.64, 25.51, 22.74, 21.48. HRMS (ESI) calcd for $C_{20}H_{30}N_2O_3Na$ $[M+Na]^+$: 369.2149, found 369.2154.

Tert-butyl (S)-(1-((1-((1-phenylethyl)carbamoyl)cyclohexyl)carbamoyl)cyclohexyl)carbamate, **Boc-Ac_6c-Ac_6c-rpy**

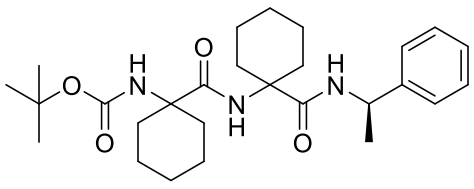

To a stirred solution of Boc-Ac_6c-Ac_6c-OH (0.2 g, 0.54 mmol, 1.0 eq) in anhydrous DMF (5 ml), DIPEA (0.28 ml, 1.63 mmol, 3.0 eq) was added. The solution was stirred for 20 mins. HATU (0.25 g, 0.65 mmol, 1.2 eq) was then added. Then the (S)-1-phenylethan-1-amine (0.069 ml 0.54 mmol, 1.0 eq) was added and the mixture was reacted for 3 days at rtp. The reaction mixture was diluted with ethyl acetate (10 ml). The organic layer was washed by 0.5 M LiCl (3 x 10 ml),5% HCl (3 x 10 ml), 0.5 M K_2CO_3 (3 x 10 ml), brine (3 x 10 ml) and then dried with anhydrous $MgSO_4$. The crude product was then purified by column chromatography (DCM/MeOH, 20/1, v/v) to obtain the desired pure white solid. **Boc-Ac_6c-Ac_6c-rpy**: (0.13 g, 0.28 mmol, 50.9%), ^{1}H NMR (400 MHz, $(CD_3)_2SO$, 298K, δ): 1.04-1.80 (m, 28H), 1.95 (d, *J* = 14.1 Hz, 4H), 4.85 (p, *J* = 7.3 Hz, 1H), 6.79 (s, 1H), 7.03 (s, 1H), 7.11-7.38 (m, 4H), 7.50 (d, *J* = 7.9 Hz, 1H). ^{13}C NMR (101 MHz, $(CD_3)_2SO$, 298K, δ): 174.37, 173.58, 155.70, 145.16, 128.45, 126.78, 126.32, 79.35, 59.37, 59.10, 48.46, 31.93, 28.58, 25.41, 22.98, 21.34, 21.21. HRMS (ESI) calcd for $C_{27}H_{41}N_3O_4Na$ $[M+Na]^+$: 494.2989, found 494.3004.

N^2,$N^{2'}$-(9,10-dioxo-9,10-dihydroanthracene-2,6-diyl)bis(N^6-(1-(((R)-1-phenylethyl)carbamoyl)cyclohexyl)pyridine-2,6-dicarboxamide), **L7**

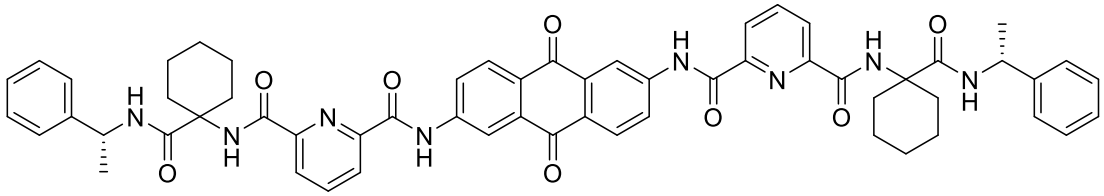

Tert-butyl (R)-(1-((1-phenylethyl)carbamoyl)cyclohexyl)carbamate (1 g, 2.89 mmol, 3.0 eq.) was dissolved in 20 ml of DCM. 5 ml of trifluoroacetic acid was added and the reaction was maintained in room temperature for 3 hrs. The solvent was then evaporated to obtain a viscous oil. The residue was dissolved in 10 ml of DMF and to

this solution is added 6,6'-(((9,10 dioxo-9,10-dihydroanthracene-2,6-diyl)bis(azanediyl))bis(carbonyl))dipicolinic acid (0.52 g, 0.96 mmol, 1.0 eq.), HATU (0.80 g, 2.12 mmol, 2.2 eq.) and DIPEA (1.17 ml, 6.73 mmol, 7.0 eq.). The reaction was stirred for 16 hrs at room temperature and pressure. The reaction mixture was diluted with ethyl acetate (30 ml). The organic layer was washed by 0.5 M LiCl (3 x 10 ml), 5% HCl (3 x 10 ml), 0.5 M K_2CO_3 (3 x 10 ml), brine (3 x 10 ml) and then dried with anhydrous $MgSO_4$. The organic layer was concentrated and then purified by HPLC with Sunfire Silica column (DCM/MeOH: 95/5; flow rate 8 ml/min). **L7**: (0.18 g, 0.18 mmol, 18.8%), ^{1}H NMR (400 MHz, $(CD_3)_2SO$, 298K, δ): 11.53 (s, 1H), 8.96 (s, 1H), 8.84 (d, *J* = 2.2 Hz, 1H), 8.42 (ddd, *J* = 7.3, 5.8, 1.9 Hz, 2H), 8.39 – 8.26 (m, 3H), 7.98 (d, *J* = 8.2 Hz, 1H), 7.35 (d, *J* = 7.6 Hz, 2H), 7.29 (t, *J* = 7.5 Hz, 2H), 7.20 (t, *J* = 7.1 Hz, 1H), 5.02 (q, *J* = 7.2 Hz, 1H), 2.44 (d, *J* = 16.3 Hz, 1H), 2.36 (d, *J* = 14.4 Hz, 1H), 1.96 (t, *J* = 12.0 Hz, 2H), 1.62 (d, *J* = 20.9 Hz, 5H), 1.38 (d, *J* = 7.0 Hz, 4H). ^{13}C NMR (101 MHz, $(CD_3)_2SO$, 298K, δ): 181.78, 173.16, 163.20, 149.87, 148.62, 145.14, 144.24, 140.24, 134.81, 129.26, 128.98, 128.51, 126.84, 125.70, 125.06, 117.63, 60.35, 48.29, 32.41, 31.88, 25.53, 22.57, 21.79. HRMS (ESI) calcd for $C_{58}H_{56}N_8O_8Na$ $[M+Na]^+$: 1015.4113, found 1015.4127.

N^2,$N^{2'}$-(9,10-dioxo-9,10-dihydroanthracene-2,6-diyl)bis(N6-(1-((1-(((R)-1-phenylethyl)carbamoyl)cyclohexyl)carbamoyl)cyclohexyl)pyridine-2,6-dicarboxamide), **L8**

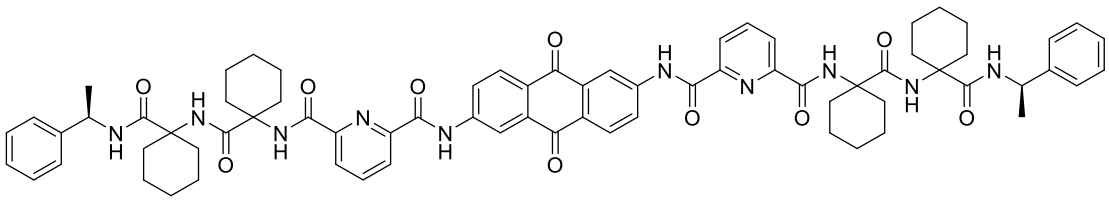

Tert-butyl (R)-(1-((1-((1-phenylethyl)carbamoyl)cyclohexyl)carbamoyl)cyclohexyl)carbamatete (1 g, 2.12 mmol, 3.0 eq.) was dissolved in 20 ml of DCM. 5 ml of trifluoroacetic acid was added and the reaction was maintained in room temperature for 3 hrs. The solvent was then evaporated to obtain a viscous oil. The residue was dissolved in 10 ml of DMF and to this solution is added 6,6'-(((9,10 dioxo-9,10-dihydroanthracene-2,6-diyl)bis(azanediyl))bis(carbonyl))dipicolinic acid (0.38 g, 0.71 mmol, 1.0 eq.), HATU (0.59 g, 2.1.55 mmol, 2.2 eq.) and DIPEA (0.86 ml, 4.95 mmol, 7.0 eq.). The reaction was stirred for 16 hrs at room temperature and pressure. The reaction mixture was diluted with ethyl acetate (30 ml). The organic layer was washed by 0.5 M LiCl (3 x 10 ml), 5% HCl (3 x 10 ml), 0.5 M K_2CO_3 (3 x 10 ml), brine (3 x 10 ml) and then dried with anhydrous $MgSO_4$. The organic layer was concentrated and then purified by HPLC with Sunfire Silica column (DCM/MeOH: 95/5; flow rate 8 ml/min). **L8**: (0.22 g, 0.18 mmol, 25.0%), ^{1}H NMR (400 MHz, $(CD_3)_2SO$, 298K, δ): 11.62 (s, 1H), 9.36 (s, 1H), 8.87 (s, 1H), 8.48 (d, *J* = 8.7 Hz, 1H), 8.42 (d, *J* = 7.7 Hz, 1H), 8.36 (d, *J* = 8.5 Hz, 1H), 8.27 (t, *J* = 7.8 Hz, 1H), 8.15 (d, *J* = 7.7 Hz, 1H), 7.82 (d, *J* = 8.2 Hz, 1H), 7.36 (d, *J* = 7.6 Hz, 2H), 7.32 – 7.21 (m, 3H), 7.17 (t, *J* = 7.2 Hz, 1H), 4.93 (q, *J* = 7.3 Hz, 1H), 2.38 – 2.12 (m, 4H), 2.03 (s, 2H), 1.80 – 1.10 (m, 17H). ^{13}C NMR (101 MHz, $(CD_3)_2SO$, 298K, δ): 181.64, 173.69, 164.01, 163.01, 149.21, 148.71, 145.48, 144.19, 140.11, 134.67, 129.17, 128.89, 128.44, 126.72, 126.41, 125.78, 124.91, 117.68, 60.18, 48.45, 33.01, 32.43, 31.71, 25.58, 23.22, 22.04, 21.58. HRMS (ESI) calcd for $C_{72}H_{78}N_{10}O_{10}Na$ $[M+Na]^+$: 1265.5795, found 1265.5807.

***Di-tert*-butyl ((1,4-phenylenebis(azanediyl))bis(2-methyl-1-oxopropane-1,2-diyl))dicarbamate**

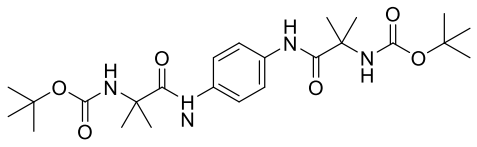

To a stirred solution of 2-((*tert*-butoxycarbonyl)amino)-2-methylpropanoic acid (3 g, 14.76 mmol, 2.2 eq) in DCM (10 ml), DIPEA (7.02 ml, 40.26 mmol, 6 eq) was added and the solution was allowed to stirred for 10 mins. HATU (5.61 g, 14.76 mmol, 2.2 eq) was then added and the solution was allowed to stir for another 10 mins. Benzene-1,4-diamine (0.73 g, 6.71 mmol, 1 eq) was added and the reaction mixture was allowed to stir for 48 hrs at rtp. Solvent was then evaporated and the crude product was washed with water (3 x 50 ml) and MeCN (3 x 50 ml) to obtained the desired white product.

***Di-tert*-butyl ((1,4-phenylenebis(azanediyl))bis(2-methyl-1-oxopropane-1,2-diyl))dicarbamate**: (3.02 g, 6.31 mmol, 94.0% yield), ^{1}H NMR (400 MHz, $(CD_3)_2SO$, 298K, δ): 9.29 (s, 2H), 7.48 (s, 4H), 6.88 (s, 2H), 1.37 (s, 15H). ^{13}C NMR (101 MHz, $(CD_3)_2SO$, 298K, δ): 173.49, 154.70, 135.10, 120.50, 78.61, 56.81, 28.57, 25.49. HRMS (ESI) calcd for $C_{24}H_{38}N_4O_6Na$ $[M+Na]^+$: 501.2684, found 501.2692.

***Di-tert*-butyl ((((1,4-phenylenebis(azanediyl))bis(2-methyl-1-oxopropane-1,2-diyl))bis(azanediyl))bis(2-methyl-1-oxopropane-1,2-diyl))dicarbamate**

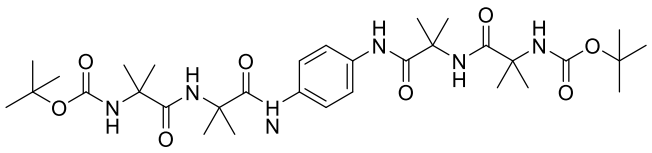

Di-tert-butyl ((1,4-phenylenebis(azanediyl))bis(2-methyl-1-oxopropane-1,2-diyl))dicarbamate (2 g, 4.18 mmol, 1.0 eq.) was dissolved in 80 ml of DCM. 20 ml of trifluoroacetic acid was added and the reaction was maintained in room temperature for 1 hr. The solvent was then evaporated to obtain white solid. The residue was dissolved in 10 ml of DMF and to this solution is added 2-((*tert*-butoxycarbonyl)amino)-2-methylpropanoic acid (1.87 g, 9.19 mmol, 2.2 eq.), HOBt (1.98 g, 14.63 mmol, 3.5 eq.), EDCI (2.27 g, 14.63 mmol, 3.5 eq.) and DIPEA (4.37 ml, 25.07 mmol, 6 eq.). Solvent was then evaporated and the crude product was washed with water (3 x 30 ml) and MeCN (3 x 30 ml) to obtained the desired white product.

***Di-tert*-butyl ((((1,4-phenylenebis(azanediyl))bis(2-methyl-1-oxopropane-1,2-diyl))bis(azanediyl))bis(2-methyl-1-oxopropane-1,2-diyl))dicarbamate**: (0.88 g, 1.36 mmol, 32.5% yield), ^{1}H NMR (400 MHz, $(CD_3)_2SO$, 298K, δ): 9.17 (s, 2H), 7.84 (s, 2H), 7.61 (s, 4H), 7.35 (s, 2H), 1.43 (s, 18H), 1.37 (s, 12H), 1.28 (s, 12H). ^{13}C NMR (101 MHz, $(CD_3)_2SO$, 298K, δ): 178.40, 177.15, 159.76, 138.59, 124.34, 84.68, 61.19, 60.64, 32.06, 29.30, 28.71. HRMS (ESI) calcd for $C_{32}H_{52}N_6O_8Na$ $[M+Na]^+$: 671.3739, found 671.3751.

***Di-tert*-butyl ((((((1,4-phenylenebis(azanediyl))bis(2-methyl-1-oxopropane-1,2-diyl))bis(azanediyl))bis(2-methyl-1-oxopropane-1,2-diyl))bis(azanediyl))bis(2-methyl-1-oxopropane-1,2-diyl))dicarbamate**

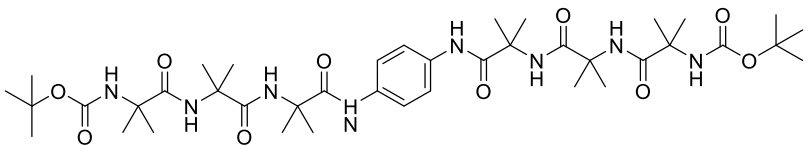

Di-tert-butyl ((((1,4-phenylenebis(azanediyl))bis(2-methyl-1-oxopropane-1,2-diyl))bis(azanediyl))bis(2-methyl-1-oxopropane-1,2-diyl))dicarbamate (0.5 g, 0.77

mmol, 1.0 eq.) was dissolved in 30 ml of DCM. 10 ml of trifluoroacetic acid was added and the reaction was maintained in room temperature for 1 hr. The solvent was then evaporated to obtain white solid. The residue was dissolved in 5 ml of DMF and to this solution is added 2-((*tert*-butoxycarbonyl)amino)-2-methylpropanoic acid (0.35 g, 1.70 mmol, 2.2 eq.), HOBt (0.36 g, 2.80 mmol, 3.5 eq.), EDCI (0.42 g, 2.80 mmol, 3.5 eq.) and DIPEA (0.81 ml, 4.62 mmol, 6 eq.). Solvent was then evaporated and the crude product was washed with water (3 x 10 ml) and MeCN (3 x 10 ml) to obtained the desired white product. ***Di-tert*-butyl ((((((1,4-phenylenebis(azanediyl))bis(2-methyl-1-oxopropane-1,2-diyl))bis(azanediyl))bis(2-methyl-1-oxopropane-1,2-diyl))bis(azanediyl))bis(2-methyl-1-oxopropane-1,2-diyl))dicarbamate**: (0.12 g, 0.15 mmol, 19.0% yield), ^{1}H NMR (400 MHz, $(CD_3)_2SO$, 298K, δ): 9.15 (s, 2H), 8.29 (s, 2H), 7.68 (s, 4H), 7.41 (s, 2H), 1.42 (d, J = 2.5 Hz, 32H), 1.34 (s, 12H), 1.29 (s, 12H). HRMS (ESI) calcd for $C_{40}H_{66}N_8O_{10}Na$ $[M+Na]^+$: 841.4794, found 841.4801.

6-(phenylcarbamoyl)picolinic acid

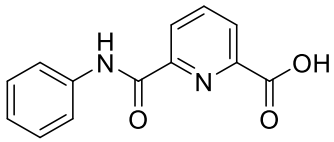

To a stirred solution of 2,6-pyridinedicarboxylic acid (5 g, 29.9 mmol, 2.5 eq.) in anhydrous DMF (75 ml), DIPEA (4.59 ml, 26.3 mmol, 2.2 eq.) was added. The solution was stirred for 20 mins. HATU (4.55 g, 12.0 mmol, 1.0 eq.) was then added. Aniline (1.11 g, 12.0 mmol, 1.0 eq.) was added after 20 mins. The reaction was allowed to stir at rtp for 16 hrs. The reaction mixture was diluted with ethyl acetate (200 ml). The organic layer was washed by 0.5 M LiCl (3 x 50 ml), 5% HCl (3 x 50 ml) and brine (3 x

50 ml) and then dried with anhydrous $MgSO_4$. The organic layer was was collected, dried and purified by column chromatography. **6-(phenylcarbamoyl)picolinic acid**: (0.88 g, 3.63 mmol, 30.4% yield), ^{1}H NMR (400 MHz, MeOD, 298K, δ): 8.44 (dd, *J* = 7.8, 1.1 Hz, 1H), 8.36 (dd, *J* = 7.8, 1.2 Hz, 1H), 8.20 (t, *J* = 7.8 Hz, 1H), 7.90 – 7.80 (m, 2H), 7.45 – 7.31 (m, 2H), 7.16 (ddt, *J* = 8.7, 7.4, 1.2 Hz, 1H). ^{13}C NMR (101 MHz, $CDCl_3$, 298K, δ): 170.22, 166.09, 154.06, 150.50, 143.23, 141.84, 132.43, 131.30, 129.54, 128.29, 124.26. HRMS (ESI) calcd for $C_{13}H_9N_2O_3$ $[M-H]^-$: 241.0619, found 241.0582.

4-(6-(phenylcarbamoyl)picolinamido)benzoic acid

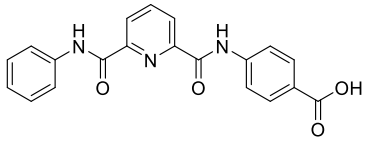

To a stirred solution of 6-(phenylcarbamoyl)picolinic acid (1 g, 4.13 mmol, 1.0 eq.) in anhydrous DMF (20 ml), DIPEA (1.59 ml, 9.1 mmol, 2.2 eq.) was added. The solution was stirred for 20 mins. HATU (1.57 g, 4.13 mmol, 1.0 eq.) was then added. Then methyl 4-aminobenzoate (0.62 g, 4.13 mmol, 1.0 eq.) was added and the mixture was reacted for 16 hrs at rtp. The reaction mixture was diluted with ethyl acetate (100 ml). The organic layer was washed by 0.5 M LiCl (3 x 30 ml), 5% HCl (3 x 30 ml), 0.5 M K_2CO_3 (3 x 30 ml), brine (3 x 30 ml) and then dried with anhydrous $MgSO_4$. The organic layer was was collected, dried to obtain the desired white solid. The white solid was then dissolved in THF (100 ml), lithium hydroxide monohydrate (0.34 g, 7.99 mmol, 3.0 eq) in minimum amount of water was added. The reaction was stirred for 16 hrs at rtp. THF was evaporated. Water (50 ml) was then added. 1% HCl was added dropwise to acidify the water phase to pH 3. Then DCM (5 x 20 ml) was added and the organic

phase was collected, dried to obtain the desired white solid. **4-(6-(phenylcarbamoyl)picolinamido)benzoic acid**: (0.84 g, 2.32 mmol, 87.3% yield), ^{1}H NMR (400 MHz, $CDCl_3$, 298K, δ): 11.24 (s, 1H), 11.05 (s, 1H), 8.43 (d, *J* = 7.7 Hz, 2H), 8.33 (dd, *J* = 8.5, 7.0 Hz, 1H), 8.09 (d, *J* = 8.8 Hz, 2H), 8.03 (d, *J* = 8.7 Hz, 2H), 7.98 – 7.89 (m, 2H), 7.46 (t, *J* = 7.9 Hz, 2H), 7.21 (t, *J* = 7.4 Hz, 1H). ^{13}C NMR (101 MHz, $(CD_3)_2SO$, 298K, δ): 167.38, 162.50, 162.04, 149.38, 148.97, 142.58, 140.53, 138.48, 130.80, 129.27, 126.67, 125.98, 124.88, 121.52, 120.66. HRMS (ESI) calcd for $C_{20}H_{15}N_3O_4Na$ $[M+Na]^+$: 384.0955, found 384.0964.

N^2,$N^{2'}$-((((((1,4-phenylenebis(azanediyl))bis(2-methyl-1-oxopropane-1,2-diyl))bis(azanediyl))bis(2-methyl-1-oxopropane-1,2-diyl))bis(azanediyl))bis(2-methyl-1-oxopropane-1,2-diyl))bis(N^6-phenylpyridine-2,6-dicarboxamide), **L9**

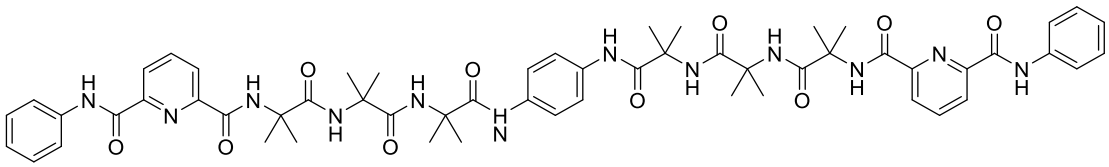

Di-tert-butyl ((((1,4-phenylenebis(azanediyl))bis(2-methyl-1-oxopropane-1,2-diyl))bis(azanediyl))bis(2-methyl-1-oxopropane-1,2-diyl))dicarbamate (0.1 g, 0.12 mmol, 1.0 eq.) was dissolved in 4 ml of DCM. 1 ml of trifluoroacetic acid was added and the reaction was maintained in room temperature for 1 hr. The solvent was then evaporated to obtain white solid. The residue was dissolved in 3 ml of DMF and to this solution is added 6-(phenylcarbamoyl)picolinic acid (0.065 g, 0.27 mmol, 2.2 eq.), HATU (0.10 g, 0.27 mmol, 2.2 eq.), and DIPEA (0.13 ml, 0.73 mmol, 6 eq.). Solvent was then evaporated and the crude product was washed with water (3 x 10 ml) and MeCN (3 x 10 ml) to obtained the desired white product. **L9**: (53.3 mg, 0.050 mmol, 41.0%

yield), ^{1}H NMR (400 MHz, $(CD_3)_2SO$, 298K, δ): 10.97 (s, 2H), 9.44 (s, 2H), 9.12 (s, 2H), 8.42 – 8.30 (m, 4H), 8.24 (d, J = 4.5 Hz, 4H), 7.89 (d, J = 7.9 Hz, 4H), 7.63 (d, J = 13.0 Hz, 6H), 7.46 (t, J = 7.8 Hz, 2H), 7.21 (t, J = 7.4 Hz, 2H), 1.63 (s, 12H), 1.54 (s, 12H), 1.29 (s, 12H). ^{13}C NMR (101 MHz, $(CD_3)_2SO$, 298K, δ): 175.20, 173.91, 173.61, 163.95, 162.14, 149.30, 148.87, 140.31, 138.37, 135.31, 129.30, 125.77, 125.53, 124.99, 121.70, 119.71, 57.04, 56.80, 25.74, 25.24. HRMS (ESI) calcd for $C_{56}H_{66}N_{12}O_{10}Na$ $[M+Na]^+$: 1089.4917, found 1089.4940.

Di-*tert*-butyl ((2*S*,2'*S*)-(((1,4-phenylenebis(azanediyl))bis(2-methyl-1-oxopropane-1,2-diyl))bis(azanediyl))bis(4-methyl-1-oxopentane-1,2-diyl))dicarbamate

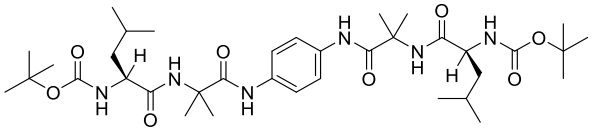

Di-tert-butyl ((1,4-phenylenebis(azanediyl))bis(2-methyl-1-oxopropane-1,2-diyl))dicarbamate (1 g, 2.09 mmol, 1.0 eq.) was dissolved in 40 ml of DCM. 10 ml of trifluoroacetic acid was added and the reaction was maintained in room temperature for 1 hr. The solvent was then evaporated to obtain white solid. The residue was dissolved in 15 ml of DMF and to this solution is added (Tert-butoxycarbonyl)-*L*-leucine (1.06 g, 4.60 mmol, 2.2 eq.), HOBt (0.99 g, 7.31 mmol, 3.5 eq.), EDCI (1.14 g, 7.31 mmol, 3.5 eq.) and DIPEA (2.19 ml, 12.54 mmol, 6 eq.) and allowed to react for 16 hrs. The reaction mixture was diluted with ethyl acetate and washed with 1M LiCl (3 x 50 ml), 5% HCl (3 x 50 ml), 0.5 M K_2CO_3 (3 x 50 ml), brine (3 x 30 ml). The organic phase was then collected and evaporated to obtain the desired white product. **Di-*tert*-butyl ((2*S*,2'*S*)-(((1,4-phenylenebis(azanediyl))bis(2-methyl-1-oxopropane-1,2-diyl))bis(azanediyl))bis(4-methyl-1-oxopentane-1,2-diyl))dicarbamate**: (1.28 g, 1.82

mmol, 86.9% yield), ^{1}H NMR (400 MHz, $(CD_3)_2SO$, 298K, δ): 8.95 (s, 1H), 8.14 (s, 1H), 7.51 (s, 2H), 7.08 (d, *J* = 6.2 Hz, 1H), 3.89 (q, *J* = 6.9 Hz, 1H), 1.68 – 1.51 (m, 1H), 1.40 (d, *J* = 31.4 Hz, 17H), 0.87 (dd, *J* = 8.4, 6.6 Hz, 6H). ^{13}C NMR (101 MHz, $CDCl_3$, 298K, δ): 173.05, 172.59, 156.59, 134.45, 120.74, 80.75, 57.84, 53.95, 40.51, 28.18, 25.62, 24.96, 24.72, 22.77, 21.79. HRMS (ESI) calcd for $C_{36}H_{60}N_6O_8Na$ $[M+Na]^+$:727.4365, found 727.4377.

Di-tert-butyl ((((2S,2'S)-(((1,4-phenylenebis(azanediyl))bis(2-methyl-1-oxopropane-1,2-diyl))bis(azanediyl))bis(4-methyl-1-oxopentane-1,2-diyl))bis(azanediyl))bis(2-methyl-1-oxopropane-1,2-diyl))dicarbamate

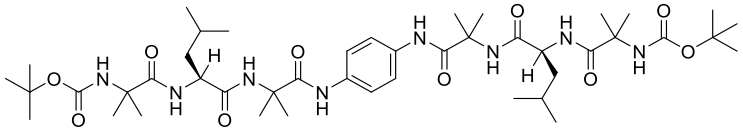

Di-*tert*-butyl ((2*S*,2'*S*)-(((1,4-phenylenebis(azanediyl))bis(2-methyl-1-oxopropane-1,2-diyl))bis(azanediyl))bis(4-methyl-1-oxopentane-1,2-diyl))dicarbamate (1 g, 1.42 mmol, 1.0 eq.) was dissolved in 40 ml of DCM. 10 ml of trifluoroacetic acid was added and the reaction was maintained in room temperature for 1 hr. The solvent was then evaporated to obtain white solid. The residue was dissolved in 15 ml of DMF and to this solution is added 2-((*tert*-butoxycarbonyl)amino)-2-methylpropanoic acid (0.63 g, 3.12 mmol, 2.2 eq.), HOBt (0.67 g, 4.97 mmol, 3.5 eq.), EDCI (0.77 g, 4.97 mmol, 3.5 eq.) and DIPEA (1.48 ml, 8.51 mmol, 6 eq.) and allowed to react for 16 hrs. The reaction mixture was diluted with ethyl acetate and washed with 1M LiCl (3 x 50 ml), 5% HCl (3 x 50 ml), 0.5 M K_2CO_3 (3 x 50 ml), brine (3 x 30 ml). The organic phase was then collected and evaporated to obtain the desired white product. **Di-tert-butyl ((((2S,2'S)-(((1,4-phenylenebis(azanediyl))bis(2-methyl-1-oxopropane-1,2-**

diyl))bis(azanediyl))bis(4-methyl-1-oxopentane-1,2-diyl))bis(azanediyl))bis(2-methyl-1-oxopropane-1,2-diyl))dicarbamate: (1 g, 1.14 mmol, 80.6%). ^{1}H NMR (400 MHz, $(CD_3)_2SO$, 298K, δ): 8.91 (s, 1H), 8.05 (s, 1H), 7.93 (s, 1H), 7.59 (s, 2H), 7.21 (s, 1H), 4.04 – 3.90 (m, 1H), 1.70 – 1.55 (m, 2H), 1.55 – 1.16 (m, 22H), 0.86 (dd, *J* = 15.6, 6.2 Hz, 6H). HRMS (ESI) calcd for $C_{44}H_{74}N_8O_{10}Na$ $[M+Na]^+$: 897.5420, found 897.5440.

6-(isopropylcarbamoyl)picolinic acid

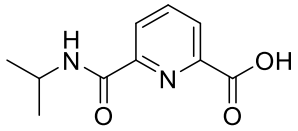

To a stirred solution of 6-(*tert*-butoxycarbonyl)picolinic acid (3 g, 13.43 mmol, 1.1 eq.) in anhydrous DMF (50 ml), DIPEA (3.2 ml, 18.33 mmol, 1.5 eq.) was added. The solution was stirred for 20 mins. HOBt (1.82 g, 13.43 mmol, 1.1 eq.), EDCI (2.09 g, 13.43 mmol, 1.1 eq.) were then added Then isopropylamine (0.72 g, 12.22 mmol, 1.0 eq.) was added and the mixture was reacted for 16 hrs at rtp. The reaction mixture was diluted with ethyl acetate (150 ml). The organic layer was washed by 0.5 M LiCl (3 x 50 ml), 5% HCl (3 x 50 ml), 0.5 M K_2CO_3 (3 x 50 ml), brine (3 x 50 ml) and then dried with anhydrous $MgSO_4$. The organic layer was was collected, dried to obtain the white solid. The white solid was then dissolved in 80 ml of DCM. 10 ml of trifluoroacetic acid was added and the reaction was maintained in room temperature for 2 hr. The solvent was then evaporated to obtain white solid. **6-(isopropylcarbamoyl)picolinic acid**: (2.06 g, 9.89 mmol, 81.0%). ^{1}H NMR (400 MHz, $CDCl_3$, 298K, δ): 8.43 (dd, *J* = 7.9, 1.2 Hz, 1H), 8.33 (dd, *J* = 7.8, 1.2 Hz, 1H), 8.16 – 8.05 (m, 2H), 4.28 (dp, *J* = 8.2, 6.5 Hz, 1H), 1.28 (d, *J* = 6.6 Hz, 6H). ^{13}C NMR (101 MHz, $CDCl_3$, 298K, δ): 166.17, 163.15, 149.33, 145.45,

139.69, 127.55, 126.75, 42.47, 22.32. HRMS (ESI) calcd for $C_{10}H_{11}N_2O_3$ $[M-H]^-$: 207.0775, found 207.0775.

4-(6-(isopropylcarbamoyl)picolinamido)benzoic acid

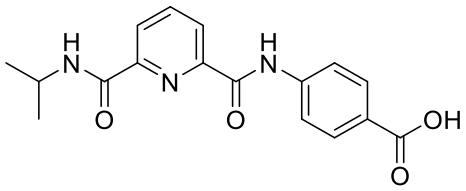

To a stirred solution of **6-(isopropylcarbamoyl)picolinic acid** (2.5 g, 12.0 mmol, 1.0 eq.) in anhydrous DMF (50 ml), DIPEA (3.14 ml, 18 mmol, 1.5 eq.) was added. The solution was stirred for 20 mins. HATU (5.02 g, 13.2 mmol, 1.1 eq.) was then added. Then methyl 4-aminobenzoate (1.81 g, 12.0 mmol, 1.0 eq.) was added and the mixture was reacted for 16 hrs at rtp. The reaction mixture was diluted with ethyl acetate (100 ml). The organic layer was washed by 0.5 M LiCl (3 x 50 ml), 5% HCl (3 x 50 ml), 0.5 M K_2CO_3 (3 x 50 ml), brine (3 x 50 ml) and then dried with anhydrous $MgSO_4$. The organic layer was was collected, dried to obtain the desired white solid. The white solid was then dissolved in THF (300 ml), lithium hydroxide monohydrate (1.53 g, 36.0 mmol, 3.0 eq) in minimum amount of water was added. The reaction was stirred for 16 hrs at rtp. THF was evaporated. Water (100 ml) was then added. 1% HCl was added dropwise to acidify the water phase to pH 3. Then DCM (5 x 50 ml) was added and the organic phase was collected, dried to obtain the desired white solid. **4-(6-(isopropylcarbamoyl)picolinamido)benzoic acid**: (1.9 g, 5.80 mmol, 48.3%). ^{1}H NMR (400 MHz, $(CD_3)_2SO$, 298K, δ): 12.78 (s, 1H), 10.97 (s, 1H), 9.05 (d, *J* = 8.0 Hz, 1H), 8.29 (dd, *J* = 7.4, 1.5 Hz, 1H), 8.25 – 8.15 (m, 2H), 7.96 (s, 4H), 4.14 (dp, *J* = 7.9, 6.5 Hz, 1H), 1.24 (d, *J* = 6.6 Hz, 6H). ^{13}C NMR (125 MHz, $(CD_3)_2SO$, 298K, δ): 167.45, 162.75, 162.63,

149.86, 148.85, 142.51, 140.19, 130.84, 126.78, 125.71, 125.45, 120.91, 41.69, 22.83. HRMS (ESI) calcd for $C_{17}H_{16}N_3O_4$ $[M-H]^-$: 326.1146, found 326.1176.

N^2,$N^{2'}$-((((2S,2'S)-(((1,4-phenylenebis(azanediyl))bis(2-methyl-1-oxopropane-1,2-diyl))bis(azanediyl))bis(4-methyl-1-oxopentane-1,2-diyl))bis(azanediyl))bis(2-methyl-1-oxopropane-1,2-diyl))bis(N6-isopropylpyridine-2,6-dicarboxamide), **L10**

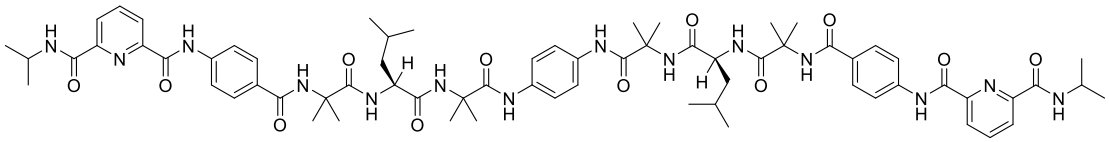

Di-tert-butyl ((((2S,2'S)-(((1,4-phenylenebis(azanediyl))bis(2-methyl-1-oxopropane-1,2-diyl))bis(azanediyl))bis(4-methyl-1-oxopentane-1,2-diyl))bis(azanediyl))bis(2-methyl-1-oxopropane-1,2-diyl))dicarbamate (0.34 g, 0.39 mmol, 1.0 eq.) was dissolved in 8 ml of DCM. 2 ml of trifluoroacetic acid was added and the reaction was maintained in room temperature for 1 hr. The solvent was then evaporated to obtain white solid. The residue was dissolved in 3 ml of DMF and to this solution is added 4-(6-(isopropylcarbamoyl)picolinamido)benzoic acid (0.28 g, 0.85 mmol, 2.2 eq.), HATU (0.32 g, 0.85 mmol, 2.2 eq.), and DIPEA (0.4 ml, 2.33 mmol, 6 eq.). Solvent was then evaporated and redissolved in EA (50 ml). The organic phase was washed with 1M LiCl (3 x 10 ml), 5% HCl (3 x 10 ml), 0.5 M K_2CO_3 (3 x 10 ml), brine (3 x 10 ml). The organic phase was then collected, evaporated and purified by column chromatography to obtained the desired white product. **L10**: (0.11 g, 0.10 mmol, 26.8% yield), ^{1}H NMR (400 MHz, $(CD_3)_2SO$, 298K, δ): 11.00 (s, 1H), 9.12 (d, *J* = 8.0 Hz, 1H), 8.91 (s, 1H), 8.61 (s, 1H), 8.35 (dd, *J* = 7.4, 1.5 Hz, 1H), 8.32 – 8.20 (m, 2H), 8.12 (d, *J* = 6.7 Hz, 1H), 8.02 (q, *J* = 8.9 Hz, 4H), 7.80 (s, 1H), 7.57 (s, 2H), 4.20 (dq, *J* = 13.7, 6.8 Hz, 1H), 4.05 – 3.93

(m, 1H), 1.70 – 1.36 (m, 13H), 1.36 – 1.21 (m, 7H), 0.85 (dd, *J* = 19.1, 6.1 Hz, 7H). ^{13}C NMR (101 MHz, $(CD_3)_2SO$, 298K, δ): 175.81, 173.23, 172.25, 166.75, 162.70, 162.52, 149.79, 148.84, 141.30, 140.15, 135.10, 129.96, 129.10, 125.61, 125.36, 120.53, 120.18, 57.09, 56.92, 53.21, 31.42, 25.85, 25.82, 25.50, 25.36, 24.84, 23.58, 22.77, 22.53, 21.67, 14.43. HRMS (ESI) calcd for $C_{68}H_{88}N_{14}O_{12}Na$ $[M+Na]^+$: 1315.6598, found 1315.6675.

4.5 References

1. Misawa, T.; Imamura, M.; Ozawa, Y.; Haishima, K.; Kurihara, M.; Kikuchi, Y.; Demizu, Y., Development of helix-stabilized antimicrobial peptides composed of lysine and hydrophobic alpha,alpha-disubstituted alpha-amino acid residues. *Bioorg. Med. Chem. Lett.* **2017,** *27* (17), 3950-3953.
2. Ishikawa, M.; Maeda, K.; Mitsutsuji, Y.; Yashima, E., An unprecedented memory of macromolecular helicity induced in an achiral polyisocyanide in water. *J. Am. Chem. Soc.* **2004,** *126* (3), 732-3.
3. Nakashima, H.; Koe, J. R.; Torimitsu, K.; Fujiki, M., Transfer and amplification of chiral molecular information to polysilylene aggregates. *J. Am. Chem. Soc.* **2001,** *123* (20), 4847-8.
4. Ishikawa, M.; Maeda, K.; Yashima, E., Macromolecular chirality induction on optically inactive poly(4-carboxyphenyl isocyanide) with chiral amines: a dynamic conformational transition of poly(phenyl isocyanide) derivatives. *J. Am. Chem. Soc.* **2002,** *124* (25), 7448-58.
5. Tanaka, M., Design and synthesis of chiral α,α-disubstituted amino acids and

conformational study of their oligopeptides. *Chem. Pharm. Bull.* **2007,** *55* (3), 349-358.

6. Byrne, L.; Sola, J.; Boddaert, T.; Marcelli, T.; Adams, R. W.; Morris, G. A.; Clayden, J., Foldamer-mediated remote stereocontrol: >1,60 asymmetric induction. *Angew. Chem. Int. Ed. Engl.* **2014,** *53* (1), 151-5.

7. Le Bailly, B. A.; Clayden, J., Dynamic foldamer chemistry. *Chem Commun (Camb)* **2016,** *52* (27), 4852-63.

8. Crisma, M.; Toniolo, C., Helical screw-sense preferences of peptides based on chiral, Calpha-tetrasubstituted alpha-amino acids. *Biopolymers* **2015,** *104* (1), 46-64.

9. Toniolo, C.; Crisma, M.; Formaggio, F.; Peggion, C., Control of peptide conformation by the Thorpe-Ingold effect (C^{α}-tetrasubstitution). *J. Pept. Sci.* **2001,** *60*, 396-491

10. Bellanda, M.; Peggion, E.; Burgi, R.; Gunsteren, W. V.; Mammi, S., Conformational study of an Aib-rich peptide in DMSO by NMR. *J. Pept. Res.* **2001,** *57*, 97-106.

11. Marshall, G. R., Hodgkin, E. E., Langs, D. A., Smith, D., Zabrocki, J., Leplawy, M. T., Factors governing helical preference of peptides containing multiple α,α-dialkyl amino acids. *Proc. Natl. Acad. Sci.* **1990,** *87*, 487-491.

12. Yeung, C.-T.; Chan, W. T. K.; Yan, S.-C.; Yu, K.-L.; Yim, K.-H.; Wong, W.-T.; Law, G.-L. Lanthanide supramolecular helical diastereoselective breaking induced by point chirality: Mixture or *P*-Helix, *M*-Helix. *Chem. Commun.* **2015**, *51*, 592-595.

13. Ousaka, N.; Takeyama, Y.; Iida, H.; Yashima, E., Chiral information harvesting

in dendritic metallopeptides. *Nat. Chem.* **2011,** *3* (11), 856-61.

14. Mamiya, F.; Ousaka, N.; Yashima, E., Remote control of the planar chirality in peptide-bound metallomacrocycles and dynamic-to-static planar chirality control triggered by solvent-induced 3(10)-to-alpha-helix transitions. *Angew. Chem. Int. Ed. Engl.* **2015,** *54* (48), 14442-6.

15. Li, J.; Sha, Y. A convenient synthesis of amino acid methyl esters. Molecules **2008**, *13* (5), 1111-1119.

General experimental procedures

Synthesis

Unless otherwise stated, all chemicals and solvents were obtained commercially and without further purification before used. All moisture-sensitive compounds were handled using standard Schlenk line techniques. All moisture-sensitive reactions were conducted under a nitrogen atmosphere in glasswares that were oven-dried at 140 ^{o}C overnight prior to use. Anhydrous dimethylformamide (DMF) and N,N-Diisopropylethylamine (DIPEA) were purchased from Acros. Solvents were used as received. Grace silica gel 60 (40–63 mesh) was used for column chromatography. 1D NMR spectra were recorded on a Bruker Ultrashield Advance Pro 400 MHz instrument and Jeol ECZ500R 500 MHz NMR spectrometer and the chemical shifts were determined with tetramethylsilane (TMS) or solvents in parts per million (ppm). 2D NMR spectra were recorded on Jeol ECZ500R 500 MHz NMR spectrometer. ESI-HRMS were performed on a Waters Synapt G2-Si Quadrupole MS. Elemental analyses were performed on an Elementar Vario EL cube elemental analyzer. All lanthanide salts were purchased from Sigma-Aldrich with purity 99.9% and used without further purification.

Photophysical measurement

Single-photon luminescence spectra were recorded using an Edinburgh Instrument FLSP920 spectrophotometer that was equipped with Xe900 continuous xenon lamp, µF920 microsecond flashlamp and a single photon counting Photomultiplier Tube. The excitation and emission spectra recorded on the FLSP920 were corrected with the correction file from the F900 software. CD spectra were recorded with a Jasco J-801 spectropolarimeter with a 1 cm cell at 25 ^{o}C. and presented as Δε in $M^{-1}cm^{-1}$. Hellma quartz cuvettes (1mm path length) were employed. All spectra were baselined subtracted with the blank solvent. UV-Visible absorption spectra were recorded with an Agilent Technologies Cary 8454 spectrophotometer. CPL spectra in chapter 2a were recorded on a Olis 17 UV/VIS/NIR/CD/CPL spectrophotometer On-Line Instrument Systems. CPL spectra in chapter 2b on a custom-build spectrometer consisting of a laserdriven light source (Energetiq EQ–99 LDLS, spectral range 170–2100 nm) coupled to an Acton SP2150 monochromator (600 g/nm, 300 nm Blaze)CPL spectra in chapter 3 were recorded with a Jasco CPL-300 circularly polarized luminescence spectrophotometer with a 1 cm cell at 25 ^{o}C. All photophysical measurement were done in triplicate.

Single crystal X-ray diffraction

Measurements of crystal data were carried out on a Bruker Smart 1000 system equipped with an APEX II CCD device for Eu_2**L1**$^{SS}{}_3$, Eu_2**L2**$^{RR}{}_3$ and **L2**^{RR} with graphite monochromated Mo-Kα radiation at room temperature (HKPolyU). Multi-scan

absorption correction was applied by SADABS program, and the SAINT program was utilized for integration of the diffraction profiles. The structures were solved by direct method and was refined by a full matrix least-squares treatment on *F*2 using the SHELXTL programme system.3 Structure $Eu_2\mathbf{L2^{RR}}_3$ contains highly disordered side arms, and were removed from the refinement using the PLATON/SQUEEZE program. Although the side arms cannot be defined clearly, the helical structure was clearly observed. Crystallographic data for the structural analysis has been deposited with Cambridge Crystallographic Data Centre, CCDC No. for $Eu_2\mathbf{L1^{SS}}_3$ is 996693; No. for $Eu_2\mathbf{L2^{RR}}_3$ is 991735; No. for $\mathbf{L2^{RR}}$ is 1003776.

$Tb_2\mathbf{L1^{SS}}_3$ was collected on a Bruker D8-Venture Diffractometer System with a micro-focus Mo-Kα radiation (HKPolyU). Of a total of 210003 reflections collected, 31661 were unique (R_{int} = 0.0893). Multi-scan absorption correction was applied by SADABS program, and the SAINT program utilised for the integration of the diffraction profile. The structure was solved by direct method and was refined by a full-matrix least-squares treatment on F^2 using the SHELXLE programme system. The final R-values were: *R*1 = 0.0524 [I>2s(I)] and *wR*2 = 0.1159 (all data). Crystallographic data for the structural analysis has been deposited with Cambridge Crystallographic Data Centre, CCDC No. for $Tb_2\mathbf{L1^{SS}}_3$ is 1009616.

Data of $Eu_4\mathbf{L3^{SS}}_6$ were collected on a Bruker D8 Venture single crystal diffractometer with a Bruker Photon II detector and an Incoatec IμS 3 Cu micro-focus X-ray source (Newcastle University). These data were then processed within the APEX3 software suite and solved and refined using the OLEX2 interface to the SHELX suite of programs. The data processing was truncated to only include the frames from

the unit cell data collection along with the first 3 experimental 'runs'. Crystallographic data for the structural analysis has been deposited with Cambridge Crystallographic Data Centre, CCDC No. for Eu_4**L3**$^{SS}_6$ is 2014348.

Single crystals of Eu_2Gd_2**L3**$^{SS}_6$ $C_{225}H_{192}Eu_2F_{27}Gd_2N_{36}O_{51}S_9$ was selected and mounted on a standard Kapton micromount, using neat paratone oil to try and reduce solvent loss during mounting procedure on a Bruker D8 Vantage diffractometer (Newcastle University). The crystal was kept at 220.0 K during data collection. Using Olex2, the structure was solved with the XT structure solution program using Intrinsic Phasing and refined with the XL refinement package using Least Squares minimisation. Crystallographic data for the structural analysis has been deposited with Cambridge Crystallographic Data Centre, CCDC No. for Eu_2Gd_2**L3**$^{SS}_6$ is 2092789.

Appendix

Chapter 2a

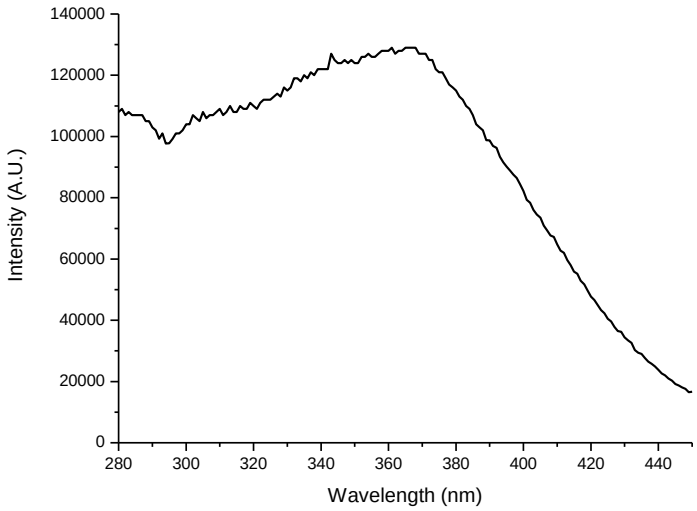

Figure S2a-1. Excitation spectrum of **$[Eu_2(L1^{RR})_3](CF_3SO_3)_6$** (powder, lem = 616 nm, slits = 5-1, filter 455nm).

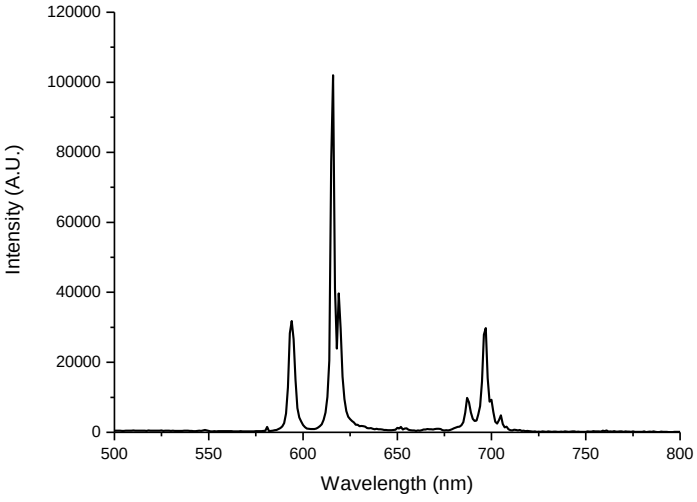

Figure S2a-2. Emission spectrum of **$[Eu_2(L1^{RR})_3](CF_3SO_3)_6$** (powder, lex = 369 nm, slits = 5-1, filter 455nm).

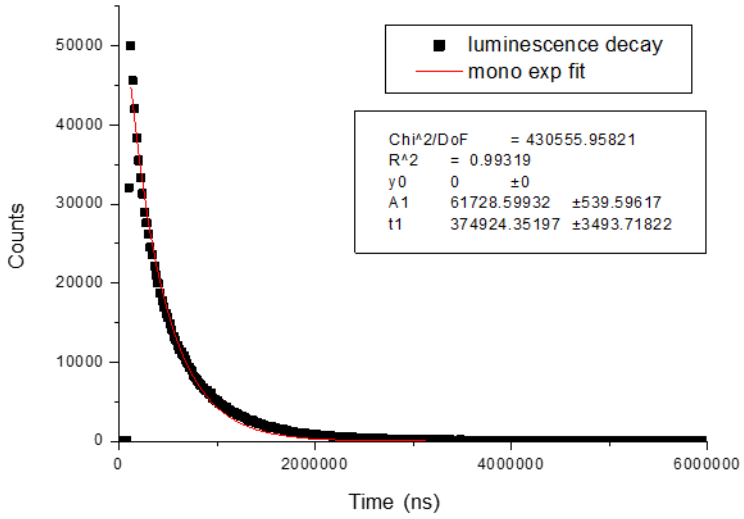

Figure S2a-3. Excited state decay curve and its mono exponential fit of **$Eu_2(L1^{RR})_3](CF_3SO_3)_6$** (powder, lex = 369 nm, slits = 15-3, filter 455nm).

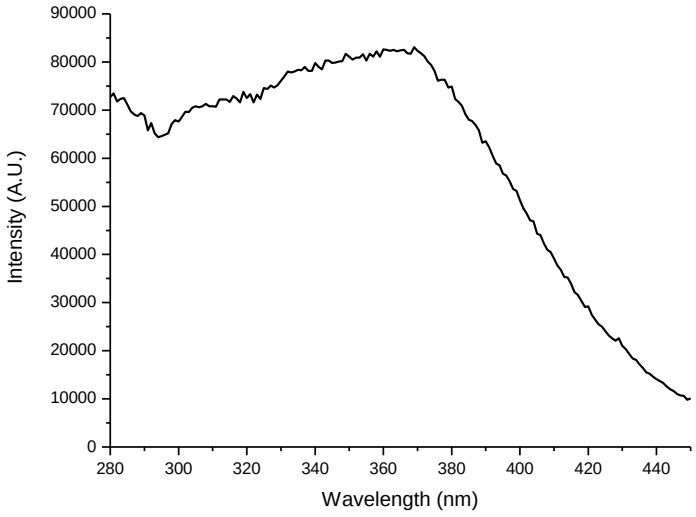

Figure S2a-4. Excitation spectrum of **$[Eu_2(L1^{SS})_3](CF_3SO_3)_6$** (powder, lem = 616 nm, slits = 5-1, filter 455nm).

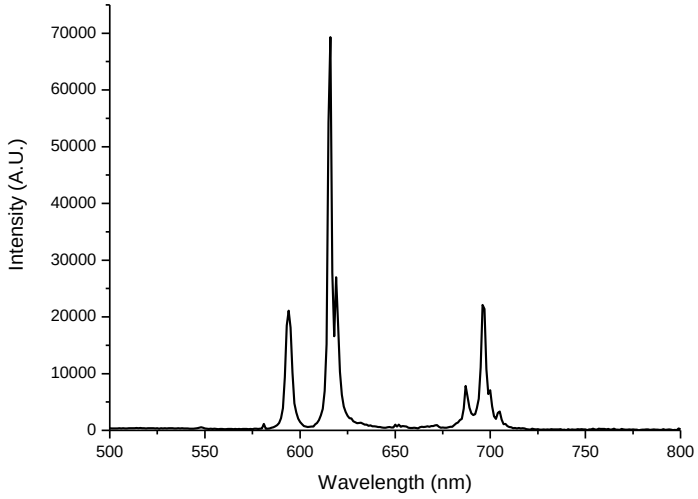

Figure S2a-5. Emission spectrum of **$[Eu_2(L1^{SS})_3](CF_3SO_3)_6$** (powder, lex = 369 nm, slits = 5-1, filter 455nm).

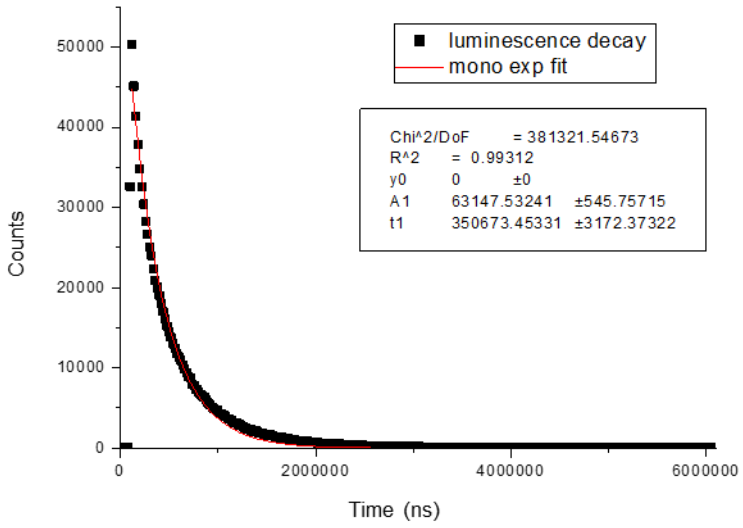

Figure S2a-6. Excited state decay curve and its mono exponential fit of **$[Eu_2(L1^{SS})_3](CF_3SO_3)_6$** (powder, lex = 369 nm, slits = 15-3, filter 455nm).

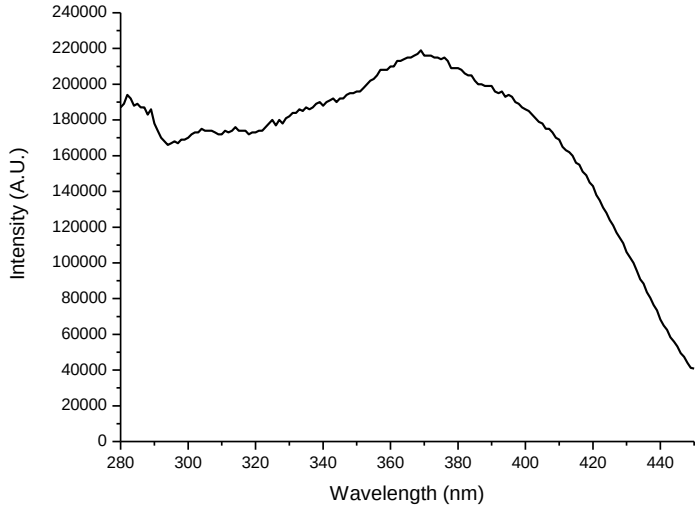

Figure S2a-7. Excitation spectrum of **$[Eu_2(L2^{RR})_3](CF_3SO_3)_6$** (powder, lem = 616 nm, slits = 5-1, filter 455nm).

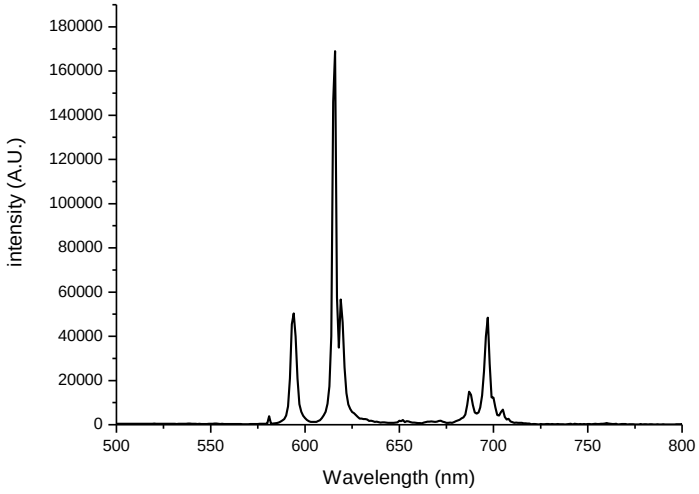

Figure S2a-8. Emission spectrum of **$[Eu_2(L2^{RR})_3](CF_3SO_3)_6$** (powder, lex = 372 nm, slits = 5-1, filter 455nm).

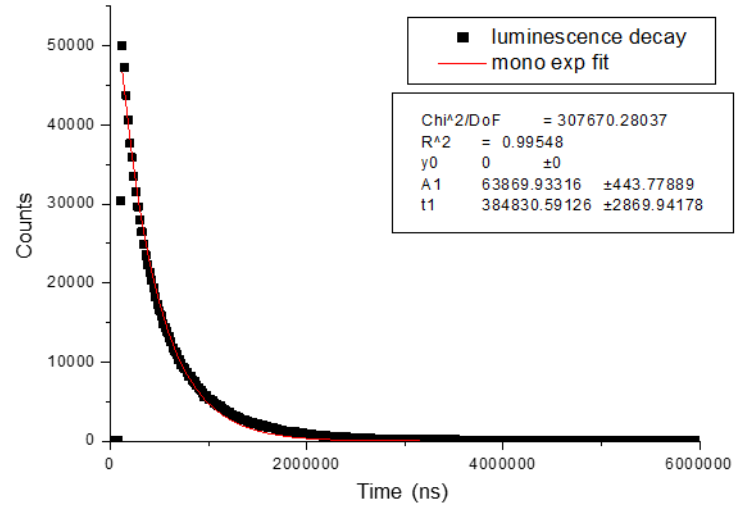

Figure S2a-9. Excited state decay curve and its mono exponential fit of **$[Eu_2(L2^{RR})_3](CF_3SO_3)_6$** (powder, lex = 372 nm, slits = 15-3, filter 455nm).

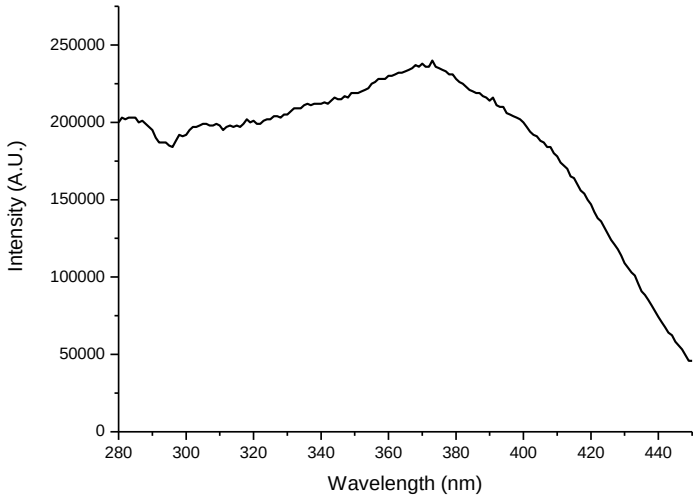

Figure S2a-10. Excitation spectrum of **$[Eu_2(L2^{SS})_3](CF_3SO_3)_6$** (powder, lem = 616 nm, slits = 5-1, filter 455nm).

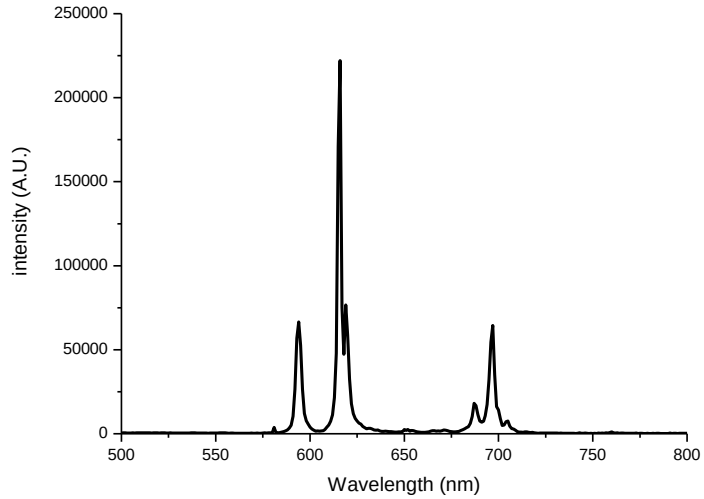

Figure S2a-11. Emission spectrum of **$[Eu_2(L2^{SS})_3](CF_3SO_3)_6$** (powder, lex = 373 nm, slits = 5-1, filter 455nm).

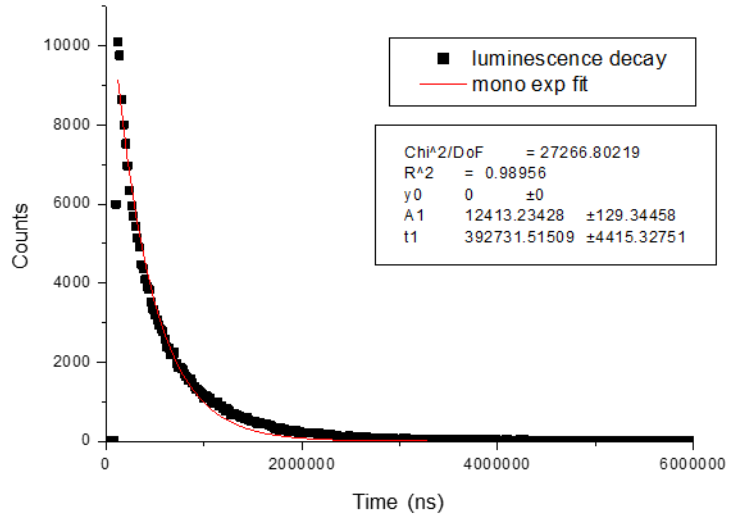

Figure S2a-12. Excited state decay curve and its mono exponential fit of **$[Eu_2(L2^{SS})_3](CF_3SO_3)_6$** (powder, lex = 373 nm, slits = 15-3, filter 455nm).

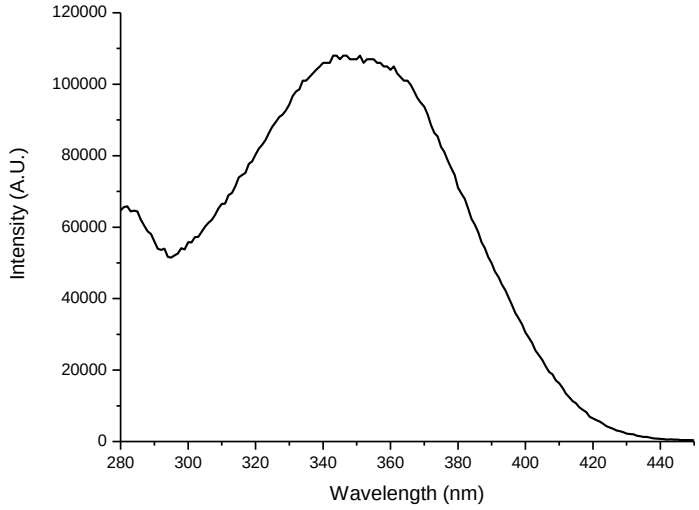

Figure S2a-13. Excitation spectrum of **$[Eu_2(L1^{RR})_3](CF_3SO_3)_6$** ($3.23 \times 10^{-5}$ M in MeCN, lem = 616 nm, slits = 5-1, filter 455nm).

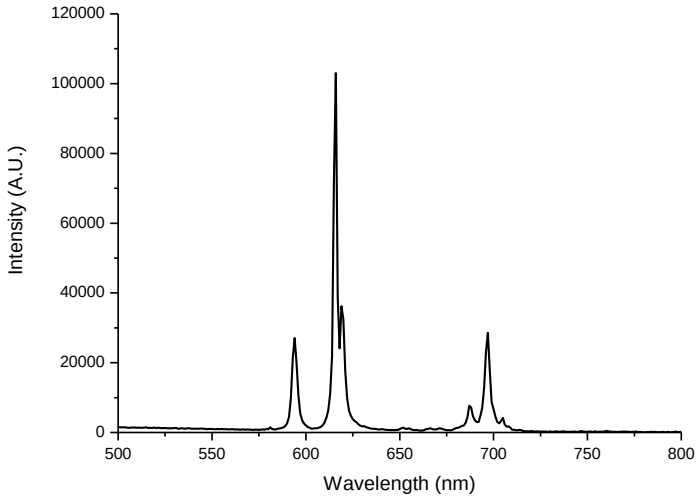

Figure S2a-14. Emission spectrum of **$[Eu_2(L1^{RR})_3](CF_3SO_3)_6$** ($3.23 \times 10^{-5}$ M in MeCN, lex = 363 nm, slits = 5-1, filter 455nm).

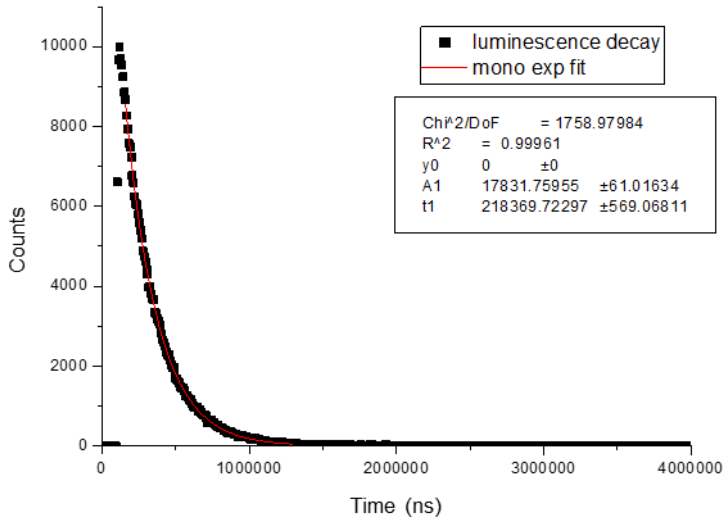

Figure S2a-16. Excited state decay curve and its mono exponential fit of **$[Eu_2(L1^{RR})_3](CF_3SO_3)_6$** ($3.23 \times 10^{-5}$ M in MeCN, lex = 363 nm, slits = 15-3, filter 455nm).

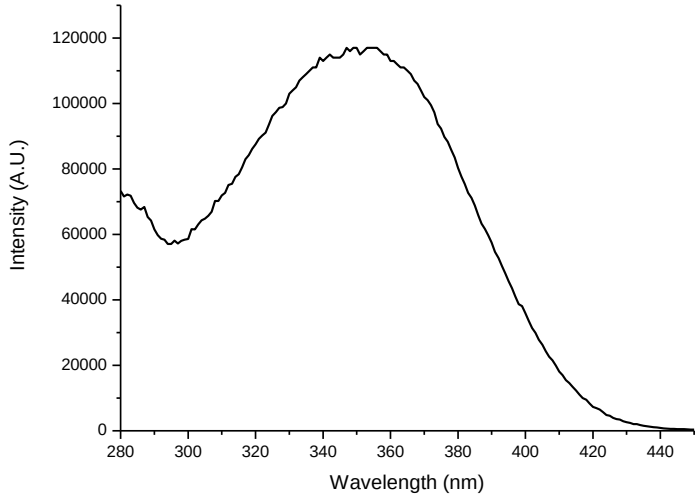

Figure S2a-16. Excitation spectrum of **$[Eu_2(L1^{SS})_3](CF_3SO_3)_6$** ($3.23 \times 10^{-5}$ M in MeCN, lem = 616 nm, slits = 5-1, filter 455nm).

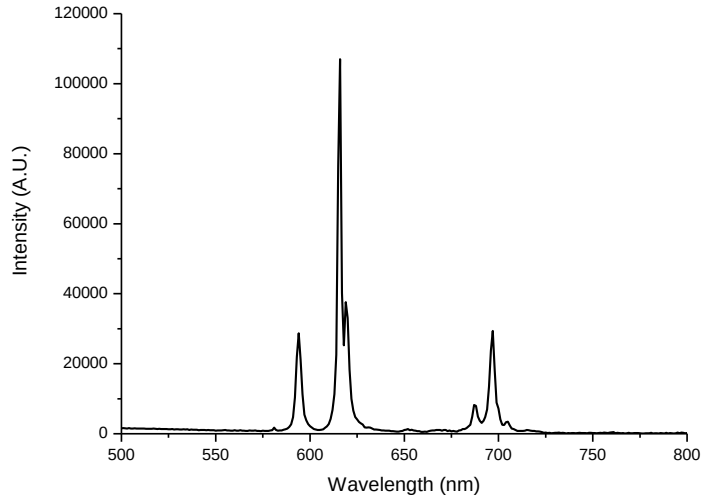

Figure S2a-17. Emission spectrum of **$[Eu_2(L1^{SS})_3](CF_3SO_3)_6$** ($3.23 \times 10^{-5}$ M in MeCN, lex = 358 nm, slits = 5-1, filter 455nm).

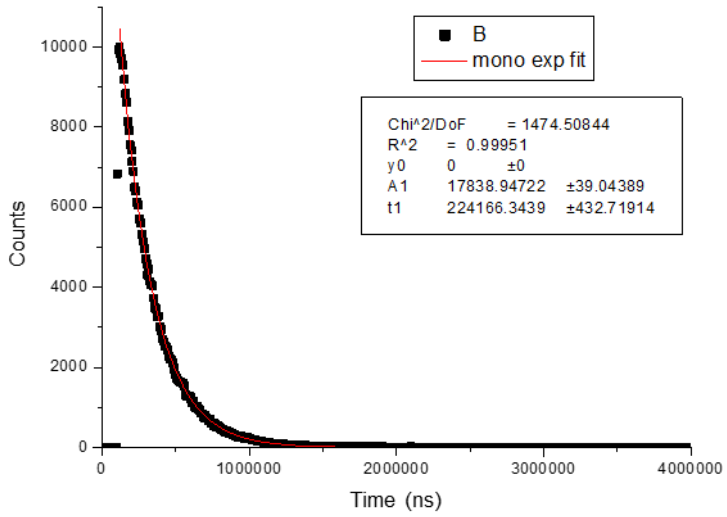

Figure S2a-18. Excited state decay curve and its mono exponential fit of **$[Eu_2(L1^{SS})_3](CF_3SO_3)_6$** ($3.23 \times 10^{-5}$ M in MeCN, lex = 358 nm, slits = 15-3, filter 455nm).

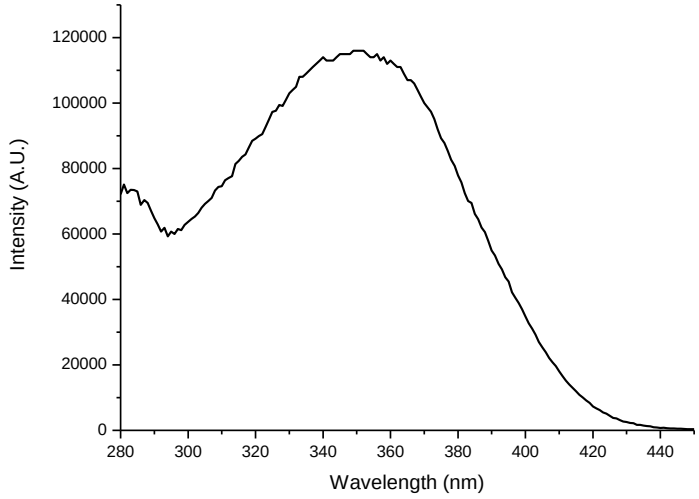

Figure S2a-19. Excitation spectrum of **$[Eu_2(L2^{RR})_3](CF_3SO_3)_6$** ($3.47 \times 10^{-5}$ M in MeCN, lem = 616 nm, slits = 5-1, filter 455nm).

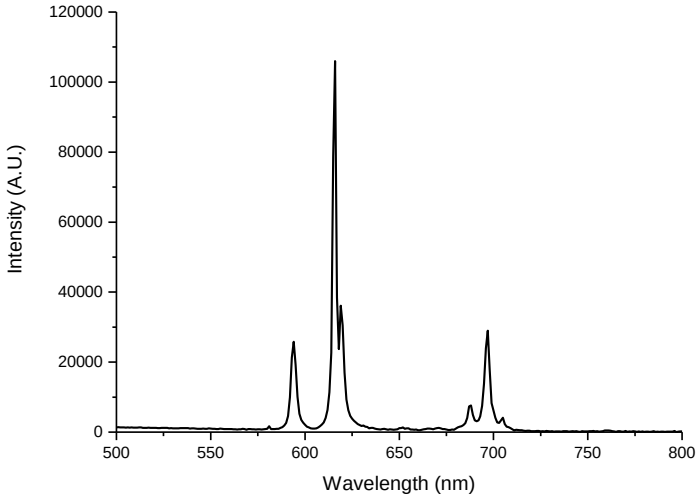

Figure S2a-20. Emission spectrum of **$[Eu_2(L2^{RR})_3](CF_3SO_3)_6$** ($3.47 \times 10^{-5}$ M in MeCN, lex = 351 nm, slits = 5-1, filter 455nm).

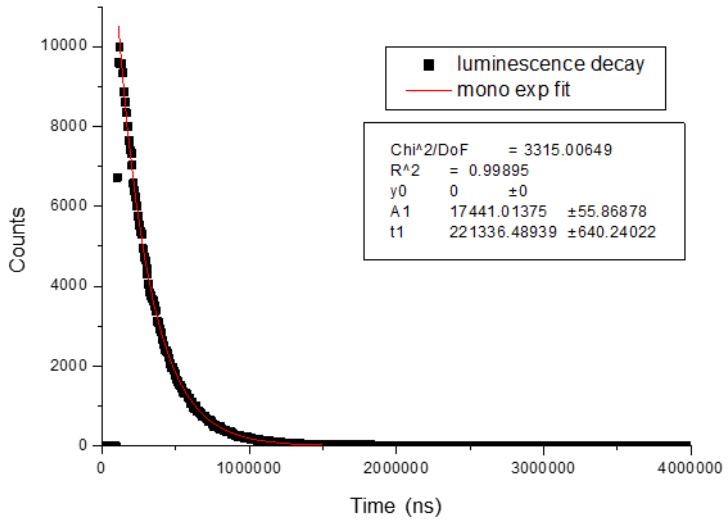

Figure S2a-21. Excited state decay curve and its mono exponential fit of **$[Eu_2(L2^{RR})_3](CF_3SO_3)_6$** ($3.47 \times 10^{-5}$ M in MeCN, lex = 351 nm, slits = 15-3, filter 455nm).

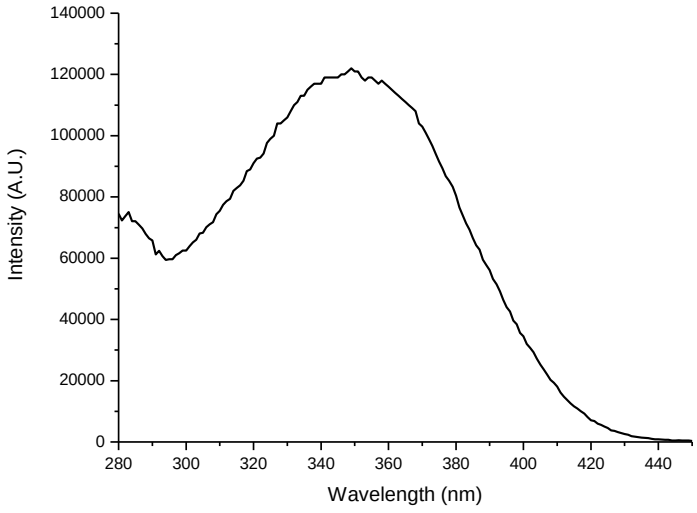

Figure S2a-22. Excitation spectrum of **$[Eu_2(L2^{SS})_3](CF_3SO_3)_6$** ($3.15 \times 10^{-5}$ M in MeCN, lem = 616 nm, slits = 5-1, filter 455nm).

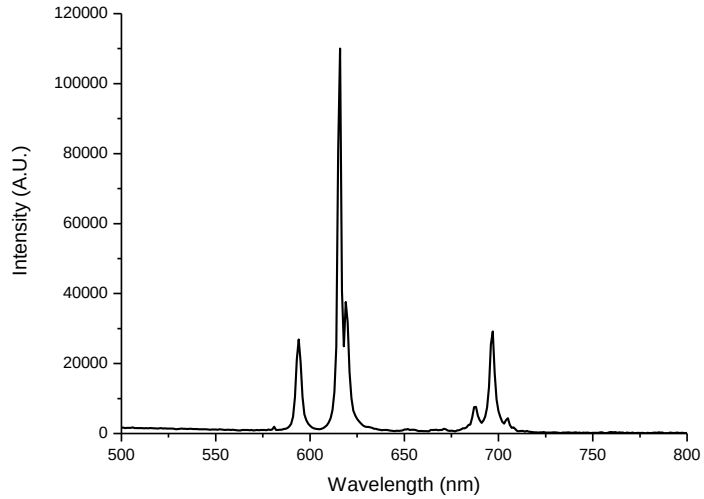

Figure S2a-23. Emission spectrum of **$[Eu_2(L2^{SS})_3](CF_3SO_3)_6$** ($3.15 \times 10^{-5}$ M in MeCN, lex = 351 nm, slits = 5-1, filter 455nm).

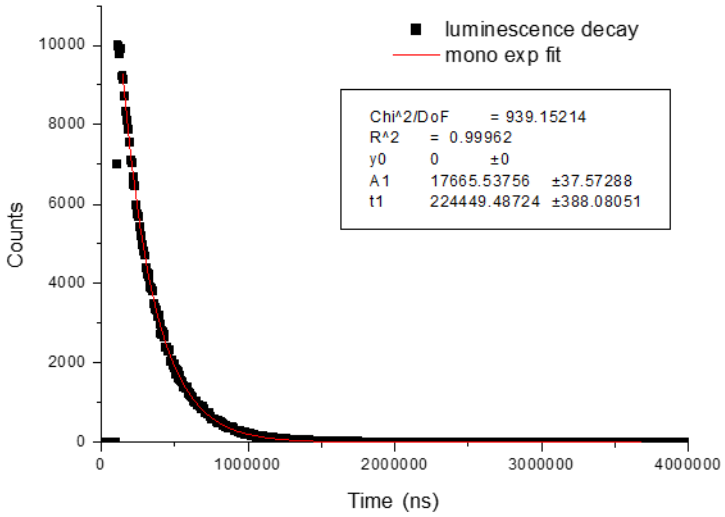

Figure S2a-24. Excited state decay curve and its mono exponential fit of **$[Eu_2(L2^{SS})_3](CF_3SO_3)_6$** ($3.15 \times 10^{-5}$ M in MeCN, lex = 351 nm, slits = 15-3, filter 455nm).

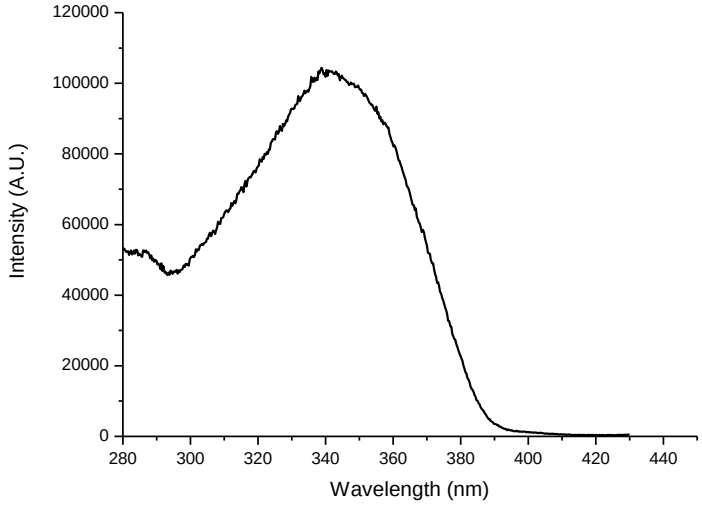

Figure S2a-25. Excitation spectrum of **$[Gd_2(L1^{SS})_3](CF_3SO_3)_6$** ($2.88 \times 10^{-6}$ M in 1:4, v/v of MeOH/EtOH at 77K, lem = 450 nm, slits = 5-1).

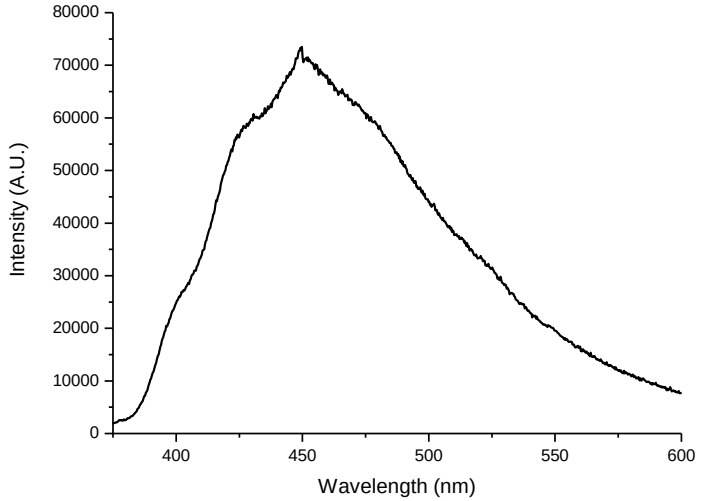

Figure S2a-26. Emission spectrum of **$[Gd_2(L1^{SS})_3](CF_3SO_3)_6$** ($2.88 \times 10^{-6}$ M in 1:4 of MeOH/EtOH at 77K, lex = 340 nm, slits = 5-1).

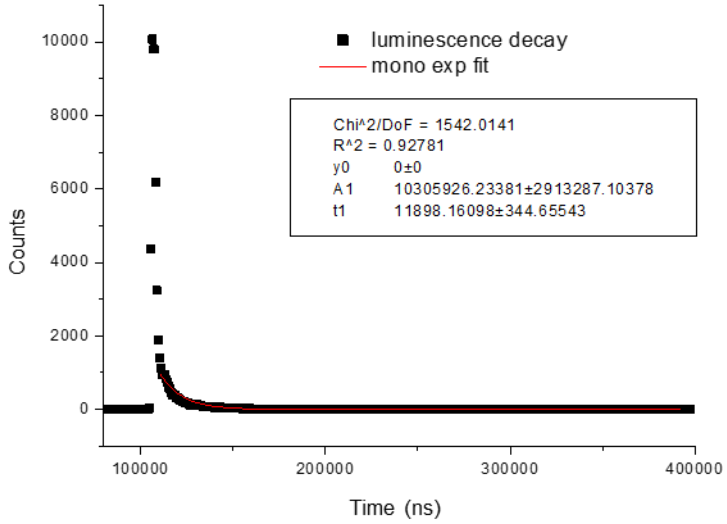

Figure S2a-27. Excited state decay curve and its mono exponential fit of **$[Gd_2(L1^{SS})_3](CF_3SO_3)_6$** ($2.88 \times 10^{-6}$ M in 1:4 of MeOH/EtOH at 77K, lex = 340 nm, slits = 15-3).

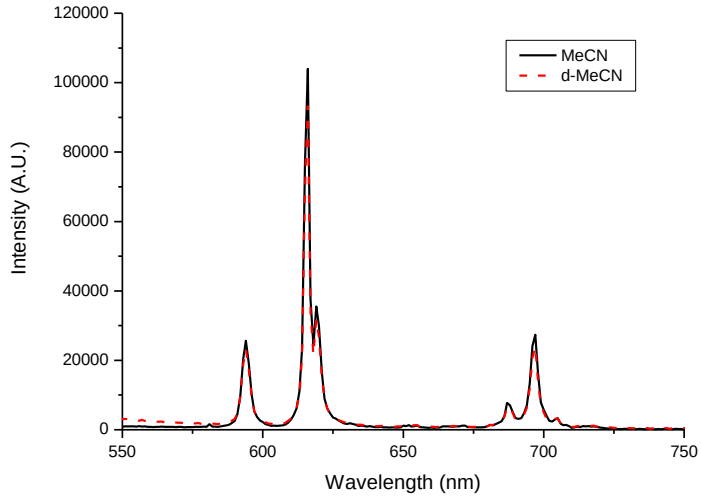

Figure S2a-28. Emission spectrum of **$[Eu_2(L2^{RR})_3](CF_3SO_3)_6$** ($3.15 \times 10^{-5}$ M in MeCN or d-MeCN, lex = 351 nm, slits = 5-1, filter 455nm).

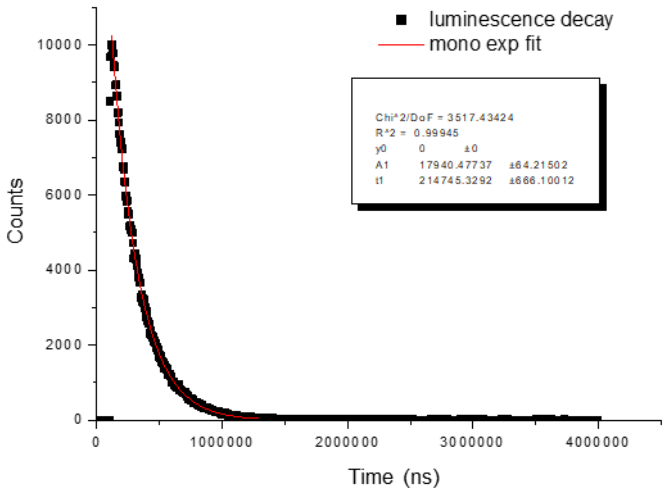

Figure S2a-29. Excited state decay curve and its mono exponential fit of **$[Eu_2(L2^{RR})_3](CF_3SO_3)_6$** ($3.15 \times 10^{-5}$ M in d-MeCN, lex = 351 nm, slits = 15-3, filter 455nm).

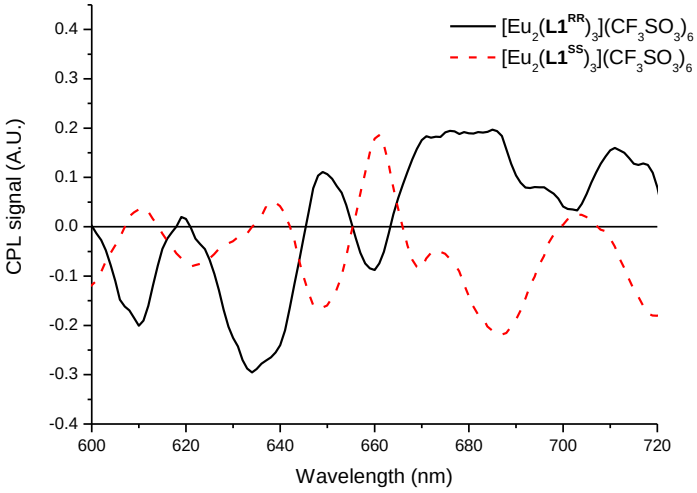

Figure S2a-30. Preliminary results of CPL for $[Eu_2(\mathbf{L1})_3](CF_3SO_3)_6$ (2.30×10^{-3} M, 10 mm cuvette, MeCN).[5]

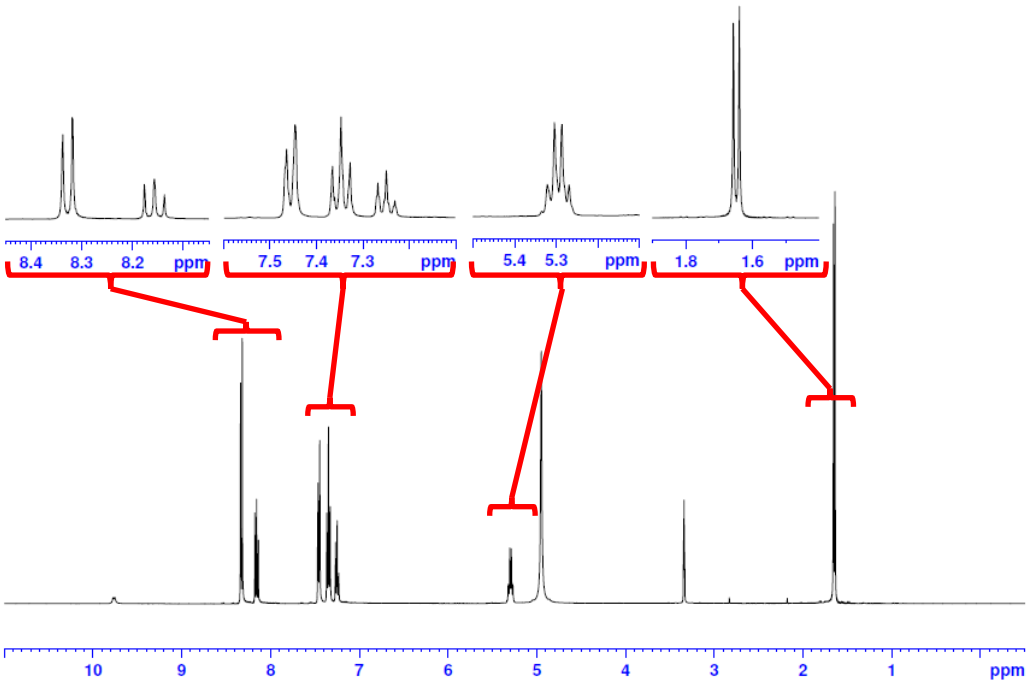

Figure S2a-31. ^{1}H NMR spectrum of **(*S*)-6-(1-phenylethyl carbamoyl)picolinic acid** in CD_3OD. The insets show the expansion of the corresponding region as indicated.

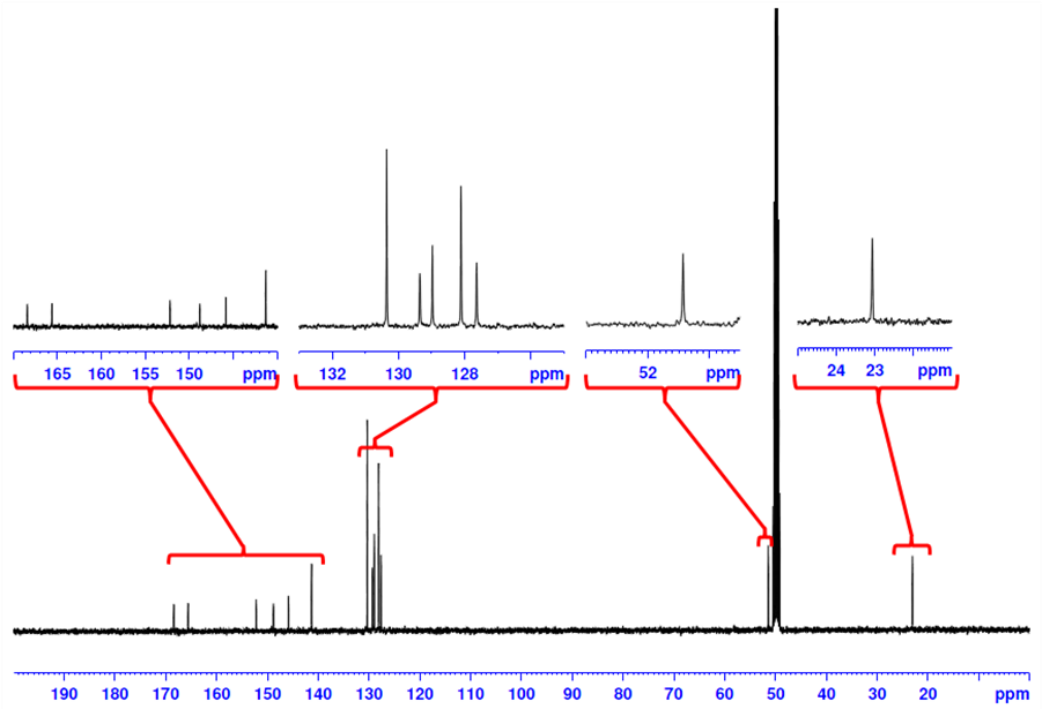

Figure S2a-32. ^{13}C NMR spectrum of **(*S*)-6-(1-phenylethyl carbamoyl)picolinic acid** in CD_3OD. The insets show the expansion of the corresponding region as indicated.

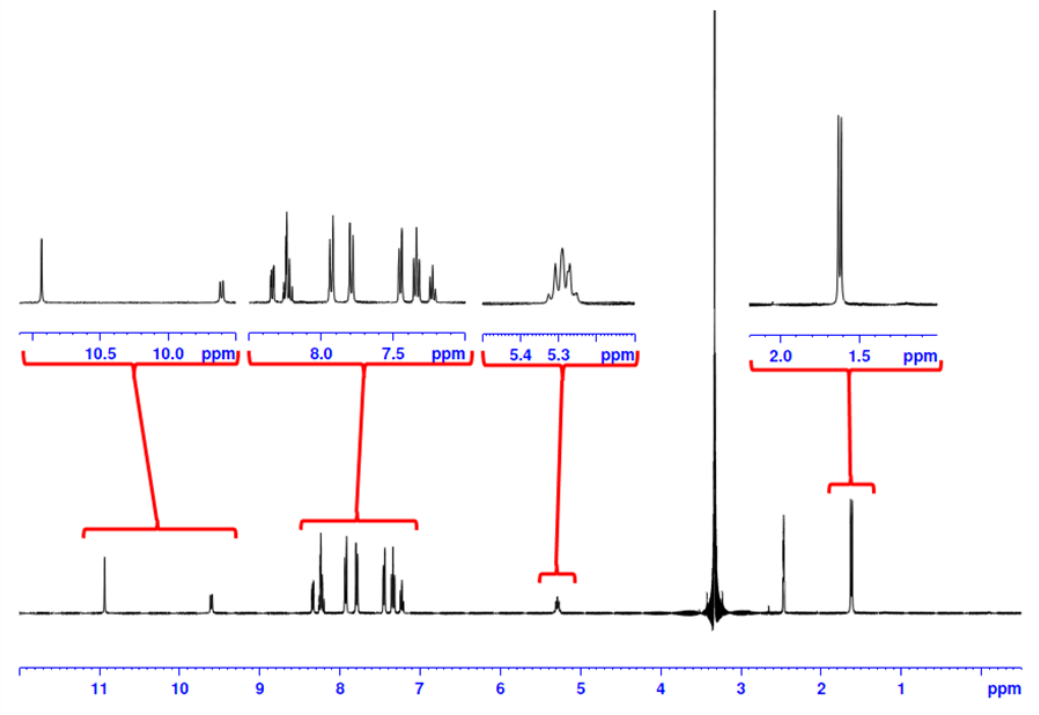

Figure S2a-33. ^{1}H NMR spectrum of **L1^{RR}** in $(CD_3)_2SO$. The insets show the expansion of the corresponding region as indicated.

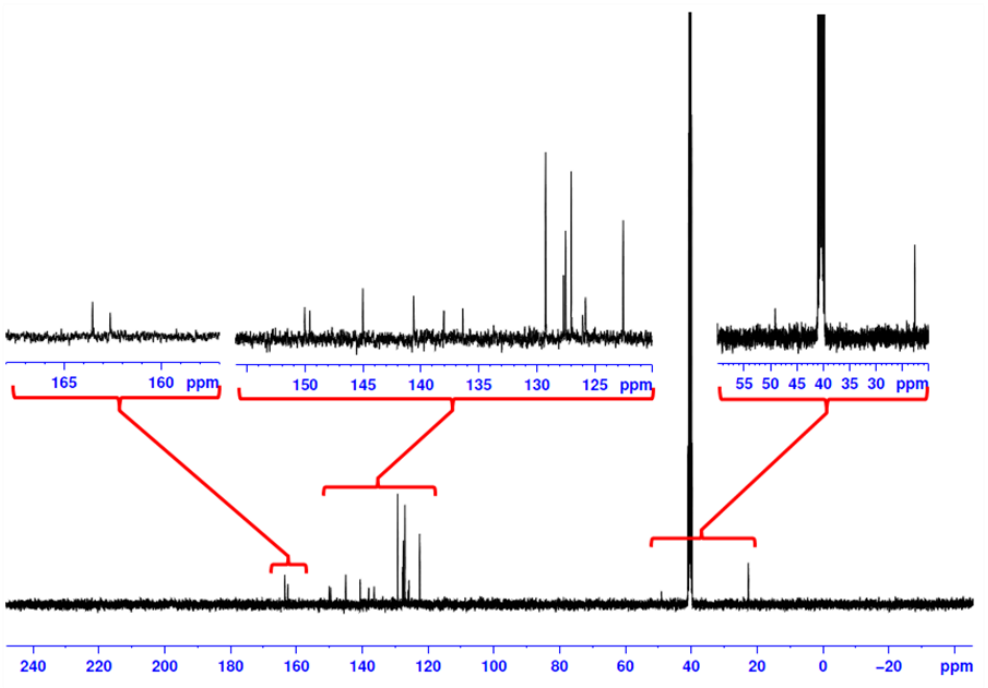

Figure S2a-34. ^{13}C NMR spectrum of **L1^{RR}** in $(CD_3)_2SO$. The insets show the expansion of the corresponding region as indicated.

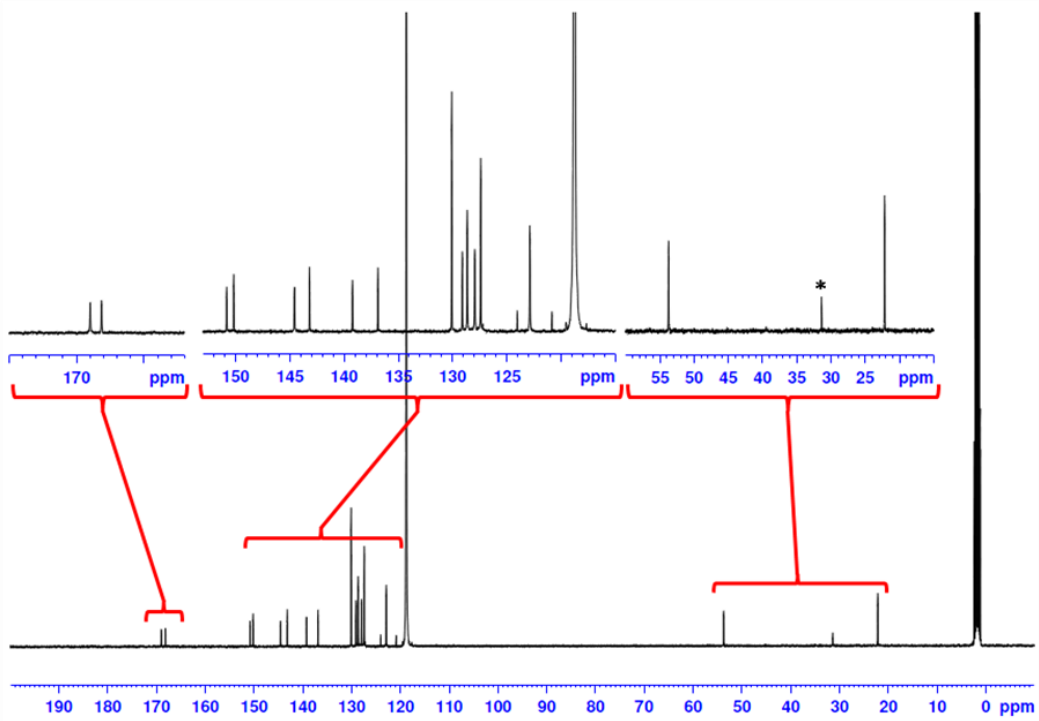

Figure S2a-35. ^{13}C NMR spectrum of **$[La_2(L1^{SS})_3](CF_3SO_3)_6$** in CD_3CN. The insets show the expansion of the corresponding region as indicated. The chemical shift with an asteroid is not very clear. It was shown to correlate a chemical shift at 2.10 ppm (singlet) in the corresponding ^1H NMR spectrum in HSQC experiment.

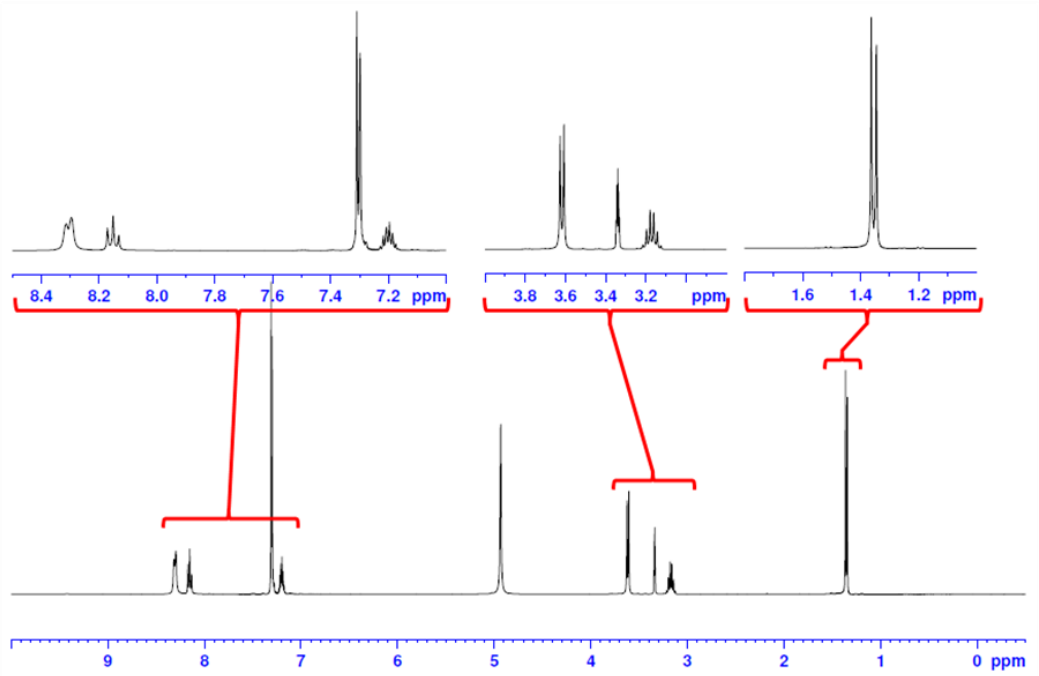

Figure S2a-36. ^1H NMR spectrum of **(*S*)-6-(2-phenylpropyl carbamoyl)picolinic acid** in CD_3OD. The insets show the expansion of the corresponding region as indicated.

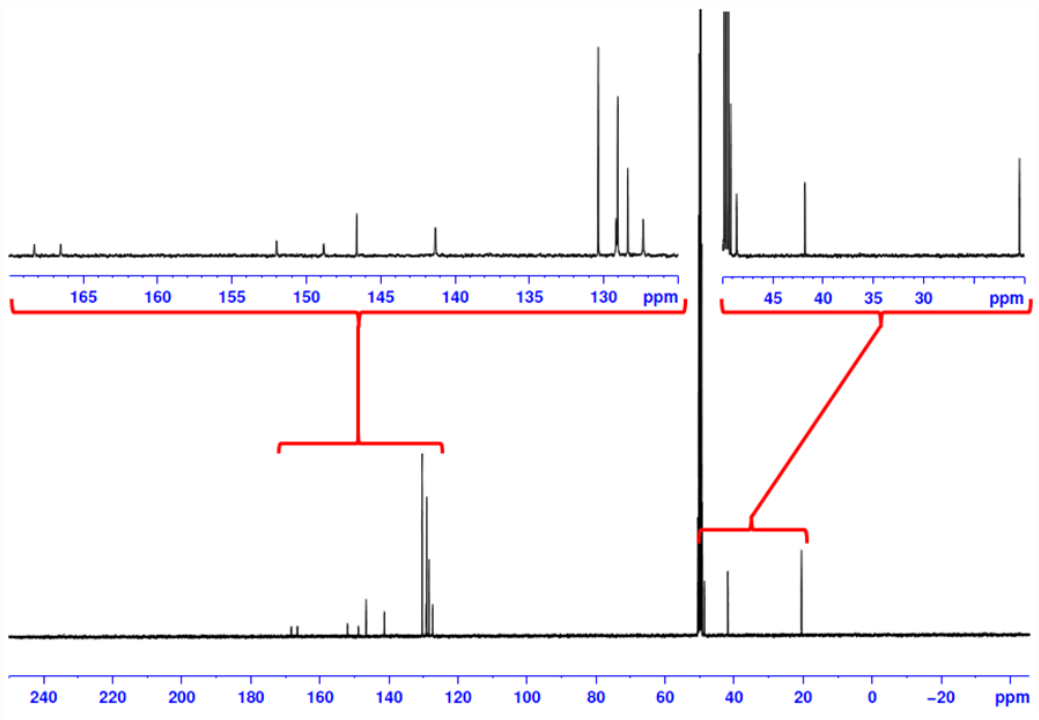

Figure S2a-37. ^{13}C NMR spectrum of **(*S*)-6-(2-phenylpropyl carbamoyl)picolinic acid** in CD_3OD. The insets show the expansion of the corresponding region as indicated.

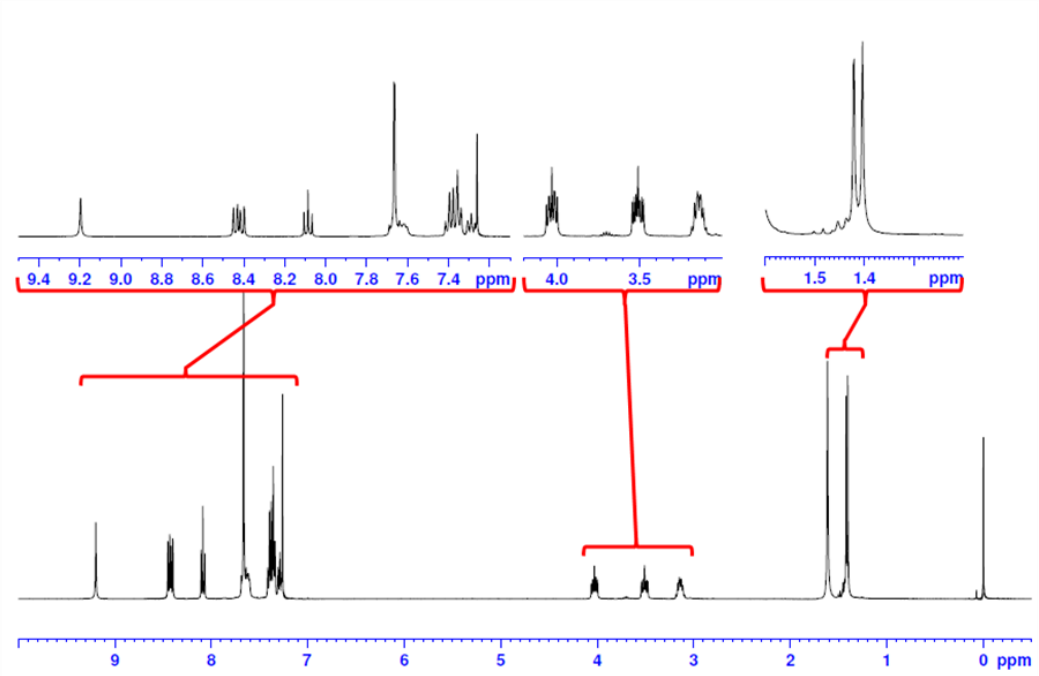

Figure S2a-38. ^{1}H NMR spectrum of **L2^{RR}** in $CDCl_3$. The insets show the expansion of the corresponding region as indicated.

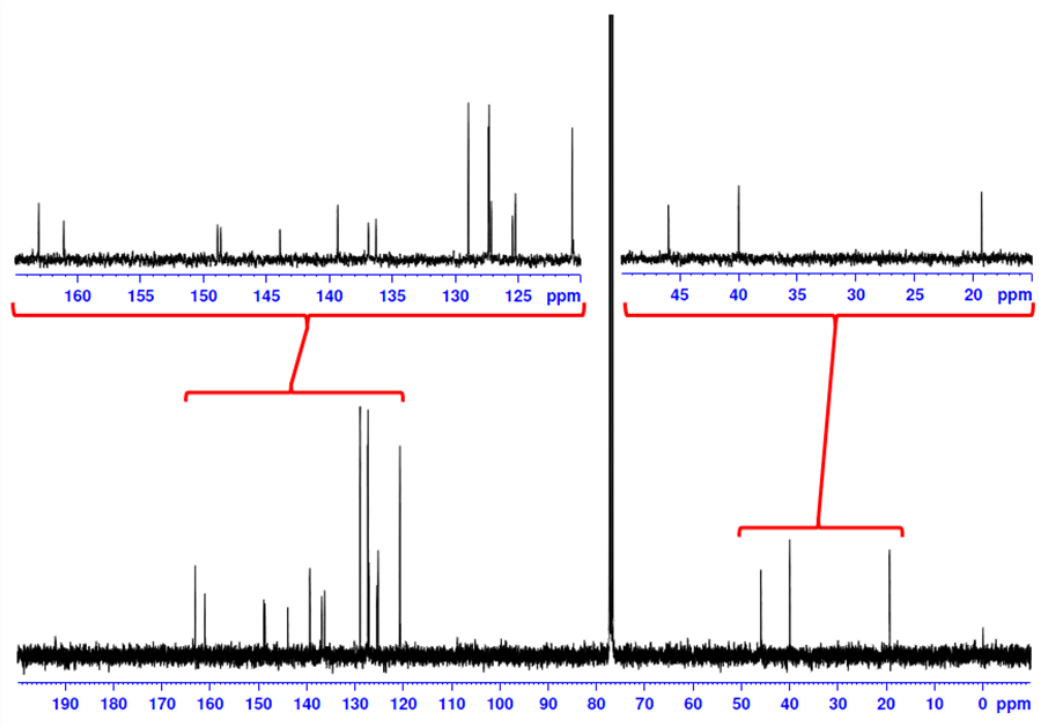

Figure S2a-39. ^{13}C NMR spectrum of **L2^{RR}** in $CDCl_3$. The insets show the expansion of the corresponding region as indicated.

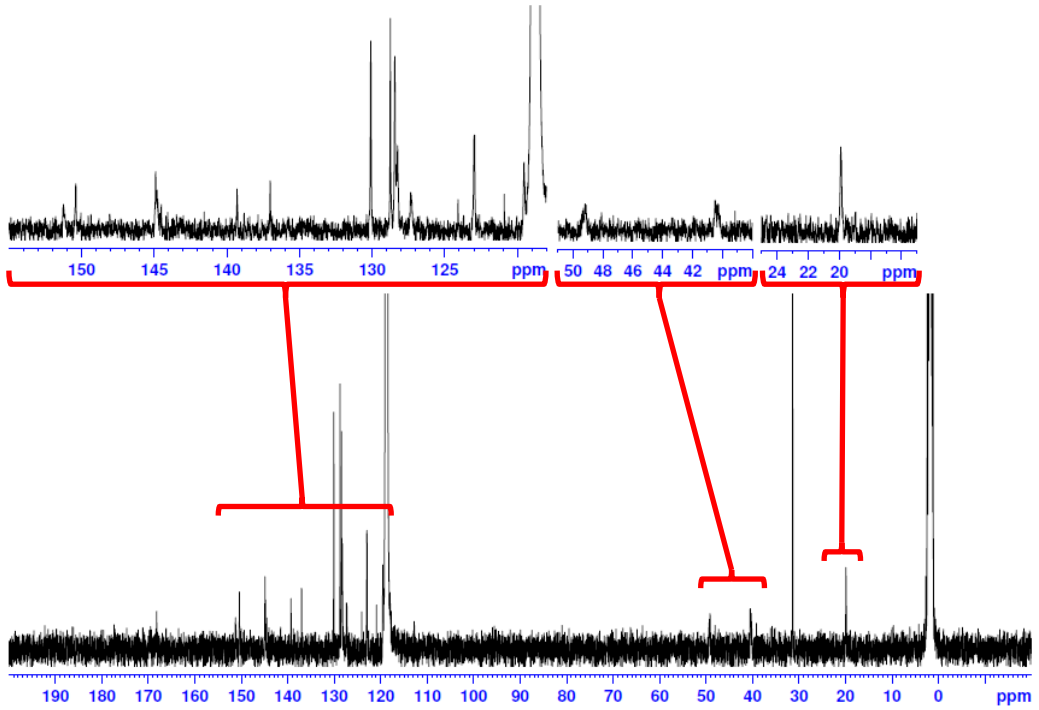

Figure S2a-40. ^{13}C NMR spectrum of **[La$_2$(L2^{RR})$_3$](CF$_3$SO$_3$)$_6$** in CD_3CN. The insets show the expansion of the corresponding region as indicated.

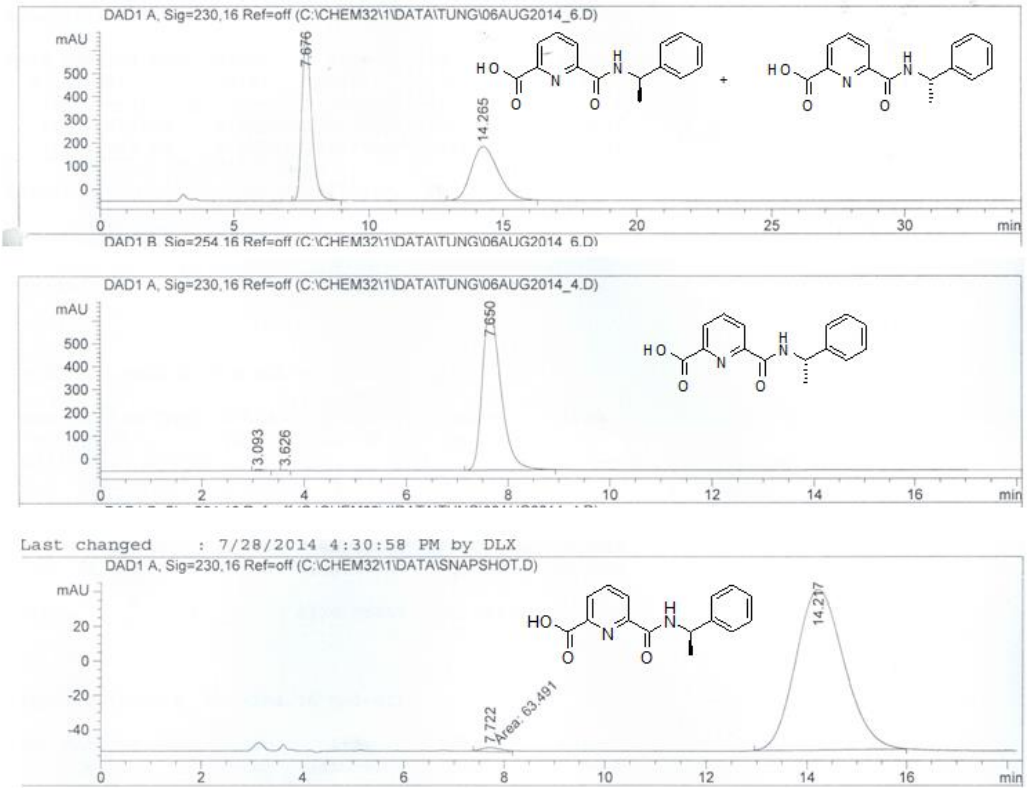

Figure S2a-41. HPLC spectra of **(*S*)-6-(1-phenylethyl carbamoyl)picolinic acid** and **(*R*)-6-(1-phenylethylcarbamoyl)picolinic acid.**

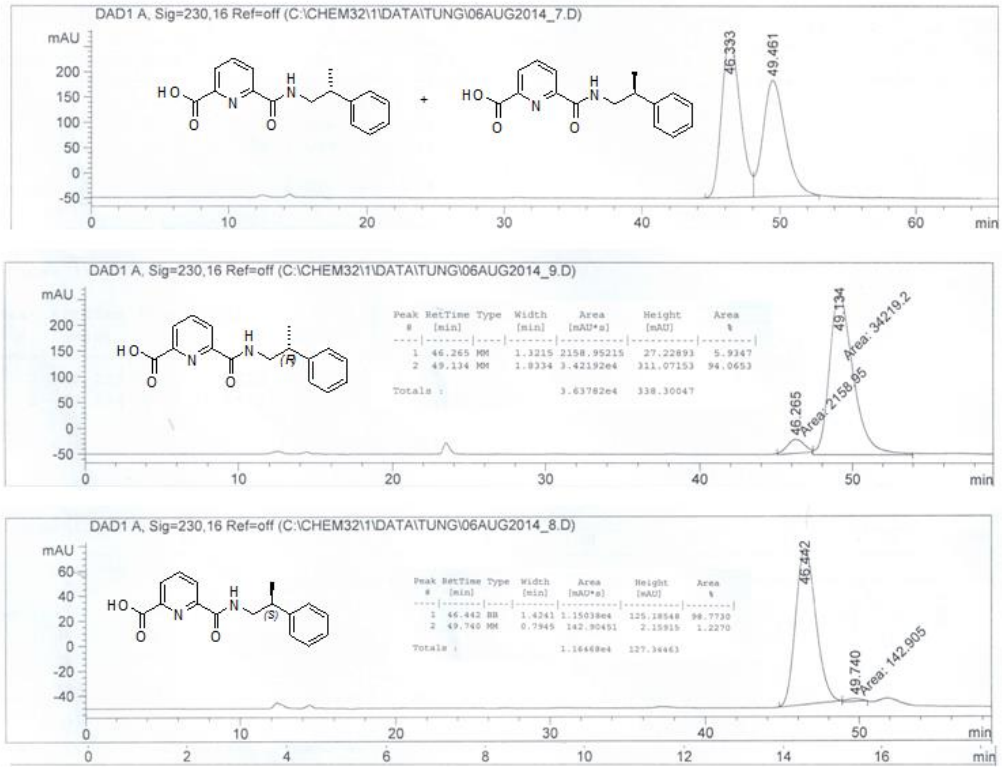

Figure S2a-42. HPLC spectra of **or (*S*)-6-(2-phenylpropyl carbamoyl)picolinic acid** and **(*R*)-6-(2-phenylpropylcarbamoyl)picolinic acid.**

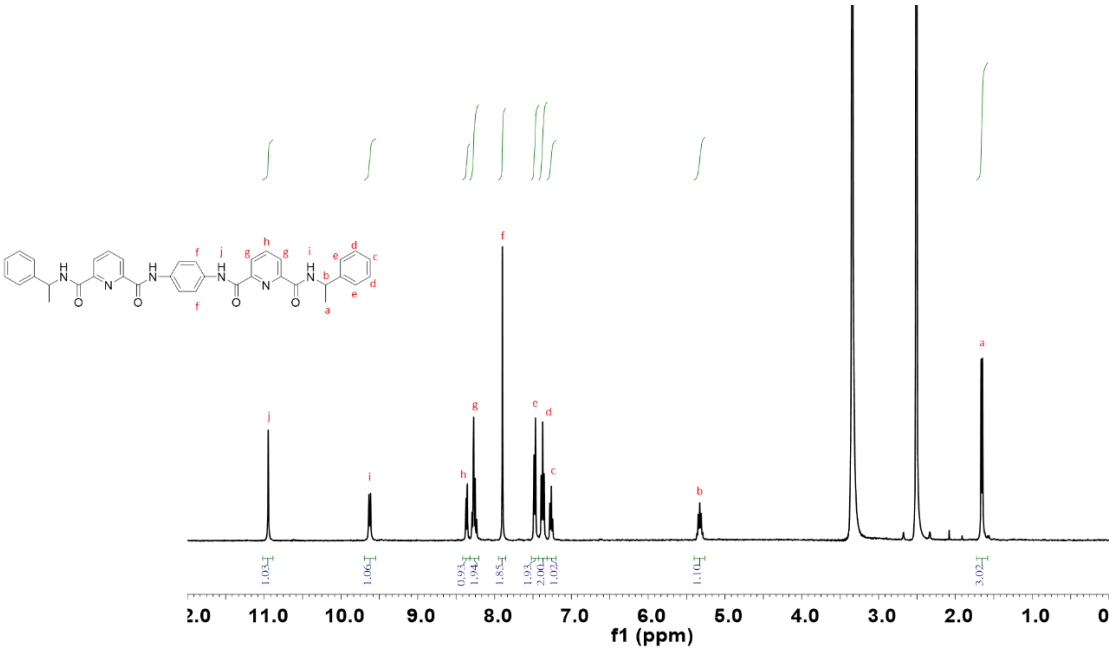

Figure S2b-1. ^{1}H NMR of **L3^{SS}** in $(CD_3)_2SO$.

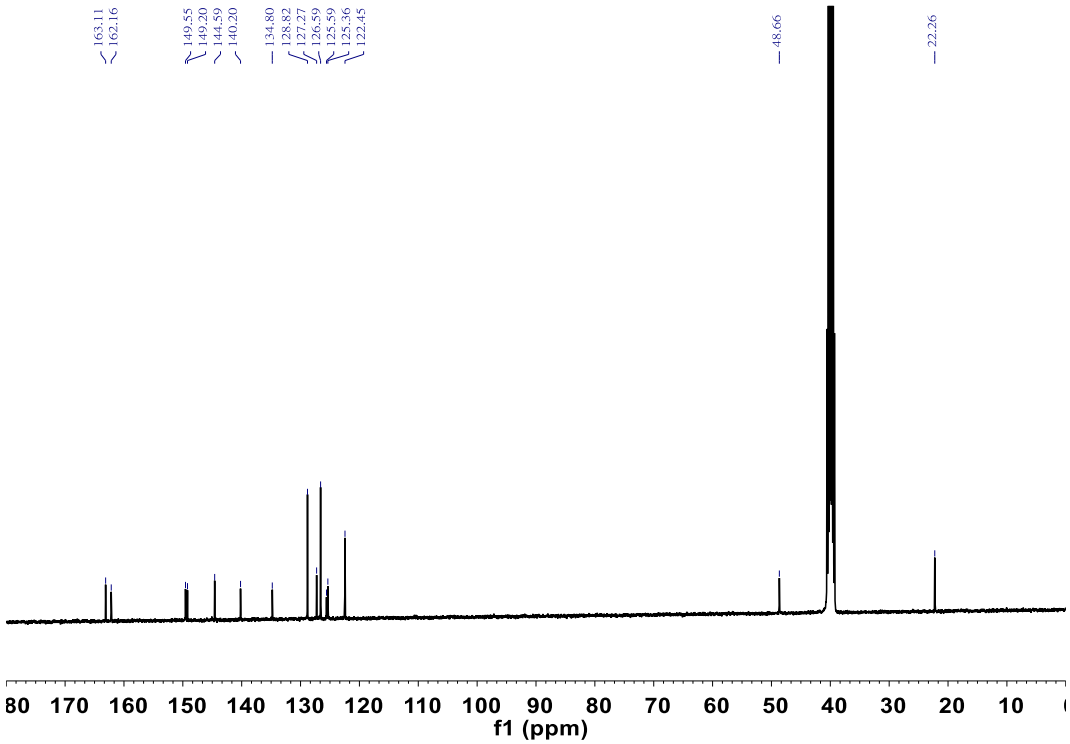

Figure S2b-2. ^{13}C NMR of **L3^{SS}** in $(CD_3)_2SO$.

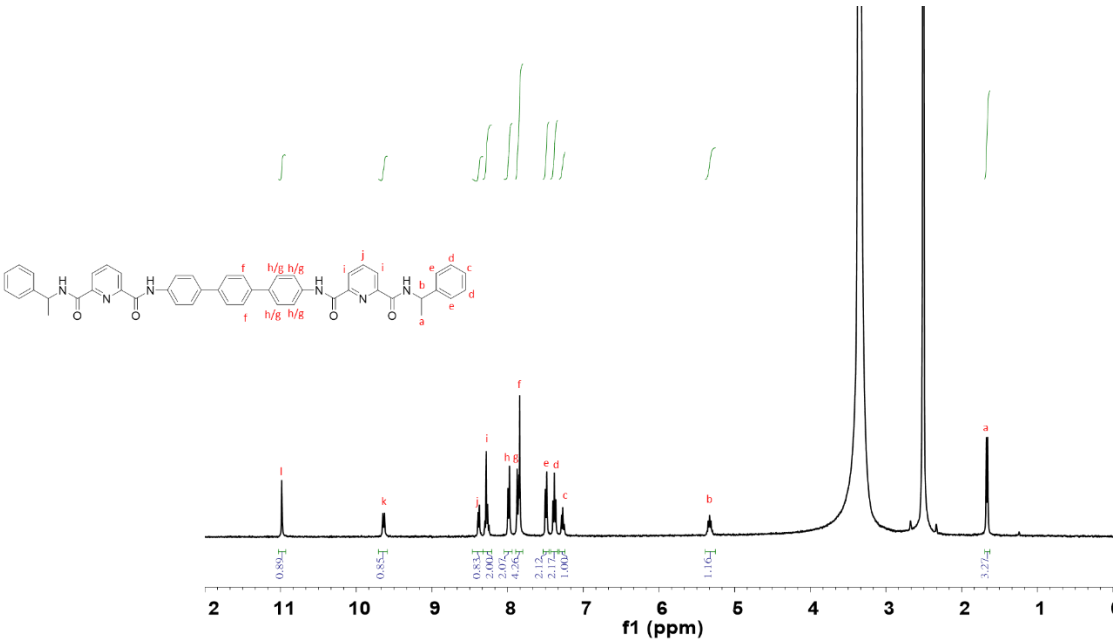

Figure S2b-3. ^{1}H NMR of **L4^{RR}** in $(CD_3)_2SO$.

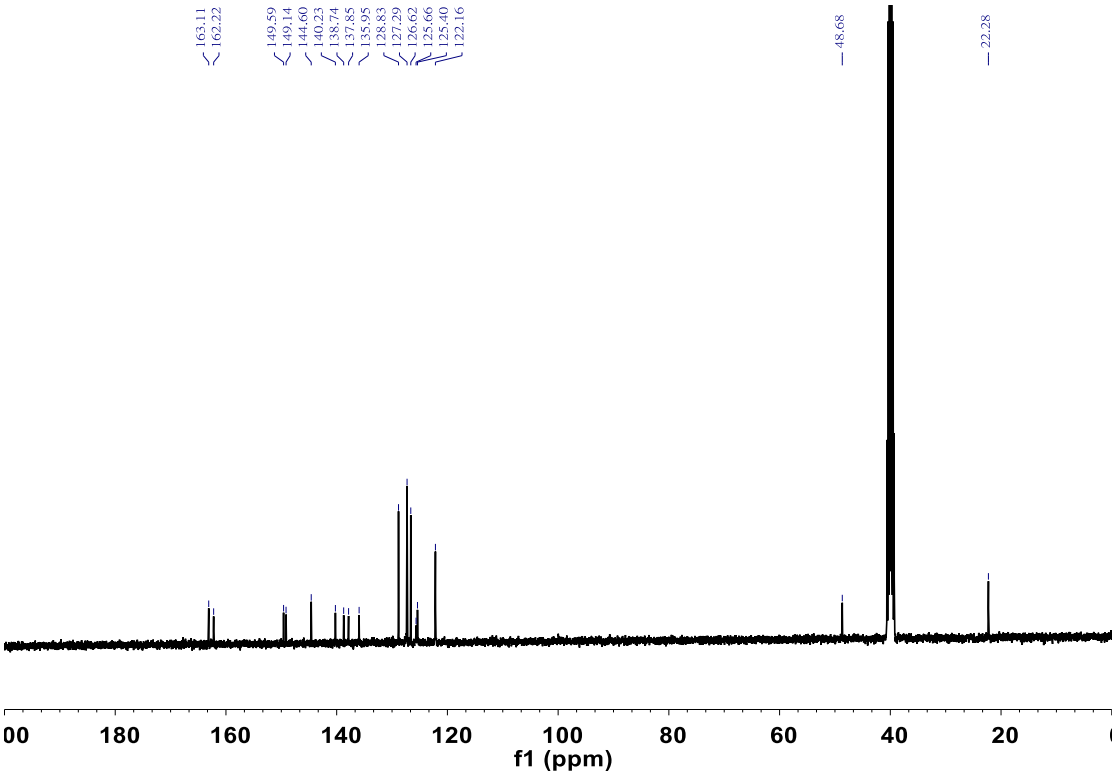

Figure S2b-4. ^{13}C NMR of **L4^{RR}** in $(CD_3)_2SO$.

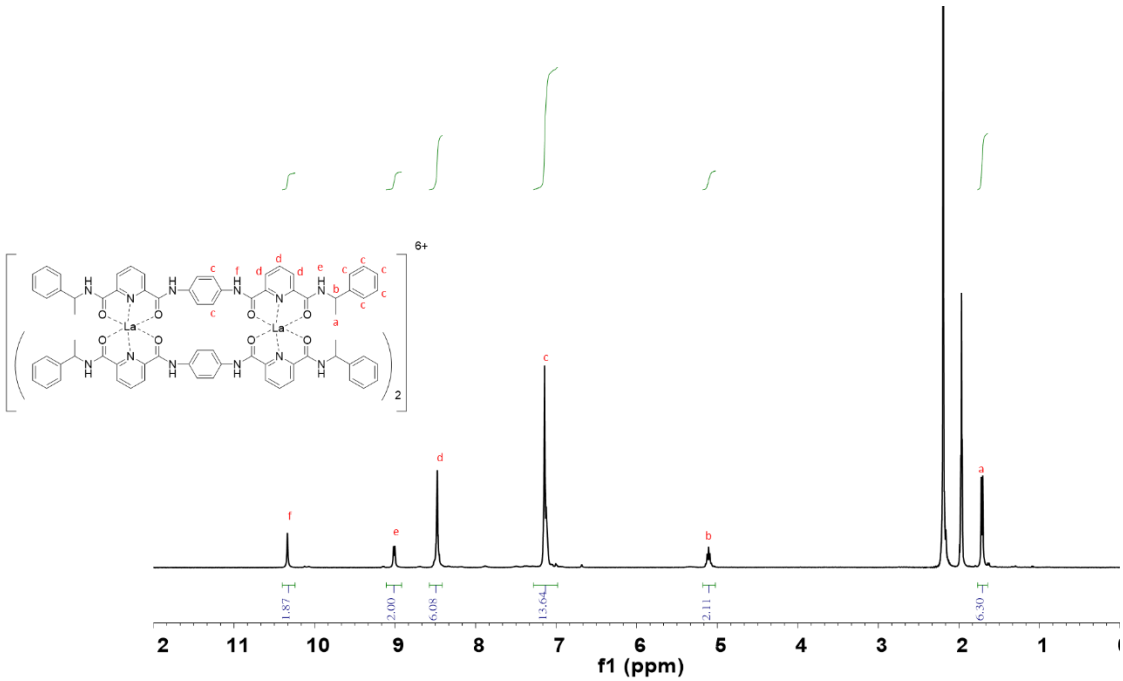

Figure S2b-5. ^{1}H NMR of $[La_2(\mathbf{L3^{SS}})_3]$ in CD_3CN.

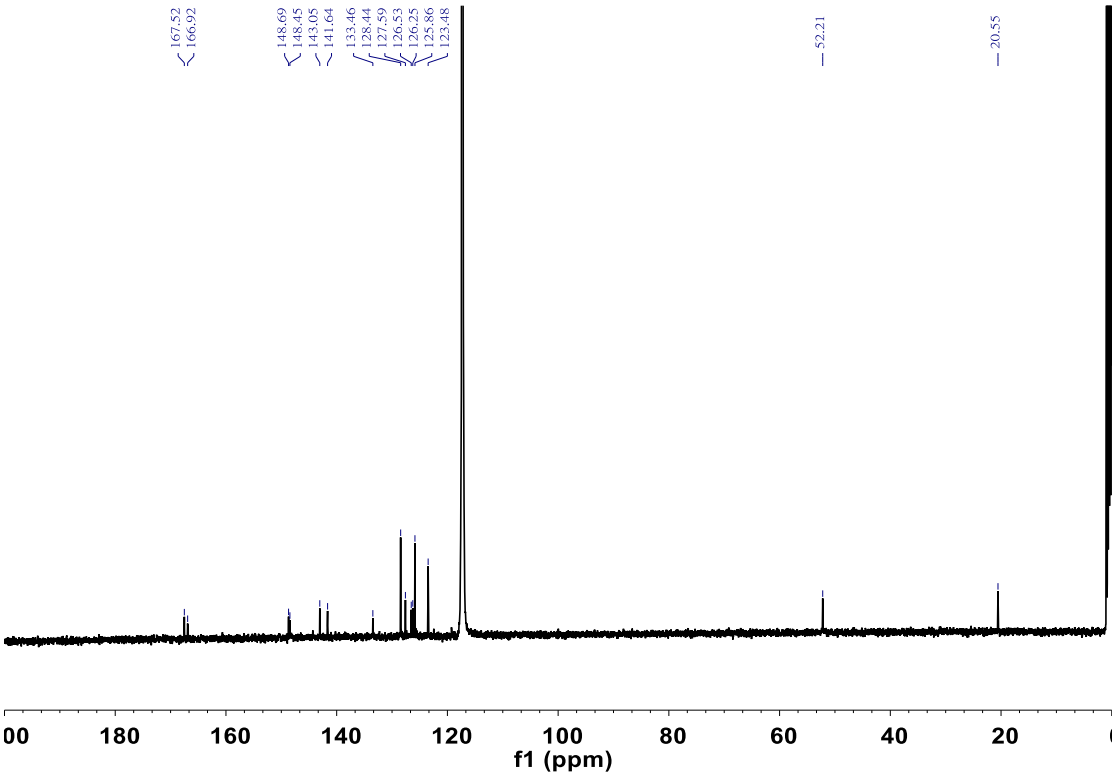

Figure S2b-6. ^{13}C NMR of $[La_2(\mathbf{L3^{SS}})_3]$ in CD_3CN.

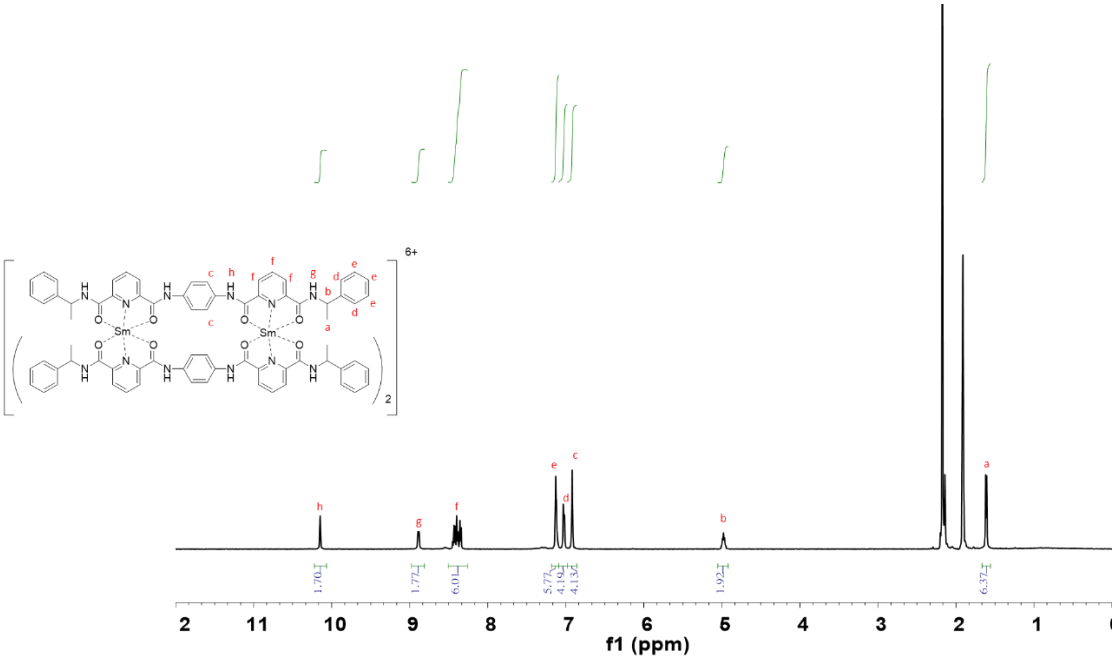

Figure S2b-7. ^{1}H NMR of [Sm_2(**L3^{RR}**)$_3$] in CD_3CN.

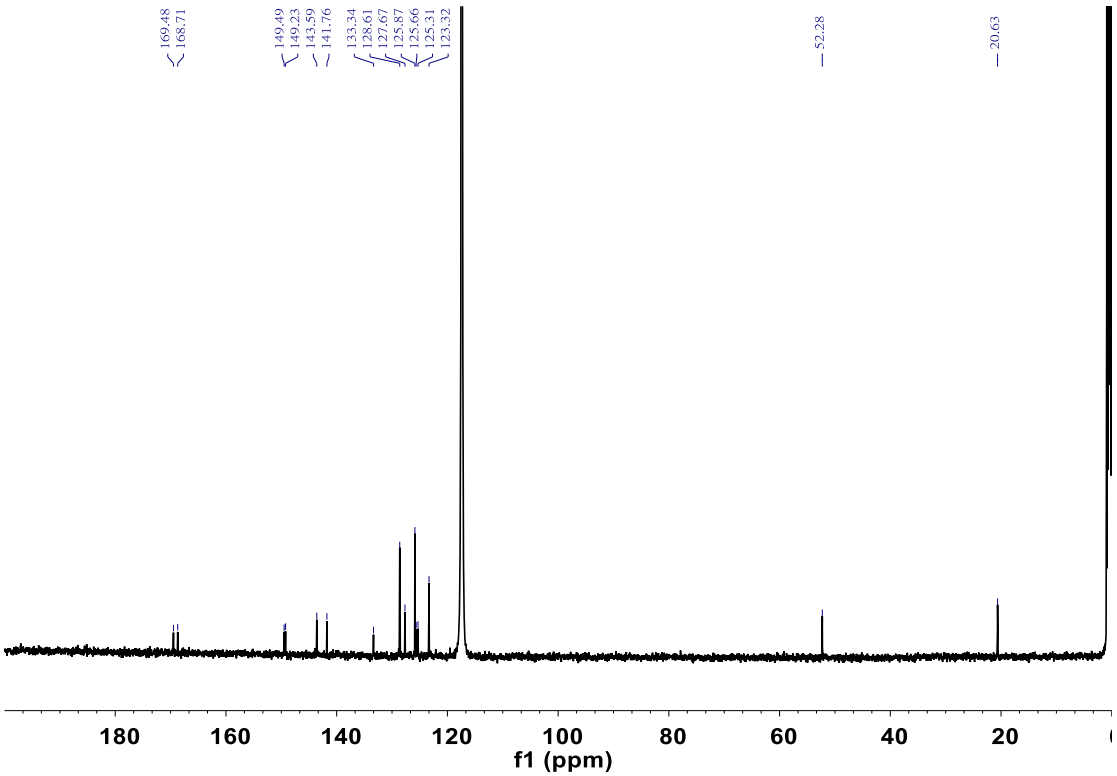

Figure S2b-8. ^{13}C NMR of [Sm_2(**L3^{RR}**)$_3$] in CD_3CN.

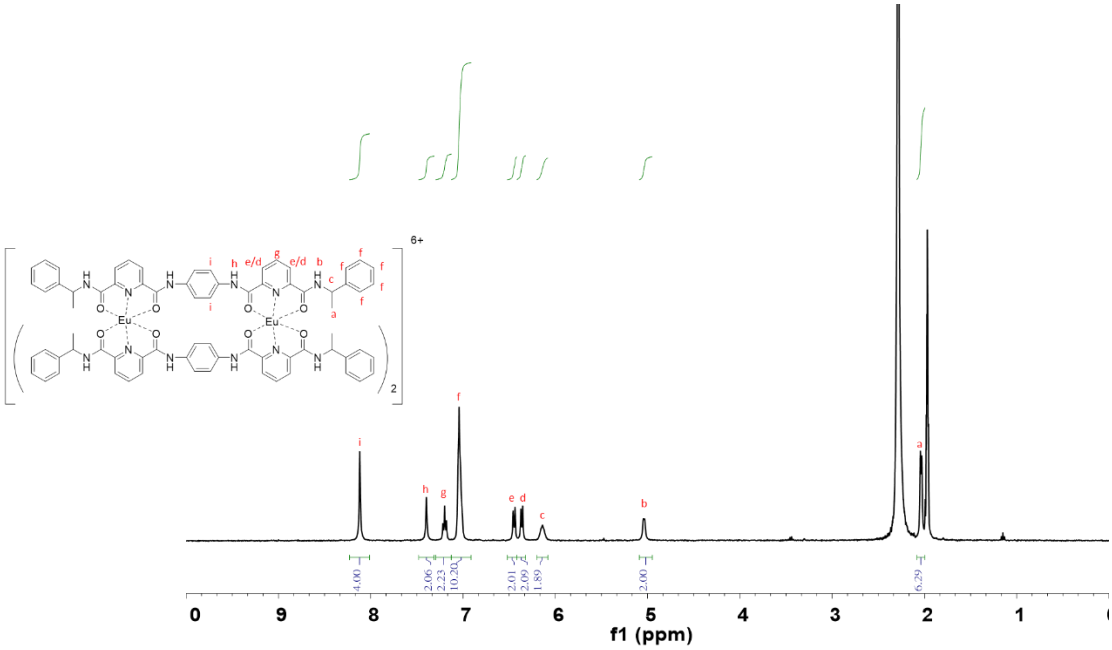

Figure S2b-9. ^{1}H NMR of [Eu_2(**L3^{SS}**)$_3$] in CD_3CN.

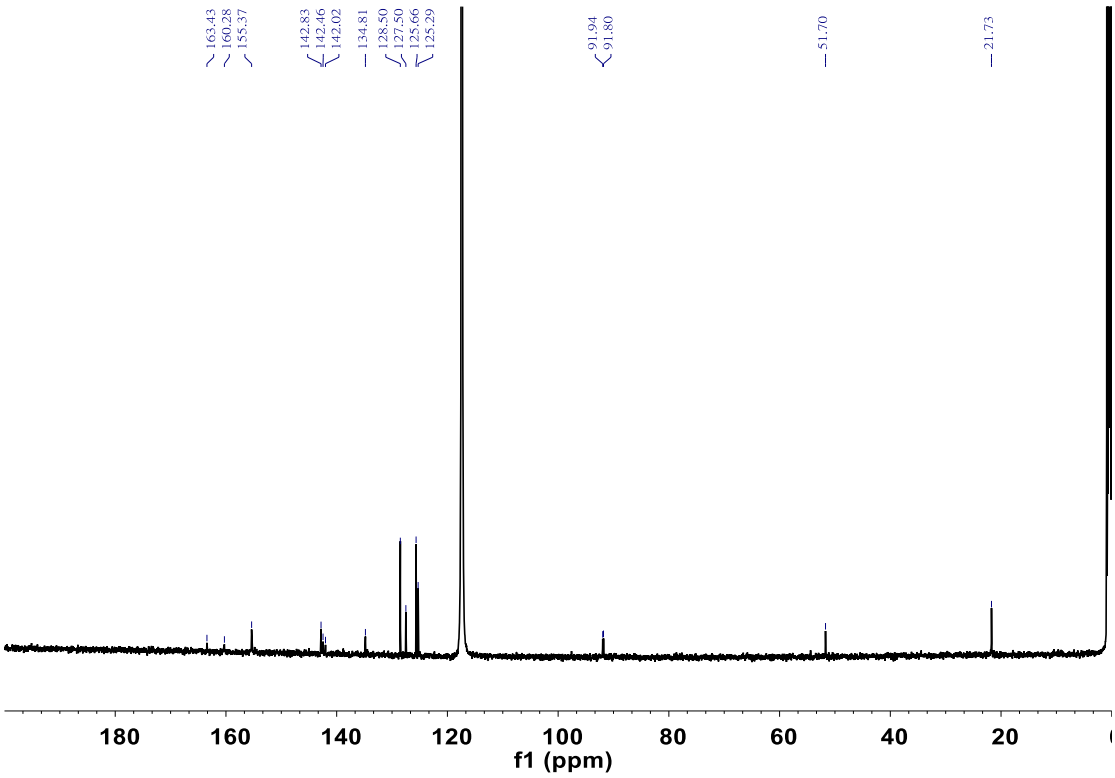

Figure S2b-10. ^{13}C NMR of [Eu_2(**L3^{RR}**)$_3$] in CD_3CN.

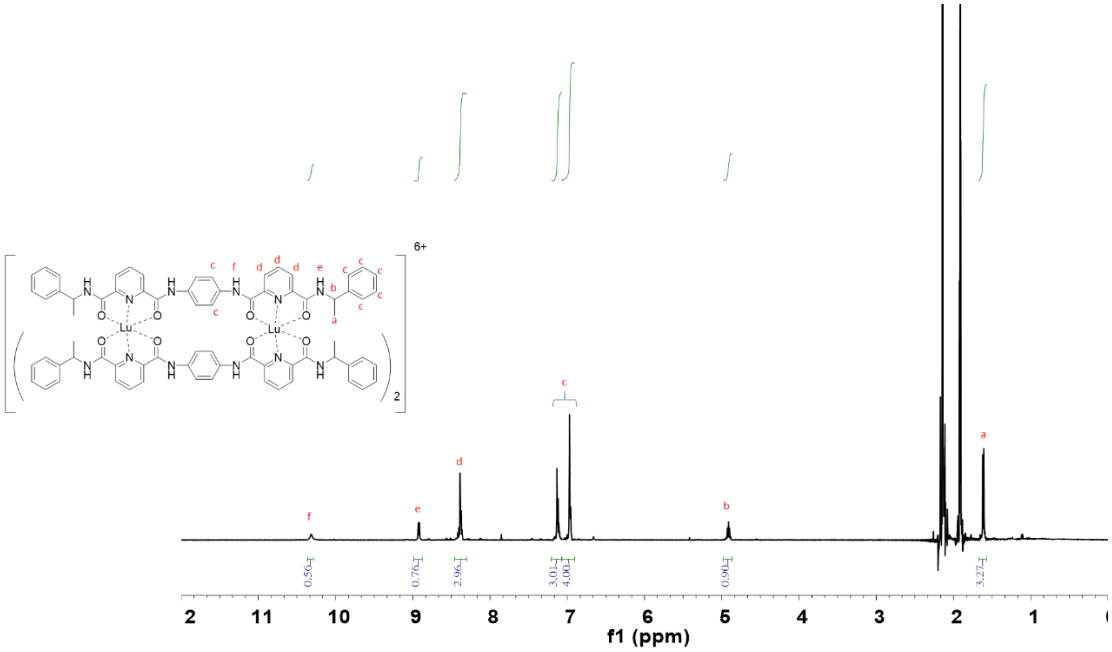

Figure S2b-11. ^{1}H NMR of [Lu_2(**L3^{RR}**)$_3$] in CD_3CN.

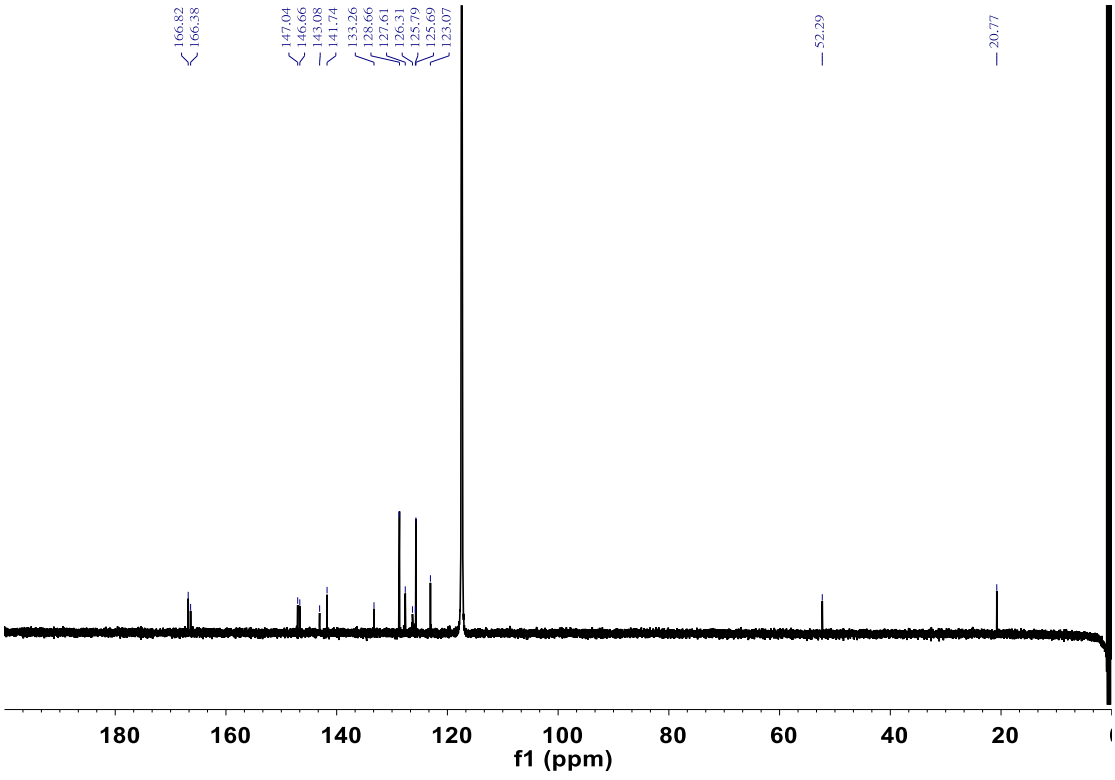

Figure S2b-12. ^{13}C NMR of [Lu_2(**L3^{SS}**)$_3$] in CD_3CN.

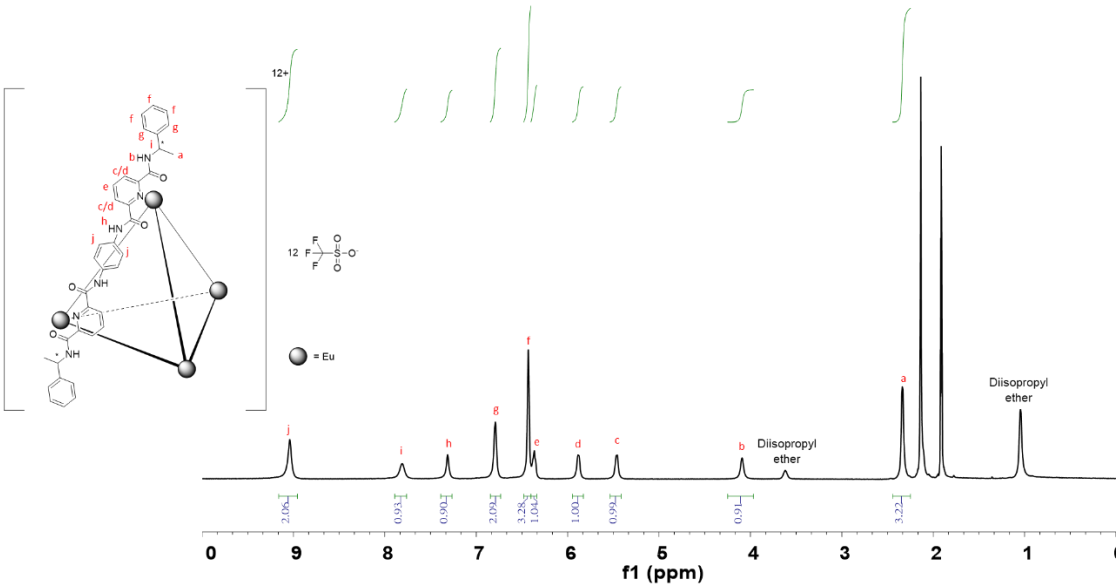

Figure S2b-13. ^{1}H NMR of [Eu_4(**L3^{SS}**)$_6$] in CD_3CN.

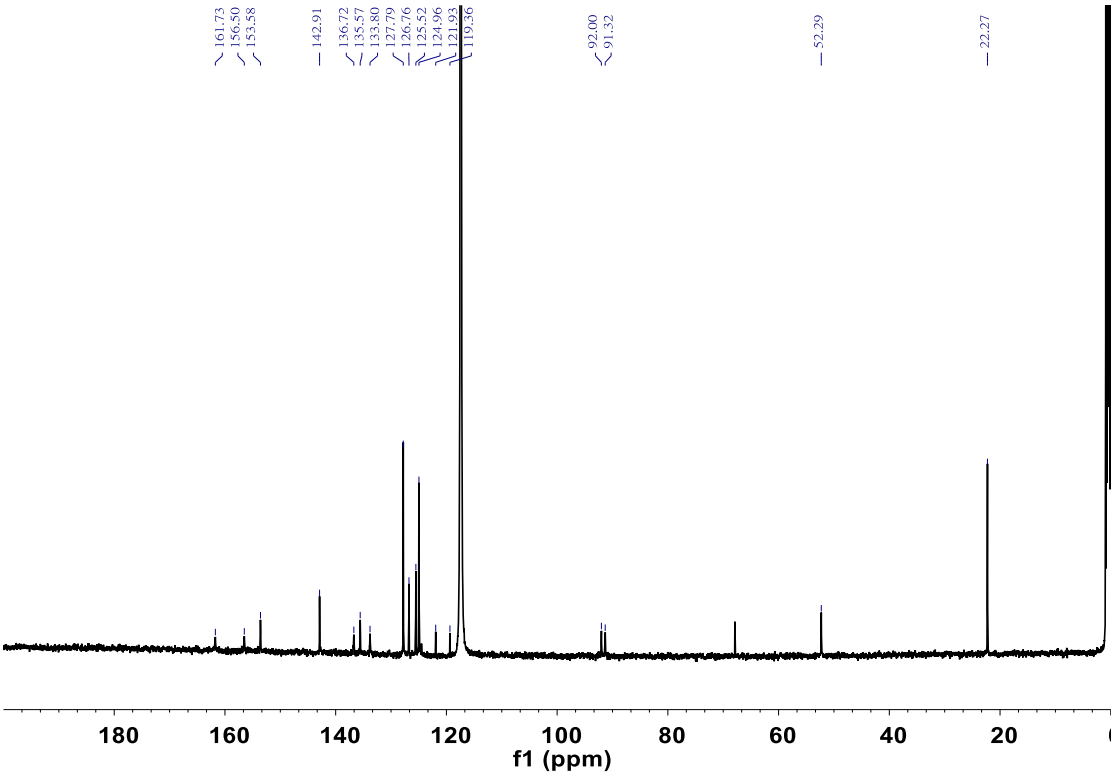

Figure S2b-14. ^{13}C NMR of [Eu_4(**L3^{SS}**)$_6$] in CD_3CN.

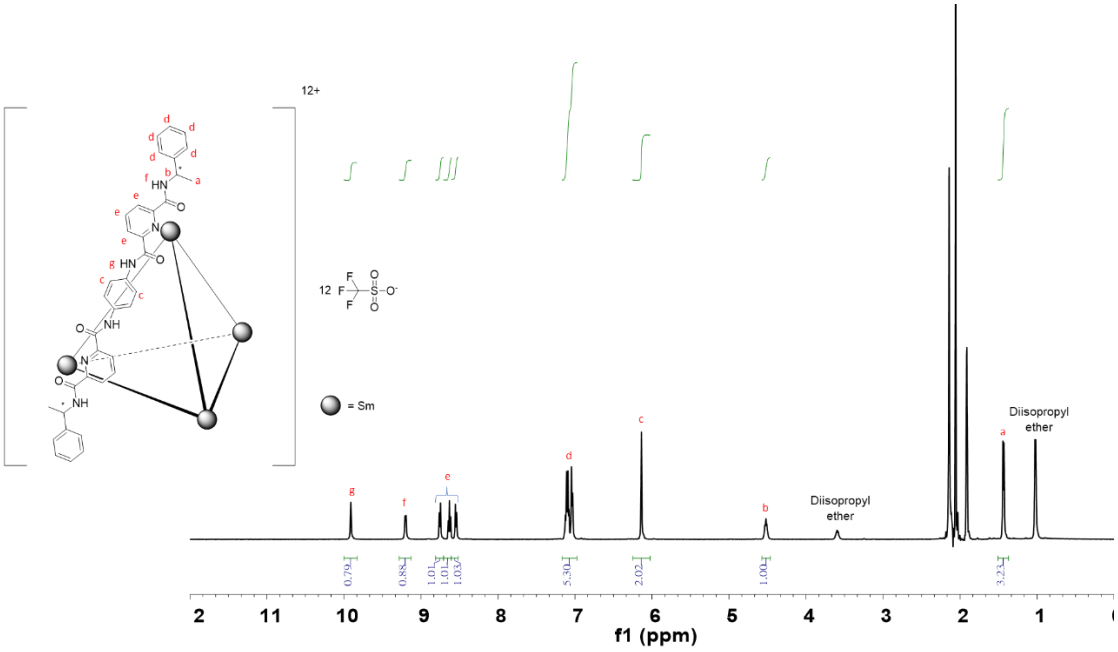

Figure S2b-15. ^{1}H NMR of [Sm_4(**L3^{SS}**)$_6$] in CD_3CN.

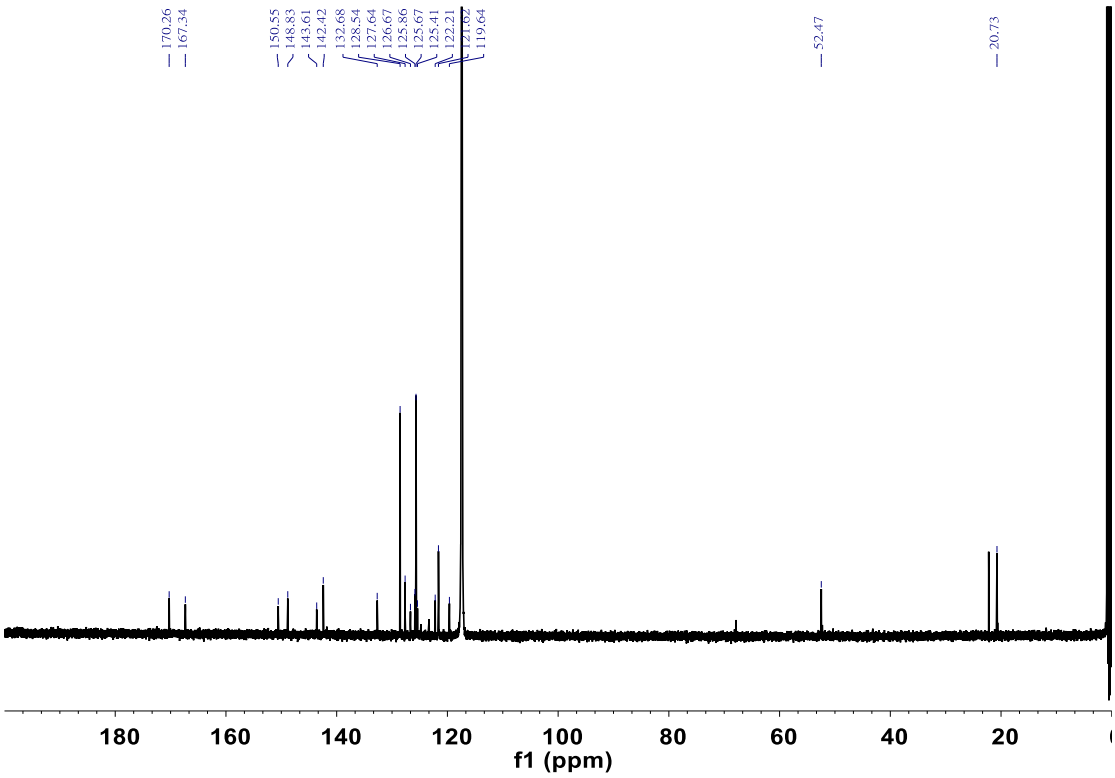

Figure S2b-16. ^{13}C NMR of [Sm_4(**L3^{RR}**)$_6$] in CD_3CN.

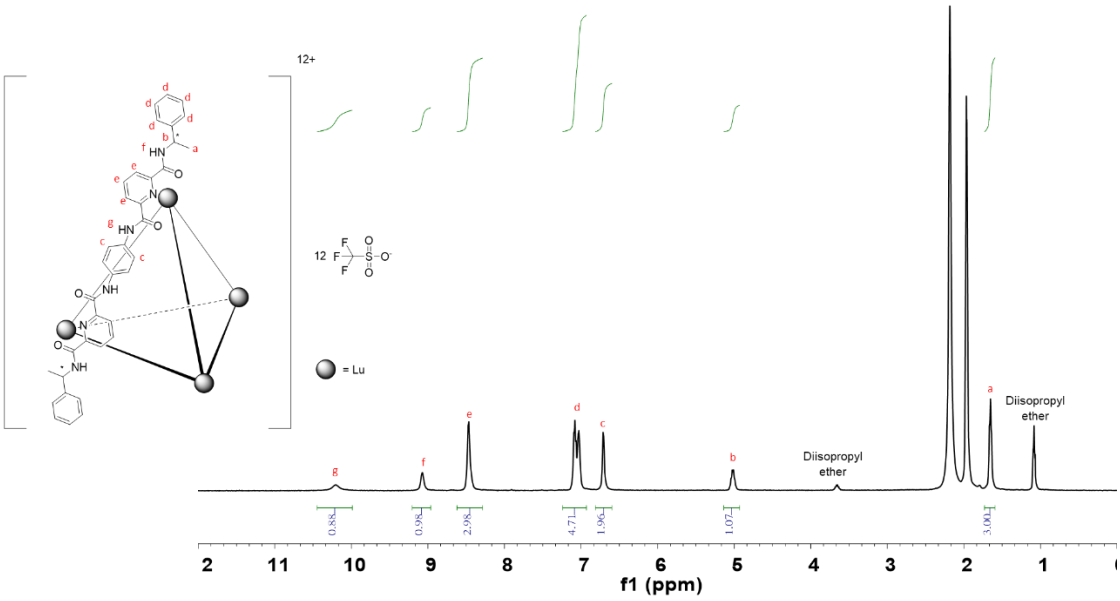

Figure S2b-17. ^{1}H NMR of [Lu_4(**L3^{SS}**)$_6$] in CD_3CN.

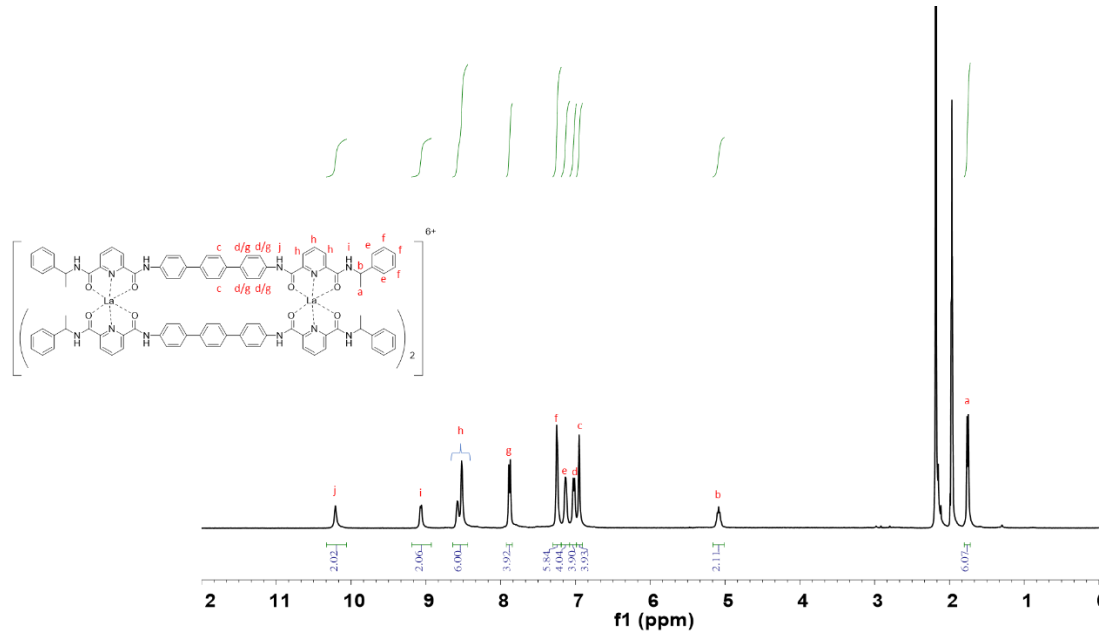

Figure S2b-18. ^{1}H NMR of [La_2(**L4^{SS}**)$_3$] in CD_3CN.

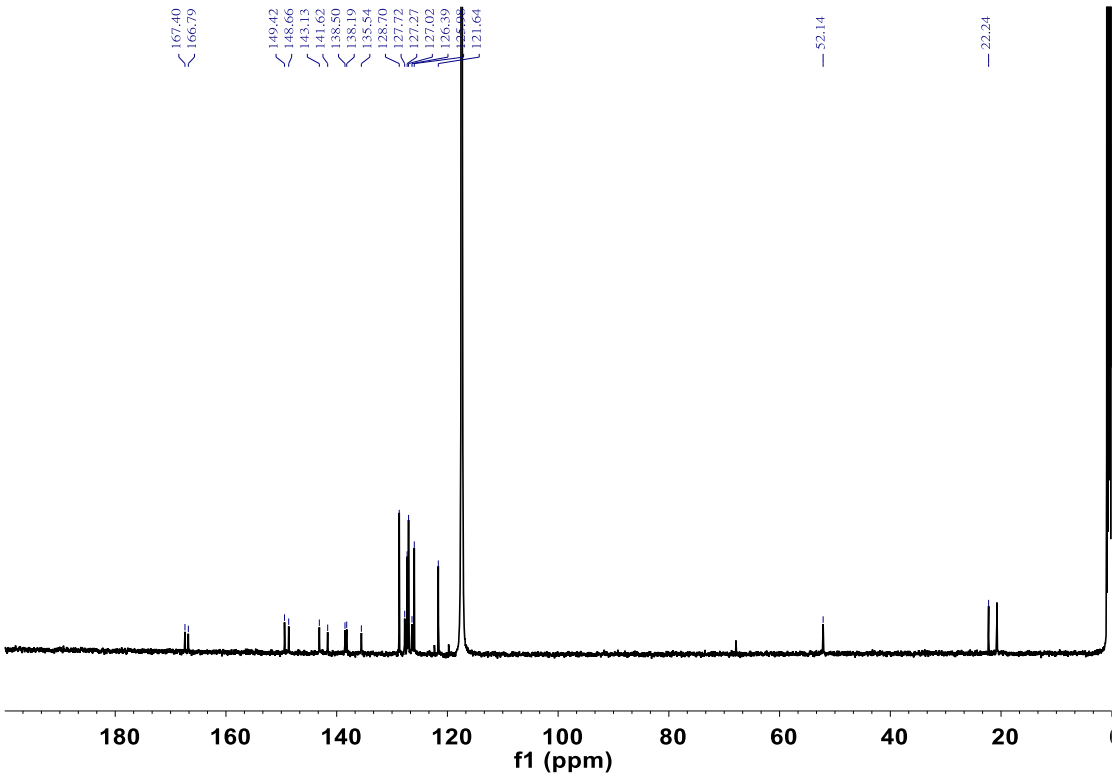

Figure S2b-19. ^{13}C NMR of $[La_2(\mathbf{L4^{RR}})_3]$ in CD_3CN.

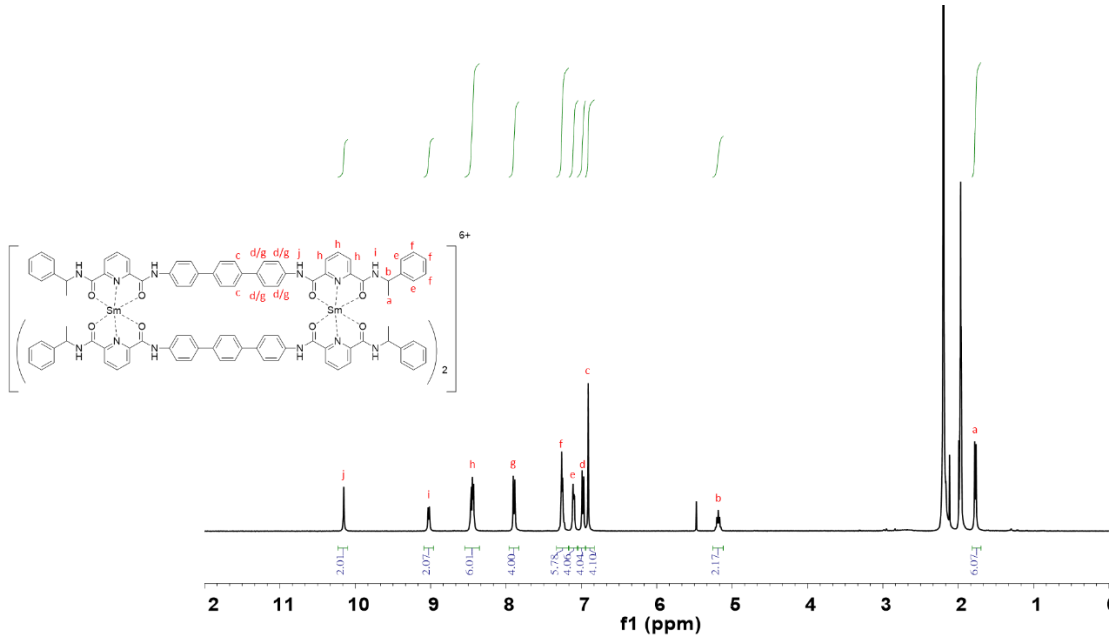

Figure S2b-20. ^{1}H NMR of $[Sm_2(\mathbf{L4^{SS}})_3]$ in CD_3CN.

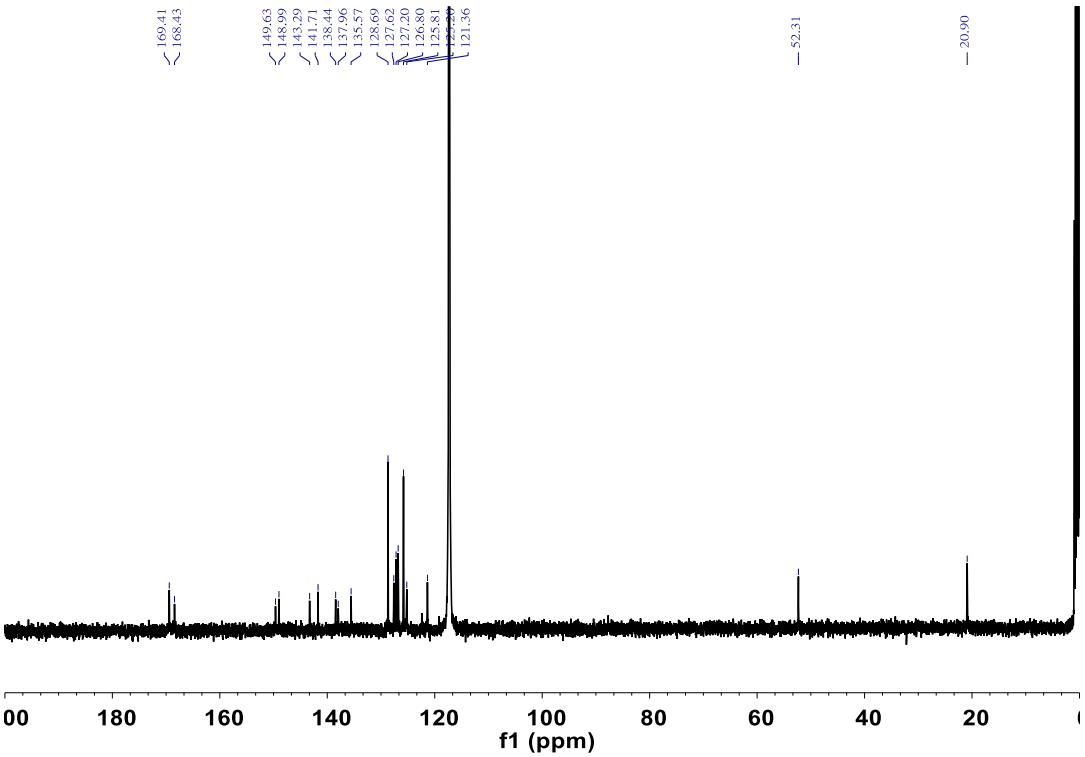

Figure S2b-21. ^{13}C NMR of $[Sm_2(\mathbf{L4^{SS}})_3]$ in CD_3CN.

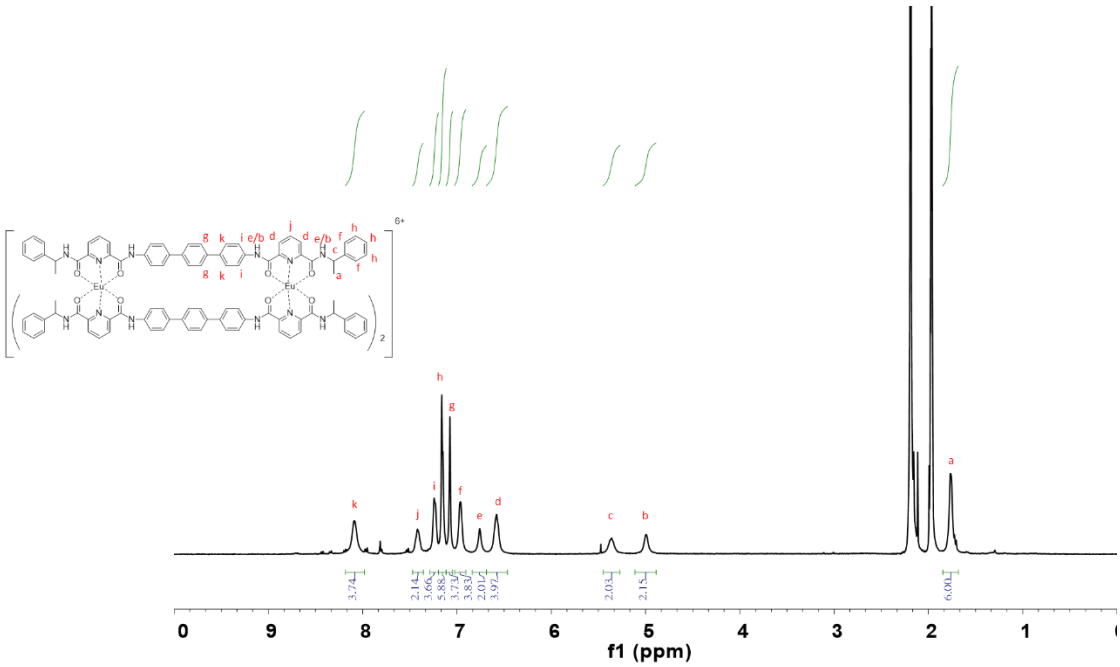

Figure S2b-22. ^{1}H NMR of $[Eu_2(\mathbf{L4^{SS}})_3]$ in CD_3CN.

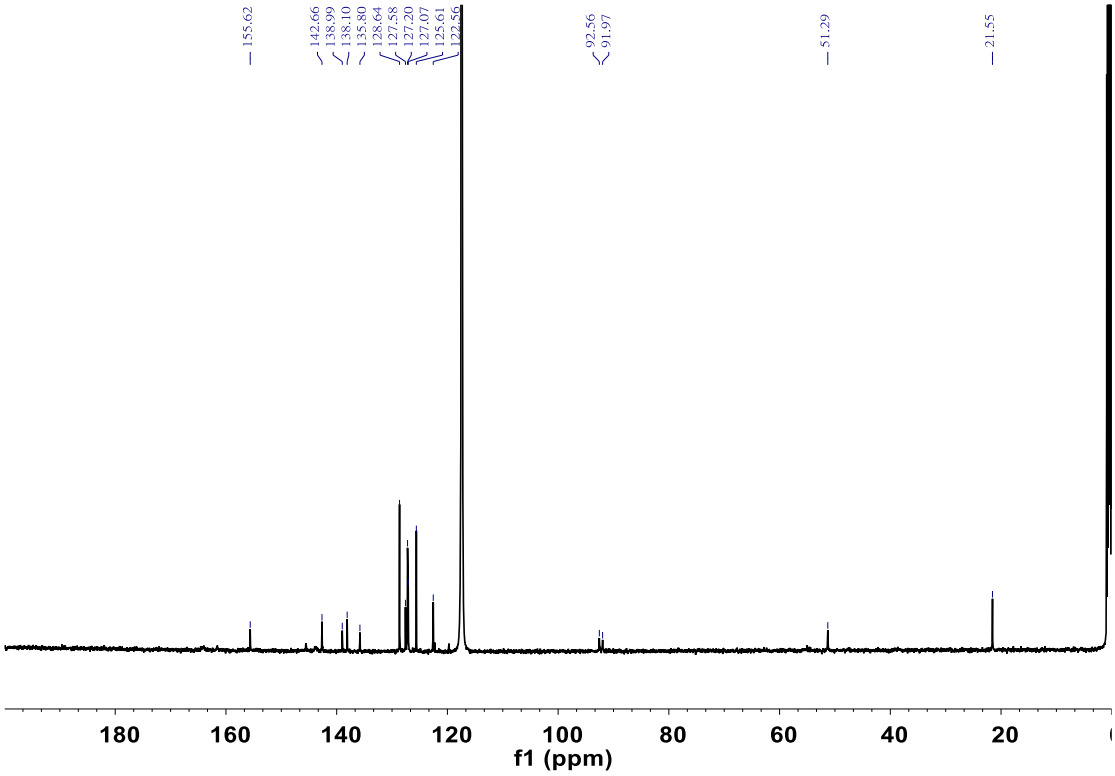

Figure S2b-23. ^{13}C NMR of $[Eu_2(\mathbf{L4^{RR}})_3]$ in CD_3CN.

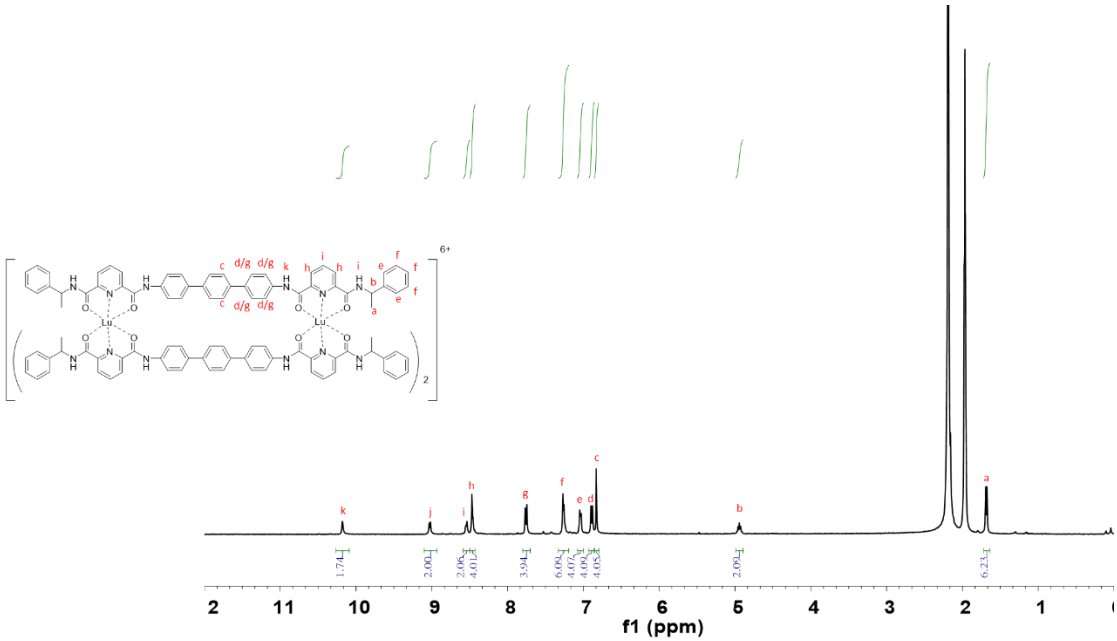

Figure S2b-24. ^{1}H NMR of $[Lu_2(\mathbf{L4^{RR}})_3]$ in CD_3CN.

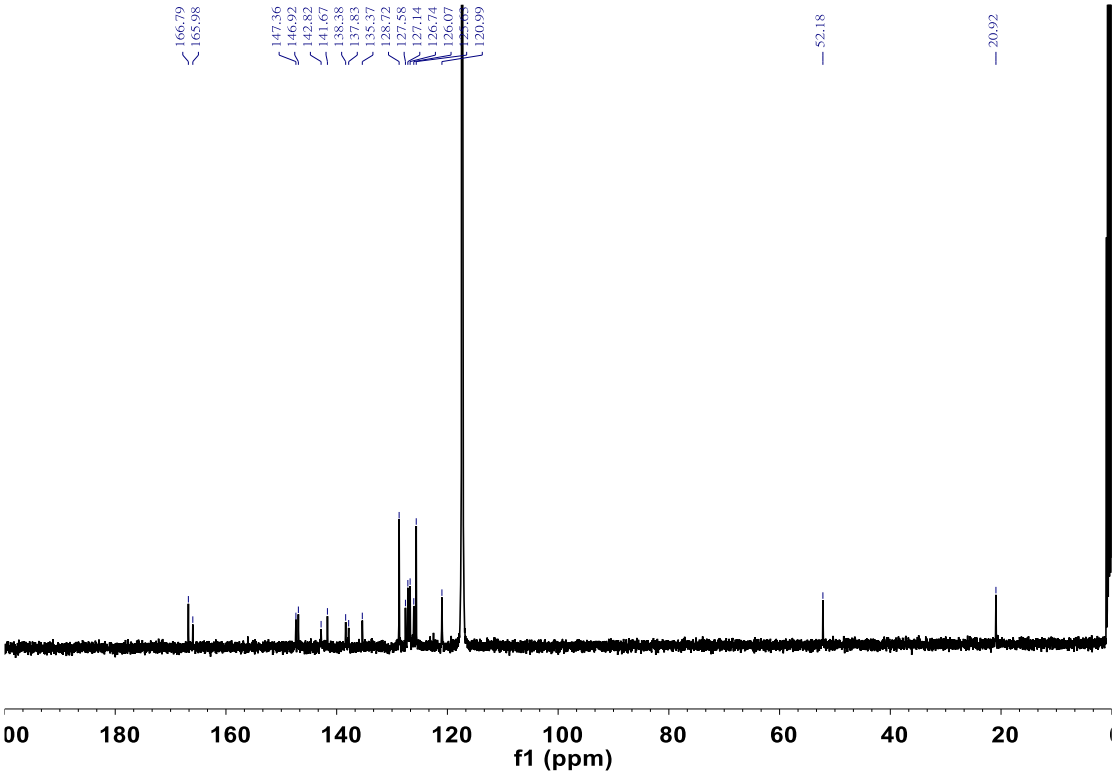

Figure S2b-25. ^{13}C NMR of $[Lu_2(\mathbf{L4^{RR}})_3]$ in CD_3CN.

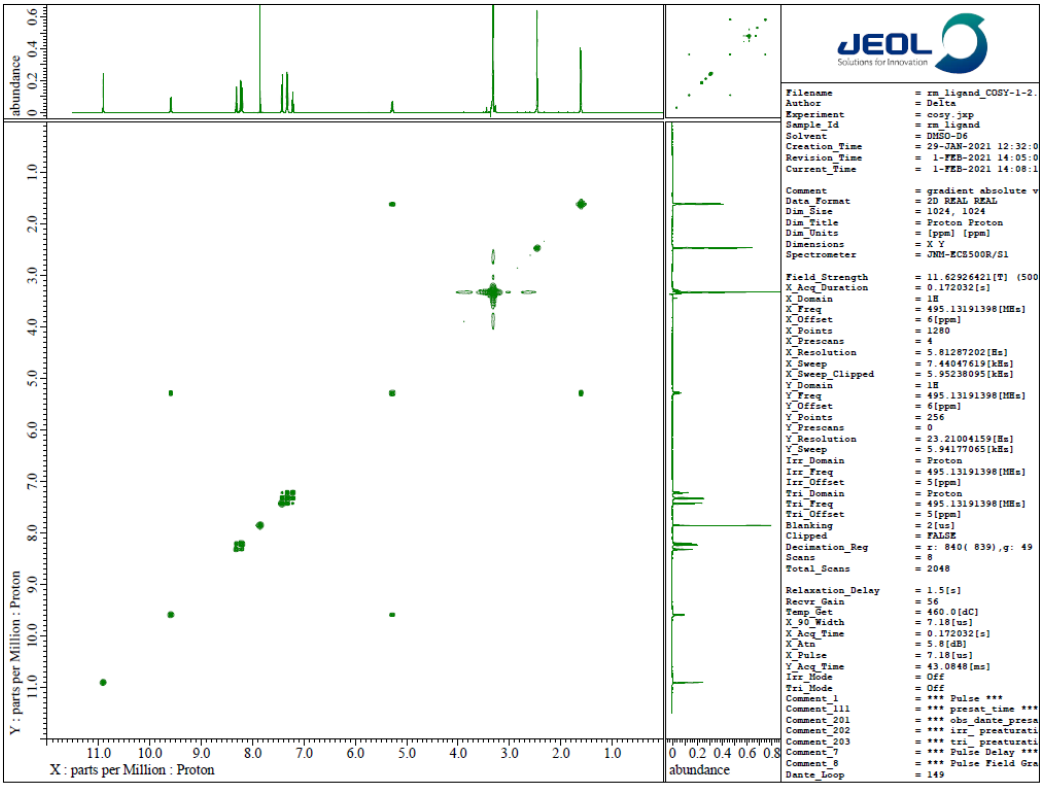

Figure S2b-26. COSY NMR of **L3** in $(CD_3)_2SO$.

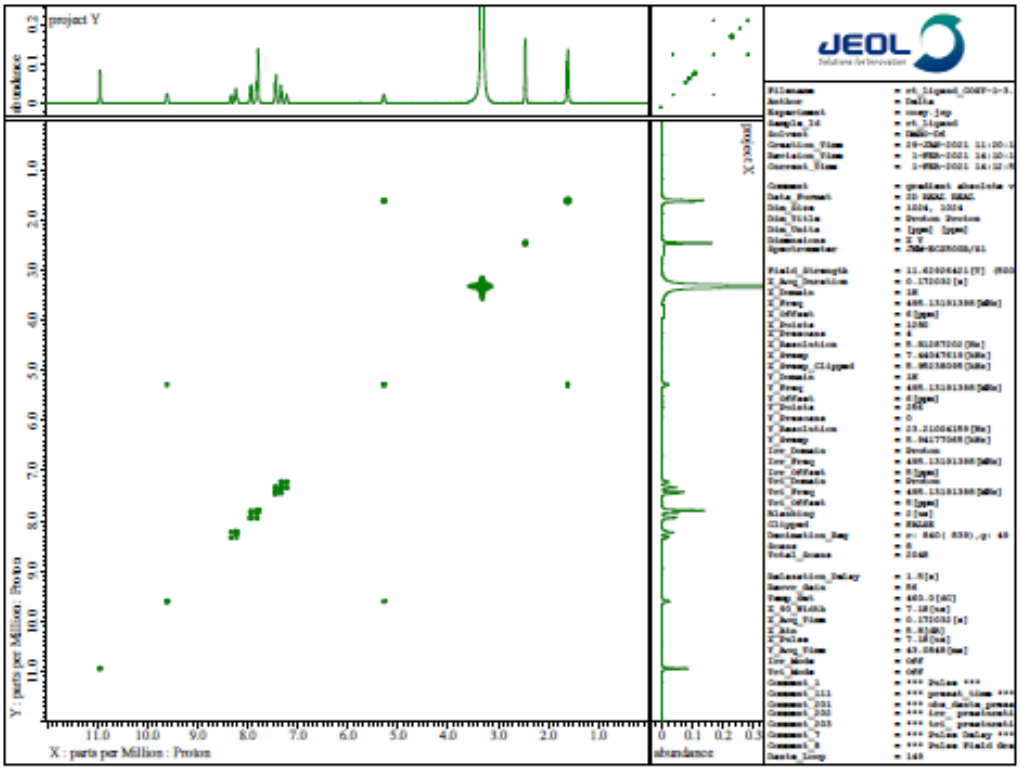

Figure S2b-27. COSY NMR of **L4** in $(CD_3)_2SO$.

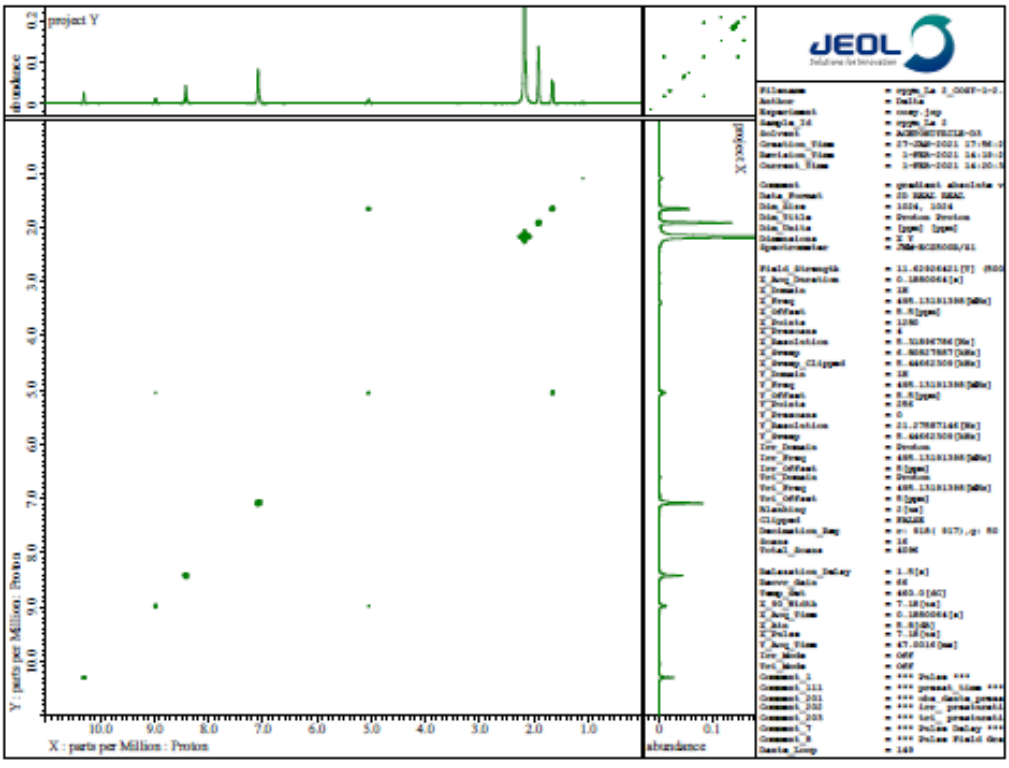

Figure S2b-28. COSY NMR of $[La_2(\mathbf{L3^{RR}})_3]$ in CD_3CN.

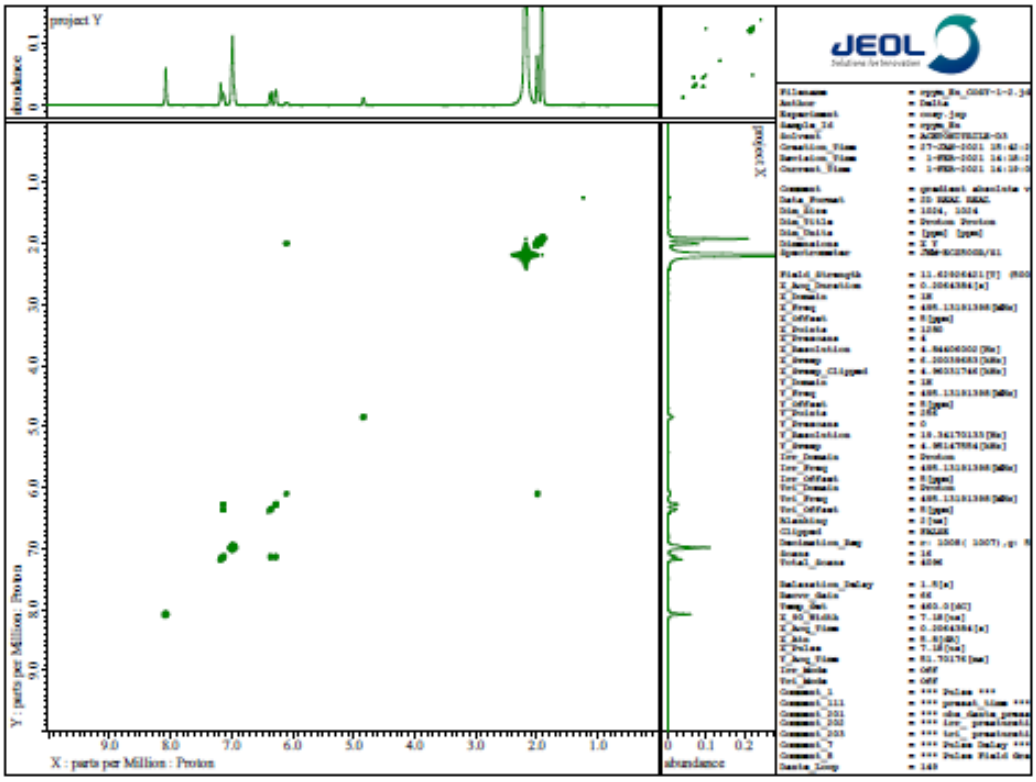

Figure S2b-29. COSY NMR of $[Eu_2(\mathbf{L3^{RR}})_3]$ in CD_3CN.

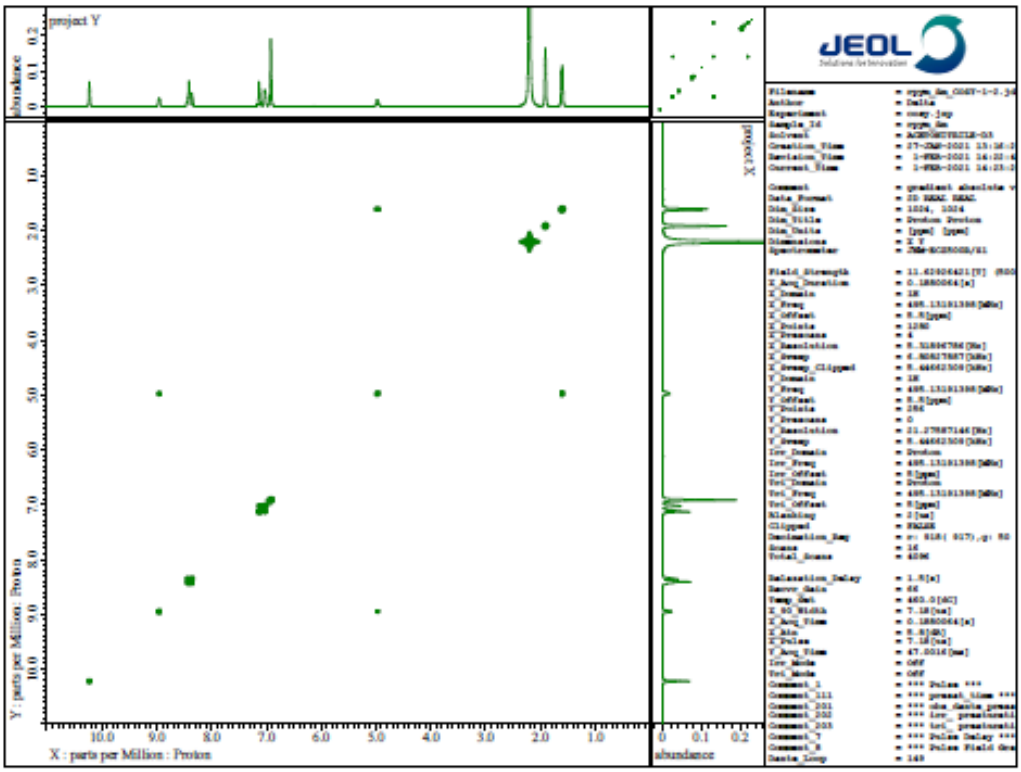

Figure S2b-30. COSY NMR of $[Sm_2(\mathbf{L3^{RR}})_3]$ in CD_3CN.

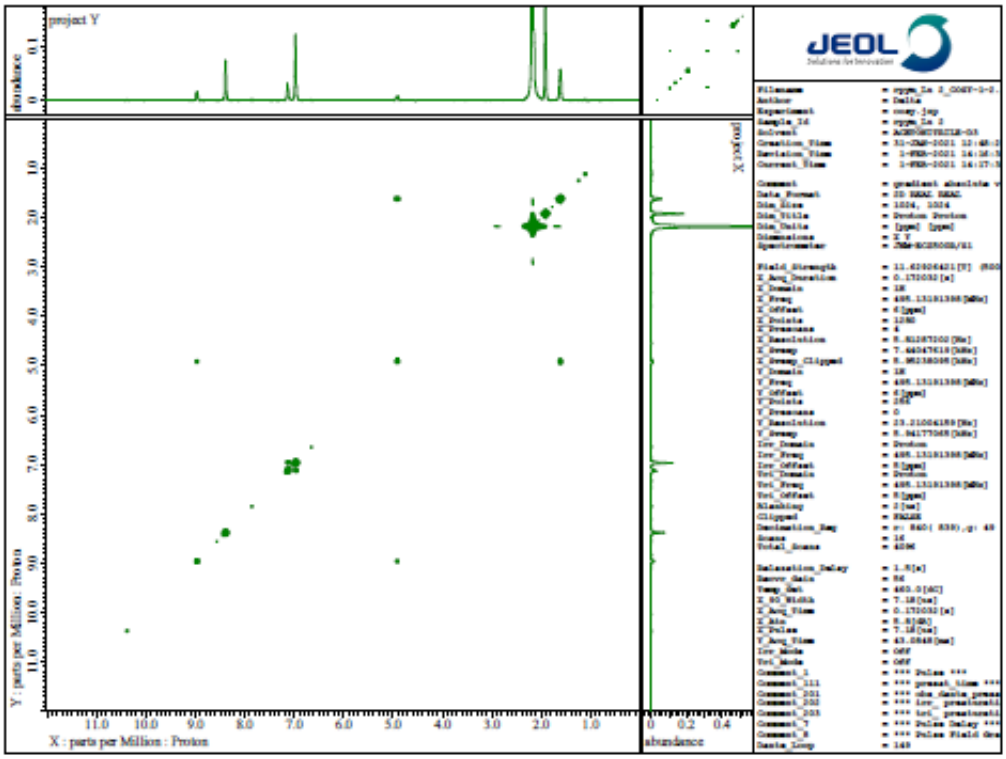

Figure S2b-31. COSY NMR of $[Lu_2(\mathbf{L3^{RR}})_3]$ in CD_3CN.

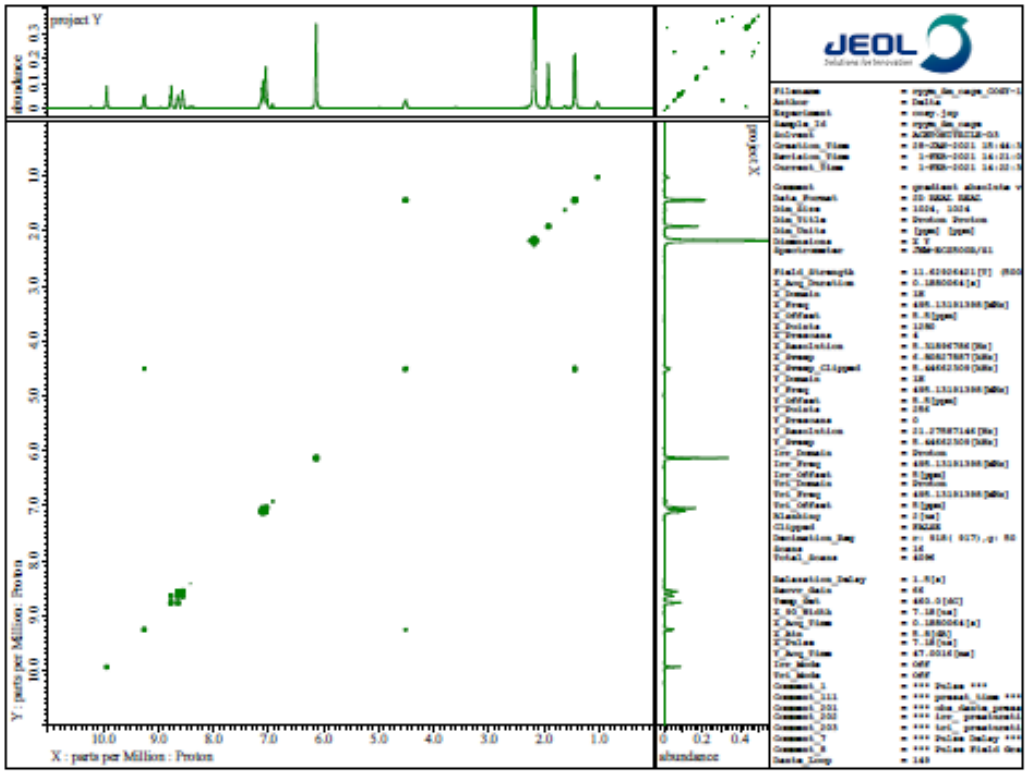

Figure S2b-32. COSY NMR of $[Sm_4(\mathbf{L3^{RR}})_6]$ in CD_3CN.

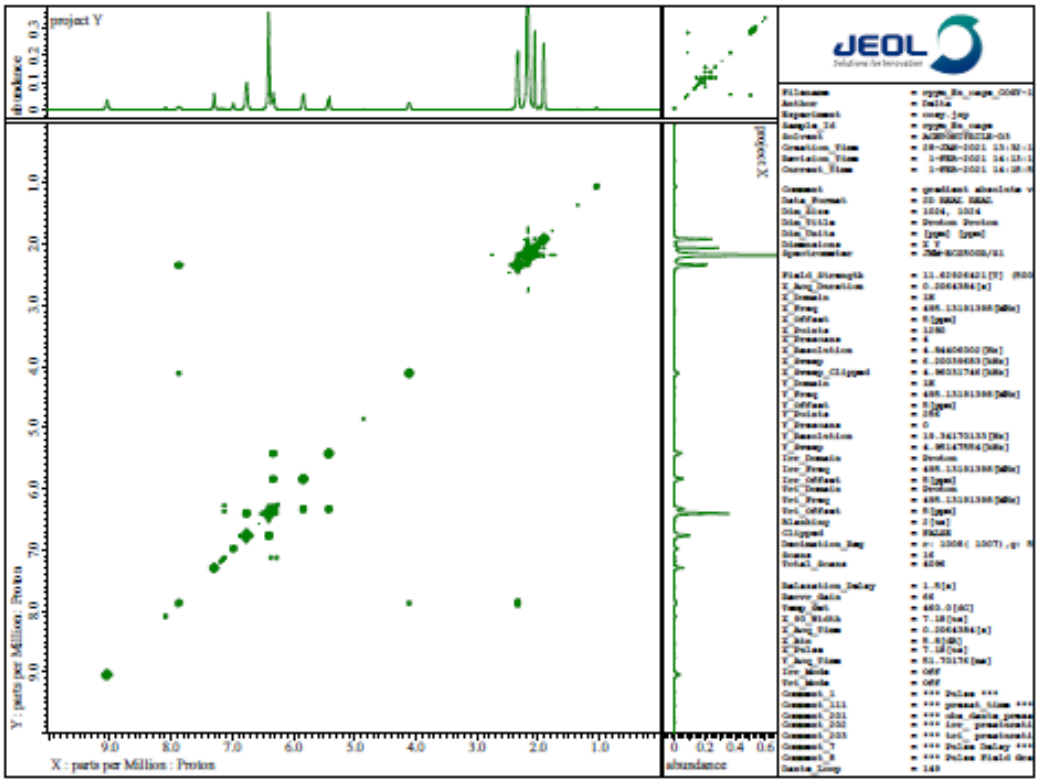

Figure S2b-33. COSY NMR of $[Eu_4(\mathbf{L3^{RR}})_6]$ in CD_3CN.

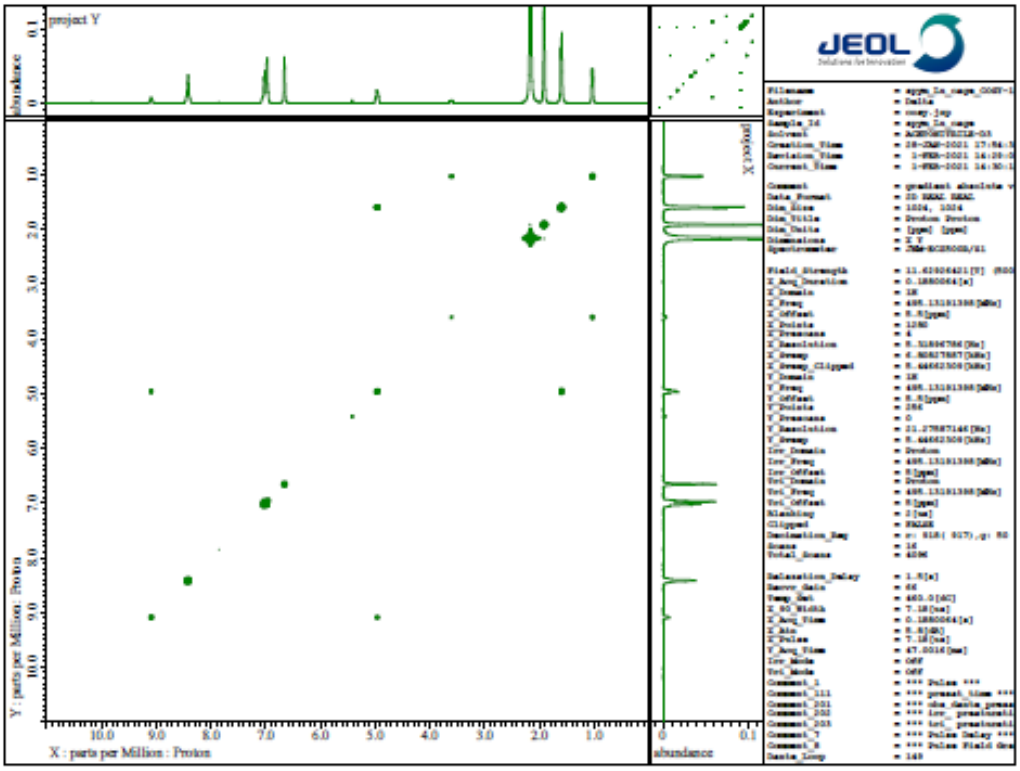

Figure S2b-34. COSY NMR of $[Lu_4(\mathbf{L3^{RR}})_6]$ in CD_3CN.

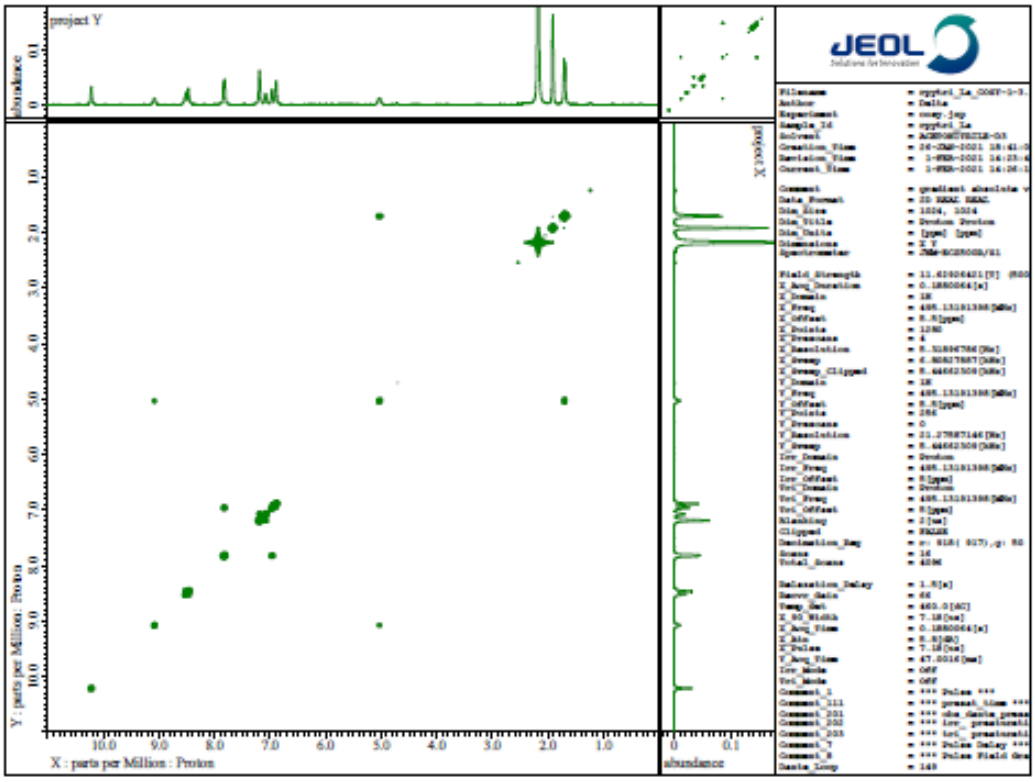

Figure S2b-35. COSY NMR of $[La_2(\mathbf{L4^{RR}})_3]$ in CD_3CN.

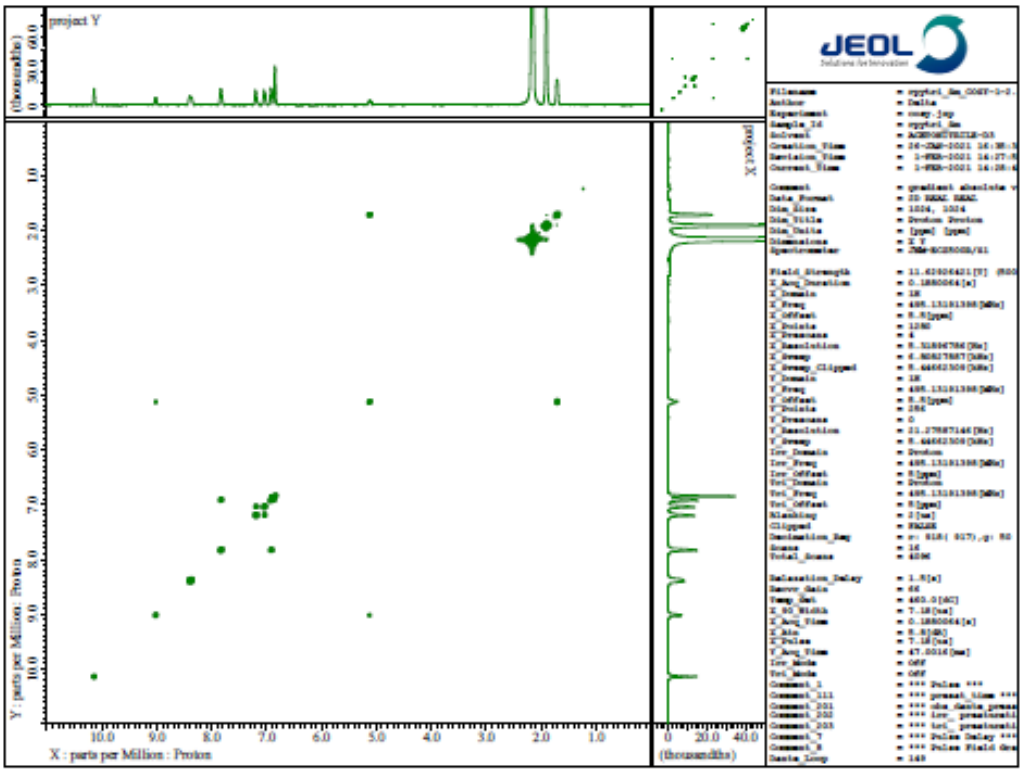

Figure S2b-36. COSY NMR of $[Sm_2(\mathbf{L4^{RR}})_3]$ in CD_3CN.

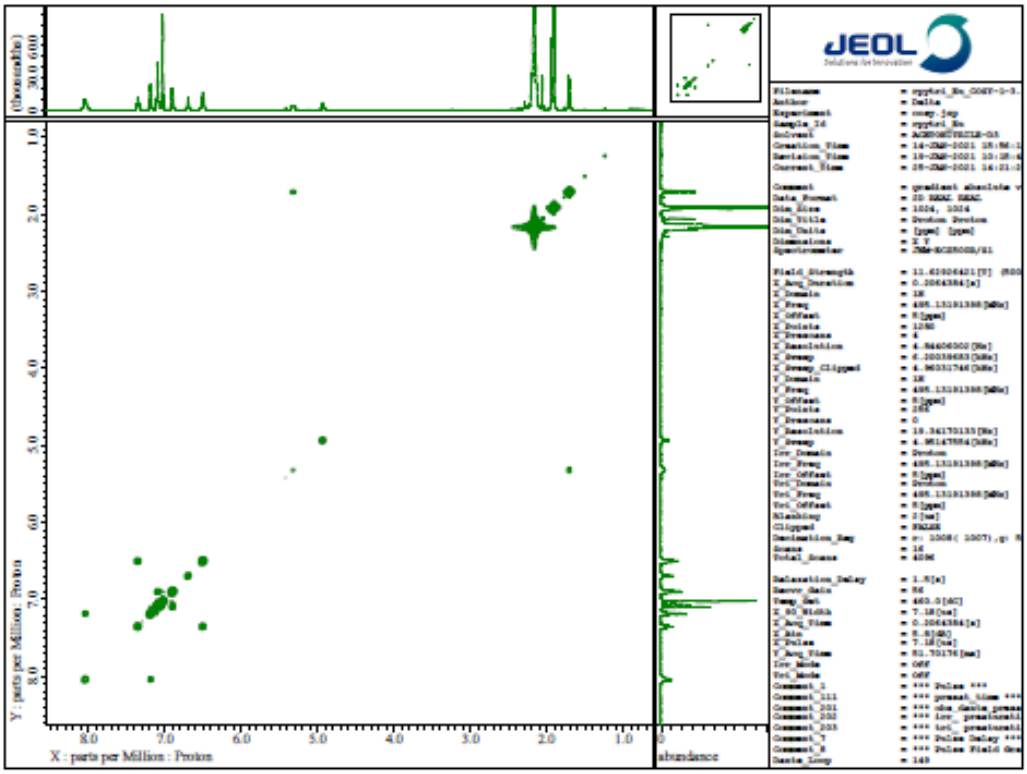

Figure S2b-37. COSY NMR of $[Eu_2(\mathbf{L4^{RR}})_3]$ in CD_3CN.

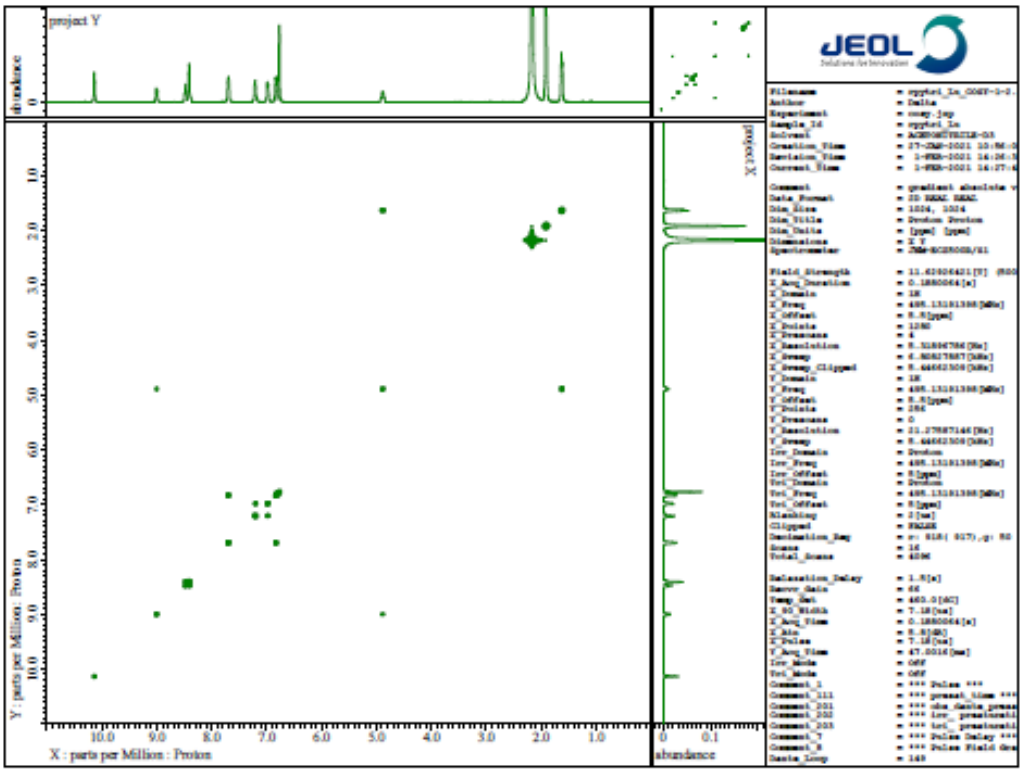

Figure S2b-38. COSY NMR of $[Lu_2(\mathbf{L4^{RR}})_3]$ in CD_3CN.

A

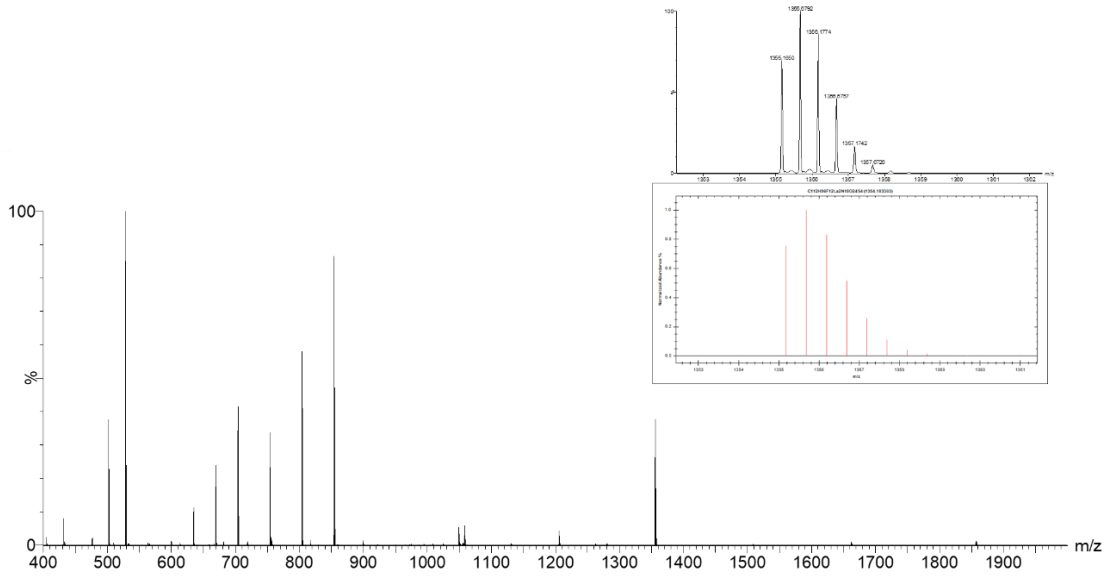

B

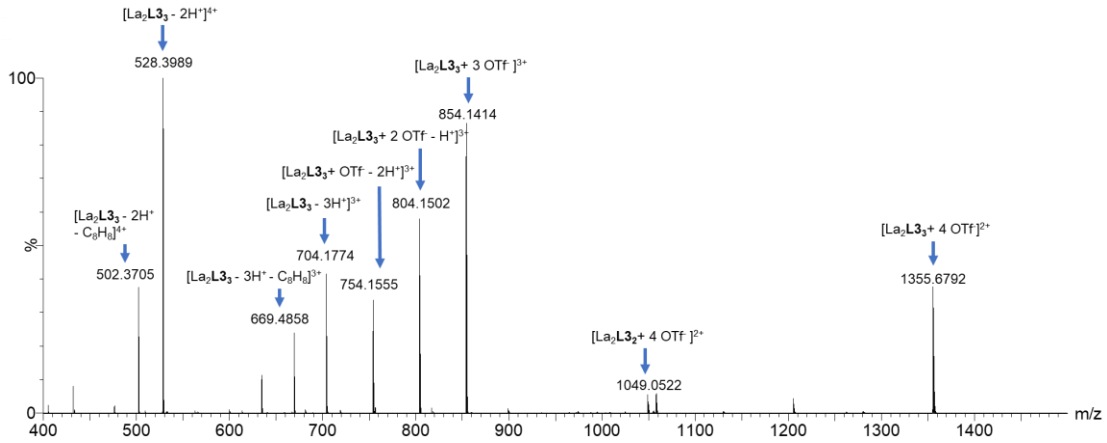

Figure S2b-39. ESI-HRMS of bimetallic helicate [La_2**L3**$_3$]. (A) The full spectrum. Simulated m/z for [La_3**L3**$_3$ + 4 OTf^-]$^{2+}$ is 1355.6841(100%), Experimental found m/z is 1355.6792(100%). Inset showing the experimental (upper) and calculated(lower) isotopic patterns. (B) Expanded region of the mass spectrum to show the possible assignments of the corresponding prominent peaks.

A

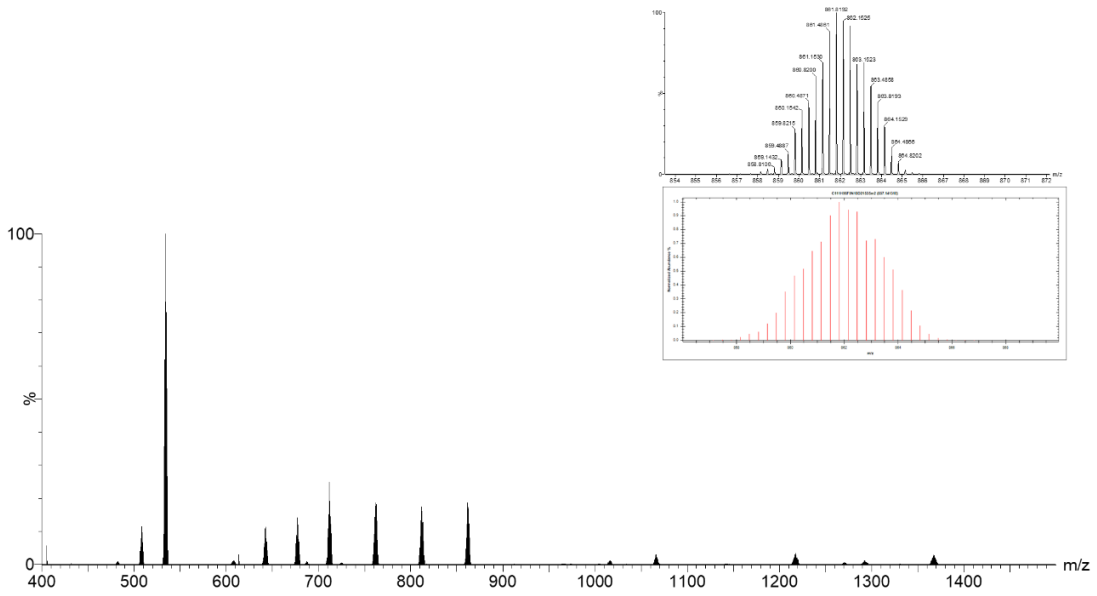

B

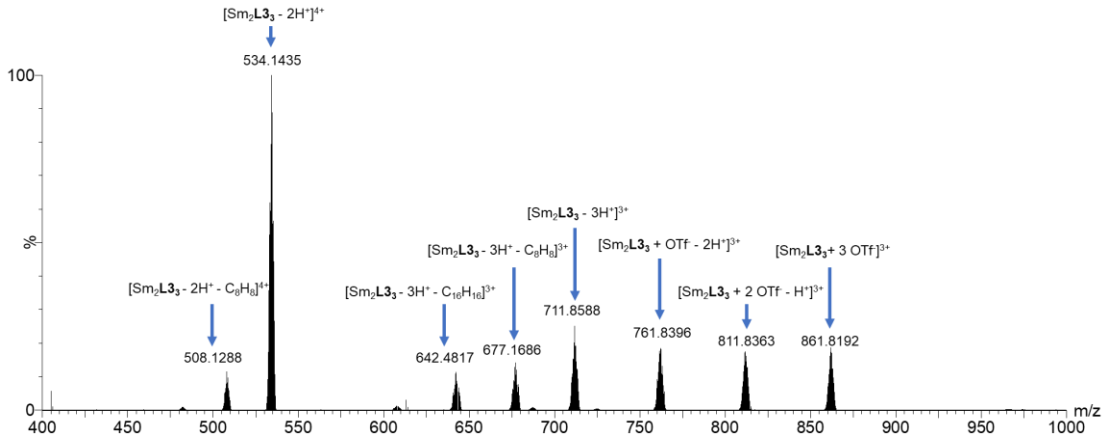

Figure S2b-40. ESI-HRMS of bimetallic helicate [Sm_2**L3**$_3$]. (A) The full spectrum. Simulated m/z for [Sm_2**L3**$_3$ + 3 OTf^-]$^{3+}$ is 861.8131(100%), Experimental found m/z is 861.8192(100%). Inset showing the experimental (upper) and calculated(lower) isotopic patterns. (B) Expanded region of the mass spectrum to show the possible assignments of the corresponding prominent peaks

A

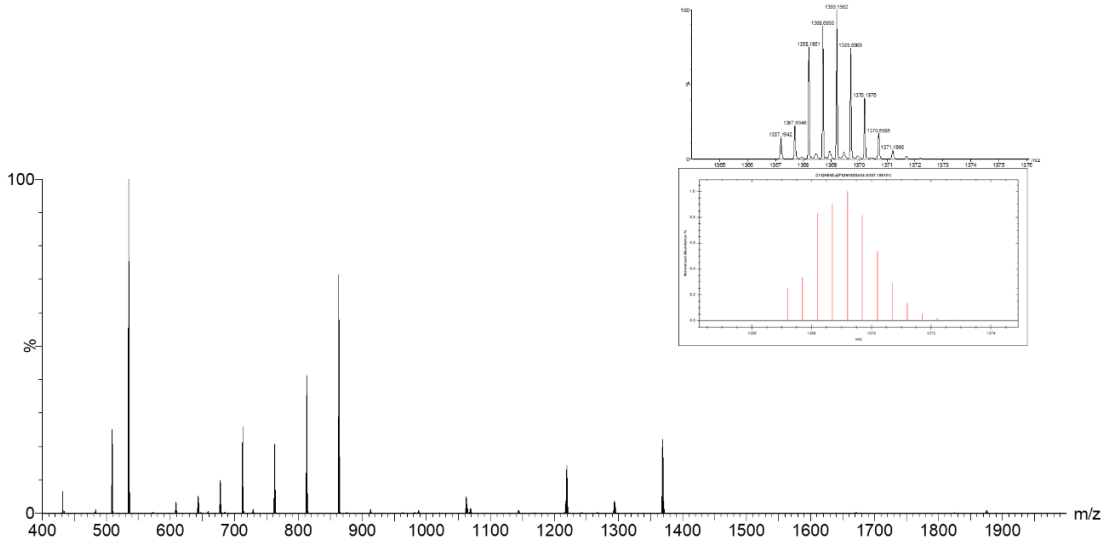

B

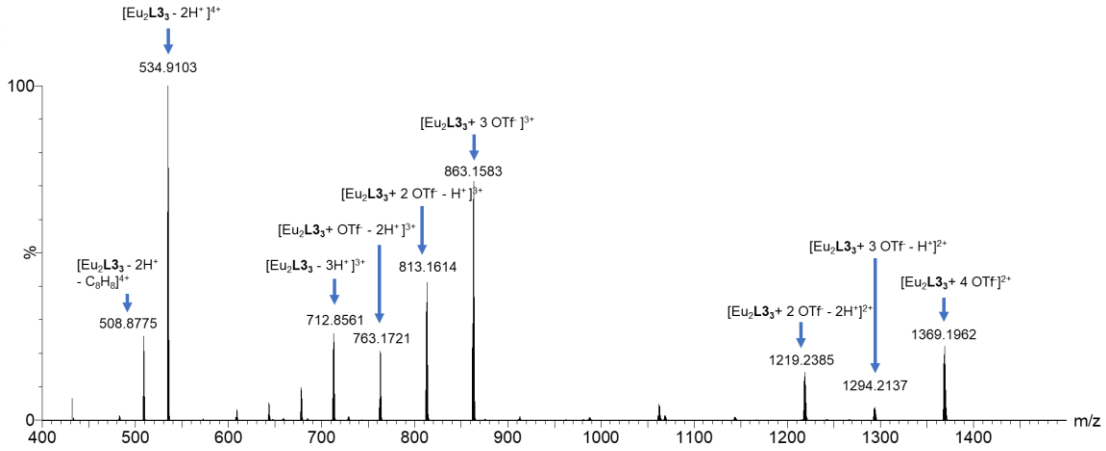

Figure S2b-41. ESI-HRMS of bimetallic helicate [Eu_2**L3**$_3$]. (A) The full spectrum. Simulated m/z for [Eu_3**L3**$_3$ + 4 OTf^-]$^{2+}$ is 1369.1985(100%), Experimental found m/z is 1369.1962(100%). Inset showing the experimental (upper) and calculated(lower) isotopic patterns. (B) Expanded region of the mass spectrum to show the possible assignments of the corresponding prominent peaks.

A

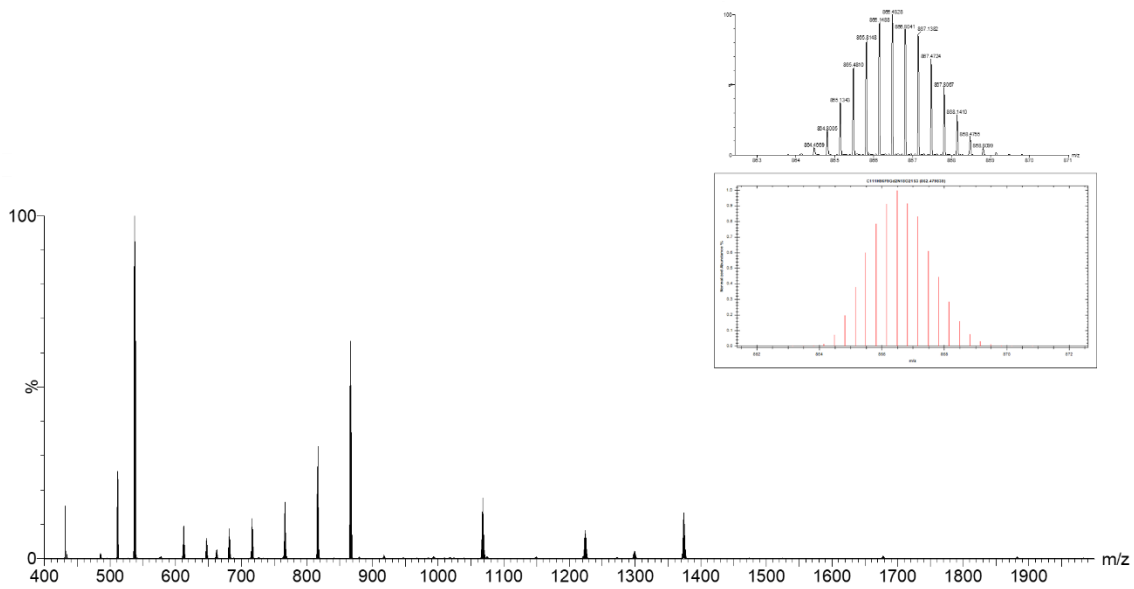

B

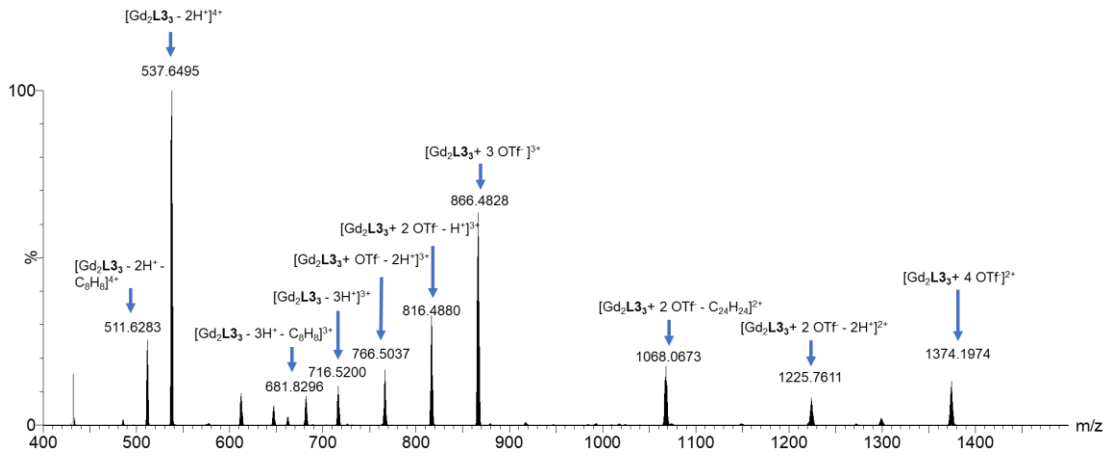

Figure S2b-42. ESI-HRMS of bimetallic helicate [Gd_2**L3**$_3$]. (A) The full spectrum. Simulated m/z for [Gd_2**L3**$_3$ + 3 OTf^-]$^{3+}$ is 866.4836 (100%), Experimental found m/z is 866.4828(100%). Inset showing the experimental (upper) and calculated(lower) isotopic patterns. (B) Expanded region of the mass spectrum to show the possible assignments of the corresponding prominent peaks.

A

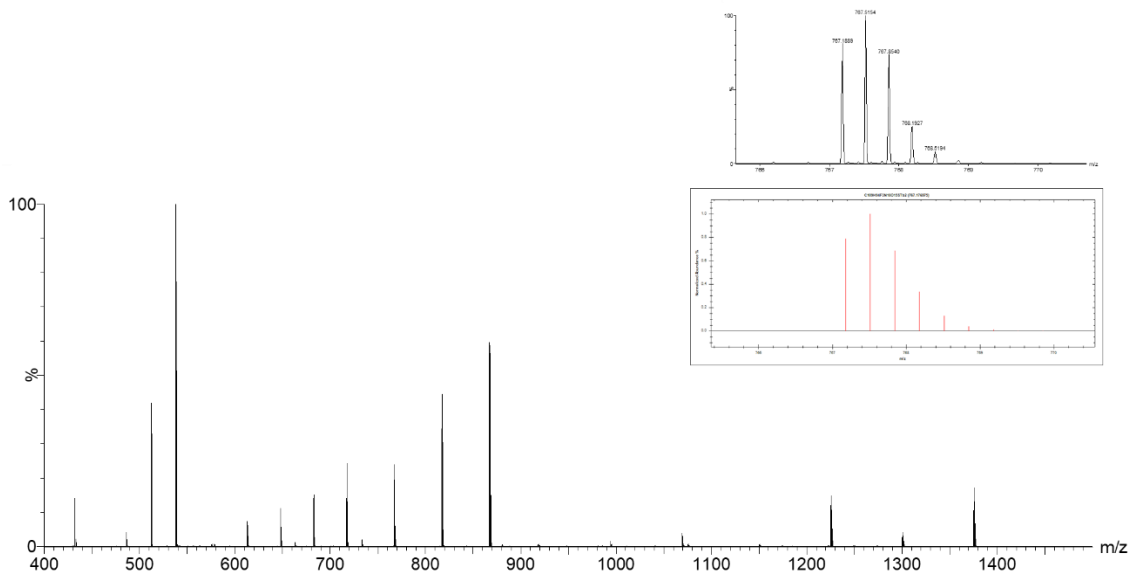

B

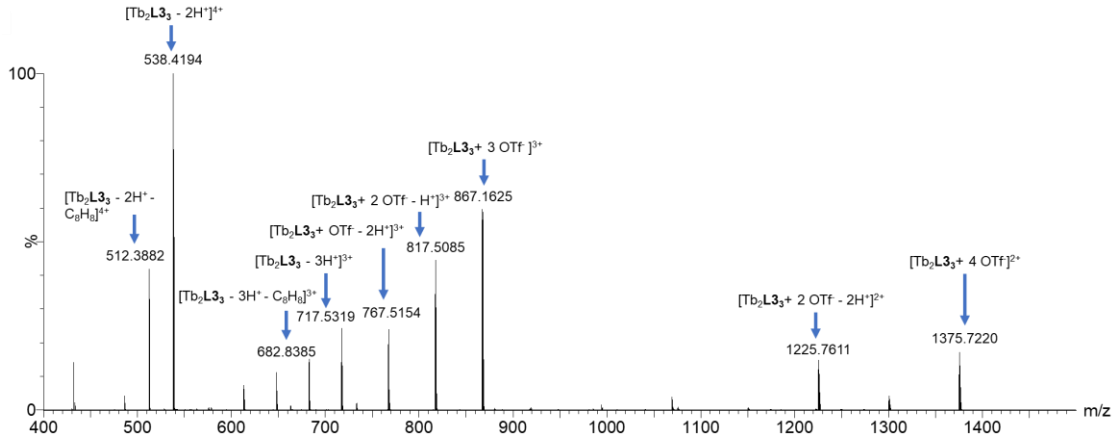

Figure S2b-43. ESI-HRMS of bimetallic helicate [Tb_2**L3**$_3$]. (A) The full spectrum. Simulated m/z for [Tb_2**L3**$_3$ + OTf^- -$2H^+$]$^{3+}$ is 767.5113(100%), Experimental found m/z is 767.5154(100%). Inset showing the experimental (upper) and calculated(lower) isotopic patterns. (B) Expanded region of the mass spectrum to show the possible assignments of the corresponding prominent peaks.

A

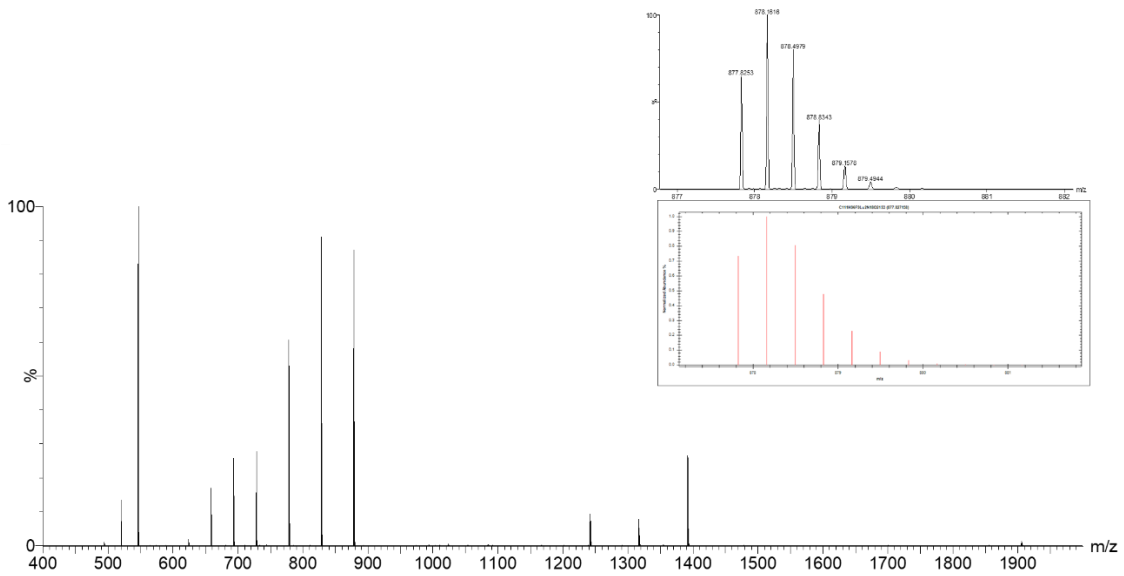

B

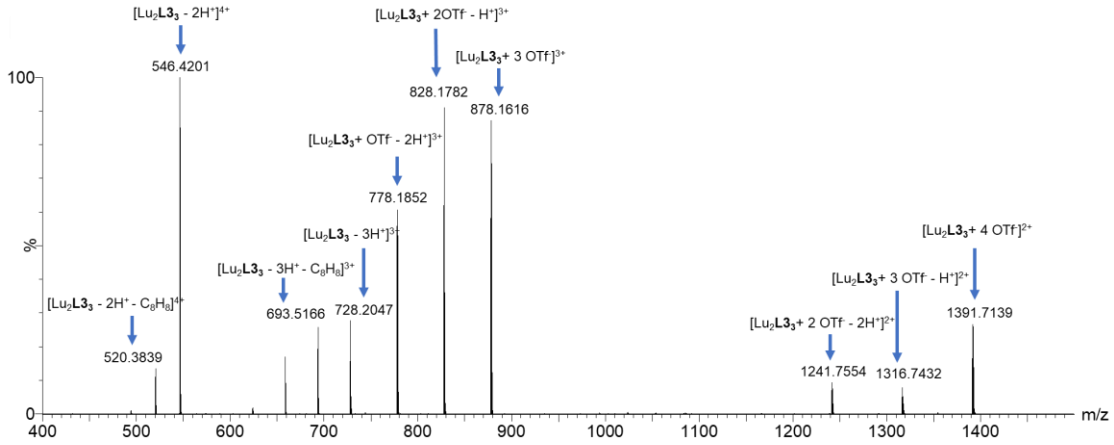

Figure S2b-44. ESI-HRMS of bimetallic helicate [Lu_2**L3**$_3$]. (A) The full spectrum. Simulated m/z for [Lu_2**L3**$_3$ + 3OTf^-]$^{3+}$ is 878.1615(100%), Experimental found m/z is 878.1616(100%). Inset showing the experimental (upper) and calculated(lower) isotopic patterns. (B) Expanded region of the mass spectrum to show the possible assignments of the corresponding prominent peaks.

A

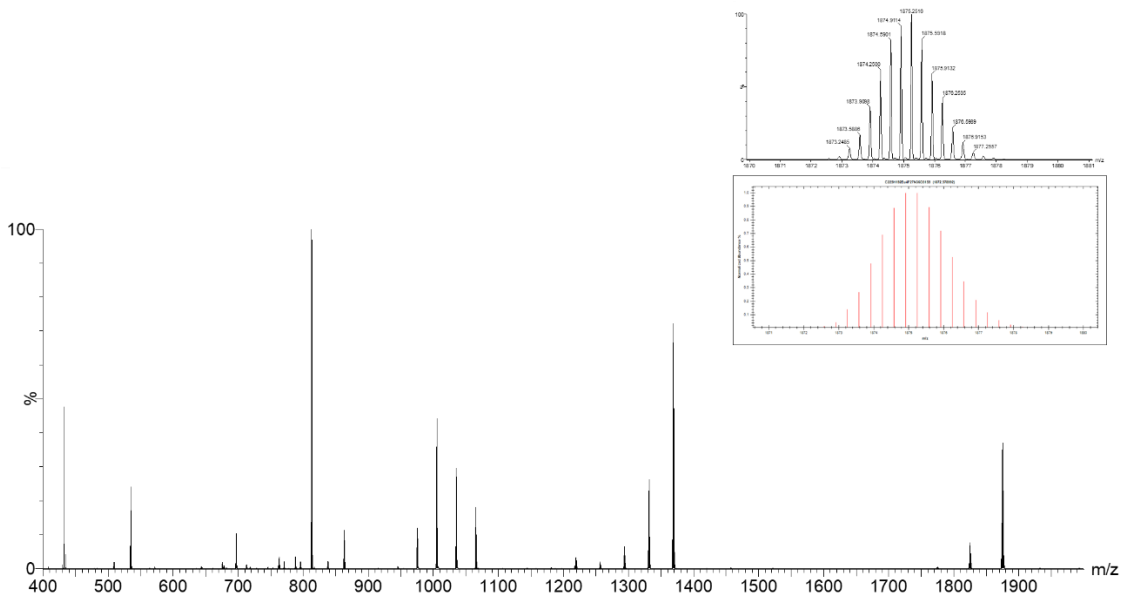

B

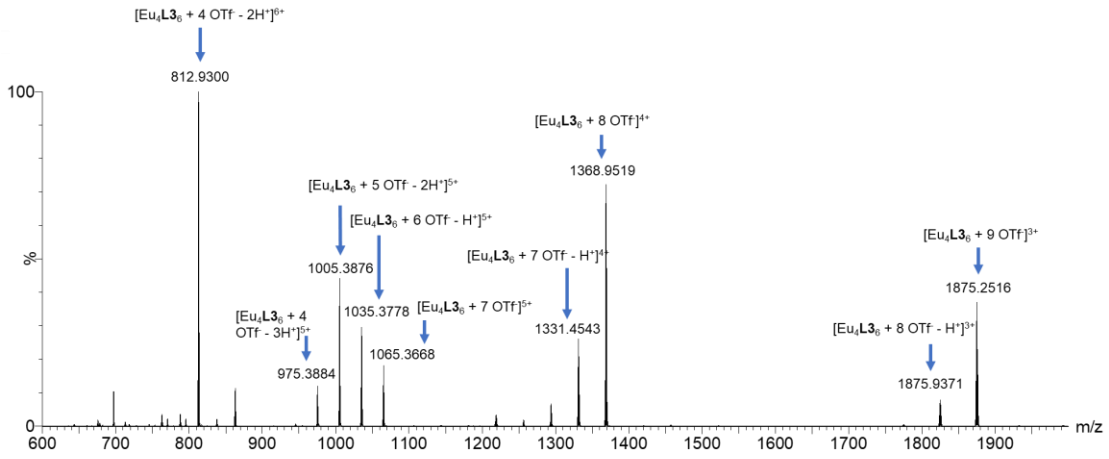

Figure S2b-45. ESI-HRMS of tetrahedron [Eu_4**L3**$_6$]. (A) The full spectrum. Simulated m/z for [Eu_4**L3**$_6$ + 9 OTf^-]$^{3+}$ is 1875.2490(100%), Experimental found m/z is 1875.2516(100%). Inset showing the experimental (upper) and calculated(lower) isotopic patterns. (B) Expanded region of the mass spectrum to show the possible assignments of the corresponding prominent peaks.

A

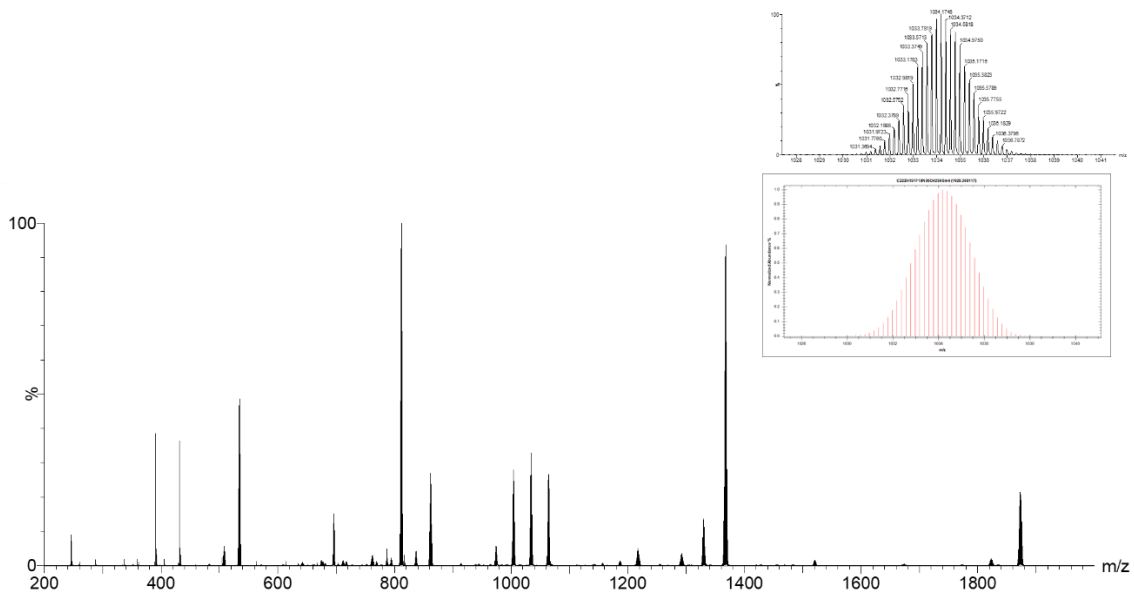

B

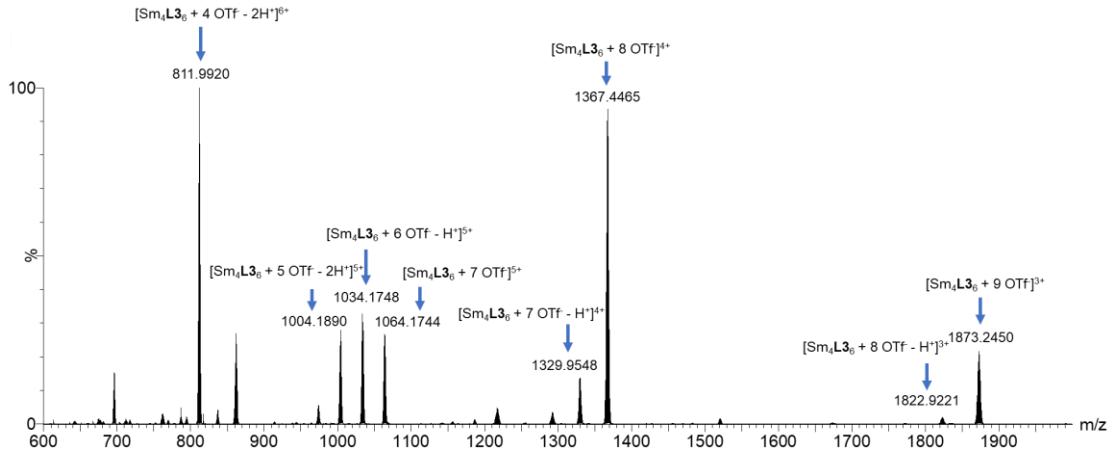

Figure S2b-46. ESI-HRMS of tetrahedron [Sm_4**L3**$_6$]. (A) The full spectrum. Simulated m/z for [Sm_4**L3**$_6$ + 6 OTf^- - H^+]$^{5+}$ is 1034.1745(100%), Experimental found m/z is 1034.1748(100%). Inset showing the experimental (upper) and calculated(lower) isotopic patterns. (B) Expanded region of the mass spectrum to show the possible assignments of the corresponding prominent peaks.

A

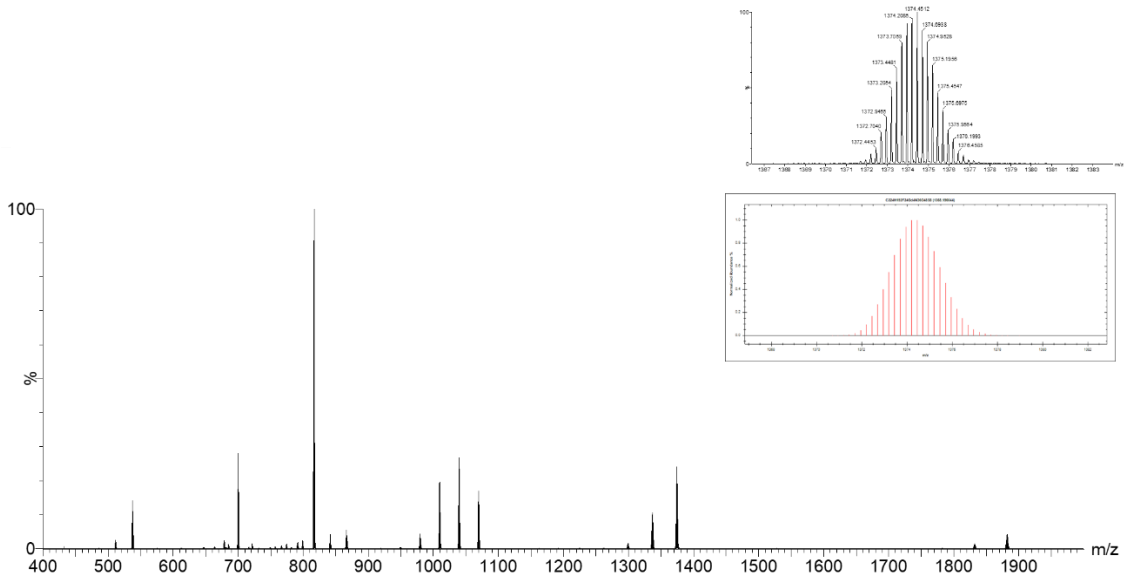

B

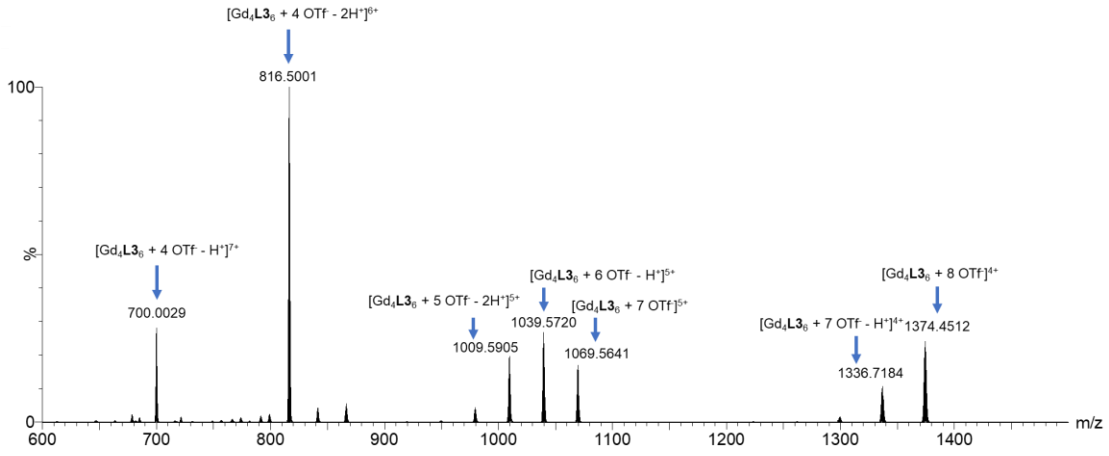

Figure S2b-47. ESI-HRMS of tetrahedron [Gd_4**L3**$_6$]. (A) The full spectrum. Simulated m/z for [Gd_4**L3**$_6$ + 8 OTf^-]$^{4+}$ is 1374.4520 (100%), Experimental found m/z is 1374.4512(100%). Inset showing the experimental (upper) and calculated(lower) isotopic patterns. (B) Expanded region of the mass spectrum to show the possible assignments of the corresponding prominent peaks.

A

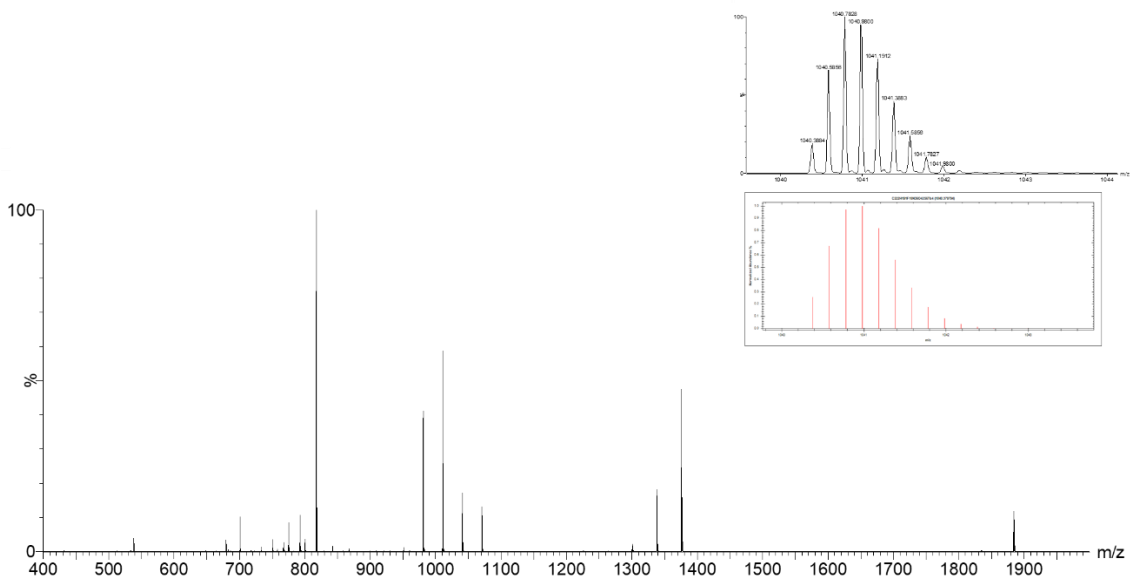

B

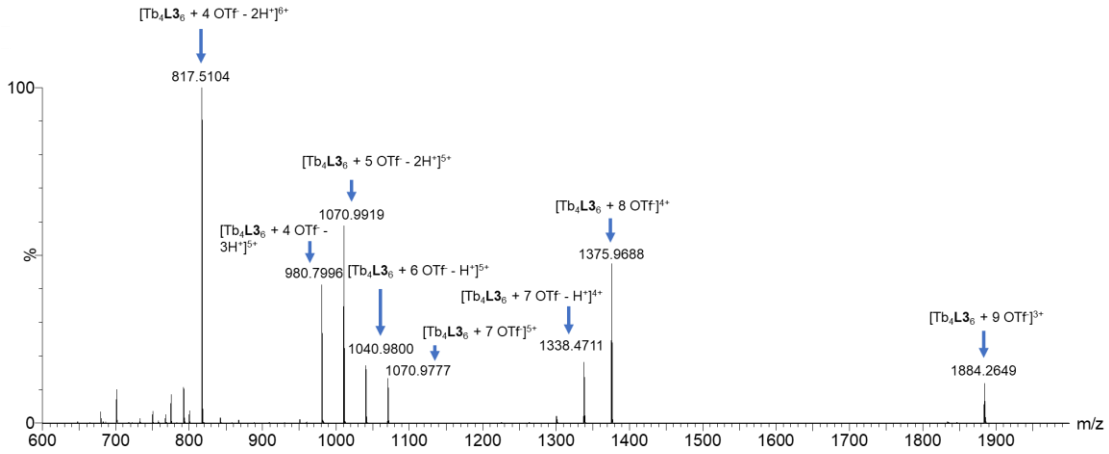

Figure S2b-48. ESI-HRMS of tetrahedron [Tb_4**L3**$_6$]. (A) The full spectrum. Simulated m/z for [Tb_4**L3**$_6$ + 6 OTf^- - H^+]$^{5+}$ is 1040.9802 (100%), Experimental found m/z is 1040.9800(100%). Inset showing the experimental (upper) and calculated(lower) isotopic patterns. (B) Expanded region of the mass spectrum to show the possible assignments of the corresponding prominent peaks.

A

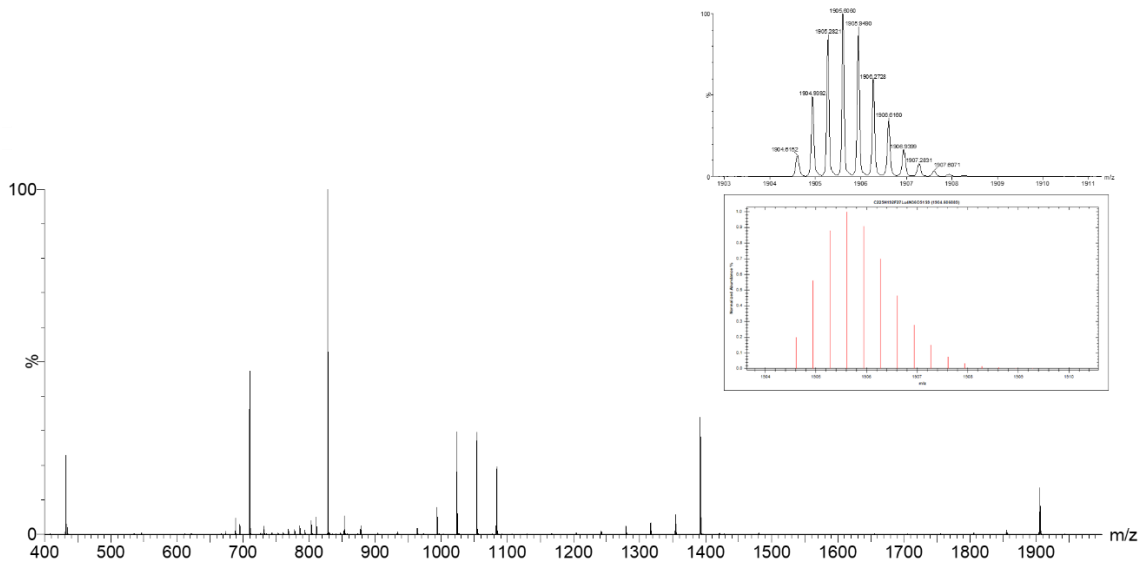

B

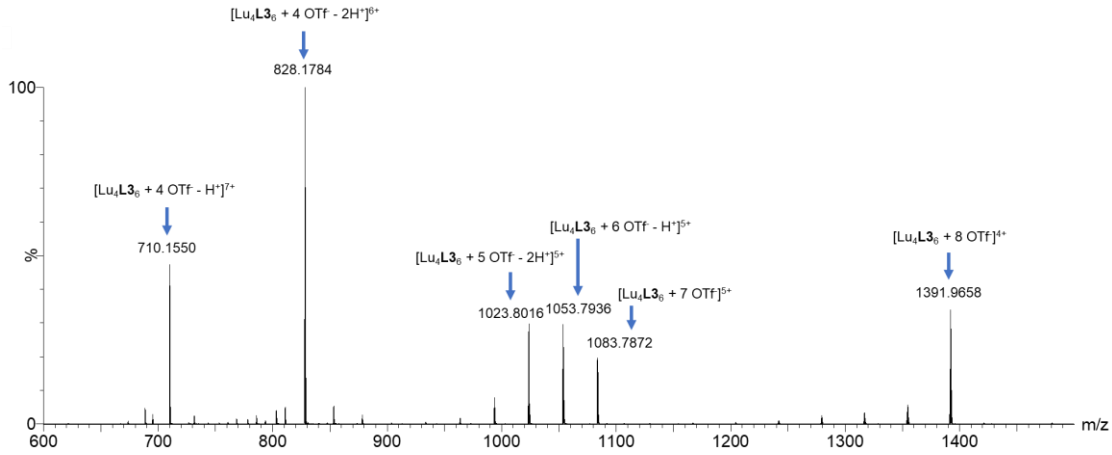

Figure S2b-49. ESI-HRMS of tetrahedron [Lu_4**L3**$_6$]. (A) The full spectrum. Simulated m/z for [Lu_4**L3**$_6$ + 9OTf^-]$^{3+}$ is 1905.6090(100%), Experimental found m/z is 1905.6060(100%). Inset showing the experimental (upper) and calculated(lower) isotopic patterns. (B) Expanded region of the mass spectrum to show the possible assignments of the corresponding prominent peaks.

A

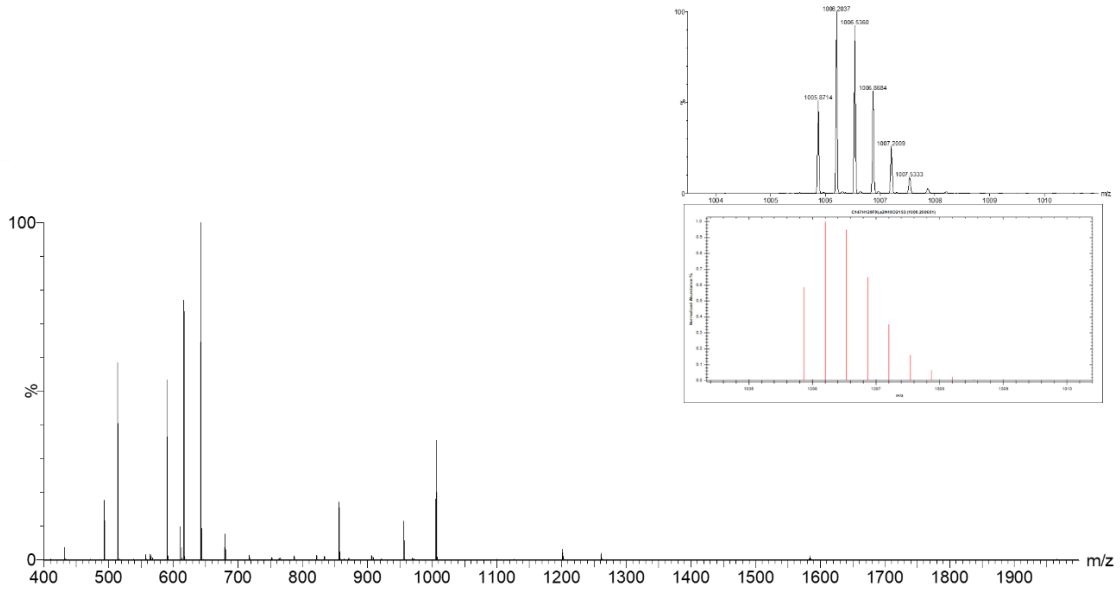

B

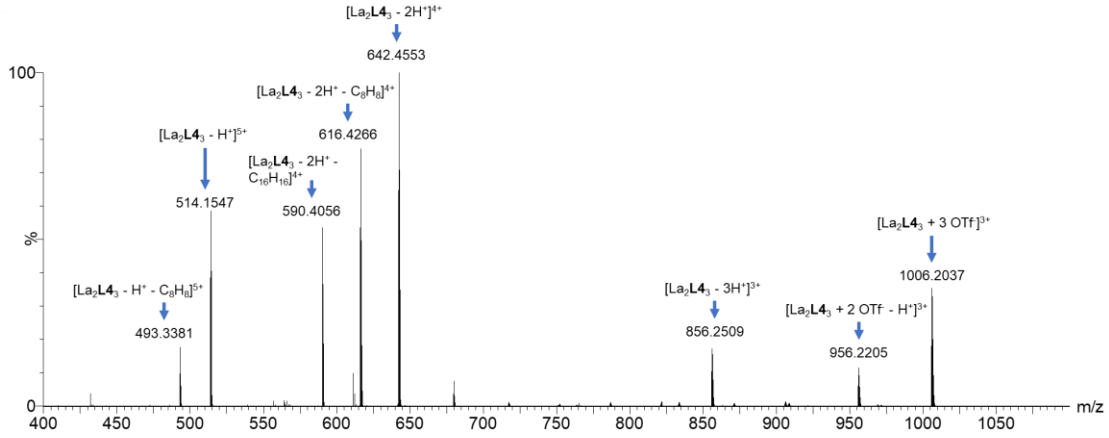

Figure S2b-50. ESI-HRMS of bimetallic helicate [La_2**L4**$_3$]. (A) The full spectrum. Simulated m/z for [La_2**L4**$_3$ + 3OTf^-]$^{3+}$ is 1006.2012(100%), Experimental found m/z is 1006.2037(100%). Inset showing the experimental (upper) and calculated(lower) isotopic patterns. (B) Expanded region of the mass spectrum to show the possible assignments of the corresponding prominent peaks.

A

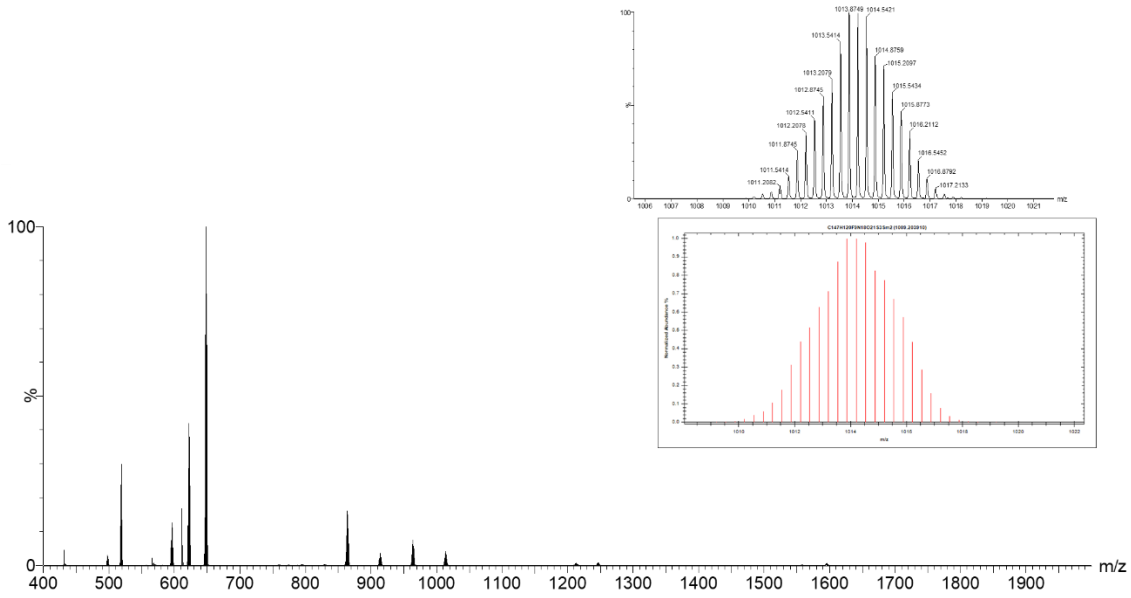

B

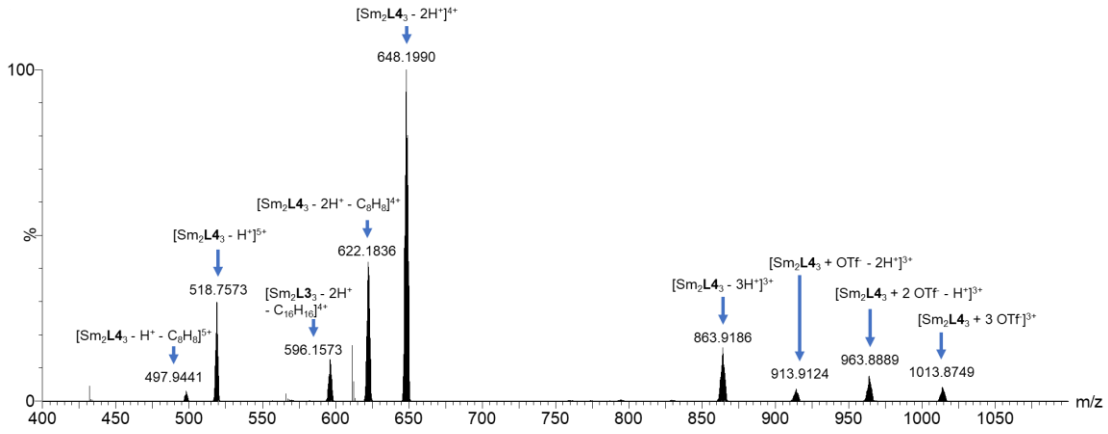

Figure S2b-51. ESI-HRMS of bimetallic helicate [Sm_2**L4**$_3$]. (A) The full spectrum. Simulated m/z for [Sm_2**L4**$_3$ + 3OTf^-]$^{3+}$ is 1013.8759(100%), Experimental found m/z is 1013.8749(100%). Inset showing the experimental (upper) and calculated(lower) isotopic patterns. (B) Expanded region of the mass spectrum to show the possible assignments of the corresponding prominent peaks.

A

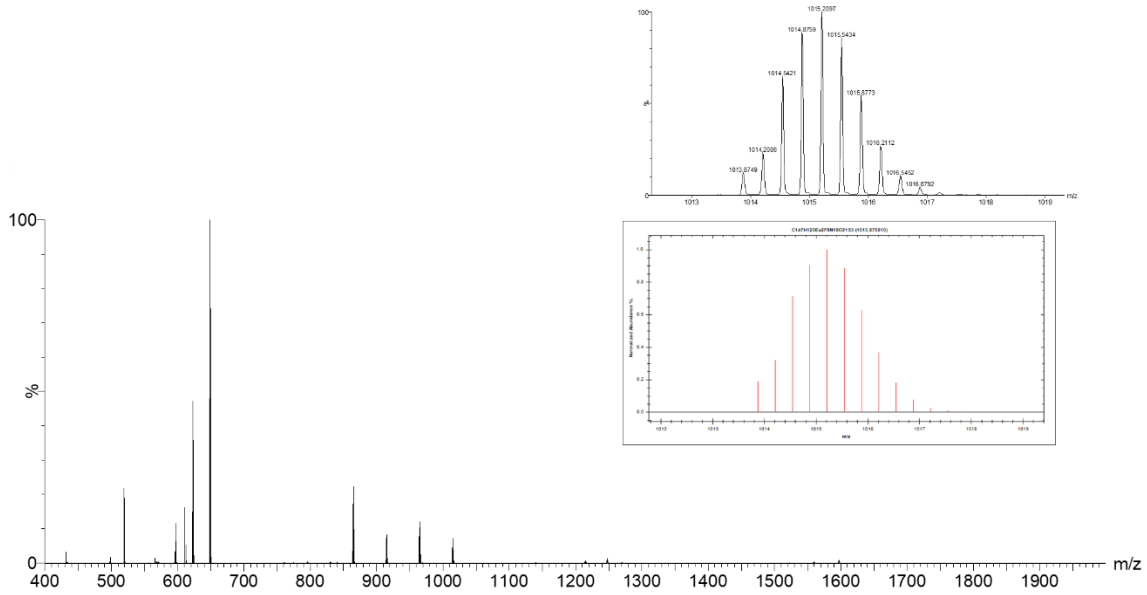

B

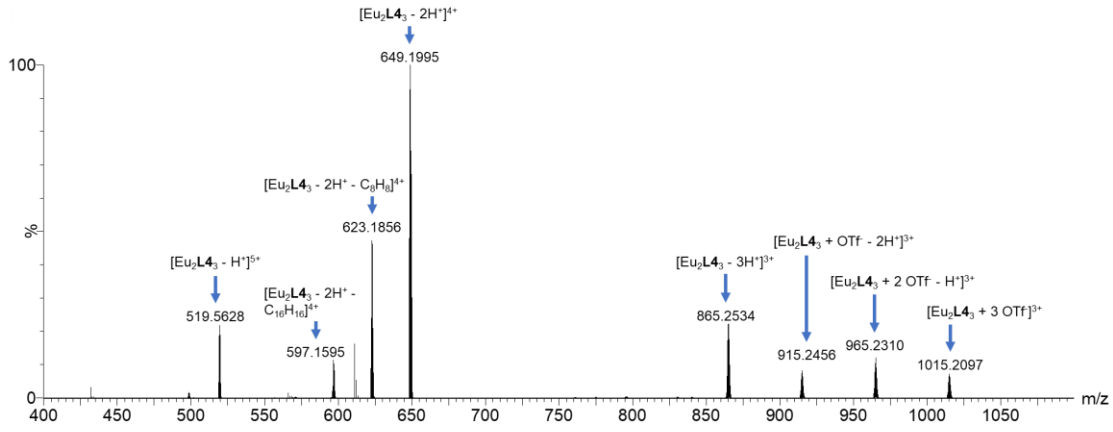

Figure S2b-52. ESI-HRMS of bimetallic helicate [Eu_2**L4**$_3$]. (A) The full spectrum. Simulated m/z for [Eu_2**L4**$_3$ + 3OTf^-]$^{3+}$ is 1015.2111(100%), Experimental found m/z is 1015.2097(100%). Inset showing the experimental (upper) and calculated(lower) isotopic patterns. (B) Expanded region of the mass spectrum to show the possible assignments of the corresponding prominent peaks.

A

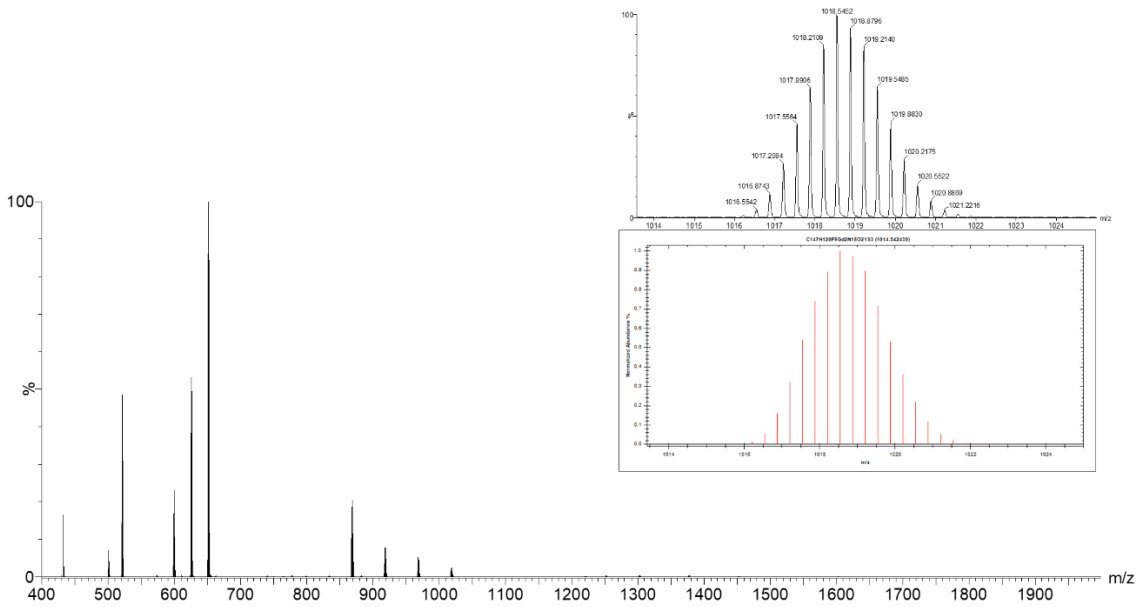

B

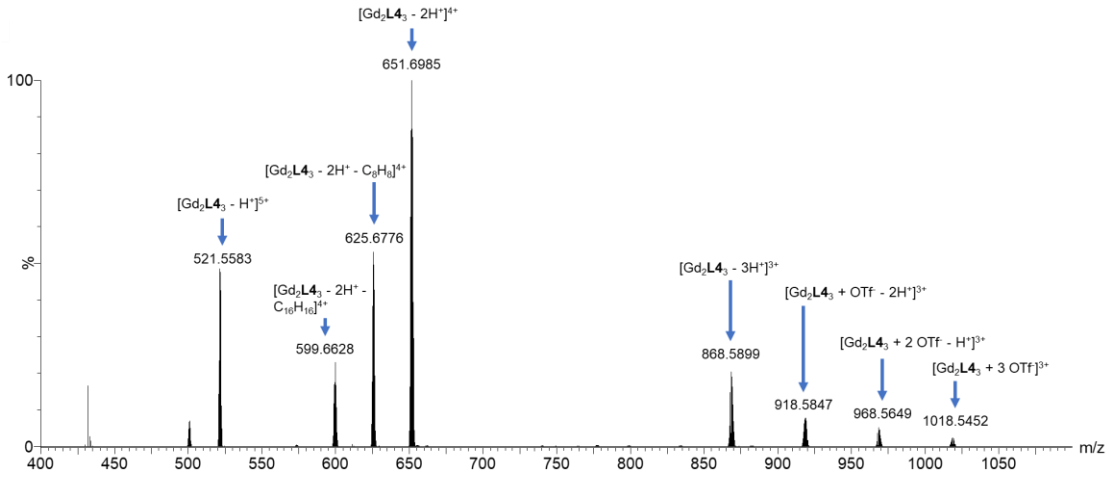

Figure S2b-53. ESI-HRMS of bimetallic helicate [Gd_2**L4**$_3$]. (A) The full spectrum. Simulated m/z for [Gd_2**L4**$_3$ + 3OTf^-]$^{3+}$ is 1018.5452(100%), Experimental found m/z is 1018.5452(100%). Inset showing the experimental (upper) and calculated(lower) isotopic patterns. (B) Expanded region of the mass spectrum to show the possible assignments of the corresponding prominent peaks.

A

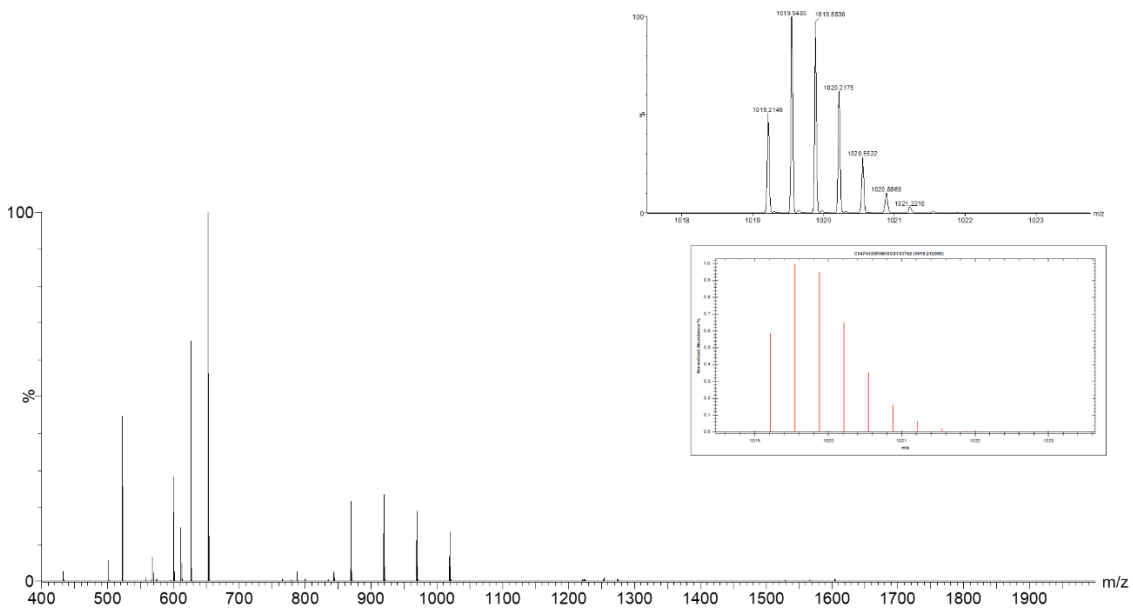

B

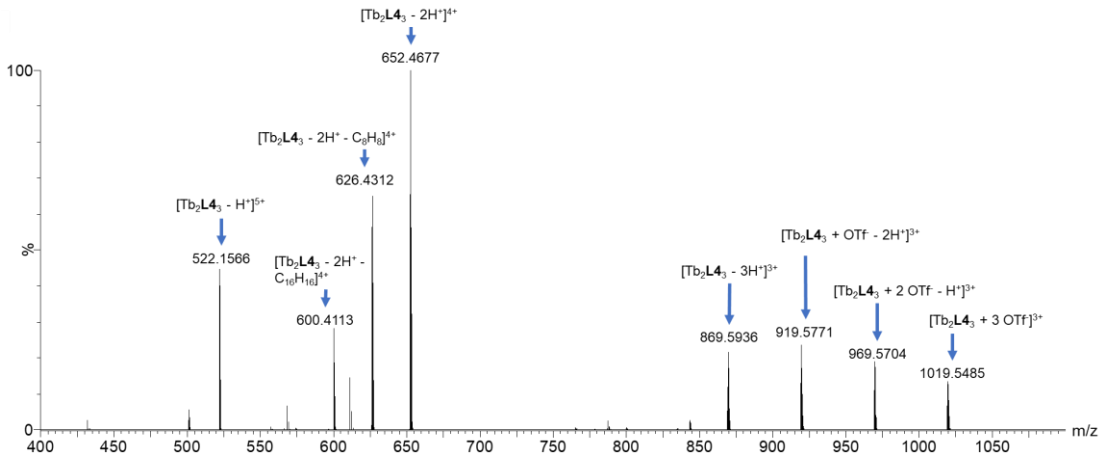

Figure S2b-54. ESI-HRMS of bimetallic helicate [Tb_2**L4**$_3$]. (A) The full spectrum. Simulated m/z for [Tb_2**L4**$_3$ + 3OTf^-]$^{3+}$ is 1019.5472(100%), Experimental found m/z is 1019.5485(100%). Inset showing the experimental (upper) and calculated(lower) isotopic patterns. (B) Expanded region of the mass spectrum to show the possible assignments of the corresponding prominent peaks.

A

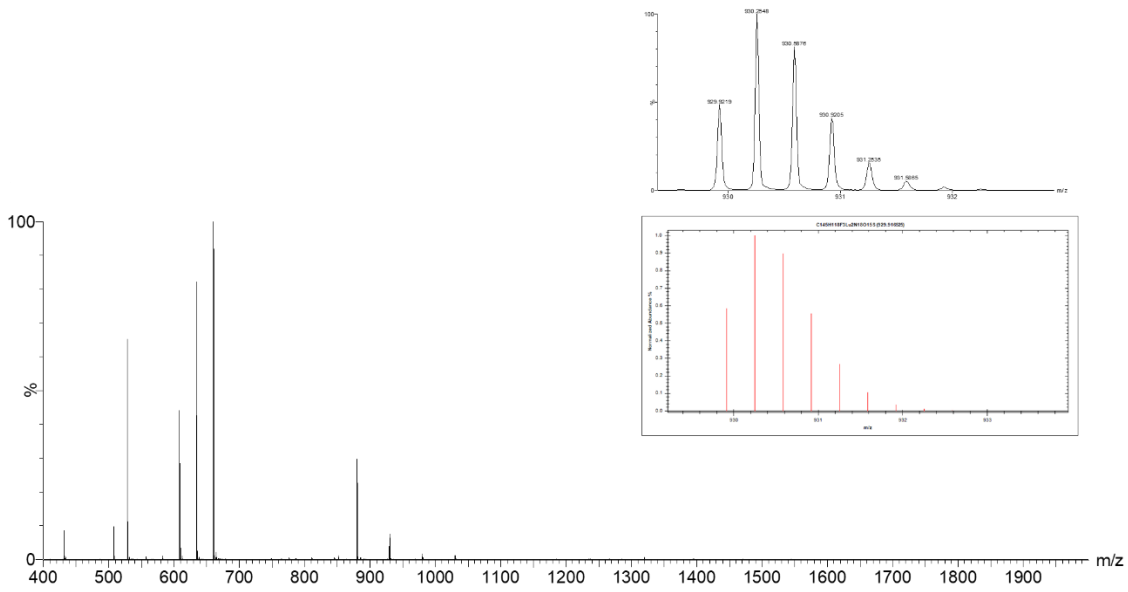

B

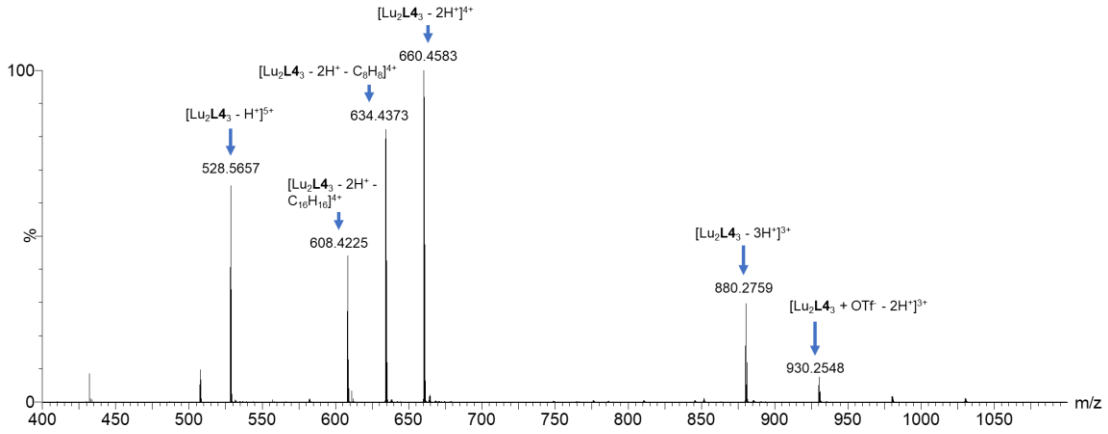

Figure S2b-55. ESI-HRMS of bimetallic helicate [Lu_2**L4**$_3$]. (A) The full spectrum. Simulated m/z for [Lu_2**L4**$_3$ + OTf^- - $2H^+$]$^{3+}$ is 930.2509(100%), Experimental found m/z is 930.2548(100%). Inset showing the experimental (upper) and calculated(lower) isotopic patterns. (B) Expanded region of the mass spectrum to show the possible assignments of the corresponding prominent peaks.

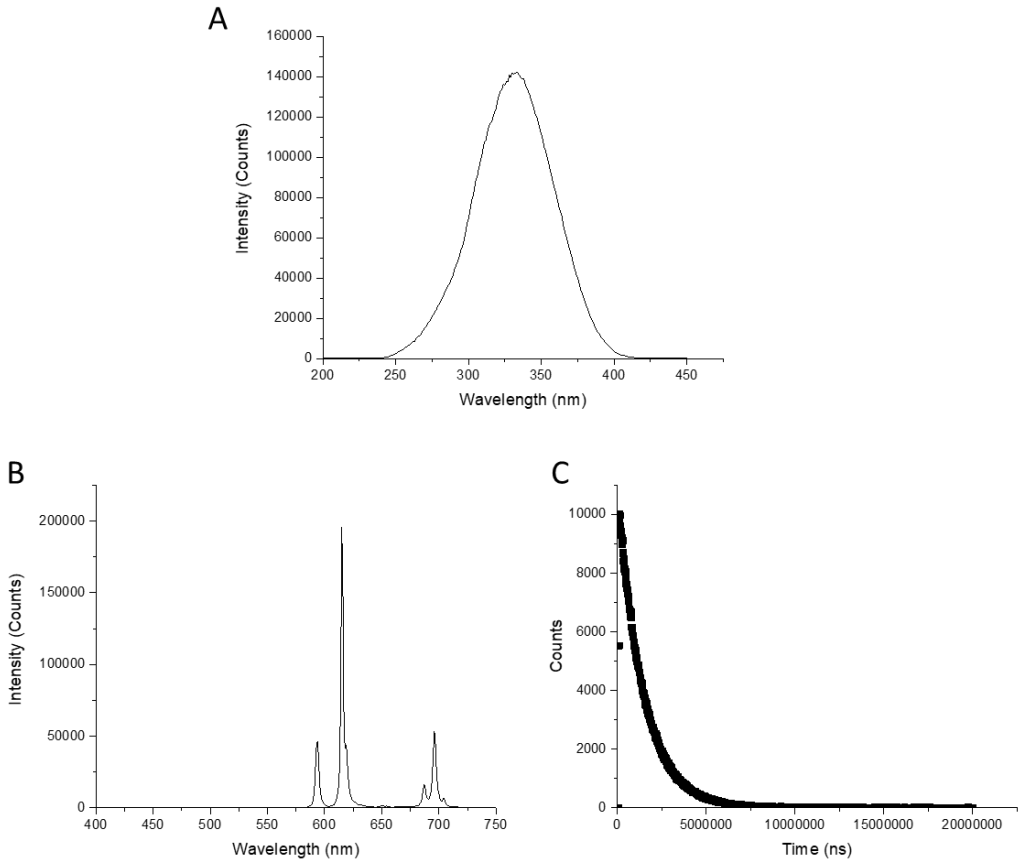

Figure S2b-56. Luminescent data of $[Eu_2(\mathbf{L3^{SS}})_3](OTf)_6$ (1.58 x 10^{-6} M in CH_3CN).(A) Excitation spectrum, λ_{em} = 616 nm, slits = 1.5-1.0, filter 380 nm. (b) Emission spectrum, λ_{ex} = 311 nm, slits = 1.5-1.0, filter 380 nm. (c) Excited state decay curve, λ_{em} = 616 nm, slits = 6-5, filter 380 nm.

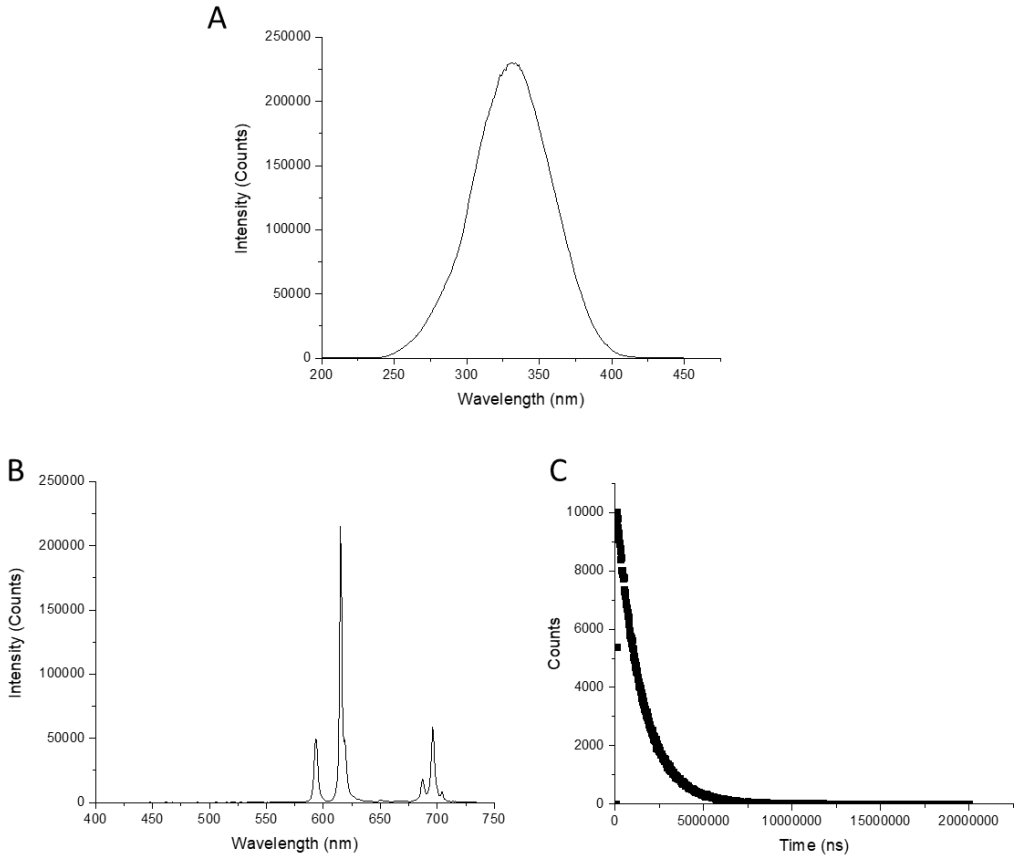

Figure S2b-57. Luminescent data of $[Eu_2(\mathbf{L3^{RR}})_3](OTf)_6$ (1.60 x 10^{-5} M in CH_3CN).(A) Excitation spectrum, λ_{em} = 616 nm, slits = 1.5-1.0, filter 380 nm. (b) Emission spectrum, λ_{ex} = 311 nm, slits = 1.5-1.0, filter 380 nm. (c) Excited state decay curve, λ_{em} = 616 nm, slits = 6-5, filter 380 nm.

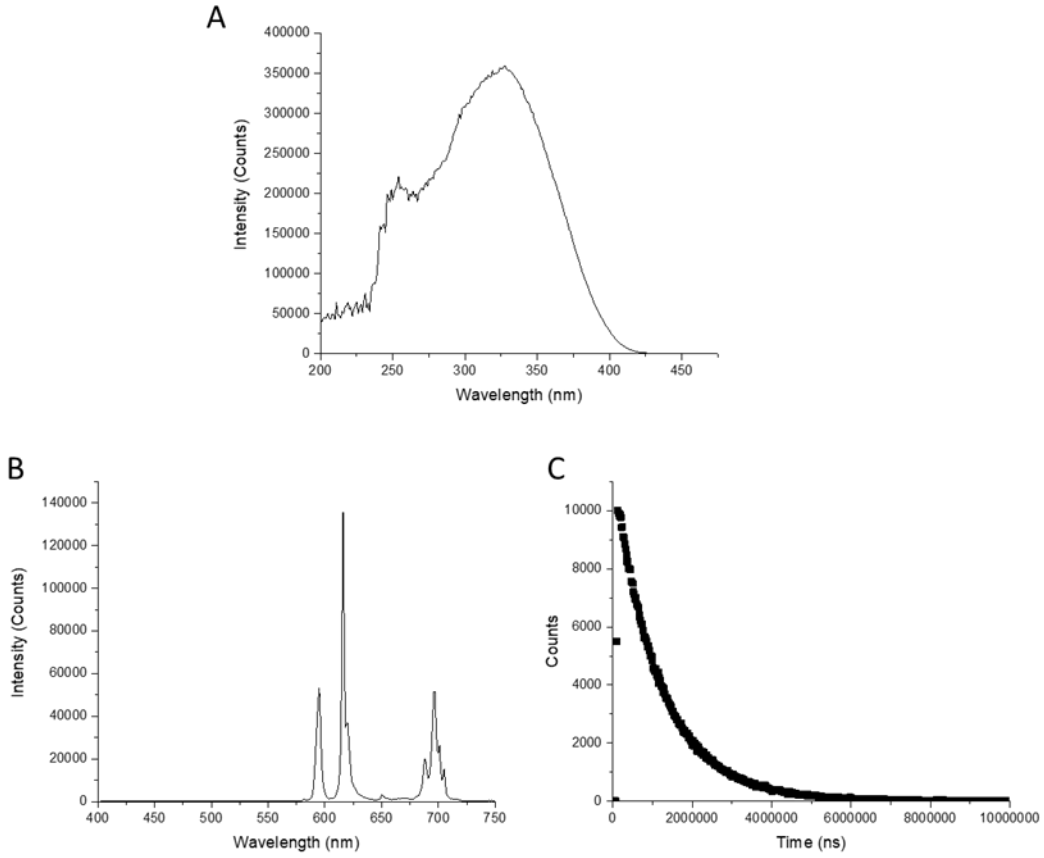

Figure S2b-58. Luminescent data of $[Eu_4(\mathbf{L3^{SS}})_6](OTf)_{12}$ (2.50 x 10^{-6} M in CH_3CN).(A) Excitation spectrum, λ_{em} = 616 nm, slits = 1.5-1.0, filter 380 nm. (b) Emission spectrum, λ_{ex} = 330 nm, slits = 1.5-1.0, filter 380 nm. (c) Excited state decay curve, λ_{em} = 616 nm, slits = 5-3, filter 380 nm.

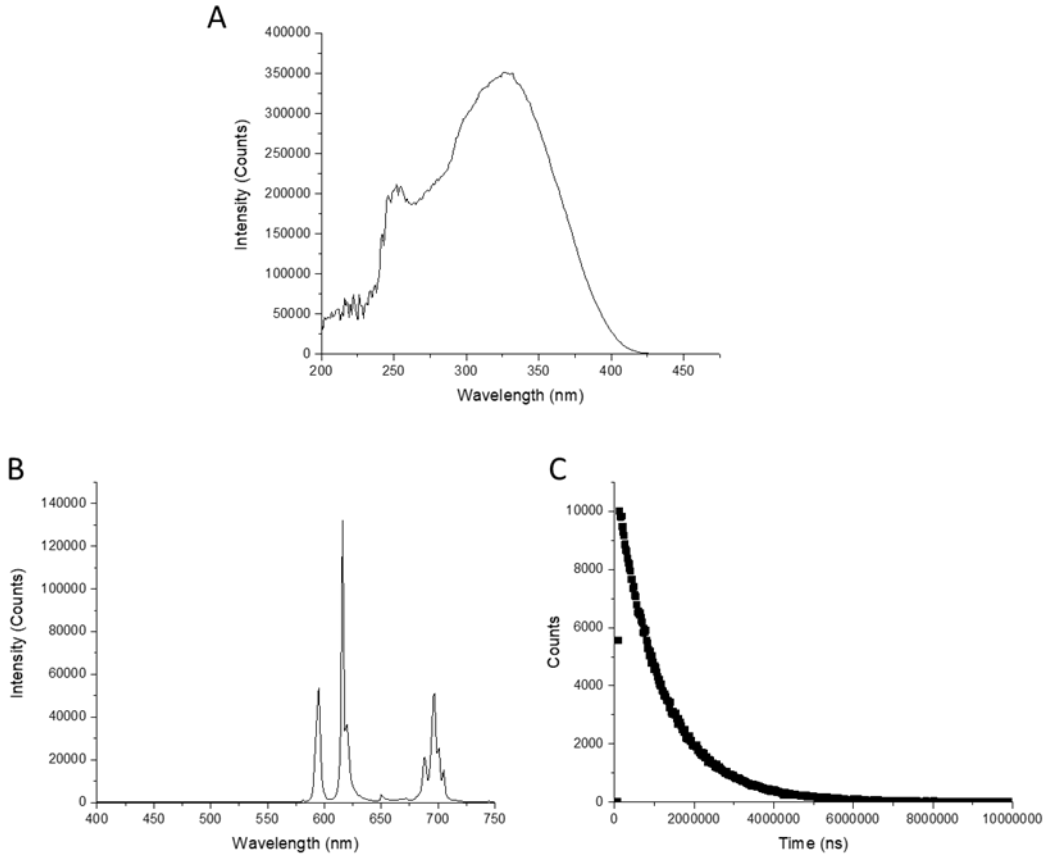

Figure S2b-59. Luminescent data of $[Eu_4(\mathbf{L3^{RR}})_6](OTf)_{12}$ (2.41 x 10^{-6} M in CH_3CN).(A) Excitation spectrum, λ_{em} = 616 nm, slits = 1.5-1.0, filter 380 nm. (b) Emission spectrum, λ_{ex} = 330 nm, slits = 1.5-1.0, filter 380 nm. (c) Excited state decay curve, λ_{em} = 616 nm, slits = 5-3, filter 380 nm.

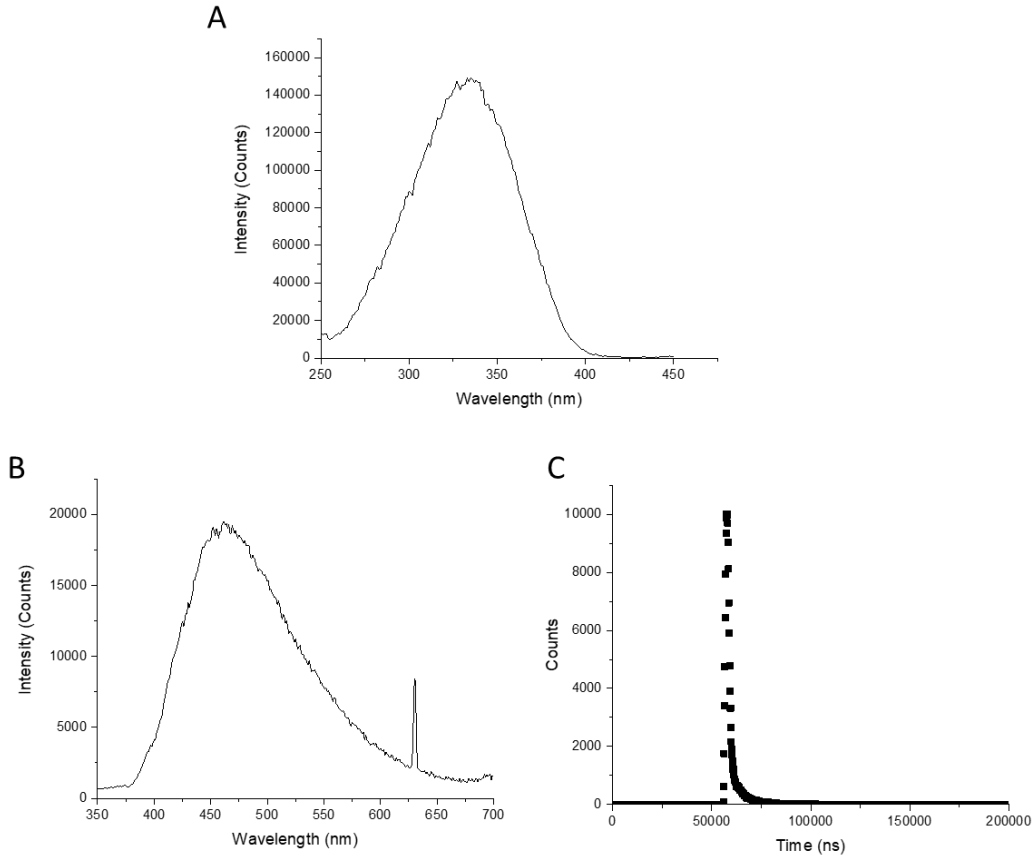

Figure S2b-60. Luminescent data of $[Gd_2(\mathbf{L3^{RR}})_3](OTf)_6$ (6.13 x 10^{-6} M in 1:4 of MeOH/EtOH at 77K).(A) Excitation spectrum, λ_{em} = 462 nm, slits = 1.0-0.5, filter 380 nm. (b) Emission spectrum, λ_{ex} = 315 nm, slits = 1.0-0.5, filter 380 nm. (c) Excited state decay curve, λ_{em} = 462 nm, filter 380 nm.

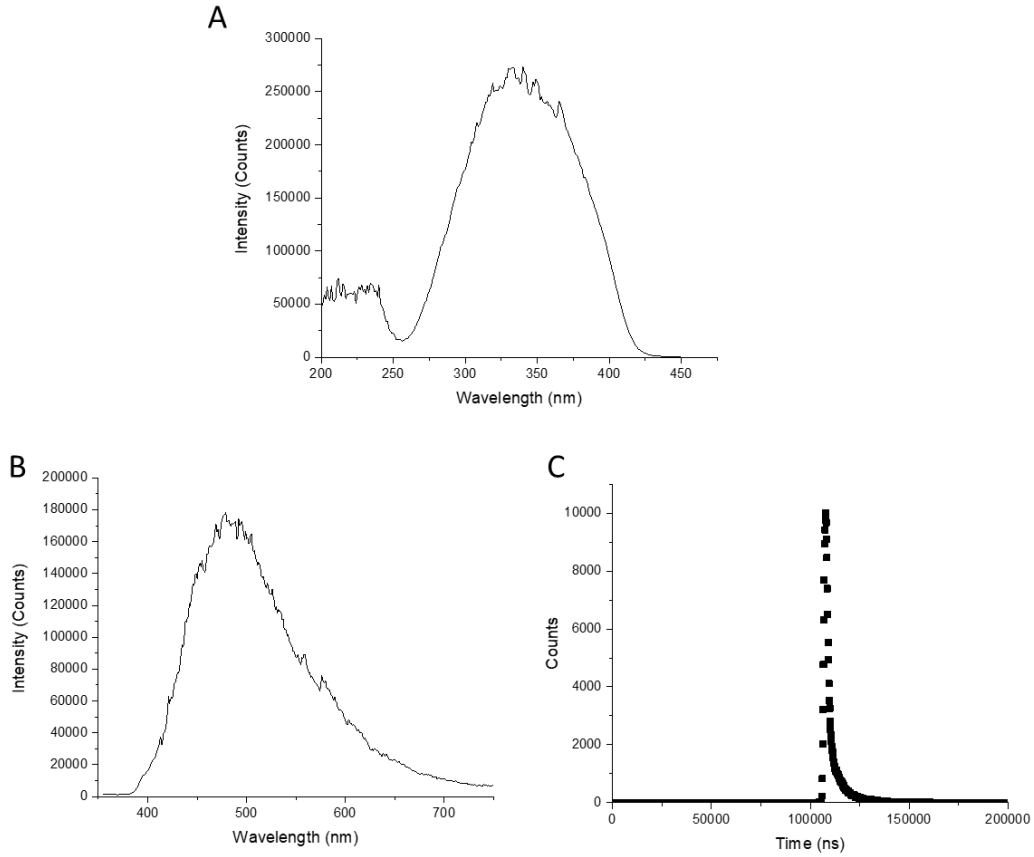

Figure S2b-61. Luminescent data of $[Gd_2(\mathbf{L4^{SS}})_3](OTf)_{12}$ (2.55 x 10^{-5} M in 1:4 of MeOH/EtOH at 77K).(A) Excitation spectrum, λ_{em} = 480 nm, slits = 2.0-0.5, filter 380 nm. (b) Emission spectrum, λ_{ex} = 345 nm, slits = 2.0-0.5, filter 380 nm. (c) Excited state decay curve, λ_{em} = 480 nm, filter 380 nm.

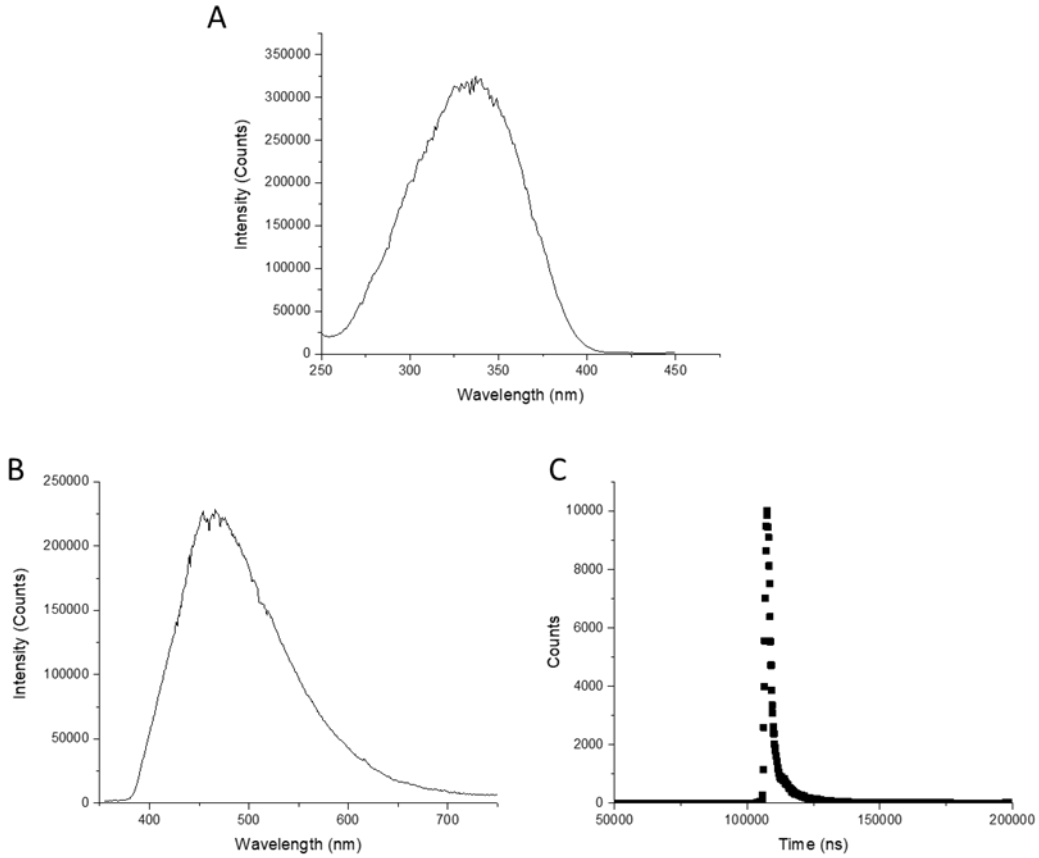

Figure S2b-62. Luminescent data of $[Gd_4(\mathbf{L3^{RR}})_6](OTf)_{12}$ (9.05 x 10^{-6} M in 1:4 of MeOH/EtOH at 77K).(A) Excitation spectrum, λ_{em} = 466 nm, slits = 2.0-0.5, filter 380 nm. (b) Emission spectrum, λ_{ex} = 330 nm, slits = 2.0-0.5, filter 380 nm. (c) Excited state decay curve, λ_{em} = 466 nm, filter 380 nm.

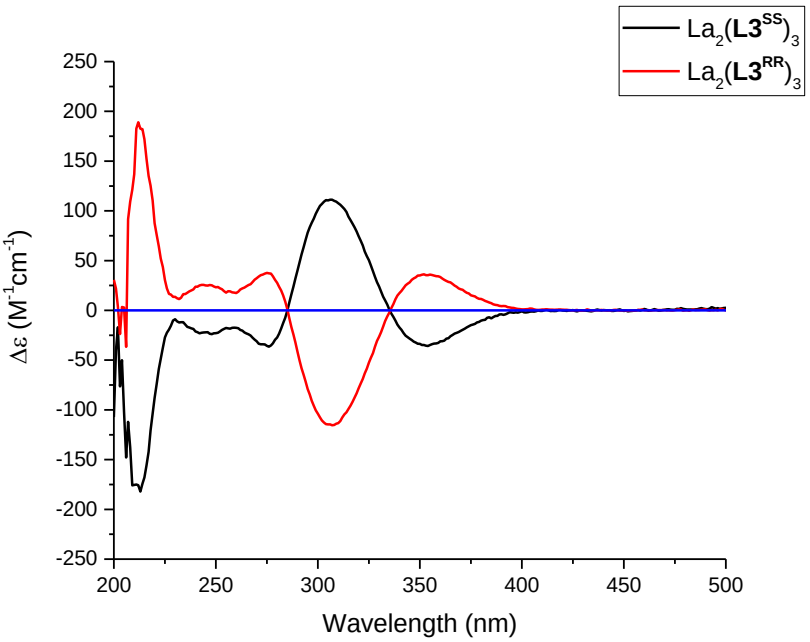

Figure S2b-63. CD spectra of $[La_2(\mathbf{L3}^{SS})_3](OTf)_6$ and $[La_2(\mathbf{L3}^{RR})_3](OTf)_6$ in CH_3CN.

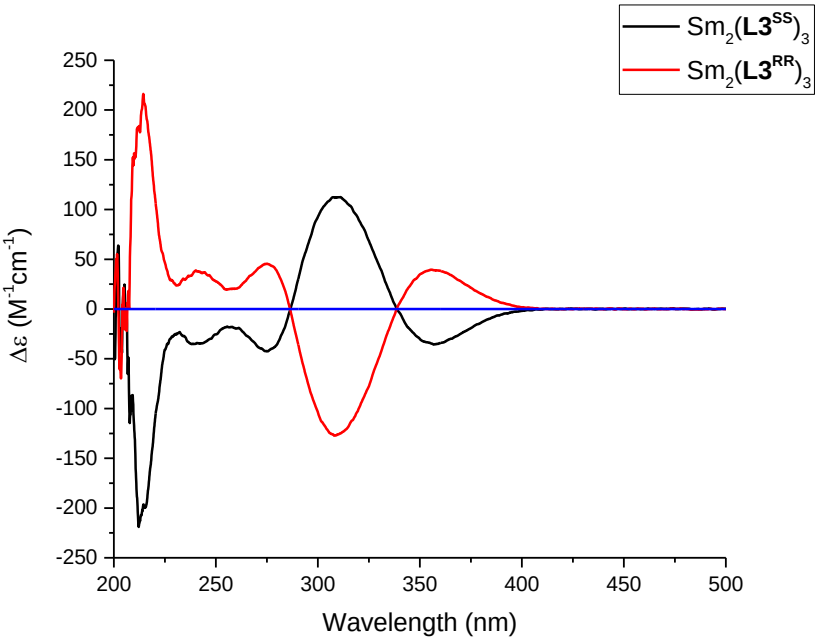

Figure S2b-64. CD spectra of $[Sm_2(\mathbf{L3}^{SS})_3](OTf)_6$ and $[Sm_2(\mathbf{L3}^{RR})_3](OTf)_6$ in CH_3CN.

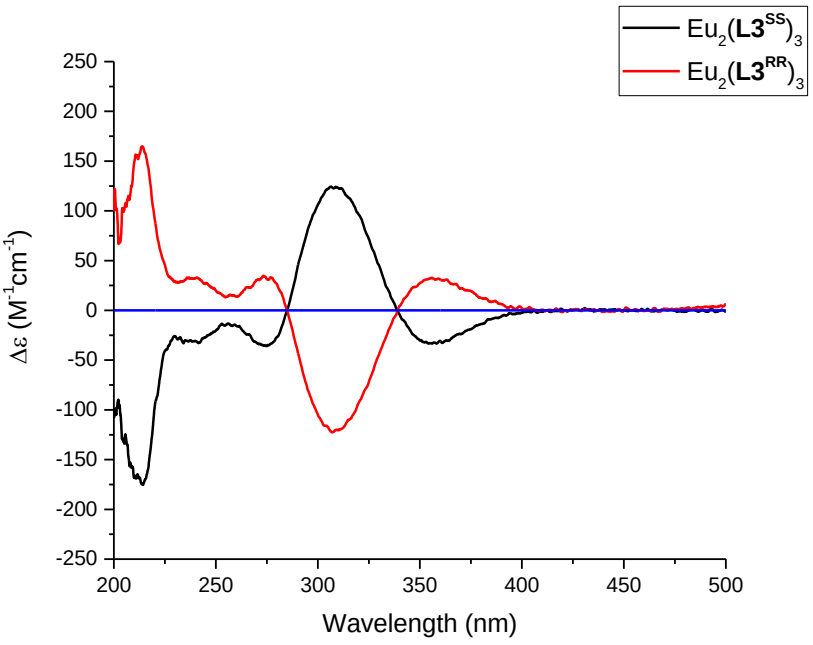

Figure S2b-65. CD spectra of $[Eu_2(\mathbf{L3}^{SS})_3](OTf)_6$ and $[Eu_2(\mathbf{L3}^{RR})_3](OTf)_6$ in CH_3CN.

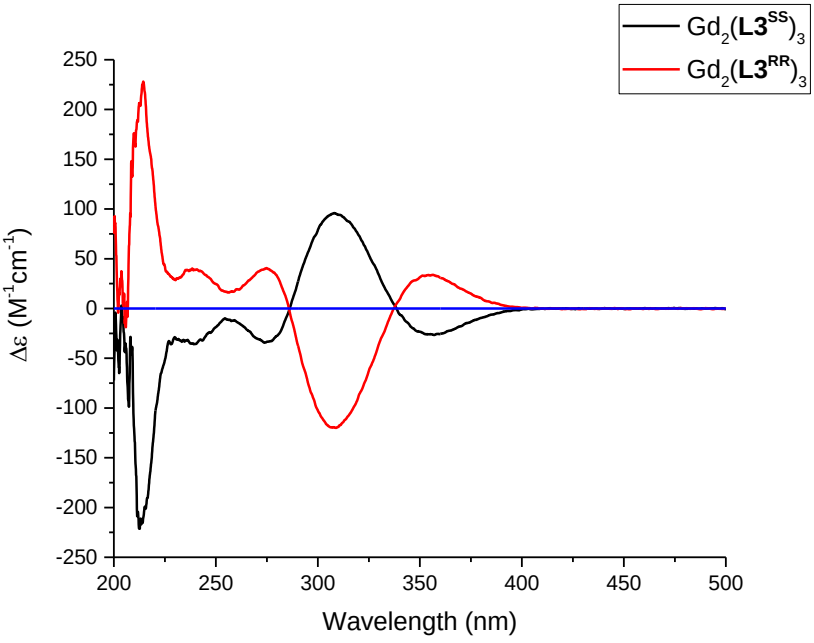

Figure S2b-66. CD spectra of $[Gd_2(\mathbf{L3}^{SS})_3](OTf)_6$ and $[Gd_2(\mathbf{L3}^{RR})_3](OTf)_6$ in CH_3CN.

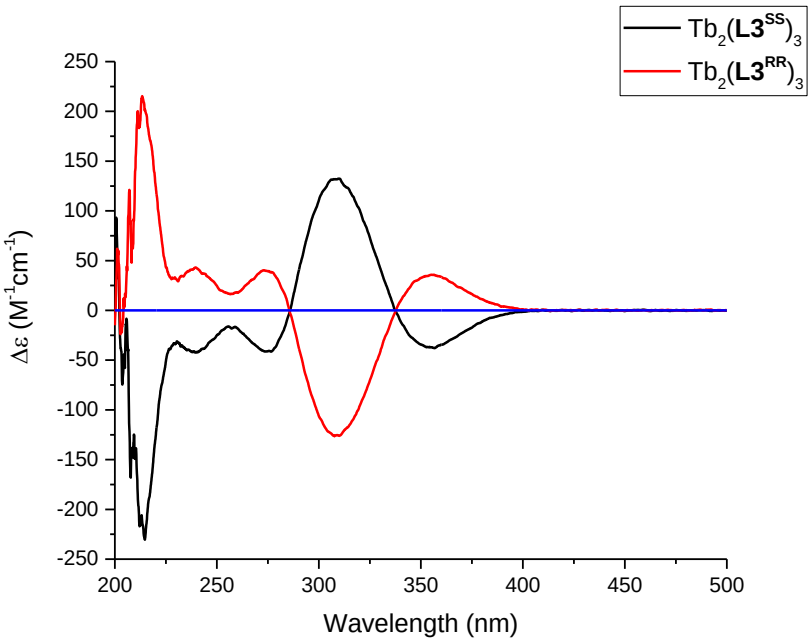

Figure S2b-67. CD spectra of $[Tb_2(\mathbf{L3^{SS}})_3](OTf)_6$ and $[Tb_2(\mathbf{L3^{RR}})_3](OTf)_6$ in CH_3CN.

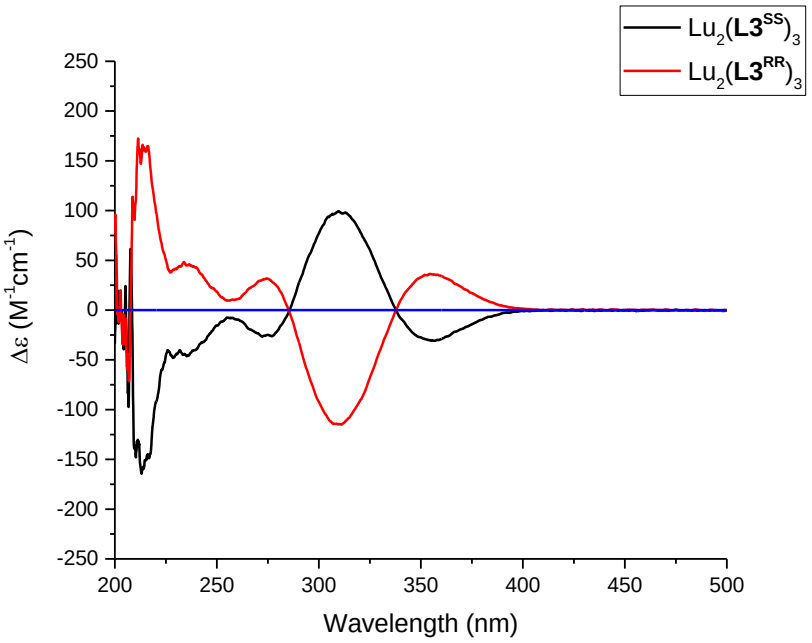

Figure S2b-68. CD spectra of $[Lu_2(\mathbf{L3^{SS}})_3](OTf)_6$ and $[Lu_2(\mathbf{L3^{RR}})_3](OTf)_6$ in CH_3CN.

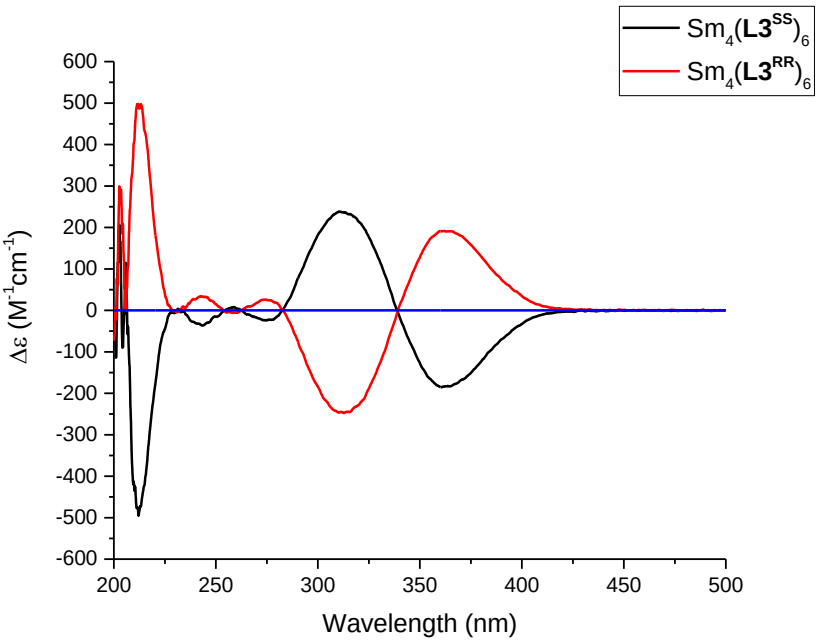

Figure S2b-69. CD spectra of $[Sm_4(\mathbf{L3^{SS}})_6](OTf)_{12}$ and $[Sm_4(\mathbf{L3^{RR}})_6](OTf)_{12}$ in CH_3CN.

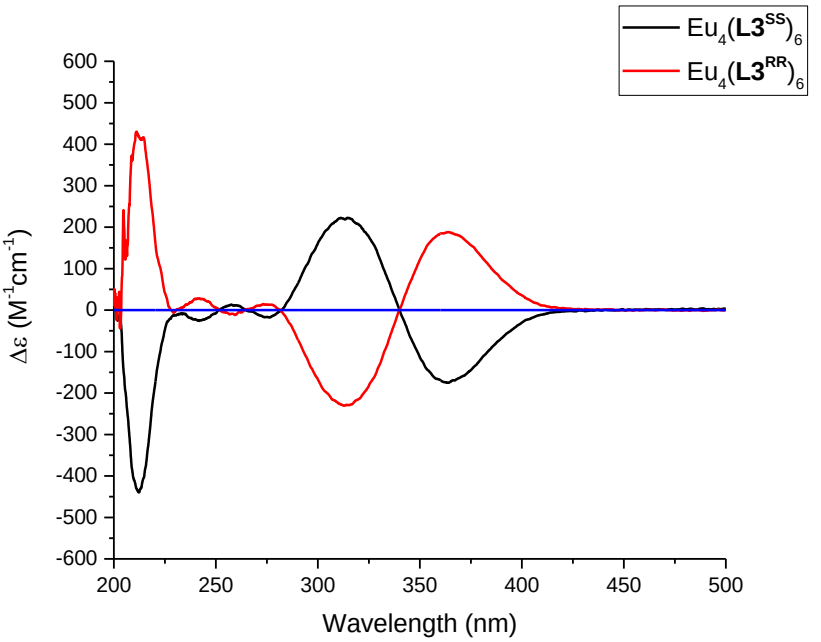

Figure S2b-70. CD spectra of $[Eu_4(\mathbf{L3^{SS}})_6](OTf)_{12}$ and $[Eu_4(\mathbf{L3^{RR}})_6](OTf)_{12}$ in CH_3CN.

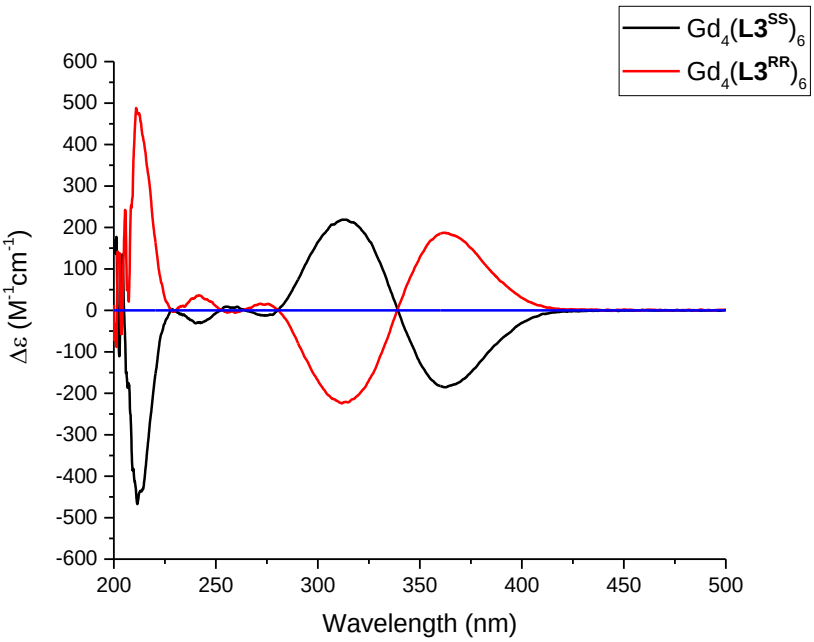

Figure S2b-71. CD spectra of $[Gd_4(\mathbf{L3^{SS}})_6](OTf)_{12}$ and $[Gd_4(\mathbf{L3^{RR}})_6](OTf)_{12}$ in CH_3CN.

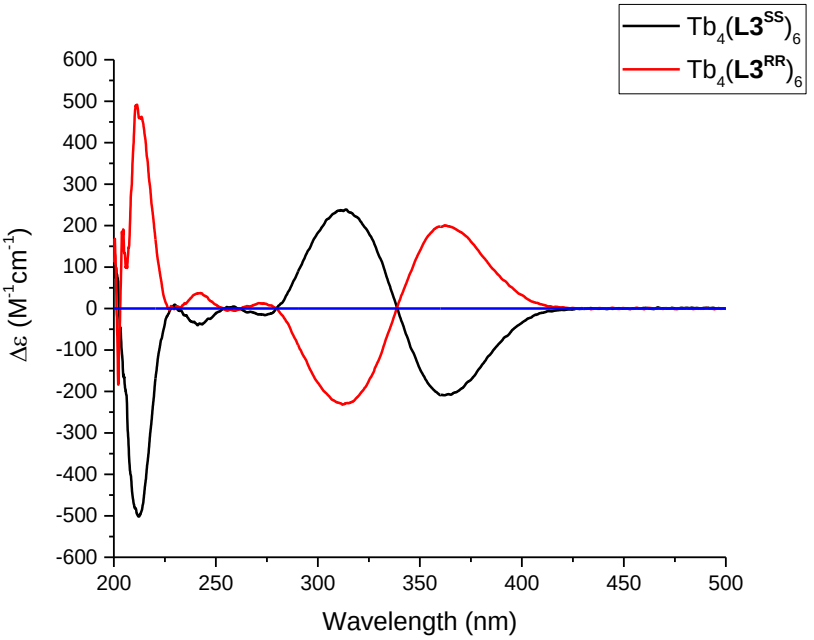

Figure S2b-72. CD spectra of $[Tb_4(\mathbf{L3^{SS}})_6](OTf)_{12}$ and $[Tb_4(\mathbf{L3^{RR}})_6](OTf)_{12}$ in CH_3CN.

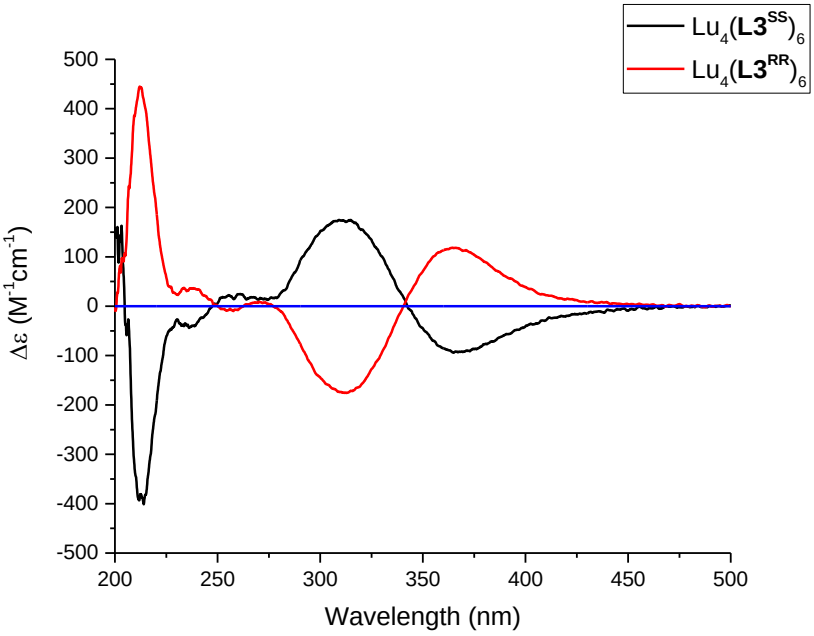

Figure S2b-73. CD spectra of $[Lu_4(\mathbf{L3^{SS}})_6](OTf)_{12}$ and $[Lu_4(\mathbf{L3^{RR}})_6](OTf)_{12}$ in CH_3CN.

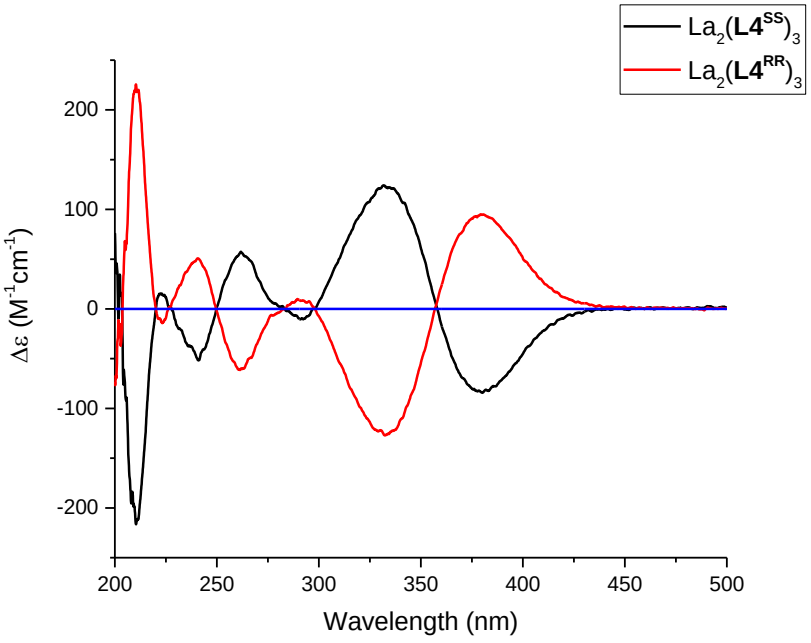

Figure S2b-74. CD spectra of $[La_2(\mathbf{L4^{SS}})_3](OTf)_6$ and $[La_2(\mathbf{L4^{RR}})_3](OTf)_6$ in CH_3CN.

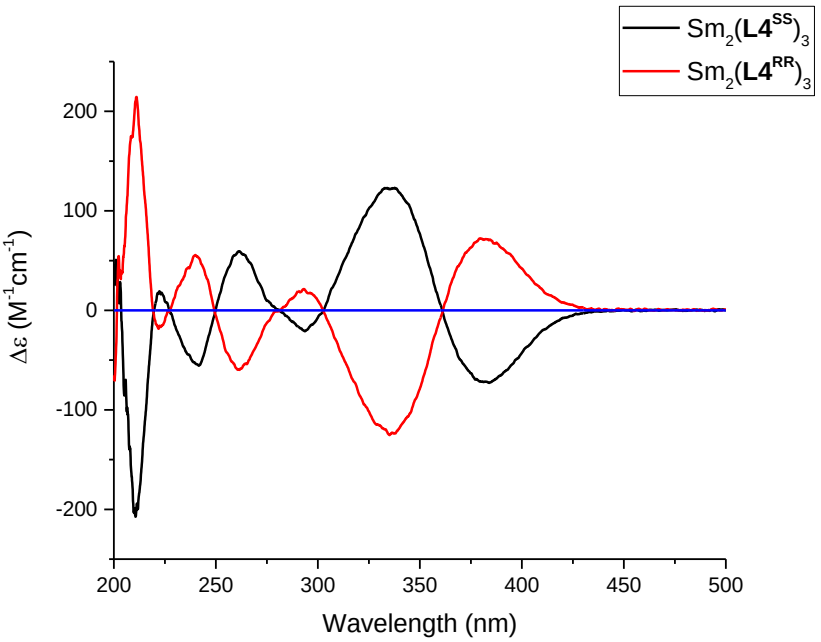

Figure S2b-75. CD spectra of $[Sm_2(\mathbf{L4}^{SS})_3](OTf)_6$ and $[Sm_2(\mathbf{L4}^{RR})_3](OTf)_6$ in CH_3CN.

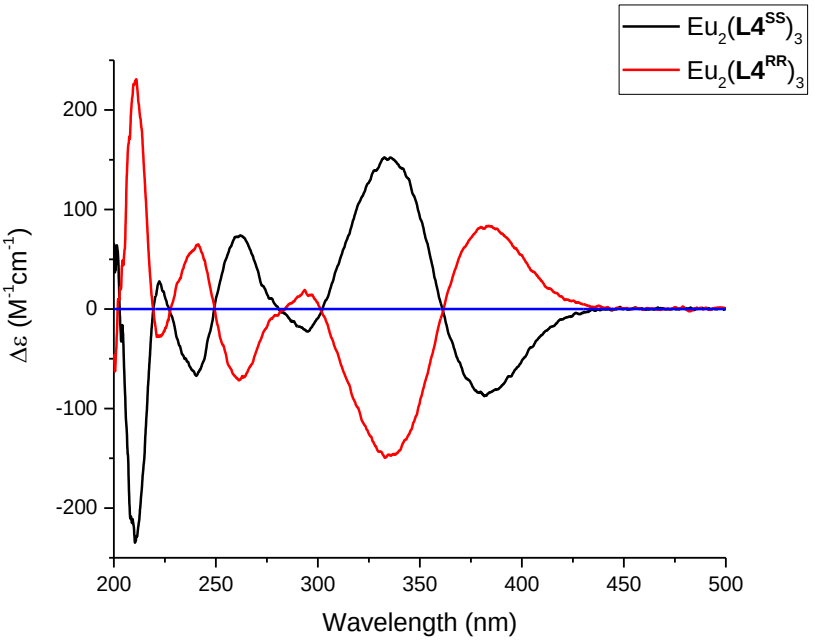

Figure S2b-76. CD spectra of $[Eu_2(\mathbf{L4}^{SS})_3](OTf)_6$ and $[Eu_2(\mathbf{L4}^{RR})_3](OTf)_6$ in CH_3CN.

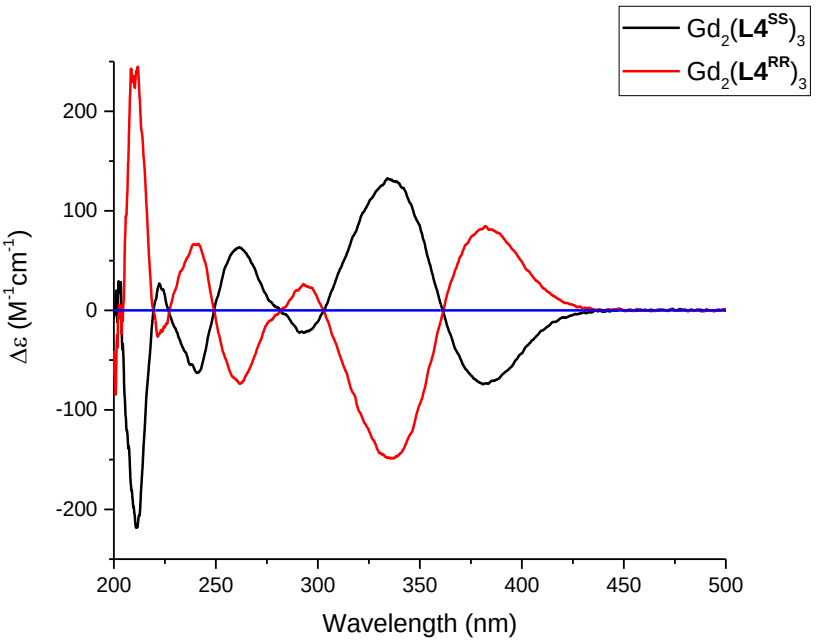

Figure S2b-77. CD spectra of $[Gd_2(\mathbf{L4}^{SS})_3](OTf)_6$ and $[Gd_2(\mathbf{L4}^{RR})_3](OTf)_6$ in CH_3CN.

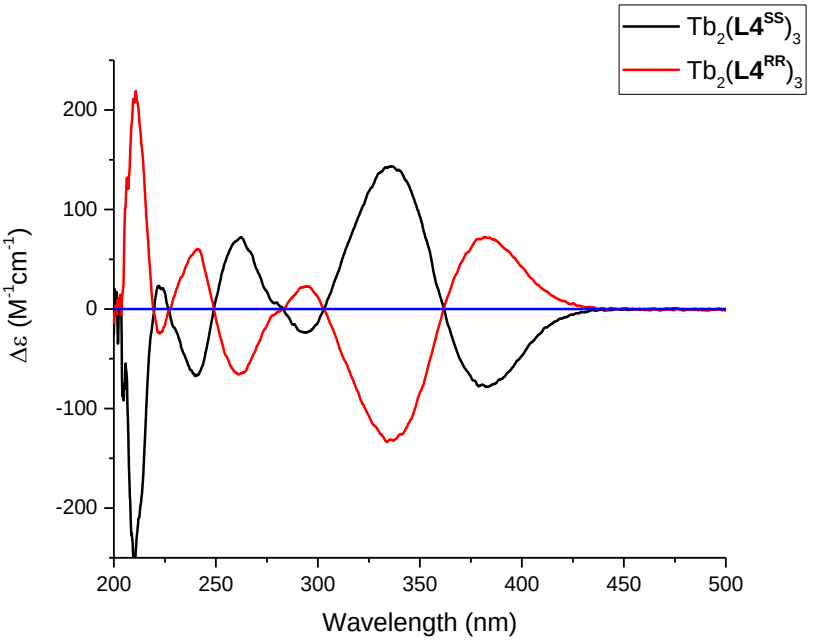

Figure S2b-78. CD spectra of $[Tb_2(\mathbf{L4}^{SS})_3](OTf)_6$ and $[Tb_2(\mathbf{L4}^{RR})_3](OTf)_6$ in CH_3CN.

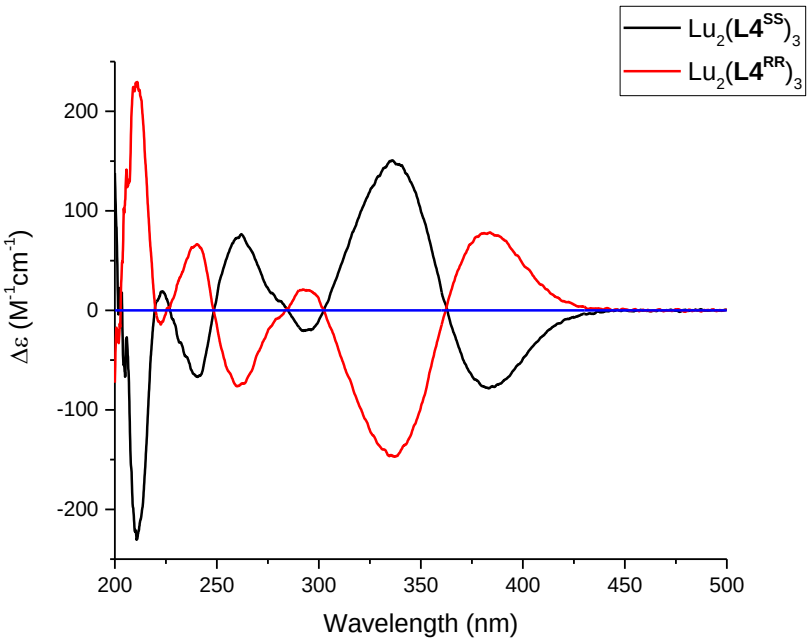

Figure S2b-79. CD spectra of $[Lu_2(\mathbf{L4}^{SS})_3](OTf)_6$ and $[Lu_2(\mathbf{L4}^{RR})_3](OTf)_6$ in CH_3CN.

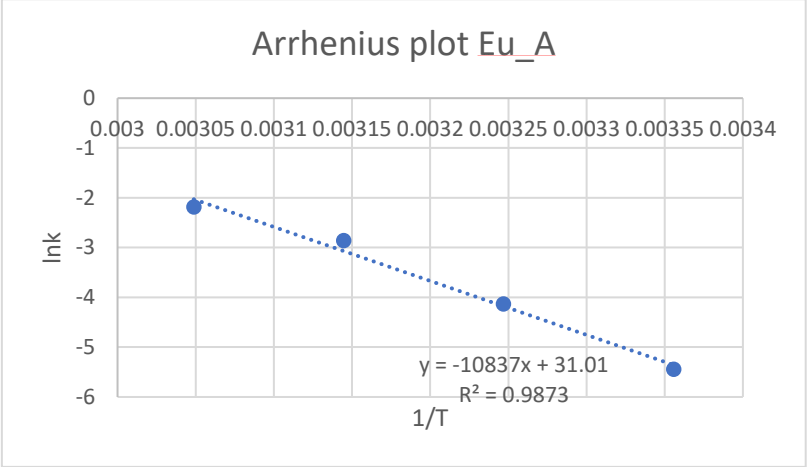

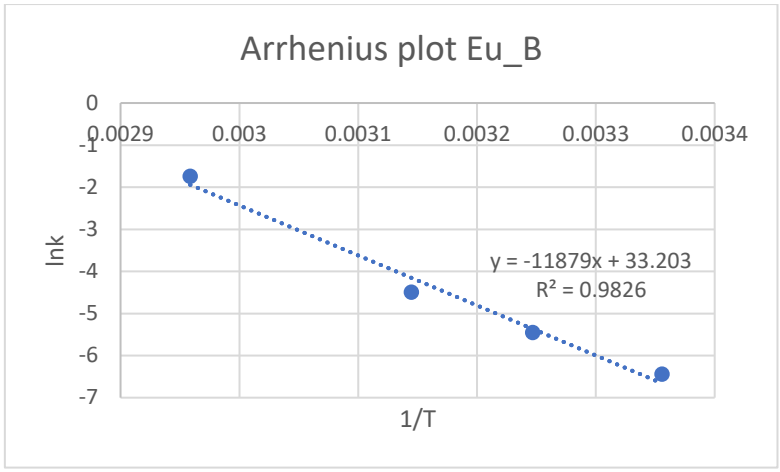

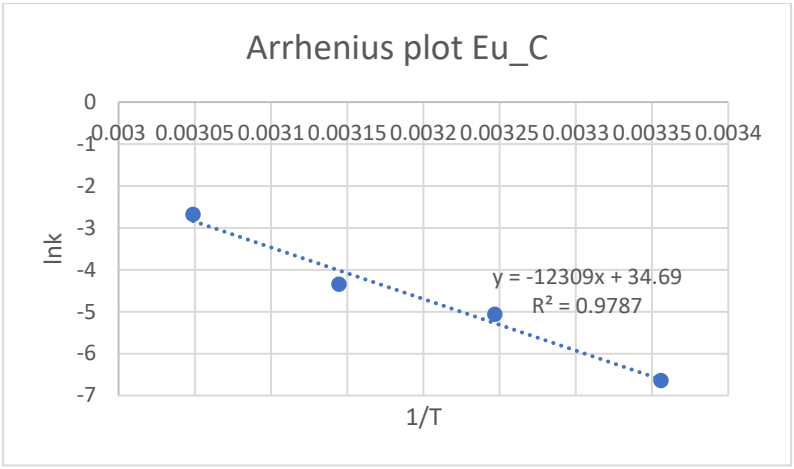

Figure S2b-80. Three sets of Arrhenius plot of Eu tetrahedron-to-helicate transformation.

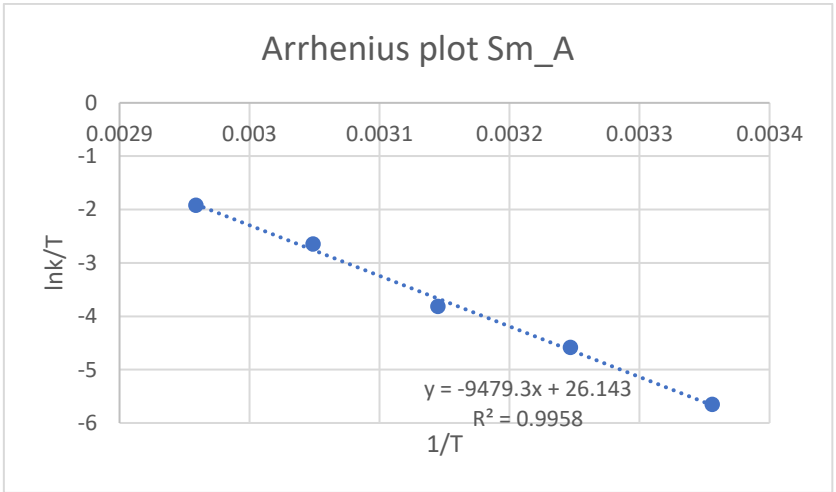

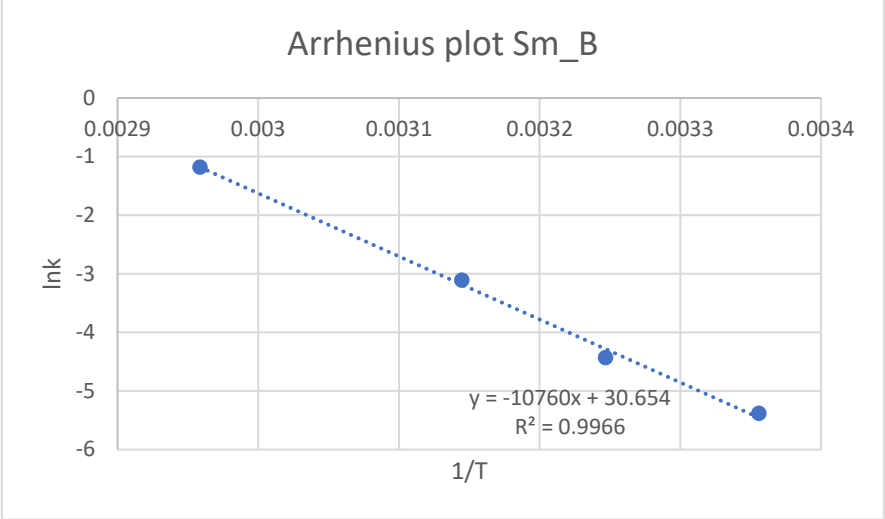

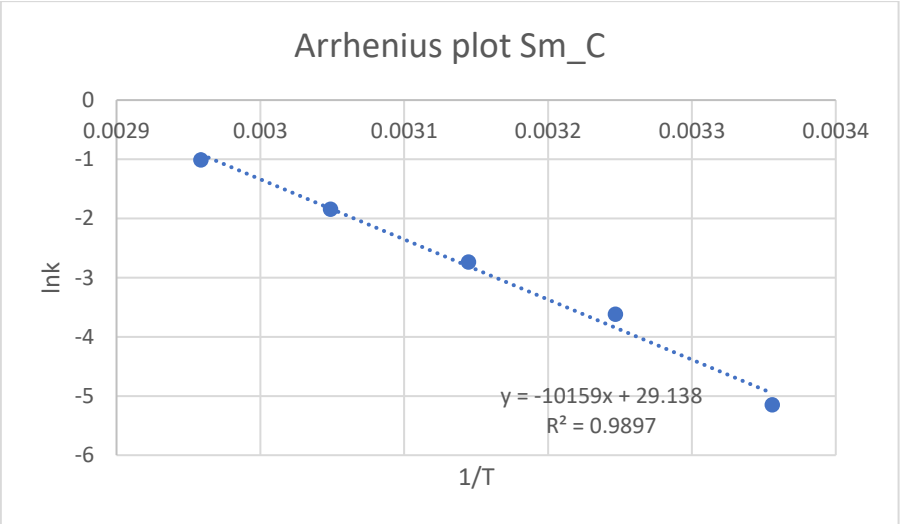

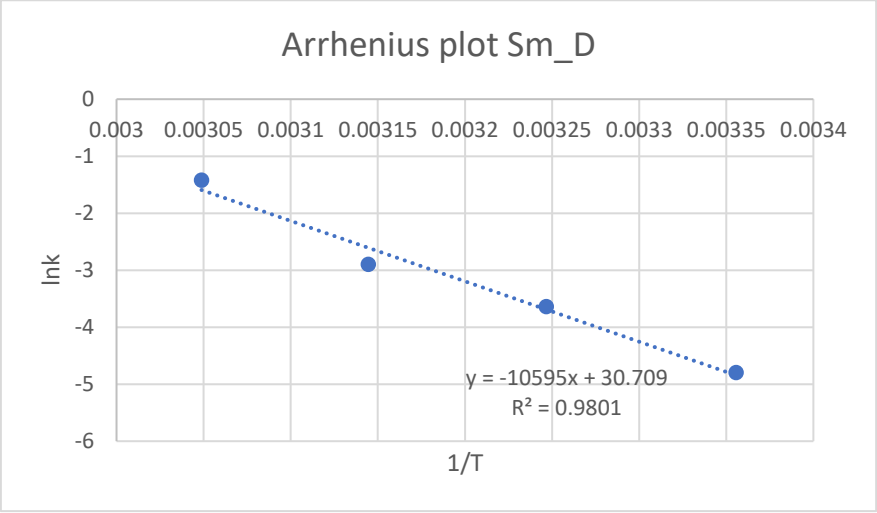

Figure S2b-81. Four sets of Arrhenius plot of Sm tetrahedron-to-helicate transformation.

A

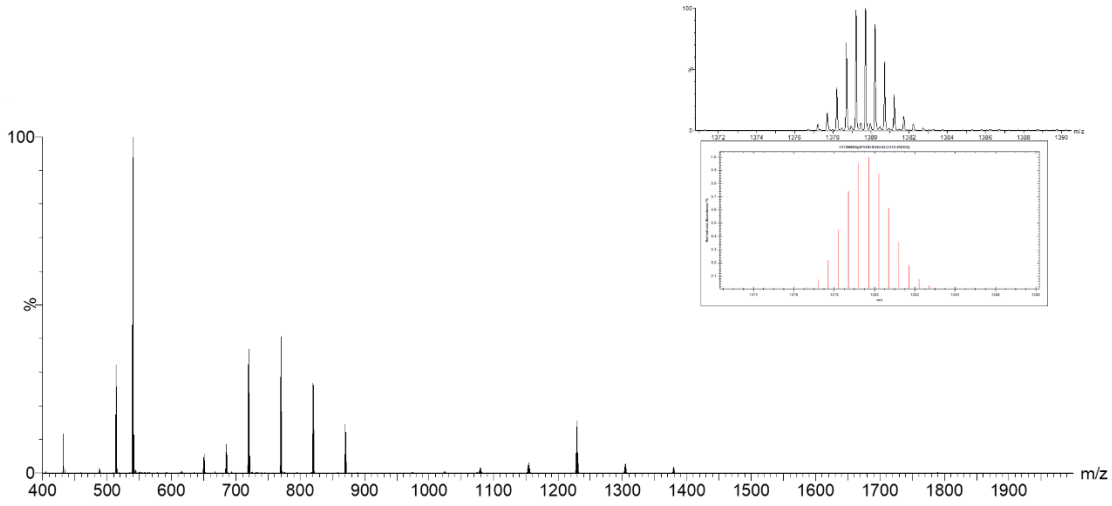

B

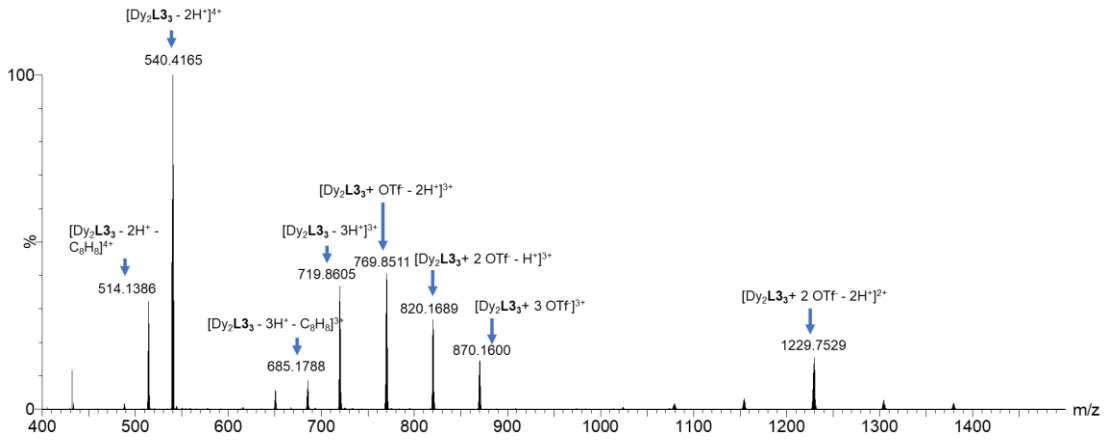

Figure S3-1. ESI-HRMS of bimetallic helicate [Dy_2**L3**$_3$]. (A) The full spectrum. Simulated m/z for [Dy_2**L3**$_3$ + 4OTf^-]$^{2+}$ is 1379.7060(100%), Experimental found m/z is 1379.7075(100%). Inset showing the experimental (upper) and calculated(lower) isotopic patterns. (B) Expanded region of the mass spectrum to show the possible assignments of the corresponding prominent peaks.

A

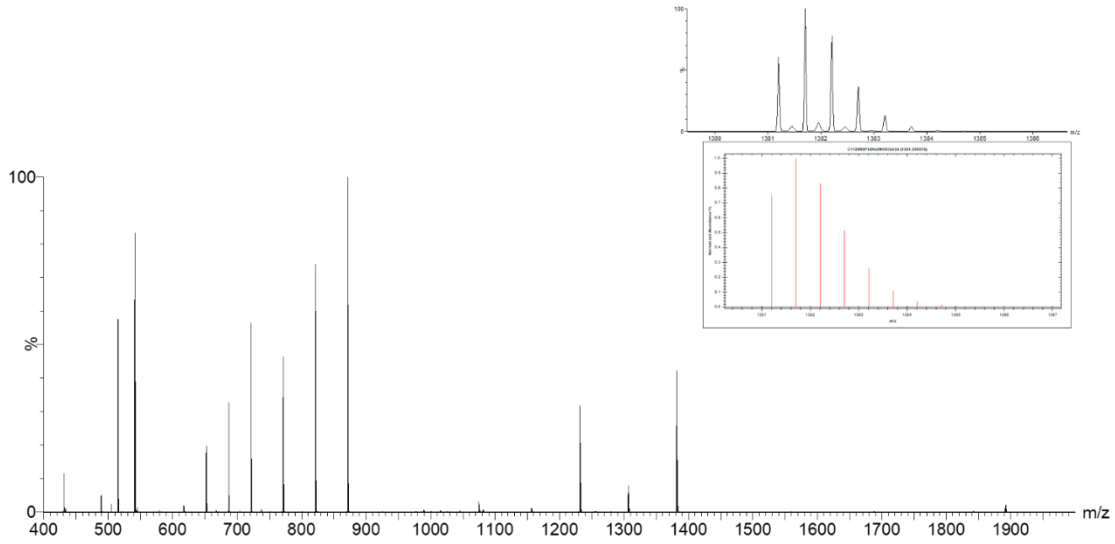

B

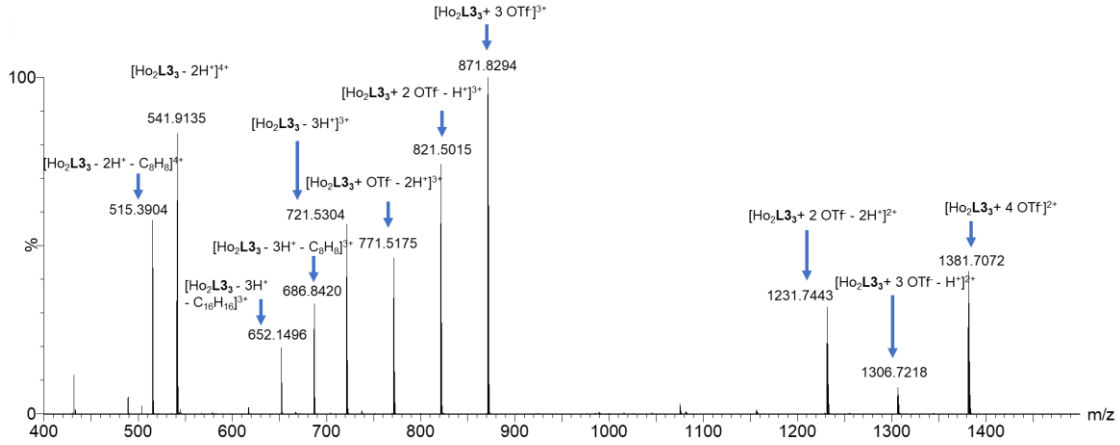

Figure S3-2. ESI-HRMS of bimetallic helicate [Ho_2**L3**$_3$]. (A) The full spectrum. Simulated m/z for [Ho_2**L3**$_3$ + 4OTf^-]$^{2+}$ is 1381.7072(100%), Experimental found m/z is 1381.7081(100%). Inset showing the experimental (upper) and calculated(lower) isotopic patterns. (B) Expanded region of the mass spectrum to show the possible assignments of the corresponding prominent peaks.

A

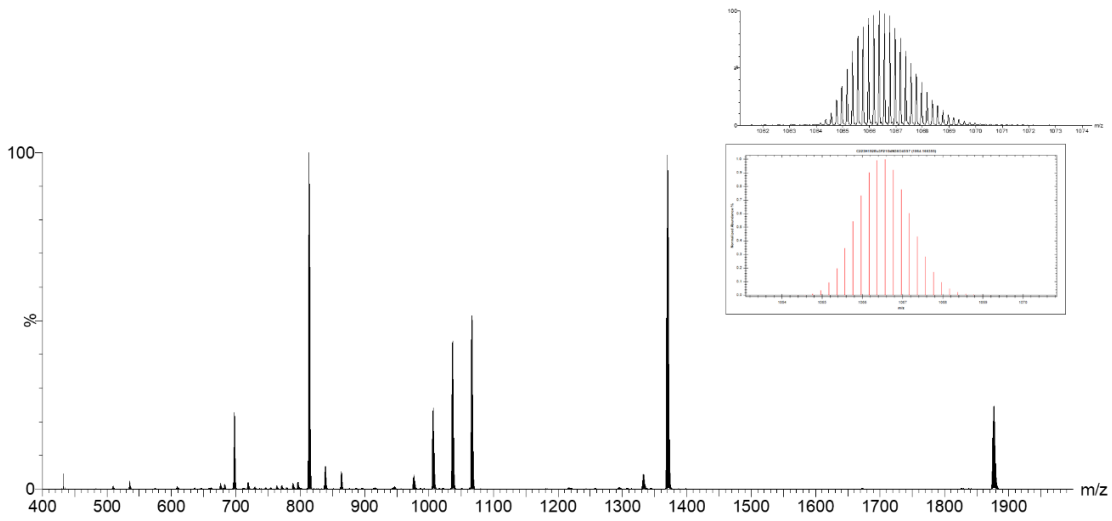

B

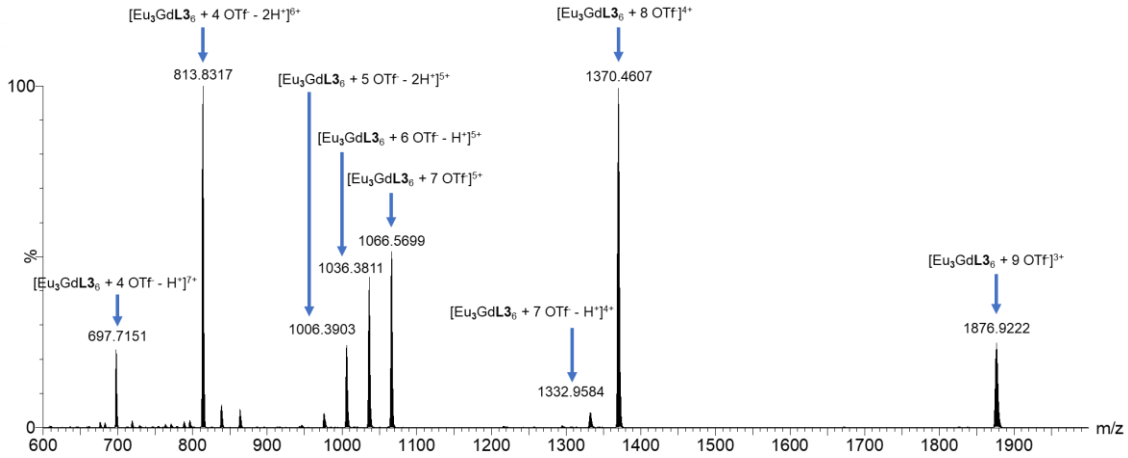

Figure S3-3. ESI-HRMS of tetrahedron [Eu_nGd_{4-n}**L3**$_6$] (prepared by ratio Eu/Gd: 3/1). (A) The full spectrum. Simulated m/z for [Eu_3Gd**L3**$_6$ + 7 OTf^-]$^{5+}$ is 1066.5690(100%), Experimental found m/z is 1066.5699(100%). Inset showing the experimental (upper) and calculated(lower) isotopic patterns. (B) Expanded region of the mass spectrum to show the possible assignments of the corresponding prominent peaks.

A

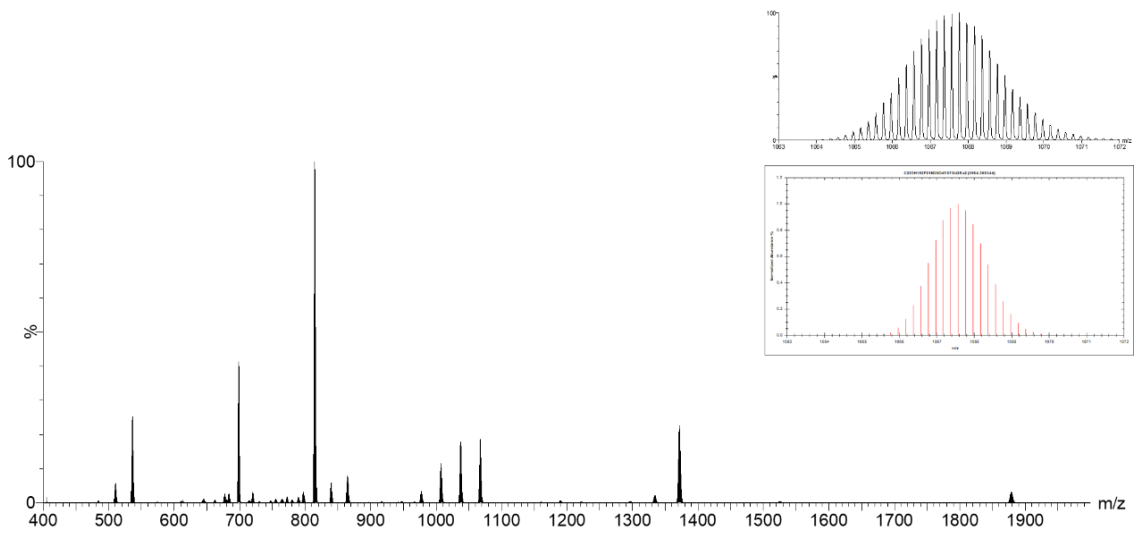

B

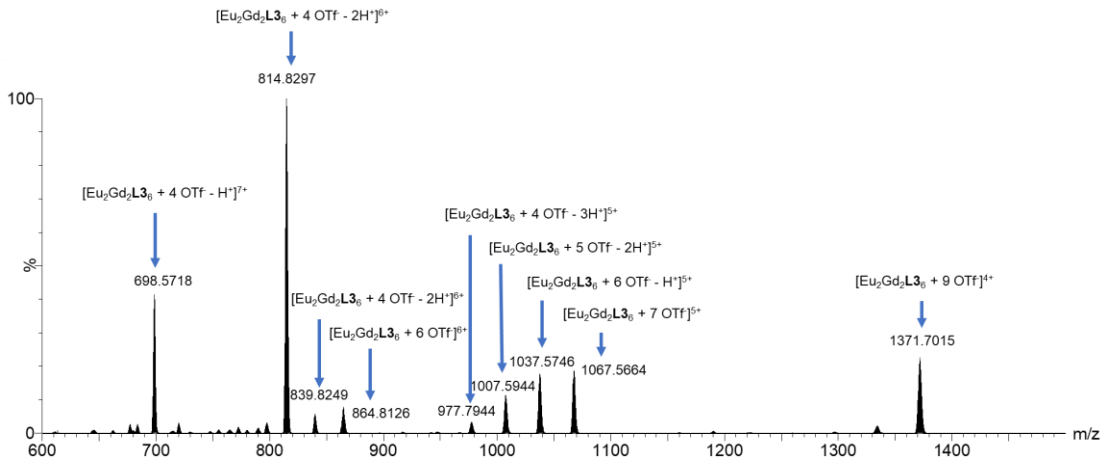

Figure S3-4. ESI-HRMS of tetrahedron $[Eu_nGd_{4-n}\mathbf{L3}_6]$ (prepared by ratio Eu/Gd: 1/1). (A) The full spectrum. Simulated m/z for $[Eu_2Gd_2\mathbf{L3}_6 + 7\ OTf^-]^{5+}$ is 1067.5697(100%), Experimental found m/z is 1067.5664(100%). Inset showing the experimental (upper) and calculated(lower) isotopic patterns. (B) Expanded region of the mass spectrum to show the possible assignments of the corresponding prominent peaks.

A

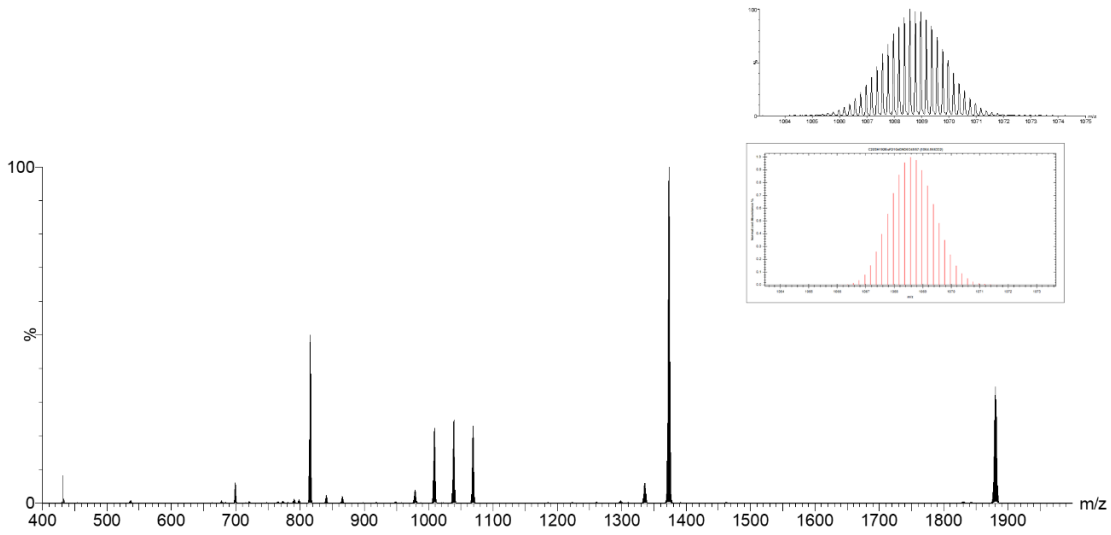

B

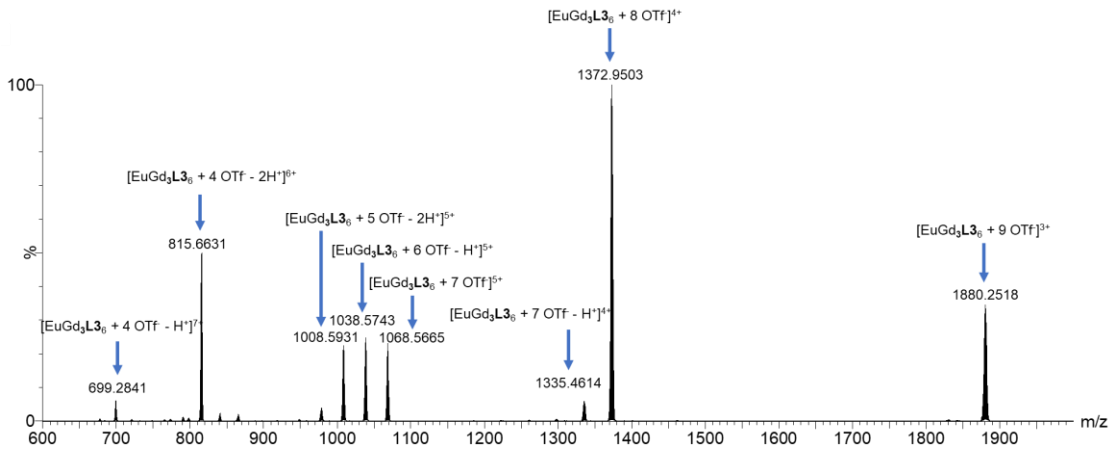

Figure S3-5. ESI-HRMS of tetrahedron [Eu_nGd_{4-n}**L3**$_6$] (prepared by ratio Eu/Gd: 1/3). (A) The full spectrum. Simulated m/z for [$EuGd_3$**L3**$_6$ + 7 OTf^-]$^{5+}$ is 1068.5703(100%), Experimental found m/z is 1068.5665(100%). Inset showing the experimental (upper) and calculated(lower) isotopic patterns. (B) Expanded region of the mass spectrum to show the possible assignments of the corresponding prominent peaks.

A

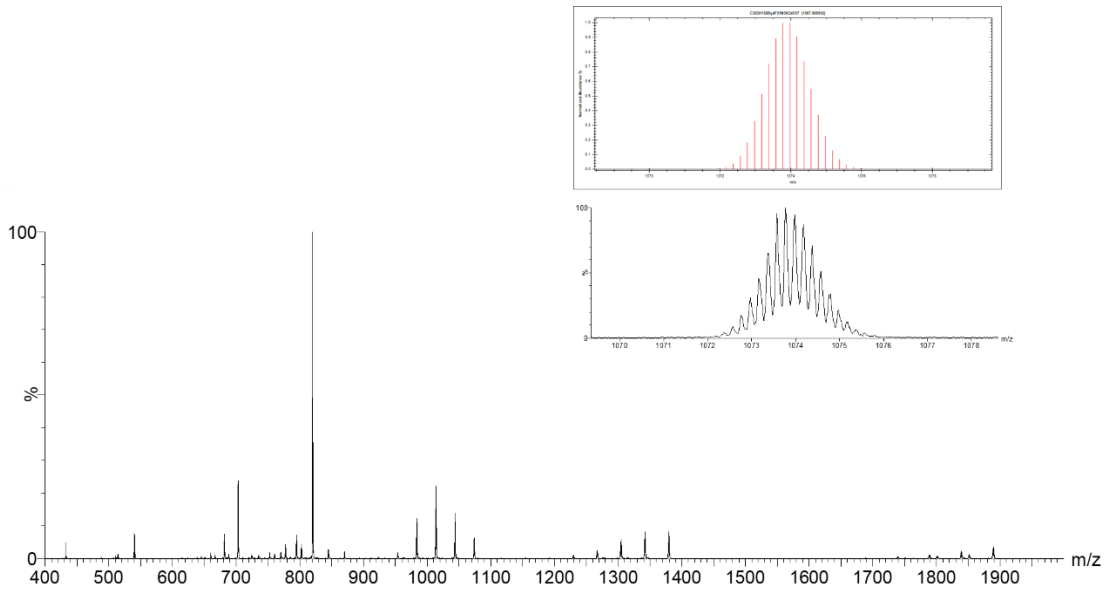

B

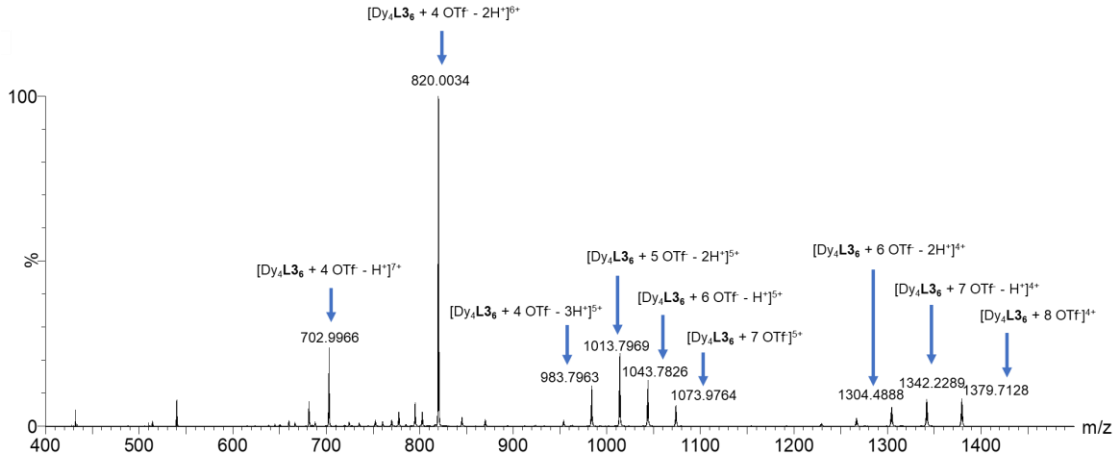

Figure S3-6. ESI-HRMS of tetrahedron [Dy_4**L3**$_6$]. (A) The full spectrum. Simulated m/z for [Dy_4**L3**$_6$ + 7 OTf^-]$^{5+}$ is 1073.9743(100%), Experimental found m/z is 1073.9764(100%). Inset showing the experimental (upper) and calculated(lower) isotopic patterns. (B) Expanded region of the mass spectrum to show the possible assignments of the corresponding prominent peaks.

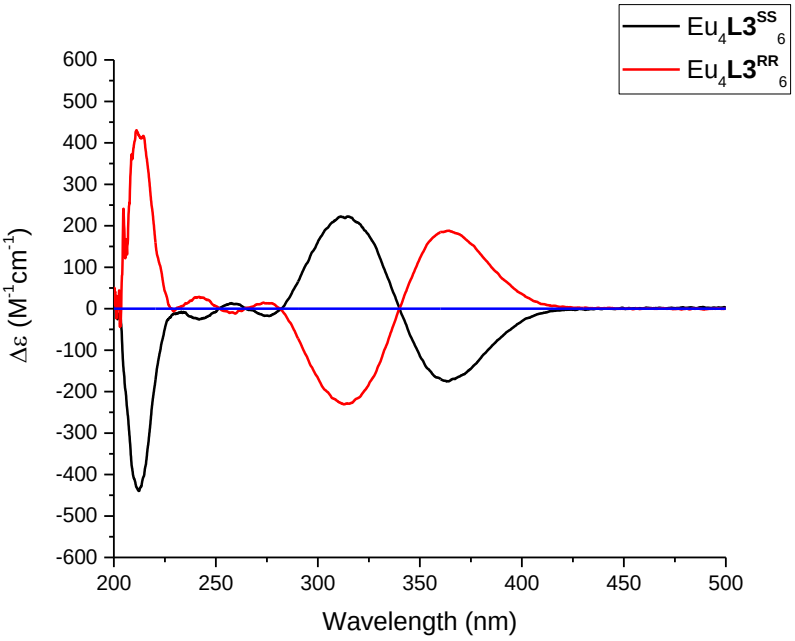

Figure S3-7. CD spectra of $[Eu_4(\mathbf{L3}^{SS})_6]$ and $[Eu_4(\mathbf{L3}^{RR})_6]$ in CH_3CN.

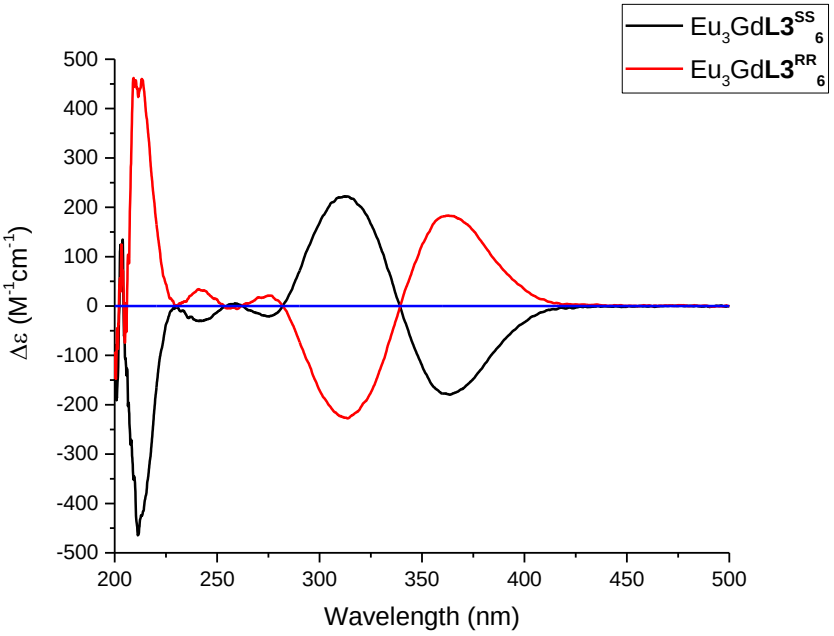

Figure S3-8. CD spectra of $[Eu_nGd_{4-n}\mathbf{L3}^{SS}_6]$ and $[Eu_nGd_{4-n}\mathbf{L3}^{RR}_6]$ in MeCN (prepared by ratio Eu/Gd: 1/3).

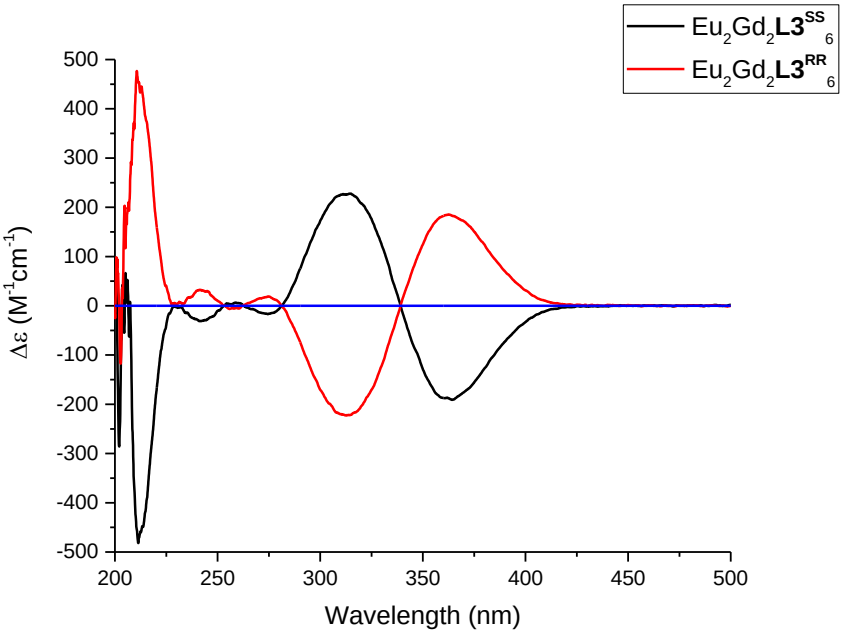

Figure S3-9. CD spectra of [Eu_nGd_{4-n}**L3**$^{SS}_6$] and [Eu_nGd_{4-n}**L3**$^{RR}_6$] in MeCN (prepared by ratio Eu/Gd: 1/1).

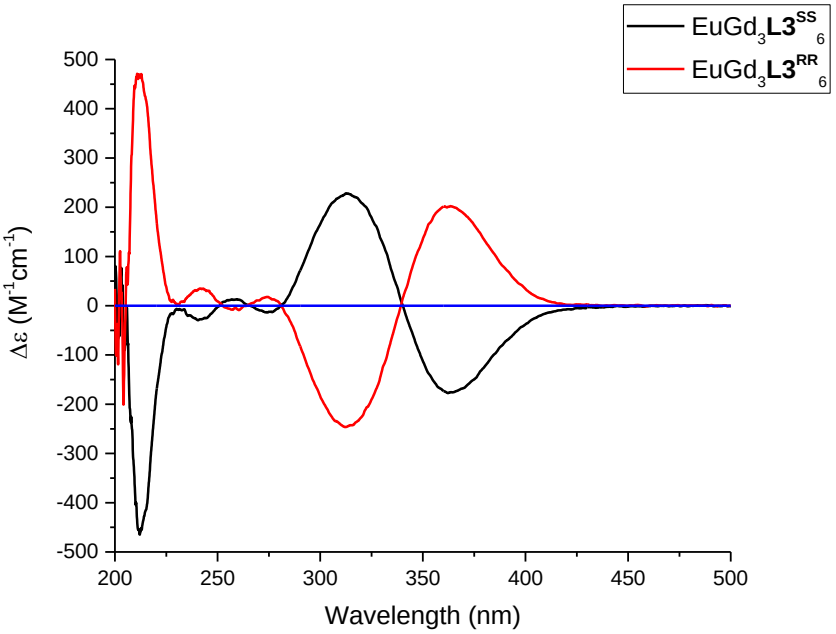

Figure S3-10. CD spectra of [Eu_nGd_{4-n}**L3**$^{SS}_6$] and [Eu_nGd_{4-n}**L3**$^{RR}_6$] in MeCN (prepared by ratio Eu/Gd: 1/2).

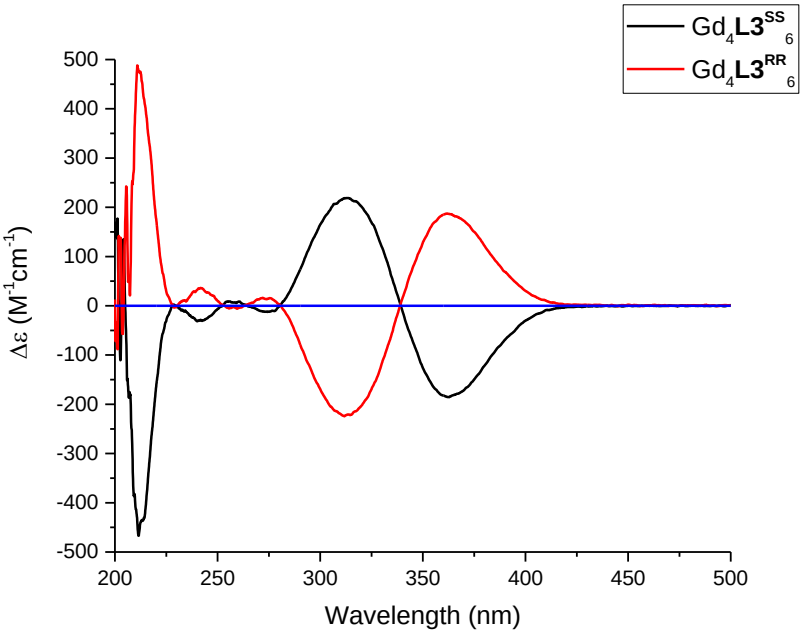

Figure S3-11. CD spectra of [Gd_4(**L3**^{SS})$_6$] and [Gd_4(**L3**^{RR})$_6$] in MeCN.

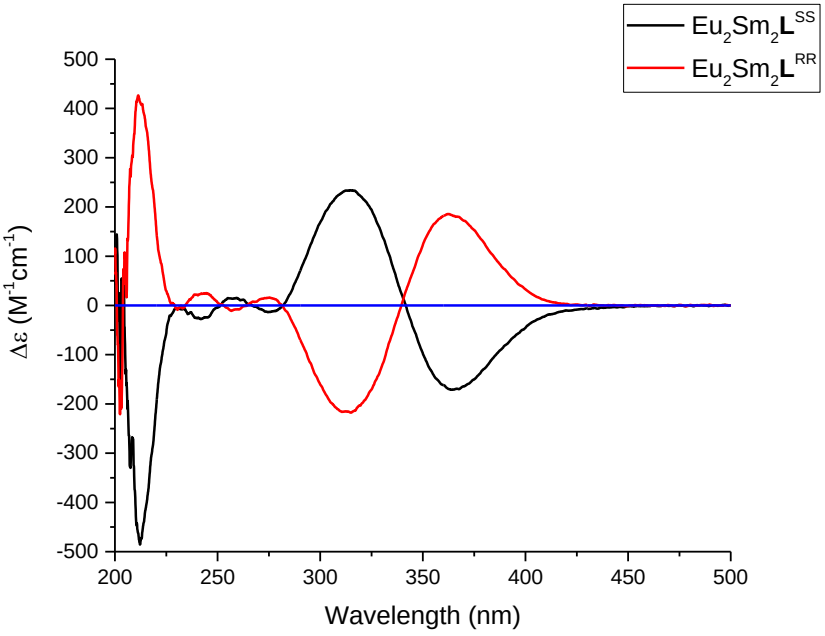

Figure S3-12. CD spectra of [Eu_nSm_{4-n}**L3**$^{SS}_6$] and [Eu_nSm_{4-n}**L3**$^{RR}_6$] in MeCN (prepared by ratio Eu/Sm: 1/1).

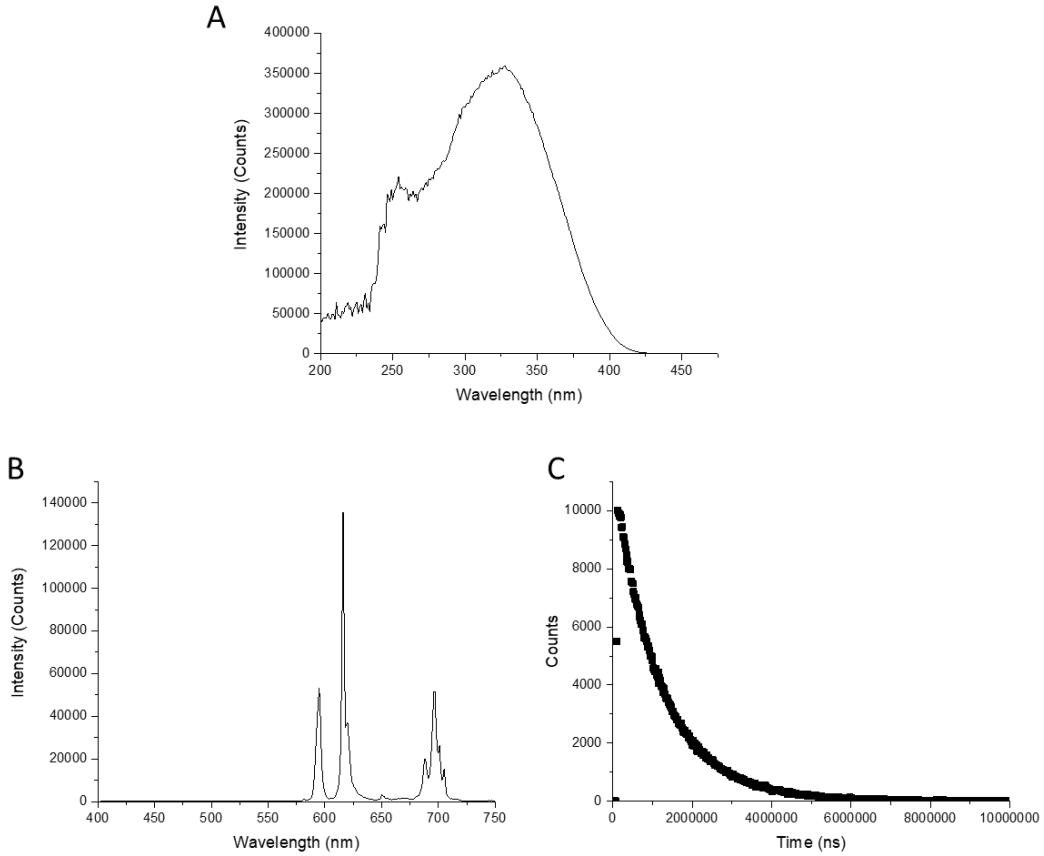

Figure S3-13. Luminescent data of $[Eu_4(\mathbf{L3^{SS}})_6]$ (2.50 x 10^{-6} M in MeCN).(A) Excitation spectrum, λ_{em} = 616 nm, slits = 1.5-1.0, filter 380 nm. (b) Emission spectrum, λ_{ex} = 330 nm, slits = 1.5-1.0, filter 380 nm. (c) Excited state decay curve, λ_{em} = 616 nm, slits = 5-3, filter 380 nm.

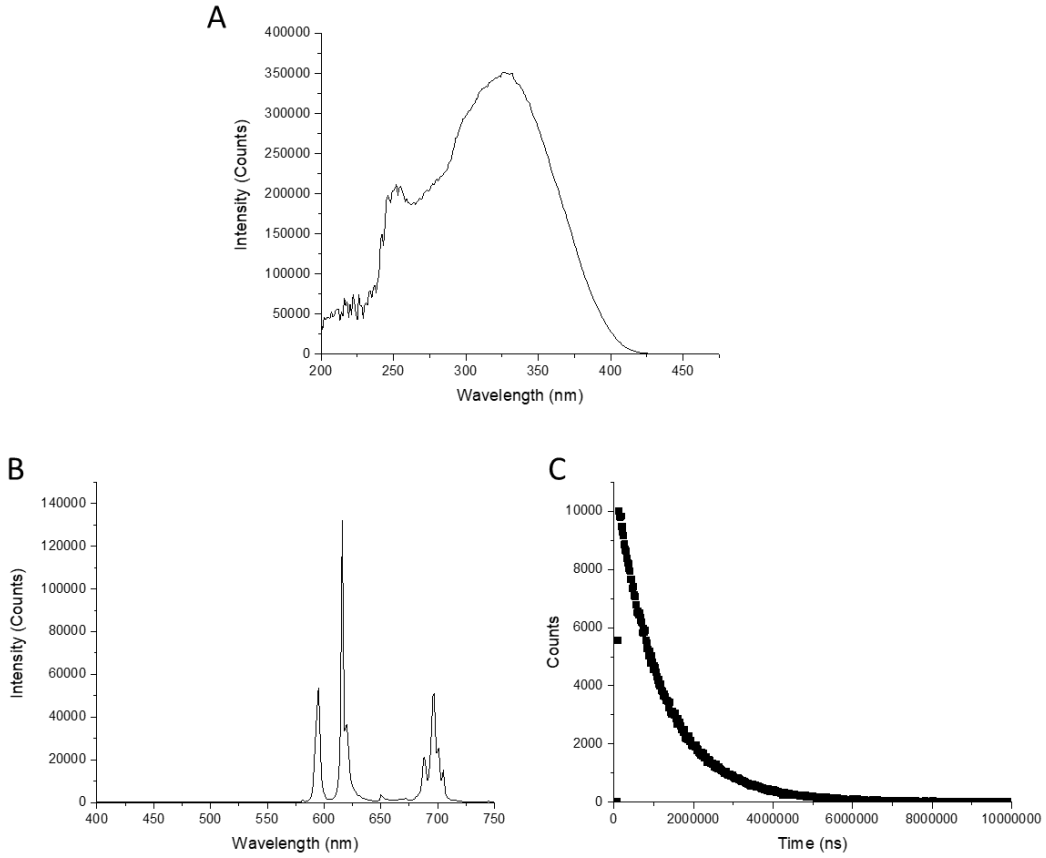

Figure S3-14. Luminescent data of $[Eu_4(\mathbf{L3^{RR}})_6]$ (2.41 x 10^{-6} M in MeCN).(A) Excitation spectrum, λ_{em} = 616 nm, slits = 1.5-1.0, filter 380 nm. (b) Emission spectrum, λ_{ex} = 330 nm, slits = 1.5-1.0, filter 380 nm. (c) Excited state decay curve, λ_{em} = 616 nm, slits = 5-3, filter 380 nm.

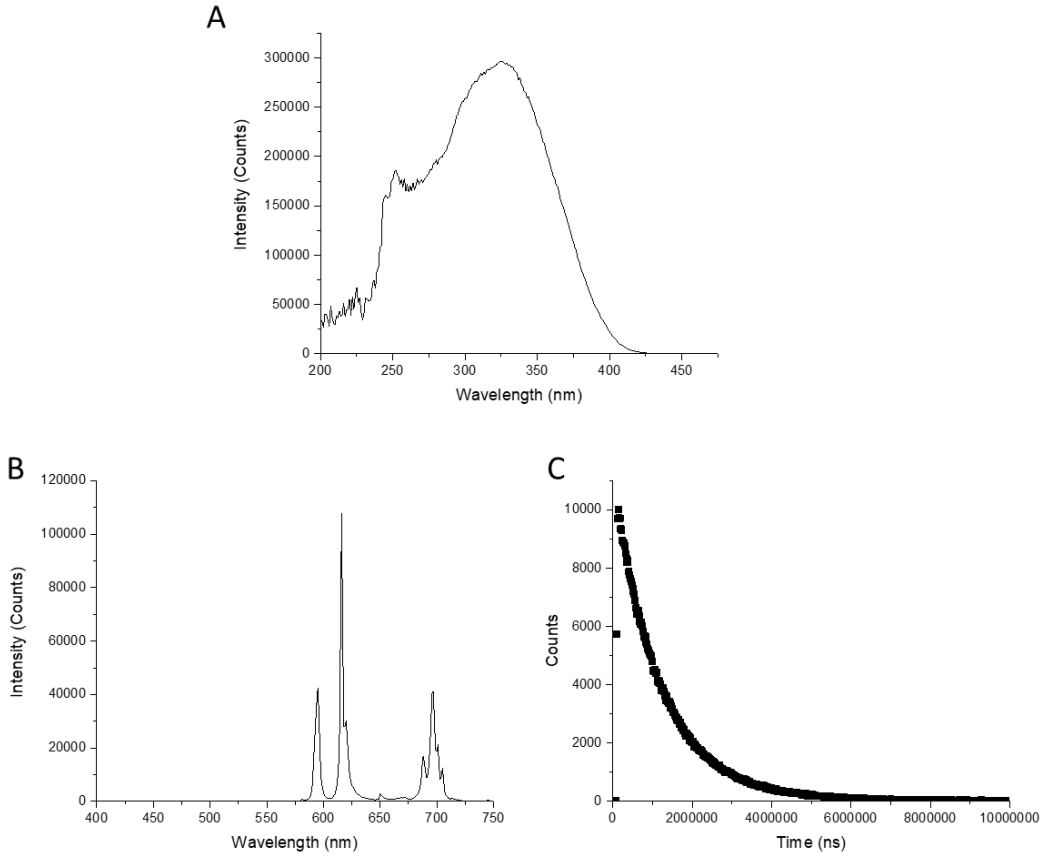

Figure S3-15. Luminescent data of [Eu_nGd_{4-n}**L3**$^{SS}_6$] (prepared by ratio Eu/Gd: 3/1), (2.29 x 10^{-6} M in MeCN).(A) Excitation spectrum, λ_{em} = 616 nm, slits = 1.5-1.0, filter 380 nm. (b) Emission spectrum, λ_{ex} = 330 nm, slits = 1.5-1.0, filter 380 nm. (c) Excited state decay curve, λ_{em} = 616 nm, slits = 5.0-3.0, filter 380 nm.

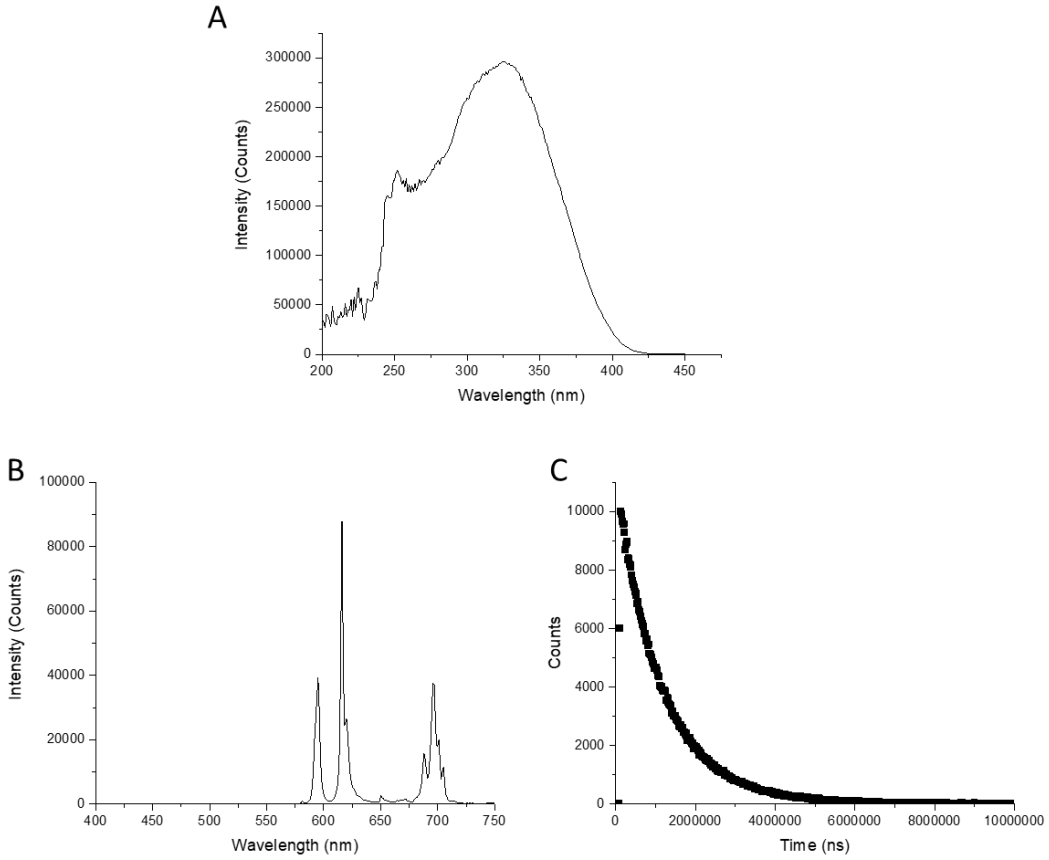

Figure S3-16. Luminescent data of [Eu_nGd_{4-n}**L3**$^{RR}{}_6$] (prepared by ratio Eu/Gd: 3/1), (2.33 x 10^{-6} M in MeCN).(A) Excitation spectrum, λ_{em} = 616 nm, slits = 1.5-1.0, filter 380 nm. (b) Emission spectrum, λ_{ex} = 330 nm, slits = 1.5-1.0, filter 380 nm. (c) Excited state decay curve, λ_{em} = 616 nm, slits = 5.0-3.5, filter 380 nm.

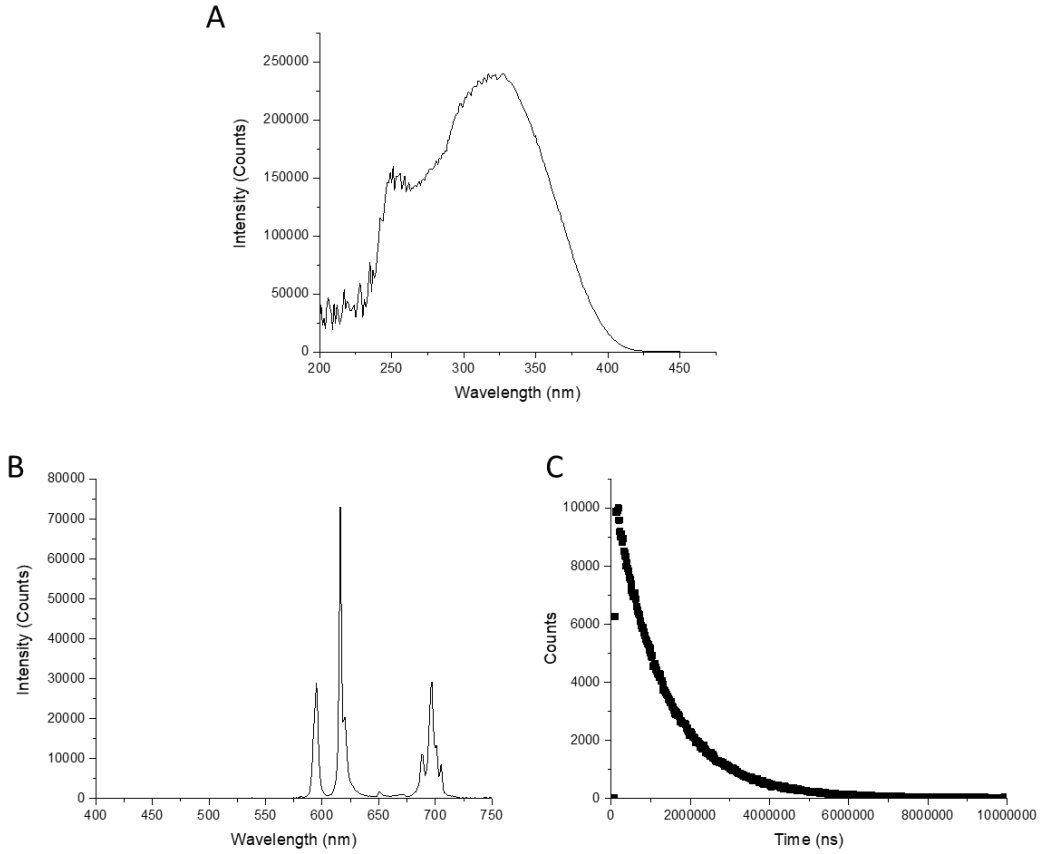

Figure S3-17. Luminescent data of [Eu_nGd_{4-n}**L3**$^{SS}_6$] (prepared by ratio Eu/Gd: 1/1), (2.60 x 10^{-6} M in MeCN).(A) Excitation spectrum, λ_{em} = 616 nm, slits = 1.5-1.0, filter 380 nm. (b) Emission spectrum, λ_{ex} = 330 nm, slits = 1.5-1.0, filter 380 nm. (c) Excited state decay curve, λ_{em} = 616 nm, slits = 5.0-4.0, filter 380 nm.

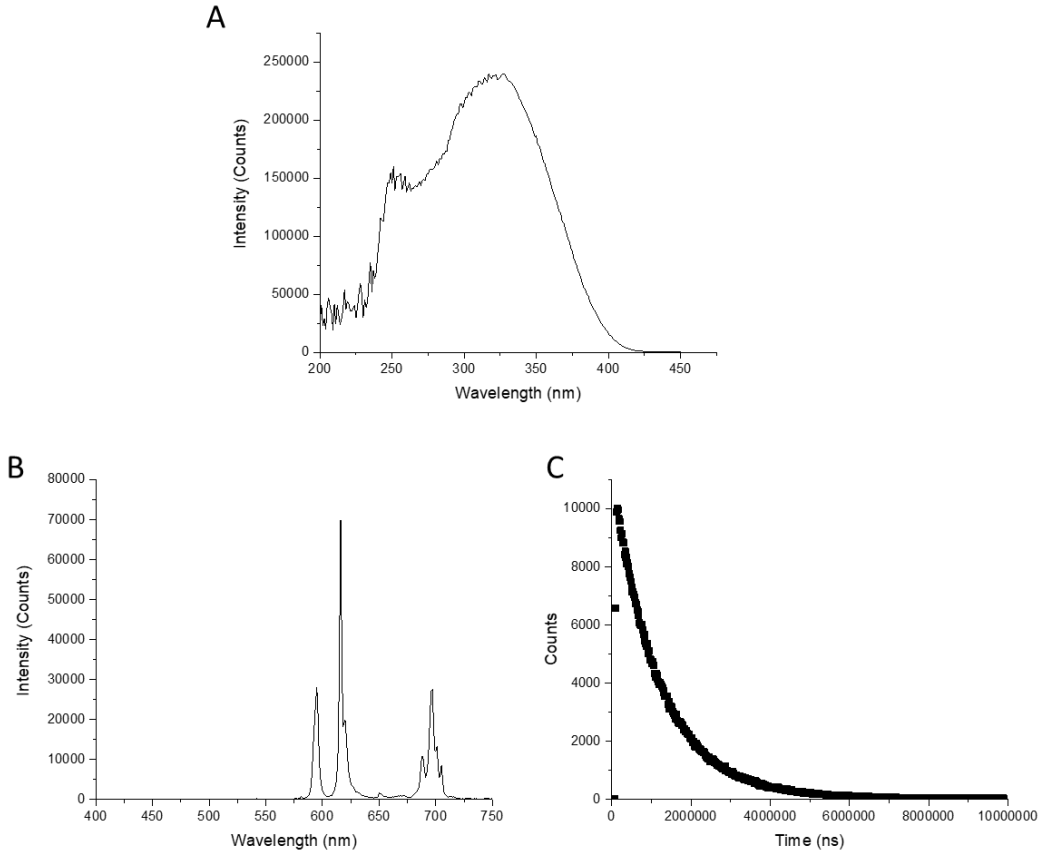

Figure S3-18. Luminescent data of [Eu_nGd_{4-n}**L3**$^{RR}_6$] (prepared by ratio Eu/Gd: 1/1), (2.60 x 10^{-6} M in MeCN).(A) Excitation spectrum, λ_{em} = 616 nm, slits = 1.5-1.0, filter 380 nm. (b) Emission spectrum, λ_{ex} = 330 nm, slits = 1.5-1.0, filter 380 nm. (c) Excited state decay curve, λ_{em} = 616 nm, slits = 5.0-4.0, filter 380 nm.

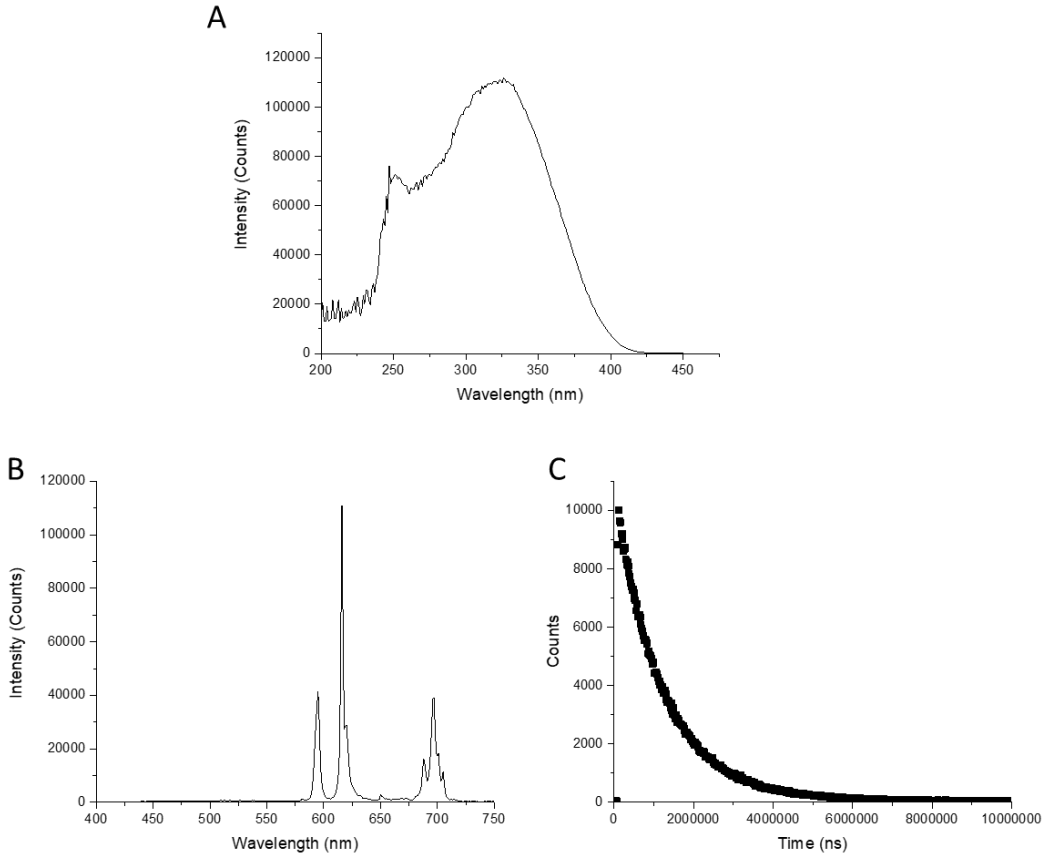

Figure S3-19. Luminescent data of [Eu_nGd_{4-n}**L3**$^{SS}_6$] (prepared by ratio Eu/Gd: 1/3), (2.44 x 10^{-6} M in MeCN).(A) Excitation spectrum, λ_{em} = 616 nm, slits = 2.5-1.0, filter 380 nm. (b) Emission spectrum, λ_{ex} = 330 nm, slits = 2.5-1.0, filter 380 nm. (c) Excited state decay curve, λ_{em} = 616 nm, slits = 6.0-5.0, filter 380 nm.

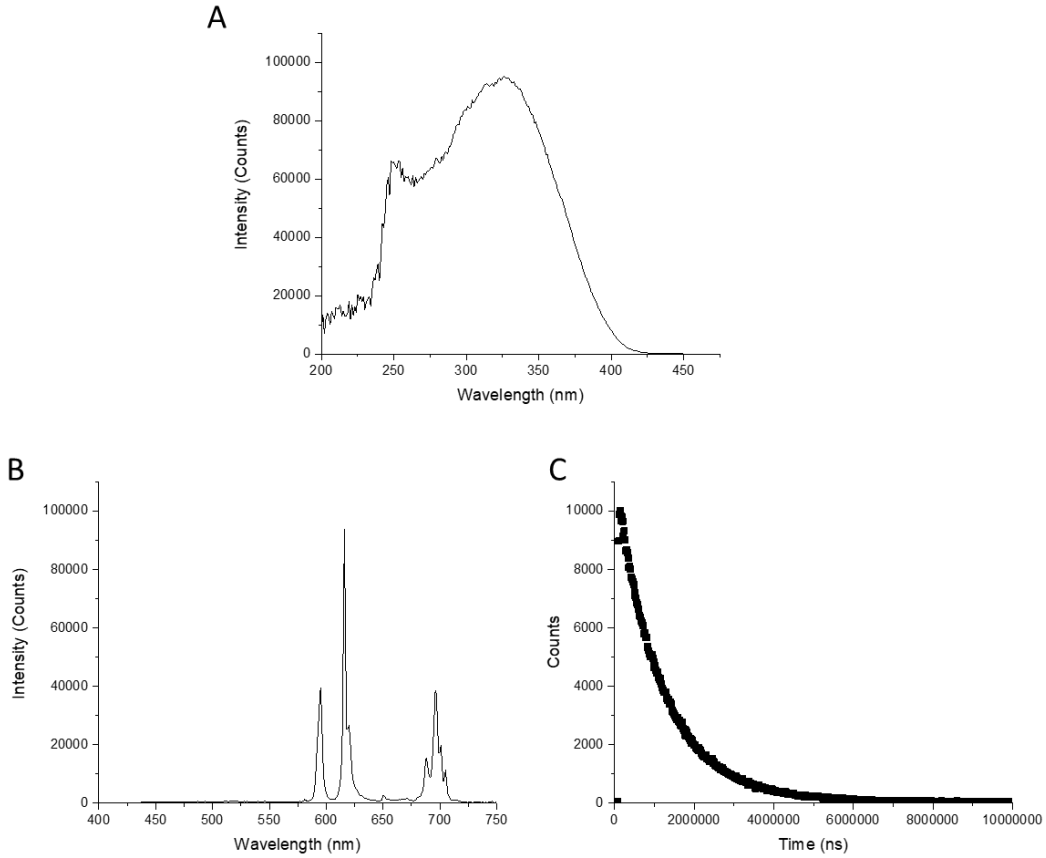

Figure S3-20. Luminescent data of [Eu_nGd_{4-n}**L3**$^{RR}_6$] (prepared by ratio Eu/Gd: 1/3), (2.59 x 10^{-6} M in MeCN).(A) Excitation spectrum, λ_{em} = 616 nm, slits = 2.5-1.0, filter 380 nm. (b) Emission spectrum, λ_{ex} = 330 nm, slits = 2.5-1.0, filter 380 nm. (c) Excited state decay curve, λ_{em} = 616 nm, slits = 6.0-5.0, filter 380 nm.

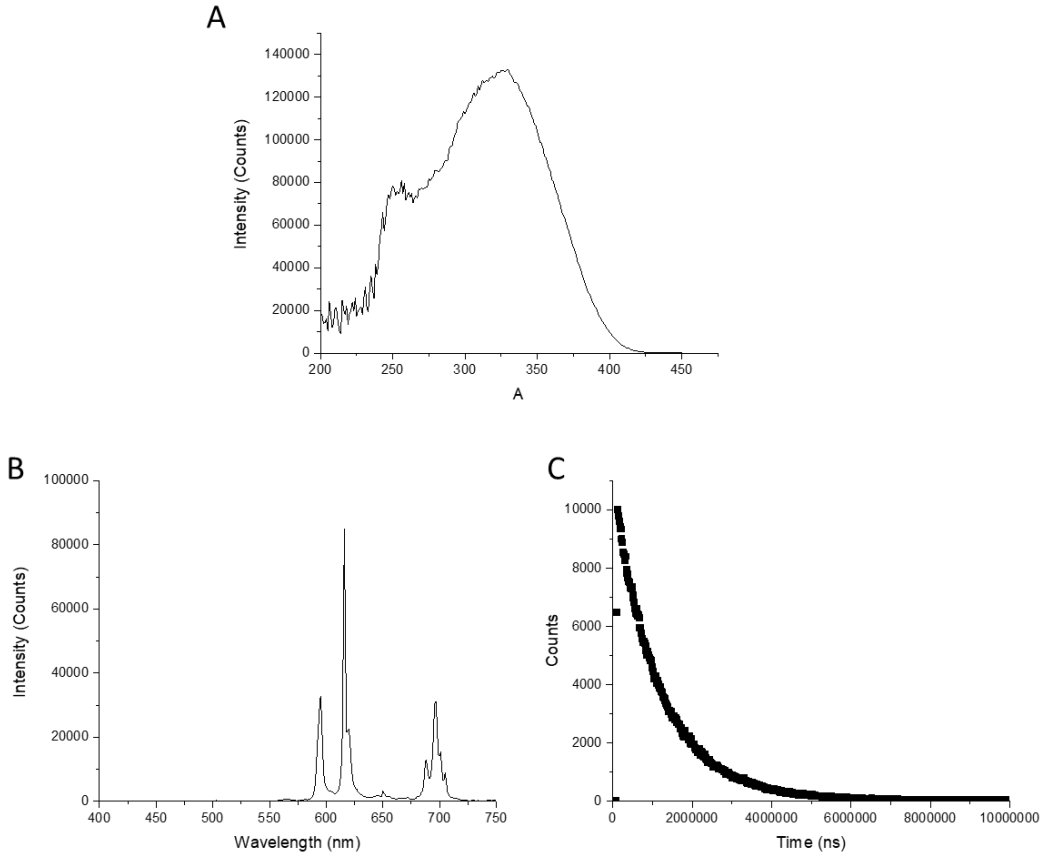

Figure S3-21. Luminescent data of [Eu_nSm_{4-n}**L3**$^{SS}_6$] (prepared by ratio Eu/Sm: 1/1), (2.19 x 10^{-6} M in MeCN).(A) Excitation spectrum, λ_{em} = 616 nm, slits = 2.0-1.0, filter 380 nm. (b) Emission spectrum, λ_{ex} = 330 nm, slits = 2.5-1.0, filter 380 nm. (c) Excited state decay curve, λ_{em} = 616 nm, slits = 6.0-4.0, filter 380 nm.

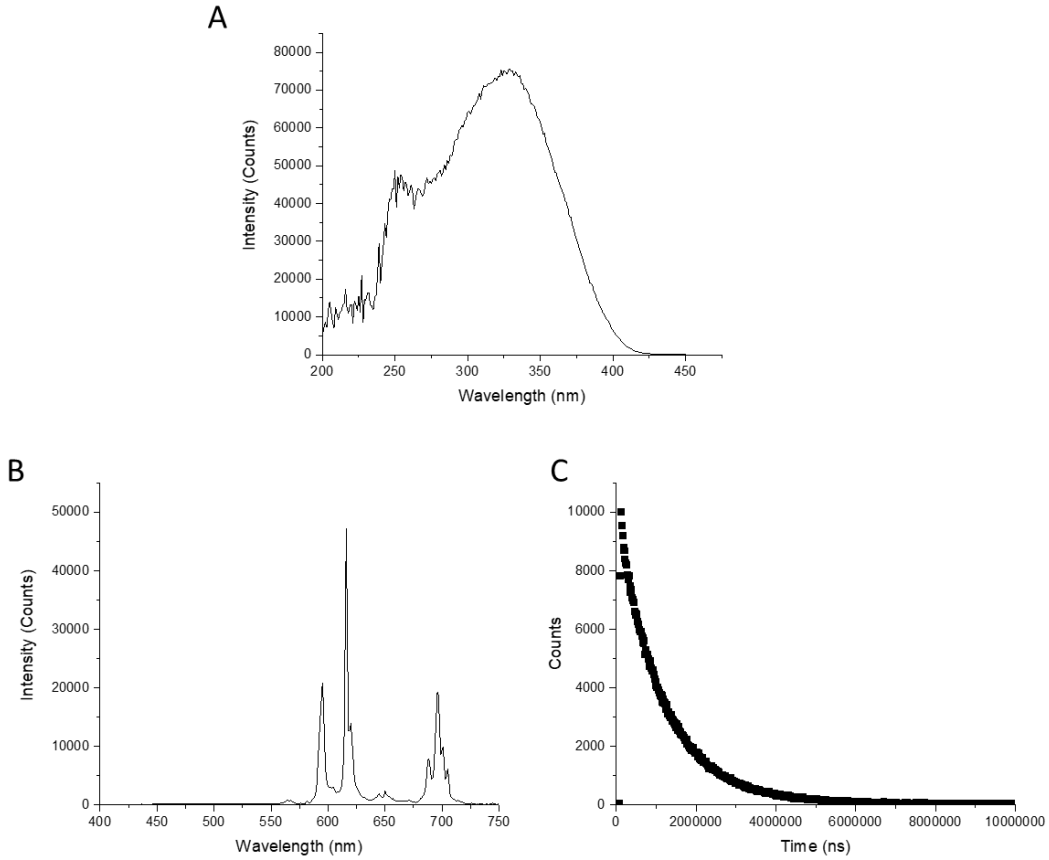

Figure S3-22. Luminescent data of [Eu_nSm_{4-n}**L3**$^{RR}_6$] (prepared by ratio Eu/Sm: 1/1), (2.48 x 10^{-6} M in MeCN).(A) Excitation spectrum, λ_{em} = 616 nm, slits = 2.0-1.0, filter 380 nm. (b) Emission spectrum, λ_{ex} = 330 nm, slits = 2.5-1.0, filter 380 nm. (c) Excited state decay curve, λ_{em} = 616 nm, slits = 6.0-4.0, filter 380 nm.

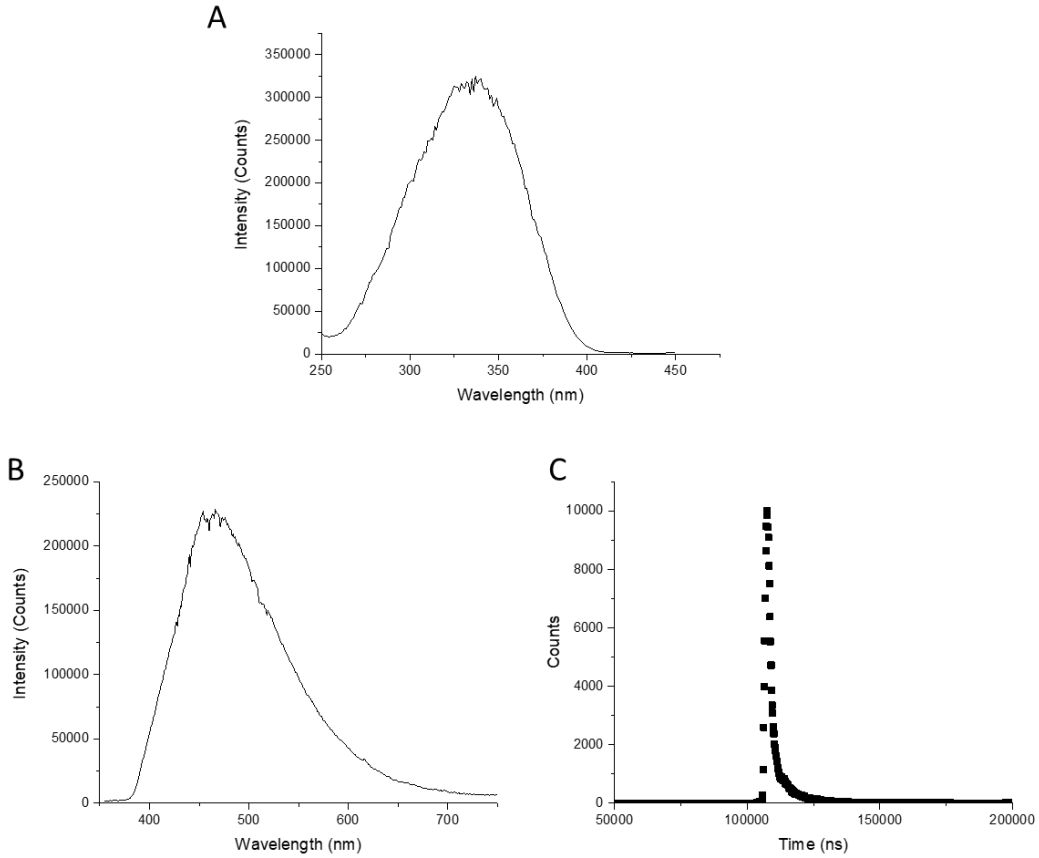

Figure S3-24. Luminescent data of $[Gd_4(\mathbf{L3^{RR}})_6](OTf)_{12}$ (9.05 x 10^{-6} M in 1:4 of MeOH/EtOH at 77K).(A) Excitation spectrum, λ_{em} = 466 nm, slits = 2.0-0.5, filter 380 nm. (b) Emission spectrum, λ_{ex} = 330 nm, slits = 2.0-0.5, filter 380 nm. (c) Excited state decay curve, λ_{em} = 466 nm, slits = 2.0-1.0, filter 380 nm.

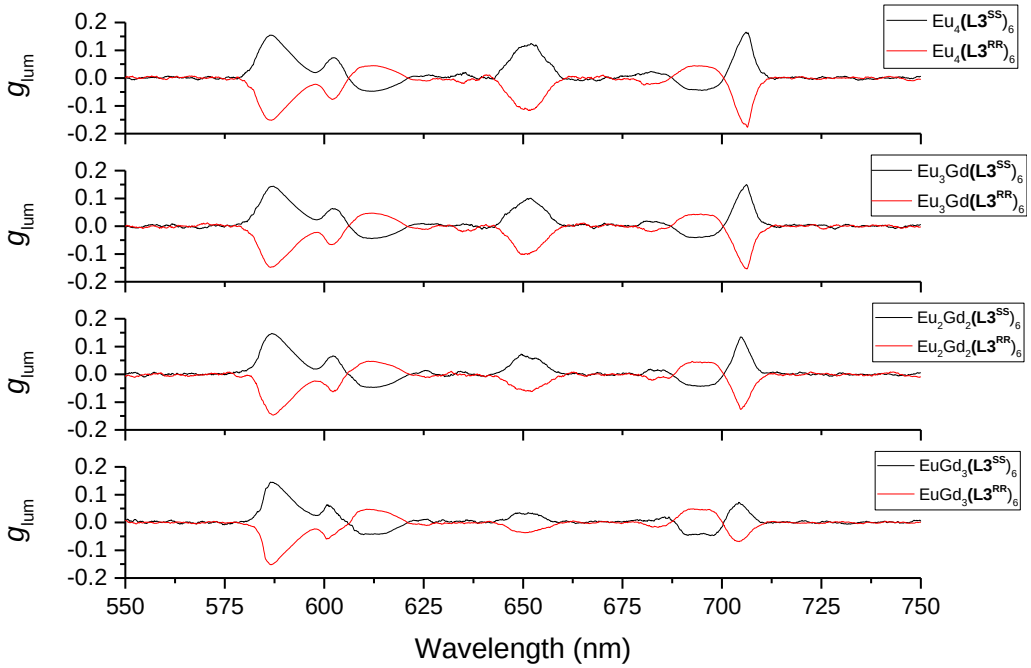

Figure S3-25. A stack of g_{lum} values of homometallic and heterometallic tetrahedra.

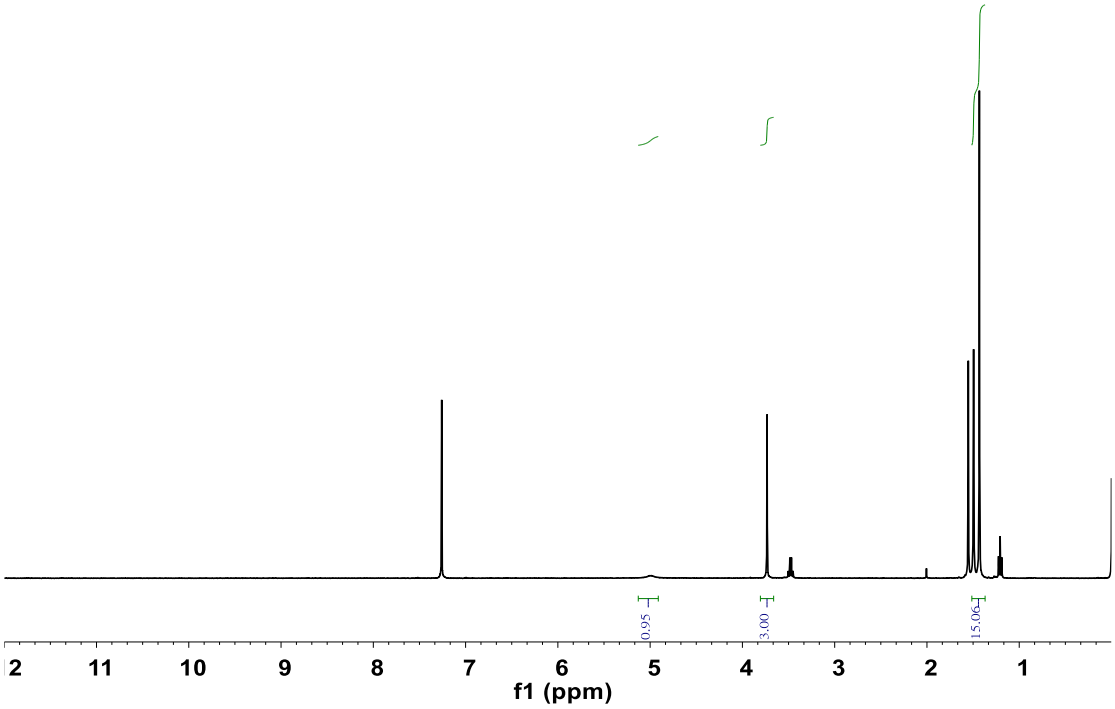

Figure S4-1. [1]HNMR of methyl 2-amino-2-methylpropanoate.

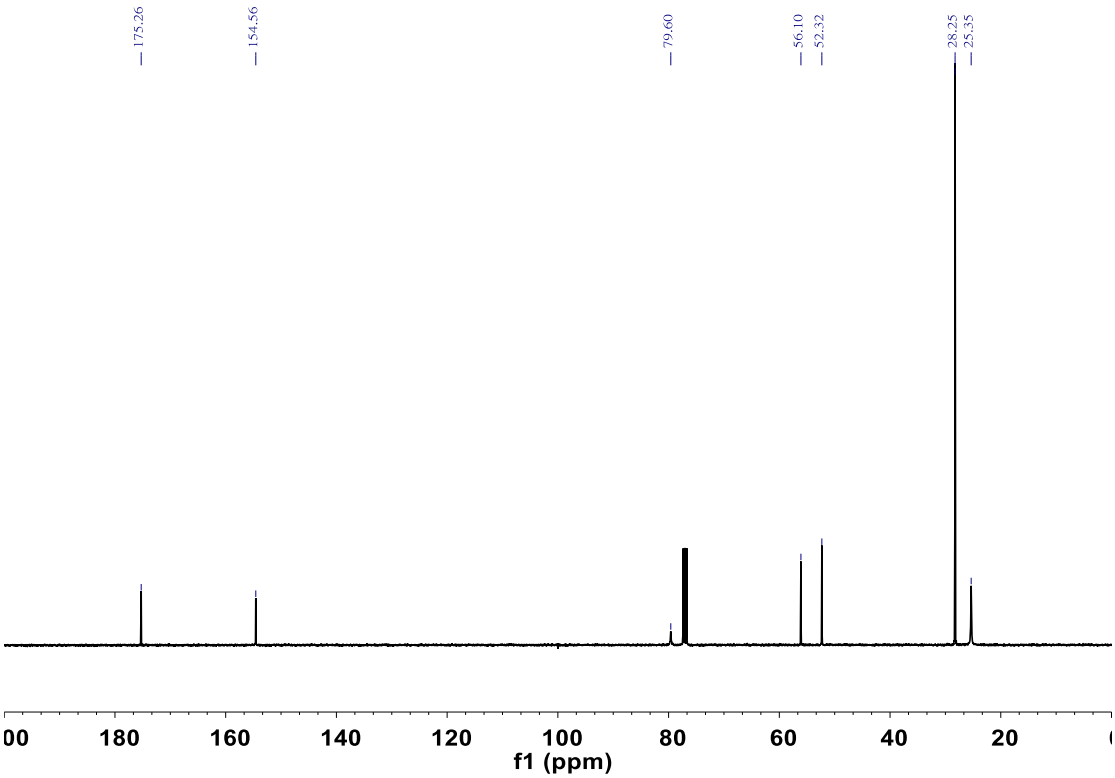

Figure S4-2. [13]CNMR of methyl 2-amino-2-methylpropanoate.

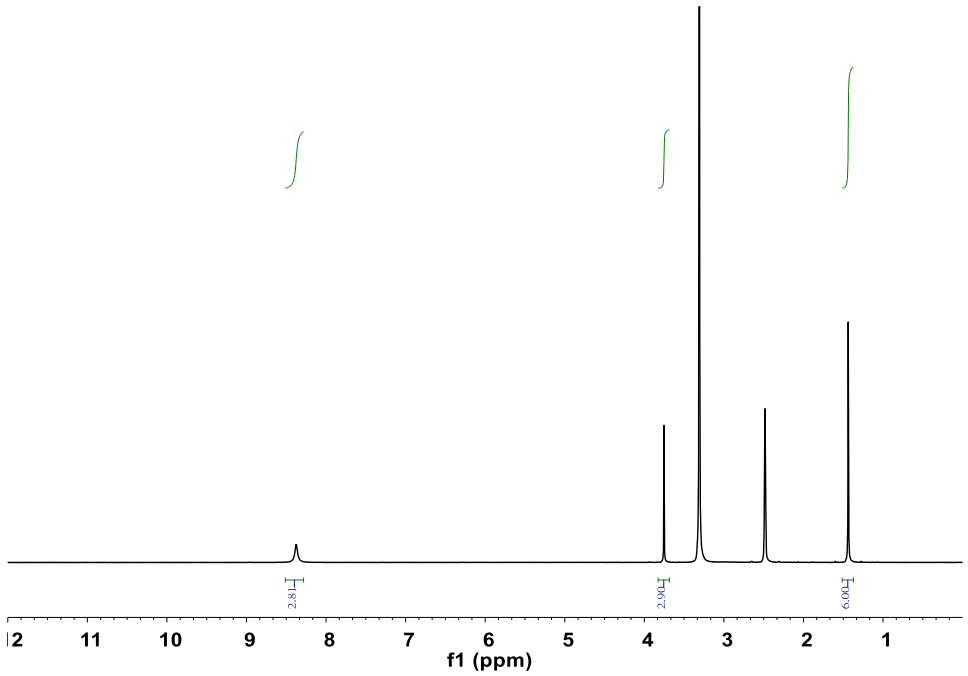

Figure S4-3. ^{1}HNMR of 1-methoxy-2-methyl-1-oxopropan-2-aminium 2,2,2-trifluoroacetate.

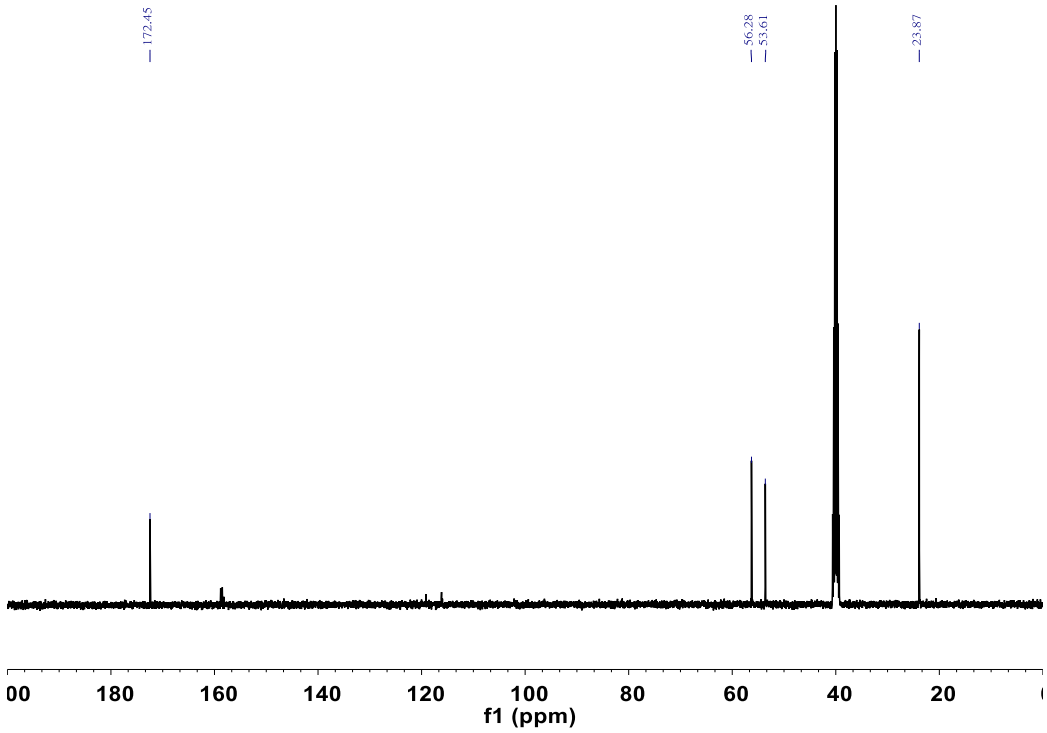

Figure S4-4. ^{13}CNMR of 1-methoxy-2-methyl-1-oxopropan-2-aminium 2,2,2-trifluoroacetate.

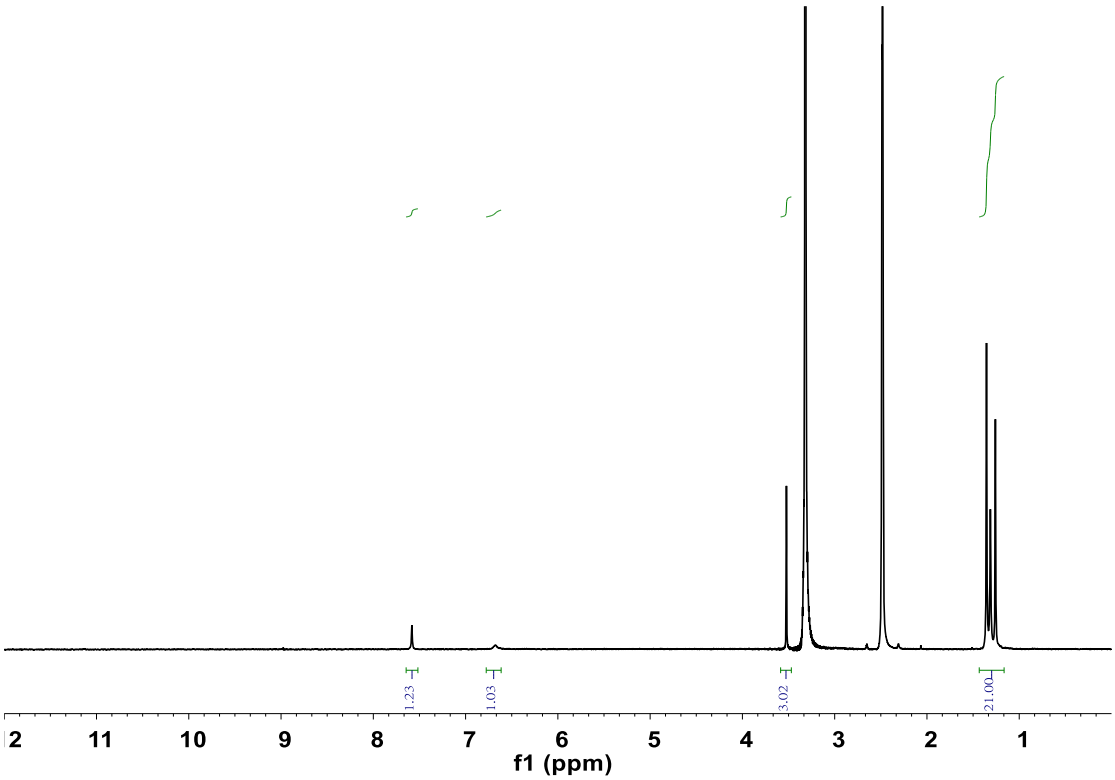

Figure S4-5. [1]HNMR of Boc-Aib-Aib-OMe.

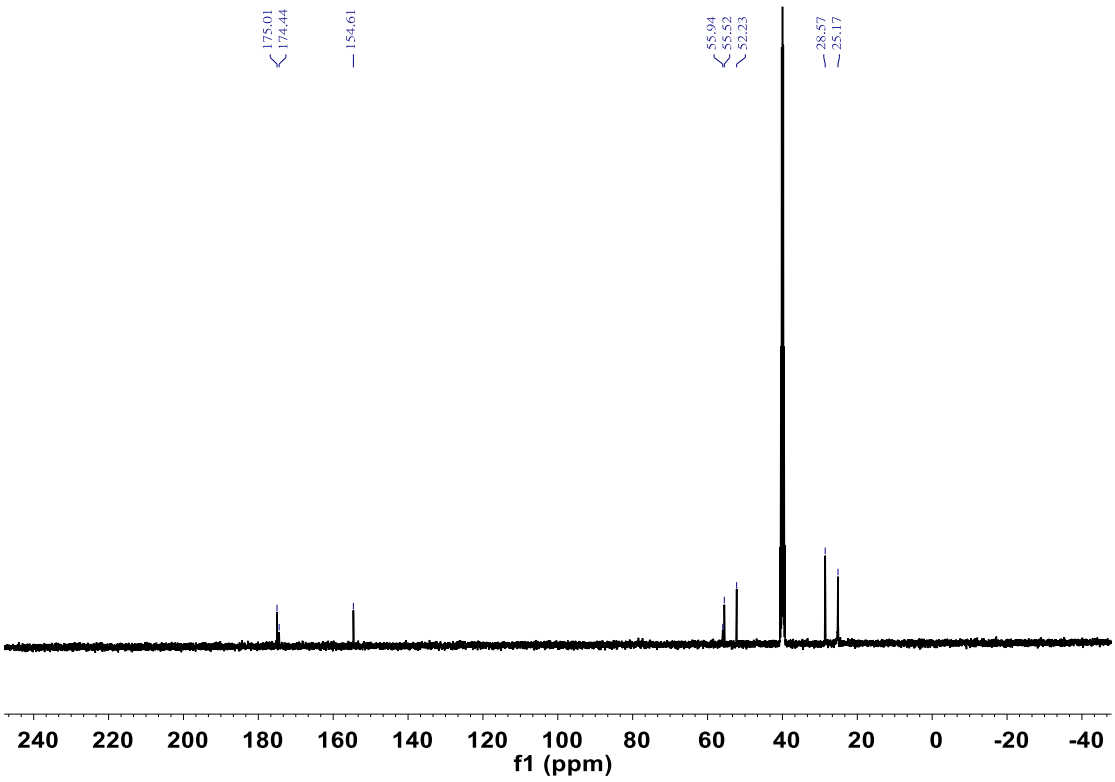

Figure S4-6. [13]CNMR of Boc-Aib-Aib-OMe.

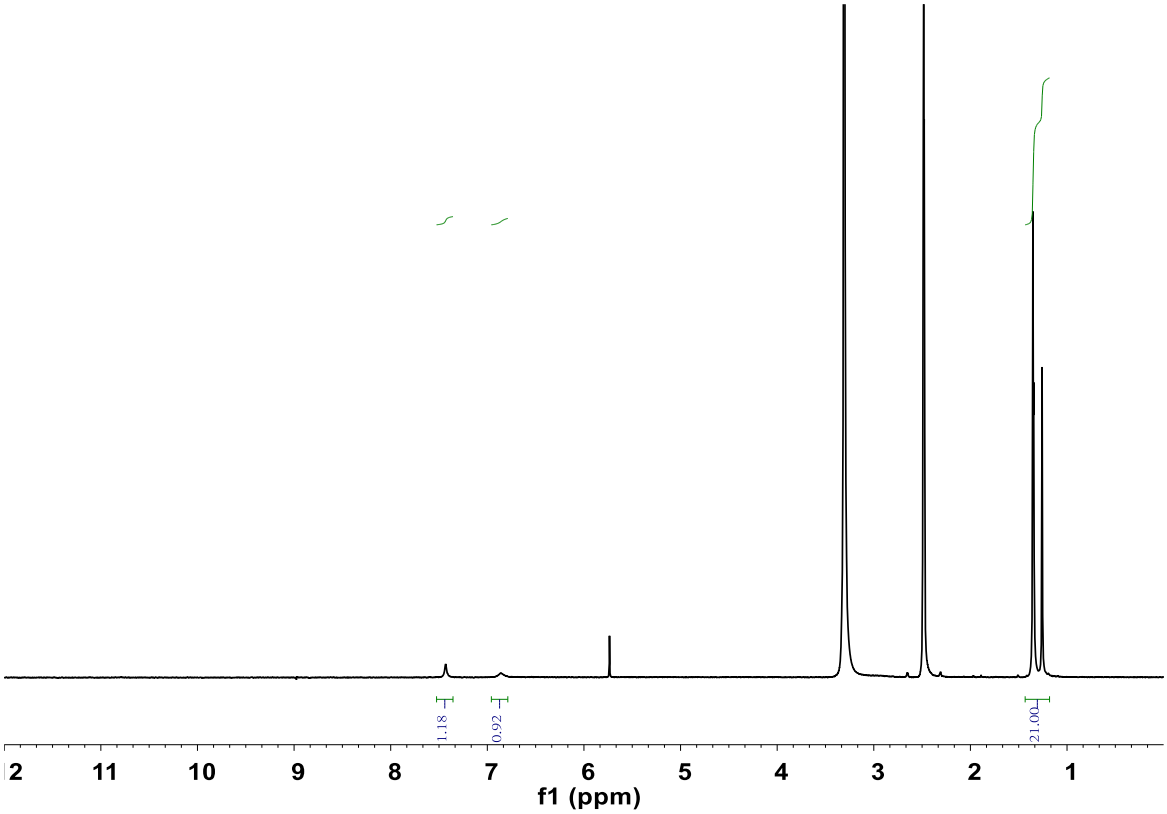

Figure S4-7. [1]HNMR of Boc-Aib-Aib-OH.

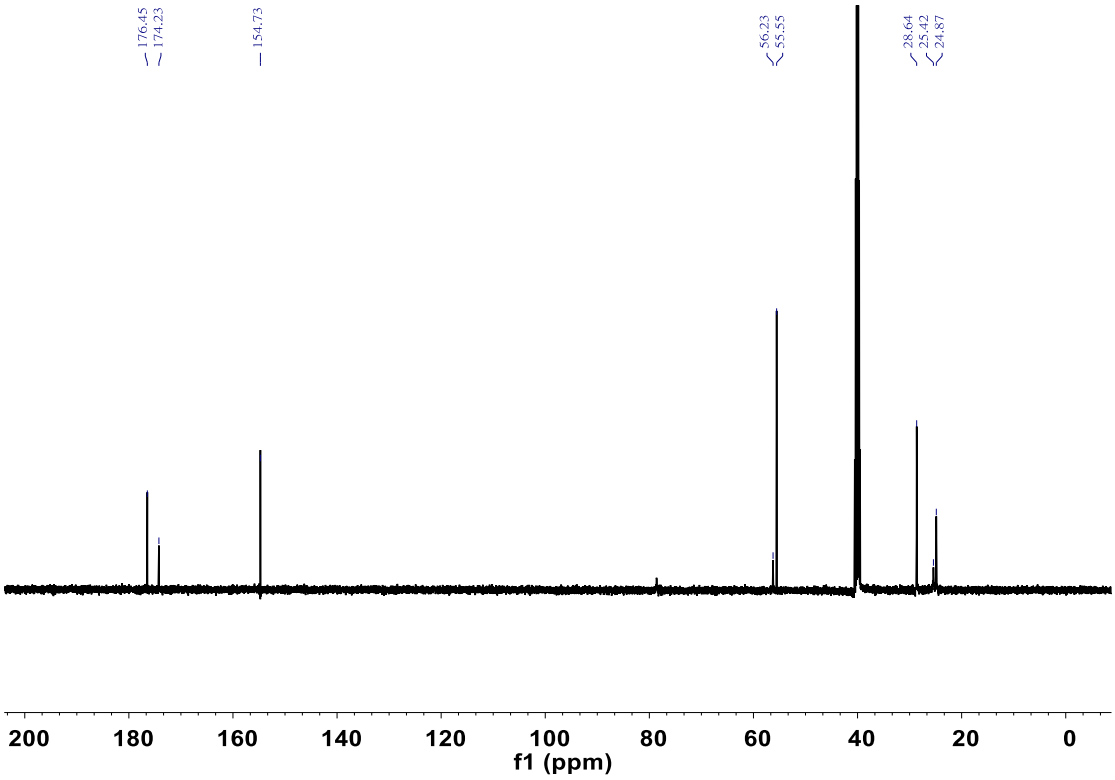

Figure S4-8. [13]CNMR of Boc-Aib-Aib-OH.

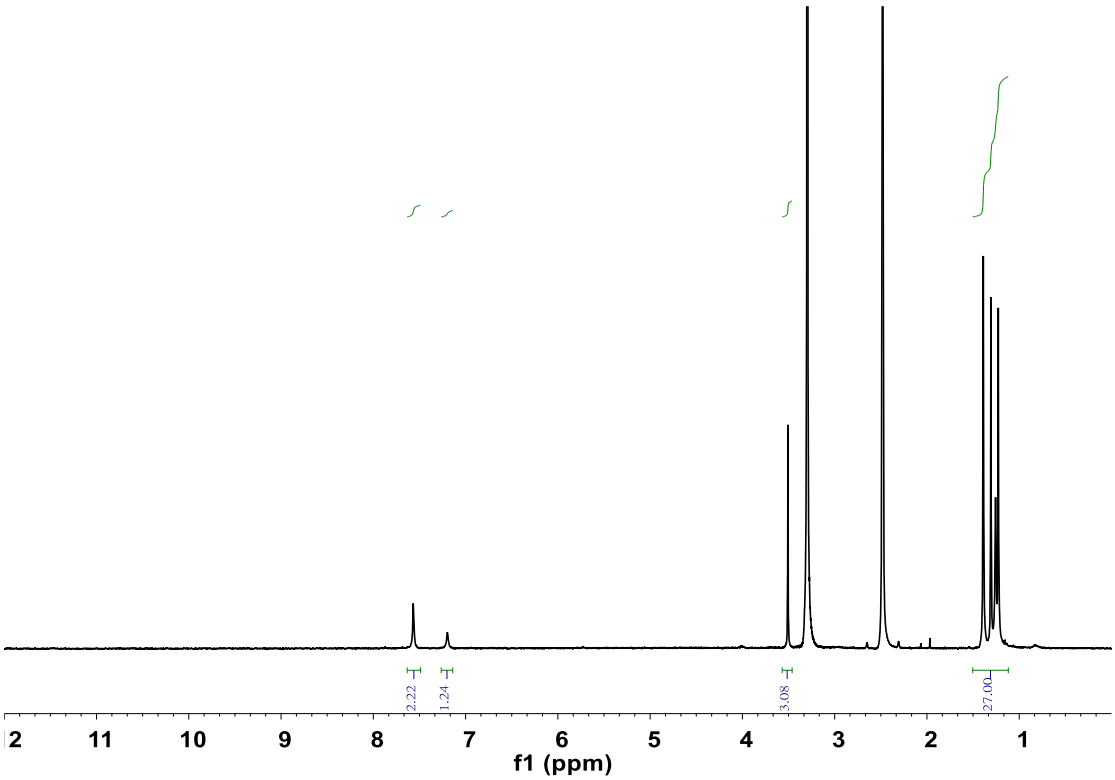

Figure S4-9. [1]HNMR of Boc-Aib-Aib-Aib-OMe.

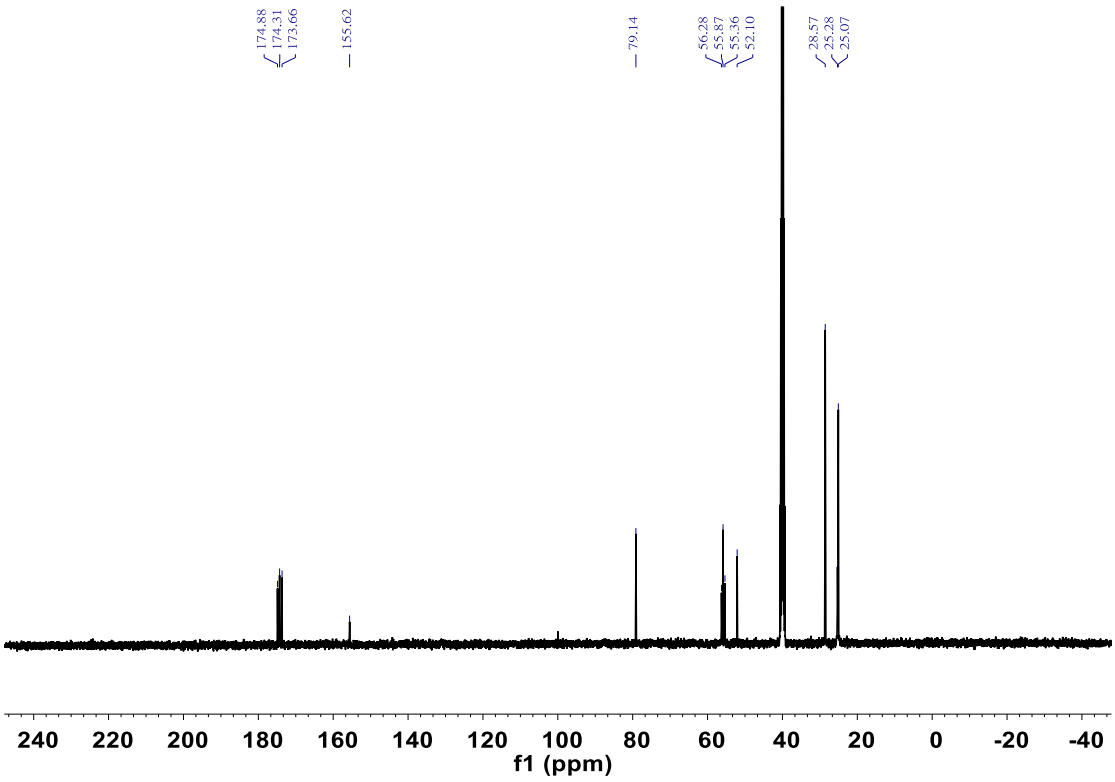

Figure S4-10. [13]CNMR of Boc-Aib-Aib-Aib-OMe.

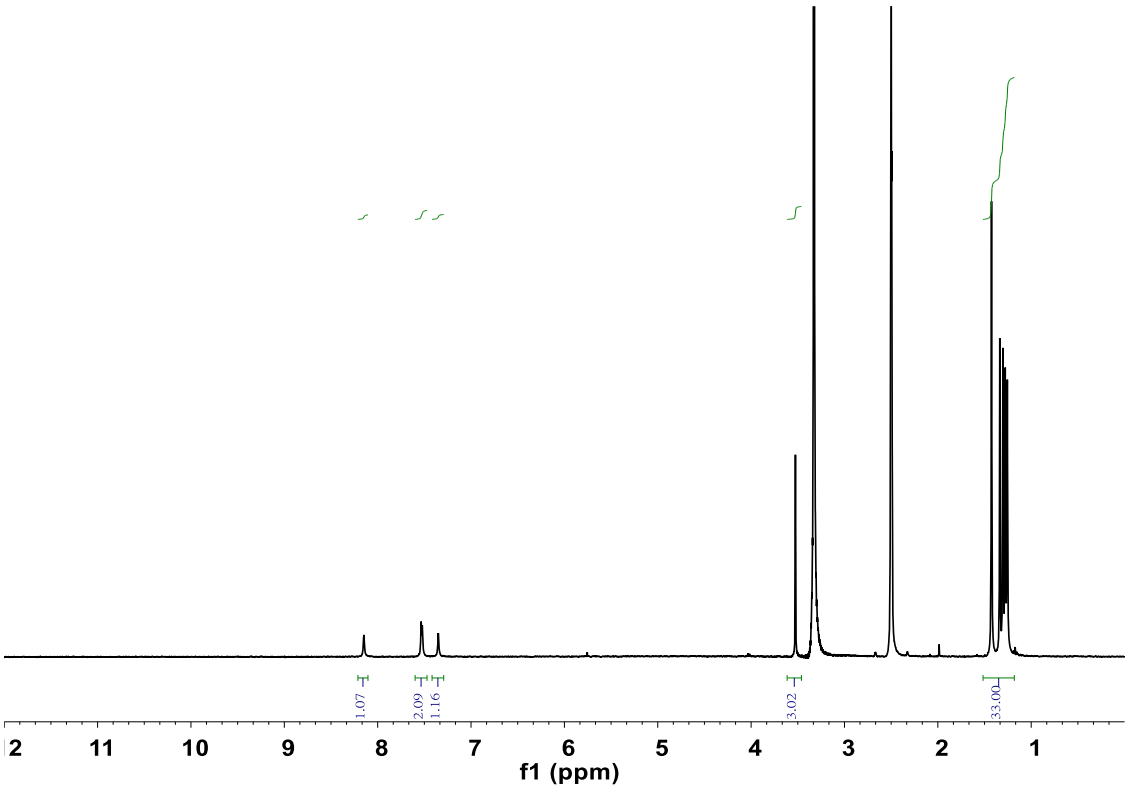

Figure S4-11. ^{1}HNMR of Boc-(Aib)$_4$-OMe.

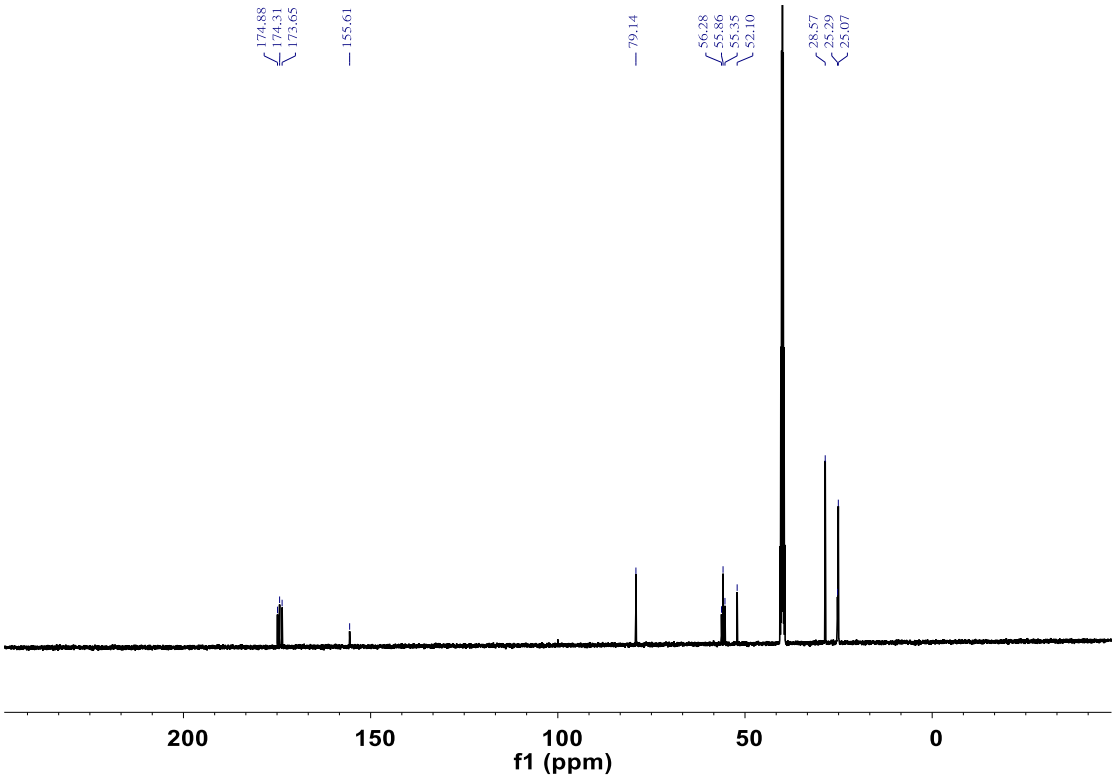

Figure S4-12. ^{13}CNMR of Boc-(Aib)$_4$-OMe.

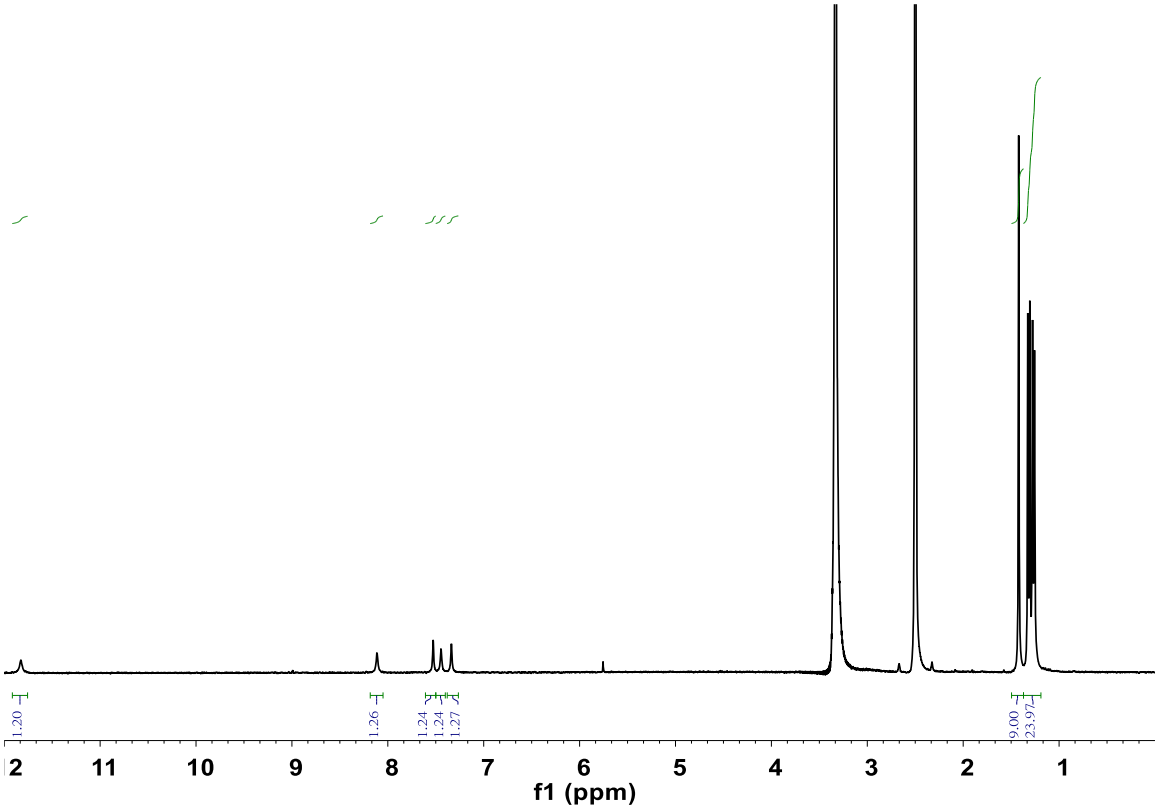

Figure S4-13. ^{1}HNMR of Boc-(Aib)$_4$-OH.

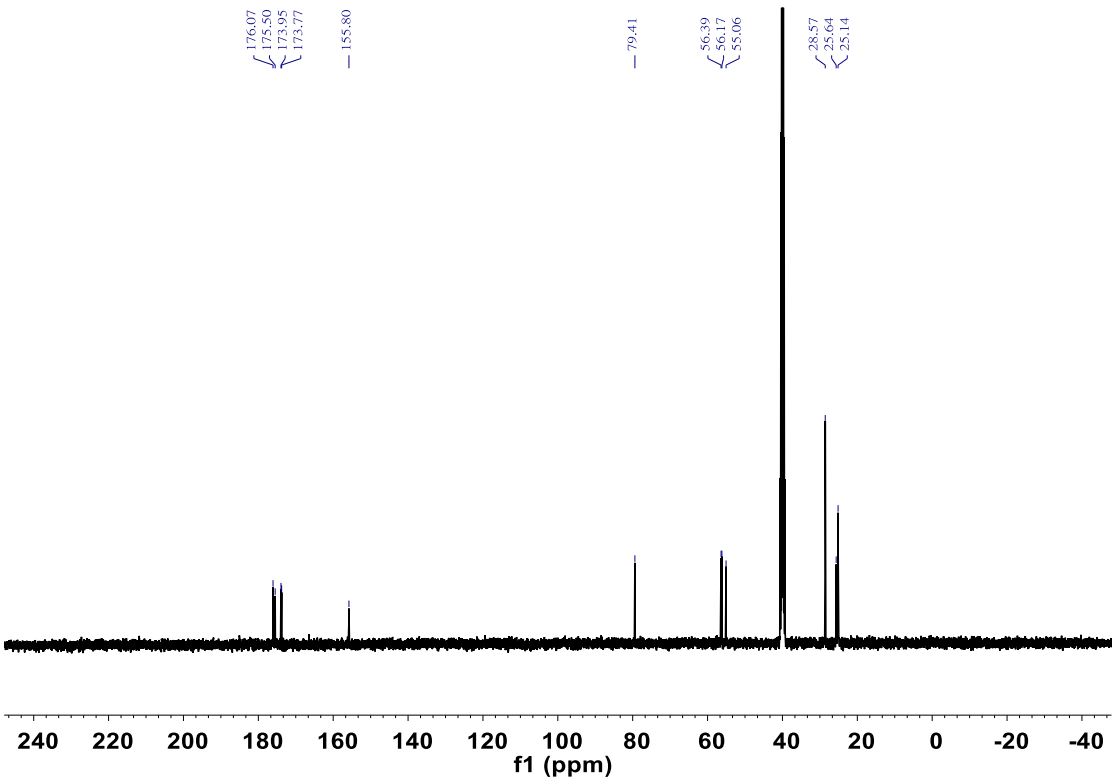

Figure S4-14. ^{13}CNMR of Boc-(Aib)$_4$-OH.

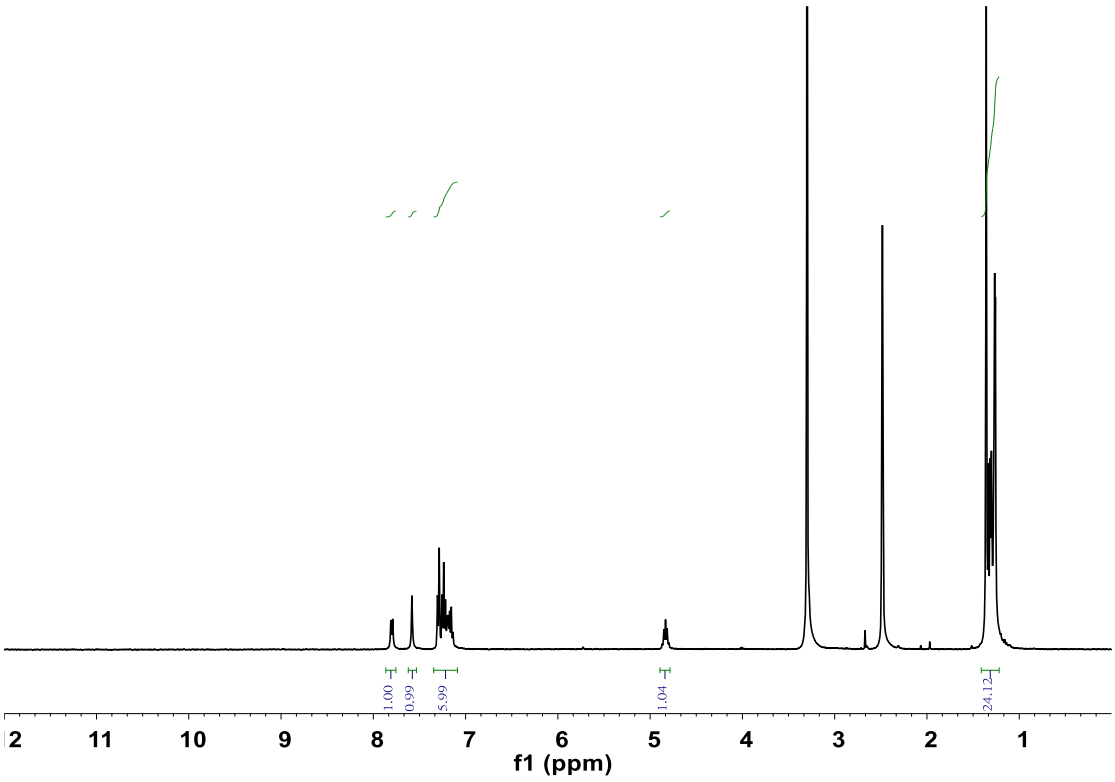

Figure S4-15. [1]HNMR of Boc-Aib-Aib-spy.

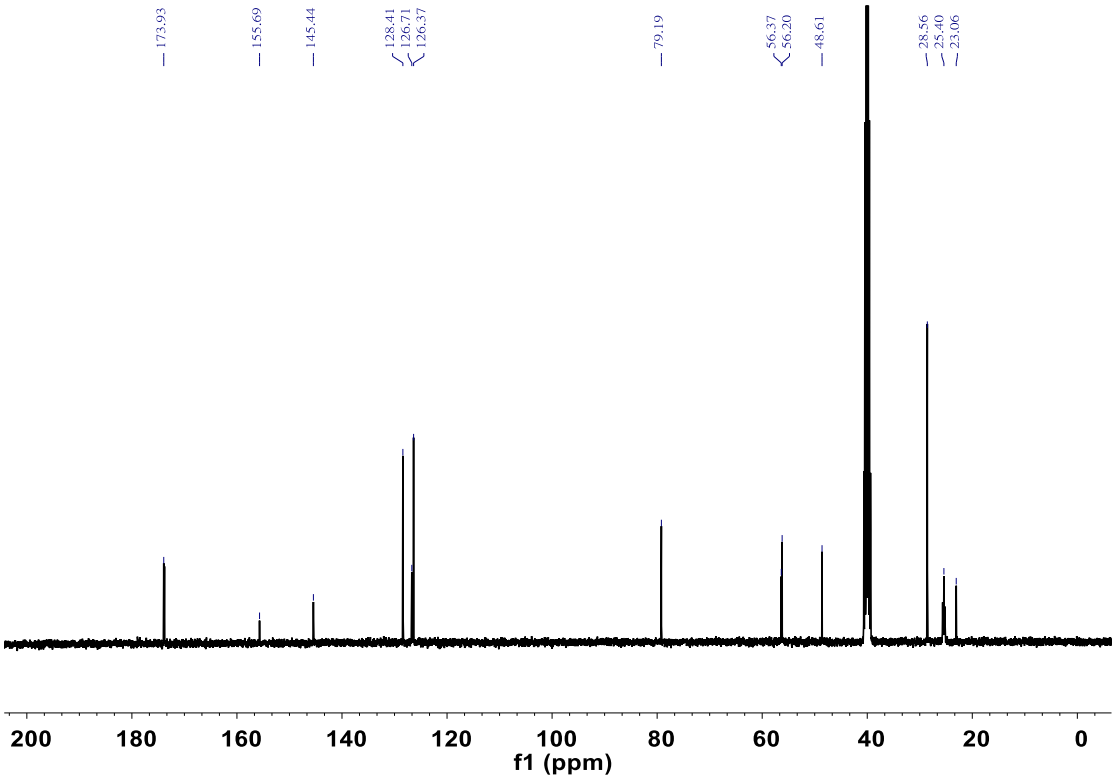

Figure S4-16. [13]CNMR of Boc-Aib-Aib-spy.

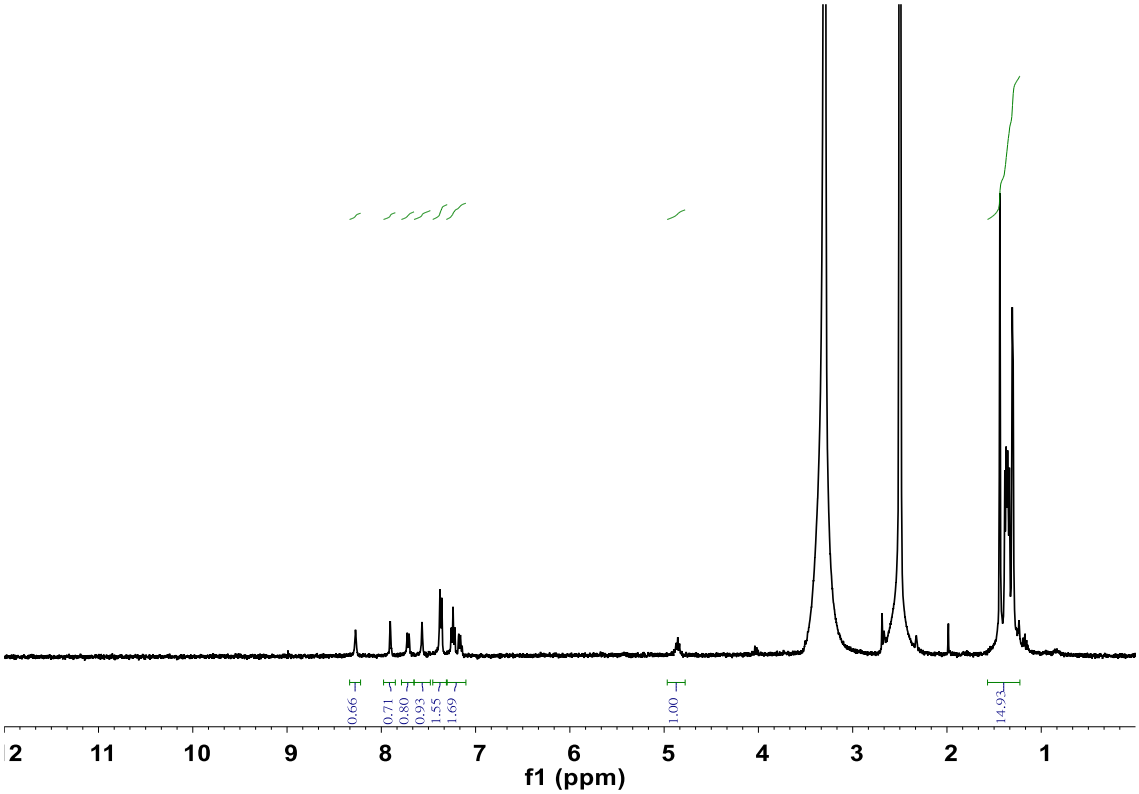

Figure S4-17. ^{1}HNMR of Boc-(Aib)$_4$-spy.

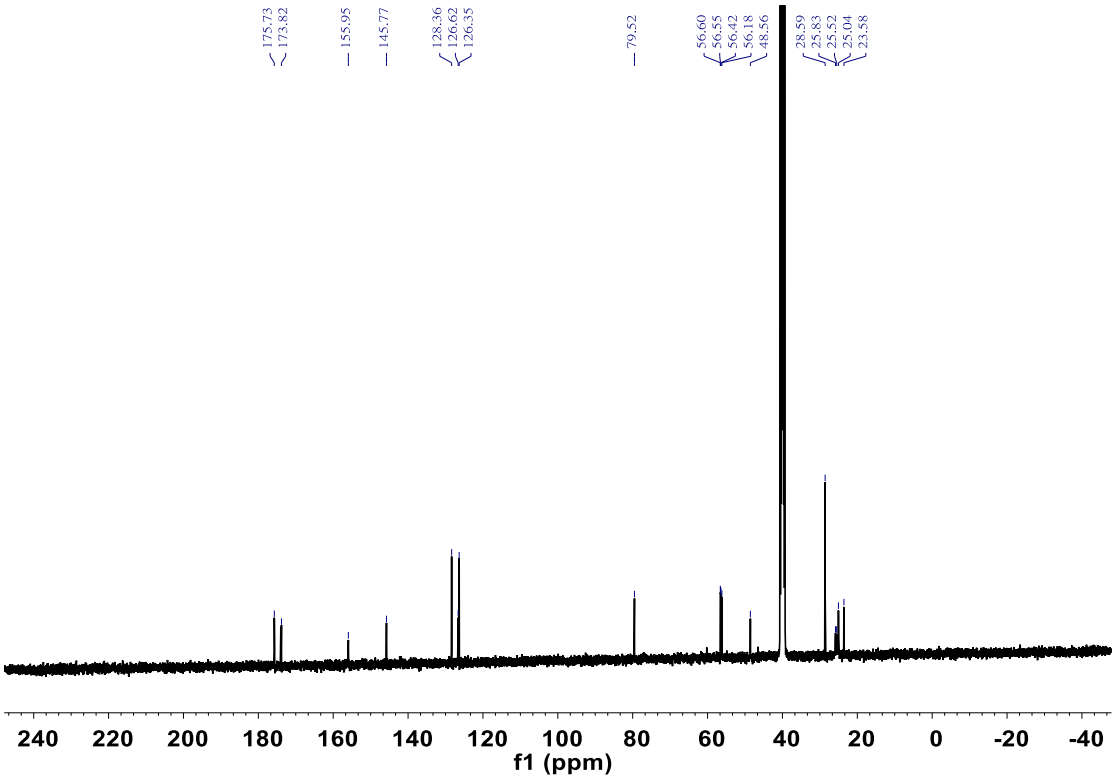

Figure S4-18. ^{13}CNMR of Boc-(Aib)$_4$-spy.

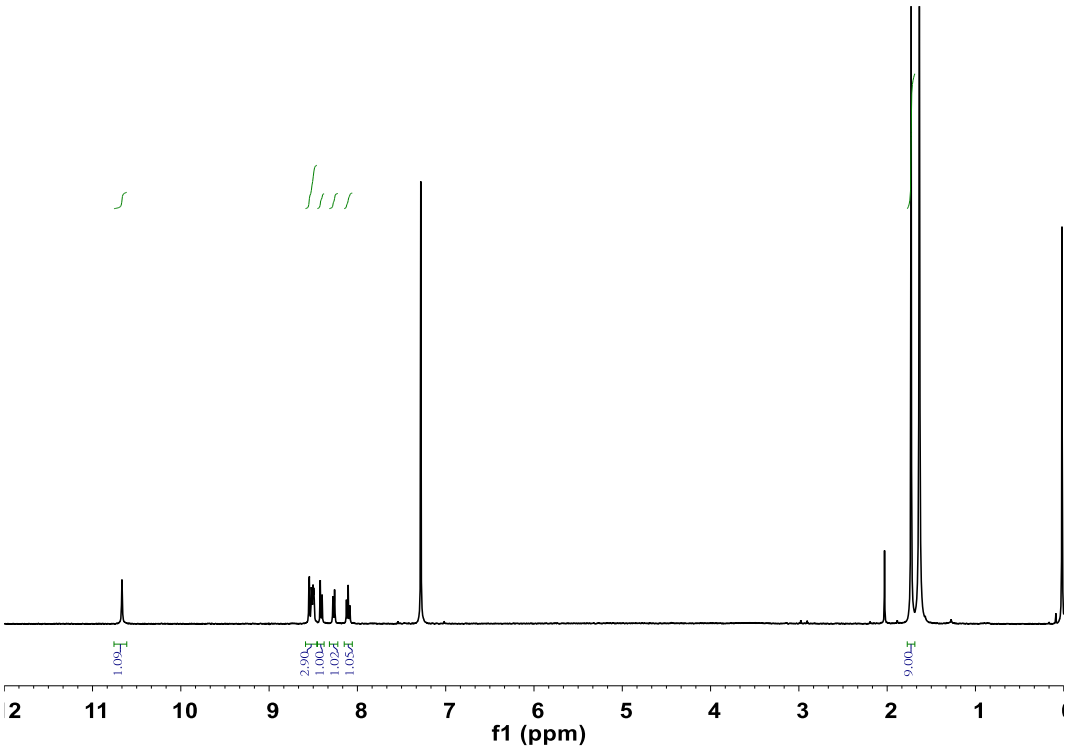

Figure S4-19. [1]HNMR of di-tert-butyl 6,6'-(((9,10-dioxo-9,10-dihydroanthracene-2,6-diyl)bis(azanediyl))bis(carbonyl))dipicolinate.

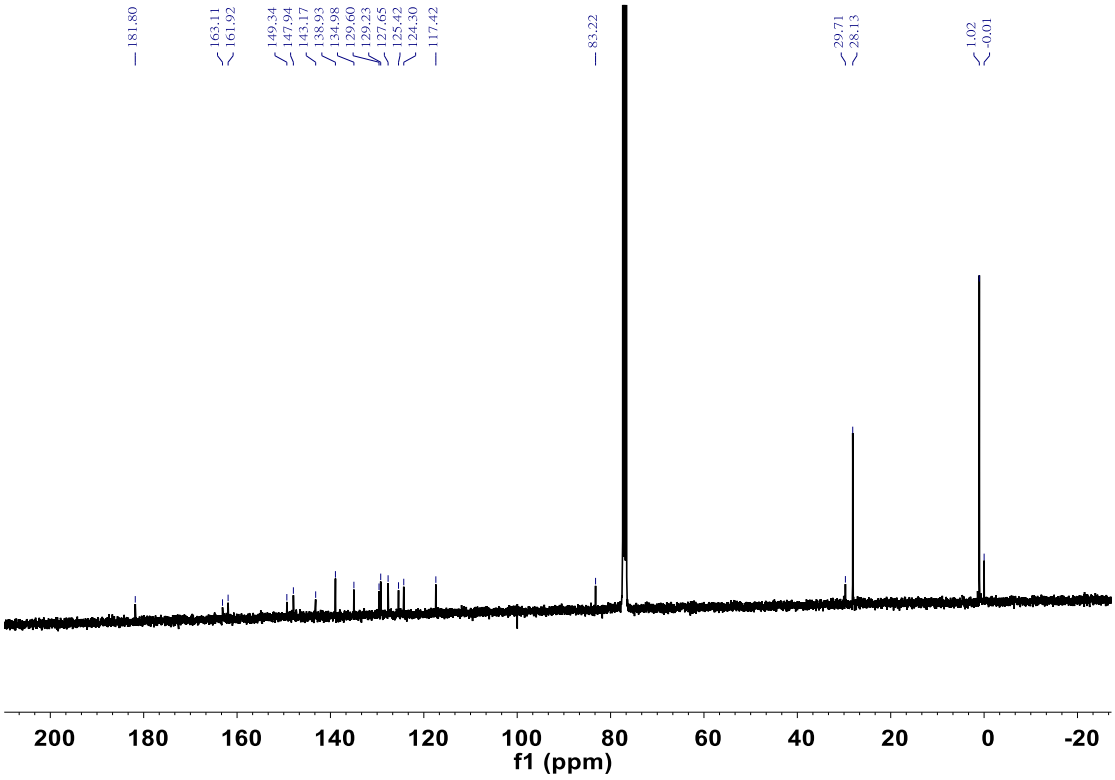

Figure S4-20. [1]HNMR of di-tert-butyl 6,6'-(((9,10-dioxo-9,10-dihydroanthracene-2,6-diyl)bis(azanediyl))bis(carbonyl))dipicolinate.

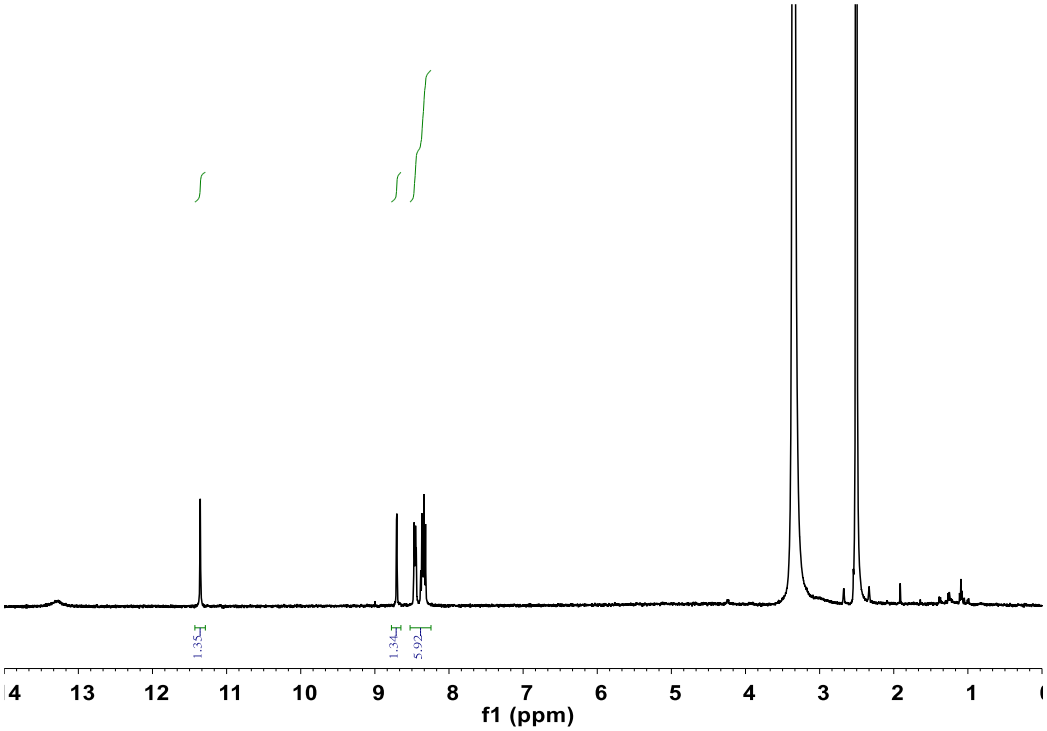

Figure S4-21. ^{1}HNMR of 6,6'-(((9,10-dioxo-9,10-dihydroanthracene-2,6-diyl)bis(azanediyl))bis(carbonyl))dipicolinic acid.

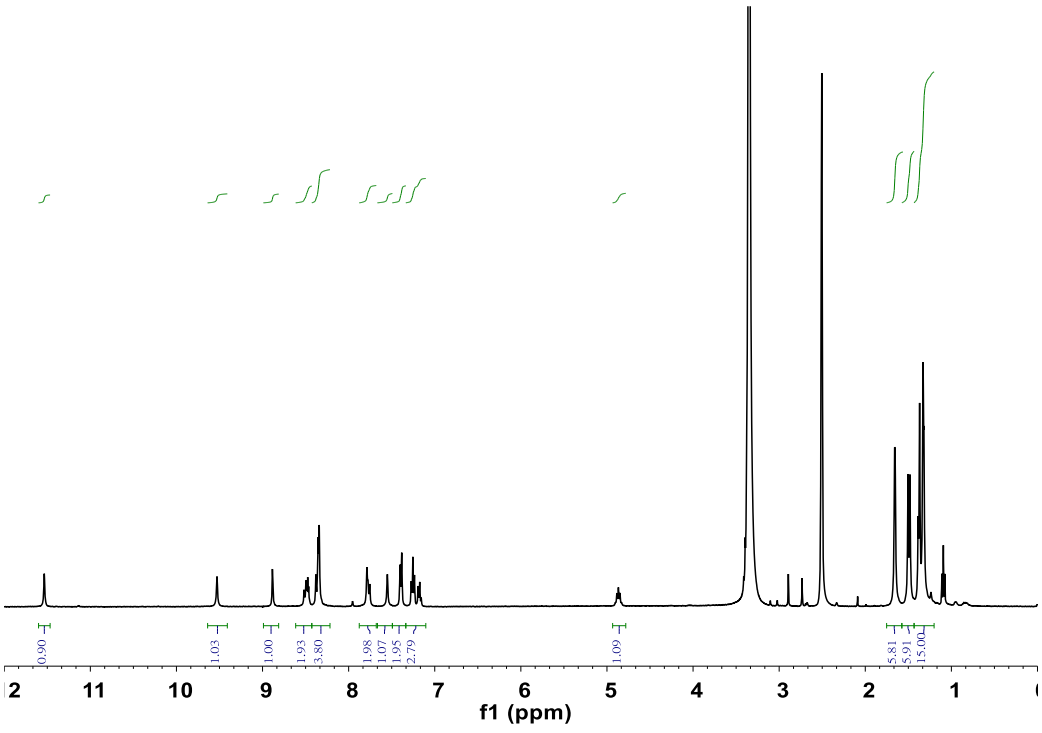

Figure S4-22. ^{1}HNMR of N^{2},$N^{2'}$-(9,10-dioxo-9,10-dihydroanthracene-2,6-diyl)bis(N^{6}-((S)-5,5,8,8,11,11,14-heptamethyl-4,7,10,13-tetraoxo-2-phenyl-3,6,9,12-tetraazapentadecan-14-yl)pyridine-2,6-dicarboxamide), **L5**.

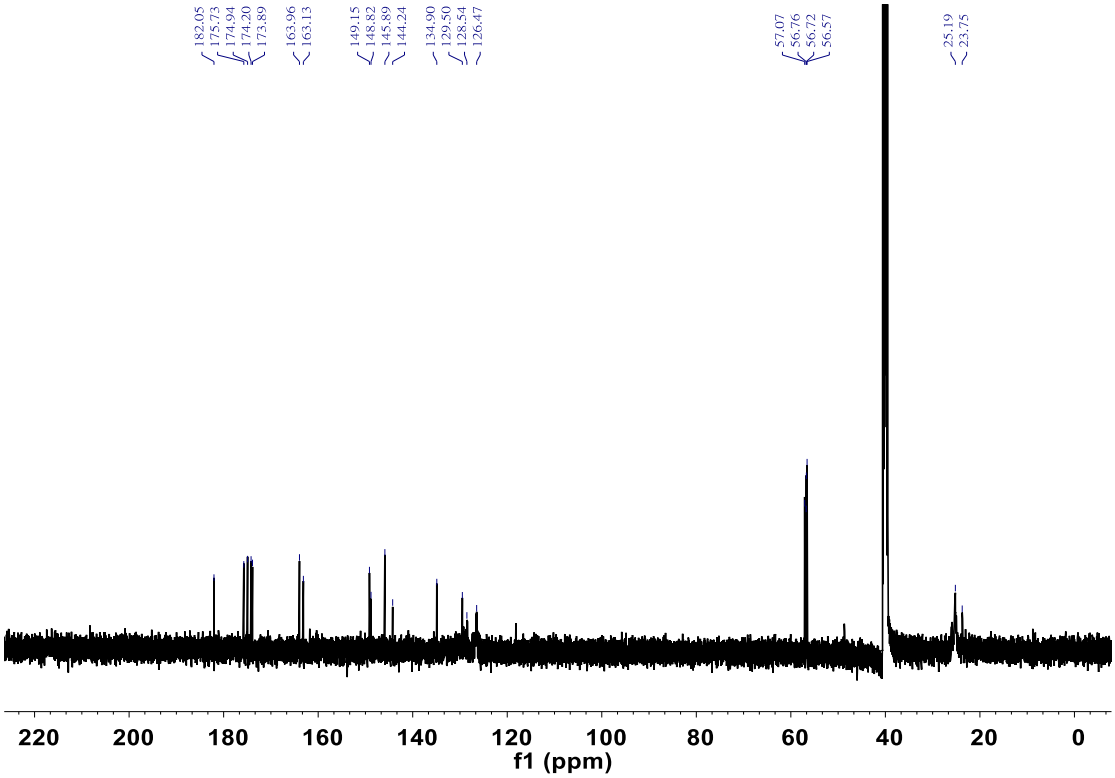

Figure S4-23. ^{13}CNMR of N^2,$N^{2'}$-(9,10-dioxo-9,10-dihydroanthracene-2,6-diyl)bis(N^6-((S)-5,5,8,8,11,11,14-heptamethyl-4,7,10,13-tetraoxo-2-phenyl-3,6,9,12-tetraazapentadecan-14-yl)pyridine-2,6-dicarboxamide), **L5**.

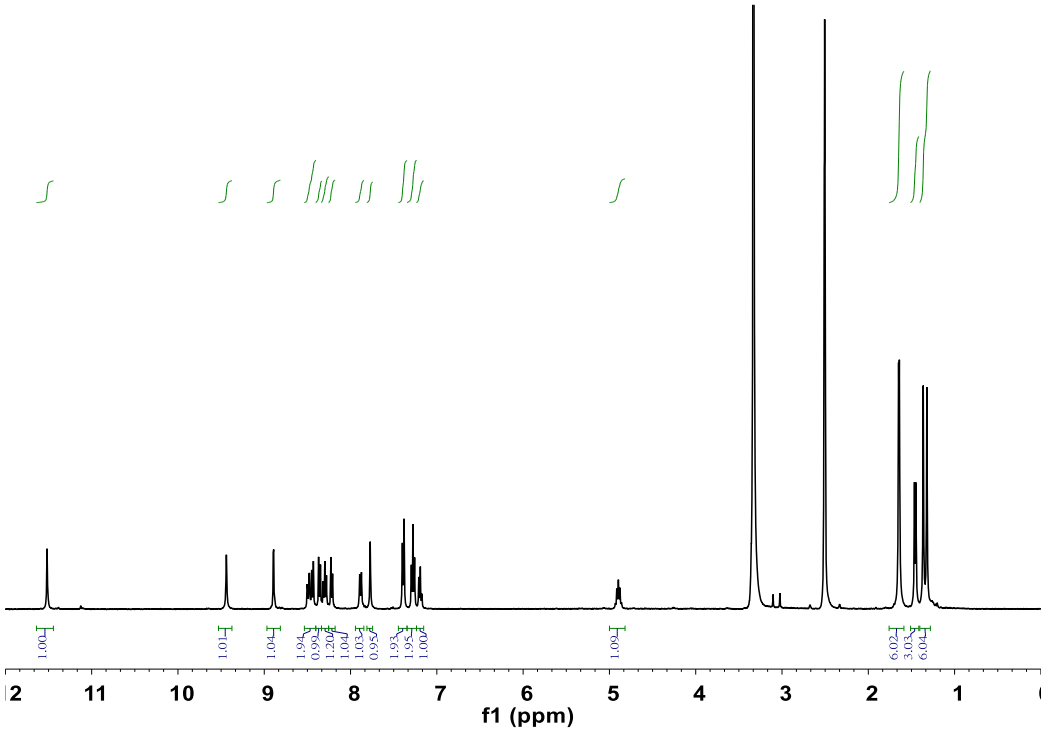

Figure S4-24. ^{1}HNMR of N^2,$N^{2'}$-(9,10-dioxo-9,10-dihydroanthracene-2,6-diyl)bis(N^6-(2-methyl-1-((2-methyl-1-oxo-1-(((S)-1-phenylethyl)amino)propan-2-yl)amino)-1-oxopropan-2-yl)pyridine-2,6-dicarboxamide), **L6**.

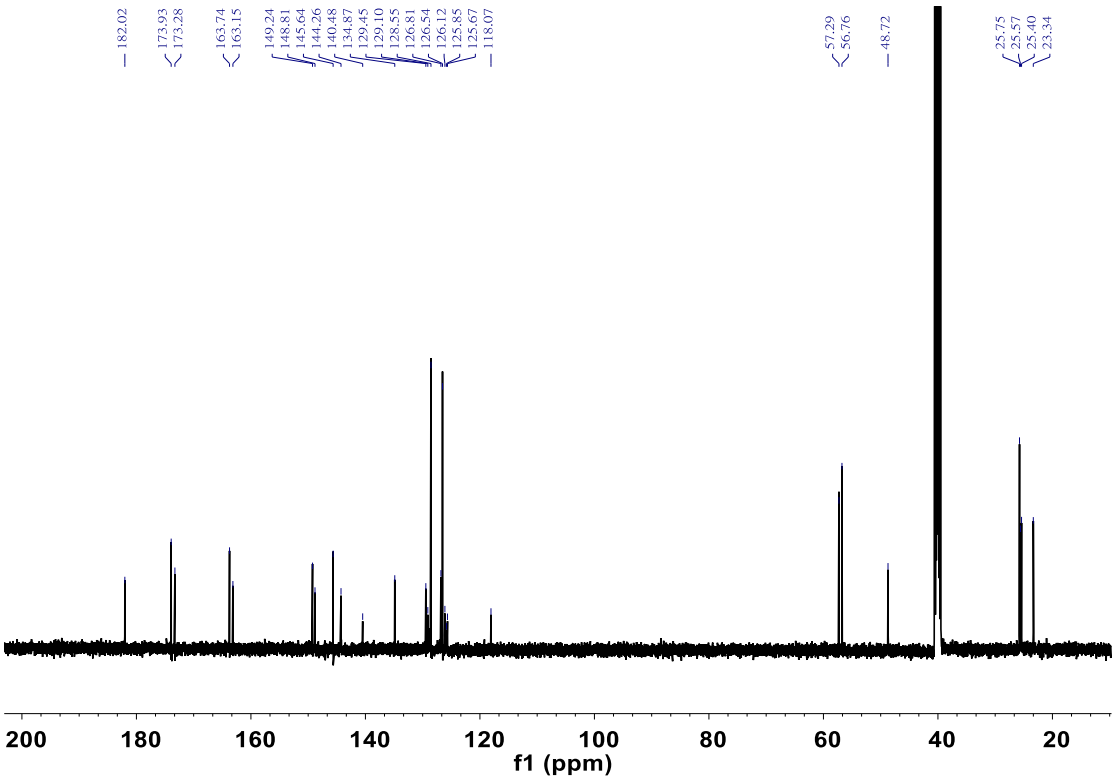

Figure S4-25. ^{13}CNMR of N^2,$N^{2'}$-(9,10-dioxo-9,10-dihydroanthracene-2,6-diyl)bis(N^6-(2-methyl-1-((2-methyl-1-oxo-1-(((S)-1-phenylethyl)amino)propan-2-yl)amino)-1-oxopropan-2-yl)pyridine-2,6-dicarboxamide), **L6**.

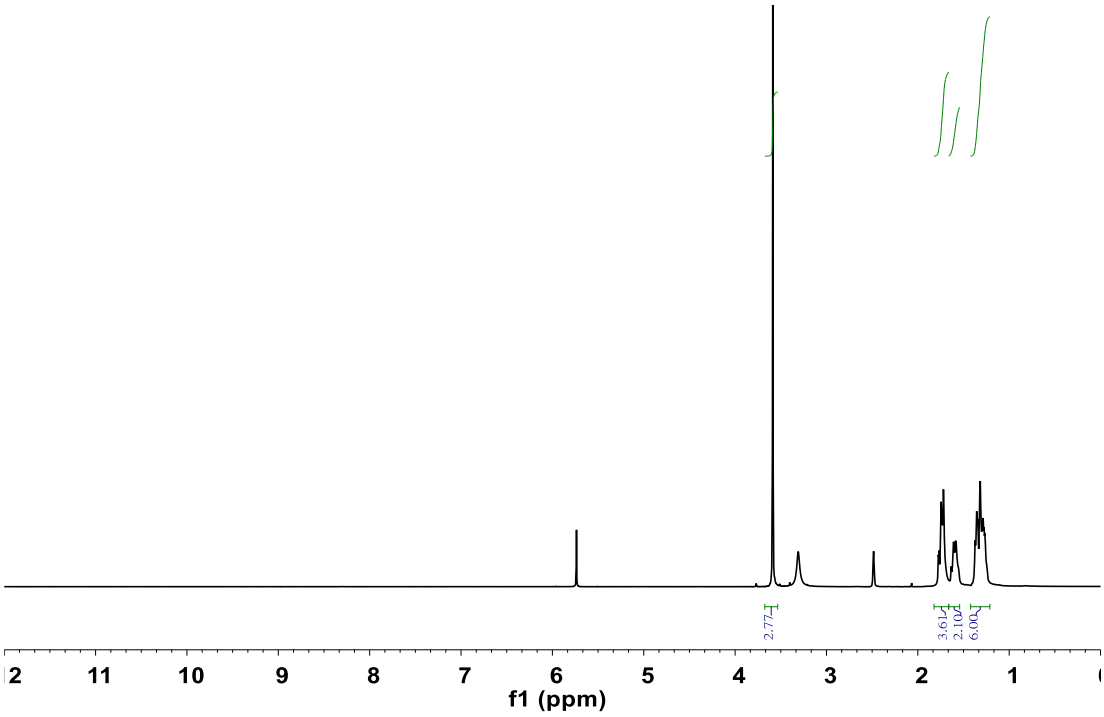

Figure S4-26. ^{1}HNMR spectrum of H_2N-Ac$_6$c-OH.

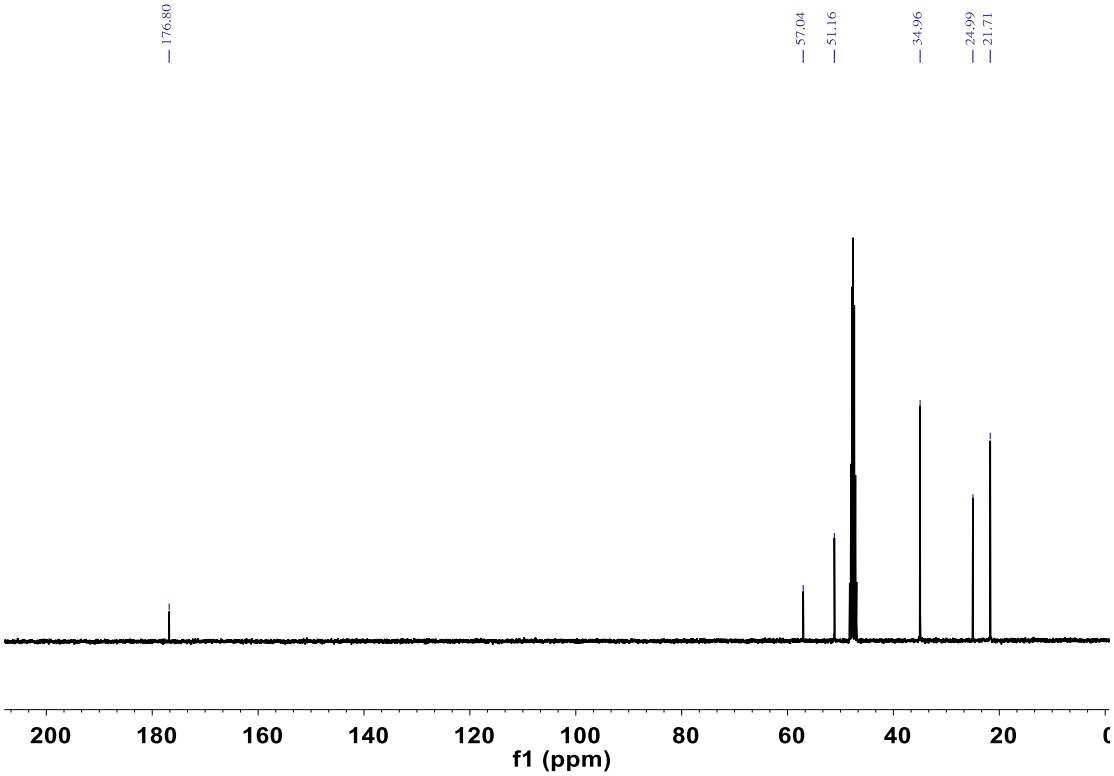

Figure S4-27. ^{13}CNMR spectrum of H_2N-Ac$_6$c-OH.

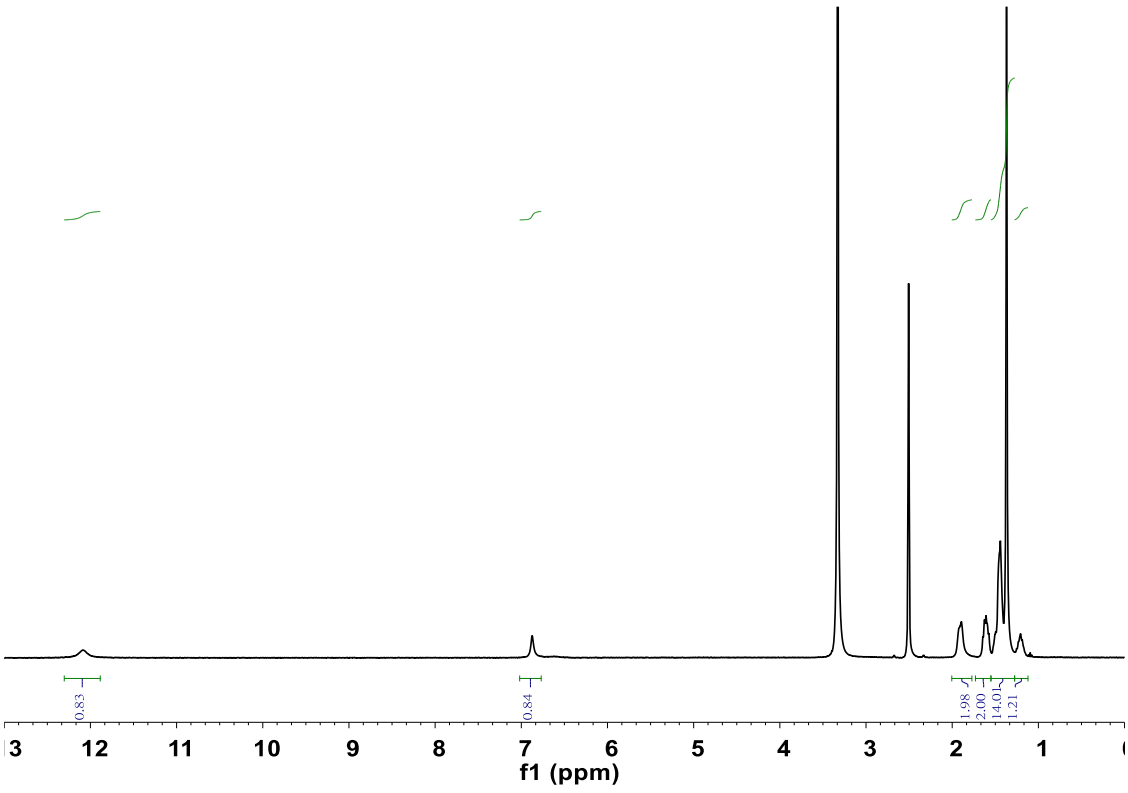

Figure S4-28. ^{1}HNMR spectrum of Boc-Ac$_6$c-OH.

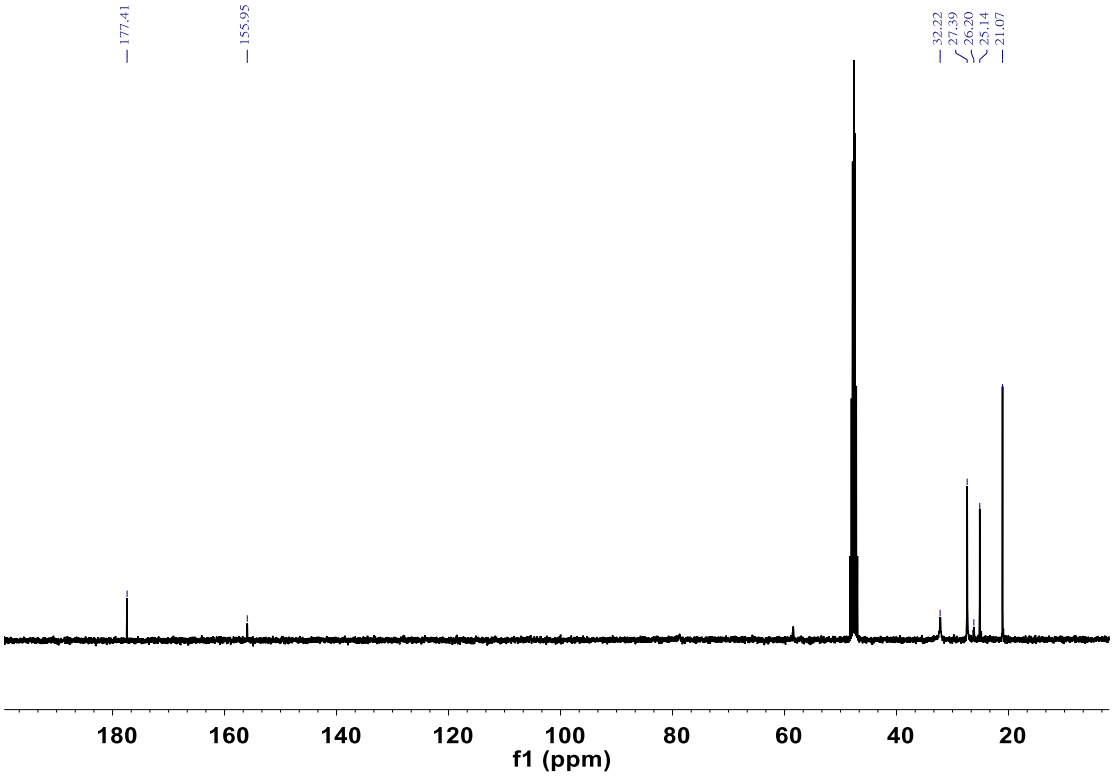

Figure S4-29. ^{13}CNMR spectrum of Boc-Ac$_6$c-OH.

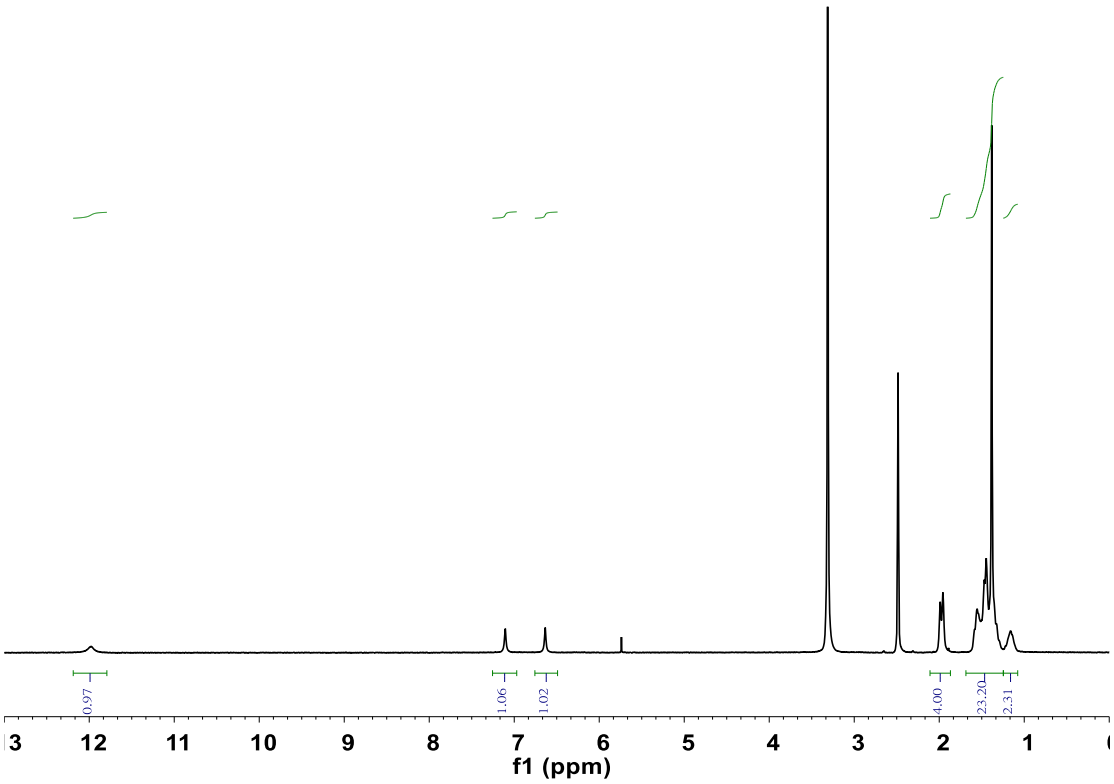

Figure S4-30. ^{1}HNMR spectrum of Boc-Ac$_6$c-Ac$_6$c-OH.

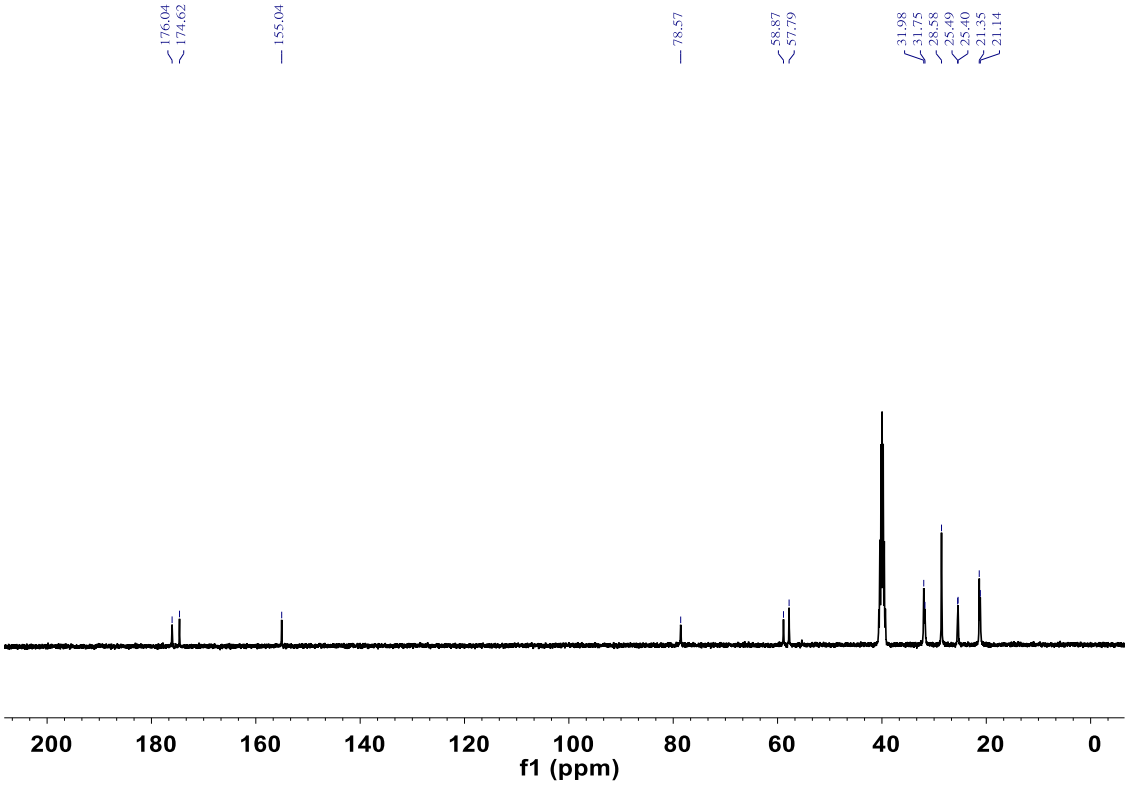

Figure S4-31. ^{13}CNMR spectrum of Boc-Ac$_6$c-Ac$_6$c-OH.

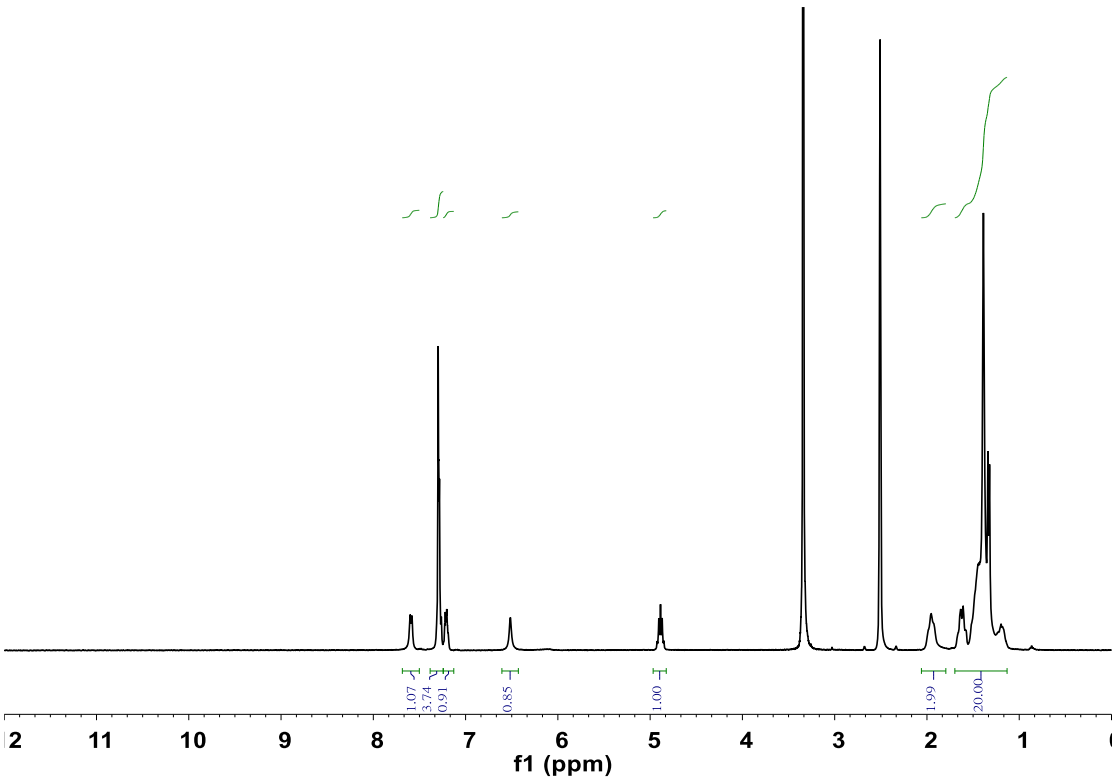

Figure S4-32. ^{1}HNMR spectrum of Boc-Ac$_6$c-rpy.

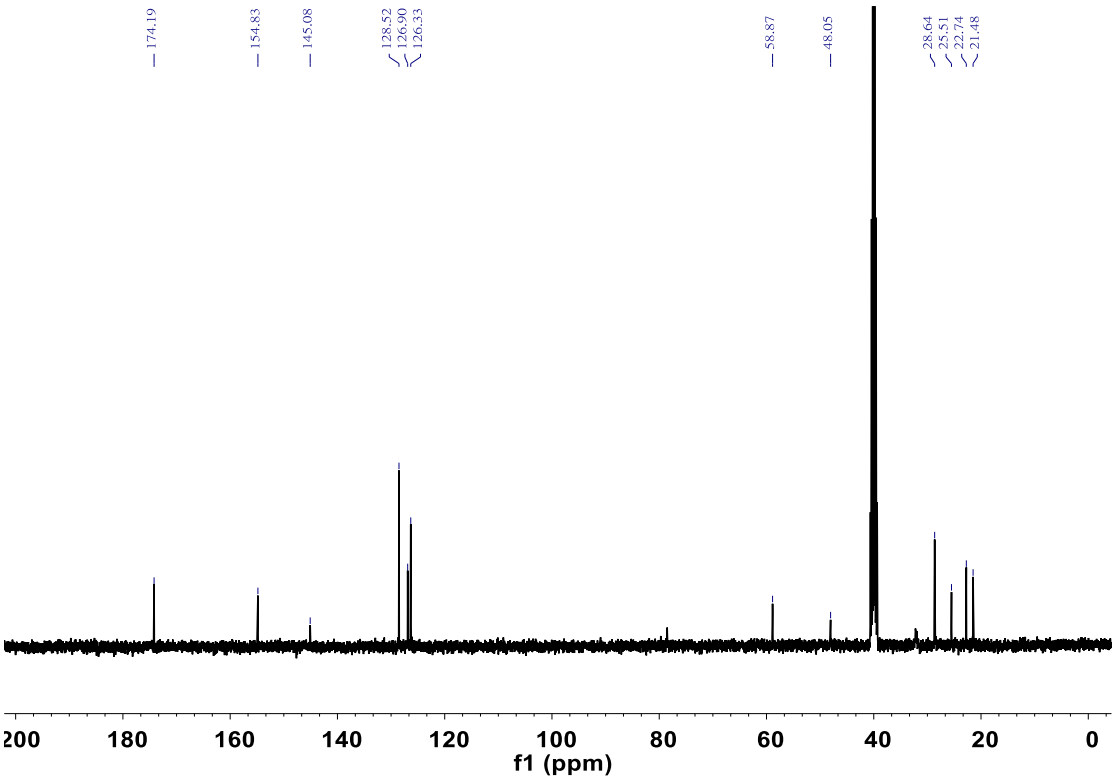

Figure S4-33. ^{13}CNMR spectrum of Boc-Ac$_6$c-rpy.

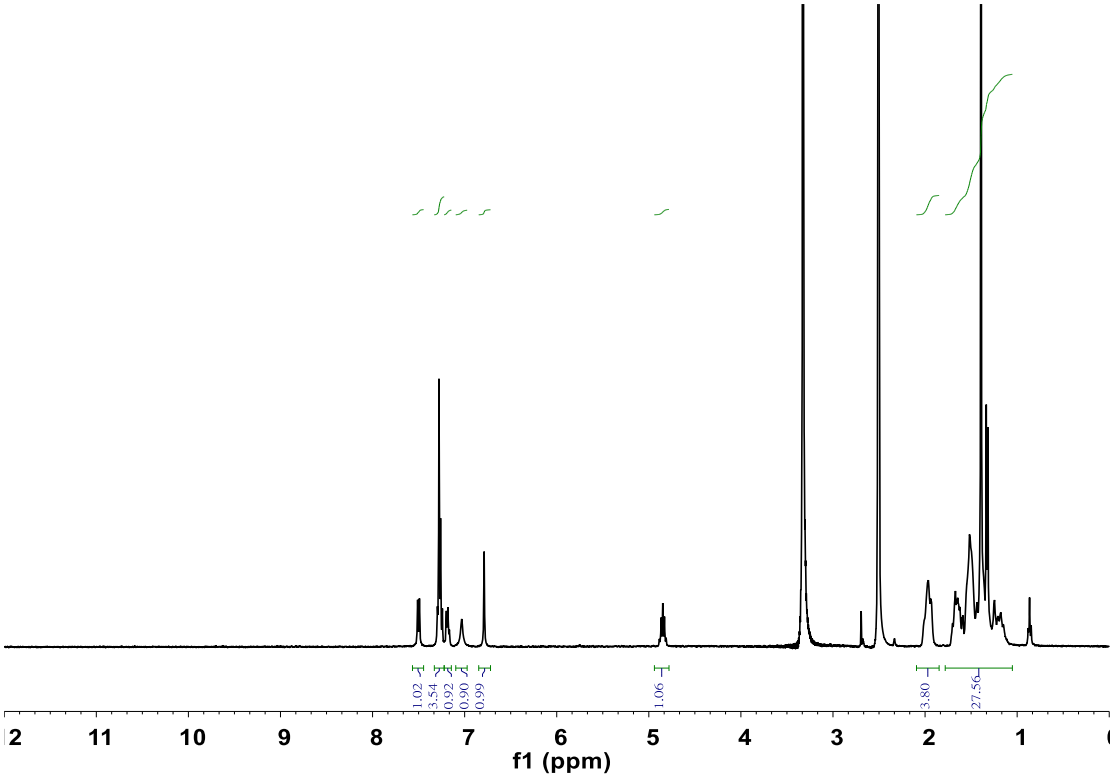

Figure S4-34. ^{13}CNMR spectrum of Boc-Ac$_6$c-Ac$_6$c-rpy.

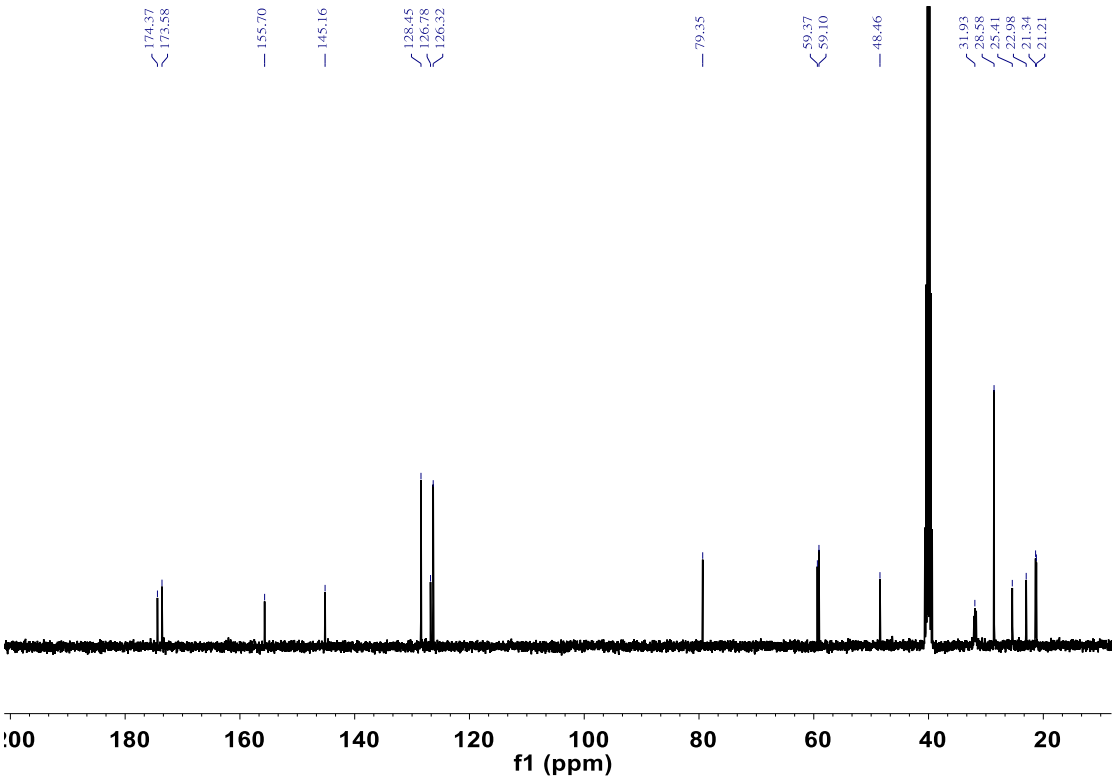

Figure S4-35. ^{13}CNMR spectrum of Boc-Ac$_6$c-Ac$_6$c-rpy.

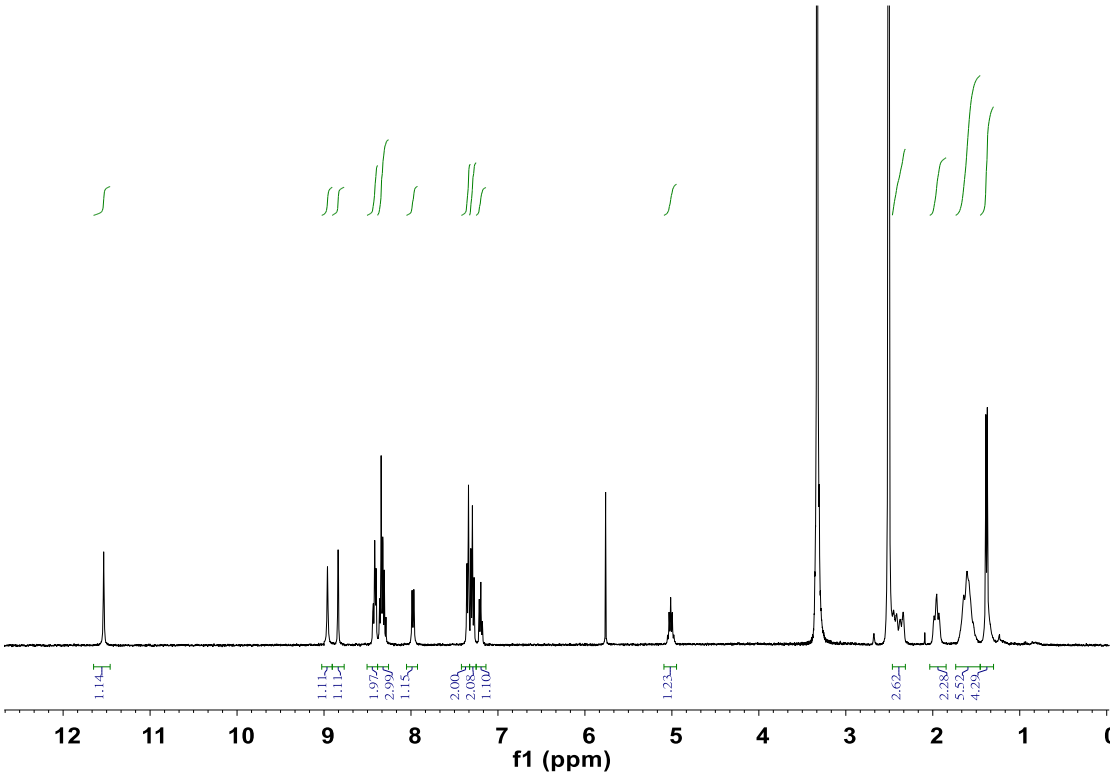

Figure S4-36. ^{1}HNMR of **L7**.

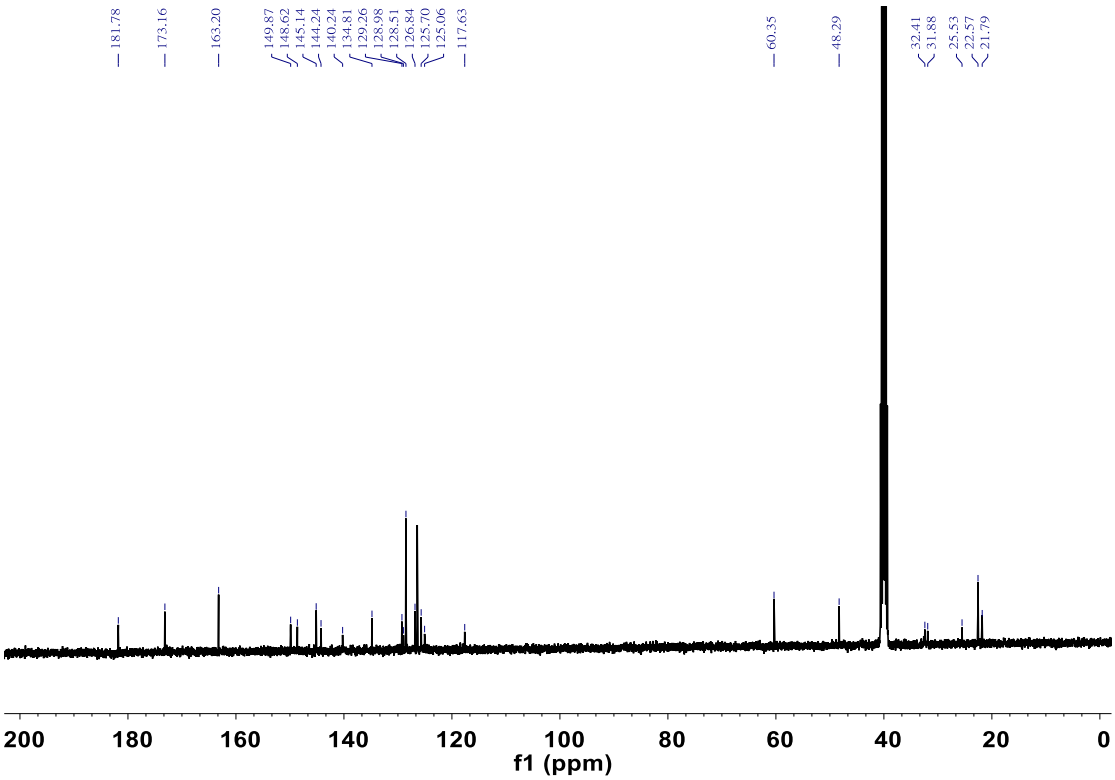

Figure S4-37. ^{13}CNMR of **L7**.

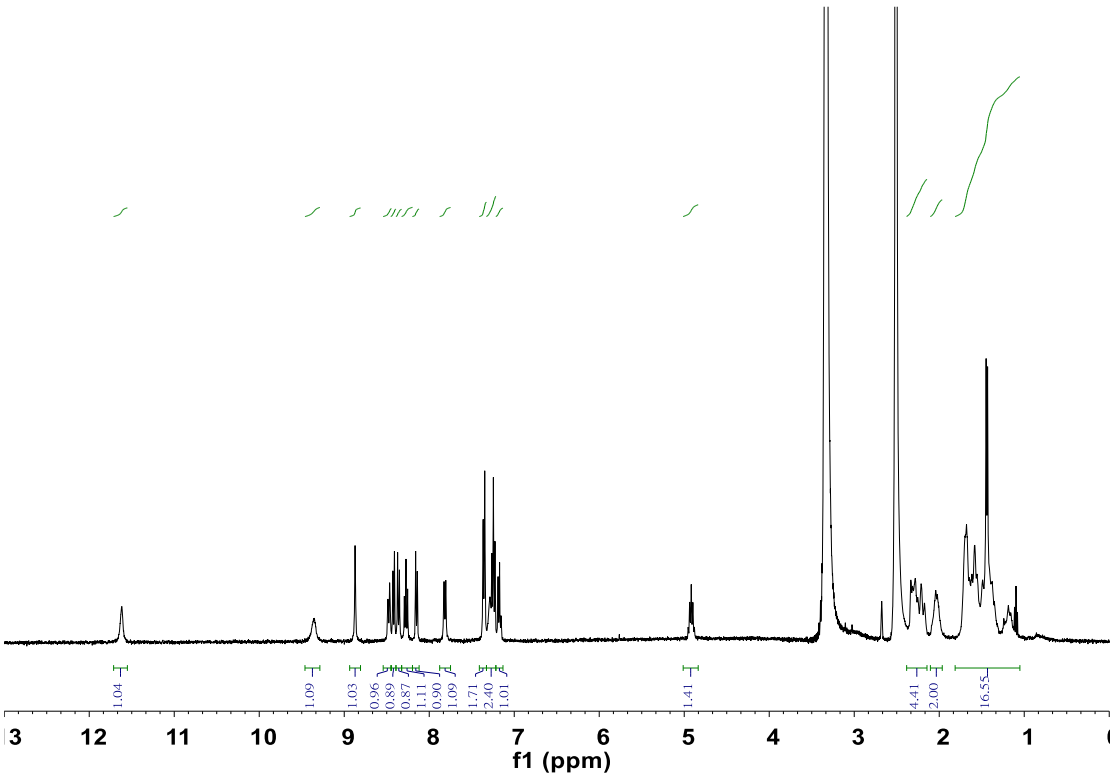

Figure S4-38. ^{1}HNMR of **L8**.

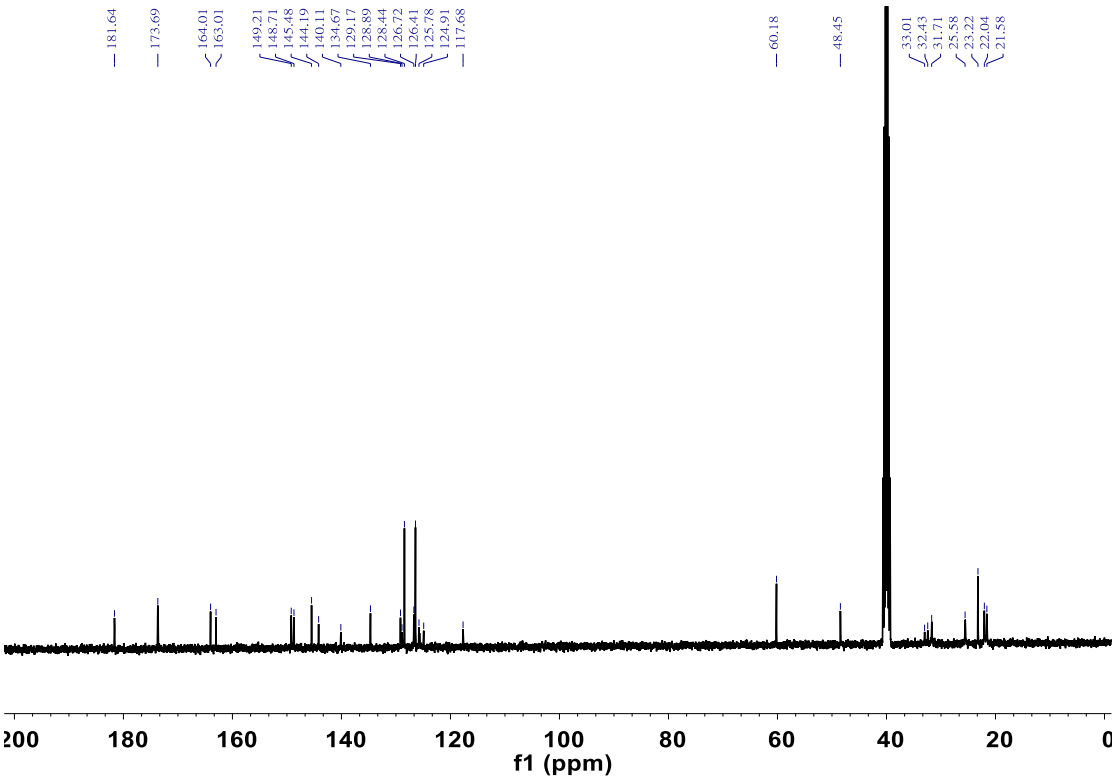

Figure S4-39. ^{13}CNMR of **L8**.

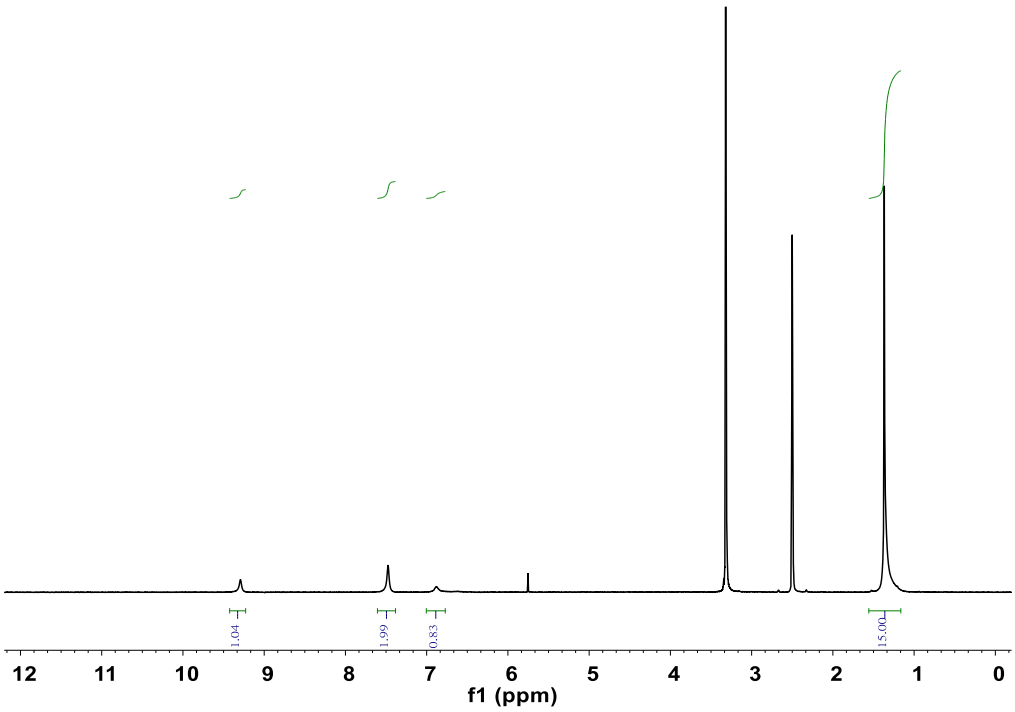

Figure S4-40. ^{1}HNMR spectrum of *di-tert*-butyl ((1,4-phenylenebis(azanediyl))bis(2-methyl-1-oxopropane-1,2-diyl))dicarbamate.

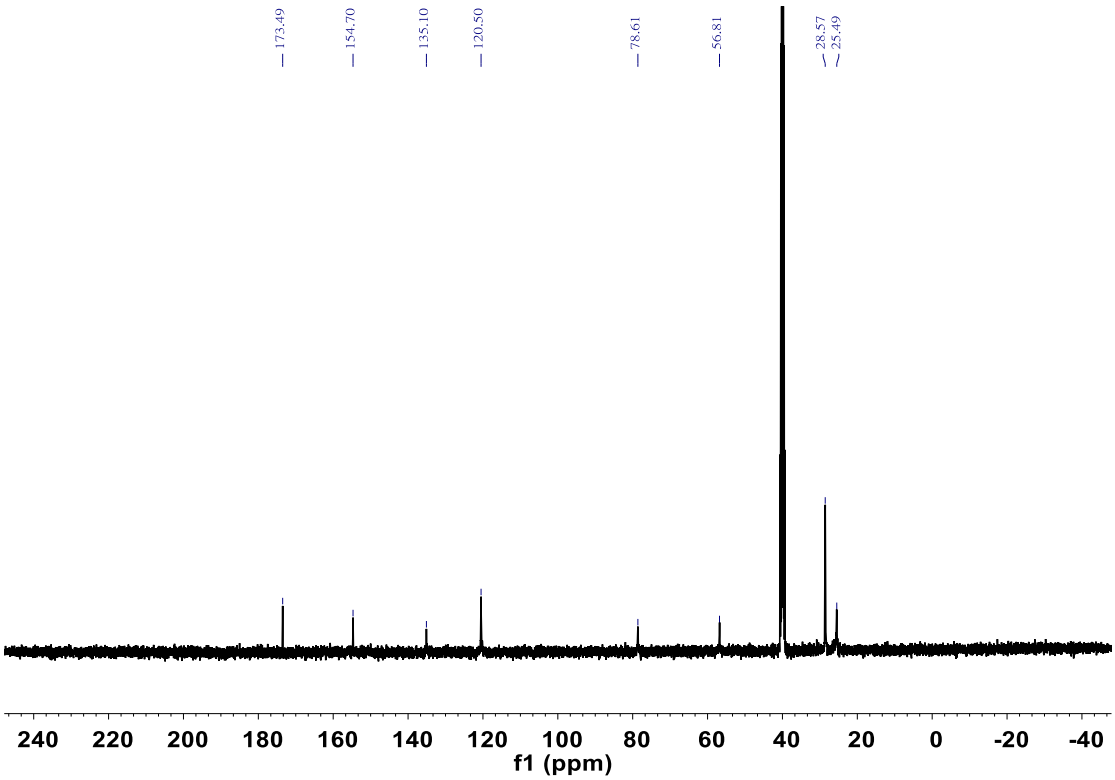

Figure S4-41. ^{13}CNMR spectrum of *di-tert*-butyl ((1,4-phenylenebis(azanediyl))bis(2-methyl-1-oxopropane-1,2-diyl))dicarbamate.

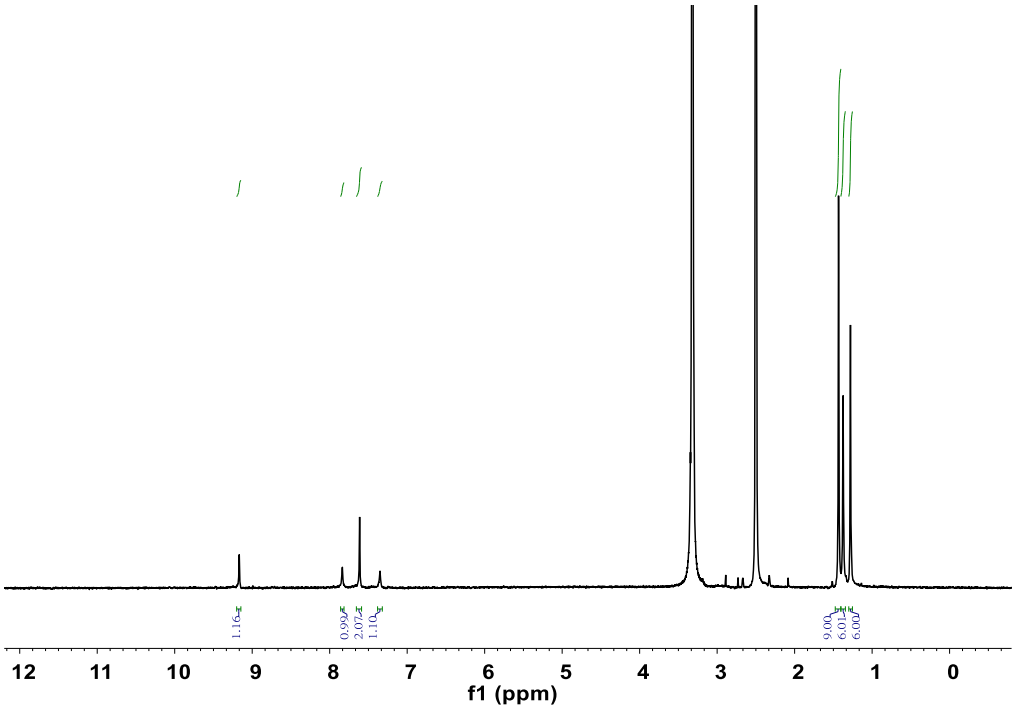

Figure S4-42. ^{1}HNMR spectrum of di-tert-butyl ((((1,4-phenylenebis(azanediyl))bis(2-methyl-1-oxopropane-1,2-diyl))bis(azanediyl))bis(2-methyl-1-oxopropane-1,2-diyl))dicarbamate.

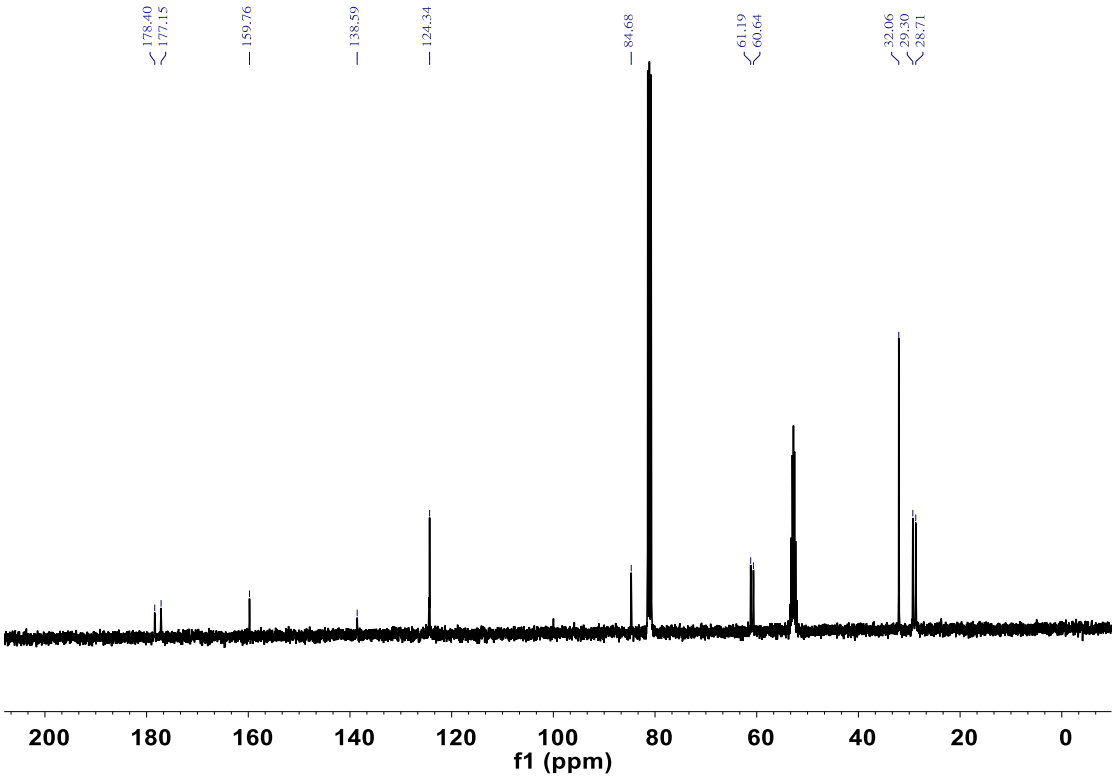

Figure S4-43. ^{13}CNMR spectrum of di-tert-butyl ((((1,4-phenylenebis(azanediyl))bis(2-methyl-1-oxopropane-1,2-diyl))bis(azanediyl))bis(2-methyl-1-oxopropane-1,2-diyl))dicarbamate.

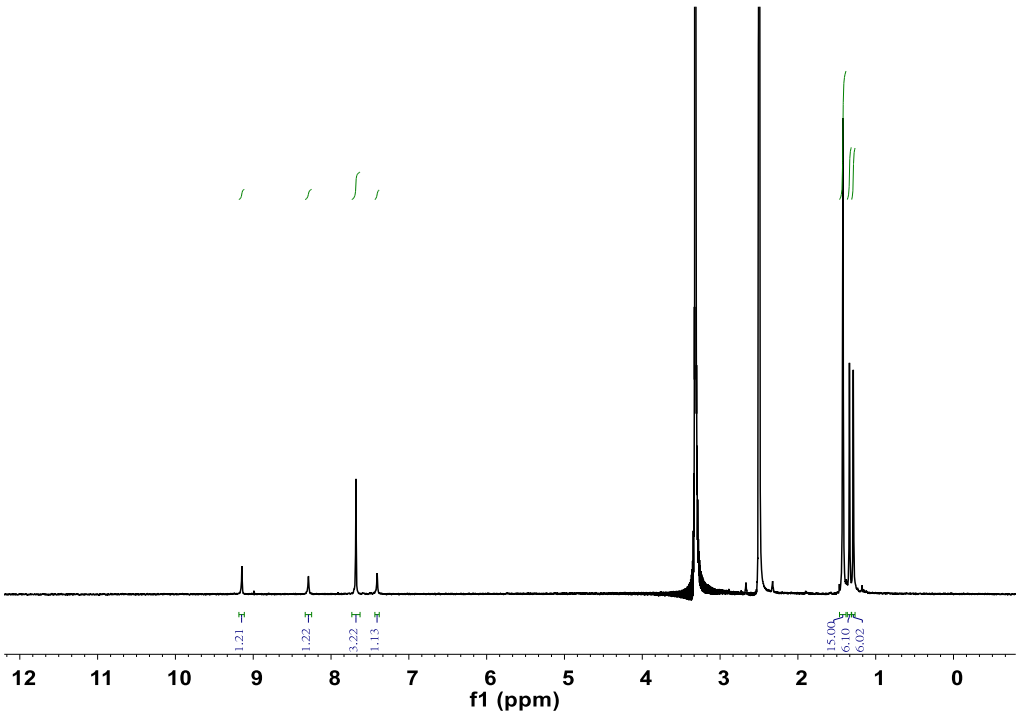

Figure S4-44. ^{1}HNMR spectrum of *Di-tert*-butyl ((((((1,4-phenylenebis(azanediyl))bis(2-methyl-1-oxopropane-1,2-diyl))bis(azanediyl))bis(2-methyl-1-oxopropane-1,2-diyl))bis(azanediyl))bis(2-methyl-1-oxopropane-1,2-diyl))dicarbamate.

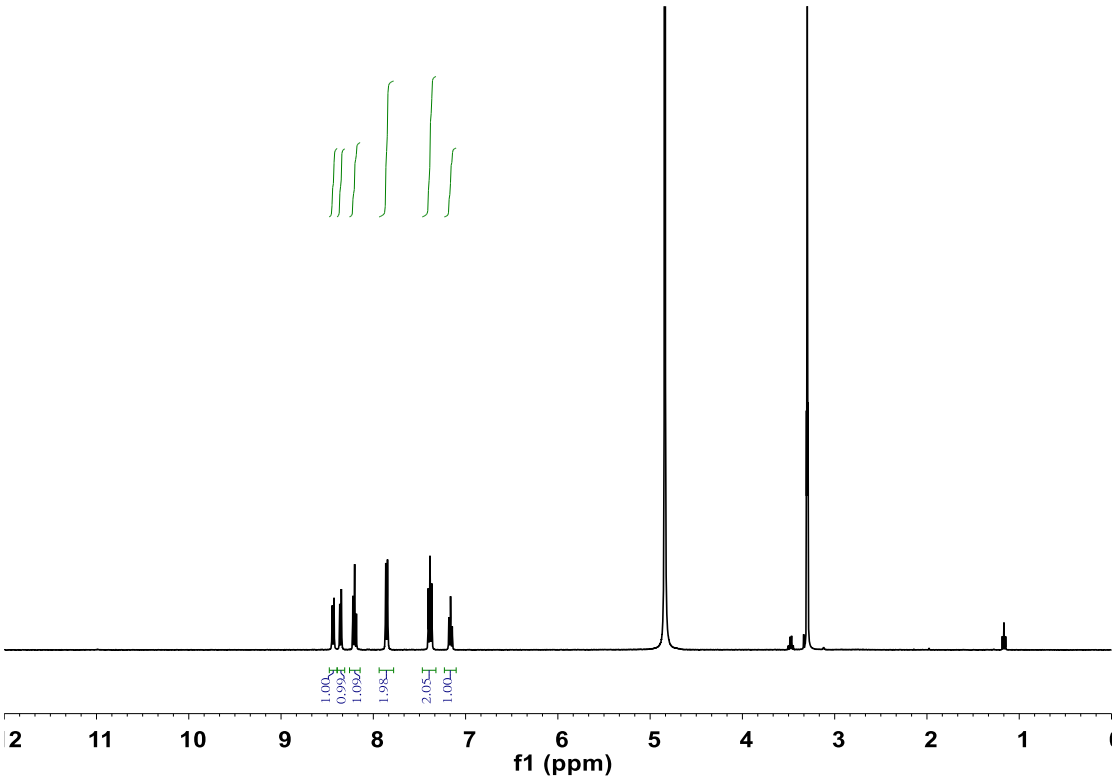

Figure S4-45. [1]HNMR spectrum of 6-(phenylcarbamoyl)picolinic acid.

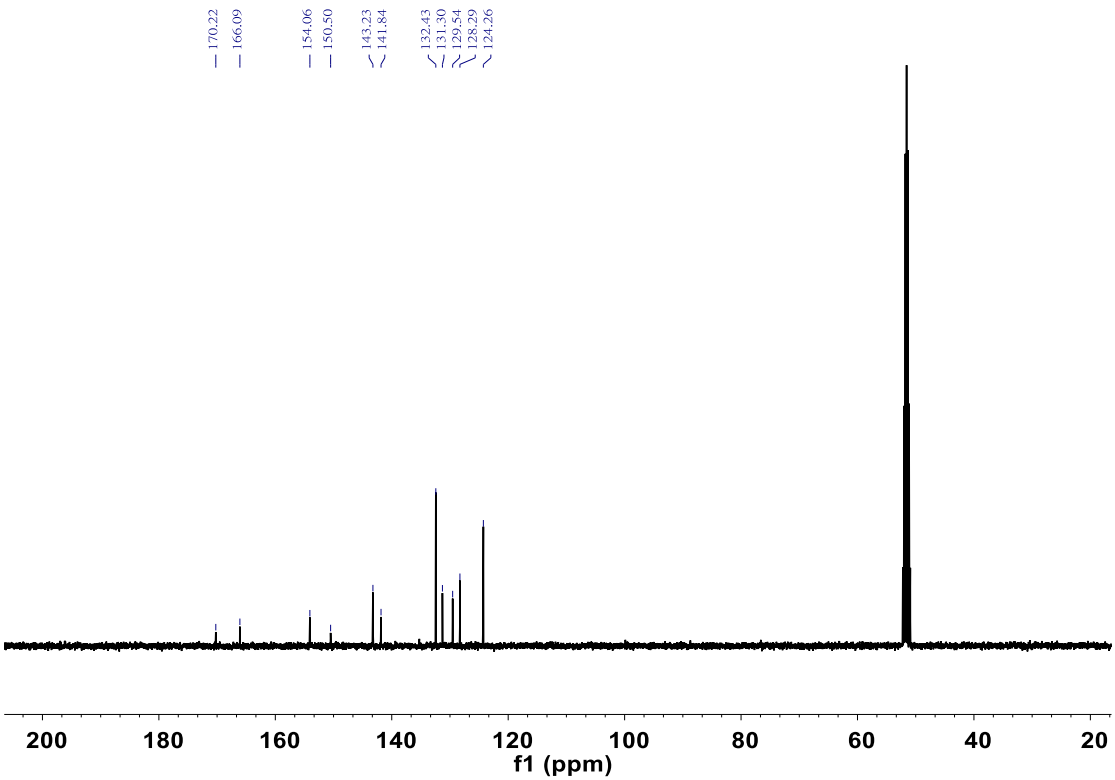

Figure S4-46. [13]CNMR spectrum of 6-(phenylcarbamoyl)picolinic acid.

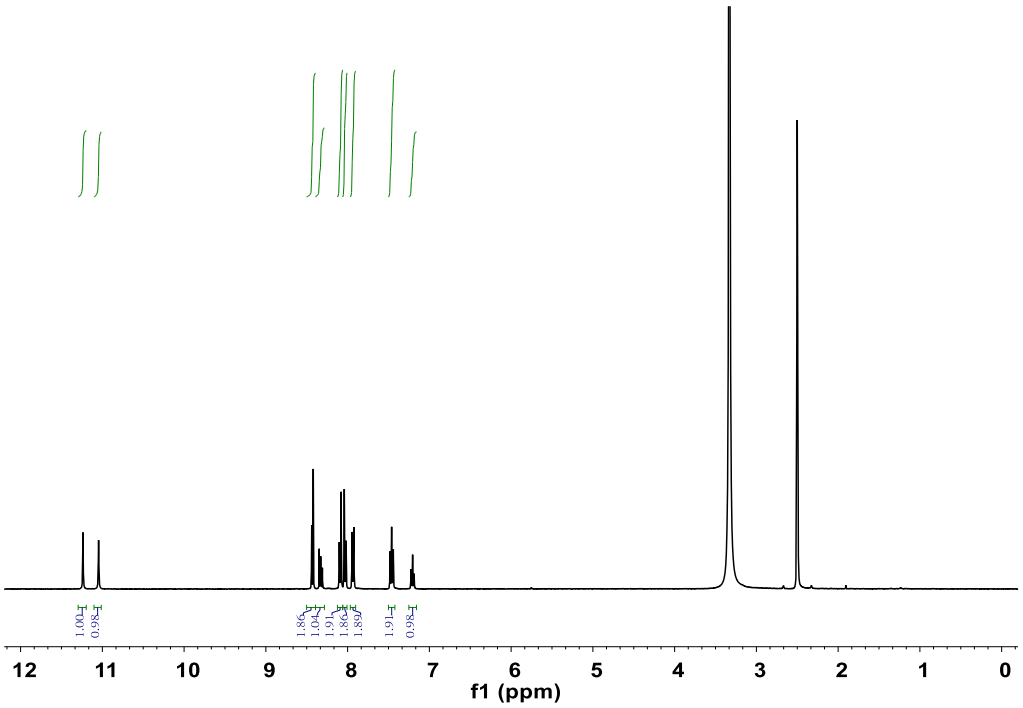

Figure S4-47. [1]HNMR spectrum of 4-(6-(phenylcarbamoyl)picolinamido)benzoic acid.

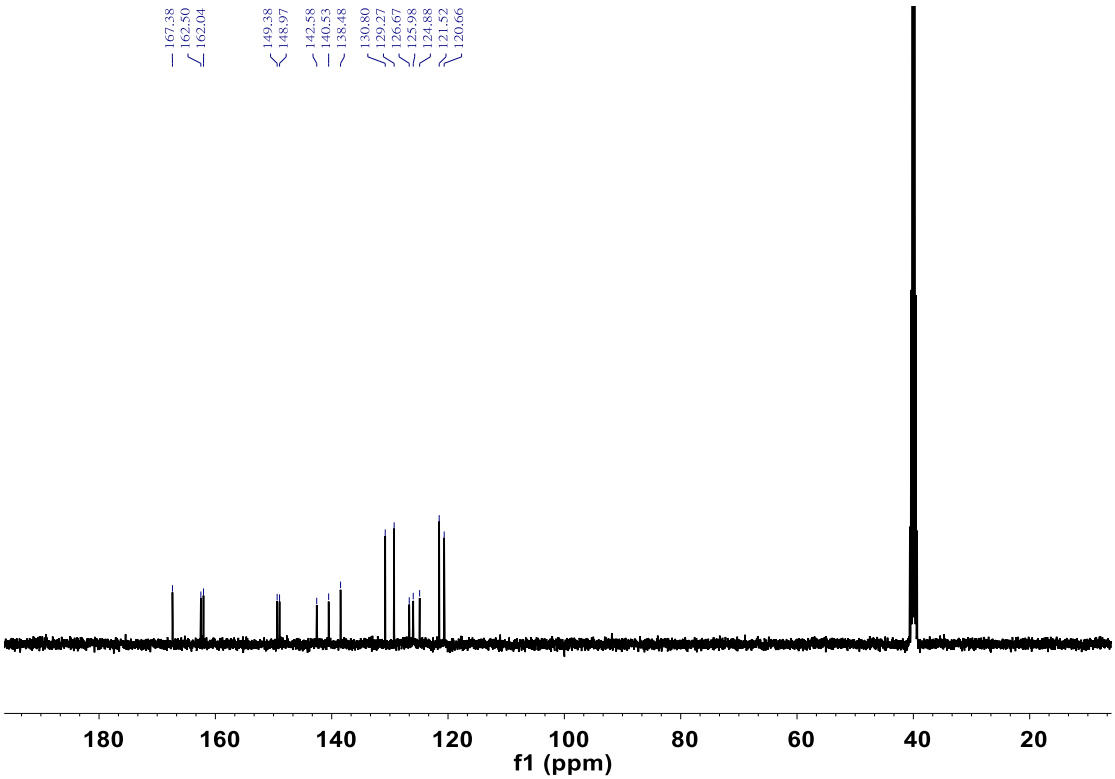

Figure S4-48. [1]HNMR spectrum of 4-(6-(phenylcarbamoyl)picolinamido)benzoic acid.

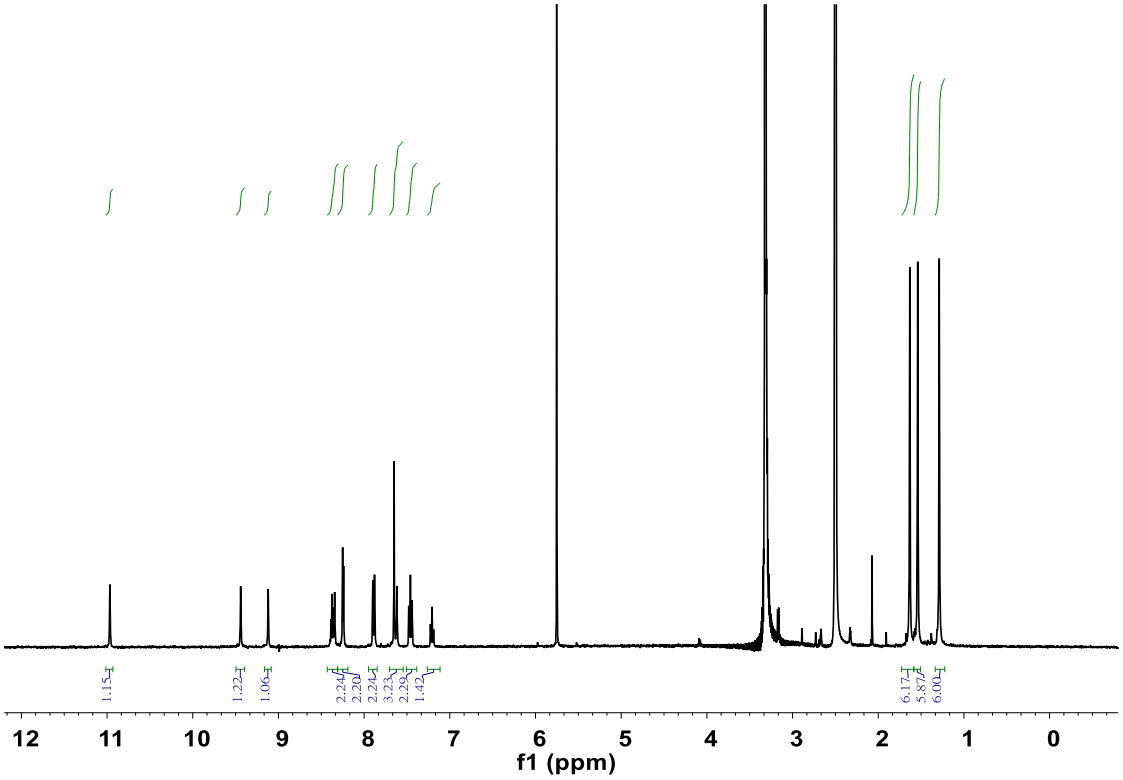

Figure S4-49. ^{1}HNMR spectrum of **L9**.

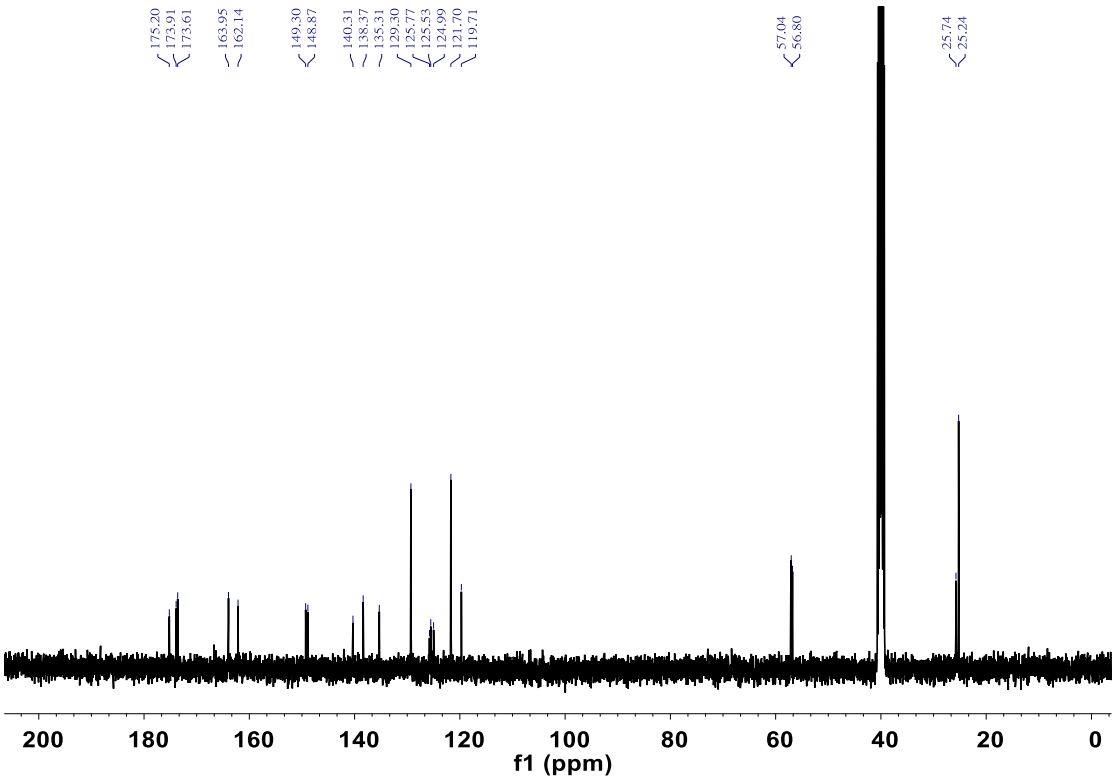

Figure S4-50. ^{13}CNMR spectrum of **L9**.

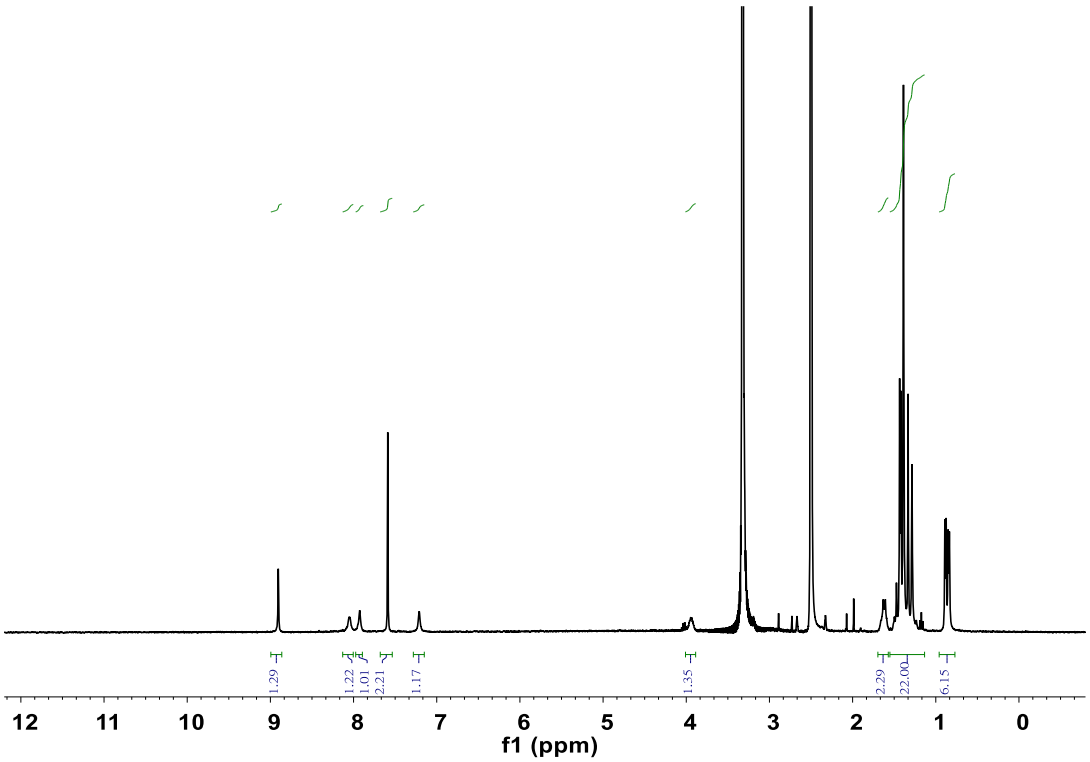

Figure S4-51. [1]HNMR spectrum of Di-*tert*-butyl ((2*S*,2'*S*)-(((1,4-phenylenebis(azanediyl))bis(2-methyl-1-oxopropane-1,2-diyl))bis(azanediyl))bis(4-methyl-1-oxopentane-1,2-diyl))dicarbamate.

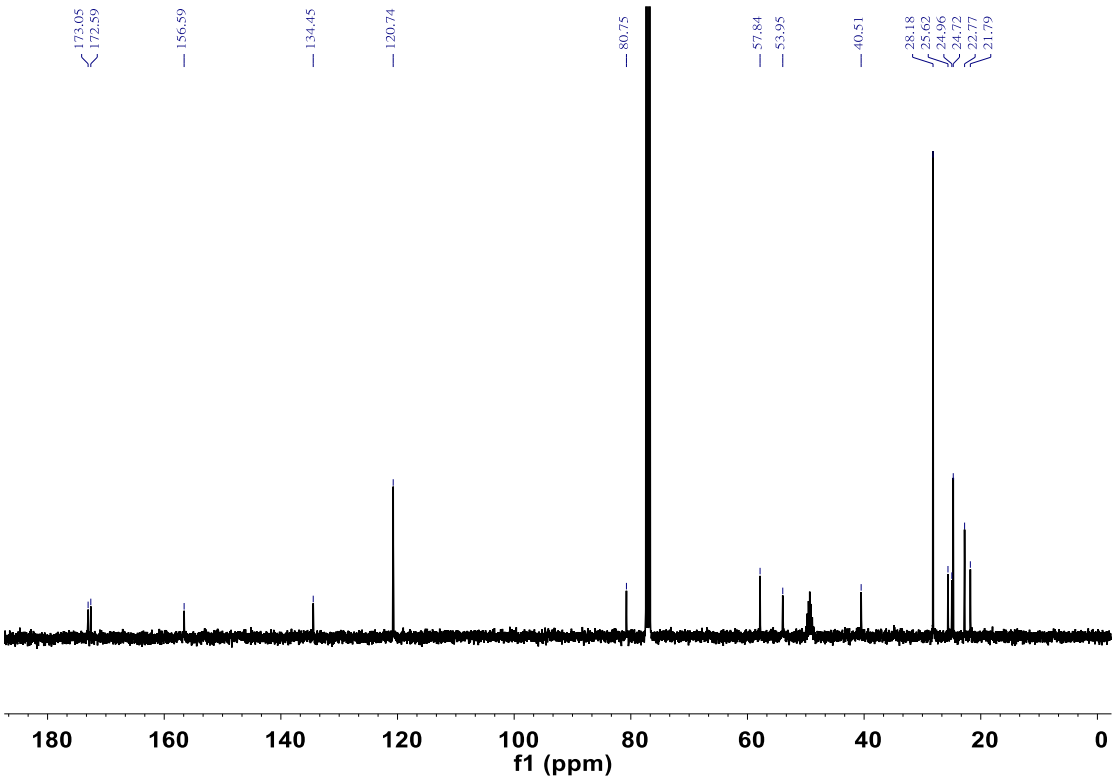

Figure S4-52. [13]CNMR spectrum of Di-*tert*-butyl ((2*S*,2'*S*)-(((1,4-phenylenebis(azanediyl))bis(2-methyl-1-oxopropane-1,2-diyl))bis(azanediyl))bis(4-methyl-1-oxopentane-1,2-diyl))dicarbamate.

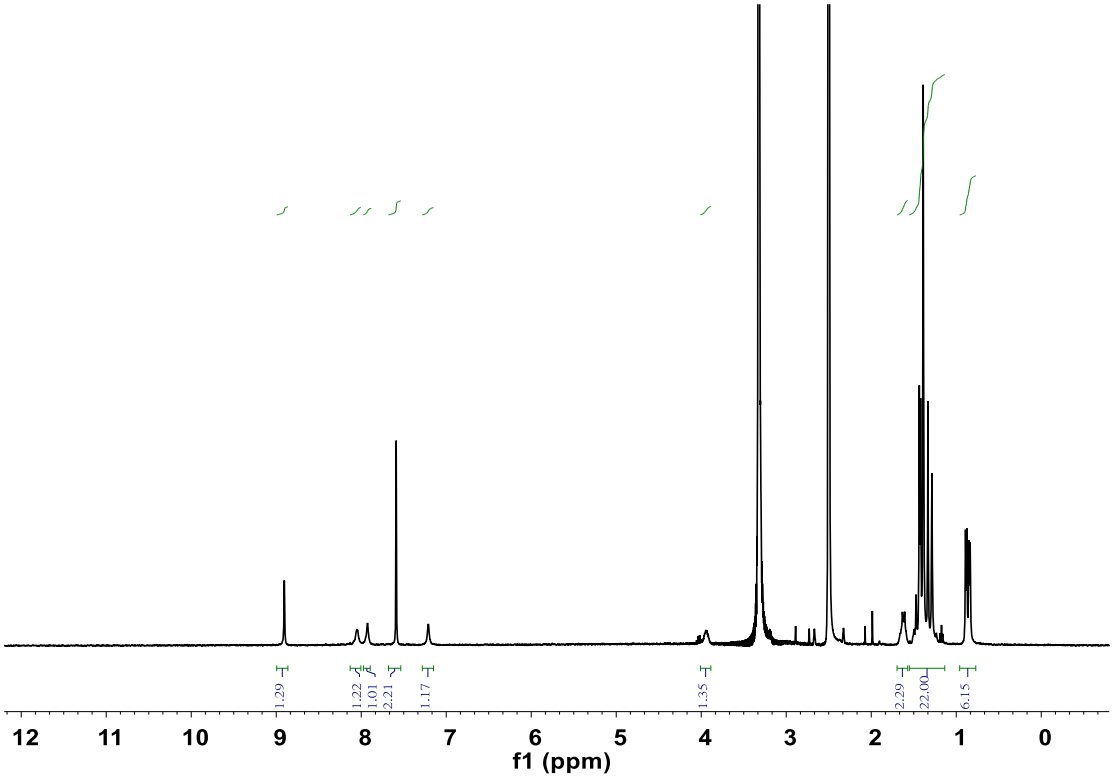

Figure S4-53. [1]HNMR spectrum of Di-tert-butyl ((((2S,2'S)-(((1,4-phenylenebis(azanediyl))bis(2-methyl-1-oxopropane-1,2-diyl))bis(azanediyl))bis(4-methyl-1-oxopentane-1,2-diyl))bis(azanediyl))bis(2-methyl-1-oxopropane-1,2-diyl))dicarbamate.

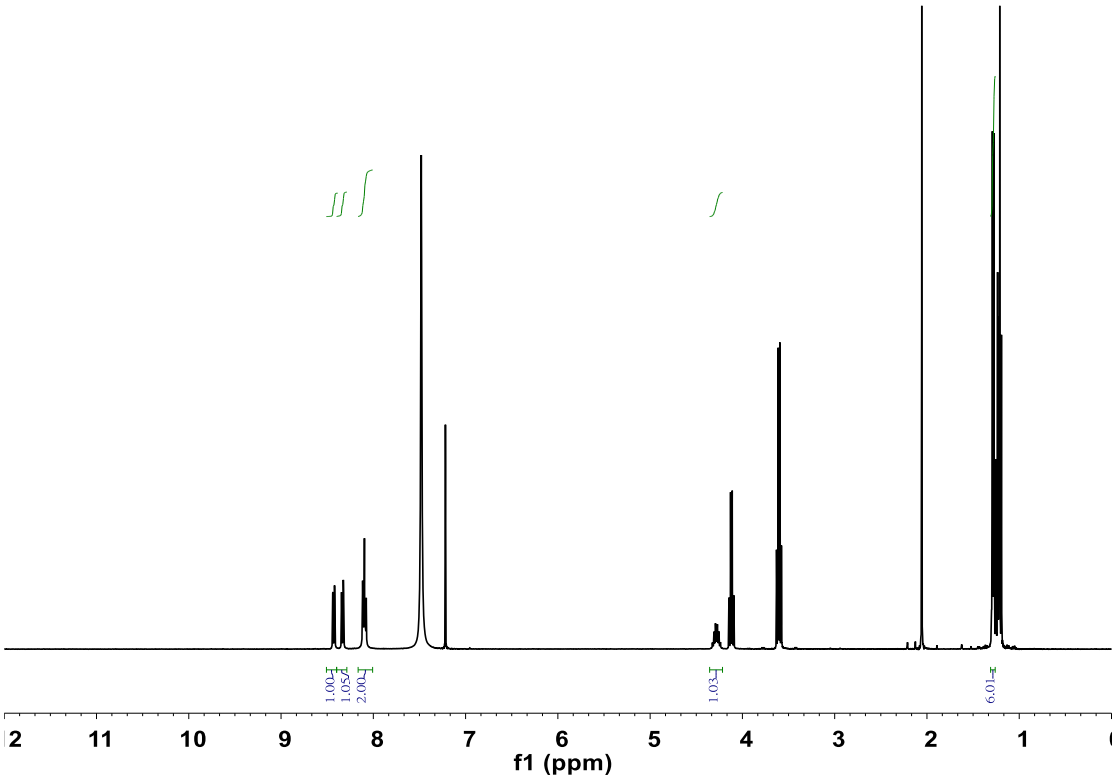

Figure S4-54. [1]HNMR spectrum of 6-(isopropylcarbamoyl)picolinic acid.

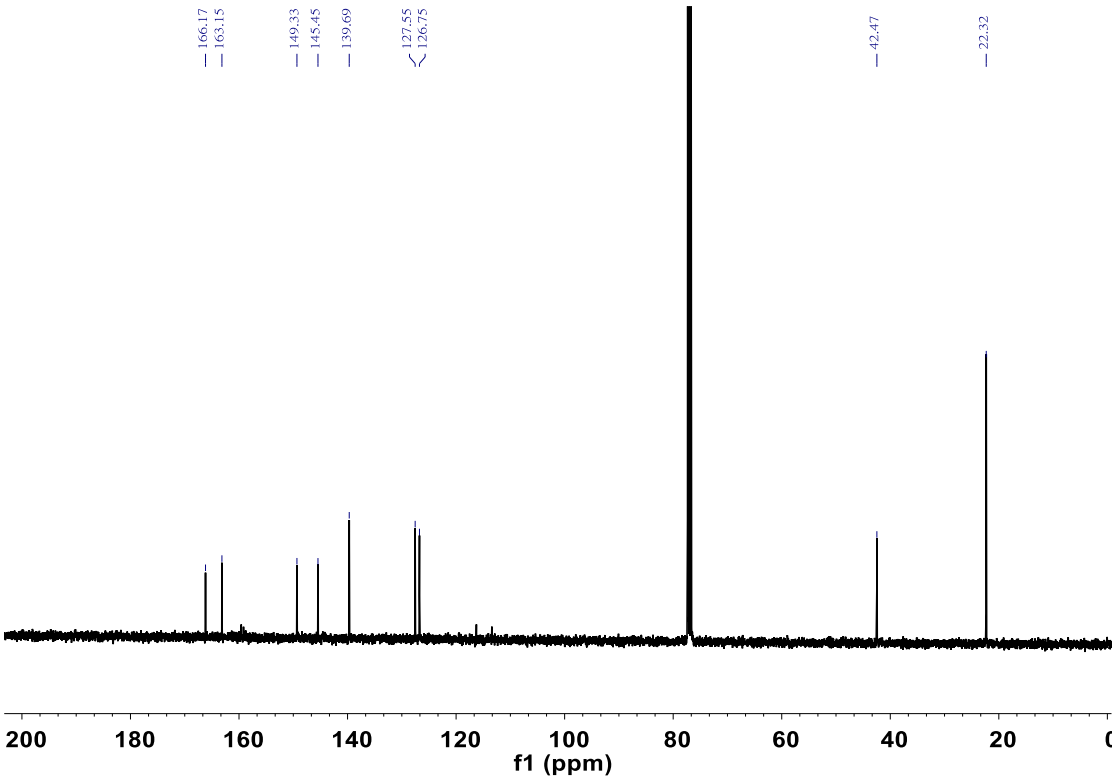

Figure S4-55. ^{13}CNMR spectrum of 6-(isopropylcarbamoyl)picolinic acid.

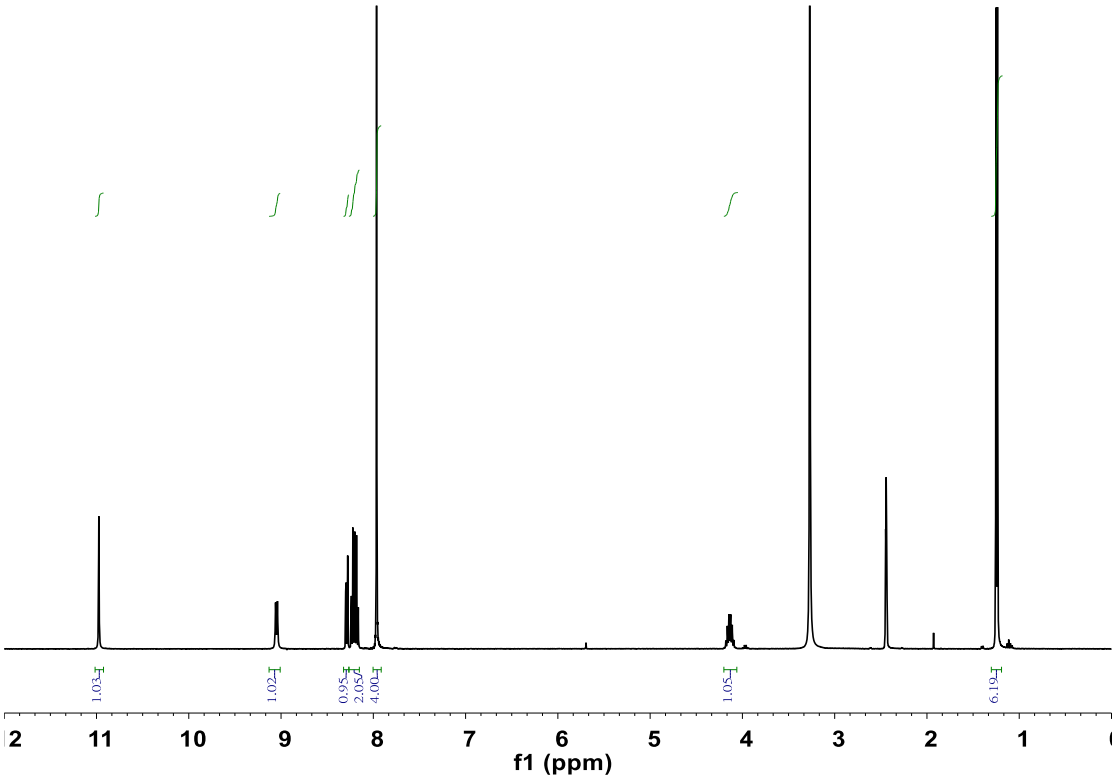

Figure S4-56. ^{1}HNMR spectrum of 4-(6-(isopropylcarbamoyl)picolinamido)benzoic acid

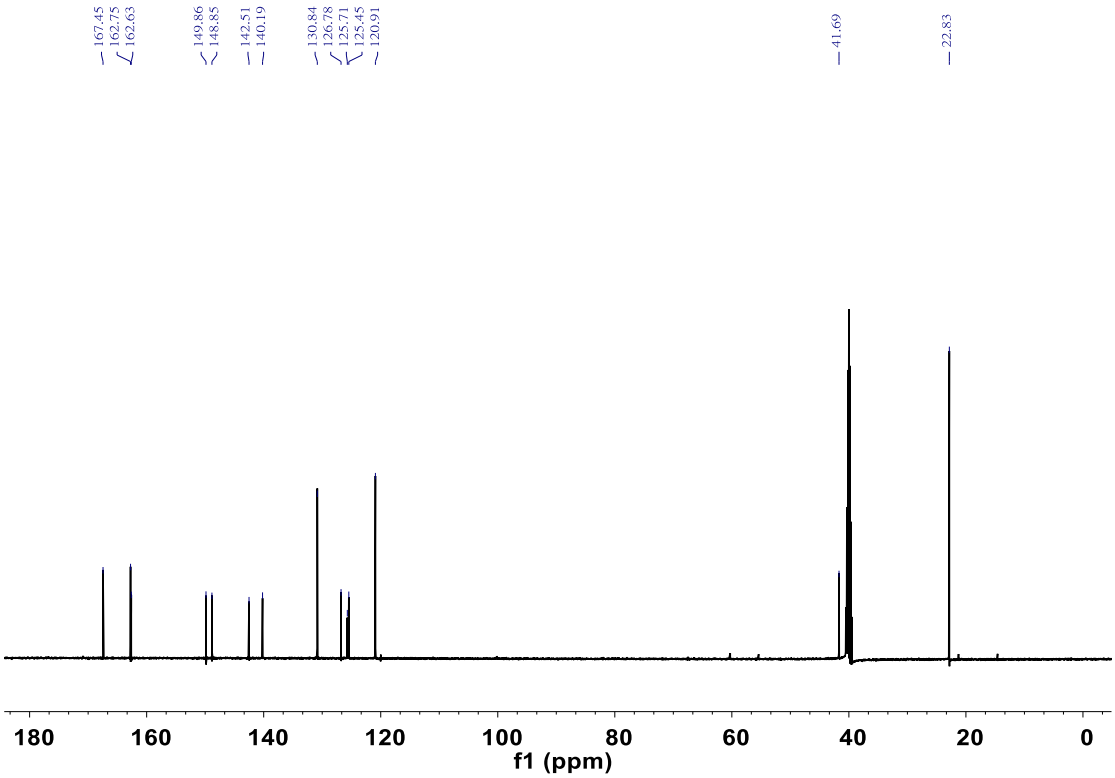

Figure S4-57. ^{13}CNMR spectrum of 4-(6-(isopropylcarbamoyl)picolinamido)benzoic acid

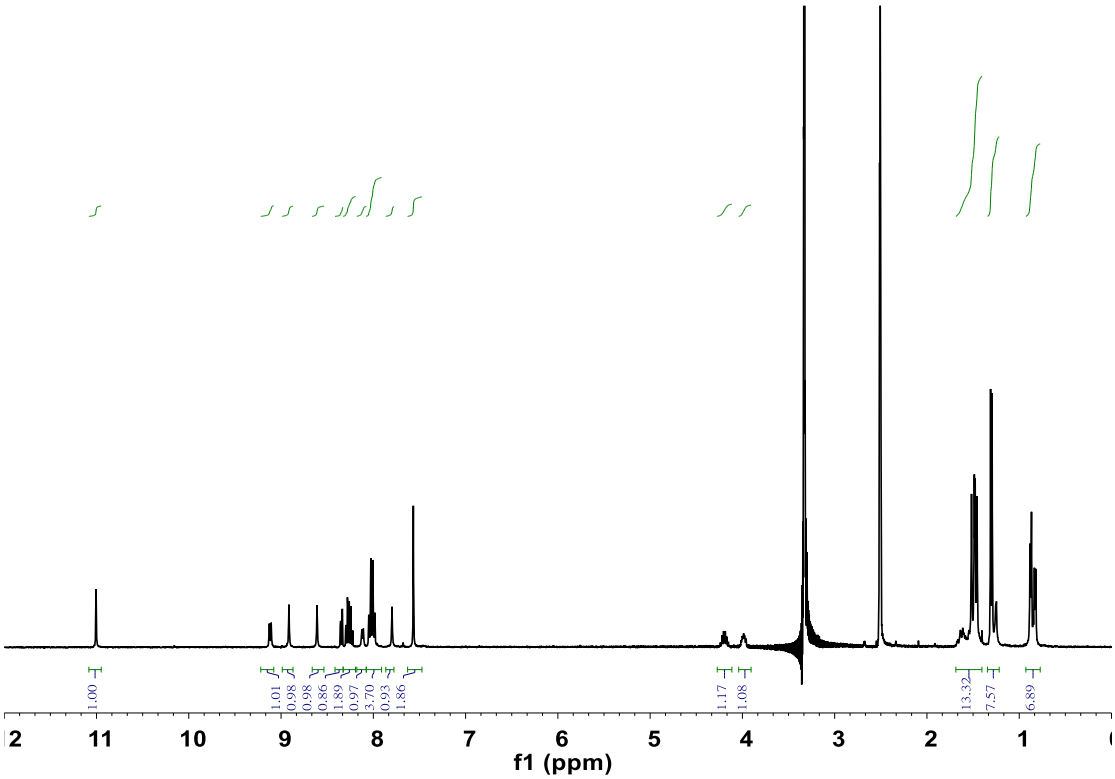

Figure S4-58. ^{1}HNMR spectrum of **L10**.

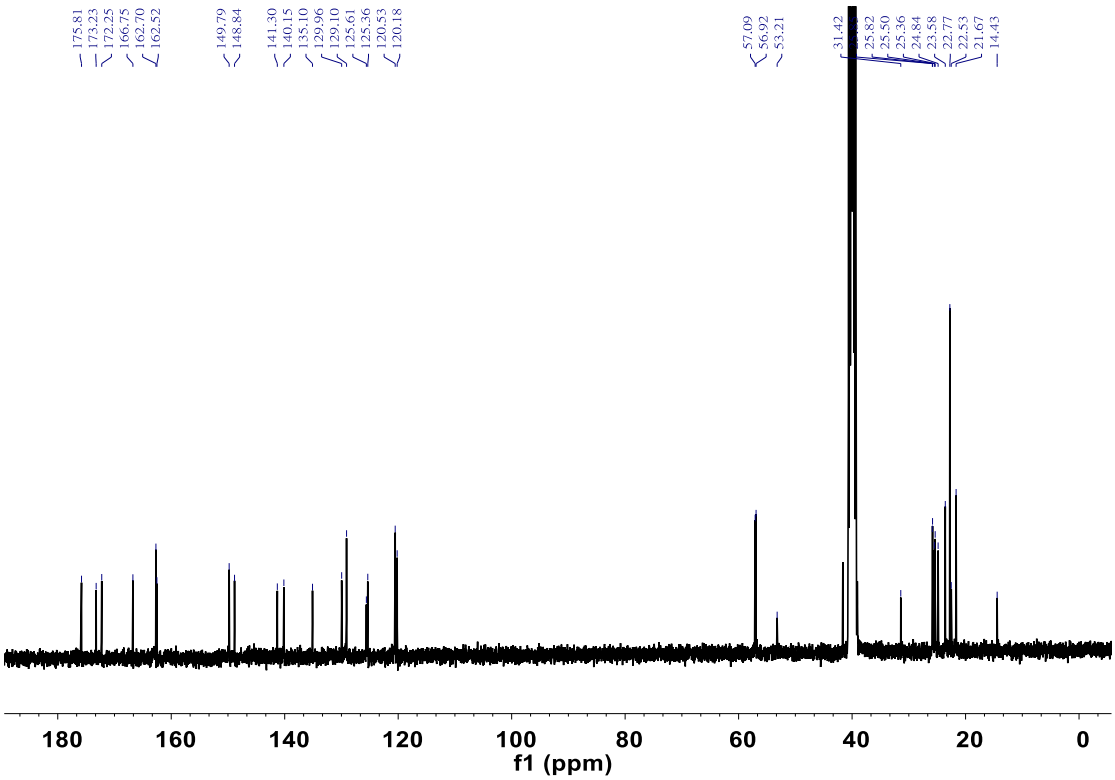

Figure S4-59. ^{13}CNMR spectrum of **L10**.